



Universidade do Minho
Escola de Engenharia

Tiago Daniel dos Santos Valente

Advanced tools for design and analysis of
fiber reinforced concrete structures

Advanced tools for design and analysis of fiber
reinforced concrete structures

Tiago Daniel dos Santos Valente

UMinho | 2019

May, 2019



FCT Fundação para a Ciência e a Tecnologia

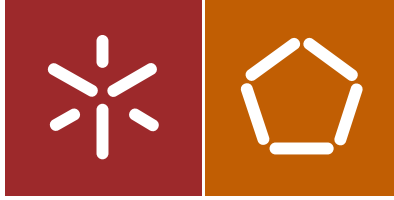
MINISTÉRIO DA CIÊNCIA, TECNOLOGIA E ENSINO SUPERIOR



GOVERNO DA REPÚBLICA
PORTUGUESA



UNIÃO EUROPEIA
Fundo Social Europeu



Universidade do Minho
Escola de Engenharia

Tiago Daniel dos Santos Valente

Advanced tools for design and analysis of
fiber reinforced concrete structures

Doctoral Thesis in Civil Engineering

Work performed under the supervision of
Professor Doctor Joaquim António Oliveira de Barros
Doctor Lúcio Abel Pereira Lourenço

May, 2019

DIREITOS DE AUTOR E CONDIÇÕES DE UTILIZAÇÃO DO TRABALHO POR TERCEIROS

Este é um trabalho académico que pode ser utilizado por terceiros desde que respeitadas as regras e boas práticas internacionalmente aceites, no que concerne aos direitos de autor e direitos conexos.

Assim, o presente trabalho pode ser utilizado nos termos previstos na licença abaixo indicada.

Caso o utilizador necessite de permissão para poder fazer um uso do trabalho em condições não previstas no licenciamento indicado, deverá contactar o autor, através do RepositóriUM da Universidade do Minho.

Licença concedida aos utilizadores deste trabalho



Atribuição
CC BY

<https://creativecommons.org/licenses/by/4.0/>

ACKNOWLEDGEMENTS

The present work was developed at the University of Minho under the supervision of Professor Joaquim António Oliveira de Barros and at CiviTest – Pesquisa de Novos Materiais para a Engenharia Civil, Lda. under the supervision of PhD Civil Engineer Lúcio Abel Pereira Lourenço.

I would like to express my deepest gratitude, support and advices to both my supervisors, Prof. Joaquim Barros and Lúcio Lourenço, that guided and motivated me at every step of the carried out work.

The financial support provided by the Portuguese Foundation for the Science and Technology (FCT, grant number SFRH/BDE/96381/2013) and CiviTest is gratefully appreciated.

I would also thank University of Minho, through the Institute for Sustainability and Innovation in Structural Engineering, the Department of Civil Engineering, and CiviTest for providing the facilities and resources to develop this project.

My special gratitude to Prof. Miguel Azenha and Patrícia Silva for their contribution in the work related to the creep of cement based materials, and to Prof. António Gouveia for his support and phenomenal assistance in the implementation of new functionalities in *FEMIX*.

I also want to thank the support and friendship provided by the CiviTest collaborators, particularly to Mr. Manuel Lopes, Delfina Gonçalves, Inês Costa and Inaldo Vasconcelos.

Finally, my gratitude to all my friends and family, particularly to my parents and life mate Delfina, for their love and support that helped and driven me throughout my life.

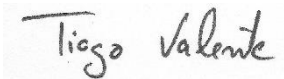
STATEMENT OF INTEGRITY

I hereby declare having conducted this academic work with integrity. I confirm that I have not used plagiarism or any form of undue use of information or falsification of results along the process leading to its elaboration.

I further declare that I have fully acknowledged the Code of Ethical Conduct of the University of Minho.

University of Minho, May 2019

Name: Tiago Daniel dos Santos Valente

Signature: 

RESUMO

A presente tese foca-se no desenvolvimento de ferramentas numéricas para a análise e dimensionamento de elementos estruturais em betão reforçado com fibras (BRF).

Neste trabalho são abordadas as mais recentes regras e recomendações de projeto expostas nos regulamentos em vigor sendo, quando necessário, complementadas com modelos mais avançados resultantes de trabalhos de investigação sobre estruturas de BRF. Com base nas atuais regras de projeto foi desenvolvido um programa de cálculo automático dedicado à análise da secção transversal de elementos estruturais de BRF, com e sem armaduras convencionais de reforço, sujeitos a esforços axial, corte e flexão, de forma a realizar as verificações de segurança relativamente aos estados limite últimos e de serviço.

Foi realizada, também, uma avaliação do desempenho dos modelos de resistência ao corte propostos no fib Model Code 2010 para elementos em BRF, através da comparação da capacidade preditiva dos modelos com os resultados experimentais de uma base de dados de ensaios de corte.

A presente tese abrange, do mesmo modo, o desenvolvimento de uma ferramenta numérica para a análise de elementos estruturais de BRF que conjuga o efeito da orientação e segregação das fibras nos elementos estruturais de BRF, e a resistência ao arranque das fibras. A capacidade preditiva do novo modelo foi verificada através da simulação de vigas entalhadas de betão reforçado com fibras de aço submetidas ao ensaio de flexão de 3-pontos.

Adicionalmente, foram abordados alguns aspetos particulares de elementos estruturais em BRF. Neste âmbito, um novo modelo de simulação da resposta viscoelástica em fluência de materiais de matriz cimentícia, desde as idades jovens, foi desenvolvido e implementado num programa baseado no método de elementos finitos – *FEMIX* – tendo sido acoplado aos modelos termo-mecânicos já aí implementados. Adicionalmente, foi desenvolvido um novo modelo constitutivo especialmente dedicado à simulação da interface entre lajes de BRF apoiadas no solo e as camadas granulares da fundação da laje, com o intuito de captar os mecanismos relevantes que induzem dano neste tipo de estruturas de BRF.

Palavras chave: Betão reforçado com fibras; projeto; simulação numérica; modelos constitutivos; programa de cálculo.

ABSTRACT

This thesis is devoted to the development of numerical tools for the analysis and design of fiber reinforced concrete (FRC) structural elements.

This work focuses on the description of the most recent design guidelines and recommendations obtained from design codes, being complemented with more advanced models published in academic works on FRC structures. Based on these guidelines a software was developed for the analysis of FRC cross-sections with and without conventional reinforcements, submitted to bending and shear with or without axial force, to assess the ultimate and serviceability limit state safety verifications of structural members.

An assessment of the shear resistance models for FRC members proposed in the fib Model Code 2010 was conducted, by evaluating its predictive performance with the results of shear tests collected in a database.

It was developed an innovative numerical tool for the analysis of FRC structures that couples the effects of fiber orientation and segregation in the FRC members, and fiber pullout resistance. The performance of the new model was assessed by simulating steel fiber reinforced concrete notched beams submitted to 3-point bending tests.

Moreover, particular topics regarding some structural application of FRC were explored. In this scope, a new model capable of predicting the aging creep response of cement-based materials, since early ages, was proposed and implemented in a finite element method software – *FEMIX* – and was coupled with the already available thermo-mechanical models.

Flooring is still the main application of FRC, and the simulation of the interface between the FRC slab and the soil supporting system is a relevant aspect for controlling crack formation and propagation, mainly due to shrinkage and thermal effects coupled with restriction to the membrane deformability of the FRC slab. A new constitutive model was developed and implemented in *FEMIX*, especially aimed to simulate the interface between FRC slabs supported on ground and the granular layers of the slab's foundation, in attempt to capture relevant mechanisms that promote damage in this type of FRC structures.

Keywords: Fiber reinforced concrete; design; numerical simulation; constitutive models; software.

TABLE OF CONTENTS

Acknowledgements.....	iii
Resumo.....	v
Abstract.....	vi
Table of Contents	vii
List of Abbreviations and Symbols.....	x
List of Figures.....	xvii
List of Tables.....	xxv
Introduction.....	1
1.1 Research significance	2
1.2 Objectives.....	3
1.3 Thesis outline	4
2 Design of fiber reinforced concrete structural elements.....	5
2.1 Introduction.....	5
2.2 Material characterization and classification	5
2.3 Constitutive laws for ULS and SLS.....	10
2.3.1 Concrete in compression	10
2.3.2 Steel in tension or compression.....	13
2.3.3 FRC in tension	14
2.4 FRC design particularities.....	22
2.5 ULS and SLS analysis of FRC structural members	25
2.5.1 Members in bending.....	25
2.5.2 Members in shear.....	27
2.5.3 Punching.....	39
2.5.4 Stress limitation	45
2.5.5 Crack control	47
2.6 Concluding remarks.....	56
3 Software for design of fiber reinforced concrete elements	58
3.1 Introduction.....	58
3.2 Plain section analysis of cross-sections.....	58
3.3 Main user interface window.....	60
3.4 Software algorithm/flowcharts.....	63
3.4.1 Data input.....	64
3.4.2 Calculation routine	68
3.4.3 Results Output.....	69

3.5 Examples.....	69
3.5.1 Example 1 – Beam	70
3.5.2 Example 2 – Slab.....	73
3.6 Concluding remarks.....	77
4 Appraisal of MC2010 shear resistance prediction models.....	78
4.1 FRC beams shear tests database	78
4.2 Residual flexural strength prediction model.....	81
4.3 Appraisal of MC2010 shear resistance prediction models.....	83
4.4 Concluding remarks.....	89
5 Analysis of FRC members considering fiber orientation, fiber segregation and fiber pullout resistance model.....	90
5.1 Introduction.....	90
5.2 New material model for FRC in tension.....	90
5.2.1 Fiber orientation profile model.....	91
5.2.2 Fiber segregation model.....	95
5.2.3 Fiber pullout constitutive model.....	96
5.2.4 Influence of the model parameters on the moment-rotation of SFRC members failing in bending.....	104
5.2.5 Assessment of the predictive performance of the new model	112
5.3 Moment-rotation procedure for analysis of cross-sections.....	125
5.3.1 Numerical simulation of FRC structural members	127
5.4 Concluding remarks.....	134
6 Creep of Cement Based Materials	136
6.1 Introduction.....	136
6.2 Time-dependent deformation.....	136
6.3 Creep fundamentals	137
6.4 Creep mechanisms and influencing factors in CBM	145
6.5 Creep compliance prediction models.....	149
6.5.1 Existing models.....	152
6.5.1.1 Double Power Law	153
6.5.1.2 Eurocode 2.....	156
6.5.1.3 Model Code 2010.....	158
6.5.1.4 B3 model.....	161
6.5.1.5 B4 model.....	164
6.5.2 Proposed model.....	167
6.6 Numerical implementation for structural analysis.....	171

6.7 Coupling of creep and thermo-mechanical models.....	177
6.8 Implementation of ACC model in FEMIX	180
6.8.1 Numerical examples	182
6.8.1.1 Concrete sample under compressive creep test.....	182
6.8.1.2 Reinforced concrete beam under flexure creep test.....	184
6.9 Concluding remarks.....	192
7 Implementation of a cyclic-hysteretic constitutive model for simulating the contact between different materials	193
7.1 Numerical implementation	193
7.2 Numerical example.....	207
7.2.1 Load combinations - set A.....	209
7.2.2 Load combinations - set B.....	210
7.2.3 Load combinations - set C.....	211
7.3 Numerical application	212
7.4 Concluding remarks.....	215
8 Conclusions.....	217
8.1 Main conclusions.....	217
8.2 Possible future developments.....	219
References	221
Appendix A	229
Appendix B.....	230
Appendix C.....	234
Appendix D.....	262
D.3 Determination of structural characteristic length.....	262
D.4 Definition constitutive models.....	266
D.5 Calculate neutral axis position and curvature for cross-section under bending and axial force	273
D.6 Determination of moment-curvature relationship.....	278
D.7 Determination of shear resistance	283
D.8 Calculation of bond transfer length and crack spacing	295
D.9 Determination of design crack width at SLS.....	297
D.10 Determination of moment-crack width relationship	300
D.11 Determination of bending moment corresponding to crack initiation	303
D.12 Verification of stress limitation criteria	305
Appendix E	309
Appendix F	312
AppendixG	314

LIST OF ABBREVIATIONS AND SYMBOLS

- 3PNBBT – Three-point notched beam bending tests
- a – Shear span
- $A_{c,ef}$ – Effective area of concrete in tension
- A_{ct} – Area of the tensile part of the concrete cross-section
- A_s – Area of steel reinforcement
- A_p – Area of prestress steel reinforcement
- A_{sl} – Cross-sectional area of the longitudinal reinforcement
- $A_{sl,min}$ – Minimum flexural reinforcement area
- A_{sw} – Area of transverse reinforcement
- A_p – Horizontally projected area of punching shear failure surface
- A_{sec} – Cross-section area
- A_f – Fiber cross-section area
- ACC – Aging creep compliance
- α_1 – Parameter that controls shape of the pre-peak branch of the $\tau - s$ relationship
- α – Transverse reinforcement inclination relative to structural element longitudinal axis
- α_2 – Parameter that controls shape of the post-peak branch of the $\tau - s$ relationship
- α_E – Modular ratio
- b_0 – Control perimeter for assessing punching shear resistance
- b_t – Width of tension zone
- b_s – Support strip width for punching analysis
- b_w – Smallest width of the tensile zone of the cross-section
- b_u – Diameter of the circle with equal area as the region inside the control perimeter
- β – Coefficient to assess mean steel strain over $l_{s,max}$
- β_μ – Ratio between maximum and residual friction coefficient
- c – Concrete cover
- c_o – Cohesion
- $C(t, t_0)$ – Specific creep.
- $C(\varphi_i)$ – Ratio between number of fibers with orientation angle φ_i and the total number of fibers in the cross-section
- CSCT – Critical Shear Crack Theory
- CMOD – Crack mouth opening displacement
- CDC – Critical diagonal crack
- COV – Coefficient of variation
- CBM – Cement based material
- χ – Curvature
- D_t – Tangential stiffness
- D_n – Normal stiffness
- d – Effective depth to main tension reinforcement

- d_{s1} – Depth of tensile longitudinal steel reinforcement
- d_{s2} – Depth of compressive longitudinal steel reinforcement
- d_p – Depth of prestress reinforcement
- d_c – Depth of resultant compressive force of concrete
- $d_{t,r}$ – Depth of tensile force of FRC inside the effective tensile zone
- $d_{t,u}$ – Depth of tensile force of FRC outside the effective tensile zone
- d_v – Shear resisting effective depth
- d_g – Maximum size of the aggregate
- d_f – Diameter of fibers
- d^j – Distance of center of gravity of the j^{th} layer of the cross-section to the cross-section top face
- D_j^p – Axial deformation of the j^{th} layer at the p^{th} rotation increment
- δ – Midspan deflection; Slip
- E_c – Concrete Young's modulus
- E_c^e – Effective modulus of concrete considering creep effects
- E_s – Reinforcing steel elastic modulus
- E_p – Prestressing steel elastic modulus
- E_{sh} – Reinforcing steel modulus of the hardening branch
- $E(t_0)$ – Elasticity modulus determined at time t_0
- E_0 – Asymptotic modulus.
- $E_s(t_0)$ – Modulus of the isolated spring of the Dirichlet series, at the time t_0 .
- $E_\mu(t_0)$ – Modulus of the μ^{th} chain of the Dirichlet series, at the time t_0 .
- e_{ui} – Eccentricity of shear forces with respect to the centroid of the basic control perimeter in the direction $i = x, y$
- e_p – Eccentricity of prestress steel reinforcement
- ε – Strain
- ε_{Fu} – Ultimate tensile strain of FRC
- ε_{ULS} – Limit tensile strain of FRC for ULS verification
- ε_{SLS} – Limit tensile strain of FRC for SLS verification
- ε_x – Longitudinal strain in the mid-depth of effective shear area
- ε_{ud} – Design value of steel ultimate strain.
- ε_{uk} – Characteristic value of steel ultimate strain
- ε_{c3} – Concrete compressive strain at the limit of elasticity
- ε_{cu3} – Concrete ultimate compressive strain
- ε_{sm} – Average strain of steel bars in the introduction length zone
- ε_{cm} – Average strain of concrete in the introduction length zone
- ε_{cs} – Strain of concrete due to shrinkage
- ε_{sh} – Strain of the concrete due to free shrinkage
- ε_{ins} – Instantaneous strain.

- ε_{cr} – Creep strain.
- ε_T – Thermal strain at time t .
- ε_0 – Stress independent strains (shrinkage and thermal) plus crack strain.
- $\varepsilon^{cr,d}$ – Delayed elastic strain.
- $\varepsilon^{cr,f}$ – Flow strain.
- $\varepsilon^{cr,v}$ – Viscoelastic aging and nonaging creep strain.
- η – Fiber orientation factor
- η_r – Coefficient to consider shrinkage contribution in the crack
- f – Maximum frictional resistance of the fiber due to snubbing effect
- f_{ck} – Characteristic value of the compressive strength of concrete, if not specified it is considered at 28 days of age
- f_{cd} – Design value of concrete compressive strength, if not specified it is considered at 28 days of age
- f_{ctm} – Mean value of the tensile strength of concrete, if not specified it is considered at 28 days of age
- f_{ctk} – Characteristic value of the tensile strength of concrete, if not specified it is considered at 28 days of age
- $f_{ctk,min}$ – Lower bound value of the characteristic tensile strength of concrete, if not specified it is considered at 28 days of age
- $\overline{f_c^{28}}$ – Mean compressive strength of concrete at 28 days of age.
- f_{cm} – Mean compressive strength of the concrete matrix
- f_{syk} – Characteristic value of yield strength of reinforcing steel
- f_{syd} – Design value of yield strength of reinforcing steel
- f_{st} – Tensile strength of reinforcing steel
- f_{Rf} – Residual flexural tensile strength
- f_L – Limit of proportionality
- f_{Ftu} – Ultimate residual tensile strength
- f_{Fts} – Serviceability residual tensile strength
- f_{ywd} – Design yield strength of the shear reinforcement
- f_{ywk} – Characteristic value of yield strength of the shear reinforcement
- f_{ct} – Concrete tensile strength
- f_{bd} – Bond strength of the steel reinforcement to concrete
- $f(\varphi_i)$ – Frequency of fibers with orientation angle φ_i
- F_{s1} – Force of tensile longitudinal steel reinforcement
- F_{s2} – Force of compressive longitudinal steel reinforcement
- F_c – Compressive force of concrete
- $F_{t,r}$ – Tensile force of FRC inside the effective tensile zone
- $F_{t,u}$ – Tensile force of FRC outside the effective tensile zone
- $F_{RE}(\eta)$ – Coefficient to account to error resultant of adopting discrete ranges of fiber orientation angles rather than a continuous function
- $F(\)$ – Cumulative distribution function of the standard Normal distribution

- FRC – Fiber reinforced concrete/cement composites
- FEM – Finite element method
- FBL – Finite bond length
- ϕ – Friction angle
- ϕ_s – Diameter of reinforcement bars
- ϕ_w – Diameter of the punching reinforcement
- φ_i – Fiber orientation angle
- $\overline{\varphi_i}$ – Mean orientation angle of the fibers in a range of fiber orientation angles interval
- φ_m – Average orientation angle of the fibers in a cross-section
- Φ – Objective function of the NLSM.
- G_f – Fracture energy of a plain concrete
- γ_c – Partial safety factor for concrete; Concrete density
- γ_F – Partial safety factor for FRC
- γ_s – Partial safety factor for steel
- $\gamma_{u,i}$ – Angle between the fiber orientation and the load direction at failure conditions
- h – Cross-section height
- $h_{c,ef}$ – Effective height of concrete in tension
- h_{sp} – Distance between the tip of the notch and the top of the cross-section
- HPFRCC – High performance fiber reinforced cement composites
- IR – Reinforcement index
- IP – Integration point
- IBL – Infinite bond length
- $J(t, t_0)$ – Creep compliance
- $\overline{J}(t_{j,i}, t_{0,i})$ – Experimental values of the creep compliance.
- $J(t_{j,i}, t_{0,i})$ – Predicted values of the creep compliance.
- $\varphi_c(t, t_0)$ – Creep coefficient
- k – Shear size effect factor. Empirical value to take the influence of the concrete cover. Coefficient to consider the non-uniform self-equilibrating cracking force
- k_c – Strength reduction factor. Coefficient that considers the stress distribution in the cross-section just before cracking occurs and the change of the inner lever arm.
- k_{dg} – Aggregate interlock coefficient at critical shear crack
- k_e – Coefficient of eccentricity
- L, l – Member span
- l_b – Crack bandwidth
- l_{cs} – Structural characteristic length
- l_p – Development length
- $l_{s,max}$ – Bond transfer length or introduction length
- l_f – Length of fibers
- $L_{bf,o}$ – Average bond length crossing the crack surface

$L_{cru,i}$	–	Critical embedment length
L_{tr}	–	Transfer bond length
L_b	–	Bond length
L_{cr}	–	Crack spacing
m_{Ed}	–	Design acting bending moment on support strip for punching analysis
M	–	Bending moment
M_{sd}	–	Design acting bending moment
M_{Rd}	–	Design resisting bending moment
M_{s1}	–	Moment of force of tensile longitudinal steel reinforcement
M_{s2}	–	Moment of force of compressive longitudinal steel reinforcement
M_c	–	Moment of compressive force of concrete
$M_{t,r}$	–	Moment of tensile force of FRC inside the effective tensile zone
$M_{t,u}$	–	Moment of tensile force of FRC outside the effective tensile zone
M_L	–	Number of discrete points of each experimental creep compliance curve.
MC2010	–	<i>fib</i> Model Code 2010
μ	–	Friction coefficient
μ_p	–	Maximum friction coefficient
N_{Ed}	–	Design acting axial force
N_f	–	Number of fibers
N_{f,φ_i}	–	Number of fibers with orientation angle φ_i
NLSM	–	Nonlinear least square method
ν	–	Poisson's ratio
ω_i	–	Initial tangent slope of the $\mu - s_a$ relationship
$P_{Rd,max}$	–	Maximum value of punching shear resistance
$P_{Rd,f}$	–	Design value of punching shear resistance provided by fiber reinforcement
$P_{Rd,c}$	–	Design value of punching shear resistance provided by concrete matrix
$P_{Rd,s}$	–	Design value of punching shear resistance provided transverse reinforcements
P_{Ed}	–	Design acting punching shear force
$P(w)$	–	Fiber pullout force
$P_{\varphi_i}^j(w)$	–	Pullout force of the total number of fibers in the j^{th} layer of the cross-section with an orientation angle φ_i
PC	–	Plain concrete
$\underline{\psi}$	–	Matrix of the defining coefficients of the ACC model.
θ	–	Inclination of the compressive stress field
$\rho_{s,ef}$	–	Effective reinforcement ratio
ρ_{sl}	–	Longitudinal reinforcement ratio
Q1	–	1 st quartile
Q3	–	3 rd quartile
r_s	–	Position where radial bending moment of slab is zero with respect to support axis
s_w	–	Spacing between shear reinforcement

s_{rm}	– Mean crack spacing
s_a	– Accumulated relative sliding displacement
$s_{a,p}$	– Accumulated relative sliding displacement corresponding to the maximum friction coefficient
SLS	– Serviceability limit state
SMCFT	– Simplified Modified Compression Field Theory
SFRC	– Steel fiber reinforced concrete
SD	– Standard deviation
s_0	– Sliding displacement at the end of the linear branch of the $\tau - s$ relationship
s_m	– Sliding displacement corresponding to the peak shear stress of the $\tau - s$ relationship
s_i	– Relative sliding displacement according to the local axis i
$\underline{\sigma}$	– Stress vector
σ_{sr}	– Maximum steel stress in a crack in the crack formation stage
σ_s	– Steel reinforcement bars stress
σ_n	– Normal stress
σ_{ct}	– FRC tensile stress
σ_{cp}	– Average axial stress acting in the cross-section
σ_{tf}	– Tensile stress of the fiber reinforcements
σ_{swd}	– Stress activated in the shear reinforcement
$\sigma_c^{SLS, char}$	– Compressive stress of concrete at characteristic load combination
$\sigma_c^{SLS, qperm}$	– Compressive stress of concrete at quasi-permanent load combination
$\sigma_t^{SLS, char}$	– Tensile stress of FRC at characteristic load combination
$\sigma_s^{SLS, char}$	– Tensile stress of longitudinal steel bars at characteristic load combination
$\sigma(\varphi_m)$	– Standard deviation of the orientation angle of the fibers in a cross-section
$\overline{\sigma_{fu}}$	– effective tensile strength of the fibers
σ_{fu}	– Fiber tensile strength
t	– Thickness of slab; time
t_0	– Loading age
$t - t_0$	– Load duration
τ	– Shear stress
τ_m	– Peak shear stress
τ_μ	– Retardation time of the μ^{th} Kelvin chain
τ_μ	– Retardation time of the μ^{th} Kelvin chain
τ_{bms}	– Mean bond strength between steel and concrete
τ_{bu}	– Average bond strength
θ	– Member rotation
U	– Perimeter of the reinforcement bars
$\underline{\Delta u}'$	– Vector of relative displacements of the interface element
ULS	– Ultimate limit states
VEM	– Variable Engadgement Model

- V_f – Fiber volume dosage
- V_{Rd} – Design value of shear resistance force
- $V_{Rd,F}$ – Design value of shear resistance of FRC member with longitudinal reinforcement and without shear reinforcement
- $V_{Rd,c}$ – Design shear resistance provided by plain concrete
- V_{Ed} – Design acting shear force
- $V_{Rd,s}$ – Design value of shear resistance provided by shear reinforcement
- $V_{Rd,max}$ – Maximum value of shear resistance
- w – Crack width
- w_u – Ultimate crack opening corresponding to the ULS criterion
- w_d – Design crack width
- w_{lim} – Nominal limiting value of crack opening
- x – Depth of the neutral axis
- ξ – Fibers segregation factor
- y – Distance between the neutral axis and the tensile side of the cross-section
- ψ – Rotation of slab outside the column region
- z – Internal lever arm
- z_s – Internal lever arm of passive reinforcement
- z_p – Internal lever arm of prestress reinforcement

LIST OF FIGURES

Figure 1 – Typical load (P) – deformation (δ) of FRC: a) Tensile strain-softening; b) Tensile strain-hardening (extracted from [33]).	6
Figure 2 – FRC composites softening and hardening characterization. V_f - volume of fibers; V_{fcri} - critical volume of fibers to obtain hardening response (extracted from [10, Ch. 3]).	7
Figure 3 – Typical load-CMOD curve of FRC [30] (dimensions in mm).	8
Figure 4 – The concept of toughness class for FRC based on the relationship between the flexural stress and CMOD [30].	8
Figure 5 – Rectangular stress-strain relationship for concrete in compression [30].	11
Figure 6 – Bilinear stress-strain relationship for concrete in compression [30].	12
Figure 7 – Bilinear stress-strain relationship considering creep for concrete in compression.	13
Figure 8 – Stress-strain diagrams for reinforcing steel in compression and tension [30].	13
Figure 9 – Tensile stress-strain relationship for plain concrete and FRC up to material tensile strength.	14
Figure 10 – Stress-crack opening constitutive laws for ULS analysis: a) rigid-plastic model; b) linear model [30].	15
Figure 11 – Example of determination of neutral axis position, x , and y for the evaluation of I_{cs} .	17
Figure 12 – Example of the analysis of a footbridge cross-section. a) Structural characteristic length; b) Crack pattern of the different components of the footbridge.	18
Figure 13 – Stress-strain relationship of a strain softening FRC, for ULS analysis: (a) complete diagram; (b) simplified diagram.	19
Figure 14 – Stress-strain relationship for SLS analysis: (a) Case I; (b) Case II; (c) Case III [30].	19
Figure 15 – SLS stress-strain case I model for situation where concrete matrix post-cracking contribution is disregarded.	21
Figure 16 – Example of SLS stress-strain Case I model where point C is disregarded.	21
Figure 17 – Typical load-displacement curve of a FRC structural element (extracted from [30, Figs. 7.7–1]).	24
Figure 18 – Stress-strain distribution for assessing flexural response of a rectangular cross-section with longitudinal steel reinforcement and FRC tension zone divided in two parts.	26
Figure 19 – Stress-strain distribution for assessing flexural response of a rectangular cross-section without longitudinal steel reinforcement.	26
Figure 20 – Simplified stress-strain distribution in the cross-section for slab design [30].	27
Figure 21 – Contribution of concrete matrix and fiber reinforcements for FRC shear resistance (extracted from [55]).	30
Figure 22 – Equilibrium at cross-section and corresponding strain profile [59].	31
Figure 23 – Example of ε_x adjustment due to proximity of rebar curtailment.	33
Figure 24 – Approach to estimate f_{R2k} and f_{R4k} based on the toughness class of the FRC.	36
Figure 25 – Ultimate crack width orthogonal to the CDC.	37

Figure 26 – Punching of slab. a) Development of critical shear crack; b) Slab’s rotation and concrete cover spalling (extracted from [67]).	39
Figure 27 – Punching of FRC slabs: (a) behavior of FRC after cracking; (b) critical shear crack in slabs; (c) assumed distribution of crack widths along the failure surface; (d) profile of fibers’ stress along the failure surface; and (e) matrix (concrete) and fiber contributions for the punching shear strength (adapted from [67]).	41
Figure 28 – Determination of eccentricity of the resultant of shear forces e_{ui} (extracted from [30]).	44
Figure 29 – Shear reinforcement activated at failure (extracted from [30]).	44
Figure 30 – Load-strain relationship for a centrically loaded tensile reinforced concrete member [68].	48
Figure 31 – Simplified representation of steel, concrete and bond stresses in the disturbed area in the crack formation stage of a RC member (adapted from [30, Figs. 7.6–3]).	49
Figure 32 – Load transmission from steel to concrete due to bond (extracted from [68]).	50
Figure 33 – Simplified representation of steel, concrete and bond stresses in the disturbed area in the crack formation stage of a FRC member.	52
Figure 34 – Determination of effective area of concrete in tension, $A_{c,ef}$, for: a) beams; b) slabs; c) walls (extracted from [30]).	54
Figure 35 – Generic rectangular FRC cross-section for determination of moment-curvature relationship.	59
Figure 36 – User interface window of the software.	60
Figure 37 – User interface window: a) Cross-section geometry; b) FRC material properties.	61
Figure 38 – User interface window: Conventional reinforcement data.	61
Figure 39 – User interface window: Data for calculation of structural characteristic length.	62
Figure 40 – User interface window: Selection of type of analysis to be performed.	62
Figure 41 – User interface window: Selection of shear capacity analysis.	63
Figure 42 – Main flowchart of <i>FRCcalc</i> .	64
Figure 43 – Idealization of the geometry of the FRC cross-section.	65
Figure 44 – Bending moment vs. curvature relationship for FRC and RC cross-section of Example no.1 beam, determined from <i>FRCcalc</i> and <i>DOCROS</i> .	71
Figure 45 – Design crack width vs. resisting bending moment at SLS relationships for FRC and RC cross-section of Example no.1 beam.	72
Figure 46 – Bending moment vs. curvature relationship for FRC and RC cross-section of Example no.2 slab, determined from <i>FRCcalc</i> and <i>DOCROS</i> .	75
Figure 47 – Design crack width vs. resisting bending moment at SLS relationship for FRC and RC cross-section of Example no.2 slab.	76
Figure 48 – Main properties of the experimental data of the database: a) Cross-section width and effective depth; b) Shear span to effective depth ratio; c) Conventional and fiber reinforcement ratio; d) Mean compressive strength.	79
Figure 49 – Residual flexural strength of SFRC beams of the DB_s .	83

Figure 50 – Statistical analysis of λ for both MC2010 shear resistance models considering the use of experimental and estimated values of f_{Ri} 84

Figure 51 - Comparison of experimental and shear strength determined from both MC2010 prediction models..... 85

Figure 52 - Statistical analysis of λ for both MC2010 shear resistance models. 85

Figure 53 – Comparison of the value of λ for each sample determined by the theoretical models.86

Figure 54 – Predictive performance of the theoretical models, safe ($\lambda \geq 1$) and unsafe ($\lambda < 1$).... 86

Figure 55 – Relationship between λ and effective shear span ratio, a/d ; the depth of longitudinal reinforcement, d ; the mean concrete compressive strength, f_{cm} ; the mean value of the ultimate residual tensile strength, f_{Fium} ; the ultimate crack width, w_u ; and the strain at mid-depth of the effective shear depth, ϵ_x 88

Figure 56 – Compressive stress vs. strain model adopted in NLMM107 constitutive model..... 91

Figure 57 – Fiber orientation profile. 92

Figure 58 – Zones of cross-section for the determination of the fiber orientation factor due to wall effect..... 94

Figure 59 – Fiber segregation model..... 96

Figure 60 – Components of the fiber pullout response..... 98

Figure 61 – Idealized bond stress vs. slip ($\tau_{b,0} - \delta$) for the pullout response of an aligned fiber. .. 99

Figure 62 – Definition of fiber bending angle, γ 99

Figure 63 – Idealized bond stress vs. slip ($\tau_{b,0} - \delta$) of the pullout response of an aligned fiber, considering the engagement length of fibers. 100

Figure 64 – Pullout force of a fiber with the orientation φ_i 101

Figure 65 – Schematic representation of coupling of the fiber orientation profile, fiber segregation and fiber pullout resistance model: a) Lateral and section cut view of a cracked FRC member; b) Determination of total number of fibers in a cracked layer, based on segregation model; c) Crack width of the j^{th} layer; d) Example to determine the fiber pullout force at the cracked j^{th} layer, considering $n\Delta\varphi = 4; \Delta\varphi_i = 22.5^\circ$ 103

Figure 66 – Cross-section geometry and reference values of the SFRC material properties considered in the case study. 104

Figure 67 – Moment vs. rotation relationship of cross-section considering $n\Delta\varphi = 4, 9, 15, 30$.. 105

Figure 68 – Moment vs. rotation relationship of cross-section, considering different engagement models..... 106

Figure 69 – Bond stress vs. slip considering three engagement models. 106

Figure 70 – Bond stress vs. slip ($\tau_{b,0} - \delta$) of the pullout response of an aligned fiber considering $\tau_{b,0,p} = 2, 5, 10, 20MPa$ 107

Figure 71 – Moment vs. rotation relationship of cross-section considering $\tau_{b,0,p} = 2, 5, 10, 20MPa$ 108

Figure 72 – Bond strength vs. slip ($\tau_{b,0} - \delta$) of the pullout response of an aligned fiber considering $\delta_p = 0.1, 0.5, 1.0, 5.0mm$ 109

Figure 73 – Moment vs. rotation relationship of cross-section considering $\delta_p = 0.1, 0.5, 1.0, 5.0mm$ 109

Figure 74 – Bond strength vs. slip ($\tau_{b,0} - \delta$) of the pullout response of an aligned fiber considering $\delta_p = 0.1, 0.5, 1.0, 5.0mm$ 110

Figure 75 – Moment vs. rotation relationship of cross-section considering $\alpha = 0.001, 0.01, 0.1, 1.0$ 110

Figure 76 – Bond strength vs. slip ($\tau_{b,0} - \delta$) of the pullout response of an aligned fiber considering $\beta = 0.1, 0.5, 1.0, 5.0$ 111

Figure 77 – Moment vs. rotation relationship of cross-section considering $\beta = 0.1, 0.5, 1.0, 5.0$ 112

Figure 78 – Division of cross-section for determination of fiber orientation factor due to the existence of notch: a) $l_f/2 > ND$; b) $l_f/2 \leq ND$ 113

Figure 79 – Derived bond stress vs. slip ($\tau_{b,0} - \delta$) of the pullout response of an aligned fiber for the numerical model of the FRC studied in :a) Pereira [110]; b) Lameiras [111]; c) Frazão et al. [112]; d) Valente et al. [113]; e) mixture c15_f45 of Salehian [49]; f) mixture c25_f60 of Salehian [49]. 117

Figure 80 – Derived bond stress vs. slip ($\tau_{b,0} - \delta$) of the pullout response of an aligned fiber for the numerical model of the FRC studied in: a) mixture c45_f90 of Salehian [49]; b) mixture c30_f45 of Salehian [49]; c) Soltanzadeh et al. [114]; d) Frazão et al. [15]; e) Amin [41]; f) Pajak et al. [115]. 118

Figure 81 – Experimental and numerical model comparison of force vs. CTOD relationship of the FRC studied in: a) Pereira [110]; b) Lameiras [111]; c) Frazão et al. [112]; d) Valente et al. [113]; e) mixture c15_f45 of Salehian [49]; f) mixture c25_f60 of Salehian [49]. 119

Figure 82 – Experimental and numerical model comparison of force vs. CTOD relationship of the FRC studied in: a) mixture c45_f90 of Salehian [49]; b) mixture c30_f45 of Salehian [49]; c) Soltanzadeh et al. [114]; d) Frazão et al. [15]; e) Amin [41]; f) Pajak et al. [115]. 120

Figure 83 – Crack propagation in the cross-section of notched FRC prisms. 121

Figure 84 – Examples of crack tortuosity and branching of notched FRC prisms submitted to 3-point bending tests (extracted from [118], [119]). 122

Figure 85 – Schematic representation of methodology to derive the crack diffusivity factor, κ . a) Fiber pullout tests; b) 3-point notched beam bending tests; c) Direct tensile tests. 123

Figure 86 – Experimental and numerical model comparison of force vs. CTOD relationship considering $\kappa = 1.20$ for the FRC studied in: a) mixture c30_f45 of Salehian [49]; b) Soltanzadeh et al. [114]. 123

Figure 87 – Derived bond stress vs. slip ($\tau_{b,0} - \delta$) of the pullout response of an aligned fiber for the numerical model considering $\kappa = 1.20$ for the FRC studied in :a) mixture c30_f45 of Salehian [49]; b) Soltanzadeh et al. [114]. 124

Figure 88 – Derived bond strength vs. slip ($\tau_{b,0} - \delta$) of the pullout response of an aligned fiber for the numerical model of all cases studies, according to type of fibers: a) hooked-end fibers; b) straight and recycled fibers..... 124

Figure 89 – Ratio between $\tau_{b,o,ave} / \tau_{b,ave,UVEM}$ 125

Figure 90 – R-FRC beams submitted to four-point bending tests (extracted from [120])..... 127

Figure 91 – Comparison between the experimental and numerical model force vs. midspan deflection for the R-FRC beams submitted to 4-point bending tests considering different FRC mixtures: a) c15_f45; b) c25_f60; and c) c45_f90 [114]...... 129

Figure 92 – Experimental and numerical model comparison of moment vs. crack width at reinforcement level for the R-FRC beams submitted to 4-point bending tests considering different FRC mixtures: a) c15_f45; b) c25_f60; and c) c45_f90 [114]...... 130

Figure 93 – Steel profiles geometry..... 131

Figure 94 – 3-point bending test setup and section cuts of composite beam (dimension in mm) [113]. 131

Figure 95 – Composite beam ready for testing [113]...... 132

Figure 96 – Experimental and numerically derived moment vs. curvature relationship at four section cuts of the composite beam studied in [113]. 133

Figure 97 – Comparison between the force vs. midspan deflection of the composite beam submitted to 3-point bending studied in [113]. 133

Figure 98 – CBM strain under constant load and temperature..... 137

Figure 99 – Viscoelastic behavior: a) Creep; b) Relaxation. 138

Figure 100 – General form of creep deformation. 138

Figure 101 – Recoverable and irrecoverable components of creep strain. 139

Figure 102 – Typical curves of creep compliance [128]...... 140

Figure 103 – Superposition principle of creep strains (adapted from [123]). 141

Figure 104 – Decomposition of time varying stress history. 142

Figure 105 – Example of specific creep curves for a material loaded at different time instants. ... 144

Figure 106 – Example of the dependence of creep strain of concrete specimens with the loading age (extracted from [130]). 147

Figure 107 – Example of loading-unloading creep response of aging material (adapted from [146]). 148

Figure 108 – Dependence of creep compliance rate with loading age t_0 in the $\log(t - t_0)$ time scale (based on [128, Fig. 2.1])..... 150

Figure 109 – Example of divergence of creep curves and nonmonotonic recovery of creep strain upon total unloading (t_r - point of recovery reversal) (adapted from [151, Fig. 1]). 151

Figure 110 – Creep curve in log-time scale (a - true elastic deformation; b - true creep; a' - conventional elastic deformation; b' - conventional creep) (adapted from [158, Fig. 1])...... 154

Figure 111 – Example of three creep functions ($L = 3$) to be fitted, where each function is defined by different number of points: $M_1=10$; $M_2=8$; $M_3=7$ 168

Figure 112 – Estimation of the creep function using the ACC model based on the experimental results of concrete samples (extracted from [179])..... 169

Figure 113 – Estimation of the creep function using the ACC model based on the experimental results of epoxy samples (extracted from [179]). 169

Figure 114 – Estimation of the creep function using the ACC model based on the experimental results [181] of concrete samples..... 170

Figure 115 – Estimation of the creep function using the ACC model based on the experimental results [182] of concrete samples..... 170

Figure 116 – Comparison between ACC and B4 models creep curves. 171

Figure 117 – Dirichlet series approximation of the creep function. a) curve of a single exponential in log-time; b) decomposition of the creep function (adapted from [128, Fig. 2.7]). 172

Figure 118 – Kelvin generalized model. 173

Figure 119 – Displacement, stress components and local coordinate system of a crack..... 178

Figure 120 – Comparison between estimated and experimental creep compliance curves of concrete studied in [197]..... 183

Figure 121 – Load history of concrete specimen [197]..... 183

Figure 122 – Experimental and numerical model comparison of the longitudinal strain of the concrete specimen submitted to the creep test. 184

Figure 123 – Beam geometry, reinforcement, support and loading configuration (dimensions in mm) [198]. 185

Figure 124 – Finite element mesh: line elements in blue line; solid elements in black line; supports in red circles (dimensions in mm)..... 186

Figure 125 – Comparison between the creep compliance curves obtained by the B4 model and by the NLMM174 model for the concrete studied in [198]. 187

Figure 126 – Trilinear tensile-softening diagram. 188

Figure 127 – Displacement along x3 obtained in the static analysis (displacements in mm, deformed mesh with 50x magnification factor)..... 189

Figure 128 – Crack pattern obtained in the static analysis (only displayed cracks with computed crack width higher than 0.005mm). 190

Figure 129 – Displacement along x3 obtained in the transient analysis (displacements in mm, deformed meshes with 50x magnification factor)..... 190

Figure 130 – Evolution of midspan deflection of the reinforced concrete beam. 191

Figure 131 – Crack pattern obtained in the transient analysis for $t = 750days$ (only displayed cracks with computed crack width higher than 0.005mm). 191

Figure 132 – Isoparametric zero-thickness finite elements available in *FEMIX*: a) linear 4-node; b) quadratic 6-node; c) Lagrangian 8-node; d) Serendipity 16-node (extracted from [199]). 193

Figure 133 – Shear stress *vs.* relative sliding displacement ($\tau - s$) monotonic response of the constitutive model. 195

Figure 134 – Schematic representation of the influence of the value of parameters α_1 and α_2 in the shape of the $\tau - s$ relationship..... 196

Figure 135 – Relationship between friction coefficient and accumulated relative sliding displacement ($\mu - s_a$) of the interface. 197

Figure 136 – Representation of the types of curves considered in the cyclic hysteretic model..... 198

Figure 137 – Representation of parameters of reversal curve 3. 199

Figure 138 – Representation of parameters of reversal curve 4. 200

Figure 139 – Representation of parameters of returning curve 5..... 201

Figure 140 – Representation of parameters of returning curve 6..... 202

Figure 141 – Representation of parameters of first transition curve 7. 203

Figure 142 – Representation of parameters of first transition curve 8. 204

Figure 143 – Representation of parameters of second transition curve 9. 205

Figure 144 – Representation of parameters of second transition curve 10. 206

Figure 145 – Representation of reversal from second transition curves of: a) Rule 9; b) Rule 10. 207

Figure 146 – Geometry, load and support conditions considered in the numerical model (dimensions in mm)..... 208

Figure 147 – Evolution of friction coefficient with the accumulated sliding displacement..... 209

Figure 148 – a) Prescribed horizontal displacement at node 9, 10 and 11 for the set A of load combinations. b) Shear stress vs sliding displacement at the IP2 of the interface element. 210

Figure 149 – Tangential stiffness at the IP2 of the interface element up to load combination 100. 210

Figure 150 – a) Prescribed horizontal displacement at node 9, 10 and 11 for the set B of load combinations; b) Shear stress vs sliding displacement at the IP2 of the interface element. 211

Figure 151 – a) Prescribed horizontal displacement at node 9, 10 and 11 for the set C of load combinations; b) Shear stress vs sliding displacement at the IP2 of the interface element. 212

Figure 152 – Test setup of slab tested in [201] (dimensions in mm)..... 213

Figure 153 – Finite element mesh. 214

Figure 154 – Horizontal load vs. displacement in the x_1 direction relationship of the slab..... 215

Figure 155 – Stress-strain distribution in 3PNBBT critical cross-section at ULS considering the rigid-plastic model for FRC. 230

Figure 156 – Stress-strain distribution in 3PNBBT critical cross-section at SLS for determination of f_{FRS} 231

Figure 157 – Values of k_a for the linear model and considering $l_{cs} = h_{sp}$ (extracted from [39]).. 232

Figure 158 – Stress-strain distribution in 3PNBBT critical cross-section at SLS for determination of f_{FRu} 233

Figure 159 – Stress, strain, compressive forces and forces depth for the compressive zone of the cross-section applying the bilinear model, for positive curvature and neutral axis position inside the cross-section. 236

Figure 160 – Stress, strain, compressive forces and forces depth for the compressive zone of the cross-section applying the bilinear model, for negative curvature and neutral axis position inside the cross-section. 237

Figure 161 – Stress, strain, compressive forces and forces depth for the compressive zone of the cross-section applying the bilinear model, for positive curvature and neutral axis position outside the cross-section. 240

Figure 162 – Stress, strain, compressive forces and forces depth for the compressive zone of the cross-section applying the bilinear model, for negative curvature and neutral axis position outside the cross-section. 242

Figure 163 – Generalized multi-linear model for FRC in tension. 245

Figure 164 – Possible distribution of stresses, strains, tensile forces and forces levers for the unreinforced tensile zone of a FRC cross-section with longitudinal conventional reinforcement, adopting quadrilinear stress-strain diagram, for positive curvature and neutral axis position inside the cross-section. 248

Figure 165 – Possible distribution of stresses, strains, tensile forces and forces levers for the unreinforced tensile zone of a FRC cross-section with longitudinal conventional reinforcement, adopting quadrilinear stress-strain diagram, for negative curvature and neutral axis position inside the cross-section. 250

Figure 166 – Possible distribution of stresses, strains, tensile forces and forces levers for the unreinforced tensile zone of a FRC cross-section with longitudinal conventional reinforcement, adopting quadrilinear stress-strain diagram, for positive curvature and neutral axis position outside the cross-section. 253

Figure 167 – Possible distribution of stresses, strains, tensile forces and forces levers for the unreinforced tensile zone of a FRC cross-section with longitudinal conventional reinforcement, adopting quadrilinear stress-strain diagram, for negative curvature and neutral axis position outside the cross-section. 256

Figure 168 – Possible distribution of stresses, strains, tensile forces and forces levers for the reinforced tensile zone of a FRC cross-section with longitudinal conventional reinforcement, adopting quadrilinear stress-strain diagram. 258

Figure 169 – Menegotto-Pinto curve..... 314

Figure 170 – Algorithm to determine the parameters that control the shape of the Menegotto-Pinto curve..... 315

LIST OF TABLES

Table 1 – Relationship between CMOD and δ [34].	9
Table 2 – Value of k_G and α depending on prism bending test standard [60].	34
Table 3 – Values of τ_{bms} , β and η_r for deformed reinforcing bars (extracted from [30]).	54
Table 4 – Verification of stress limitation criteria for Example no.1 beam.	73
Table 5 – Verification of stress limitation criteria for Example no.2 slab.	76
Table 6 – Prism bending test standards adopted for the evaluation of the residual flexural strength, f_{Ri} , considering the different SFRC mixes present in the DB_s .	80
Table 7 – Statistical results of the residual flexural strength prediction model [66].	81
Table 8 – Statistical analysis of the ratio between the experimental and estimated values of the residual flexural strength, f_{Ri} .	82
Table 9 – Adapted version of the <i>Demerit Points Classification</i> .	87
Table 10 – Algorithm to determine number of fibers within each orientation angle interval.	95
Table 11 – Material properties of the FRC mixtures considered in the assessment of the predictive performance of the new model.	116
Table 12 – Basic creep compliance evolution of DPL model.	154
Table 13 - Creep coefficient function based on EC2 model [37].	157
Table 14 – Creep coefficient function based on MC2010 model [30].	159
Table 15 – Creep compliance function based on B3 model [170].	162
Table 16 – Creep compliance function based on B4 model [175].	165
Table 17 – Properties of the steel reinforcements [198].	185
Table 18 – Maximum stress level of the steel reinforcements obtained in the static analysis.	189
Table 19 – Maximum stress level of the steel reinforcements obtained in the transient analysis for $t = 750days$.	191
Table 20 – Material properties of the constitutive model of the interface.	208
Table 21 - Material properties of the constitutive model of the interface.	214
Table 22 – Reference values of concrete mechanical properties for each strength class [30].	229
Table 23 – Algorithm for determination of structural characteristic length of FRC member.	262
Table 24 – Algorithm to set the formulas for effective height of tensile zone of cross-section.	264
Table 25 – Algorithm for definition of constitutive model for concrete in compression.	266
Table 26 – Algorithm for definition of constitutive model for steel in compression or tension.	267
Table 27 – Algorithm for definition of constitutive model for FRC in tension at ULS.	268
Table 28 – Algorithm for definition of constitutive model for FRC in tension at SLS.	270
Table 29 – Algorithm to determine neutral axis and curvature of a FRC or RC cross-section.	273
Table 30 – Algorithm to set the formulas for forces in a FRC cross-section.	275
Table 31 – Algorithm to set the formulas for forces depth and moments in a FRC cross-section.	276
Table 32 – Algorithm to set the formulas compatibility equations.	277

Table 33 – Algorithm to resolve the equilibrium equations and find solution for neutral axis position and cross-section curvature.	277
Table 34 – Algorithm to determine the moment-curvature relationship of a FRC or RC cross-section.	279
Table 35 – Algorithm to resolve the equilibrium equations and find solution for neutral axis position and bending moment.	282
Table 36 – Algorithm to check if tensile failure of FRC is reached.	283
Table 37 – Algorithm to determine shear resistance of FRC cross-section.	284
Table 38 – Algorithm to determine shear resistance of FRC cross-section without longitudinal and shear reinforcements.	285
Table 39 – Algorithm to determine shear resistance of FRC cross-section with longitudinal reinforcement, based on empirical model.	285
Table 40 – Algorithm to determine shear resistance of FRC cross-section with longitudinal reinforcement and with or without transversal reinforcements, based on VEM/SMCFT model.	288
Table 41 – Algorithm to determine shear resistance of RC cross-section.	291
Table 42 – Algorithm to determine shear resistance of RC cross-section with longitudinal reinforcement.	292
Table 43 – Algorithm to determine shear resistance of RC cross-section with longitudinal and transverse reinforcements.	293
Table 44 – Algorithm to determine the bond transfer length in a FRC and RC cross-section.	296
Table 45 – Main algorithm to determine the design crack width of a FRC and RC cross-section at SLS.	297
Table 46 – Algorithm to determine the design crack width of a FRC and RC cross-section.	298
Table 47 – Algorithm to determine moment-crack width relationship of FRC and RC cross-section.	300
Table 48 – Algorithm to determine the moment at crack initiation.	304
Table 49 – Algorithm of routine of stress limitation serviceability verifications.	305
Table 50 – Database of beams shear tests and results of theoretical models.	309
Table 51 – B4 model creep parameters dependent on cement type [175].	312
Table 52 – B4 model shrinkage parameter dependent on aggregate type [175].	313

INTRODUCTION

Concrete is a cement-based material that can exhibit a high compressive strength. Its main disadvantage consists in its brittleness, i.e. relatively low tensile strength and low tensile deformability. The use of tensile reinforcements in concrete structural elements improves their tensile and flexural response, limits the crack opening to acceptable values, and increases the stiffness of the structural elements after crack initiation. These reinforcements can be incorporated in a discrete manner, e.g. conventional steel or fiber reinforced polymer (FRP) in the form of bars or grids, or by dispersing fibers into the concrete matrix. In the market exist fibers of several types of materials (metallic, synthetic, vegetable, etc.) and geometric configurations (longitudinal and transversal shape). Although the employment of natural fiber reinforcements in concrete is dated to the beginning of the 1900's [1], it was majorly since its modern age development, in the 1960's [2], that fiber reinforced concrete (FRC) has being showing enormous potentialities for use in structural elements.

The use of fiber reinforced concrete in the construction of structural systems has being progressively increasing in the last decades for new construction and repair operations of building's structural elements (slabs, beams, columns and foundations), shell type structures, pre-fabrication elements, pavements, roads, tunnel linings, decks of bridges, marine structures, etc.[1], [3].

The use of short and randomly distributed fibers increases concrete post-cracking tensile capacity, its ductility, energy absorption capacity and impact resistance when compared to plain concrete (PC) [4], [5]. Additionally, the restrain to crack propagation, provided by the different fiber reinforcement mechanisms enhances the durability and integrity of cement based materials. The fundamental reinforcement mechanism of fibers consists in the capacity of ensuring relatively high stress transfer between the faces of cracks, by restraining the degeneration of micro-cracks in meso- and macro-cracks, which increases the stiffness and load carrying capacity of concrete structures in their cracking stage, as well as their durability [6]–[9]. For FRC's with regular content of dispersed fibers, which generally ranges from 0.2 to 2.0% in volume of FRC, the pre-cracking response and tensile strength of concrete remain unaltered [3], [6]. Conversely, fiber contribution after cracking depends mainly on the content of fibers, their orientation and distribution towards the potential cracks, the material and geometric characteristics of the fibers, and the mechanical properties of the concrete, which are designated as the variables that mainly affect the fiber reinforcement mechanisms. Likewise, the compressive strength of FRC's is similar to plain concrete, while the post-peak load and deformation

capacity increase with the variables that have a favorable influence on the fiber reinforcement mechanisms [10]–[12].

When used in structural elements, fiber reinforcement can: improve the tensile and flexural response [13]–[15]; increase the shear and punching resistance of concrete [16]–[19]; restrain the crack opening [20], [21]; reduce the deformation of members [22]–[24]; decrease the tensile stress in conventional reinforcement [24]; improve the bond performance of conventional reinforcement to surrounding concrete [25], [26] and improve concrete fire resistance [27], [28]. From the design point of view, the use of FRC can benefit the ultimate and serviceability limit states verifications. Additionally, fiber reinforcement can replace partially or even totally conventional steel bars, mainly in statically indeterminate structures. Fiber reinforcement is being also explored with appreciable success on the partial or integral replacement of transverse reinforcement, such in the shear reinforcement of beams [29] and in the punching reinforcement of slabs [19]; decreasing the construction time; and reducing construction and maintenance costs.

Different types of fibers can be used in the production of FRCs, namely [1], [6]:

- Steel fibers, with different shapes, aspect ratio (length to diameter ratio) and tensile strength;
- Glass fibers, namely alkali-resistant glass fibers;
- Synthetic fibers, like polypropylene (PP), polyvinyl alcohol (PVA), aramid, etc.;
- Carbon fibers, namely pitch and polyacrylonitrile (PAN);
- Natural fibers, like sisal, cellulose, asbestos, etc.

Generally, fibers with high modulus of elasticity and tensile strength can improve significantly the post-cracking strength of cement based materials, like steel, carbon and PVA fibers, while low-modulus fibers are mostly used to control cracking shrinkage at early ages [1]. Polypropylene fibers can also be used to avoid concrete spalling in a fire scenario, as they melt when submitted to high temperatures, creating channels that can relieve water pressure in concrete pores [10].

1.1 Research significance

Although several research activities have been carried out, including the description of fiber reinforcements potentialities and development of design rules and codes [30]–[32], in the designer's

community there is still a lack of knowledge in the dimensioning of FRC structures. Furthermore, the available analysis and design numerical tools dedicated to FRC structural members is scarce or even inexistent in some design aspects. These circumstances are avoiding a faster use of this material, with economic and technical detrimental impact in the construction sector.

This work aims to contribute for the design process of structural elements with FRC using the recommendations of one of the most recent and comprehensive design codes, the fib Model Code 2010 (MC2010), while complementing the design guidelines with the findings of the most recent academic works. In addition, are developed numerical tools that consider the relevant specificities of this FRC and improve the simulation capabilities of some particularities of structural members where this material is adopted.

It is expected that this work constitutes a valuable contribute to the dissemination of knowledge related to the design and analysis of FRC structures. The developed numerical tools will be readily used in the analysis and design of fiber reinforced concrete members, which can ultimately contribute to the increase of the use of FRC in structural elements.

1.2 Objectives

This thesis is focused on the development and implementation of numerical tools to be used in the analysis and design of fiber reinforced concrete structural elements. The main objectives are:

- Development of software for the evaluation of the flexural and shear behavior of FRC members according to MC2010 design guidelines and recommendations;
- Appraisal of the MC2010 FRC shear resistance models considering an extensive shear test database;
- Implementation of an integrated approach coupling the effect of fiber orientation profile, fiber segregation, and fiber pullout resistance on a numerical tool for the evaluation of the flexural response of FRC members.
- Development and implementation in FEM-based software of an aging creep model for the simulation of the nonlinear behavior of cement based materials since early ages, coupling the creep model to the other thermo-mechanical constitutive model, by considering the concrete maturation, shrinkage and cracking;
- Development of a cyclic-hysteretic constitutive model for the simulation of the contact between different materials, which is a relevant modeling aspect on FRC slabs supported on soil.

1.3 Thesis outline

The thesis is divided in eight chapters. This chapter corresponds to the introduction, while the last chapter is dedicated to the conclusions and possible recommendations for future research.

In the second chapter is presented the design guidelines and recommendations for FRC structures provided in the *fib* Model Code 2010, which, when applicable, are complemented with the more advanced models published in academic works.

The third chapter is dedicated to present a new software – *FRCcalc* – developed for the analysis and design of FRC member considering the design rules provided in the second chapter.

In the fourth chapter is appraised the performance of the shear resistance prediction models considering an extended version of a database of results of experimental tests of FRC elements.

The fifth chapter is devoted to the development of a novel model for predicting the flexural capacity of FRC members failing in bending, capable of considering the relevant fiber reinforcement mechanism, namely: fiber orientation profile, fiber segregation and fiber pull-out resistance. This model was implemented in a software for the prediction of the moment-rotation response of this type FRC members, and its predictive performance was assessed by simulating FRC notched beams submitted to 3 points bending tests

Chapter sixth is dedicated to the development of a creep model for cement based materials and its implementation into the *FEMIX* computer program in order to increase the potentialities of this software for modeling the time dependent phenomena and cracking of these materials since their early age. In this context the developed creep model was coupled with a thermo, maturation, shrinkage and cracking model components available in *FEMIX*.

In the seventh chapter, a new cyclic-hysteretic constitutive model is described and implemented into the *FEMIX* for the simulation of contact between different materials, namely FRC slabs supported on ground and the foundation granular layers.

2 DESIGN OF FIBER REINFORCED CONCRETE STRUCTURAL ELEMENTS

2.1 Introduction

In the last decades, an extensive research has been conducted on FRC structures, mainly concerning the description of fiber reinforcement potentialities and experimental characterization from the material to the structural level. Although some design rules and codes have been developed, as is the case of the *fib* Model Code 2010 [30], the ACI 544.4R-88 [32] and the RILEM TC 162-TDF [31], in the designer's community there is still a lack of knowledge in the analysis of FRC structures, which avoids a faster use of this material, with economic and technical detrimental impact in the construction sector.

The present chapter aims to present a comprehensive analysis of the design process of structural elements with FRC using the recommendations of one of the most recent and comprehensive design codes, the *fib* Model Code 2010 (MC2010) [30].

2.2 Material characterization and classification

When assessing the uniaxial tensile behavior of a FRC, two types of responses can be obtained: (i) strain-softening or (ii) strain-hardening. A FRC has a tensile strain-softening behavior when a reduction of load carrying capacity with the increase of crack width opening occurs after the formation of the first crack (Figure 1a). Conversely, in a strain-hardening material the load carrying capacity increases with the material deformation (Figure 1b), up to a strain of $\varepsilon_{Fu} = 1.0\%$. In strain-softening FRC a major failure crack is formed, while in strain-hardening a diffuse crack pattern is observed. Commonly, for usual volume contents of fibers, FRC's exhibit a tensile strain-softening behavior, while for high performance matrix and high fiber contents (>1.5% in volume of FRC) is possible to attain a strain-hardening behavior [33].

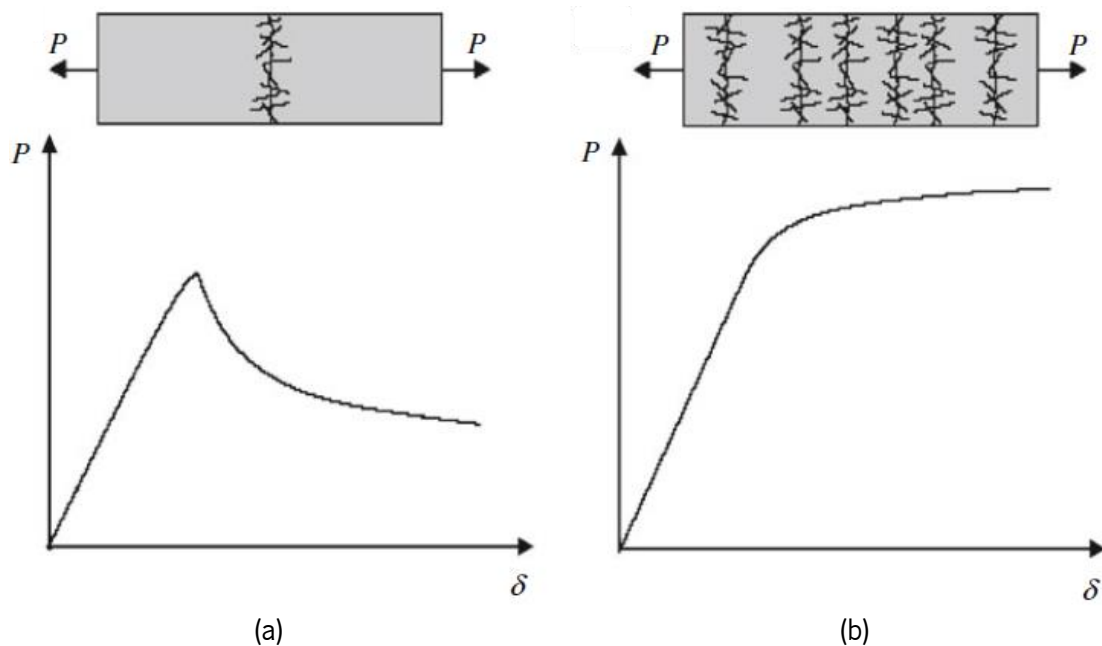


Figure 1 – Typical load (P) – deformation (δ) of FRC: a) Tensile strain-softening; b) Tensile strain-hardening (extracted from [33]).

The tensile behavior of a specific composition of a FRC can be determined by performing uniaxial tensile tests. Nevertheless, the execution of these tests is quite cumbersome, namely direct tensile tests. Therefore, for material characterization, 3-point notched beam bending tests (3PNBBT) are executed according to EN 14651 [34] or RILEM 162-TDF [35]. However, due to the strain variation profile obtained during bending tests and stress redistribution provided by the fiber reinforcements, it can be observed that in 3PNBBT the peak load arises after the first crack load. This response characterizes a material as deflection-hardening and cannot be confused with the tensile strain-hardening behavior that can only be assessed in uniaxial tensile tests. While tensile strain-hardening materials always exhibit a deflection-hardening behavior, strain-softening materials can present a deflection-hardening or softening response in 3PNBBT. In Figure 2 is presented a summary of the possible softening and hardening characterization of FRC's. In this figure is also provided additional information regarding the critical volume of fibers needed to achieve a strain-hardening or deflection-hardening response.

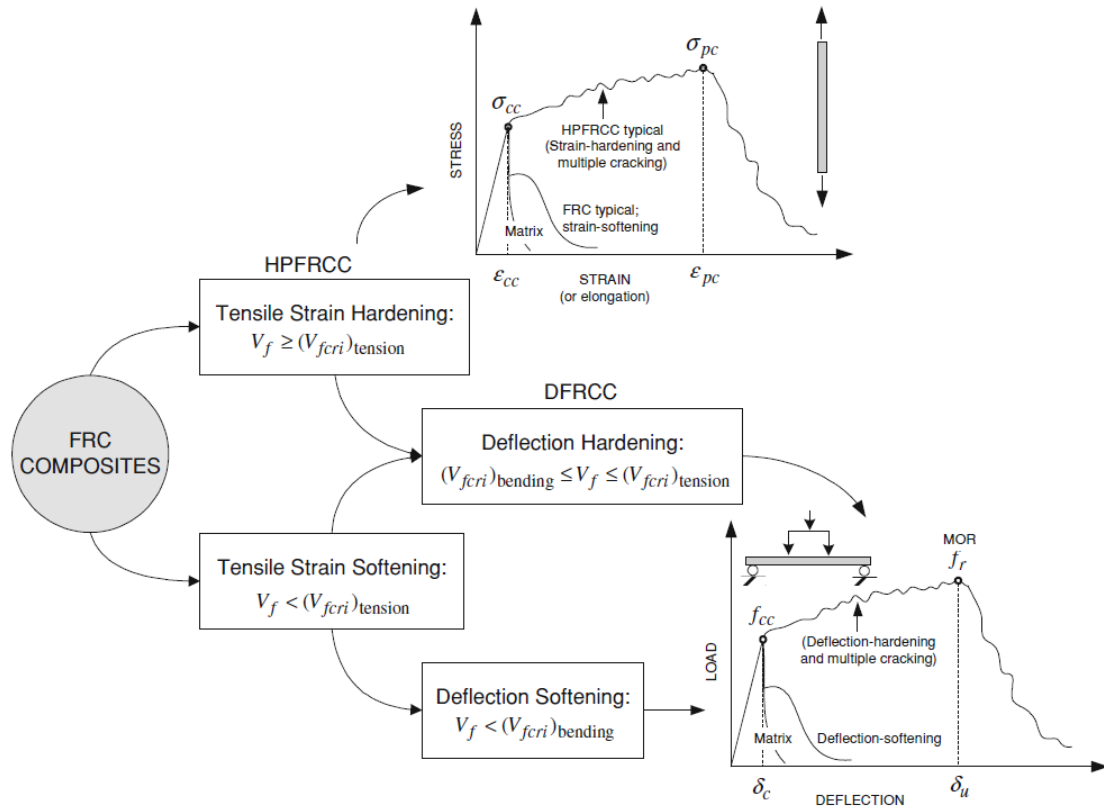


Figure 2 – FRC composites softening and hardening characterization. V_f - volume of fibers; V_{fcri} - critical volume of fibers to obtain hardening response (extracted from [10, Ch. 3]).

From the execution of 3PNBBT, it is possible to evaluate the post-cracking tensile strength of a FRC. The test setup and typical load *vs.* crack mouth opening displacement (CMOD) relationship are presented in Figure 3. Based on the force values, F_j ($j = 1, 2, 3, 4$) corresponding to specific values of CMOD, the residual flexural tensile strength, f_{Rj} , is determined from the following expression:

$$f_{Rj} = \frac{3 \cdot F_j \cdot l}{2 \cdot b \cdot h_{sp}^2} \quad \text{Eq. (2.1)}$$

where l is the span length of the test beam; b is the width of the specimen's cross section; and h_{sp} is the distance between the notch tip and the beam top face. By specifying the values of the residual flexural strength, it is possible to compare the post-cracking behavior of different FRC's compositions.

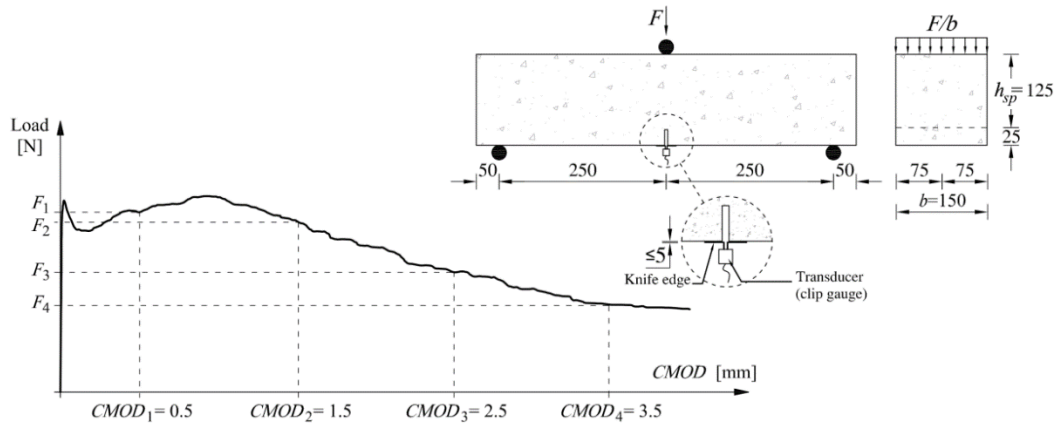


Figure 3 – Typical load-CMOD curve of FRC [30] (dimensions in mm).

In fact, the MC2010 resorts to the residual flexural strength concept to classify the post-cracking performance of a FRC, by adopting a toughness class. The toughness class is determined from the characteristic values of the residual flexural tensile strength of FRC for serviceability, f_{R1k} , and ultimate state conditions, f_{R3k} . The value of f_{R1k} corresponds to $CMOD_1 = 0.5\text{mm}$ and f_{R3k} to $CMOD_3 = 2.5\text{mm}$. The toughness class is defined by a value associated to an interval of f_{R1k} , and a letter corresponding to the residual strength ratio, f_{R3k}/f_{R1k} . The f_{R1k} can be selected from the series: 1.0, 1.5, 2.0, 2.5, 3.0, 4.0, 5.0, 5.0, 6.0, 7.0, 8.0, ... [MPa], while the letter corresponding to f_{R3k}/f_{R1k} is determined from the following intervals $a = [0.5; 0.7[$; $b = [0.7; 0.9[$; $c = [0.9; 1.1[$; $d = [1.1; 1.3[$; $e = [1.3; +\infty[$. For example, after the execution of six 3PNBBT (Figure 4), the tested FRC presents a characteristic residual strength $f_{R1k} = 7.2\text{MPa}$ and a residual strength ratio of $f_{R3k}/f_{R1k} = 0.72$. According to MC2010 classification, this FRC has a toughness class “7b”.

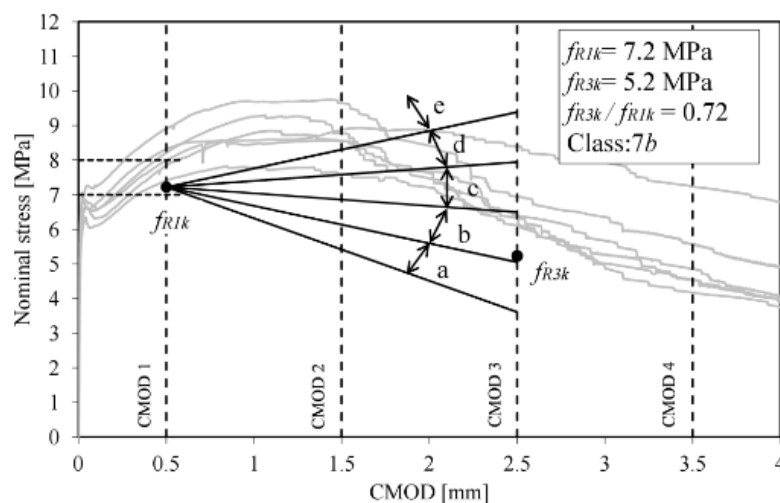


Figure 4 – The concept of toughness class for FRC based on the relationship between the flexural stress and CMOD [30].

In the execution of 3PNBBT the midspan deflection (δ) of the beams is, usually, also recorded, and the following average relationship between δ and CMOD can be used in the post-peak region of the load-CMOD curve [34]:

$$\delta [mm] = 0.85 \cdot \text{CMOD} [mm] + 0.04 \quad \text{Eq. (2.2)}$$

In Table 1 is presented the conversion of the CMOD_j ($j = 1, 2, 3, 4$) to δ .

Table 1 – Relationship between CMOD and δ [34].

j	CMOD [mm]	δ [mm]
1	0.50	0.47
2	1.50	1.32
3	2.50	2.17
4	3.50	3.02

For structural applications, MC2010 specifies that a minimum ratio between the residual tensile strength at $\text{CMOD} = 2.5\text{mm}$ and $\text{CMOD} = 0.5\text{mm}$ (Eq. (2.3)) should be verified in order to consider the tensile contribution of FRC in the ultimate limit state (ULS) resistance of a structural element [30].

$$f_{R3k} / f_{R1k} > 0.50 \quad \text{Eq. (2.3)}$$

An additional condition is also specified in MC2010, related with the ratio between the characteristic value of the limit of proportionality, f_{Lk} , and the residual strength, f_{R1k} (Eq. (2.4)) [30]. The value of f_{Lk} is given by Eq. (2.1), considering the maximum load value, F_L , registered on the 3PNBBT up to $\text{CMOD} = 0.05\text{mm}$ [34], [35].

$$f_{R1k} / f_{Lk} > 0.40 \quad \text{Eq. (2.4)}$$

For structural applications, when designers prescribe an FRC based on its performance, the toughness class should be defined and coupled with the existing performance based grades applicable to plain and reinforced concrete according to EN 206 [36], namely the compressive strength class, the exposure class, the chloride content class and the consistence class, among others. These grading classes are universally adopted by designers and producers. On the other hand, the concrete manufacturer and construction supplier must define the concrete composition, specifications, type

and amount of fibers, and also provide validation of the FRC's mechanical and rheological properties considering the prescribed performance based classes.

In the dimensioning process, a conservative approach should be adopted by considering the lower value of the residual flexural strength interval of the FRC toughness class. For example, when prescribing a FRC of the 4d toughness class ($f_{R1k} = [4.0; 5.0[$ and $f_{R3k} / f_{R1k} = [1.1; 1.3[$), the post-cracking response should be defined by the following residual strength values: $f_{R1k} = 4.0MPa$ and $f_{R3k} = 1.1 \times 4.0 = 4.4MPa$. Additionally, the clauses for structural application of FRC must be verified. At the design process, the value of the limit of proportionality is unknown. Therefore, for the verification of the 2nd structural application clause (Eq. (2.4)), it can be considered that the limit of proportionality is equal to the characteristic value of the tensile strength of concrete ($f_{Lk} = f_{ctk}$). For example, if the compressive strength class of the FRC is C30/37, the upper bound of the characteristic tensile strength of concrete is $f_{ctk,max} = 3.8MPa$ [30], and, therefore, the residual tensile strength, f_{R1k} , shall be $f_{R1k} > 1.52MPa$ to comply with the 2nd structural application clause (Eq. (2.4)).

2.3 Constitutive laws for ULS and SLS

2.3.1 Concrete in compression

For the usual fiber concentrations used in FRC's, its compressive behavior is similar to the one observed in PC. Accordingly, the stress-strain relationships defined in MC2010 or Eurocode 2 [37] for PC can also be used for characterizing the compressive behavior of FRC. The rectangular and bilinear stress-strain relationships are usually used in the dimensioning process of concrete in compression.

The rectangular stress-strain distribution, presented in Figure 5, is defined by the following equation:

$$\begin{aligned} \sigma &= \eta \cdot f_{cd} & ; 0 < \varepsilon \leq \varepsilon_{cu3} \\ \sigma &= 0 & ; \varepsilon > \varepsilon_{cu3} \end{aligned} \quad \text{Eq. (2.5)}$$

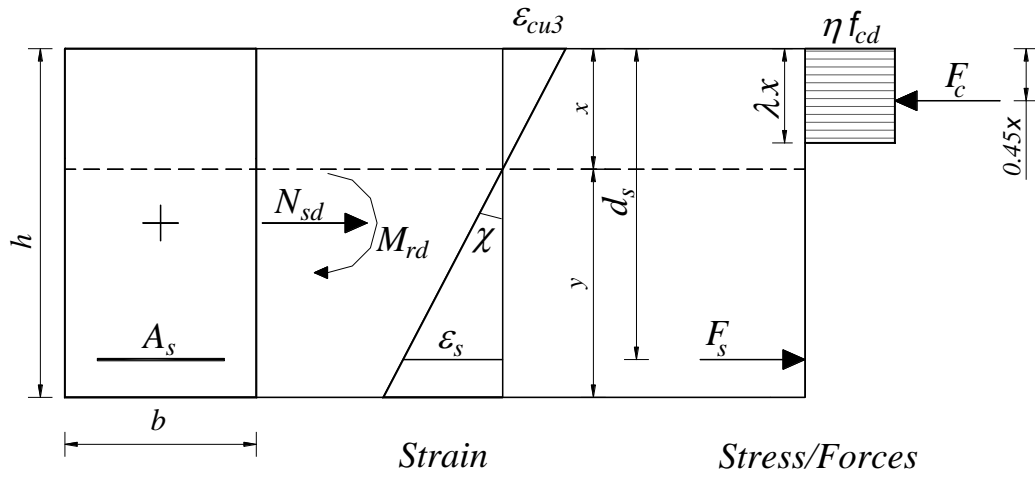


Figure 5 – Rectangular stress-strain relationship for concrete in compression [30].

The value of the ultimate compressive strain, ε_{cu3} , is defined according to the concrete compressive strength and can be obtained from Table 7.2-1 of MC2010 and Appendix A, based on the concrete strength class. The factor η is determined according to Eq. (2.6), and the parameter λ that affects the height of the compression zone is determined from Eq. (2.7) [30]. If the width of the compression zone decreases in the direction of the extreme compression fiber, the value of the effective strength, $\eta \cdot f_{cd}$, must be reduced in 10% [30].

$$\eta = \begin{cases} 1.0 & ; f_{ck} \leq 50 \text{ MPa} \\ 1.0 - (f_{ck} - 50)/200 & ; 50 \leq f_{ck} \leq 100 \text{ MPa} \end{cases} \quad \text{Eq. (2.6)}$$

$$\lambda = \begin{cases} 0.8 & ; f_{ck} \leq 50 \text{ MPa} \\ 0.8 - (f_{ck} - 50)/400 & ; 50 \leq f_{ck} \leq 100 \text{ MPa} \end{cases} \quad \text{Eq. (2.7)}$$

The bilinear stress-strain relationship, presented in Figure 6, is defined according to the following equations:

$$\begin{aligned} \sigma &= \frac{f_{cd}}{\varepsilon_{c3}} \cdot \varepsilon & ; \varepsilon_{c3} \leq \varepsilon \leq 0 \\ \sigma &= f_{cd} & ; \varepsilon_{cu3} < \varepsilon \leq \varepsilon_{c3} \\ \sigma &= 0 & ; \varepsilon < \varepsilon_{cu3} \end{aligned} \quad \text{Eq. (2.8)}$$

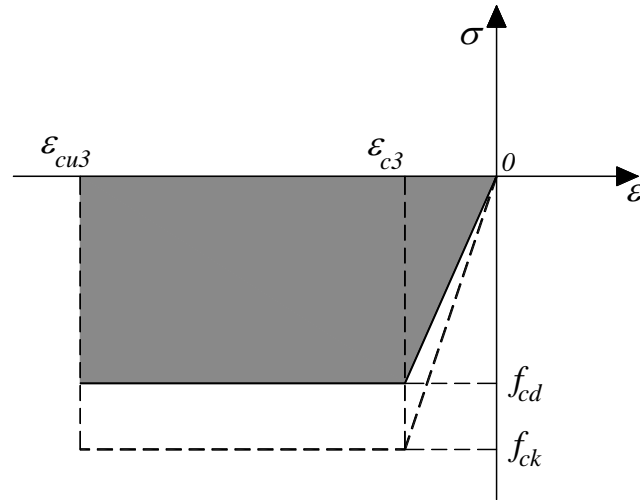


Figure 6 – Bilinear stress-strain relationship for concrete in compression [30].

In Eq. (2.5) and Eq. (2.8), both compressive stresses and strains adopt negative values.

In both types of relationships for concrete in compression, the design compressive strength, f_{cd} , is obtained from the following expression:

$$f_{cd} = \alpha_{cc} \cdot \frac{f_{ck}}{\gamma_c} \quad \text{Eq. (2.9)}$$

where: α_{cc} is a coefficient to take into account long term effects on the compressive strength of concrete and of unfavorable effects from the way loads are applied; and γ_c is the partial safety factor for concrete, taking the value of $\gamma_c = 1.5$ for ULS design situations and $\gamma_c = 1.0$ for serviceability limit state (SLS) [30]. For normal design situations, where the first variable loads of the structure are applied only after few months after casting, and the long-term compressive strength increase provided by continuous hydration of cement compensates the unfavorable effect of sustained loading, is appropriate to consider $\alpha_{cc} = 1.0$. Otherwise, $\alpha_{cc} = 0.85$ is more suitable [30].

When concrete creep effects need to be considered in the analysis of a member cross-section, the stress-strain relationship previously presented can be modified in order to take into account the increased deformation of concrete under creep. Therefore, in the analysis the strains values of the points defining the stress-strain diagram are multiplied by the factor $(1 + \varphi_c(t, t_0))$. $\varphi_c(t, t_0)$ is the creep coefficient defined as the relation between the creep strain $\varepsilon_{cr}(t)$ evaluated at the instant t and the instantaneous strain $\varepsilon_{ins}(t_0)$ at the instant t_0 when the load is applied. However, during analysis the compressive strain in the cross-section cannot exceed the ultimate compressive strain, ε_{cu3} . The model is illustrated in Figure 7 and formulated in Eq. (2.10).

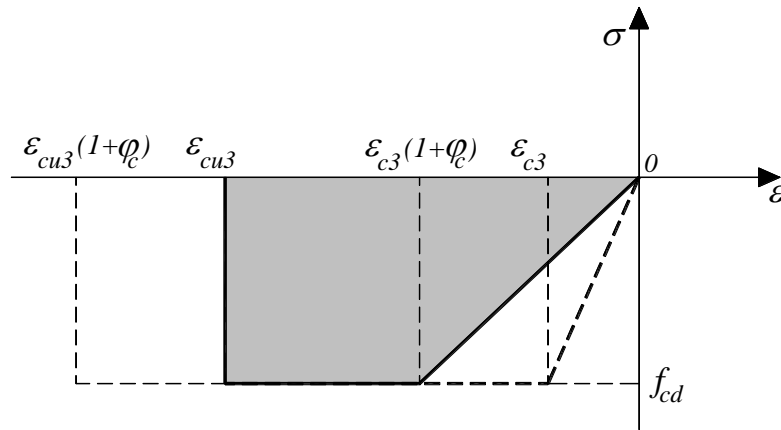


Figure 7 – Bilinear stress-strain relationship considering creep for concrete in compression.

$$\begin{aligned}
 \sigma &= \frac{f_{cd}}{\varepsilon_{c3} \cdot (1 + \varphi_c)} \cdot \varepsilon & ; \varepsilon_{c3} \cdot (1 + \varphi_c) \leq \varepsilon < 0 \wedge \varepsilon \geq \varepsilon_{cu3} \\
 \sigma &= f_{cd} & ; \varepsilon_{cu3} \leq \varepsilon < \varepsilon_{c3} \cdot (1 + \varphi_c) \\
 \sigma &= 0 & ; \varepsilon < \varepsilon_{cu3}
 \end{aligned}
 \tag{Eq. (2.10)}$$

2.3.2 Steel in tension or compression

When conventional steel bars are provided for flexural reinforcement, the stress-strain laws defined in MC2010 or Eurocode 2 are adopted. In Figure 8 are presented the stress-strain relationship for steel in tension and compression. When analyzing a cross-section, it is possible to consider one of two models: (i) an elastic-perfectly plastic model; and (ii) an elastic branch followed by a hardening branch. The elastic-perfectly plastic model is presented in Eq. (2.11). When using this model, it is considered that reinforcing steel has an unlimited deformation capacity. The model with the hardening branch is presented in Eq. (2.12) and in this case is considered that steel fails when ultimate design strain, ε_{ud} , is reached. The modulus of the hardening branch, E_{sh} , is determined according to Eq. (2.13).

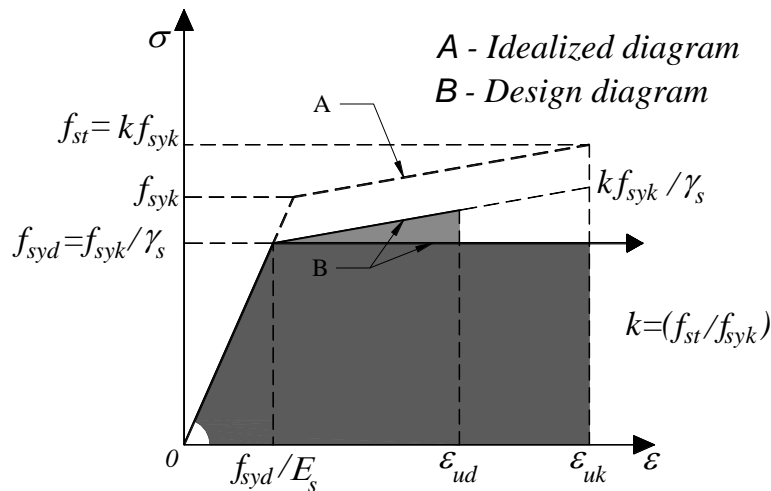


Figure 8 – Stress-strain diagrams for reinforcing steel in compression and tension [30].

$$\left\{ \begin{array}{l} \sigma = E_s \cdot \varepsilon \quad ; 0 \leq \varepsilon \leq \frac{f_{syd}}{E_s} \\ \sigma = f_{syd} \quad ; \varepsilon > \frac{f_{syd}}{E_s} \end{array} \right. \quad \text{Eq. (2.11)}$$

$$\left\{ \begin{array}{l} \sigma = E_s \cdot \varepsilon \quad ; 0 \leq \varepsilon \leq \frac{f_{syd}}{E_s} \\ \sigma = f_{syd} + E_{sh} \cdot \left(\varepsilon - \frac{f_{syd}}{E_s} \right) \quad ; \frac{f_{syd}}{E_s} < \varepsilon \leq \varepsilon_{ud} \end{array} \right. \quad \text{Eq. (2.12)}$$

$$E_{sh} = \frac{k \cdot f_{syd} - f_{syd}}{\varepsilon_{uk} - \frac{f_{syd}}{E_s}} \quad \text{Eq. (2.13)}$$

2.3.3 FRC in tension

Contrarily to PC where the tensile strength is usually disregarded in the design process of structural elements, FRC can exhibit a significant post-cracking tensile capacity. In the pre-peak stage it is possible to assume that FRC and PC have similar response, and the existing stress-strain relationship used for PC is also applicable to FRC until this stage [30], see Figure 9:

$$\left\{ \begin{array}{l} \sigma = E_c \cdot \varepsilon \quad ; 0 \leq \varepsilon \leq 0.9 \cdot f_{ct} / E_c \\ \sigma = f_{ct} \cdot \left(1 - 0.1 \cdot \frac{0.15 \times 10^{-3} - \varepsilon}{0.15 \times 10^{-3} - 0.9 \cdot f_{ct} / E_c} \right) \quad ; 0.9 \cdot f_{ct} / E_c < \varepsilon \leq (\varepsilon_p = 0.15\%) \end{array} \right. \quad \text{Eq. (2.14)}$$

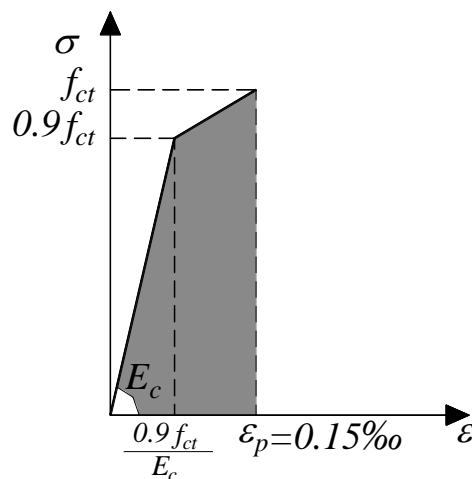


Figure 9 – Tensile stress-strain relationship for plain concrete and FRC up to material tensile strength.

As the formation of cracks in concrete is a discrete phenomenon, a stress-crack opening relationship is the most suitable formulation to describe FRC post-cracking behavior, mainly in FRC of tensile-softening nature, which is the most current in structural applications. In MC2010 different approaches are used to characterize the post-cracking tensile behavior of FRC, depending on the type of limit state verification.

For the ULS analysis two models can be used: the (i) rigid-plastic model; and the (ii) linear model. Both models are schematically presented in Figure 10, where: w_u is the ultimate crack opening corresponding to the ULS criterion; f_{Ftu} is the ultimate residual tensile strength; and f_{Fts} is the serviceability residual tensile strength. For FRC with a softening post-cracking behavior (solid lines in Figure 10) the value f_{Ftu} is lower than f_{Fts} , while for a hardening post-cracking response (dashed lines in Figure 10) the value f_{Ftu} is higher than f_{Fts} .

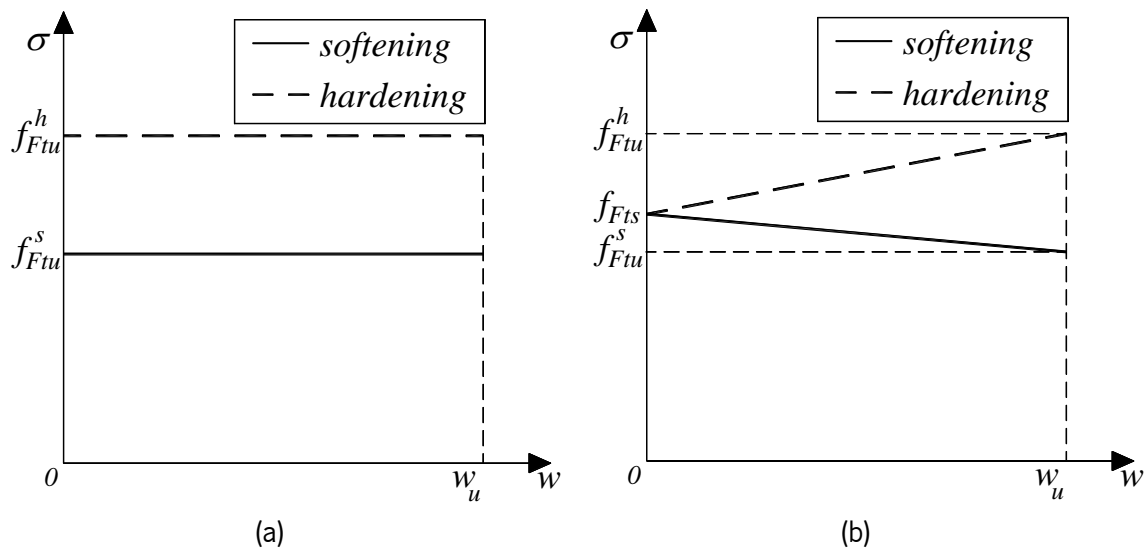


Figure 10 – Stress-crack opening constitutive laws for ULS analysis: a) rigid-plastic model; b) linear model [30].

For the rigid-plastic model, the ultimate residual tensile strength is determined from [30]:

$$f_{Ftu} = \frac{f_{R3}}{3} \quad \text{Eq. (2.15)}$$

For the linear model, the serviceability and ultimate residual tensile strength are obtained from [30]:

$$f_{Fts} = 0.45 \cdot f_{R1} \quad \text{Eq. (2.16)}$$

$$f_{Ftu} = f_{Fts} - \frac{w_u}{CMOD_3 (= 2.5mm)} \cdot (f_{Fts} - 0.5 \cdot f_{R3} + 0.2 \cdot f_{R1}) \geq 0 \quad \text{Eq. (2.17)}$$

In appendix B are presented the derivation of Eq. (2.15), Eq. (2.16) and Eq. (2.17) for the rigid-plastic and linear models.

For the rigid-plastic model the value of the ultimate crack opening is equal to $w_u = \text{CMOD}_3 = 2.5\text{mm}$, while for the linear model it depends on the ductility required, namely [30]:

$$w_u = \min(2.5\text{mm}; l_{cs} \cdot \varepsilon_{Fu}) \quad \text{Eq. (2.18)}$$

where, ε_{Fu} is the ultimate tensile strain of FRC; and l_{cs} is the structural characteristic length.

According to the MC2010, the ultimate tensile strain, ε_{Fu} , depends on the strain distribution along the cross-section. For a constant tensile strain (section under pure normal tensile force), $\varepsilon_{Fu} = 1\%$. For variable strain distribution in the cross-section (section under pure bending or combined axial-bending load), $\varepsilon_{Fu} = 2\%$ [30].

In structural elements with steel bars reinforcement, the structural characteristic length is determined from [30]:

$$l_{cs} = \min(y, s_m) \quad \text{Eq. (2.19)}$$

where, y is the distance between the neutral axis position (whose depth from the top surface is represented by x) and the tensile side of the cross-section (see Figure 11); and s_m is the mean crack spacing. In the calculation of the neutral axis position, x , a loading situation corresponding to the cracking serviceability criteria is assumed, generally the quasi-permanent load combination; and the tensile contribution of FRC can be disregarded [30]. An example of stress-strain distribution in a cross-section for the calculation of the neutral axis is presented in Figure 11. For sections without traditional reinforcements, the value of the structural characteristic length, l_{cs} , is considered equal to the cross-section height, h [30]. When necessary, the creep effect of concrete in compression can be considered following the methodology presented in Figure 7 and Eq. (2.10).

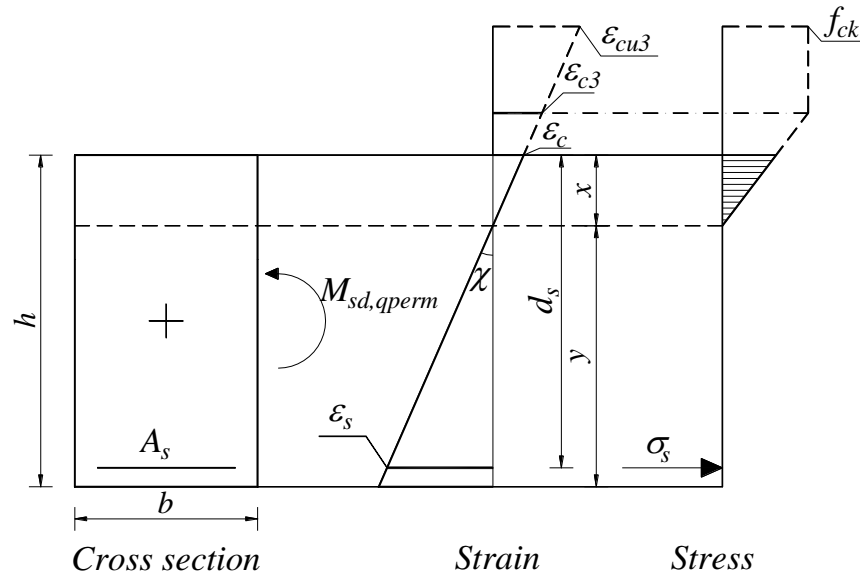


Figure 11 – Example of determination of neutral axis position, x , and y for the evaluation of l_{cs} .

For conventionally reinforced cross-sections, the mean crack spacing, s_m , can be estimated from the bond transfer length, $l_{s,max}$. The determination of mean crack spacing and bond transfer length are presented in section 2.5.

When analyzing a FRC member with conventional steel reinforcement, the cross-section must be divided due to the different structural characteristic lengths of each zone (the effective tensile zone and the remaining area of the cross-section), which requires different post-cracking constitutive laws for each zone (due to different ultimate crack opening, w_u , which has a direct influence on the structural characteristic length, l_{cs}).

As an example, in Figure 12 is presented the analysis of a U-shape cross-section of a FRC footbridge, being formed with two longitudinal hybrid reinforced beams (conventional steel bars plus fiber reinforcement) connected with a deck of a thin FRC layer. In Figure 12a) is illustrated the division of the cross-section based on the structural characteristic length of each part, where three l_{cs} are considered, one for the FRC deck, l_{cs}^D , and two for the hybrid reinforced beams, l_{cs}^{R1} and l_{cs}^{R2} . The two l_{cs} values adopted for the hybrid reinforced beams aims to better simulate the different cracking process formed in these beams due to the presence of the conventional reinforcement in the bottom part of the beam (of a depth defined by $h_{c,ef}$), and the exclusive use of FRC in the zone out of the area under the influence of this reinforcement. In Figure 12b) is schematically presented the crack pattern of the different components of the footbridge.

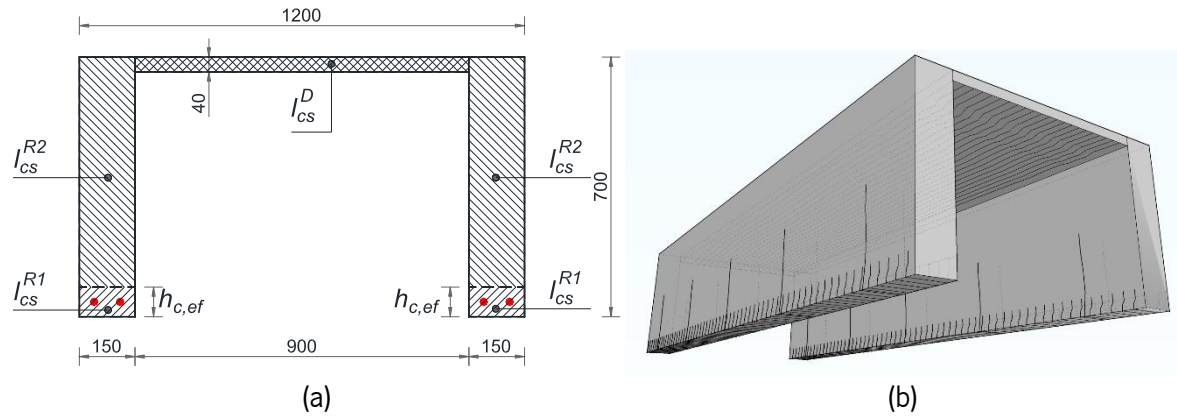


Figure 12 – Example of the analysis of a footbridge cross-section. a) Structural characteristic length; b) Crack pattern of the different components of the footbridge.

Although the stress-crack opening relationship is the most suitable model to describe the FRC post-cracking tensile response [38], the stress-strain diagram is the most used in engineering practice. Consequently, to transform the stress-crack opening relationship in a stress-strain diagram, the MC2010 [30] proposes to convert the concept of crack opening, w , in tensile strain, ε , by using the structural length parameter:

$$\varepsilon = \frac{w}{l_{cs}} \quad \text{Eq. (2.20)}$$

In Figure 13a is presented the complete stress-strain diagram for a strain softening FRC, assuming that $f_{Fts} < f_{ct}$ and the FRC's post-cracking linear model (Figure 10b). However, for the usual cases where $\varepsilon_{ULS} \gg \varepsilon_p$, and for manual calculation of the cross-section flexural capacity, the pre-cracking contribution of FRC can be disregarded and the simplified stress-strain diagram presented in Figure 13b can be adopted without a significant loss of precision. During the analysis of a cross-section, if $\varepsilon > \varepsilon_{ULS}$ a stress cut-off is assumed. The complete tensile stress-strain diagram presented in Figure 13a is mathematically described by Eq. (2.21), while in Eq. (2.22) is presented the simplified model.

$$\left\{ \begin{array}{l} \sigma = E_c \cdot \varepsilon \quad ; 0 \leq \varepsilon \leq \frac{0.9 \cdot f_{ct}}{E_c} \\ \sigma = 0.9 \cdot f_{ct} + \left(\frac{f_{ct} - 0.9 \cdot f_{ct}}{\varepsilon_p - 0.9 \cdot f_{ct} / E_c} \right) \cdot \left(\varepsilon - 0.9 \cdot f_{ct} / E_c \right) \quad ; \frac{0.9 \cdot f_{ct}}{E_c} < \varepsilon \leq \varepsilon_p \\ \sigma = f_{Fts} + \left(\frac{f_{Ftu} - f_{Fts}}{\varepsilon_{ULS} - \varepsilon_p} \right) \cdot (\varepsilon - \varepsilon_p) \quad ; \varepsilon_p < \varepsilon \leq \varepsilon_{ULS} \\ \sigma = 0 \quad ; \varepsilon > \varepsilon_{ULS} \end{array} \right. \quad \text{Eq. (2.21)}$$

$$\begin{cases} \sigma = f_{Fts} + \left(\frac{f_{Ftu} - f_{Fts}}{\epsilon_{ULS} - \epsilon_p} \right) \cdot \epsilon & ; 0 \leq \epsilon \leq \epsilon_{ULS} \\ \sigma = 0 & ; \epsilon > \epsilon_{ULS} \end{cases} \quad \text{Eq. (2.22)}$$

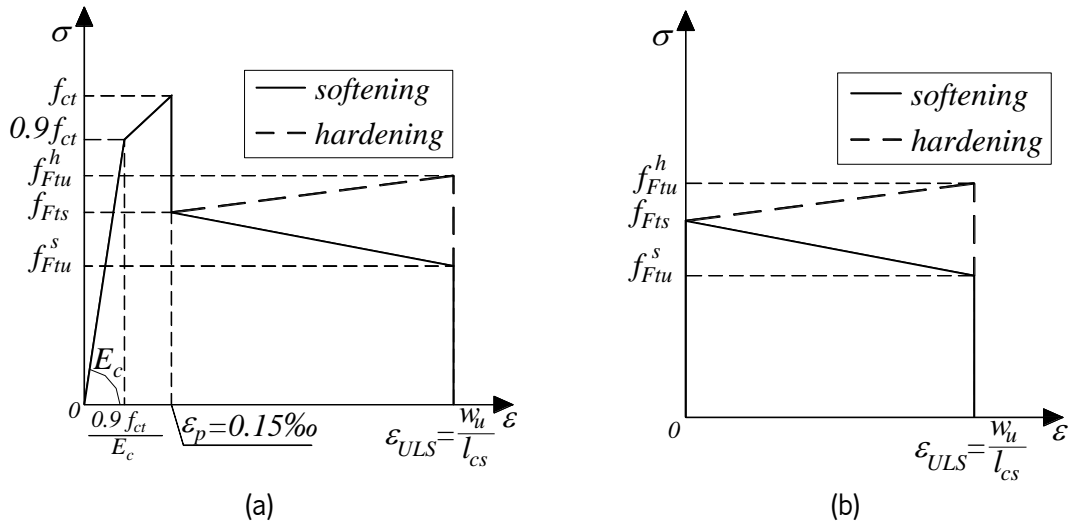


Figure 13 – Stress-strain relationship of a strain softening FRC, for ULS analysis: (a) complete diagram; (b) simplified diagram.

For the verification of the serviceability limit states (SLS), one of the three stress-strain models presented in MC2010 (Figure 14) is applicable. The residual tensile strength f_{Fts} and f_{Ftu} are determined from Eq. (2.16) and Eq. (2.17), respectively.

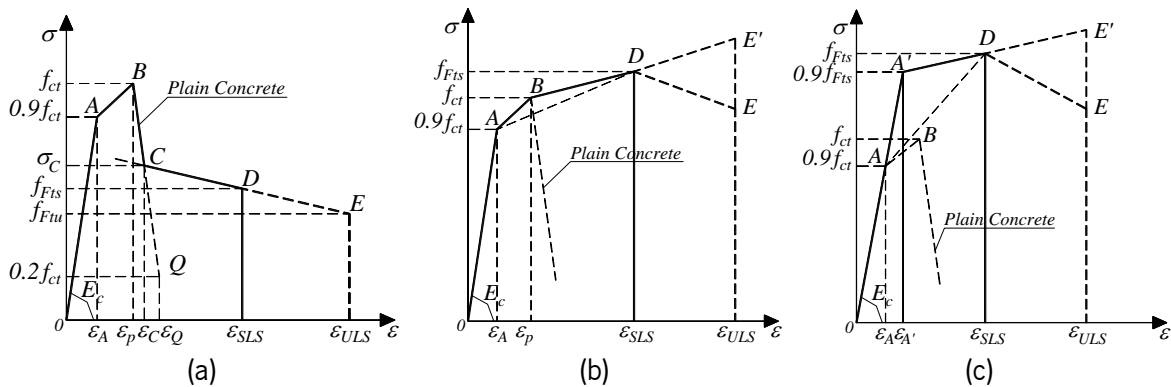


Figure 14 – Stress-strain relationship for SLS analysis: (a) Case I; (b) Case II; (c) Case III [30].

The constitutive models presented in Figure 14 have common defining points, namely points A , B , D and E . Points A and B correspond to the stress and strain values defined for un-macro-cracked plain concrete (Figure 9). Point D and E correspond, respectively, to the serviceability and ultimate deformation criteria of the material, which are determined by [30]:

$$\begin{cases} \varepsilon_{SLS} = \frac{CMOD_1}{l_{cs}} \\ \varepsilon_{ULS} = \frac{w_u}{l_{cs}} \end{cases} \quad \text{Eq. (2.23)}$$

where $CMOD_1 = 0.5mm$ and l_{cs} is determined as previously described. The corresponding stress of points D and E , f_{Fts} and f_{Ftu} , are determined according to Eq. (2.16) and Eq. (2.17), respectively.

The first model, Case I (Figure 14a), is applicable for softening materials with $f_{Fts} < f_{ct}$. The stress of point Q is equal to $\sigma_Q = 0.2 \cdot f_{ct}$, and its corresponding strain is determined from the following equation [30]:

$$\varepsilon_Q = \frac{G_f}{f_{ct} \cdot l_{cs}} + \left(\varepsilon_p - \frac{0.8 \cdot f_{ct}}{E_c} \right) \quad \text{Eq. (2.24)}$$

where G_f represents the fracture energy of a plain concrete of the same strength class of the FRC, which can be estimated from the following expression [30]:

$$G_f = \frac{73 \cdot f_{cm}^{0.18}}{1000} \left[\frac{N}{mm} \right] \quad \text{Eq. (2.25)}$$

where f_{cm} is the mean compressive strength of concrete, in MPa, that can be determined from the following expression [30]:

$$f_{cm} = f_{ck} + 8MPa \quad \text{Eq. (2.26)}$$

Point C coordinates are determined from the intersection of lines \overline{BQ} and \overline{DE} , which represents the intersection of the concrete matrix post-cracking strength with the post-cracking residual strength of FRC. Due to the dependence of ε_Q on the values of f_{ct} and l_{cs} , the application of Eq. (2.24) can result a value of strain lower than that for the tensile strength, $\varepsilon_Q < \varepsilon_p$, which has no physical meaning. In this situation, the concrete matrix post-cracking contribution is discarded, and it is assumed that $\varepsilon_Q = \varepsilon_p = 0.15\%$, as presented in Figure 15.

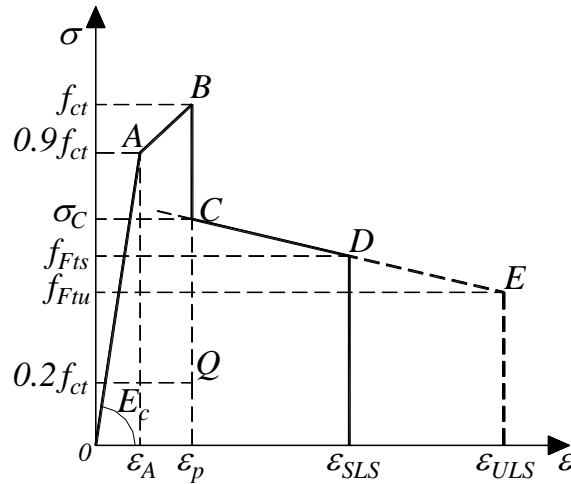


Figure 15 – SLS stress-strain case I model for situation where concrete matrix post-cracking contribution is disregarded.

Additionally, the present formulation can also result in a situation where the intersection of both lines yields $\varepsilon_C < \varepsilon_p$ (see Figure 16). In this circumstance, point C is disregarded, and point D is connected to point B.

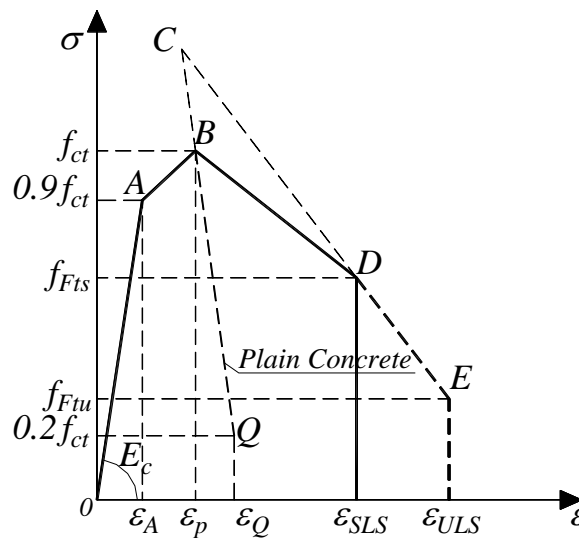


Figure 16 – Example of SLS stress-strain Case I model where point C is disregarded.

Cases II and III are applicable for materials exhibiting a stable crack propagation up to ε_{SLS} , with $f_{Fts} > f_{ct}$. Case II is applicable when:

$$\frac{\sigma_D - \sigma_A}{\varepsilon_{SLS} - \varepsilon_A} \leq \frac{\sigma_B - \sigma_A}{\varepsilon_p - \varepsilon_A} \Leftrightarrow \frac{f_{Fts} - 0.9 \cdot f_{ct}}{\varepsilon_{SLS} - 0.9 \cdot f_{ct} / E_c} \leq \frac{f_{ct} - 0.9 \cdot f_{ct}}{\varepsilon_p - 0.9 \cdot f_{ct} / E_c} \quad \text{Eq. (2.27)}$$

otherwise Case III is adopted. The equation Eq. (2.27) compares the slope of lines \overline{AD} and \overline{AB} . If the slope of line \overline{AD} is lower than the slope of line \overline{AB} , Case II is applied, otherwise Case III should

be chosen. Case III has an additional point, A' , which stress value is $\sigma_{A'} = 0.9 \cdot f_{Fts}$ and corresponding strain is $\varepsilon_{A'} = 0.9 \cdot f_{Fts} / E_c$.

In the safety assessment of a member at SLS, the principal tensile strain cannot exceed ε_{SLS} , where a stress cut-off is admitted.

Similarly to the consideration adopted for the ULS stress-strain diagram, in the common situation where $\varepsilon_{SLS} \gg \varepsilon_p$, for manual calculation of the cross-section flexural capacity, the pre-cracking contribution of FRC can be disregarded without a significant loss of precision.

Likewise to concrete in compression, for ULS and SLS analysis of a structure are used design values of the material tensile strength parameters, X_d , by adopting a partial safety factor γ_F , namely:

$$X_d = X_k / \gamma_F \quad \text{Eq. (2.28)}$$

For converting the characteristic values of the tensile strength parameters, X_k , in design values, X_d , partial safety factor, γ_F , equal to 1.0 and 1.5 are adopted for SLS and ULS, respectively.

Regarding the suitability of the MC2010 constitutive model to describe the tensile response of FRC, in [39], [40] was verified a satisfactory agreement between the measured experimental response and the numerical response obtained from a plain-section analysis of the cross-section and from numerical simulations of four-point bending tests of steel fiber reinforced concrete beams without conventional reinforcement. A has been found out However, recently carried out research pointed that the MC2010 model results in the overestimation of the residual tensile strength of steel fiber reinforced concrete when compared to experimental data obtained from uniaxial tensile tests [41].

2.4 FRC design particularities

For certain FRC applications, namely for thin walled members and for casting operations that resort to vibration, the fiber dispersion can be strongly influenced during casting procedure [39], [42]–[47]. In MC2010 these situations can be considered in the design process, by applying the orientation factor, K . The orientation factor influence is considered by modifying the serviceability and ultimate residual tensile strength of FRC, namely:

$$f_{Ftsd,mod} = f_{Ftsd} / K ; f_{Ftud,mod} = f_{Ftud} / K \quad \text{Eq. (2.29)}$$

In general, it is assumed an isotropic fiber distribution in the element and the orientation factor takes the value $K = 1.0$. For situations where the fiber distribution has been experimentally proven to have a favorable effect on the element performance, the orientation factor assumes a value lower than 1.0, while for unfavorable effect it assumes a value higher than 1.0 [30]. A scientific approach for the determination of the orientation factor, and its influence on the behavior of FRC elements is proposed in [42], [48], [49]. In chapter 5 is explored a model to consider the fibers orientation profile and fiber segregation in the analysis of FRC structural members.

The fiber dispersion on FRC elements promotes the occurrence of stress redistribution, which is quite favorable effect in statically indeterminate structures in terms of ultimate load carrying capacity and deformation performance. During the material characterization of FRC in 3PNBBT, a small volume of the material is involved in the crack propagation process at failure, leading to relatively high scatter for the f_{Rj} values. For structural applications where the volume of the material involved in the crack propagation process increases and the degree of support redundancy allows a significant stress redistribution, an increase of the ultimate load capacity of the structure, P_{Rd} , is obtained. In MC2010 this effect is given by the coefficient K_{Rd} , namely [30]:

$$P_{Rd} = K_{Rd} \cdot P(f_{Fd}) \quad \text{Eq. (2.30)}$$

where $P(f_{Fd})$ is the ultimate load that is computed considering the design strength of FRC, considering the FRC residual tensile strength derived from standard material characterization tests.

The determination of the coefficient K_{Rd} can be experimentally derived and, among other methods, by performing a statistical analysis on the variation of the ultimate load capacity, P_{max} , of a structure considering a standard deviation of the mechanical constitutive law of the FRC, namely [30]:

$$K_{Rd} = \frac{P_{max,k}}{P_{max,m}} \cdot \frac{f_{Ftum}}{f_{Ftuk}} \leq 1.4 \quad \text{Eq. (2.31)}$$

where $P_{max,k}$ and $P_{max,m}$ are, respectively, the characteristic and mean value of the maximum load; f_{Ftum} and f_{Ftuk} are, respectively, the mean and characteristic value of the ultimate residual tensile strength of FRC.

Due to the increased post-cracking tensile strength, FRC's are capable of replacing conventional rebars for flexural reinforcement. However, an assessment of the ductility capacity of the structural element

should be performed. According to MC2010, if the conventional flexural reinforcement area is higher than the minimum required area for the member, $A_{sl,min}$, which is determined by Eq. (2.32), it is possible to consider the ductility requirement satisfied.

$$A_{sl,min} = 0.26 \cdot \frac{f_{ctm}}{f_{yk}} \cdot b_t \cdot d \quad \text{Eq. (2.32)}$$

If the element reinforcement area is lower than $A_{sl,min}$, MC2010 specifies the need to verify if the ultimate displacement, δ_u , of the structural element is higher than 20 times the displacement at maximum service load, δ_{SLS} . Alternatively, if the displacement corresponding to the maximum load, δ_{peak} , is higher to 5 times the displacement at maximum service load δ_{SLS} , the ductility requirement of the member is satisfied. The ultimate displacement is related with the maximum allowable deformation of the structure or structural element. These ductility requirement conditions are presented in Eq. (2.33) and Eq. (2.34), respectively, and the variables are illustrated in Figure 17 [30]. For the estimation of the FRC's elements deformation, MC2010 suggests the execution of linear elastic analysis of the structure, assuming uncracked concrete and initial elastic Young's modulus of concrete. The ultimate load P_u should always be higher than load at crack initiation, P_{cr} , and higher than the maximum service load P_{SLS} . In the case of beam or column types of elements, subjected to a tensile-only strain distribution in the cross-section, MC2010 denotes the need to prescribe an FRC with tensile-hardening behavior, in order to avoid a fragile collapse of structures.

$$\delta_u \geq 20 \cdot \delta_{SLS} \quad \text{Eq. (2.33)}$$

$$\delta_{peak} \geq 5 \cdot \delta_{SLS} \quad \text{Eq. (2.34)}$$

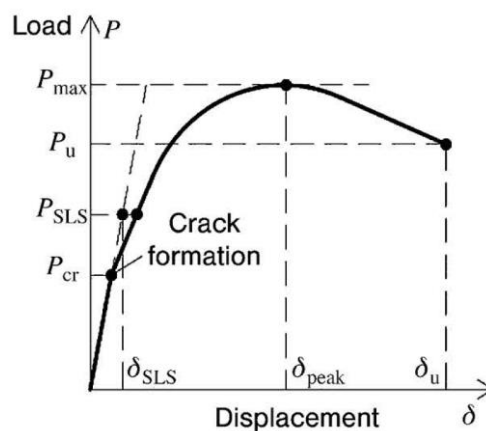


Figure 17 – Typical load-displacement curve of a FRC structural element (extracted from [30, Figs. 7.7–1]).

2.5 ULS and SLS analysis of FRC structural members

2.5.1 Members in bending

The improvement provided by the use of FRC in the flexural capacity of structural elements is granted by the post-cracking residual tensile strength contribution of the FRC in the tensile region. In order to assess the flexural response of a FRC member (beams, slabs or columns) it is necessary to define the constitutive models of the involving materials, namely the stress-strain models presented in section 2.3. To express the stress-strain law for FRC in tension it is necessary to previously determine the structural characteristic length, l_{cs} , of the cross-section and the ultimate crack width of the FRC, w_u .

In Figure 18 is presented the stress-strain distribution that can be used to determine the flexural capacity at ULS of a generic rectangular cross-section, considering the bilinear compressive stress-strain law for concrete in compression and the linear model for post-cracking response of tensile-softening FRC. Considering the existence of conventional steel reinforcements, the tension zone of the section is divided in two. The reinforced zone is limited by the extreme fiber in tension and the height of the effective tension zone, $h_{c,ef}$, while the unreinforced zone is limited by $h_{c,ef}$ and the neutral axis position. In order to establish the tensile stress-strain relationship of FRC in the section, is necessary to determine the corresponding structural characteristic length of each zone. The procedure to determine the structural characteristic length for the reinforced zone, l_{cs}^r , is presented in section 2.3, namely Eq. (2.19). The structural characteristic length of the unreinforced zone, l_{cs}^u , is equal to the element height, h , minus the height of the effective tension zone of the section, $h_{c,ef}$, namely:

$$l_{cs}^u = h - h_{c,ef} \quad \text{Eq. (2.35)}$$

Since the structural characteristic length of both zones are different, it is possible that the ultimate crack width, w_u , for each tensile zone present distinct values. Since the ultimate tensile strain for ULS verification, ε_{ULS} , and the design value of the ultimate residual tensile strength, f_{Ftud} , are dependent of w_u , the post-cracking tensile stress-strain model is different for both tensile zone of the cross-section, as it is illustrated in Figure 18.

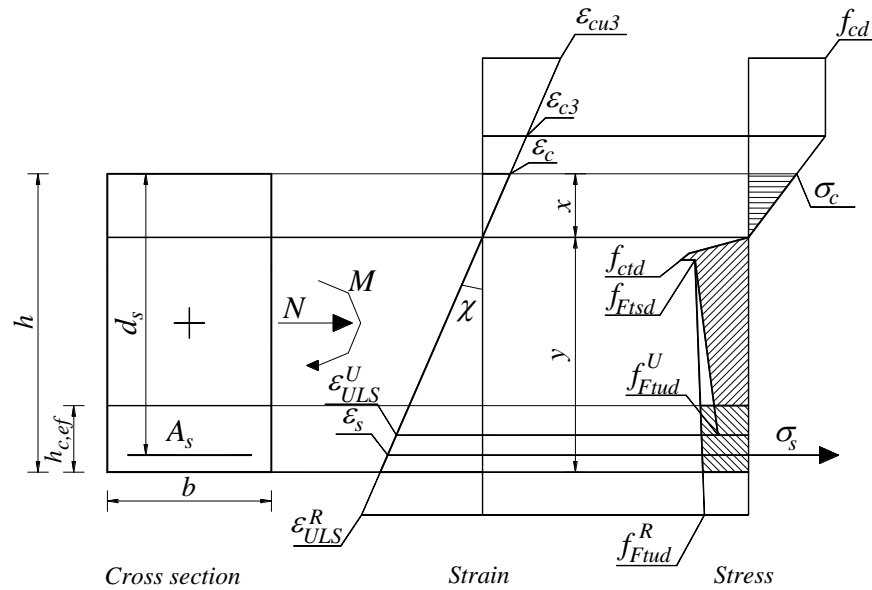


Figure 18 – Stress-strain distribution for assessing flexural response of a rectangular cross-section with longitudinal steel reinforcement and FRC tension zone divided in two parts.

On the other hand, if the longitudinal steel bars are discarded, a unique model would be used to describe the FRC post-cracking tensile stress-strain relationship, as is illustrated in Figure 19.

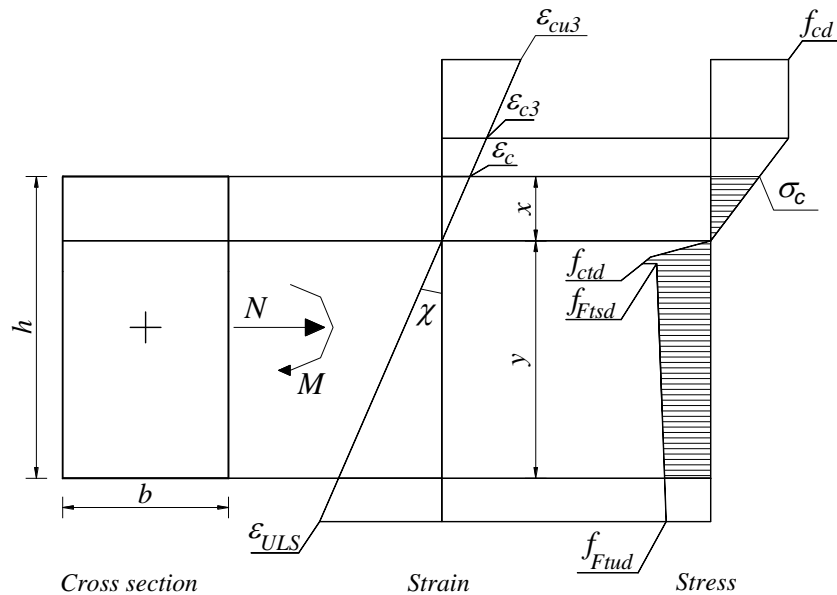


Figure 19 – Stress-strain distribution for assessing flexural response of a rectangular cross-section without longitudinal steel reinforcement.

A similar approach is used when analyzing the flexural response of a FRC cross-section for serviceability safety verifications. In this case, the tensile stress-strain model would be one of the three models presented in Figure 14.

After the definition of the constitutive models of the FRC and steel rebars, and assuming the appropriate stress-strain distribution in the cross-section, the flexural response of the structural member can be determined by considering the force and moment equilibrium in the cross-section. The resisting moment-curvature relationship of the section can be obtained by adopting an iterative approach. In each iteration, a strain increment is applied to the upper or lower fiber of section, and resorting to the resolution of the equilibrium system of equations, it is possible to determine the position of the neutral axis, and, therefore, the moment and curvature corresponding to the strain profile for the adopted strain increment. Performing this approach up to a certain strain limit in the selected control fiber of the section it is obtained the corresponding moment-curvature diagram.

For ULS analysis of slabs without conventional reinforcements and predominantly submitted to the action of bending moments, MC2010 allows the use of a simplified stress-strain distribution in the slab's cross-section (Figure 20) to evaluate the resisting moment of the slab cross-section. The FRC stress-strain distribution is based on the rigid-plastic model (Figure 10a). When performing a linear-elastic analysis of the structure, the safety verification can be easily performed by comparing the maximum principal moment with the resisting bending moment, m_{Rd} , determined from [30]:

$$m_{Rd} = \frac{f_{Ftud} \cdot t^2}{2} [\text{kN.m/m}] \quad \text{Eq. (2.36)}$$

where t is the thickness of the slab and f_{Ftud} is determined according to Eq. (2.15) and Eq. (2.28).

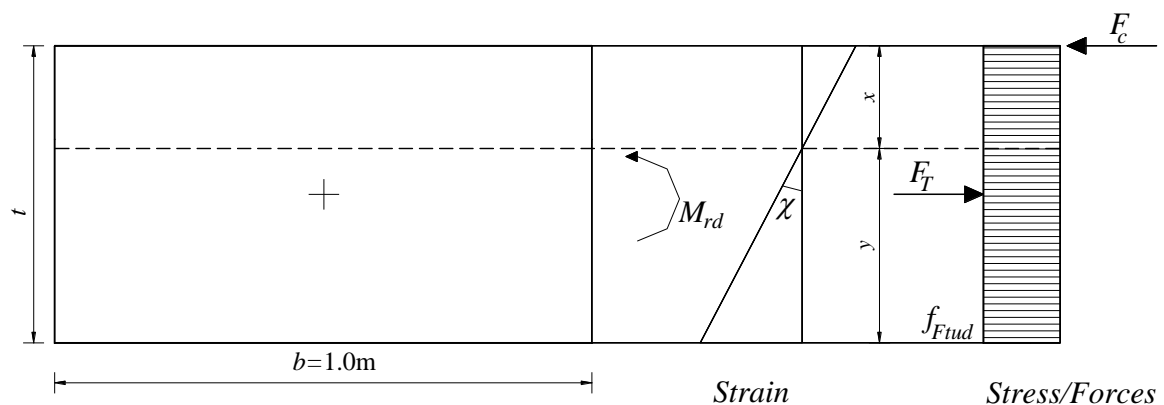


Figure 20 – Simplified stress-strain distribution in the cross-section for slab design [30].

2.5.2 Members in shear

Fiber reinforcement enhances the shear capacity of concrete, and allows a partial or total replacement of steel stirrups in structural elements [18], [50]–[54]. According to MC2010, the design value of the

shear resistance of an FRC structural element with longitudinal steel rebars and without shear reinforcement, $V_{Rd,F}$, can be evaluated by employing the expression [30]:

$$V_{Rd,F} = \left(\frac{0.18}{\gamma_c} \cdot k \cdot \left(100 \cdot \rho_{sl} \cdot \left(1 + 7.5 \cdot \frac{f_{Ftuk}}{f_{ctk}} \right) \cdot f_{ck} \right)^{1/3} + 0.15 \cdot \sigma_{cp} \right) \cdot b_w \cdot d \quad \text{Eq. (2.37)}$$

where $\gamma_c = 1.5$ is the partial safety factor for concrete without fibers; $k = 1 + \sqrt{200/d} \leq 2.0$ is a factor that takes into account the size effect; d is the effective depth of the cross section [mm]; $\rho_{sl} = A_{sl}/(b_w \cdot d)$ is the longitudinal reinforcement ratio; A_{sl} is the cross-sectional area of the longitudinal reinforcement [mm²]; f_{Ftuk} is the characteristic value of the ultimate residual tensile strength of the FRC that is computed from Eq. (2.17) considering the characteristic values of the residual flexural strength of FRC and $w_u = 1.5 \text{ mm}$ [MPa]; f_{ctk} is the characteristic tensile strength for the concrete without fibers [MPa]; f_{ck} is the characteristic compressive strength [MPa]; $\sigma_{cp} = N_{Ed}/A_c < 0.2 \cdot f_{cd}$ is the average axial stress acting in the cross-section [MPa] (considered positive in compression); and b_w is the smallest width of the tensile zone of the cross-section [mm].

The previous equation is based on the one proposed by Eurocode 2 [37] for shear contribution of plain concrete members without transverse reinforcements, by adding the contribution of FRC residual flexural strength. The effect of the dispersed fibers to shear resistance provided by the increased post-cracking toughness and crack-opening restriction is empirically considered by multiplying the longitudinal reinforcement ratio by the factor $(1 + 7.5 f_{Ftuk}/f_{ctk})$. Therefore, the contribution of fiber reinforcement is regarded as an extra flexural reinforcement, whose favorable mechanism for the shear capacity derives from the dowel effect.

It should be noticed that in Eurocode 2 is considered an upper limit of to the value of the longitudinal reinforcement ratio $\rho_{sl} \leq 0.02$ to be used in the calculation of the shear resistance of plain concrete members. Although this condition is not established in MC2010 for FRC members, a similar limit should be applied in Eq. (2.37) [55].

According to *fib* Bulletin 57 [56], the applicability of Eq. (2.37) is limited to elements where shear diagonal failure is expected and arch action is insignificant, namely for elements with ratio $a/d \geq 2.5$, being a the shear span.

The shear resistance, $V_{Rd,F}$, is assumed to be not smaller than the minimum value, $V_{Rd,F,\min}$, obtained from:

$$V_{Rd,F,\min} = (v_{\min} + 0.15 \cdot \sigma_{cp}) \cdot b_w \cdot d \quad \text{Eq. (2.38)}$$

$$v_{\min} = 0.035 \cdot k^{3/2} \cdot f_{ck}^{1/2} \quad \text{Eq. (2.39)}$$

In MC2010, for structural members with transverse reinforcements is considered the following relation:

$$V_{Rd} = V_{Rd,F} + V_{Rd,s} \leq V_{Rd,\max} \quad \text{Eq. (2.40)}$$

where, $V_{Rd,s}$ is the shear resistance provided by the web reinforcement and $V_{Rd,\max}$ is the maximum shear capacity without concrete crushing. According to MC2010, $V_{Rd,s}$ is determined according to the model proposed for RC elements, where is only possible to consider the added contribution of $V_{Rd,s}$ and $V_{Rd,F}$ for the level of approximation III (based on the simplified modified compression field theory) and IV, and the same principle must be applicable to FRC. However, the use of the same model to determine $V_{Rd,s}$ for FRC and RC cross-sections is dubious, due to the expected difference in the rotation of the critical diagonal crack between RC and FRC elements. Due to this, the added contribution of $V_{Rd,s}$ and $V_{Rd,F}$ is not recommended when adopting this shear model to determine the shear resistance of a FRC structural element.

Although Eq. (2.37) generally returns reasonably good estimates when compared with available experimental data, its empirical based formulation, when compared to the physical approach to describe shear of reinforced plain concrete members, can be seen as a drawback [55]. Therefore, the combination of both models, as considered, can be questionable.

A more recent model describing fiber reinforcement contribution to shear resistance based on the Variable Engagement Model (VEM) [57] and on the Simplified Modified Compression Field Theory (SMCFT) [58] is also presented in MC2010. Based on this model, the design value of shear resistance of FRC members with longitudinal and transverse reinforcements is equal to:

$$V_{Rd} = V_{Rd,F} + V_{Rd,s} \leq V_{Rd,\max} \quad \text{Eq. (2.41)}$$

The FRC shear resistance, $V_{Rd,F}$, is the result of the added shear resistance of the concrete matrix, $V_{Rd,c}$, and fiber reinforcements bridging the shear cracks, $V_{Rd,f}$, and is determined from [30]:

$$V_{Rd,F} = V_{Rd,c} + V_{Rd,f} = \frac{1}{\gamma_F} \cdot (v_{Rd,c} + v_{Rd,f}) \cdot z \cdot b_w \quad \text{Eq. (2.42)}$$

where, z is the internal lever arm, that can be estimated as $z = 0.9 \cdot d$ [mm] [30].

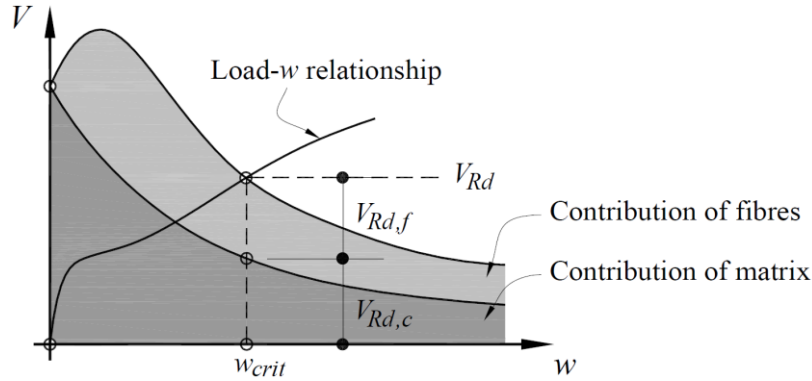


Figure 21 – Contribution of concrete matrix and fiber reinforcements for FRC shear resistance (extracted from [55]).

The concrete matrix shear strength is provided by the aggregate interlock, which is dependent on the concrete compressive strength, size of aggregate particles and on the shear crack width, namely [30]:

$$v_{Rd,c} = k_v \cdot \sqrt{f_{ck}} \quad \text{Eq. (2.43)}$$

where k_v is the parameter that determines the contribution of the aggregate interlock mechanism for the shear strength of the cross section (Eq. (2.44)). The parameter k_v is function of the parameter that considers the aggregate size influence (Eq. (2.45)), k_{dg} , and of the longitudinal strain at the mid depth of the effective shear area, ε_x . Although in MC2010 is not specified a limit for the value of $\sqrt{f_{ck}}$, a limiting value of $\sqrt{f_{ck}} \leq 8 \text{ MPa}$ should be implemented in Eq. (2.43), similarly to the expression used to determine the concrete matrix contribution for plain concrete.

$$k_v = \begin{cases} \frac{0.4}{1+1500 \cdot \varepsilon_x} \cdot \frac{1300}{1000+z \cdot k_{dg}} & \text{for } \rho_w < 0.08 \cdot \sqrt{f_{ck}/f_{yk}} \\ \frac{0.4}{1+1500 \cdot \varepsilon_x} & \text{for } \rho_w \geq 0.08 \cdot \sqrt{f_{ck}/f_{yk}} \end{cases} > 0.0 \quad \text{Eq. (2.44)}$$

$$k_{dg} = \begin{cases} \frac{32}{16+d_g} \geq 0.75 & \text{for } f_{ck} \leq 70 \text{ MPa} \\ 2.0 & \text{for } f_{ck} > 70 \text{ MPa and for lightweight concrete} \end{cases} \quad \text{Eq. (2.45)}$$

In Eq. (2.44), the term ρ_w represents the transverse reinforcement ratio of the cross-section, that is given by [30]:

$$\rho_w = \frac{A_{sw}}{b_w \cdot s_w \cdot \sin \alpha} \quad \text{Eq. (2.46)}$$

where, A_{sw} is the shear reinforcement area [mm²]; s_w is the longitudinal spacing between shear reinforcement bars [mm]; and α is the inclination of the transverse reinforcements with the element longitudinal axis.

In Eq. (2.45) the term d_g is the maximum aggregate dimension in the concrete matrix [mm].

In Figure 22 is illustrated the simple truss model of a beam subjected to bending, shear and axial load that, by conducting a plane section analysis ignoring the tension stiffening effect, allows the determination of the “representative” longitudinal strain, ε_x , at the mid-depth of the effective shear area, which is required in the analysis of shear reinforced members [30], [59]. Considering the equilibrium of forces and $A_p = 0$, it is possible to obtain the tension chord force, as [59]:

$$F_t = \frac{M_{Ed}}{z} + \frac{V_{Ed}}{2} \cot \theta + N_{Ed} \cdot \left(\frac{1}{2} \pm \frac{\Delta e}{z} \right) \quad \text{Eq. (2.47)}$$

where:

- M_{Ed} and V_{Ed} assume positive values and N_{Ed} value is positive for tension and negative for compression;
- Δe is the eccentricity of the beam axis with respect to its mid-depth of the shear height.

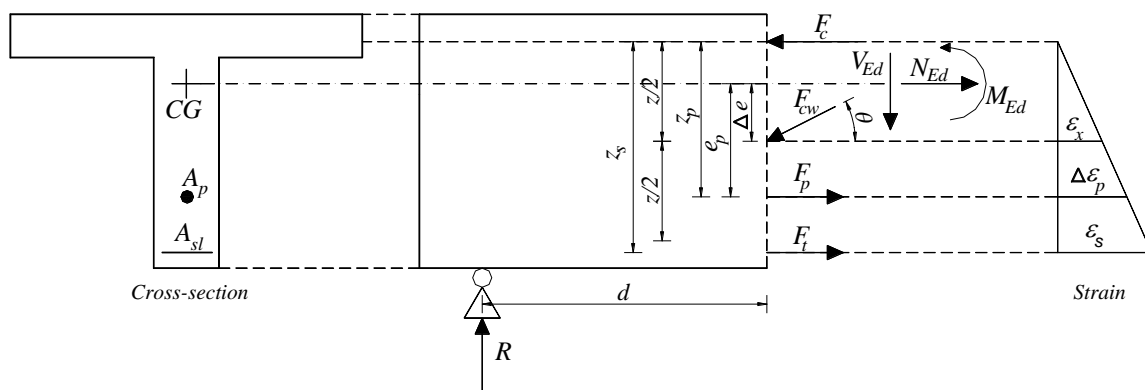


Figure 22 – Equilibrium at cross-section and corresponding strain profile [59].

Assuming the simplification that the strain in the compressive chord is equal to zero, the strain, ε_x , at mid-depth of the effective shear depth is defined as half the tension chord strain, ε_s , namely [30], [59]:

$$\varepsilon_x = 0 \leq \frac{\varepsilon_s}{2} \leq 0.003 \Leftrightarrow$$

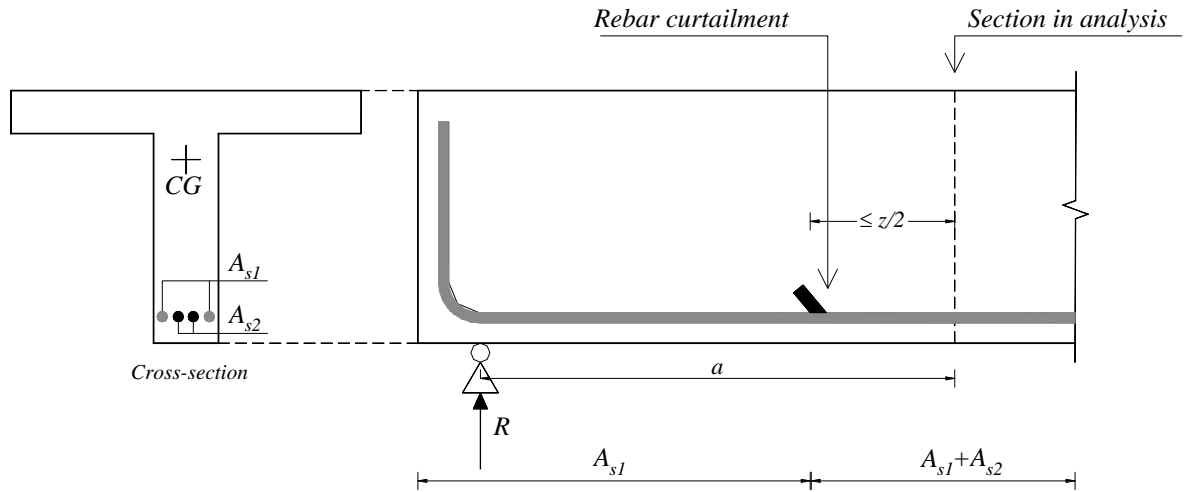
$$\varepsilon_x = 0 \leq \frac{1}{2 \cdot E_s \cdot A_{sl}} \cdot \left(\frac{M_{Ed}}{z} + \frac{V_{Ed}}{2} \cot \theta + N_{Ed} \cdot \left(\frac{1}{2} \pm \frac{\Delta e}{z} \right) \right) \leq 0.003 \quad \text{Eq. (2.48)}$$

In order to avoid an iterative process to calculate ε_x , the second term of Eq. (2.47) can be approximated by $V_{Ed}/2 \cot \theta \approx V_{Ed}$ [59].

$$\varepsilon_x = 0 \leq \frac{1}{2 \cdot E_s \cdot A_{sl}} \cdot \left(\frac{M_{Ed}}{z} + V_{Ed} + N_{Ed} \cdot \left(\frac{1}{2} \pm \frac{\Delta e}{z} \right) \right) \leq 0.003 \quad \text{Eq. (2.49)}$$

MC2010 presents the following conditions for application of Eq. (2.49):

- A_{sl} comprises the main longitudinal reinforcement in the tensile chord, while any other distributed longitudinal reinforcement must be disregarded;
- If longitudinal reinforcement bars do not respect the required development length, l_p , (§6.1.8.6 MC2010) from the section under consideration, the value of A_{sl} must be reduced proportionally to the lack of development length;
- The strain ε_x must not exceed 3.0‰ ;
- If the strain ε_x is negative (compression), it must be taken as zero;
- When analyzing sections within a distance $z/2$ of a significant rebar curtailment (see Figure 23), the calculated value of ε_x must be multiplied by 1.5;
- If the axial tension is large enough to crack the flexural compression face of the section, the value of ε_x must be multiplied by 2.0.


 Figure 23 – Example of ε_x adjustment due to proximity of rebar curtailment.

For a prestressed FRC member ($A_p > 0$), the longitudinal strain ε_x , can be obtained from [30]:

$$\varepsilon_x = 0 \leq \frac{\left(\frac{M_{Ed}}{z} + V_{Ed} \cdot \cot \theta + N_{Ed} \cdot \left(\frac{z_p - e_p}{z} \right) \right)}{2 \cdot \left(\frac{z_s}{z} \cdot E_s \cdot A_s + \frac{z_p}{z} \cdot E_p \cdot A_p \right)} \leq 0.003 \quad \text{Eq. (2.50)}$$

with z_s and z_p represent the internal lever arm of the passive and prestress reinforcements, respectively, e_p is the prestress eccentricity and z is considered as the effective shear depth, that can be taken as [30]:

$$z = \frac{z_s^2 \cdot A_{sl} + z_p^2 \cdot A_p}{z_s \cdot A_{sl} + z_p \cdot A_p} \quad \text{Eq. (2.51)}$$

According to MC2010, the value of θ can be freely chose in the interval of $\theta_{\min} \leq \theta \leq 45^\circ$, while the value of θ_{\min} is related with the longitudinal strain level in the mid-depth of the cross-section, ε_x , which can be obtained from [30]:

$$\theta_{\min} = \left(29^\circ + 7000 \cdot \varepsilon_x \right) \quad \text{Eq. (2.52)}$$

The shear strength provided by the fiber reinforcements bridging the shear diagonal cracks is obtained from [30]:

$$v_{Rd,f} = k_{fd} \cdot f_{Tk} (w_u) \cdot \cot \theta \quad \text{Eq. (2.53)}$$

where, k_{fd} is a fiber dispersion reduction factor [55], assuming the value of $k_{fd} = 0.8$ [30]; $f_{Tk}(w_u)$ is the characteristic value of the post-cracking tensile capacity of FRC, evaluated at the ultimate crack width, w_u , that can be determined from direct tensile tests. As the execution of direct tensile tests is quite cumbersome, alternatively, $f_{Tk}(w_u)$ can be estimated according to Eq. (2.54), considering $w = w_u$ [60]:

$$f_{Tk}(w) = k_o \min(0.4f_{R2k} + 1.2(f_{R4k} - f_{R2k}) \xi(w), f_{ctk,\min}) \quad \text{Eq. (2.54)}$$

$$\xi(w) = \alpha \cdot w - 0.25 \quad \text{Eq. (2.55)}$$

Eq. (2.54) is based on the work of [61] that derived the $\sigma - \varepsilon$ relationship of FRC from inverse analysis using the results of prism bending tests. The factor k_G considers the fiber alignment due to casting bias and wall influences that occur in the prism bending test. In Table 2 is presented the value of k_G considering the different prism bending test standards. The value of factor α also depends on the prism bending test configuration and is presented in Table 2.

Table 2 – Value of k_G and α depending on prism bending test standard [60].

Prism bending test normative	k_G	α
ASTM 1609 [62]	0.70	1/3
EN 14651 [34]	0.60	5/12
RILEM TC 162-TDF [35]	0.60	5/12
UNI 11039 [63]	0.60	43/84

For design situations, where it may only be prescribed the toughness and strength class of the FRC, it is possible to estimate the characteristic values of the residual flexural strength f_{R2k} and f_{R4k} , based on the work of Moraes Neto, et al. [64], [65], that derived relationships between the reinforcement index ($IR = V_f \cdot l_f / d_f$) and the post peak residual flexural strength of hooked end steel fiber reinforced concrete based on inverse analysis of the results of 3PNBBT, namely:

$$f_{R1k} = 7.5 \cdot \left(V_f \cdot \frac{l_f}{d_f} \right)^{0.8} \quad \text{Eq. (2.56)}$$

$$f_{R2k} = 6.8 \cdot \left(V_f \cdot \frac{l_f}{d_f} \right)^{0.75} \quad \text{Eq. (2.57)}$$

$$f_{R3k} = 6.0 \cdot \left(V_f \cdot \frac{l_f}{d_f} \right)^{0.7} \quad \text{Eq. (2.58)}$$

$$f_{R4k} = 5.5 \cdot \left(V_f \cdot \frac{l_f}{d_f} \right)^{0.65} \quad \text{Eq. (2.59)}$$

Alternatively, in the work developed by Moussa [66] it was also derived a relationship (Eq. (2.61)) between the residual flexural strength and the reinforcement index, IR , and the concrete average tensile strength, f_{ctm} , based on the analysis of 89 samples of hooked end steel fiber reinforced concrete notched beams submitted to 3-point bending tests according to EN 14651 [34].

$$f_{R1} = \frac{k_{1,R1} \cdot f_{ctm} \cdot (IR)^{k_{2,R1}}}{\gamma_F} \quad \text{Eq. (2.60)}$$

Additionally, it was also derived a relationship between the residual flexural strength f_{Ri} , $i = 2, 3, 4$ and f_{R1} , namely:

$$f_{Ri} = \frac{k_{1,Ri}}{\gamma_F} \cdot (f_{R1})^{k_{2,Ri}} \quad i = 2, 3, 4 \quad \text{Eq. (2.61)}$$

In Eq. (2.60) and Eq. (2.61) γ_F is the partial safety factor, that assumes the value of $\gamma_F = 1.5$ for design situations; $k_{1,Ri}$ and $k_{2,Ri}$, ($i = 1, 2, 3, 4$) are obtained from Eq. (2.62) to Eq. (2.69), considering the intervals of the FRC mean compressive strength, f_{cm} . The use of Eq. (2.61), and Eq. (2.62) to Eq. (2.69) is restricted for $f_{cm} \leq 70MPa$, as the formulation tends to overestimate the residual flexural strength of SFRC for $f_{cm} > 70MPa$ (few data existed in this interval when deriving the expressions).

$$k_{1,R1} = \begin{cases} 3.2 & , f_{cm} < 25MPa \\ 1.1 \times 10^{-3} \cdot f_{cm}^2 - 0.1 \cdot f_{cm} + 5 & , 25MPa \leq f_{cm} \leq 65MPa \\ 3.2 & , f_{cm} > 65MPa \end{cases} \quad \text{Eq. (2.62)}$$

$$k_{2,R1} = \begin{cases} 0.5 & , f_{cm} < 25MPa \\ 8 \times 10^{-3} \cdot f_{cm} + 0.32 & , 25MPa \leq f_{cm} \leq 65MPa \\ 0.85 & , f_{cm} > 65MPa \end{cases} \quad \text{Eq. (2.63)}$$

$$k_{1,R2} = \begin{cases} 0.9 & , f_{cm} < 25MPa \\ -3.8 \times 10^{-4} \cdot f_{cm}^2 + 3.2 \times 10^{-2} \cdot f_{cm} + 0.35 & , 25MPa \leq f_{cm} \leq 65MPa \\ 0.8 & , f_{cm} > 65MPa \end{cases} \quad \text{Eq. (2.64)}$$

$$k_{2,R2} = \begin{cases} 1.1 & , f_{cm} < 25MPa \\ 3 \times 10^{-4} \cdot f_{cm}^2 - 2.8 \times 10^{-2} \cdot f_{cm} + 1.6 & , 25MPa \leq f_{cm} \leq 65MPa \\ 1.1 & , f_{cm} > 65MPa \end{cases} \quad \text{Eq. (2.65)}$$

$$k_{1,R3} = \begin{cases} 0.88 & , f_{cm} < 25MPa \\ -8 \times 10^{-4} \cdot f_{cm}^2 + 6.05 \times 10^{-2} \cdot f_{cm} - 0.14 & , 25MPa \leq f_{cm} \leq 65MPa \\ 0.4 & , f_{cm} > 65MPa \end{cases} \quad \text{Eq. (2.66)}$$

$$k_{2,R3} = \begin{cases} 1.12 & , f_{cm} < 25MPa \\ 8 \times 10^{-4} \cdot f_{cm}^2 - 6.78 \times 10^{-2} \cdot f_{cm} + 2.31 & , 25MPa \leq f_{cm} \leq 65MPa \\ 1.3 & , f_{cm} > 65MPa \end{cases} \quad \text{Eq. (2.67)}$$

$$k_{1,R4} = \begin{cases} 0.8 & , f_{cm} < 25MPa \\ -1.06 \times 10^{-3} \cdot f_{cm}^2 + 8.4 \times 10^{-2} \cdot f_{cm} - 0.66 & , 25MPa \leq f_{cm} \leq 65MPa \\ 0.3 & , f_{cm} > 65MPa \end{cases} \quad \text{Eq. (2.68)}$$

$$k_{2,R4} = \begin{cases} 1.12 & , f_{cm} < 25MPa \\ 1.1 \times 10^{-3} \cdot f_{cm}^2 - 9.26 \times 10^{-2} \cdot f_{cm} + 2.75 & , 25MPa \leq f_{cm} \leq 65MPa \\ 1.38 & , f_{cm} > 65MPa \end{cases} \quad \text{Eq. (2.69)}$$

Considering the value of f_{R1k} and f_{R3k} defined by the toughness, it is possible to estimate f_{R2k} and f_{R4k} following the one of the two approaches defined in Figure 24. For the approach using the expressions derived by Moussa [66] it is also necessary to consider the mean compressive and tensile strength of concrete.

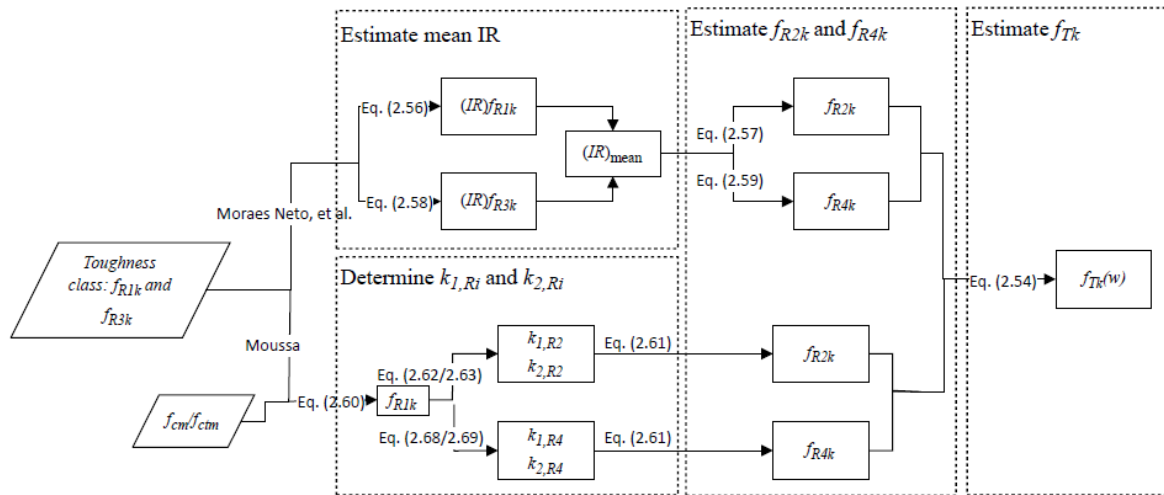


Figure 24 – Approach to estimate f_{R2k} and f_{R4k} based on the toughness class of the FRC.

According to MC2010, the ultimate crack width orthogonal to the critical diagonal crack (CDC), w_u , is determined according to Eq. (2.70). In Figure 25 is presented the definition of w_u .

$$w_u = (0.2 + 1000 \cdot \varepsilon_x) \geq 0.125 \text{ mm} \quad \text{Eq. (2.70)}$$

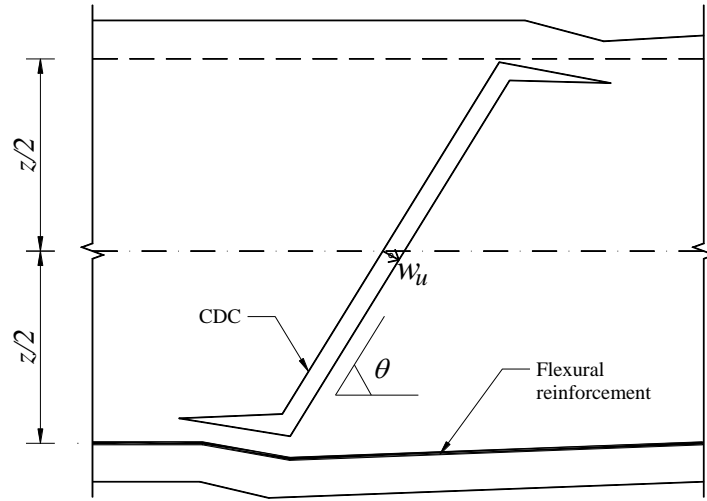


Figure 25 – Ultimate crack width orthogonal to the CDC.

The shear reinforcement resistance, $V_{Rd,s}$, is determined according to the following expression [30]:

$$V_{Rd,s} = \frac{A_{sw}}{s_w} \cdot z \cdot f_{ywd} \cdot (\cot \theta + \cot \alpha) \cdot \sin \alpha \quad \text{Eq. (2.71)}$$

where, A_{sw} is the shear reinforcement area [mm²]; and f_{ywd} is design value of the yield strength of the shear reinforcement.

The design shear resistance cannot exceed the crushing capacity of concrete in the web, determined as [30]:

$$V_{Rd,max} = k_c \cdot \frac{f_{ck}}{\gamma_c} \cdot b_w \cdot z \cdot \frac{\cot \theta + \cot \alpha}{1 + \cot^2 \theta} \quad \text{Eq. (2.72)}$$

where, k_c is a strength reduction factor, defined by $k_c = k_\epsilon \cdot \eta_{fc}$; k_ϵ is a factor that takes into account the strain in the web of the structural element, and is determined according to the level of approximation defined in MC2010 (level of approximation I : $k_\epsilon = 0.55$; level of approximation II and III : Eq. (2.73)); η_{fc} is a factor to consider the effect of more brittle failure for high strength concrete compositions, and is determined from Eq. (2.75); and θ is the inclination of the principal compressive stress in the web, relative to the longitudinal axis of the member.

$$k_\epsilon = \frac{1}{1.2 + 55 \cdot \epsilon_1} \leq 0.65 \quad \text{Eq. (2.73)}$$

$$\epsilon_1 = \epsilon_x + (\epsilon_x + 0.002) \cdot \cot^2 \theta \quad \text{Eq. (2.74)}$$

$$\eta_{fc} = \left(\frac{30}{f_{ck}} \right)^{1/3} \leq 1.0 \quad (f_{ck} \text{ in MPa}) \quad \text{Eq. (2.75)}$$

The shear model that combines VEM and SMCFT prediction capacity was assessed in [55] and [56] by comparison with experimental results of steel fiber reinforced concrete beams failing in shear, and was observed good agreement between the model and the experimental results. In chapter 4 is presented a comparison of the results of the shear resistance prediction models, whose formulation was applied to a database of shear tests of FRC beams.

The exclusive use of fibers for shear reinforcement, i.e. members without shear or longitudinal reinforcements, is limited to tensile-hardening FRC's. In this situation, the principal tensile stress, σ_1 , in the member must accomplish the following condition [30]:

$$\sigma_1 \leq \frac{f_{Ftuk}}{\gamma_F} \quad \text{Eq. (2.76)}$$

where, f_{Ftuk} is the characteristic ultimate residual tensile strength of FRC computed according to Eq. (2.17) considering $w_u = 1.5mm$.

Additionally, for FRC slabs without conventional reinforcements or prestressing, it can be considered that shear failure is not dominant as flexural failure, unless significant concentrated loads are applied near supports [30].

Due to the crack-opening resistance provided by FRC, the minimum shear reinforcement for beams can be disregarded if an appropriate value of ultimate residual tensile strength of FRC is guaranteed in order to assure sufficient ductility. According to MC2010, this condition is verified if:

$$f_{Ftuk} \geq 0.08 \cdot \sqrt{f_{ck}} \quad \text{Eq. (2.77)}$$

where, f_{Ftuk} is the characteristic value of the residual tensile strength of FRC determined according to Eq. (2.17), considering $w_u = 1.5mm$.

When Eq. (2.77) is not fulfilled, a minimum reinforcement area, $A_{sw,min}$ must be adopted. According to MC2010, the value of $A_{sw,min}$ for beams is determined from Eq. (2.78).

$$A_{sw,min} = 0.08 \cdot \sqrt{f_{ck}} \cdot \frac{b_w \cdot s_w \cdot \sin \alpha}{f_{yk}} \quad \text{Eq. (2.78)}$$

2.5.3 Punching

The punching shear analysis of FRC slabs can be conducted according to the Critical Shear Crack Theory (CSCT) [67]. The CSCT is based on the assumption that shear strength in members without shear reinforcement is governed by the tensile stresses and aggregate interlocking that develop along the critical shear crack [67]. With the formation of the critical shear crack (Figure 26a), the associated failure mode is characterized by the rotation of the slab (ψ) and spalling of concrete cover of the flexural reinforcement (Figure 26b).

For plain concrete, with the increase of slab's rotation, the favorable effects of aggregate interlock and tensile strength of concrete decrease [67]. Due to the enhanced post-cracking behavior and crack-opening restriction provided by fiber reinforcements, the punching shear resistance of FRC's slabs can be significantly improved.

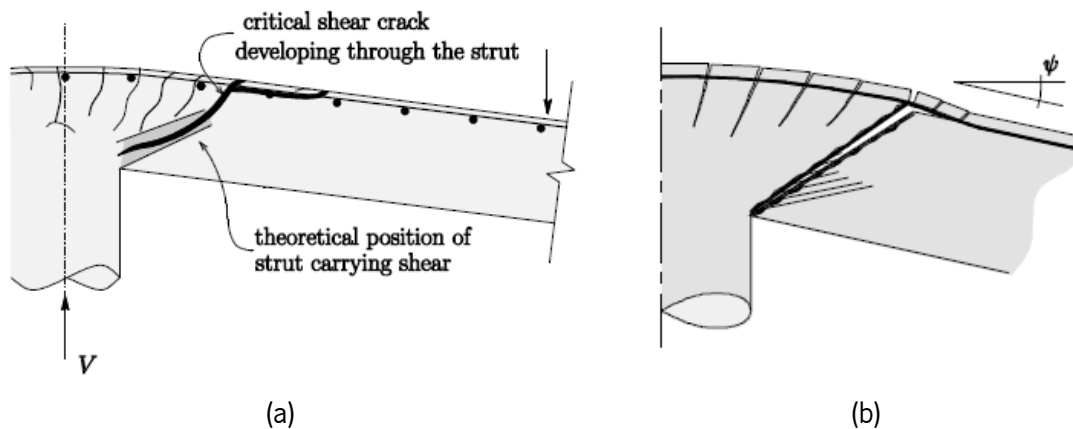


Figure 26 – Punching of slab. a) Development of critical shear crack; b) Slab's rotation and concrete cover spalling (extracted from [67]).

The FRC can be considered as a composite material, whose behavior after cracking depends on the matrix strength, $P_{Rd,c}$, and fiber post-cracking strength, $P_{Rd,f}$. According to MC2010, the punching shear resistance of a FRC slab, P_{Rd} can be taken as:

$$P_{Rd} = P_{Rd,F} + P_{Rd,s} \quad \text{Eq. (2.79)}$$

$$P_{Rd,F} = P_{Rd,c} + P_{Rd,f} \quad \text{Eq. (2.80)}$$

where $P_{Rd,s}$ is the design punching shear resistance ensured by transverse reinforcement.

The punching shear resistance provided by the fiber reinforcements is a consequence of the improved post-cracking strength of FRC, which is dependent on the crack width opening of the critical shear crack. The crack width can be estimated by the following relationship (Figure 27b,c) [67]:

$$w = \kappa \cdot \psi \cdot \xi \quad \text{Eq. (2.81)}$$

where ψ is the slab rotation, ξ is the distance from the soffit of the slab and κ is a coefficient relating total rotation and critical crack width opening, which for design purposes can take the value of $\kappa = 0.5$. In this manner, the tensile stress of the fibers can be related with the slab's rotation and position of the fibers, $\sigma_{tf}(\psi, \xi)$. By integration of this law to the failure surface, the punching shear-carrying capacity of the fiber reinforcements is [67]:

$$P_{Rd,f} = \int_{A_p} \sigma_{tf}(\psi, \xi) dA_p \quad \text{Eq. (2.82)}$$

where A_p is the horizontally projected area of the failure surface (Figure 27d).

The punching shear strength of the FRC slab can be determined by the intersection of the load-rotation relationship of the slab with the similar relation of the added contribution of the matrix and fiber shear resistance (Figure 27e) [67].

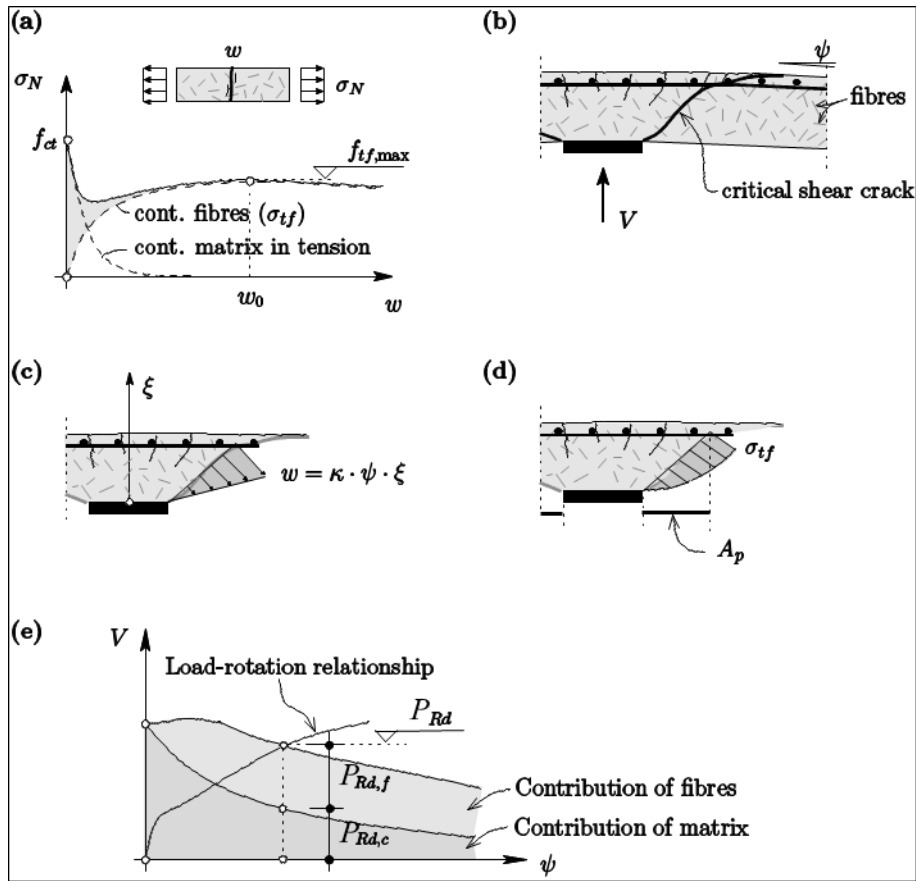


Figure 27 – Punching of FRC slabs: (a) behavior of FRC after cracking; (b) critical shear crack in slabs; (c) assumed distribution of crack widths along the failure surface; (d) profile of fibers' stress along the failure surface; and (e) matrix (concrete) and fiber contributions for the punching shear strength (adapted from [67]).

A simplified method has been implemented in MC2010, also based in the CSCT theory, which consists on the consideration of an average value of the fiber's stress. The full integral is converted to a multiplication of the average fiber's stress with the projected area of the failure surface, namely:

$$P_{Rd,f} = \int_{A_p} \sigma_{tf}(\psi, \xi) \cdot dA_p = A_p \cdot \sigma_{tf}(\psi, h_c) \quad \text{Eq. (2.83)}$$

where h_c is the control distance from the soffit of the slab at which the average stress is considered. According to [67], the value of $h_c = d/3$ leads to results in agreement with experimental evidence. According to Eq. (2.81), the estimated crack width opening takes the value:

$$w_u = 0.5 \cdot \psi \cdot \frac{d}{3} = \frac{\psi \cdot d}{6} \quad \text{Eq. (2.84)}$$

For design purposes, in MC2010 is presented a simplified methodology to compute the punching shear contribution provided by the fiber reinforcement, $P_{Rd,f}$, that overcomes the need to determine

the slab's rotation ψ . The formulation is based in Eq. (2.83) and Eq. (2.84). The projected area of the failure surface is taken as:

$$A_p = b_0 \cdot d_v \quad \text{Eq. (2.85)}$$

where, b_0 is the punching shear resistance control perimeter; d_v is the shear resisting effective depth, considered as the mean value of longitudinal reinforcement depth applied in the x and y directions of the slab.

Additionally, it is considered that the average tensile stress of fibers σ_{ff} is equal to:

$$\sigma_{ff} \left(w_u = \frac{\psi \cdot d}{6} \right) = f_{Ftu} (w_u = 1.5mm) \quad \text{Eq. (2.86)}$$

The design value of the punching shear contribution provided by the fiber reinforcement proposed by MC2010 results in:

$$P_{Rd,f} = \frac{f_{Ftuk}}{\gamma_F} \cdot b_0 \cdot d_v \quad \text{Eq. (2.87)}$$

where, $\gamma_F = 1.5$ is the partial safety factor for FRC for ULS analysis; f_{Ftuk} is the characteristic value of the ultimate residual tensile strength of the FRC that is computed from Eq. (2.17) considering the characteristic value of the residual flexural strength parameters of FRC, in MPa; and $w_u = 1.5mm$;

The FRC punching resistance contribution should be added to the matrix shear strength, $V_{Rd,c}$ and conventional transverse reinforcement contribution.

According to MC2010, the concrete matrix punching shear strength is determined as follows:

$$V_{Rd,c} = k_\psi \cdot \frac{\sqrt{f_{ck}}}{\gamma_c} \cdot b_0 \cdot d_v \quad \text{Eq. (2.88)}$$

where, k_ψ is a factor accounting for opening and roughness of cracks, and is dependent on the slab's rotation (Eq. (2.89)).

$$k_\psi = \frac{1}{1.5 + 0.9 \cdot k_{dg} \cdot \psi \cdot d_v} \quad \text{Eq. (2.89)}$$

In Eq. (2.89) the variable k_{dg} represents an aggregate's size effect coefficient that influences the aggregate interlocking in the critical shear crack, and is determined according to Eq. (2.90), where d_g is the maximum aggregate dimension in the concrete matrix [mm]. For high strength and lightweight concrete, due to possibility of aggregate breaking, this variable assumes the value of $d_g = 0$ [30].

$$k_{dg} = 1.0 \quad \text{if } d_g \leq 16\text{mm}$$

$$k_{dg} = \frac{32}{16 + d_g} \geq 0.75 \quad \text{if } d_g > 16\text{mm} \quad \text{Eq. (2.90)}$$

For the determination of the slab rotation, ψ , MC2010 presents four levels of approximation. The lower levels of approximation imply lower computational costs, but leads to more conservative results. By adopting higher levels of approximation, the calculation effort and precision increase.

In level of approximation I, the rotation of the slabs is determined from [30]:

$$\psi = 1.5 \cdot \frac{r_s}{d_v} \cdot \frac{f_{yd}}{E_s} \quad \text{Eq. (2.91)}$$

where r_s represents the position where the radial bending moment is zero with respect to the support axis. For regular flat slabs where the ratio between the spans in both slab's direction (L_x/L_y) is between 0.5 and 2.0, the value of r_s can be approximated to the maximum value of $r_{s,x} = 0.22 \cdot L_x$ or $r_{s,y} = 0.22 \cdot L_y$.

For the level of approximation II the rotation of slab is estimated from the following expression [30]:

$$\psi = 1.5 \cdot \frac{r_s}{d_v} \cdot \frac{f_{yd}}{E_s} \cdot \left(\frac{m_{Ed}}{m_{Rd}} \right)^{1.5} \quad \text{Eq. (2.92)}$$

where m_{Ed} is the average acting bending moment per unit length for the calculation of the flexural reinforcement in the support strip; m_{Rd} is the design average flexural strength per unit length in the support strip. The width of the mentioned support strip, b_s is equal to:

$$b_s = 1.5 \cdot \sqrt{r_{s,x} \cdot r_{s,y}} \leq L_{\min} \quad \text{Eq. (2.93)}$$

where L_{\min} is the minimum span for x and y directions of the slab.

MC2010 also presents several methods for estimating the acting bending moment m_{Ed} in the support strip, depending on the shear force and eccentricity of shear forces with respect to the centroid of the basic control perimeter, e_{ui} . The determination of e_{ui} is illustrated in Figure 28.

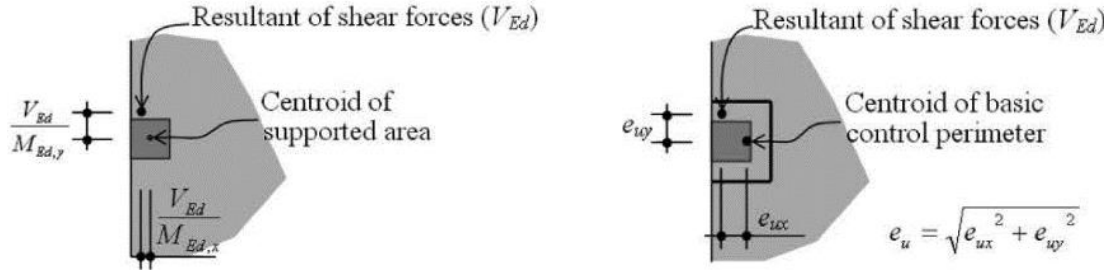


Figure 28 – Determination of eccentricity of the resultant of shear forces e_{ui} (extracted from [30]).

The level III of approximation is based on a more detailed analysis of the structure. If a linear elastic analysis is performed, considering an uncracked constitutive model for concrete, to determine the value of r_s and m_{Ed} , the coefficient 1.5 in Eq. (2.92) can be replaced by 1.2.

The level IV of approximation resorts to the performance of nonlinear numerical simulations, considering the phenomenon of cracking, tension-stiffening, yielding of reinforcements and other nonlinear effects that can be considered relevant to determine the rotation of slabs.

The design punching shear resistance provided by transverse reinforcement is calculated as:

$$P_{Rd,s} = \sum A_{sw} \cdot k_e \cdot \sigma_{swd} \quad \text{Eq. (2.94)}$$

where, A_{sw} is the sum of the cross-section area of all shear reinforcement that intersect the potential failure surface within the zone bounded by $0.35 \cdot d_v$ and d_v from the edge of the supported area (Figure 29); σ_{swd} is the stress that is activated in the shear reinforcement, determined by Eq. (2.95); and k_e is the coefficient of eccentricity that is determined from Eq. (2.96).

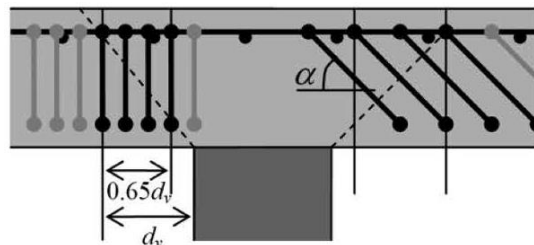


Figure 29 – Shear reinforcement activated at failure (extracted from [30]).

$$\sigma_{swd} = \frac{E_s \cdot \psi}{6} \cdot \left(1 + \frac{f_{bd}}{f_{ywd}} \cdot \frac{d_v}{\phi_w} \right) \leq f_{ywd} \quad \text{Eq. (2.95)}$$

$$k_e = \frac{1}{1 + \frac{e_u}{b_u}} \quad \text{Eq. (2.96)}$$

In Eq. (2.95) the variable ϕ_w represents the diameter of the punching shear reinforcement and f_{bd} represents the bond strength of the steel reinforcement to concrete.

In Eq. (2.96) $e_u = \sqrt{e_{u,x}^2 + e_{u,y}^2}$ is the norm of the eccentricity of resultant of shear forces (Figure 28), and b_u is the diameter of the circle with equal area as the region inside the basic control perimeter.

In order to prevent crushing of concrete struts in the supported zone, the design punching shear resistance determined according to Eq. (2.79) is limited to a maximum value, $P_{Rd,max}$, namely [30]:

$$P_{Rd,max} = k_{sys} \cdot k_{\psi} \cdot \frac{\sqrt{f_{ck}}}{\gamma_c} \cdot b_0 \cdot d_v \leq \frac{\sqrt{f_{ck}}}{\gamma_c} \cdot b_0 \cdot d_v \quad \text{Eq. (2.97)}$$

where k_{sys} is a coefficient that considers the performance of punching shear reinforcing systems to control cracking and to suitably confine compression struts at the soffit of the slab. The standard value for k_{sys} is 2.0. However, if enhanced detailing rules are adopted, the value of k_{sys} can be increased.

When transverse reinforcement is needed to guarantee sufficient punching resistance, a minimum amount of fibers is required to ensure sufficient deformation capacity at failure. According to MC2010 is possible to assume this condition if:

$$P_{Rd,s} + P_{Rd,f} \geq 0.5 \cdot P_{Ed} \quad \text{Eq. (2.98)}$$

where P_{Ed} is the acting punching shear force.

2.5.4 Stress limitation

Under service loads conditions the stress on FRC and steel reinforcements shall be limited in order to reduce the probability of concrete cracking and avoid excessive member deformation.

According to MC2010, for members of FRC with tension-hardening behavior, the tensile stress at the SLS must be limited to:

$$\sigma_t^{SLS,char} \leq 0.6 \cdot f_{Ftsk} \quad \text{Eq. (2.99)}$$

where $\sigma_t^{SLS, char}$ is the principal tensile stress in the member determined for the characteristic load combination, and f_{Ftsk} is the characteristic value of the serviceability residual tensile strength, given in Eq. (2.16).

For FRC members having a tensile-softening behavior after cracking, the tensile stress limitation of Eq. (2.99) is not necessary [30].

Similarly to reinforced plain concrete elements, MC2010 provides conditions regarding compressive stress limitation of concrete and tensile stress of flexural reinforcements.

The compressive stress limitation of concrete is divided in two clauses. For the characteristic combination of actions, the following condition applies [30]:

$$\sigma_c^{SLS, char}(t) < 0.6 \cdot f_{ck}(t) \quad \text{Eq. (2.100)}$$

For the quasi-permanent combination of actions, the following condition applies [30]:

$$\sigma_c^{SLS, qperm}(t) < 0.4 \cdot f_{ck}(t) \quad \text{Eq. (2.101)}$$

If Eq. (2.100) is verified, it indicates that longitudinal cracking of the member is unlikely to occur. In other hand, if Eq. (2.101) is accomplished it represents that creep linearity is ensured, and nonlinear creep deformation is avoided.

In order to prevent inelastic deformations of the steel longitudinal reinforcements, MC2010 introduces a steel stress limitation:

$$\sigma_s^{SLS, char} < 0.8 \cdot f_{yk}(t) \quad \text{Eq. (2.102)}$$

where, $\sigma_s^{SLS, char}$ is the steel stress determined for the characteristic load combination of actions. However, if the stress is due to imposed deformations, is acceptable that the steel stress can reach $1.0 \cdot f_{yk}$.

When more than 50% of the stresses arise from quasi-permanent actions, the concrete creep effects on the member should be considered when evaluating the steel stress. The methodology considered in section 2.3.1 can be adopted for considering concrete creep effects when performing plain-section analysis of a cross-section.

The stresses in FRC members can be determined by evaluating the acting moments and forces by performing a linear elastic analysis of the structure and conducting a plain-section analysis, considering the stress-strain relationships presented in section 2.3. Alternatively, more advanced analysis procedures can be conducted regarding the nonlinear behavior of the involving materials, e.g., finite element models.

2.5.5 Crack control

The limit state of cracking for any concrete member should be verified to assure that the requirements concerning functionality, durability and appearance are met. The MC2010 adopts a cracking serviceability criterion in the form of limiting a calculated crack width, w_d , to a nominal limiting value,

w_{lim} :

$$w_d \leq w_{lim} \quad \text{Eq. (2.103)}$$

The variable w_d represents the design value of crack width at the concrete member surface and is determined for the appropriate combination of actions. The nominal limit value of crack width at the concrete surface, w_{lim} , must be chosen according to the design situation, or is a project stipulated value.

The method proposed in MC2010 for the calculation of the design crack width of a concrete member is based on the basic case of a prismatic reinforced concrete member subjected to axial tension. As illustrated in Figure 30, when a RC member is subjected to a steadily increasing elongation it develops an approximately regular crack pattern. In Figure 30 it is also represented the relationship between the load and mean strain of the member, where it is possible to detect the following stages:

1. Uncracked stage;
2. Crack formation stage;
3. Stabilized crack stage;
4. Reinforcement steel yielding.

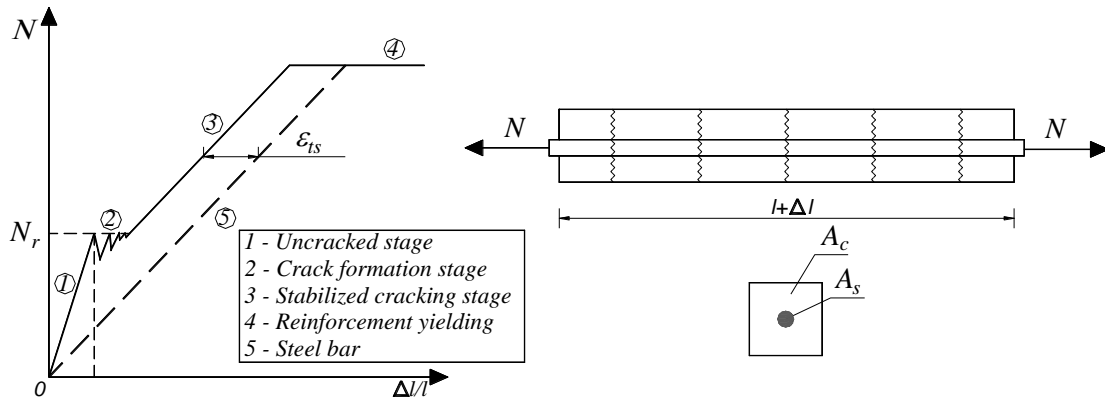


Figure 30 – Load-strain relationship for a centrally loaded tensile reinforced concrete member [68].

In stage 1 (uncracked stage) concrete has not been cracked yet, and the stiffness of the member is at the maximum level. At this stage, the axial load applied to the member can be determined from:

$$N^1 = \varepsilon \cdot E_c \cdot A_c \cdot (1 + \alpha_E \cdot \rho_{sl}) \quad \text{Eq. (2.104)}$$

where $\alpha_E = E_s / E_c^e$ is the modular ratio and $\rho_{sl} = A_{sl} / A_c$ is the ratio of longitudinal reinforcement, being E_c^e the effective modulus of concrete taking into consideration creep effects, $E_c^e = E_c / (1 + \varphi_c)$, where φ_c is the concrete creep coefficient.

The stage 2 corresponds to the formation of the cracks, which occurs when the tensile strength of concrete is reached, $\sigma_{ct} = f_{ctm}$. When the first crack takes place the axial tensile load in the member is equal to:

$$N_R^2 = f_{ctm} \cdot A_c \cdot (1 + \alpha_E \cdot \rho_{sl}) \quad \text{Eq. (2.105)}$$

As illustrated in Figure 31, when cracking occurs the stress in concrete decreases almost to zero at crack location (depending on the fracture energy and crack width of the material, but to simplify it can be considered a null value), $\sigma_{ct} = 0$, and the axial tensile load is carried by the steel. At this stage the steel stress is [68]:

$$\sigma_{sr} = \frac{N_R^2}{A_s} = \frac{f_{ctm}}{\rho} \cdot (1 + \alpha_E \cdot \rho_{sl}) = \frac{A_c \cdot f_{ctm}}{A_s} + f_{ctm} \cdot \alpha_E \quad \text{Eq. (2.106)}$$

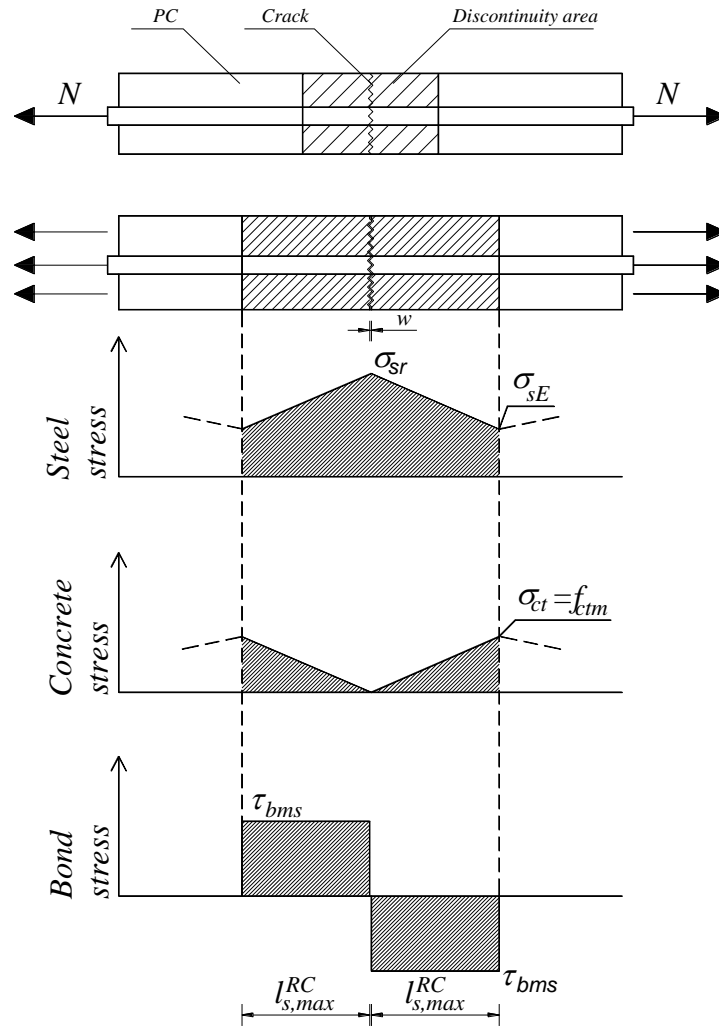


Figure 31 – Simplified representation of steel, concrete and bond stresses in the disturbed area in the crack formation stage of a RC member (adapted from [30, Figs. 7.6–3]).

Due to bond strength between steel and concrete, stress is transferred from steel to concrete along both sides of the crack, corresponding to the discontinuity zone illustrated in Figure 31. In a simplified assumption, it is considered a constant value for the bond-slip relationship between concrete and steel (Figure 32). Nevertheless, several authors have proposed different models [69], [70].

To the length needed for concrete to reach again its tensile strength, $\sigma_{ct} = f_{ctm}$, due to bond action, is called the transmission length or bond transfer length, $l_{s,max}^{RC}$. Therefore, new cracks cannot occur within the distance $l_{s,max}^{RC}$ from the existing cracks, as stress on concrete does not reach its tensile strength within this transition zone. At a distance $l_{s,max}^{RC}$ from the crack, steel stress at the undisturbed zone takes the value of:

$$\sigma_{sE} = f_{ctm} \cdot \alpha_E \quad \text{Eq. (2.107)}$$

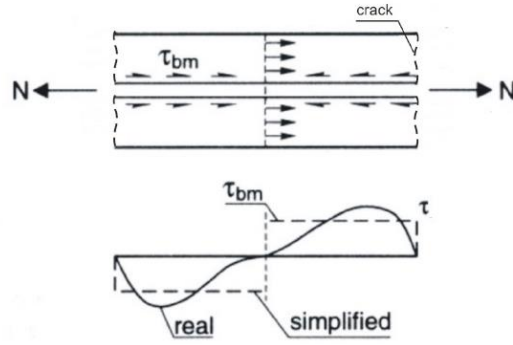


Figure 32 – Load transmission from steel to concrete due to bond (extracted from [68]).

At the end of $l_{s,max}$, the force carried by concrete is equal to:

$$N_c = A_c \cdot f_{ctm} \quad \text{Eq. (2.108)}$$

This force, N_c , must be transferred by the steel reinforcement by bond over the length $l_{s,max}$. Considering that the generated action due to bond capacity is equal to [68]:

$$N_{bond} = \tau_{bms} \cdot l_{s,max}^{RC} \cdot \sum U \quad \text{Eq. (2.109)}$$

where τ_{bms} is the mean bond strength between steel and concrete (Figure 32) and $\sum U$ is the total perimeter of the reinforcement bars, the theoretical value of the transmission length for reinforced concrete members, $l_{s,max}^{RC}$, can be determined from equating Eq. (2.108) and Eq. (2.109), namely [68]:

$$N_c = N_{bond} \Leftrightarrow l_{s,max}^{RC} = \frac{f_{ctm}}{4 \cdot \tau_{bms}} \cdot \frac{\phi_s}{\rho} \quad \text{Eq. (2.110)}$$

Regarding the load-strain response at the crack formation stage presented in Figure 30, since the member is under an imposed deformation action, when a crack arises the axial load drops due to the reduction of stiffness of the member. The axial tensile load return to increase with the deformation in the member, but it cannot exceed the value of N_R^2 because the concrete tensile strength is reached again outside the discontinuity zone, and a new crack is formed [68]. This behavior, illustrated in Figure 30 by the saw-tooth line, is simplified in MC2010 by assuming a constant load-strain relationship in the crack formation stage.

The stabilized crack stage starts when the entire RC member is constituted by discontinuity zones, and no more cracks can be formed due to impossibility of concrete stress attains again its tensile

strength in between the already formed cracks. In this stage the distance between cracks varies between $l_{s,max}$ and $2 \cdot l_{s,max}$, having a mean value $s_{rm} = 1.5 \cdot l_{s,max}$ [68].

The stabilized crack stage is characterized by the widening of existing cracks. Due to the deterioration of bond, the contribution of concrete between cracks (tension-stiffening effect) decreases with the applied deformation up to the attainment of the yield of the steel reinforcement, after which the tension-stiffening effect is null. To model this effect in a simply approach, the load-strain response is assumed parallel to the line of the unembedded steel response (dashed line in Figure 30), where the difference between the two lines represents the tension-stiffening effect, ε_{ts} .

According to MC2010, the tension-stiffening effect takes the value of:

$$\varepsilon_{ts} = \frac{\beta \cdot \sigma_{sr}}{E_s} \quad \text{Eq. (2.111)}$$

where β is a coefficient to assess the mean steel strain over $l_{s,max}$, and depends on the type of loading.

Considering the analogous situation for a FRC member with longitudinal reinforcement, subjected to axial tension, the main differences rely on the fibers capacity to transfer tensile stresses between the faces of the cracks they are bridging. At stage 2, when cracking is processing, this stress transfer capacity of the fibers is considered $\sigma_{ct} = f_{Fism}$, thereby the steel stress at crack location is reduced when compared to the analogous RC member, namely:

$$\sigma_{sr} = \frac{(f_{ctm} - f_{Fism})}{\rho} \cdot (1 + \alpha_E \cdot \rho_{sl}) \quad \text{Eq. (2.112)}$$

where, f_{Fism} is the mean value of the serviceability residual tensile strength of FRC, and can be determined according to:

$$f_{Fism} = \frac{f_{Ftsk}}{0.7} \quad \text{Eq. (2.113)}$$

where f_{Ftsk} is determined according to Eq. (2.16).

Due to the reduced steel stress, the force transmitted from steel to concrete due to bond (analogous to Eq. (2.108)) is also reduced due to the effect of the post-cracking residual strength of FRC, by:

$$N_{bond} = A_c \cdot (f_{ctm} - f_{Ftism}) \quad \text{Eq. (2.114)}$$

and, therefore, the transmission length for a FRC member, $l_{s,max}^{FRC}$, takes the value of:

$$l_{s,max}^{FRC} = \frac{f_{ctm} - f_{Ftism}}{4 \cdot \tau_{bms}} \cdot \frac{\phi_s}{\rho} \quad \text{Eq. (2.115)}$$

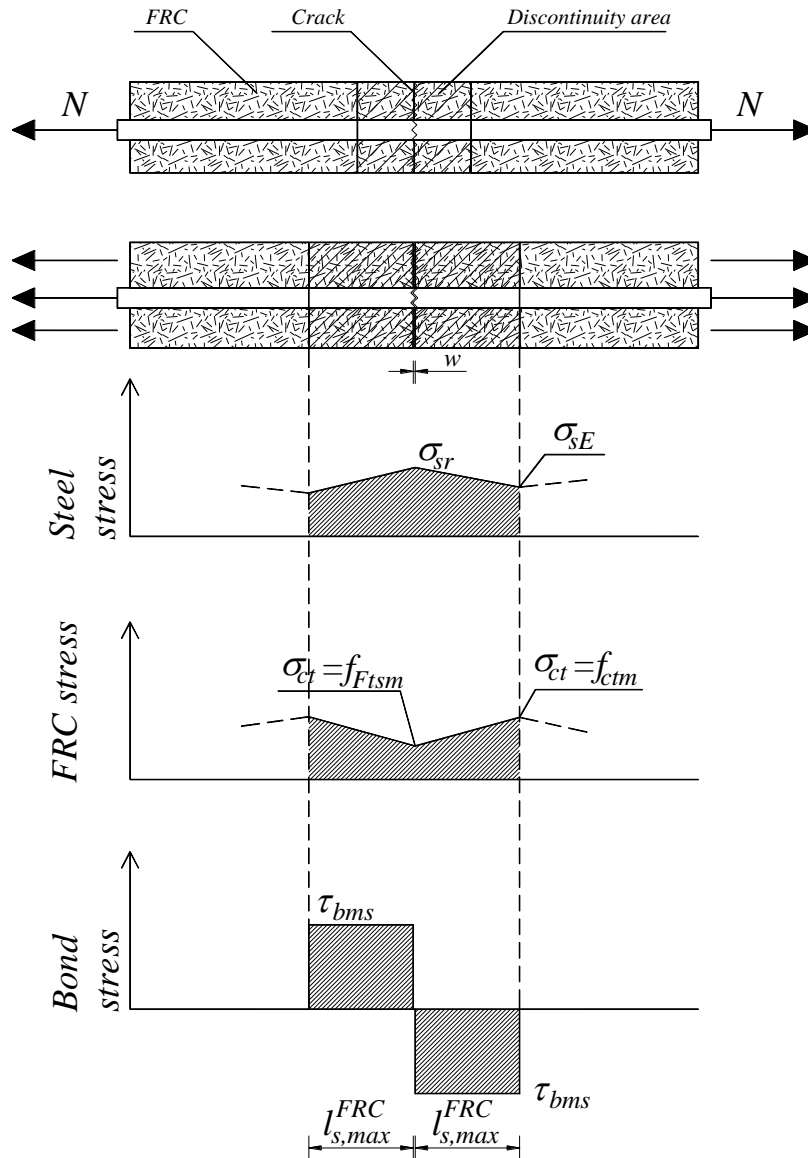


Figure 33 – Simplified representation of steel, concrete and bond stresses in the disturbed area in the crack formation stage of a FRC member.

The expressions to calculate the introduction length of a RC and FRC member, Eq. (2.110) and Eq. (2.115), respectively, do not fully describe the expressions presented in MC2010, which considers the concrete cover influence in the length of $l_{s,max}$, namely:

$$l_{s,\max} = k \cdot c + \frac{1}{4} \cdot \frac{f_{ctm}}{\tau_{bm}} \cdot \frac{\phi_s}{\rho_{s,ef}} \quad (\text{RC}) \quad \text{Eq. (2.116)}$$

$$l_{s,\max} = k \cdot c + \frac{1}{4} \cdot \frac{(f_{ctm} - f_{Ft5m})}{\tau_{bms}} \cdot \frac{\phi_s}{\rho_{s,ef}} \quad (\text{FRC}) \quad \text{Eq. (2.117)}$$

where k is an empirical value to take the influence of the concrete cover, and as a simplification can be assumed equal to $k = 1.0$; c is the concrete cover; ϕ_s corresponds to flexural reinforcement bar diameter; τ_{bms} is the mean bond strength between steel and concrete; and $\rho_{s,ef}$ is the effective reinforcement ratio. MC2010 indicates that the validity of previous expressions is limited for member with cover thickness lesser than 75mm. In Eq. (2.116) and Eq. (2.117) is used the definition of effective reinforcement ratio, $\rho_{s,ef}$, instead of the regular reinforcement ratio, ρ . In fact, $\rho_{s,ef}$ is used to generalize the presented formulation to the crack analysis for other types of member different than axially reinforced prisms [71]. Due to this, in the previous expressions presented in this section, the variable ρ should be replaced by $\rho_{s,ef}$. According to MC2010, the variable $\rho_{s,ef}$ can be determined by the following expression:

$$\rho_{s,ef} = \frac{A_s}{A_{c,ef}} \quad \text{Eq. (2.118)}$$

where $A_{c,ef}$ is the effective area of concrete in tension and A_s is the reinforcement area inside $A_{c,ef}$. The effective area of concrete in tension can be approximated by the methodology presented in [30], considering the type of structural element in analysis.

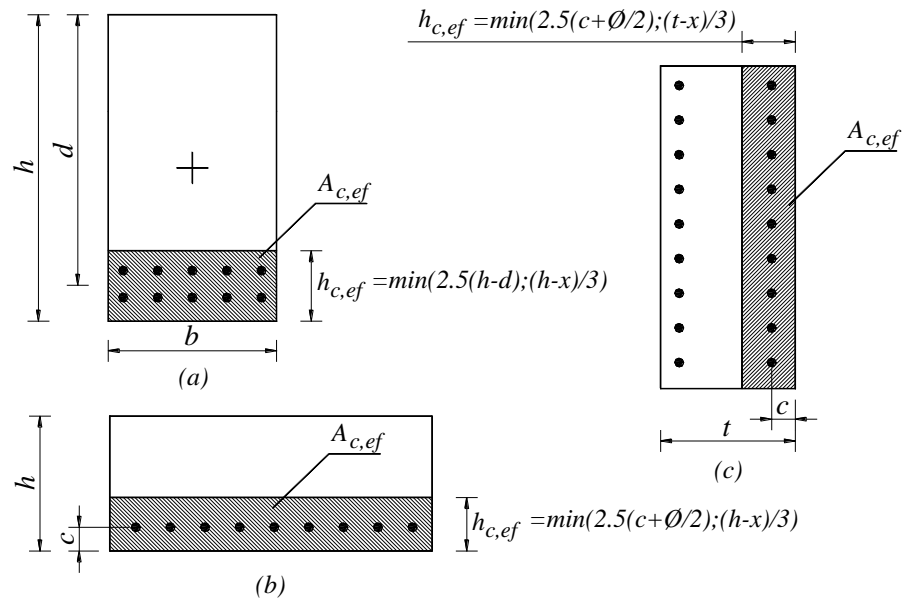


Figure 34 – Determination of effective area of concrete in tension, $A_{c,ef}$, for: a) beams; b) slabs; c) walls (extracted from [30]).

As previously presented, in MC2010 is considered a simplified bond-slip relationship. The bond strength, τ_{bms} , assumes a constant value that is proportional to the concrete tensile strength and is also dependent on the cracking stage and type of loading. The expressions to determine τ_{bms} are presented in Table 3.

Table 3 – Values of τ_{bms} , β and η_r for deformed reinforcing bars (extracted from [30]).

Type of loading	Crack formation stage	Stabilized cracking stage
Long term, repeated loading	$\tau_{bms} = 1.35 \cdot f_{ctm}(t)$	$\tau_{bms} = 1.8 \cdot f_{ctm}(t)$
	$\beta = 0.60$	$\beta = 0.40$
	$\eta_r = 0$	$\eta_r = 1$
Short term, instantaneous loading	$\tau_{bms} = 1.8 \cdot f_{ctm}(t)$	
	$\beta = 0.60$	
	$\eta_r = 0$	

Due to crack formation, the compatibility of strains of concrete and steel is not maintained. The sum of strain differences results in the development of relative slip between concrete and steel. The crack width is the result of the sum of the two slip values at both sides of the crack [72]. The relative slip between concrete and steel at each side of the crack can be estimated by the difference between the average strain of concrete and steel over the introduction length, $l_{s,max}$. Considering the effect of concrete shrinkage, the crack width at the steel reinforcement level can be determined from:

$$w_d = 2 \cdot l_{s,\max} \cdot (\varepsilon_{sm} - \varepsilon_{cm} - \varepsilon_{cs}) \geq 0 \quad \text{Eq. (2.119)}$$

where, ε_{sm} is the average strain of the steel bars; ε_{cm} is the average strain of concrete; and ε_{cs} is the concrete shrinkage strain.

According to MC2010, the relative mean strain ($\varepsilon_{sm} - \varepsilon_{cm} - \varepsilon_{cs}$) can be determined by:

$$\varepsilon_{sm} - \varepsilon_{cm} - \varepsilon_{cs} = \frac{\sigma_s - \beta \cdot \sigma_{sr}}{E_s} + \eta_r \cdot \varepsilon_{sh} \quad \text{Eq. (2.120)}$$

where ε_{sh} is the strain of the concrete due to free shrinkage; σ_s is the stress in the conventional steel rebars in a crack; σ_{sr} is the maximum steel stress in a crack in the crack formation stage; β is a coefficient to assess the mean steel strain over $l_{s,\max}$; η_r is a coefficient for considering the shrinkage contribution in the crack; E_s is the modulus of elasticity of steel. The values of β and η_r can be obtained in Table 7.6-2 of the MC2010.

Combining Eq. (2.119) and Eq. (2.120), the crack width of a FRC member can be determined from [30]:

$$w_d = 2 \cdot l_{s,\max} \cdot \frac{1}{E_s} \cdot (\sigma_s - \beta \cdot \sigma_{sr} - \eta_r \cdot \varepsilon_{sh} \cdot E_s) \geq 0 \quad \text{Eq. (2.121)}$$

where σ_{sr} can be determined from the Eq. (2.106) and Eq. (2.112), respectively, for RC and FRC members, and considering the variable $\rho_{s,ef}$.

As expressed in Eq. (2.116) and Eq. (2.117), due to post-cracking residual strength of FRC, the necessary length for concrete reaches the tensile strength is smaller than for a RC member, which means that crack spacing and crack width of a FRC member is smaller than for RC members. This fact has already been proved in carried out experimental investigations [20], [73]. It is also possible to state that the steel stress at crack location, σ_s , is reduced for FRC members (Eq. (2.112)).

As stated in Eq. (2.121) for evaluation of the design value of crack width of a FRC member, it is necessary to determine the steel stress, σ_s , considering the acting forces and moments corresponding to the serviceability criteria load combination. The steel rebars stress can be calculated by conducting a plain-section analysis and considering the appropriate stress-strain relationship for SLS analysis presented in section 2.3. For long-term evaluation of the member crack width, the

influence of concrete creep in the increase of the rebars stress should be considered. In section 2.3.1 is presented a methodology to consider creep effect on the concrete compression stress-strain relationship.

The MC2010 formulation to determine the design value of crack width is only valid for conventionally reinforced FRC members.

For crack control of members in bending, MC2010 provides a design rule regarding the definition of a minimum required area of conventional reinforcement to withstand the tensile forces gradient resulting from concrete tensile stress reduction at cracking initiation, namely:

$$A_{s,\min} = k_c \cdot k \cdot (f_{ctm} - f_{Ftsm}) \cdot \frac{A_{ct}}{\sigma_s} \quad \text{Eq. (2.122)}$$

where, k_c is a coefficient taking into account the stress distribution in the cross-section just before cracking occurs and the change of the inner lever arm, taking the value $k_c = 1.0$ for rectangular cross-sections; A_{ct} is the area of the tensile part of the concrete cross-section, evaluated at the limit of the elastic stress distribution; σ_s is the maximum tensile stress in the reinforcement in the cracked state, which can be considered equal to the yielding stress of the steel; and k is a coefficient to take into account the non-uniform self-equilibrating cracking force, taking the value $k = 1.0$ for webs with $h \leq 300\text{mm}$ or flanges with width lesser than 300mm, and the value $k = 0.65$ for webs with $h \leq 800\text{mm}$ or flanges with width greater than 800mm.

2.6 Concluding remarks

This chapter presents an overview of the design guidelines and recommendations presented in MC2010 for the design of FRC structures. The main topics focused were related to the classification of FRC, namely the meaning and determination of the mechanical properties related to the toughness class, the calculation of the post-cracking residual tensile strength; and the definition of constitutive relationship of FRC, namely the stress-crack width and stress-strain diagrams.

It is also presented the methodology of MC2010 to account the increase of ultimate load capacity due to stress redistribution and the ductility requirements for FRC structures.

The approach proposed in MC2010 to consider the influence of the fiber distribution in the behavior of the FRC members is also presented. In this scope, and taking into account the absence of a generalized formulation to determine the fiber orientation factor, this topic is further developed in chapter 5.

The models proposed by MC2010 to perform the ULS and SLS verifications were thoroughly described, with special focus to some particular topics for FRC members, namely the determination of the structural characteristic length of members with and without conventional longitudinal reinforcements, the background and outline of the available shear models and the description of the model to determine the FRC crack width and spacing. Additionally, the shear and punching models presented in MC2010 are complemented with the more advanced models published in academic works.

3 SOFTWARE FOR DESIGN OF FIBER REINFORCED CONCRETE ELEMENTS

3.1 Introduction

This chapter is dedicated to present a new software, denominated *FRCcalc*, that, in the context of this thesis, was developed for the analysis and design of FRC members based on the recommendations and design guidelines presented in chapter 2. The software is guided for the analysis of FRC cross-sections with and without conventional reinforcements, submitted to bending and shear with or without axial force, in order to assess the ultimate and serviceability limit state safety verifications of structural members.

A main feature of the software is the possibility to run a comparative analysis between FRC and RC cross-sections, which was implemented to assess the improvement provided by the addition of fiber reinforcement to concrete and to assess the potentialities of replacing conventional reinforcement by fibers.

The software allows to perform the following analysis, for FRC and RC members:

- Ultimate flexural capacity;
- Evaluation of the moment vs. curvature relationship at ULS;
- Ultimate shear capacity;
- Evaluation of design crack width;
- Determination of moment vs. design crack width relationship at SLS;
- Evaluation of stress limitation criteria at SLS.

3.2 Plain section analysis of cross-sections

An essential requirement of an analysis and design software of FRC and RC members is the development of a versatile calculation module to perform plain-section analysis of cross-sections. In the present section is presented the methodology adopted in *FRCcalc* to conduct plain-section analysis of cross-sections submitted to bending with or without axial force.

Assuming that the cross-section of a structural element remains plane after bending and shear deformation can be ignored, the set of equilibrium and compatibility equations of a generic rectangular cross section, composed of FRC with longitudinal conventional reinforcements, can be obtained in accordance to Figure 35. Due to the presence of conventional steel reinforcements, the tensile zone of the cross-section is divided in two parts: one with a height equal to the effective tensile depth, $h_{c,ef}$; and, the other, corresponding to the depth $y - h_{c,ef}$. If no conventional tensile reinforcement is applied, the division of the cross-section is discarded.

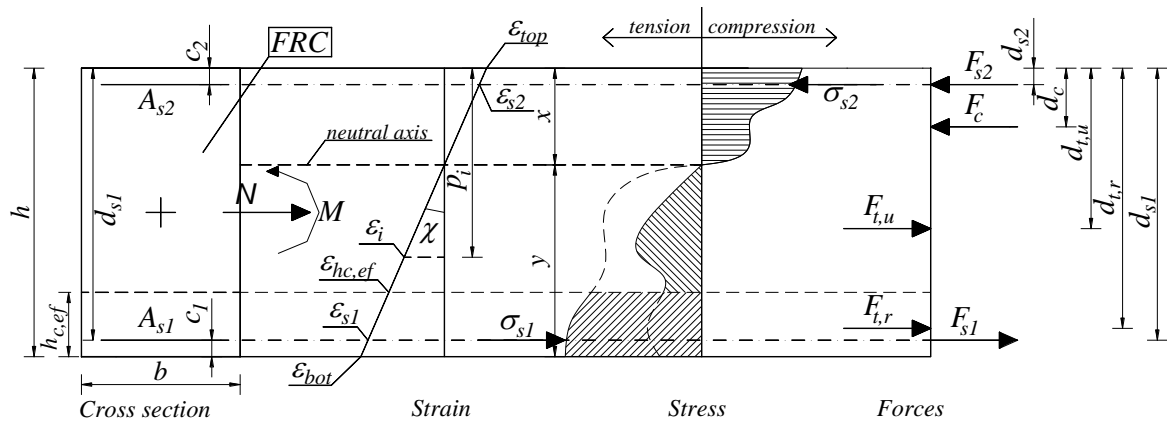


Figure 35 – Generic rectangular FRC cross-section for determination of moment-curvature relationship.

Based on Figure 35 the forces and moment equilibrium equations in the cross-section are:

$$\begin{cases} \sum F = N \\ \sum F_i \cdot d_i = M \end{cases} \Leftrightarrow \begin{cases} F_s + F_{t,u} + F_{t,r} + F_c = N \\ M_s + M_{t,u} + M_{t,r} + M_c + N \cdot \frac{h}{2} = M \end{cases} \quad \text{Eq. (3.1)}$$

The further development of the compatibility and equilibrium equation in the cross-section are presented in Appendix C.

For FRC cross-sections without conventional steel reinforcements, the tensile zone is not divided and a unique stress-strain relationship is applied in the plain section analysis. For this situation the value of $h_{c,ef} = 0$, turning $F_{t,r} = 0$ and $M_{t,r} = 0$.

In *FRCcalc* the resolution of the set of equilibrium equations (presented in Eq. (C.1)) can be used to determine two sets of solutions:

- The neutral axis position, x , and bending moment of the cross-section, M ;
- The neutral axis position, x , and curvature, χ .

In situation a), it is necessary to consider the application of a strain in the cross-section in order to obtain the resisting bending moment of the cross-section, M , and neutral axis position, x . In situation b), it is necessary to consider the application of the acting bending moment, M , in order to obtain the neutral axis position, x , and curvature, χ .

The resolution of forces and moment equilibrium equations in a cross-section is obtained by considering an iterative approach for the determination of the set of variables a) or b) and adopting the compatibility and constitutive models equations (Eq. (C.2) to Eq. (C.39)). The iterative approach resorts to Microsoft Office Excel Solver algorithm [74].

3.3 Main user interface window

In Figure 36 is presented the user interface window of the software. In this window, the geometry of the cross-section and material properties data are inputted, and the user can select the type of ULS and/or SLS analysis to be conducted.

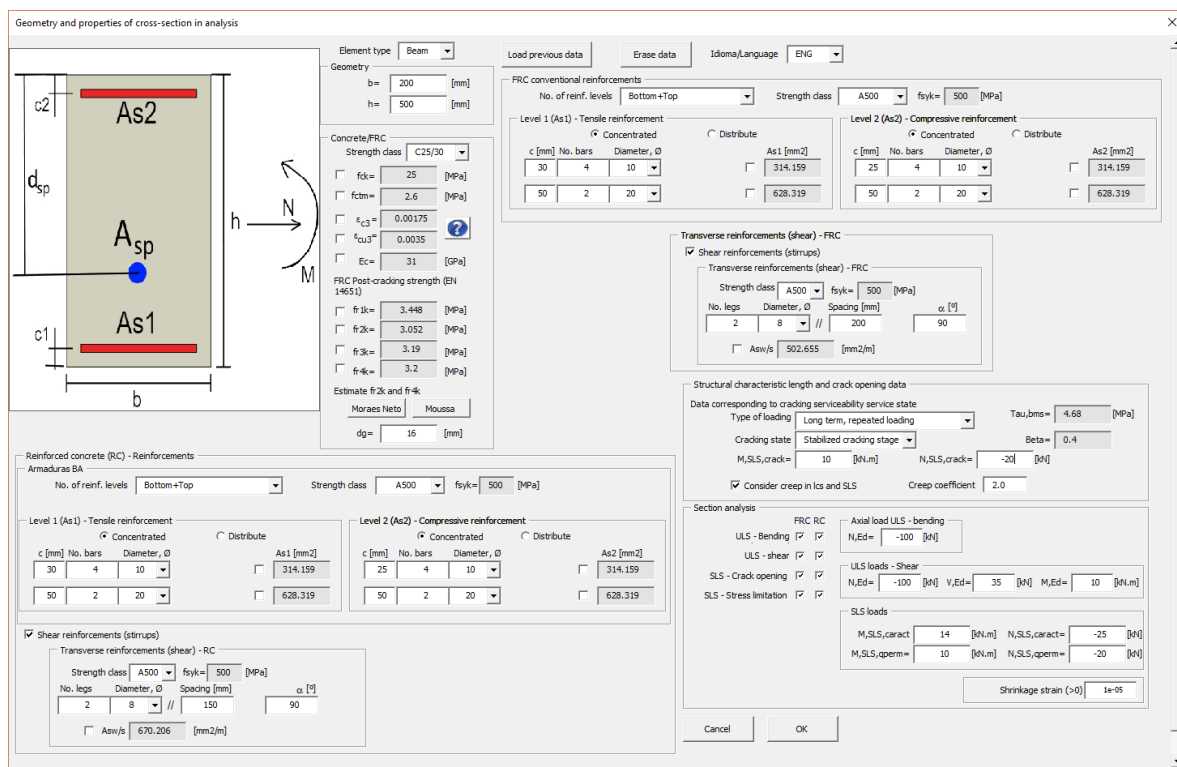


Figure 36 – User interface window of the software.

The available cross-section geometry to be adopted is limited to rectangular shapes. The cross-section general data for user to input corresponds to the element width and height, as well as the type of member: beam, slab or walls (Figure 37a).

The material properties can be manually defined or can be chosen according to the reference values of the existing strength classes defined in MC2010 and Eurocode 2, except for the characteristic residual flexural strength of FRC and the maximum size of the aggregate, whose values must be manually inputted (Figure 37b). The software also has a built-in function that estimates the value of f_{R2k} and f_{R4k} based on the work of Moraes Neto et al. [64], [65] or Moussa [66].

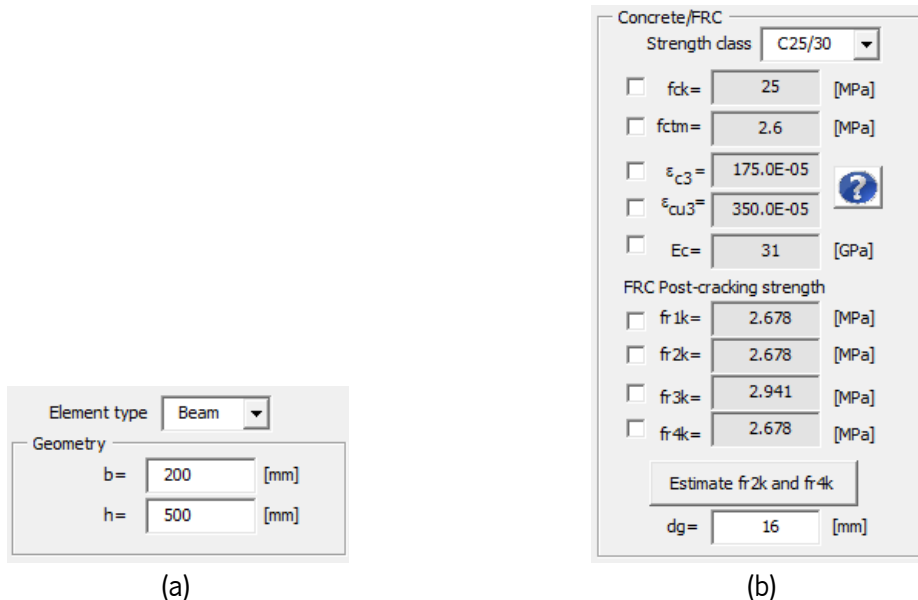


Figure 37 – User interface window: a) Cross-section geometry; b) FRC material properties.

The software also allows the definition of two sets of bottom and top conventional reinforcement positioning (Figure 38) to be considered in the analysis of the FRC and RC cross-sections. The conventional reinforcement area can be manually inputted or a distribution can be defined according to the number and diameter of bars or diameter and spacing of bars. The top and bottom bars cover can be individually defined and the strength class of steel can be chosen according to pre-existing strength classes.

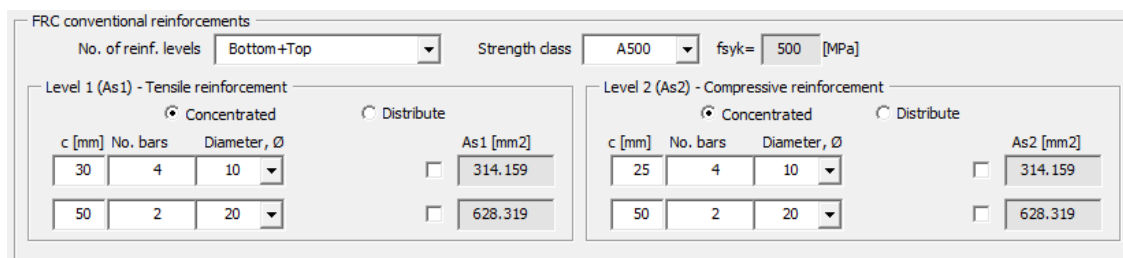


Figure 38 – User interface window: Conventional reinforcement data.

In order to determine the FRC tensile stress-strain relationship defined according to MC2010, it is necessary to specify the essential data to determine the structural characteristic length of the member

(Figure 39), namely: type of loading, cracking stage, the bending moment corresponding to the cracking serviceability criteria load combination (generally is assumed the quasi-permanent load combination). Additionally, is also possible to specify the creep coefficient for concrete in compression to be adopted in the determination of the structural characteristic length and in the SLS safety verifications.

Figure 39 – User interface window: Data for calculation of structural characteristic length.

FRCcalc was developed to determine the flexural and shear performance, with or without axial load, of FRC and RC cross-sections at ULS, and to assist in the assessment of the SLS safety verifications, namely crack control and stress limitation (Figure 40).

Figure 40 – User interface window: Selection of type of analysis to be performed.

The flexural response of the FRC cross-section is evaluated by determining the moment-curvature relationship and the ultimate design resisting moment at ULS, considering the value of the axial load acting in the cross-section for the ULS combination, with optional consideration of conventional longitudinal reinforcement bars.

The shear resistance of the FRC cross-section at ULS can be determined considering the fiber contribution, the longitudinal rebars contribution and conventional shear reinforcements (Figure 41). The conventional shear reinforcements are defined by selecting the steel strength class, inclination of the stirrups, and manually defining the value of the shear reinforcement area per meter or by providing the number of stirrups legs, diameter and longitudinal spacing of the stirrups. To determine the longitudinal strain in the mid-depth of effective shear area, ε_x , the axial and shear forces and bending

moment acting in the cross-section at ULS load combination must be inputted. In addition, for the evaluation of the shear resistance of the FRC cross-section is required the input of the concrete maximum aggregate size and the values of the residual flexural strength f_{R2k} and f_{R4k} .

Figure 41 – User interface window: Selection of shear capacity analysis.

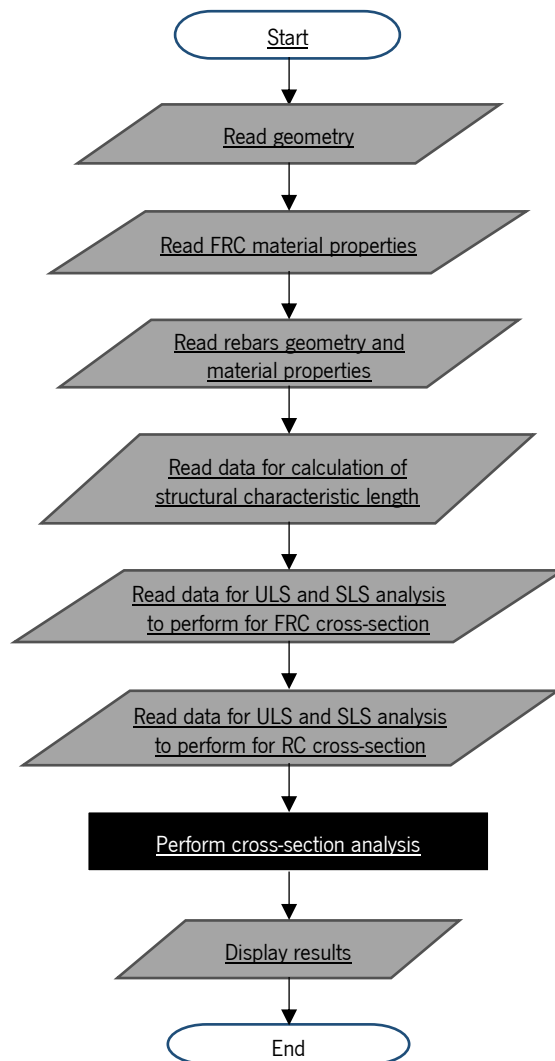
The software allows the determination of the design crack width of FRC and RC cross-sections, according to MC2010 formulation (presented in section 2.5). In addition, the moment-crack width response at SLS analysis for cross-sections considering the value of the axial force for the quasi-permanent load combination is also outputted. In the analysis is possible to consider the concrete creep effect, by inputting the creep coefficient of concrete, and is also necessary to specify the free shrinkage strain of the member (Figure 40).

Using *FRCcalc* is also possible to easily analyze the verification of the serviceability criteria of stress limitation for FRC and RC cross-sections, presented in section 2.5.4. For conducting this analysis, it is necessary to input the quasi-permanent and characteristic load combinations results (axial load and bending moment) - Figure 40.

3.4 Software algorithm/flowcharts

FRCcalc was developed in Visual Basic for Application programming language and can be used in Microsoft Office Excel.

The main flowchart of *FRCcalc* is presented in Figure 42.

Figure 42 – Main flowchart of *FRCcalc*.

3.4.1 Data input

The idealization of the cross-section geometry is presented in Figure 43. The rectangular section geometry is defined by its width, b [mm], and its height, h [mm]. It is possible to consider two sets of bottom and two sets of top conventional steel reinforcements, that are characterized by its area, A_{si-1} / A_{si-2} [mm²], cover, c_{i-1} / c_{i-2} [mm], diameter, ϕ_{i-1} / ϕ_{i-2} [mm], and strength class, with $i = 1$ for bottom reinforcement and $i = 2$ for top reinforcements.

The FRC cross-section is divided in two zones, a reinforced zone delimited by the effective tensile zone height, $h_{c,ef}$ [mm], and the unreinforced zone.

All the variables that define the geometry of the cross-section must be greater than zero.

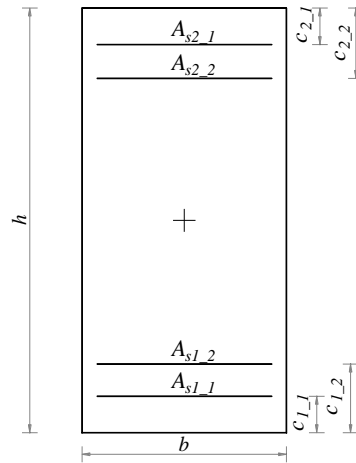


Figure 43 – Idealization of the geometry of the FRC cross-section.

The software adopts the bilinear stress-strain relationship for concrete in compression presented in Figure 6. The model input variables are:

- f_{ck} , the characteristic compressive strength of concrete, in MPa. This value must be positive;
- ε_{c3} , the concrete compressive strain at the limit of elasticity (see Figure 6). This value must be positive;
- ε_{cu3} , the concrete ultimate compressive strain (see Figure 6). This value must be positive;
- E_c , the concrete modulus of elasticity (Young's modulus), in GPa. This value must be positive;
- φ , the concrete creep coefficient. This value must assume a positive value. If concrete creep effect is disregarded, it must assume the value zero.

During the calculation procedure, the values of the variables, f_{ck} , ε_{c3} and ε_{cu3} are converted to its opposite values.

For FRC in tension the stress-strain relationships presented in section 2.3.3 are used. The input variables to define these models are:

- f_{cm} , the mean tensile strength of concrete, in MPa. This value must be positive;
- f_{R1k} , the characteristic value of the residual flexural strength of FRC corresponding to $CMOD_1 = 0.5mm$, in MPa. This value must be positive;
- f_{R3k} , the characteristic value of the residual flexural strength of FRC corresponding to $CMOD_3 = 2.5mm$, in MPa. This value must be positive.

The partial safety factor for concrete and FRC are defined within the calculation routines.

In Appendix A are presented the reference values that characterize the concrete matrix mechanical properties based on the existing strength classes.

For the reinforcement steel bars is considered the elastic-perfectly plastic model presented in section 2.3.2. The input variable of the model is:

- f_{syk} , the characteristic yield strength of reinforcing steel bars, in MPa. This value must be positive;

For steel rebars is considered that the elastic modulus takes the value of $E_s = 200GPa$. The partial safety factor for steel reinforcement is defined within the calculation routines.

All the input fields that define the constitutive models of the materials must be greater than zero.

The additional input variables for the calculation of the structural characteristic length are:

- Loading type, which can take the following options:
 - o Short term, instantaneous loading;
 - o Long term, repeated loading.
- Cracking stage, which can take the following options:
 - o Crack formation stage;
 - o Stabilized cracking stage.
- $M_{Ed,crack}$, acting bending moment for the combination of actions corresponding to the cracking serviceability criteria, in kN.m. This value must be greater than zero;
- $N_{Ed,crack}$, acting axial force for the combination of actions corresponding to the cracking serviceability criteria, in kN. Compressive forces must be inputted as negative values and tensile forces must assume positive values.

The additional variable used for the determination of flexural resistance of the cross-section is:

- $N_{Ed,ULS}$, axial force for the ULS load combination, in kN. Compressive forces must be inputted as negative values and tensile forces must assume positive values.

The additional variables used for the definition of the FRC shear resistance are:

- Maximum size of the aggregates, d_g , in mm;
- f_{R2k} , the characteristic value of the residual flexural strength of FRC corresponding to $CMOD_2 = 1.5mm$, in MPa. This value must be positive;
- f_{R4k} , the characteristic value of the residual flexural strength of FRC corresponding to $CMOD_4 = 3.5mm$, in MPa. This value must be positive;
- $N_{Ed,Shear,ULS}$, axial force for the ULS load combination for shear resistance assessment, in kN. Compressive forces must be inputted as negative values and tensile forces must assume positive values;
- $V_{Ed,Shear,ULS}$, shear force for the ULS load combination for shear resistance assessment, in kN. This value must be positive;
- $M_{Ed,Shear,ULS}$, bending moment for the ULS load combination for shear resistance assessment, in kN.m. This value must be positive.

The additional input variables for the definition of the shear reinforcement properties are:

- f_{ywk} , the characteristic yield strength of transverse reinforcement steel bars, in MPa;
- $\frac{A_{sw}}{s_w}$, the transverse reinforcement area, in mm^2/m ;
- α , the inclination of the shear reinforcements relative to member axis, in degrees.

For the SLS stress limit verification is necessary to input the following variables:

- $M_{Ed,char}$, acting bending moment for the characteristic combination of actions, in kN.m. This value must be greater than zero;
- $M_{Ed,qperm}$, acting bending moment for the quasi-permanent combination of actions, in kN.m. This value must be greater than zero.

For the SLS crack control verification is necessary to input the following variables:

- $M_{Ed,crack}$, acting bending moment for the combination of actions corresponding to the cracking serviceability criteria, in kN.m. This value must be greater than zero;

- $N_{Ed,crack}$, acting axial force for the combination of actions corresponding to the cracking serviceability criteria, in kN. Compressive forces must be inputted as negative values and tensile forces must assume positive values;
- ε_{sh} , is the shrinkage strain. The input value must assume a positive value.

In *FRCcalc* all the data regarding geometry, material and loads are stored in the class *cData*, that is called during the calculation routines.

3.4.2 Calculation routine

The core of the software calculation routine resides in the performance of the cross-section analysis. In Appendix D are presented all algorithms that perform the following calculation subroutines:

- Calculation of the structural characteristic length, l_{cs} ;
- Definition of constitutive models:
 - o Concrete in compression;
 - o Steel in compression or tension;
 - o FRC in tension.
- Calculation neutral axis position and curvature for cross-section under bending;
- Determination of moment vs. curvature relationship;
- Determination of shear resistance:
 - o FRC shear resistance without longitudinal reinforcement;
 - o FRC shear resistance with longitudinal reinforcements;
 - o RC shear resistance without transverse reinforcement;
 - o Shear resistance contribution of transverse reinforcements;
- Calculation of bond transfer length, $l_{s,max}$;
- Determination of design crack width;
- Determination of moment vs. crack width relationship;
- Determination of bending moment corresponding to crack initiation;

- Verification of stress limitation criteria:
 - o Compressive stress in compression;
 - o Tensile stress in FRC;
 - o Tensile stress in steel rebars.

3.4.3 Results Output

The outputs of *FRCcalc* are presented in the form of a datasheet and graphs, namely:

- Structural characteristic length of the FRC cross-section, l_{cs}^r and l_{cs}^u ;
- Maximum resisting bending moment of the FRC and RC cross-sections;
- Ultimate shear resistance of the FRC and RC cross-sections;
- Plot of the resisting moment vs. curvature of the FRC and RC cross-sections;
- Design crack width and mean crack spacing of the FRC and RC cross-sections;
- Plot of the moment vs. design crack width of the FRC and RC cross-sections;
- Assessment of stress limitation at SLS for FRC and RC cross-sections.

3.5 Examples

In the present section are presented some examples of the analysis of FRC and RC cross-section using *FRCcalc*, which allow to demonstrate the benefits provided using fiber reinforcements in the performance of concrete structural elements and the possibility of fiber reinforcements to partially replace the conventional steel bar reinforcements.

Additionally, to appraise *FRCcalc* accuracy to evaluate the flexural response of FRC and RC cross-sections, a comparison with the results obtained with *DOCROS* software [75] is presented. *DOCROS* is a software used in the analysis of cross-sections subjected to axial load and increasing curvature and it was developed by the Structural Composites research group of the Department of Civil Engineering of University of Minho. In *DOCROS* a cross-section is discretized in layers, for which is assigned a specific constitutive law to describe the material behavior of the layer. A detailed description of *DOCROS* can be found in [75].

3.5.1 Example 1 – Beam

The first example corresponds to FRC/RC cross-section of a beam. The main objective of this example is to demonstrate the increase of structural performance provided by the use of fiber reinforcements when compared to a RC cross-section. The cross-section has the following properties:

- Geometry: $b = 200mm$ | $h = 500mm$;
- Concrete strength class: C25/30 | toughness class: 2.5c | $f_{R1k} = 2.678MPa$ | $f_{R2k} = 2.508MPa$ | $f_{R3k} = 2.941MPa$ | $f_{R4k} = 2.950MPa$ | $\varphi_c = 0.0$ | $d_g = 16mm$;
- Conventional reinforcement for FRC and RC cross-section:
 - Tensile steel reinforcement: A500NR | $A_{s1} = 314.16mm^2 (4\phi10)$ | $c_1 = 30mm$;
 - Compressive steel reinforcement: A500NR | $A_{s2} = 157.08mm^2 (2\phi10)$ | $c_2 = 30mm$;
 - Transverse reinforcement: A500NR | $A_{sw} = 502.66mm^2/m (\phi8 / /200mm)$ | $\alpha = 90^\circ$.
- Data for determination of structural characteristic length:
 - Type of loading: Long term, repeated loading;
 - State of cracking: Stabilized cracking stage;
 - Load combination corresponding to cracking serviceability criteria:
 $M_{Ed,crack} = 40.0kN.m$ | $N_{Ed,crack} = -50.0kN$.
- Axial force at ULS load combination for determination of flexural resistance:
 $N_{Ed,ULS} = -100.0kN / m$
- ULS load combination for determination of shear resistance: $N_{Ed,Shear,ULS} = -100.0kN$ | $V_{Ed,Shear,ULS} = 75kN$ | $M_{Ed,Shear,ULS} = 12.5kN.m$;
- Characteristic combination of actions: $M_{Ed,char} = 50.0kN.m$ | $N_{Ed,char} = -80.0kN.m$;
- Quasi-permanent combination of actions: $M_{Ed,qperm} = 40.0kN.m$ | $N_{Ed,qperm} = -50.0kN.m$;

- Shrinkage strain: $\varepsilon_{sh} = 1.5 \times 10^{-4}$.

In Figure 44 is presented the moment vs. curvature relationship for the FRC and RC cross-sections determined by *FRCcalc* and *DOCROS*. It is possible to observe that the accuracy of *FRCcalc* to describe the flexural response of the cross-sections is similar to *DOCROS*. For this example, the effective tensile zone height is mainly limited to $h_{c,ef} = 75\text{mm}$ due to the geometry of the cross-section, with exception of the initial cases where the $\chi \leq 2.3 \times 10^{-3} \text{m}^{-1}$ where $h_{c,ef} < 75\text{mm}$. It is noted that in analysis performed in *DOCROS* it is not possible to consider the variation of the effective tensile zone height due to the changes of the neutral axis position, and a fixed value of $h_{c,ef} = 75\text{mm}$ was assumed.

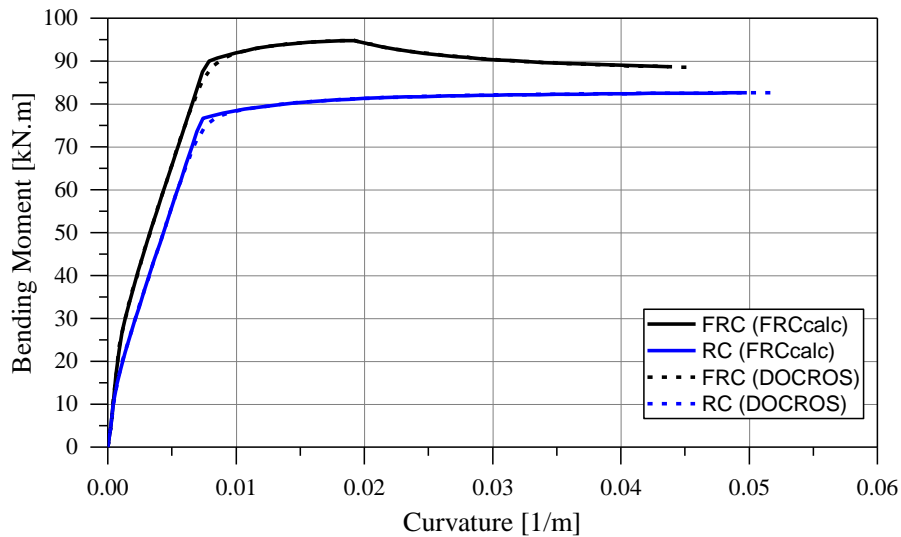


Figure 44 – Bending moment vs. curvature relationship for FRC and RC cross-section of Example no.1 beam, determined from *FRCcalc* and *DOCROS*.

The structural characteristic length of the FRC cross-section presents the following values:

$$l_{cs}^r = 78.61\text{mm} \text{ and } l_{cs}^u = 425\text{mm}.$$

The maximum resisting bending moment of the FRC cross-section is $M_{Rd,ULS}^{FRC} = 94.802\text{kN.m}$ and of the RC cross-section is $M_{Rd,ULS}^{RC} = 82.602\text{kN.m}$. As can be seen, the post-cracking residual strength of the FRC provided a flexural capacity improvement of the beam in 14.8% when compared to the RC cross-section.

The design shear resistance of the FRC and RC cross-sections are, respectively, $V_{Rd}^{FRC} = 232.341\text{kN}$ and $V_{Rd}^{RC} = 203.243\text{kN}$, which represents a 14.3% improvement of the shear strength provided by

the fiber reinforcements. The FRC shear resistance was determined according to the model based on the VEM/SMCFT theory.

In Figure 45 is presented the relationship between the design crack width and the acting moment in the cross-section evaluated at SLS conditions. For the load combination corresponding to cracking serviceability criteria, the design crack width in the FRC and RC cross-section are, respectively, $w_d^{FRC} = 0.047\text{mm}$ and $w_d^{RC} = 0.191\text{mm}$, which represent a decrease of crack opening of 4.06x provided by the fiber reinforcements. In addition, the mean crack spacing of the FRC and RC beams are, respectively, $s_{sm}^{FRC} = 78.607\text{mm}$ and $s_{sm}^{RC} = 144.472\text{mm}$.

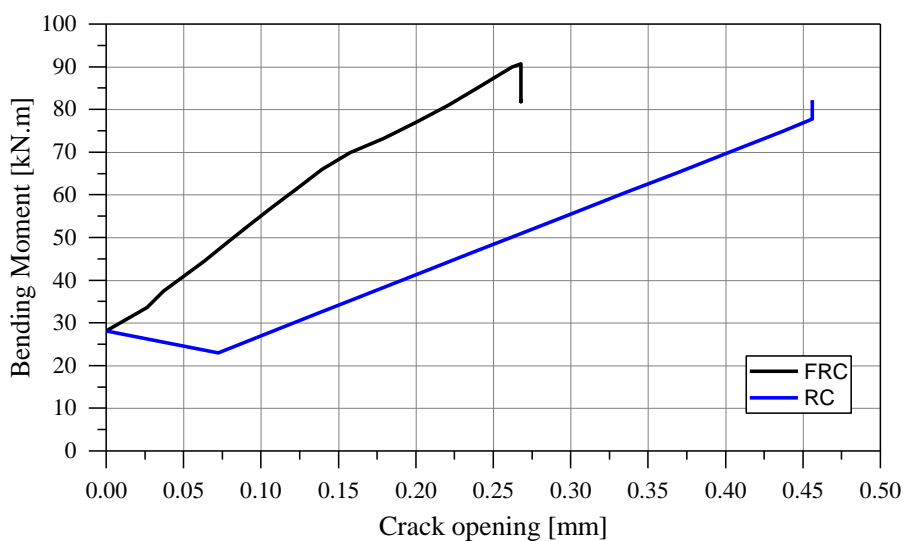


Figure 45 – Design crack width vs. resisting bending moment at SLS relationships for FRC and RC cross-section of Example no.1 beam.

Regarding the verification of the stress limitation criteria defined in MC2010, in Table 4 is presented a summary of the verification check. As can be seen, the use of fiber reinforcements provides a decrease of the stress in the cross-section when compared to the performance of a RC cross-section, particularly of the steel bars stress (54.1%).

Table 4 – Verification of stress limitation criteria for Example no.1 beam.

Concrete compressive stress			
Stress		Limit	Result
$\sigma_{c,FRC}^{SLS,char} = 7.765MPa$	\leq	$0.6 \cdot f_{ck} (t = 28) = 15MPa$	Verified
$\sigma_{c,RC}^{SLS,char} = 9.218MPa$	\leq	$0.6 \cdot f_{ck} (t = 28) = 15MPa$	Verified
$\sigma_{c,FRC}^{SLS,qperm} = 5.729MPa$	\leq	$0.4 \cdot f_{ck} (t = 28) = 10MPa$	Verified
$\sigma_{c,RC}^{SLS,qperm} = 7.320MPa$	\leq	$0.4 \cdot f_{ck} (t = 28) = 10MPa$	Verified
Steel tensile stress			
Stress		Limit	Result
$\sigma_{s,FRC}^{SLS,char} = 118.304MPa$	\leq	$0.8 \cdot f_{yk} = 400MPa$	Verified
$\sigma_{s,RC}^{SLS,char} = 257.690MPa$	\leq	$0.8 \cdot f_{yk} = 400MPa$	Verified
FRC tensile stress			
Stress		Limit	Result
Not applicable: $f_{Ftsk} < f_{ctk}$			Verified

3.5.2 Example 2 – Slab

The second example corresponds to FRC/RC cross-section of a slab. The purpose of this example is to demonstrate the possibility of partial replacement of conventional steel reinforcement by the addition of fibers to concrete. The cross-section has the following properties:

- Geometry: $b = 1000mm$ | $h = 200mm$;
- Concrete strength class: C25/30 | toughness class: 3b | $f_{R1k} = 3.0MPa$ | $f_{R2k} = 2.552MPa$ | $f_{R3k} = 2.1MPa$ | $f_{R4k} = 2.352MPa$ | $\varphi_c = 0.0$ | $d_g = 16mm$;
- Conventional reinforcement for FRC cross-section:
 - Tensile steel reinforcement: A500NR | $A_{s1} = 251.327mm^2 (\phi 8 / / 200mm)$ | $c_1 = 25mm$;
 - Compressive steel reinforcement: none;
 - Transverse reinforcement: none;
- Conventional reinforcement for RC cross-section:
 - Tensile steel reinforcement: A500NR | $A_{s1} = 392.699mm^2 (\phi 10 / / 200mm)$ | $c_1 = 25mm$;

- Compressive steel reinforcement: none;
- Transverse reinforcement: none;
- Data for determination of structural characteristic length:
 - Type of loading: Long term, repeated loading;
 - State of cracking: Stabilized cracking stage;
 - Load combination corresponding to cracking serviceability criteria: $N_{Ed,crack} = 0kN / m$
| $M_{Ed,crack} = 18.0kN.m / m$;
- ULS load combination: $N_{Ed,ULS} = 0.0kN / m$ | $V_{Ed,ULS} = 35kN / m$ |
 $M_{Ed,ULS} = 10.0kN.m / m$;
- Characteristic combination of actions: $N_{Ed,char} = 0kN / m$ | $M_{Ed,char} = 28.0kN.m / m$;
- Quasi-permanent combination of actions: $N_{Ed,qperm} = 0kN / m$ |
 $M_{Ed,qperm} = 18.0kN.m / m$;
- Shrinkage strain: $\varepsilon_{sh} = 2.1 \times 10^{-4}$.

In Figure 46 is presented the moment vs. curvature relationship for a FRC and RC cross-sections determined by *FRCcalc* and *DOCROS*. For this example, the effective tensile zone height varies between $23.5mm \leq h_{c,ef} \leq 62.8mm$. Due to the restriction to use a fixed value of effective tensile zone height in the analysis performed in *DOCROS*, it was assumed a constant value of $h_{c,ef} = 60mm$. Although this limitation, it is also possible to observe that the flexural response of the cross-section is similar between *FRCcalc* and *DOCROS*.

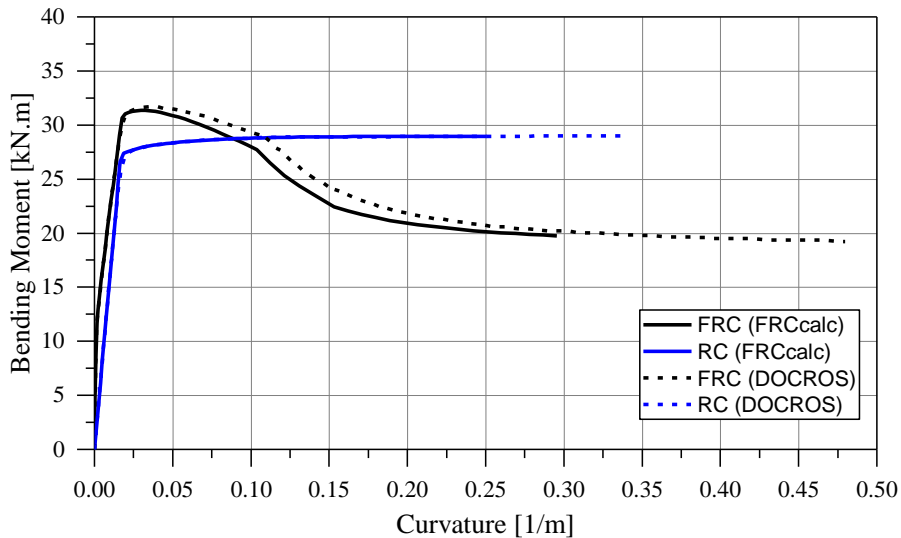


Figure 46 – Bending moment vs. curvature relationship for FRC and RC cross-section of Example no.2 slab, determined from *FRCcalc* and *DOCROS*.

The structural characteristic length of the FRC cross-section presents the following values: $l_{cs}^r = 133.544mm$ and $l_{cs}^u = 143.917mm$.

The maximum resisting bending moment of the FRC cross-section is $M_{Rd,ULS}^{FRC} = 31.337kN.m$ and of the RC cross-section is $M_{Rd,ULS}^{RC} = 28.971kN.m$. Although the area of tensile reinforcement of the FRC is about 65% of the RC cross-section, the ultimate flexural capacity of the FRC slab is slightly higher than the RC counterpart due to the post-cracking tensile strength improvement provided by the fiber reinforcements.

The design shear resistance of the FRC and RC cross-sections are, respectively, $V_{Rd}^{FRC} = 171.375kN$ and $V_{Rd}^{RC} = 121.541kN$, which represents a 41.0% increase of the shear strength of the cross-section provided by fiber reinforcement. The presented FRC shear resistance was determined according to the model based on the VEM/SMCFT theory where the tensile strength of the FRC was estimated according to Figure 24 considering the work of Moraes Neto, et al. [65].

In Figure 47 is presented the relationship between the design crack width and the acting moment in the cross-section evaluated at SLS conditions. For a load combination corresponding to cracking serviceability criteria, the FRC cross-section presents a design crack width equal to $w_d^{FRC} = 0.019mm$ and a mean crack spacing of $s_{m}^{FRC} = 91.271mm$, while the RC cross-section presents a design crack width value of $w_d^{RC} = 0.378mm$ and a mean crack spacing of $s_{m}^{RC} = 322.721mm$, which corresponds to a 20x reduction of the design crack width. For a crack width corresponding to the minimum and maximum value of crack opening commonly adopted in the SLS verifications, the

resisting bending moment of the FRC cross-section is considerably higher than the RC cross-section (2.3x higher for $w = 0.1mm$ and 2.4x for $w = 0.3mm$).

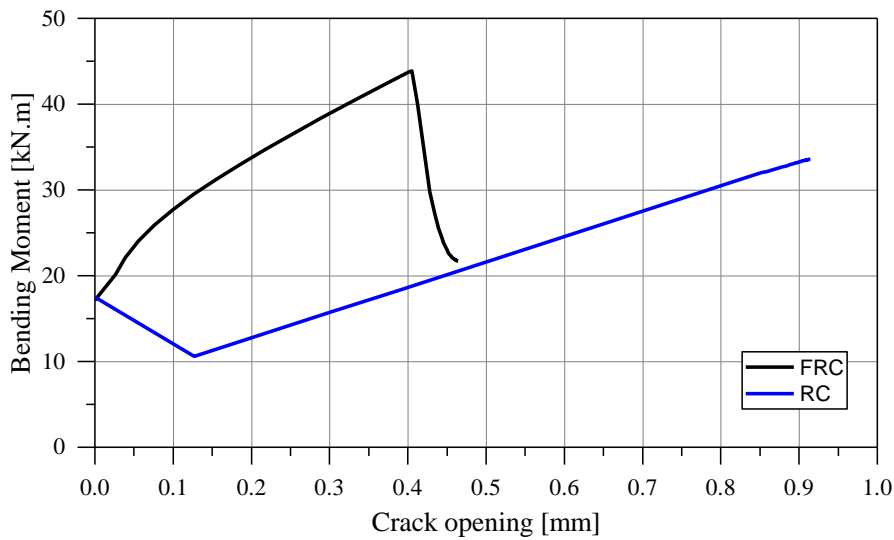


Figure 47 – Design crack width vs. resisting bending moment at SLS relationship for FRC and RC cross-section of Example no.2 slab.

Regarding the verification of the stress limitation criteria defined in MC2010, in Table 5 is presented a summary of the verification check. As can be seen, the use of fiber reinforcements provides a decrease of the stress in the cross-section when compared to the performance of a RC cross-section, especially of the steel bars stress, where for the RC cross-section the limitation criteria for the steel bars tensile stress is not verified.

Table 5 – Verification of stress limitation criteria for Example no.2 slab.

Concrete compressive stress			
Stress		Limit	Result
$\sigma_{c,FRC}^{SLS,char} = 6.826MPa$	\leq	$0.6 \cdot f_{ck} (t = 28) = 15MPa$	Verified
$\sigma_{c,RC}^{SLS,char} = 8.924MPa$	\leq	$0.6 \cdot f_{ck} (t = 28) = 15MPa$	Verified
$\sigma_{c,FRC}^{SLS,qperm} = 2.700MPa$	\leq	$0.4 \cdot f_{ck} (t = 28) = 10MPa$	Verified
$\sigma_{c,RC}^{SLS,qperm} = 5.737MPa$	\leq	$0.4 \cdot f_{ck} (t = 28) = 10MPa$	Verified
Steel tensile stress			
Stress		Limit	Result
$\sigma_{s,FRC}^{SLS,char} = 145.563MPa$	\leq	$0.8 \cdot f_{yk} = 400MPa$	Verified
$\sigma_{s,RC}^{SLS,char} = 439.871MPa$	$>$	$0.8 \cdot f_{yk} = 400MPa$	Not verified
FRC tensile stress			
Stress		Limit	Result
Not applicable: $f_{Frsk} < f_{ctk}$			Verified

3.6 Concluding remarks

This chapter was devoted to the presentation of a new software – *FRCcalc* - developed to perform analysis of the ULS and SLS safety verifications of FRC members, according to the MC2010 design guidelines and recommendations presented in chapter 2. The *FRCcalc* can be used for assessing the effectiveness of fiber reinforcement by comparing the design outputs at SLS and ULS conditions of members reinforced with fibers and with traditional reinforcements. The user interface, input variables, calculation principles and routines were also presented.

The chapter ends by carrying the analysis of two examples of FRC members, which demonstrate the benefits provided by the use of fiber reinforcements in the performance of concrete structural members and the possibility of replacing conventional steel reinforcements by fiber reinforcements. In addition, the accuracy of *FRCcalc* was also confirmed by comparing the flexural response of FRC and RC cross-section with another software.

4 APPRAISAL OF MC2010 SHEAR RESISTANCE PREDICTION MODELS

In the present chapter both shear models available in MC2010 and presented in section 2.5.2 are appraised by comparing the prediction of the shear resistance delivered by the models with an extended version of a database of results of experimental tests of FRC elements, DB_s [76]. The complete database is presented in Appendix E.

4.1 FRC beams shear tests database

The DB_s comprises the results of 113 samples of steel fiber reinforced concrete (SFRC) elements submitted to three-point shear tests, collected from the following sources [16], [18], [61], [77]–[90]. The beams cross-section of the database includes rectangular shape (99) and T-shape (14). Within the 113 samples, 99 represent SFRC deep beams ($d/b_w > 1.0$) and 14 are SFRC shall beams ($d/b_w \leq 1.0$). The effective shear span ratio, a/d , ranges from 2.0 to 4.0, therefore it is assured that the applied load is not directly conducted to the closest support of the beams.

All specimens comprise the use of longitudinal reinforcements in the form of passive steel bars. The passive reinforcement ratio varies between 1.0 to 3.1%. The effective depth of the cross-section, d , is within the interval 150 to 1440mm. None of the samples adopts conventional shear reinforcements.

The fibers incorporated in FRC specimens are exclusively of the hooked-end type, with a fiber aspect ratio, l_f/d_f , varying between 48 to 80. The fiber reinforcement volume ratio ranges from 0.25% to 1.5%.

The concrete maximum aggregate size, d_g , varies between 10 and 25mm, while the mean compressive strength, f_{cm} , of the FRC ranges between 19.6 to 64.6MPa.

The main properties of the experimental data of the DB_s are plotted in Figure 48.

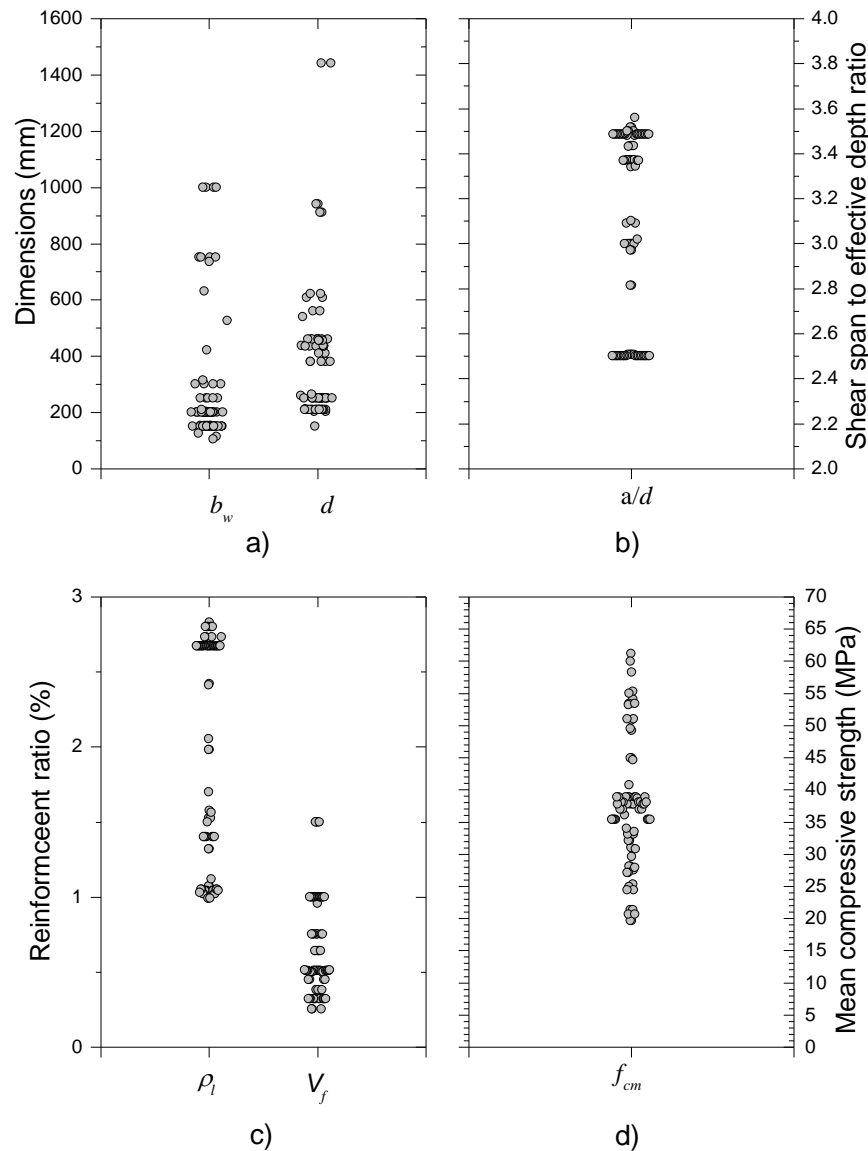


Figure 48 – Main properties of the experimental data of the database: a) Cross-section width and effective depth; b) Shear span to effective depth ratio; c) Conventional and fiber reinforcement ratio; d) Mean compressive strength.

Regarding the SFRC residual flexural tensile strength, the average values of f_{R1} and f_{R3} are not reported for 39 samples, while for f_{R2} and f_{R4} are not provided for 59 samples. In the DB_s , three different prism bending test standards were used, namely the EN 14651 [34], RILEM TC 162-TDF[35], the ASTM C1609 [62] and the UNI 11039 [63]. Considering the main differences for the evaluation of the residual flexural strength using the referenced standards, the EN 14651 and RILEM TC 162-TDF adopt a 3-point bending test configuration with notched FRC beams, while the ASTM C1609 and UNI 11039 adopt a 4-point bending test, the former one with un-notched beams, and the later with notched beams.

Due to the use of un-notched SFRC samples on the prisms bending tests performed according to the ASTM C1609, the crack appears at the weakest point between the two loading points, and the measurement of the crack mouth opening displacement (CMOD) is not possible due to the unknown location of the crack. Consequently, in order to calculate the residual flexural strength of the SFRC samples of the database, the CMODs were obtained by correlating the CMOD with the measured mid-span deflection of the SFRC prisms using the methodology proposed in [91] that considers a rigid body kinematic mechanism similar to the one adopted in 3-point bending tests of notched beams [92]. Due to this simplification, the residual flexural strength values that were determined according to the ASTM C1609 can present some additional inaccuracy.

A first analysis of the DB_s has consisted in the exclusion of test results where a flexural-shear failure mechanism could be feasible. For this purpose, the flexural capacity of each SFRC beam was assessed using the software *FRCcalc* (chapter 3), that follows the design guidelines of MC2010. For the samples where the ultimate resisting bending moment was lower than 95% of the acting bending moment (due to shear capacity registered experimentally), the shear test results were not considered. After this analysis, a total of 80 SFRC beams were considered for the assessment of the shear resistance prediction models, within which the complete data of the post-cracking residual flexural strength (f_{Ri} , $i = 1, 2, 3, 4$) was available for 42 beams, and partial information (f_{Ri} , $i = 1, 3$) was provided for 59 beams. Since some of the beams in the DB_s are casted with the same SFRC mix, the results of the experimental characterization of the post-cracking residual strength for these beams are the same. The 59 beams with experimental data of f_{R1} and f_{R3} were casted from 44 different SFRC mixes, while the 42 beams with f_{R2} and f_{R4} resulted from 35 different SFRC mixes. In Table 6 is presented the different standards considered in the evaluation of the available residual flexural strength values, considering the different SFRC mixes present in the DB_s .

Table 6 – Prism bending test standards adopted for the evaluation of the residual flexural strength, f_{Ri} , considering the different SFRC mixes present in the DB_s .

Number of samples	Prism bending standards				Total
	EN 14651	RILEM TC 16	ASTM C1609	UNI 11039	
f_{R1} and f_{R3}	9	9	25	1	44
f_{R2} and f_{R4}	9	0	25	1	35

4.2 Residual flexural strength prediction model

Due to the significant number of SFRC beams of the DB_s where the residual flexural strength is not reported, the residual flexural strength of these SFRC beams was predicted based on the relationships derived by Moussa [66], that are presented in Eq. (2.61), and Eq. (2.62) to Eq. (2.69).

In the database analyzed by Moussa [66], was found a very good agreement between the experimental, $f_{Ri,exp}$, and predicted, $f_{Ri,mod}$, values of the residual flexural strength, as the ratio $f_{Ri,exp}/f_{Ri,mod}$ ranged between 1.02 to 1.09, while the coefficient of variation varied between 17.8% to 28.9% (Table 7). It is verified that the coefficient of variation has increased with the crack opening at which the f_{Ri} is evaluated, which is a consequence of the increase of the dispersion of the results from f_{R1} to f_{R4} .

Table 7 – Statistical results of the residual flexural strength prediction model [66].

Residual flexural strength	$f_{Ri,exp}/f_{Ri,mod}$		
	Average	SD	COV (%)
f_{R1}	1.02	0.18	17.8
f_{R2}	1.08	0.22	20.6
f_{R3}	1.09	0.26	23.7
f_{R4}	1.05	0.30	28.9

A preliminary assessment was conducted by applying the prediction model for the SFRC mixes used in the beams of the DB_s where the residual flexural strength was experimentally characterized. In Table 8 is presented the average and coefficient of variation (COV) of the ratio between experimental, $f_{Ri,exp}$, and estimated values, $f_{Ri,est}$, of the residual flexural strength, considering the prism bending test standard adopted in the evaluation of the experimental values, considering in Eq. (2.61) is considered that $\gamma_F = 1.0$. Globally, the prediction model exhibited a good agreement between the experimental and estimated values of the residual flexural strength. It is possible to verify that when comparing the estimated and experimental f_{Ri} values determined from the test configuration that adopts notched beams (EN 14651/RILEM TC 162-TDF/UNI 11039), the model exhibits an higher dispersion and average values of the ratio $f_{Ri,exp}/f_{Ri,est}$ than the observed in [66]. For the samples tested according to the ASTM C1609, the model presents in average a slight underestimation of the SFRC residual flexural strength, which can be related with lower values of $f_{Ri,exp}$ due to cracking on

the weakest section between the loading points of the un-notched beams, and to the simplification adopted in the adopted correlation between the mid-span deflection and CMOD.

Table 8 – Statistical analysis of the ratio between the experimental and estimated values of the residual flexural strength, f_{Ri} .

Residual flexural strength	$f_{Ri,exp} / f_{Ri,est}$					
	Global		EN 14651/RILEM TC 162-TDF/UNI 11039		ASTM C1609	
	Average	COV (%)	Average	COV (%)	Average	COV (%)
f_{R1}	1.06	26.9	1.23	24.4	0.92	19.4
f_{R2}	1.14	28.9	1.49	21.0	0.99	20.2
f_{R3}	1.14	31.9	1.35	27.6	0.99	27.8
f_{R4}	1.09	37.9	1.49	28.3	0.93	30.4

For the prediction of the missing values of the residual flexural strength of the SFRC beams of the DB_s , was considered in Eq. (2.60) and Eq. (2.61) a partial safety factor $\gamma_F = 1.0$. In addition, to determine the value of f_{R1m} with Eq. (2.60), the mean tensile strength of the SFRC was determined from the expression provided in MC2010, namely:

$$f_{ctm} = \begin{cases} 0.3 \cdot (f_{ck})^{2/3} & , f_{ck} \leq 50MPa \\ 2.12 \cdot \ln(1 + 0.1 \cdot (f_{ck} + 8)) & , f_{ck} > 50MPa \end{cases} \quad \text{Eq. (4.1)}$$

In order to use Eq. (4.1) the characteristic value of the SFRC compressive strength was determined from the mean compressive strength by the following relationship:

$$f_{ck} = f_{cm} - 8MPa \quad \text{Eq. (4.2)}$$

The complete set of values of the residual flexural strength of the SFRC beams of the DB_s after implementation of the prediction model is presented in Figure 49. The interval data ranges between $f_{R1} = [1.5 - 8.5]MPa$, $f_{R2} = [1.8 - 8.9]MPa$, $f_{R3} = [1.5 - 8.9]MPa$ and $f_{R4} = [1.1 - 7.9]MPa$.

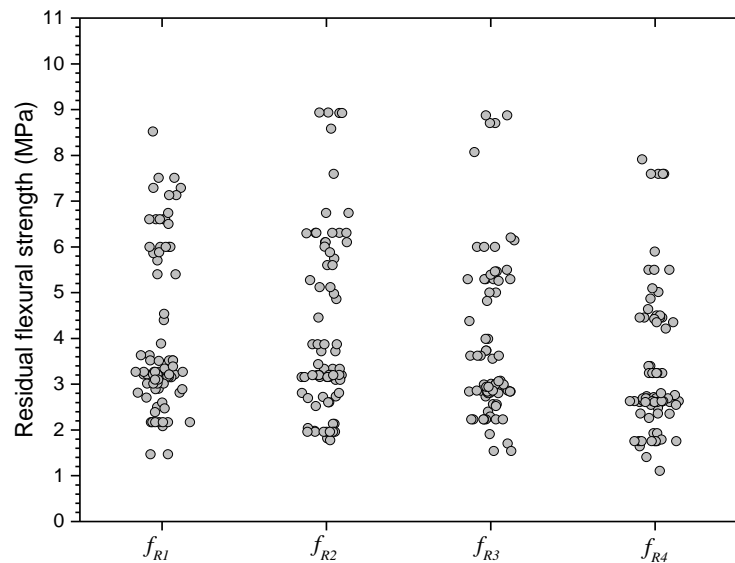


Figure 49 – Residual flexural strength of SFRC beams of the DB_s .

4.3 Appraisal of MC2010 shear resistance prediction models

The predictive performance of both shear models presented in section 2.5.2 is appraised by using the information collected in the DB_s . The shear resistance, $V_{u,model}$, obtained by the empirical based model (Eq. (2.37)), denoted as MC2010_EEN, and by the VEM/SMCFT (Eq. (2.41)), denoted as MC2010_MCFT is compared with the experimentally obtained shear resistance of each specimen, $V_{u,exp}$, and the ratio $\lambda = V_{u,exp}/V_{u,model}$ is appraised, being the predictive performance of the model considered as better as closer to 1.0 is λ . For the determination of the strain at mid-depth of the effective shear area, ε_x , the internal forces in the member were determined for a control section at the distance $a/2$ from the beam's support. During the analysis, the partial safety factors adopted in the theoretical models are set to 1.0, and average values of the FRC material properties are adopted, to properly compare the experimental and theoretical results.

In Figure 50 is presented the statistical analysis of the relationship, λ , between the experimental and theoretical shear resistance determined from both models, considering the source of the residual flexural strength values (experimental/estimated). When assessing the influence of the use of experimental or estimated values of the residual flexural strength of SFRC for the MC2010_EEN and MC2010_MCFT, it is possible to denote that the average values of the prediction ratio, λ , is slightly higher when using estimated values of f_{Ri} , which is related to the slight underestimation of the estimated values of f_{Ri} , as shown in the column "Global" of Table 8. However, the average values of the prediction ratio, λ , for the analyzed scenarios have very small differences, including the

coefficients of variation. Due to this, it is possible to conclude that the residual flexural strength prediction model presented in the previous section is suitable to be used in the evaluation of the shear resistance of SFRC beams, when the values of f_{Ri} are absent in the database.

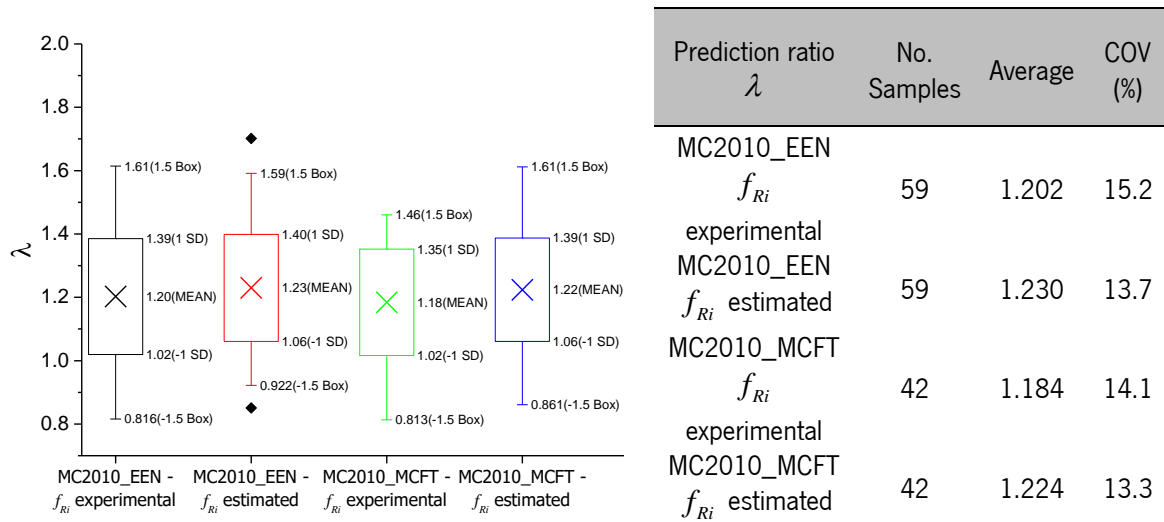


Figure 50 – Statistical analysis of λ for both MC2010 shear resistance models considering the use of experimental and estimated values of f_{Ri} .

In Figure 53 is presented the comparison between the experimental and prediction values of the shear resistance for each beam of the DB_s . The results are divided in two categories considering the source of the residual flexural strength values considered in the shear resistance model (experimental and estimated values). As can be seen, the predictive performance of the shear models is very similar and a satisfactory agreement with the experimental values of the DB_s is attained. Considering the influence of the source of the residual flexural strength values, it is possible to observe that the use of the f_{Ri} prediction model appears to be related with a more pronounced underestimation of the shear resistance (a relatively high percentage of results is in the interval of $V_{u,exp} = 1.5 \cdot V_{u,model}$ to $V_{u,exp} = 2.0 \cdot V_{u,model}$) for the SFRC beams under analysis.

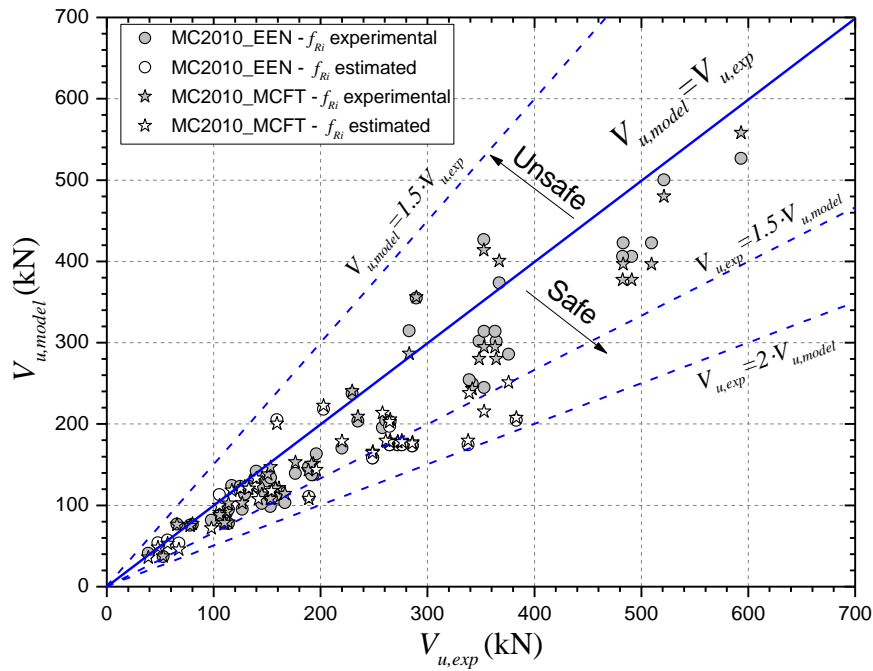


Figure 51 - Comparison of experimental and shear strength determined from both MC2010 prediction models

In Figure 52 is presented the statistical analysis of the ratio, λ , between the experimental and theoretical shear resistance determined from both models, for all samples analyzed (80 SFRC beams). In average, both models present a satisfactory approximation to the experimental results (average value of λ equal to 1.26), with acceptable values of dispersion (coefficient of variation lower than 20%). It should be noticed the existence of only one outlier in 80 samples ($\approx 1\%$), which corresponds to a sample of the MC2010_EEN model.

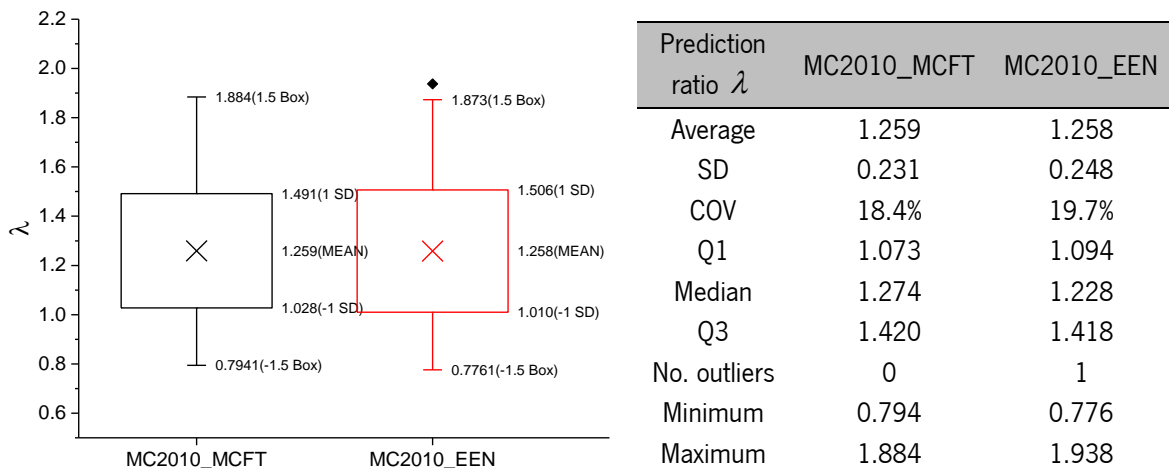


Figure 52 - Statistical analysis of λ for both MC2010 shear resistance models.

In Figure 53 is presented the comparison of the prediction ratio, λ , for each test sample. As can be clearly seen, the results of both models are very similar, which could indicate that the quality of the

prediction of the shear strength provided by the MC2010_EEN and MC2010_MCFT is being influenced by the same set of variables.

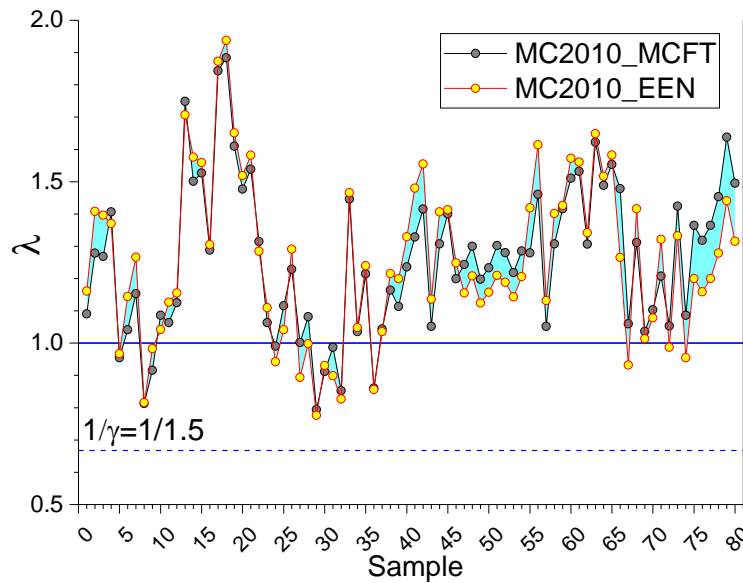


Figure 53 – Comparison of the value of λ for each sample determined by the theoretical models.

In Figure 54 is presented the overall analysis of both models, regarding that the prediction values are safe for $\lambda \geq 1$ and unsafe for $\lambda < 1$. From these results is possible to verify that the MC2010_MCFT model presents a slightly higher percentage of safe predictions when compared to the MC2010_EEN model. When a safety factor equal to $\gamma = 1.5$ is considered in the shear strength prediction (discontinuous line in Figure 53), both models always return safe prediction of the shear resistance of the SFRC beams.

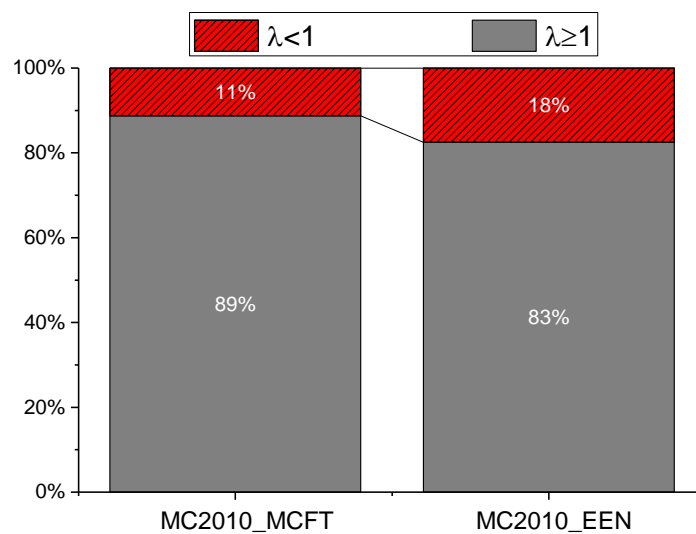


Figure 54 – Predictive performance of the theoretical models, safe ($\lambda \geq 1$) and unsafe ($\lambda < 1$).

In addition, the comparison between the performance of both MC2010 models was assessed according to an adapted version of the *Demerit Points Classification* proposed in [93]. This classification is based on the determination of the cumulative number of penalties for each value of λ . The penalty points scale is defined in Table 9, and the lower the number of penalties is, the safer is the performance of the model. For this case, both models present a very similar number of total penalties points, with a slight better performance of the MC2010_MCFT model presenting 62 penalty points while the MC2010_EEN model has 68 penalty points.

Table 9 – Adapted version of the *Demerit Points Classification*.

$\lambda = V_{u,exp} / V_{u,model}$	Classification	Penalty
< 0.50	Extremely Dangerous	10
[0.50-0.85[Dangerous	5
[0.85-1.15[Appropriate Safety	0
[1.15-2.00[Conservative	1
≥ 2.00	Extremely Conservative	2

In Figure 55 is presented the relationship between the ratio λ with some variables of the shear tests and of the shear models. For clarification, in Figure 55 the ultimate crack width, w_u , and the strain at mid-depth of the effective shear area, ε_x , are only determined for the MC2010_MCFT model. It is visible a slight correlation between the increase of the ultimate crack width and strain at mid-depth of the effective shear area, and the increase of the predictive performance of the MC2010_MCFT model. This may indicate that the aggregate interlock effect is being estimated too conservatively, since this favorable shear resisting mechanism is inversely proportional to the crack width at shear failure. Another possibility is a too conservative estimation of the adopted approach for the contribution of the fiber reinforcement for the shear capacity in the cases where shear failure occurs at relatively small crack width.

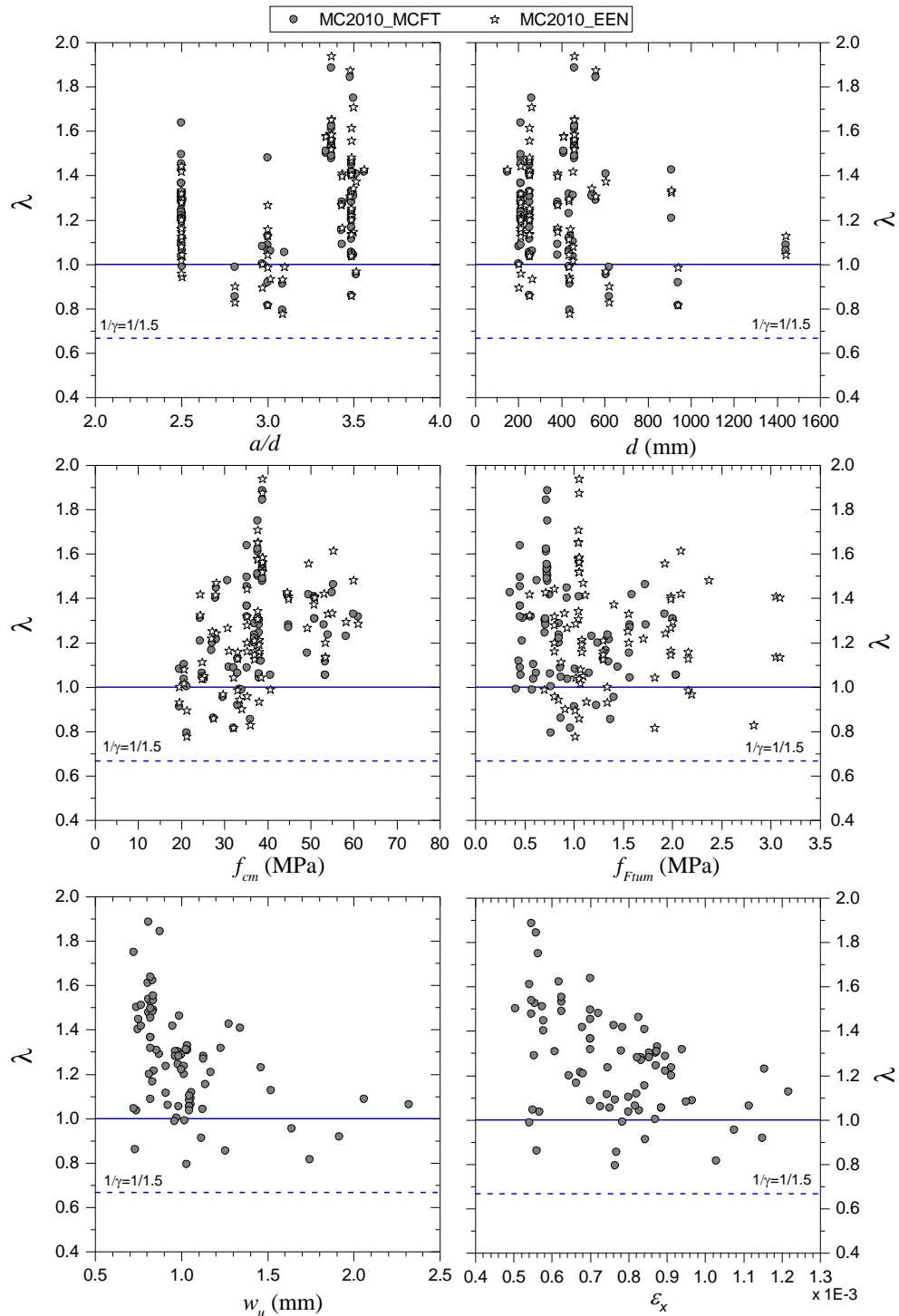


Figure 55 – Relationship between λ and effective shear span ratio, a/d ; the depth of longitudinal reinforcement, d ; the mean concrete compressive strength, f_{cm} ; the mean value of the ultimate residual tensile strength, f_{Fum} ; the ultimate crack width, w_u ; and the strain at mid-depth of the effective shear depth, ϵ_x .

4.4 Concluding remarks

In the present work was assessed the performance of the two shear resistance models available in MC2010 by comparing its predictive capability in a database that includes the results of 80 samples of SFRC beams submitted to shear.

Due to the absence of the characterization of the residual flexural strength of the SFRC used in several tests, a model that estimates these mechanical parameters based on the reinforcement index and concrete strength class was proposed and coupled with the shear resistance models.

For the assessment of the suitability of the residual flexural strength prediction model, a comparison of the prediction ratio, λ , was performed, which was computed by considering estimated and experimentally obtained values of the residual flexural strength of the SFRC. The obtained results demonstrated a very small difference between the average and dispersion of the prediction ratio, λ , which validates the use of the residual flexural strength prediction model in the assessment of the shear resistance of FRC elements.

For evaluating the overall performance of the shear models, a statistical analysis of the prediction ratio, λ , was conducted, which revealed that the performance of the MC2010_MCFT and MC2010_EEN models is very similar. For the majority of the cases, both MC2010 shear models predict safe values for the shear resistance of the SFRC beams, and when the partial safety factor is introduced, the models always return safe predictions. An additional comparison of the MC2010 shear models was done considering the Demerit Points Classification, having both approaches presented similar performance in this regard (the difference was only 6 penalty points between both models).

5 ANALYSIS OF FRC MEMBERS CONSIDERING FIBER ORIENTATION, FIBER SEGREGATION AND FIBER PULLOUT RESISTANCE MODEL

5.1 Introduction

This chapter describes an integrated approach for the prediction of the flexural capacity of FRC members. This approach considers the orientation and segregation of fibers along the cross-section of the FRC members and the pullout constitutive law of each fiber bridging the two faces of a crack.

This model is implemented in a software developed for the analysis of the flexural response and cracking behavior of FRC structural elements.

5.2 New material model for FRC in tension

In order to describe the flexural behavior of FRC, a new model was implemented in *DOCROS*, an already existing software for the analysis of cross-sections of R-FRC members failing in bending [94]. The acronym R-FRC means a FRC member that is flexurally reinforced with conventional reinforcements like bars or meshes.

As previously mentioned, *DOCROS* is a software used in the analysis of cross-sections, where a cross-section is discretized in N layers, for which is assigned a specific constitutive law to describe the material behavior of the layers. In this scope, the fiber orientation profile, fiber segregation and fiber pullout constitutive law were coupled to form a new material model, named NLMM107, to simulate the nonlinear material behavior of FRC.

For the pre-cracking tensile behavior of the FRC is considered a linear elastic stress-strain response up to tensile strength, f_{ct} , is reached. In Eq. (5.1) is presented the expression to determine the tensile stress at the j^{th} layer that discretizes the cross-section, considering that ε^j is the strain at the level of the center of gravity of the j^{th} layer.

$$\sigma^j = E_c \cdot \varepsilon^j \quad ; \quad \varepsilon^j \leq f_{ct} / E_c \quad \text{Eq. (5.1)}$$

For the post-cracking tensile response of FRC, the contribution of the fiber pullout resistance, $P(w)$, is added to the post-cracking residual strength of FRC matrix, $\sigma_{ct}(w)$, namely:

$$\sigma^j = \frac{P^j(w^j)}{b^j \cdot t^j} + \sigma_{ct}^j(w^j) \quad \text{Eq. (5.2)}$$

where b^j and t^j are, respectively, the width and thickness of the generic j^{th} layer that discretizes the cross-section, and w^j is the crack width at the level of the center of gravity of the j^{th} layer.

The adopted stress-crack width relationship of the concrete matrix is based on the model presented in [20]. The tensile softening response is defined by the following expression [95]:

$$\sigma_{ct}^j(w) = c_1 \cdot \sigma_0 \cdot e^{-c_2 \cdot w^j} \quad \text{Eq. (5.3)}$$

where c_1 is a coefficient that accounts for beneficial effect of the fibers on the tensile strength of the matrix; c_2 is a coefficient that controls the steepness of the softening branch; and σ_0 for fracture Mode I is equal to the matrix tensile strength, f_{ct} . For fracture Mode I, in [96] is adopted a value of $c_1 = 1.0$, while $c_2 = 15$ and $c_2 = 30$ are proposed in [97] for concrete and mortar, respectively.

To simulate the compressive behavior of the FRC, the NLMM107 model, resorts to the compressive monotonic stress-strain relationship presented in Figure 56, where f_{cc} is the FRC compressive strength, ε_{cc} is the concrete strain at peak compressive stress, and ε_{cr} is the critical strain for FRC in compression [98], which is already implemented in *DOCROS*.

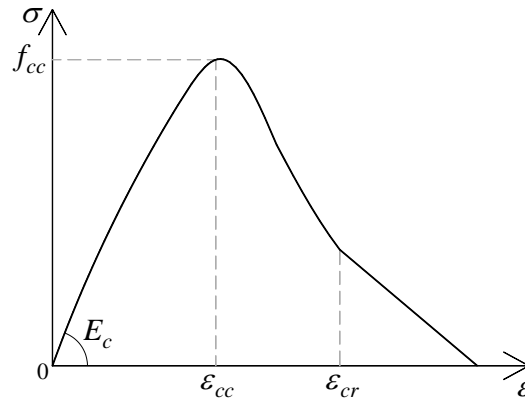


Figure 56 – Compressive stress vs. strain model adopted in NLMM107 constitutive model.

5.2.1 Fiber orientation profile model

In this section is presented a model capable of predicting the distribution of orientation angles of the fibers, φ_i , on a cross-section of a FRC member, based on the definition of an orientation factor, η . The orientation factor corresponds to the average length of the projection of all fibers crossing a crack

plane on its orthogonal direction, divided by the fiber length [42]. The fiber orientation factor can vary between 0.0 and 1.0, corresponding, respectively, to fibers parallel and orthogonal to the analyzed cross-section (herein representing the crack plane) [99]. The fiber orientation factor relates the theoretical number of fibers, N_{th} , into the concrete medium with the number of fibers to be encountered in a cross-section, N_f , according to the expression [100]:

$$N_f = N_{th} \cdot \eta = \frac{A_{sec}}{A_f} \cdot V_f \cdot \eta \quad \text{Eq. (5.4)}$$

where A_{sec} is the cross-section area of the FRC element, A_f is the cross sectional area of a fiber, and V_f is the fiber volume dosage.

The fiber orientation profile model is based on the work of [42], where the distribution of the orientation of the fibers in a cross-section is arranged in discrete intervals, $n\Delta\varphi$, and the number of fibers within each orientation angle interval, $N_{f,\bar{\varphi}_i}$ is determined according to the expression:

$$N_{f,\bar{\varphi}_i} = C(\bar{\varphi}_i) \cdot N_f \quad \text{Eq. (5.5)}$$

where $C(\bar{\varphi}_i)$ is the ratio between the number of fibers within each interval range with a mean orientation angle $\bar{\varphi}_i$ and the total number of fibers in the cross-section (Figure 57).

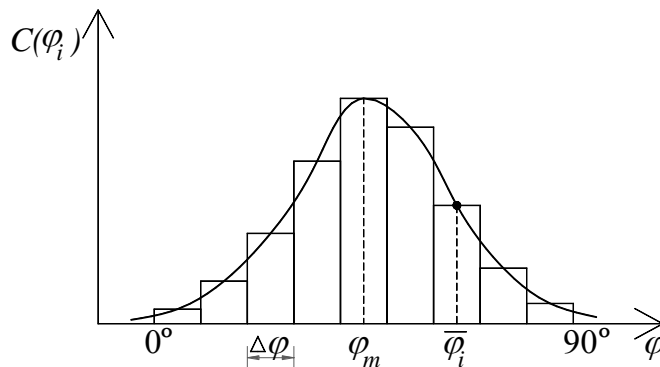


Figure 57 – Fiber orientation profile.

According to [42] the parameter $C(\varphi_i)$ can be determined by the expression:

$$C(\bar{\varphi}_i) = f(\bar{\varphi}_i) \cdot F_{RE}(\eta) \quad \text{Eq. (5.6)}$$

where $f(\bar{\varphi}_i)$ is the frequency of fibers within the interval of orientation angles $\varphi_i \pm \Delta\varphi_i/2$, $\Delta\varphi_i = 90/n\Delta\varphi$, considering a Gaussian law to describe the frequency distribution, and $F_{RE}(\eta)$ is

a coefficient to account to the error resultant of adopting discrete ranges of fiber orientation angles rather than considering a continuous function, which is determined with Eq. (5.7).

$$F_{RE} = \begin{cases} 1.29 - 0.38 \cdot \eta & ; \eta < 0.75 \\ 1.0 & ; \eta \geq 0.75 \end{cases} \quad \text{Eq. (5.7)}$$

According to [42], based on the orientation factor, η , is possible to determine the average orientation angle of the fibers in the cross-section, φ_m , and the corresponding standard deviation, $\sigma(\varphi_m)$, using the following equations:

$$\varphi_m = \arccos(\eta) \cdot 180/\pi \quad [^\circ] \quad \text{Eq. (5.8)}$$

$$\sigma(\varphi_m) = 90 \cdot \eta \cdot (1 - \eta) \quad [^\circ] \quad \text{Eq. (5.9)}$$

The methodology adopted to determine the fiber orientation factor, η , is based on the work of Krenchel [100]. Due to the wall effect on the orientation of the fibers, the cross-section of the FRC member is divided in three zones with different orientation factors (Figure 58). The fiber orientation factor of the cross-section is determined by the expression:

$$\eta = \frac{\eta \cdot (b - l_f) \cdot (h - l_f) + \eta \cdot l_f \cdot [(b - l_f) + (h - l_f)] + \eta_3 \cdot l_f^2}{b \cdot h} \quad \text{Eq. (5.10)}$$

where l_f is the length of the adopted fiber type, and η_z ($z = 1, 2, 3$) is the fiber orientation factor for each zone of the cross-section.

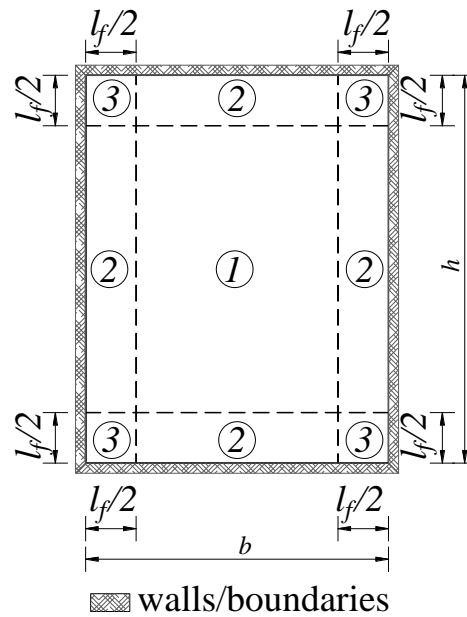


Figure 58 – Zones of cross-section for the determination of the fiber orientation factor due to wall effect.

The values of the orientation factor for each zone of the cross-section are based on previous research, namely:

- Zone 1: corresponds to the zone where the fiber orientation is not influenced by any boundary condition, and the orientation factor is equal to $\eta_1 = 0.50$ [101], [102];
- Zone 2 : corresponds to the situation where the fiber orientation is affected by one boundary, leading to a zone of average orientation factor equal to $\eta_2 = 2/\pi$ [102];
- Zone 3: zone within the influence of two boundaries, with an average orientation factor equal to $\eta_3 = 0.84$ [101];

The boundaries correspond to the formwork that usually are adopted in the bottom and lateral surfaces of the cross-section, and to the top surface (the smoothing process of the concrete element top surface is considered to have a similar influence on fiber orientation as a mold [101]).

The number of fibers within each orientation angle interval, N_{f,φ_i} is determined according to the algorithm presented in Table 10.

Table 10 – Algorithm to determine number of fibers within each orientation angle interval.

ROUTINE TITLE: <i>Calc_Fiber_Orientation_Profile</i>
<p>INPUT:</p> <ul style="list-style-type: none"> • Cross-section width, b, and height, h; • Length (l_f) and diameter (d_f) of fibers; • Fiber volume dosage, V_f; • Number of divisions in the fiber orientation domain, $n\Delta\varphi$.
<p>OUTPUT:</p> <ul style="list-style-type: none"> • Number of fibers within each orientation angle interval, $N_{f,\overline{\varphi_i}}$.
<p>i) Determine fiber orientation factor value according to Eq. (5.10);</p> <p>ii) Determine number of fibers in the cross-section, N_f, according to Eq. (5.4);</p> <p>iii) Determine the coefficient $F_{RE}(\eta)$ using Eq. (5.7);</p> <p>iv) Determine the average orientation angle, φ_m, and the corresponding standard deviation, $\sigma(\varphi_m)$ using Eq. (5.8) and Eq. (5.9);</p> <p>v) Divided the fiber orientation domain $[0-90^\circ]$ into $n\Delta\varphi$ intervals. For each interval determine:</p> <ol style="list-style-type: none"> a. Mean orientation angle of the interval: $\overline{\varphi_i} = (\varphi_i + \varphi_{i-1})/2$; $\varphi_i = 90/n\Delta\varphi$; $i = 1, \dots, n\Delta\varphi$; b. Determine the frequency of fibers within the interval, $f(\overline{\varphi_i}) = F(\varphi_i, \varphi_m, \sigma(\varphi_i)) - F(\varphi_{i-1}, \varphi_m, \sigma(\varphi_i))$, where $F(\dots)$ is the cumulative distribution function of the standard Normal distribution; c. Determine $C(\varphi_i)$ according to Eq. (5.6); d. Determine the number of fibers within the orientation angle interval, $N_{f,\overline{\varphi_i}}$, using Eq. (5.5).

5.2.2 Fiber segregation model

In order to analyze the fiber segregation phenomena that can occur during FRC casting, a segregation model is implemented. The model is defined by a segregation factor, ξ , varying between -1.0 to

+1.0. The segregation model assumes a linear variation of the fiber's distribution along the depth of the cross-section. The cross-section is divided in N layers, and considering the thickness t^j ($j=1, \dots, N$) and depth of center of gravity of the j^{th} layer to the top face of the FRC elements d^j ($j=1, \dots, N$), the number of fibers in each layer is determined by the following expression:

$$N_f^j = \left(N_f^{\text{top}} \left(1 - \frac{d^j}{h} \right) + N_f^{\text{bot}} \cdot \frac{d^j}{h} \right) \cdot t^j ; j=1, \dots, N \quad \text{Eq. (5.11)}$$

where h is the cross-section height, N_f^{top} and N_f^{bot} are, respectively, the number of fibers at top and bottom faces of the cross-section that are determined according to:

$$N_f^{\text{top}} = \frac{N_f}{h} \cdot (1 - \xi) \quad \text{Eq. (5.12)}$$

$$N_f^{\text{bot}} = \frac{N_f}{h} \cdot (1 + \xi) \quad \text{Eq. (5.13)}$$

where N_f is the total number of fibers in the cross-section.

The model variables and schematic distribution of the fibers along the depth of the cross-section is presented in Figure 59.

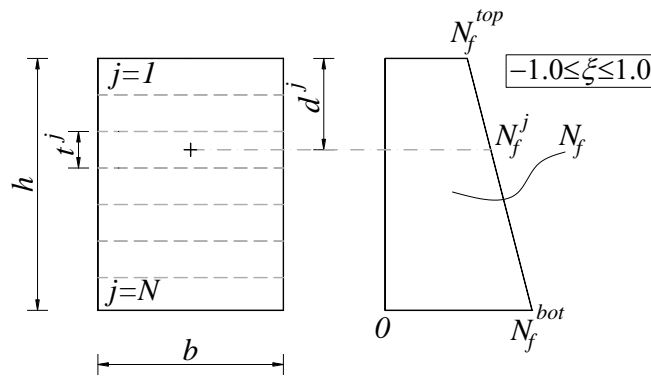


Figure 59 – Fiber segregation model.

For a homogenous distribution of the fibers in the cross-section, the segregation factor assumes a value of $\xi = 0$, and $N_f^{\text{top}} = N_f^{\text{bot}}$. If $\xi = 1.0$ is assumed, $N_f^{\text{top}} = 0$, while $N_f^{\text{bot}} = 0$ if $\xi = -1.0$.

5.2.3 Fiber pullout constitutive model

Based on the execution of pullout tests of fibers from cementitious matrix, it has been demonstrated that the pullout response, particularly for the case of steel fibers, is primarily influenced by the type,

geometry and length of the fibers, and by the mechanical properties of the fiber and of the matrix, as is summarized in [103].

The considered fiber pullout constitutive model is based on the Unified Variable Engagement Model (UVEM) proposed by [96], [103], [104]. The UVEM combines Mode I and Mode II fracture process of SFRC.

The proposed model adopts the following assumptions [103]:

- It is admitted that all the fiber slip from the matrix occurs from the shorter embedded length of the fiber, and the slip between the longer embedded part of the fiber and its surrounding matrix is negligible. This assumption leads to the slip of the shorter embedded length being equal to the crack opening displacement of the cementitious matrix;
- The elastic deformation of the fibers is insignificant in comparison with the slip of the fibers during pullout;
- In comparison with the pullout of the fibers, the energy expended by bending the fibers is small and can be disregarded.

The pullout force carried by a steel fiber bridging a crack of a cementitious matrix is the sum of three components (Figure 60): i) friction of the embedded straight part of the fibers; ii) mechanical anchorage provided by end appendages of the fibers; and iii) a mechanical anchorage provided by the snubbing effect [105], [106]. The snubbing effect is characterized by a scrape and constrain of the cementitious matrix against the fibers that occurs during the pullout mechanism of inclined fibers [107].

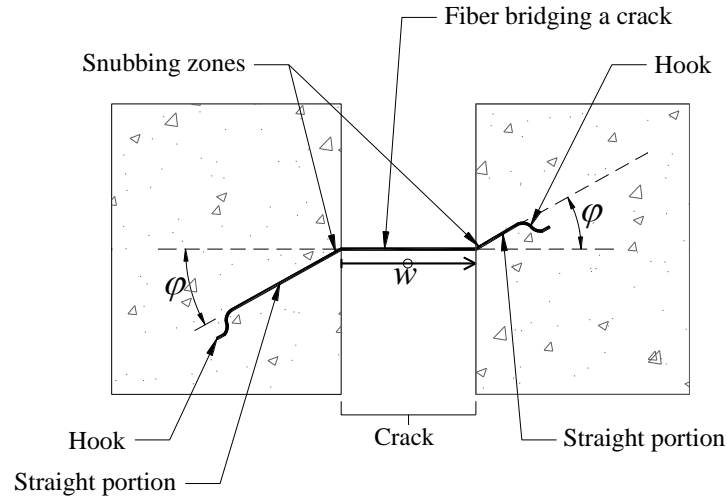


Figure 60 – Components of the fiber pullout response.

Similarly to the UVEM model, in the proposed model is adopted an uniform bond strength, τ_b , along the fiber embedded length. With this methodology, the contribution of each component (hooked-end, straight portion and snubbing zones) is not individually discretized, being rather defined the bond strength vs. slip relationship of the combined effect of all components contributing to the pullout resistance of a fiber.

In the present model it is idealized a variable bond strength, as a function of the slip displacement of the fiber, while in the UVEM it is considered a constant bond strength. In Figure 61 is illustrated the adopted bond strength vs. slip model ($\tau_{b,0} - \delta$), which is idealized for the pullout response of an aligned fiber ($\varphi = 0^\circ$). The bond strength vs. slip model is defined by the following four parameters (Figure 61 and Eq. (5.14)): the peak bond strength, $\tau_{b,0,p}$; the slip corresponding to the peak bond strength, δ_p ; and the exponents α and β , which define the $\tau_{b,0} - \delta$ variation in its pre-peak and post-peak stage.

$$\tau_{b,o} = \begin{cases} \tau_{b,0,p} \cdot \left(\frac{\delta}{\delta_p} \right)^\alpha & \delta \leq \delta_p \\ \tau_{b,0,p} \cdot \left(\frac{\delta}{\delta_p} \right)^{-\beta} & \delta > \delta_p \end{cases} \quad \text{Eq. (5.14)}$$

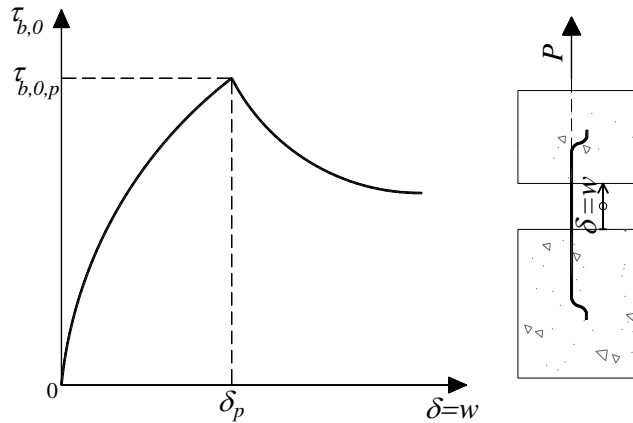


Figure 61 – Idealized bond stress vs. slip ($\tau_{b,0} - \delta$) for the pullout response of an aligned fiber.

In order to consider the snubbing effect in the pullout resistance of the fiber, the expression presented in [103] is adopted:

$$\tau_b(s) = \tau_{b,0}(s) + 0.25 \cdot \gamma^3 \quad \text{Eq. (5.15)}$$

where γ is the fiber bending angle, being defined as the angle between the fiber longitudinal axis and pullout force direction (Figure 62). For Mode I fracture, the crack sliding is null ($s = 0$), and the fiber bending angle is equal to the fiber orientation angle ($\gamma = \varphi$).

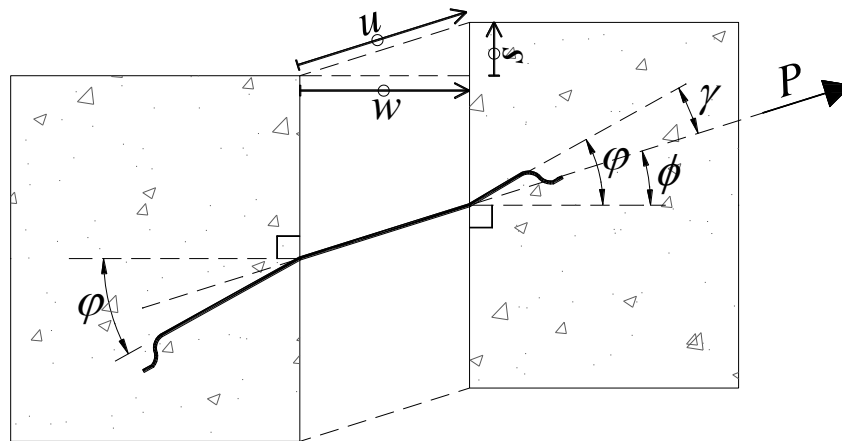


Figure 62 – Definition of fiber bending angle, γ .

In the UVEM model is proposed the minimum crack displacement necessary to a fiber submitted to a pullout force to be considered engaged. This engagement model is a function of the fiber bending angle, γ , and the engagement crack opening, w_e , is defined by [103]:

$$w_e = \frac{d_f}{3.5} \cdot \tan^3 \left(\frac{\gamma}{\gamma_{\max}} \cdot \frac{\pi}{2} \right) \quad \text{Eq. (5.16)}$$

where for Mode I fracture process $\gamma_{\max} = \pi/2$, and for Mode II $\gamma_{\max} = \pi$ [96].

The engagement model defined by Eq. (5.16) was experimentally derived from individual fiber shear test data, assuming that a fiber is considered engaged at the point where the force is 50% of the peak pullout force [103].

By adopting this engagement model in the UVEM, at the initial stage of the crack formation and propagation, the contribution of the most inclined fibers in relation to the load direction is neglected while the crack opening displacement necessary to engage the most inclined fibers has not yet been reached. As in the deduction of the engagement model a fiber is engaged if the pullout force is at least 50% of the maximum pullout load, the UVEM is disregarding 50% of the pullout force for the most inclined fibers up to w_e is reached. As is presented in the section 5.2.4 (Figure 68), this assumption can lead to a significant deviation of the response of a FRC submitted to tension. Due to this, in the present model, a new approach is assumed that considers a linear variation of the bond stress up to the w_e is reached, as is illustrated in Figure 63 and described in Eq. (5.17) and Eq. (5.18).

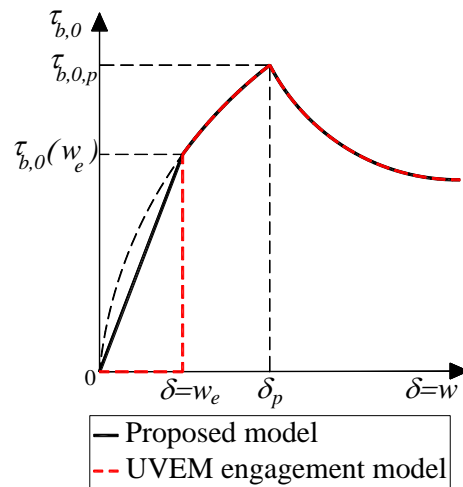


Figure 63 – Idealized bond stress vs. slip ($\tau_{b,0} - \delta$) of the pullout response of an aligned fiber, considering the engagement length of fibers.

$$\tau_{b,o} = \begin{cases} \tau_{b,0}(w_e) \cdot \frac{\delta}{w_e} & ; \delta \leq w_e \\ \tau_{b,0,p} \cdot \left(\frac{\delta}{\delta_p}\right)^\alpha & ; \delta \leq \delta_p \wedge \delta > w_e \\ \tau_{b,0,p} \cdot \left(\frac{\delta}{\delta_p}\right)^{-\beta} & ; \delta > \delta_p \wedge \delta > w_e \end{cases} \quad \text{Eq. (5.17)}$$

$$\tau_{b,o}(w_e) = \begin{cases} \tau_{b,0,p} \cdot \left(\frac{w_e}{\delta_p}\right)^\alpha & w_e \leq \delta_p \\ \tau_{b,0,p} \cdot \left(\frac{w_e}{\delta_p}\right)^{-\beta} & w_e > \delta_p \end{cases} \quad \text{Eq. (5.18)}$$

As illustrated in Figure 64, the pullout force of a fiber with an orientation angle φ_i , P_{φ_i} , corresponding to a crack opening displacement, w , is equal to:

$$P_{\varphi_i}(w) = \pi \cdot d_f \cdot \tau_b(\varphi_i, \delta = w) \cdot L_{bf,o}(w) \quad \text{Eq. (5.19)}$$

where d_f is the diameter of the fibers; τ_b is the average fiber bond strength determined according to Eq. (5.15), Eq. (5.17) and Eq. (5.18), function of the crack width and orientation angle of the fiber; $L_{bf,o}$ is the fiber embedment length that is equal to its initial value minus the crack opening displacement. For the initial value of the fiber embedment length, which corresponds to a crack width equal to zero ($w = 0$), it is assumed $L_{bf,o} = l_f / 4$ for the shortest embedment side, considering that it has been verified to be the average length of embedment of the fibers according to the work of [108].

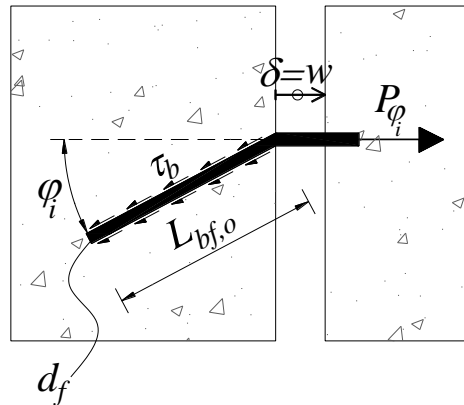


Figure 64 – Pullout force of a fiber with the orientation φ_i .

Due to the increased bond strength, as result of improved mechanical anchorage provided by the snubbing effect and geometry irregularities (providing mechanical anchorage mechanisms), fibers may be susceptible to fracture during the pullout process, particularly the case of the most inclined fibers. In the present model is considered that a fiber fractures if the tensile stress, σ_f , reaches the effective ultimate tensile strength of the fiber, $\overline{\sigma_{fu}}$. For the effective ultimate tensile strength of the fibers is proposed the expression considered in the UVEM model, namely [103]:

$$\overline{\sigma}_{fu} = \sigma_{fu} \cdot \frac{\pi}{2 \cdot \gamma_{\max}} \quad \text{Eq. (5.20)}$$

where σ_{fu} is the fiber tensile strength.

The failure criterion of the fibers with circular cross-section is verified by the following expression:

$$\overline{\sigma}_{fu} \geq \sigma_f = \frac{4 \cdot \tau_b \cdot L_{bf,o}(w)}{d_f} \quad \text{Eq. (5.21)}$$

Considering that the cross-section of a FRC member is discretized in N layers ($j = 1, \dots, N$), and that the fiber orientation domain is divided into $n\Delta\varphi$ intervals (Figure 65a), at the j^{th} cracked layer the pullout resistance is equal to:

$$P^j(w) = \sum_{i=1}^{n\Delta\varphi} P_{\varphi_i}^j(w) \quad \text{Eq. (5.22)}$$

$$P_{\varphi_i}^j(w) = N_{f,\varphi_i}^j \cdot \pi \cdot d_f \cdot \tau_{bu,i} \cdot L_{bf,o}(w) \quad \text{Eq. (5.23)}$$

where $P_{\varphi_i}^j(w)$ is the pullout resistance of the N_{f,φ_i}^j fibers with a mean orientation angle $\overline{\varphi}_i$ at the j^{th} cracked layer, determined according to the fiber orientation and segregation models. In Figure 65c-d is schematically presented an example of the calculation of the pullout force of the fibers bridging the crack at the j^{th} layer of a FRC cross-section.

To determine N_{f,φ_i}^j , at first, the number of fibers at each orientation angle interval is evaluated for the whole cross-section, according to the algorithm presented in Table 10. Afterwards, the corresponding number of fibers within each orientation angle interval, at the j^{th} layer, is determined according to the segregation model, namely Eq. (5.11) to Eq. (5.13) (Figure 65b).

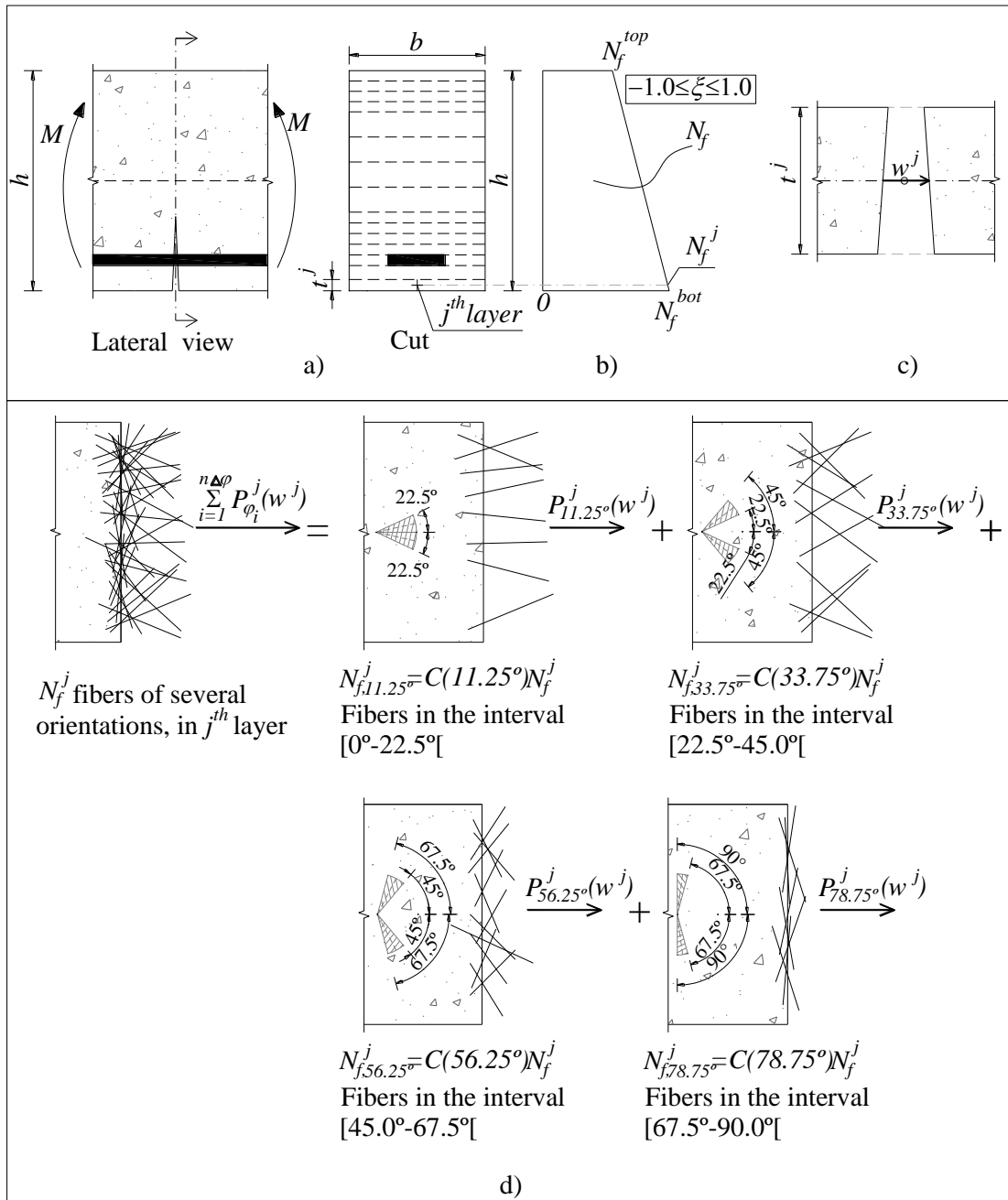


Figure 65 – Schematic representation of coupling of the fiber orientation profile, fiber segregation and fiber pullout resistance model: a) Lateral and section cut view of a cracked FRC member; b) Determination of total number of fibers in a cracked layer, based on segregation model; c) Crack width of the j^{th} layer; d) Example to determine the fiber pullout force at the cracked j^{th} layer, considering $n\Delta\varphi = 4$; $\Delta\varphi_i = 22.5^\circ$.

5.2.4 Influence of the model parameters on the moment-rotation of SFRC members failing in bending

In the present section is assessed the influence of the parameters of the new model on the moment-rotation of SFRC members failing in bending. In Figure 66 is presented the cross-section geometry and reference values of SFRC material properties of the case study. The influence of the variation of the NLM107 parameters on the flexural response of the cross-section is analyzed, specifically in the moment vs. rotation ($M - \theta$) response.

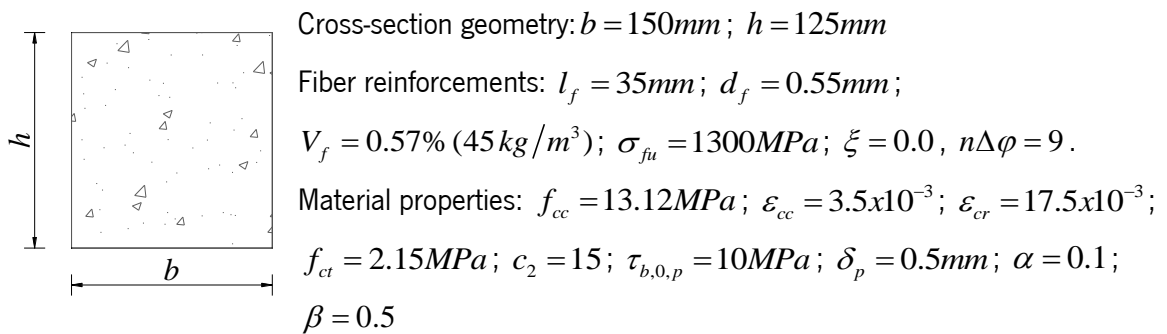


Figure 66 – Cross-section geometry and reference values of the SFRC material properties considered in the case study.

The moment-rotation cross-sectional analysis is performed according to the methodology presented in section 5.3. At each loading step, the crack width of the bottom layer of the cross-section is increased by $\Delta w^p = 5 \times 10^{-3}\text{mm}$, up to a maximum crack width of $w = 7.0\text{mm}$. The cross-section is divided in 125 layers of 1mm of thickness and with equal to 150mm.

According to the fiber orientation model described in section 5.2.1, the reference cross-section presents a fiber orientation factor equal to $\eta = 0.574$, which leads to a total number of fibers in the cross-section under analysis equal to $N_f = 260$. Since fiber segregation factor is assumed equal to zero ($\xi = 0.0$) all layers have the same number of fibers $N_f^j = 2.08$.

Number of divisions of the fiber orientation domain

In Figure 67 is presented the $M - \theta$ response of the cross-section considering four levels of division of the fiber orientation domain, namely for $n\Delta\varphi = 4, 9, 15, 30$, which lead to an interval angle between each division of the fiber orientation profile equal to, respectively, $\Delta\varphi = 22.5^\circ, 10.0^\circ, 6.0^\circ, 3.0^\circ$. As can be seen, the number of divisions of the fiber orientation

profile influence the flexural response of the cross-section when the division level of the fiber orientation domain is relatively small ($n\Delta\varphi = 4$). However, no influence in the response of the cross-section is observed when the domain is decomposed in higher or equal 9 intervals ($n\Delta\varphi > 9$).

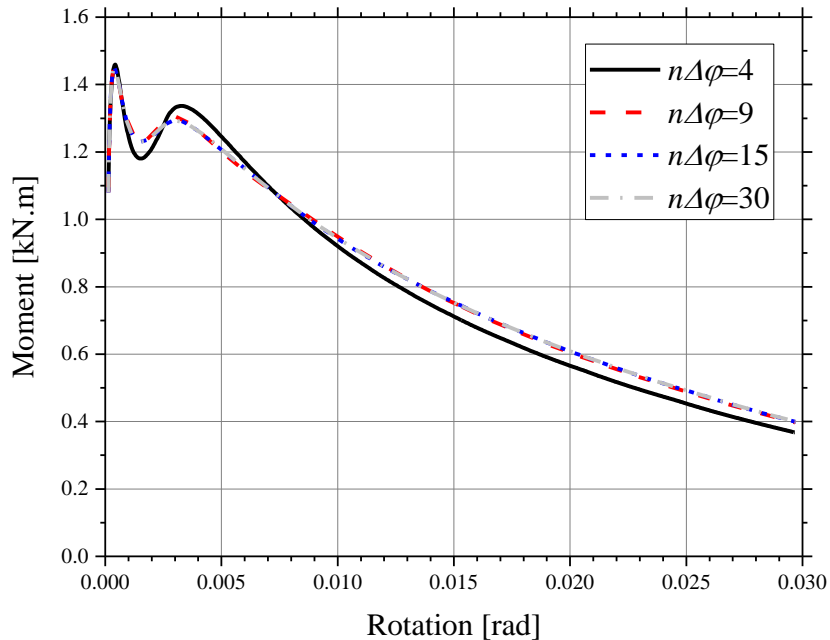


Figure 67 – Moment vs. rotation relationship of cross-section considering $n\Delta\varphi = 4, 9, 15, 30$.

Engagement model

In Figure 68 is analyzed the influence of the engagement model in the $M - \theta$ response the cross-section. Three situations are considered in the analysis, as presented in Figure 69, namely: i) the engagement model as considered in the present model; ii) the engagement model as considered in the UVEM; iii) no engagement model.

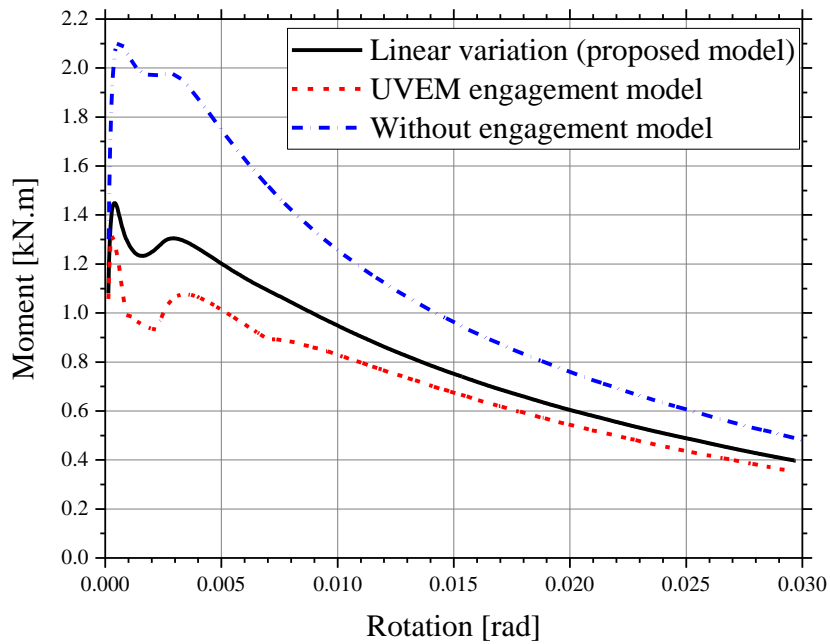


Figure 68 – Moment vs. rotation relationship of cross-section, considering different engagement models.

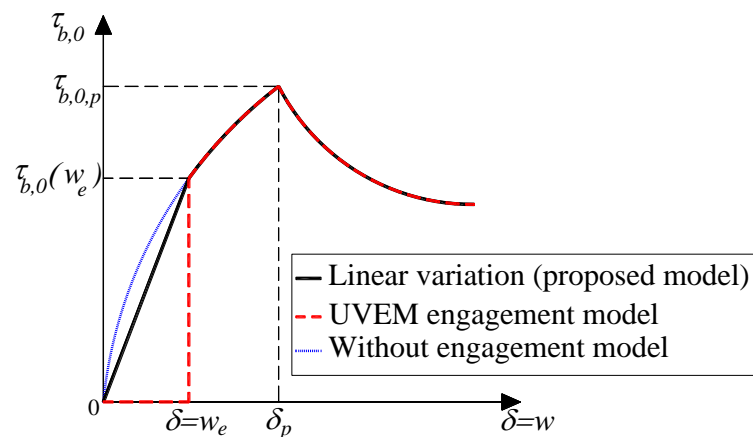


Figure 69 – Bond stress vs. slip considering three engagement models.

It is clear that the consideration of the engagement models has a significant influence in the resisting moment of the cross-section, particularly in the initial stage of the flexural response. When comparing the engagement model of the proposed model (linear variation of the bond strength up to the engagement crack opening) with the UVEM model, at the early stage of the flexural response ($\theta \approx 0.003 \text{ rad}$) there is a difference of about 25% of the resisting moment of the cross-section, with the proposed model exhibiting a higher resisting moment. For the residual flexural response ($\theta \approx 0.03 \text{ rad}$), the increase of the resisting moment of the proposed engagement model, when compared to the engagement model considered in the UVEM, is only of 13%.

Bond strength of the fiber pullout local constitutive law

The influence of the bond strength of the pullout response of aligned fibers, $\tau_{b,0,p}$ (Figure 63), in the flexural response of the cross-section is evaluated taking in consideration different levels of $\tau_{b,0,p}$, namely $\tau_{b,0,p} = 2, 5, 10, 20MPa$. The bond stress vs. slip relationship adopted in the pullout response of aligned fiber is presented in Figure 70. As can be seen in Figure 71, the bond strength of the pullout response of fibers has a significant impact in the flexural response of the cross-section. For the case of $\tau_{b,0,p} = 20MPa$, both the pre-peak and post-peak $M - \theta$ response of the cross-section is influenced, as the member exhibits a pronounced deflection hardening behavior. For the cases where $\tau_{b,0,p} \leq 10MPa$, the influence of the different levels of $\tau_{b,0,p}$ is only significant in the post-peak stage of the $M - \theta$ response.

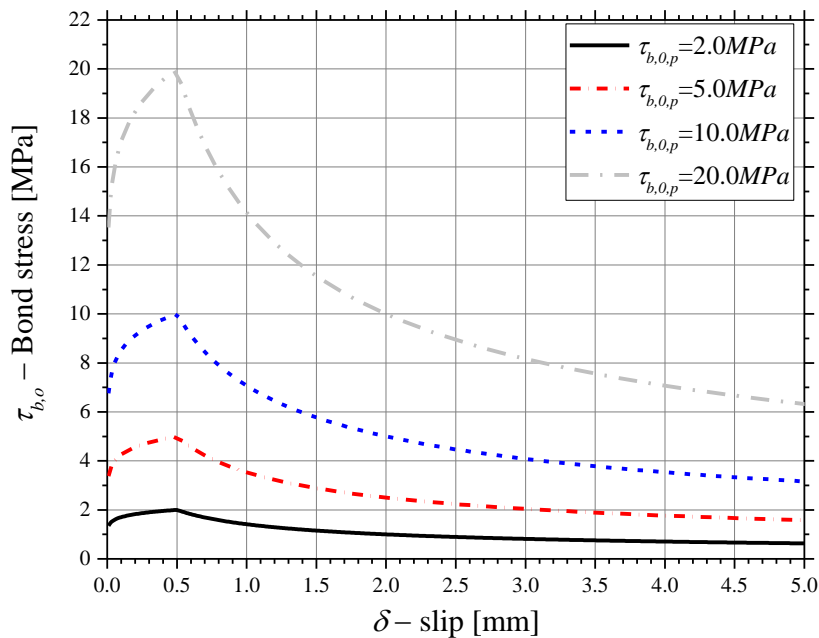


Figure 70 – Bond stress vs. slip ($\tau_{b,0} - \delta$) of the pullout response of an aligned fiber considering $\tau_{b,0,p} = 2, 5, 10, 20MPa$.

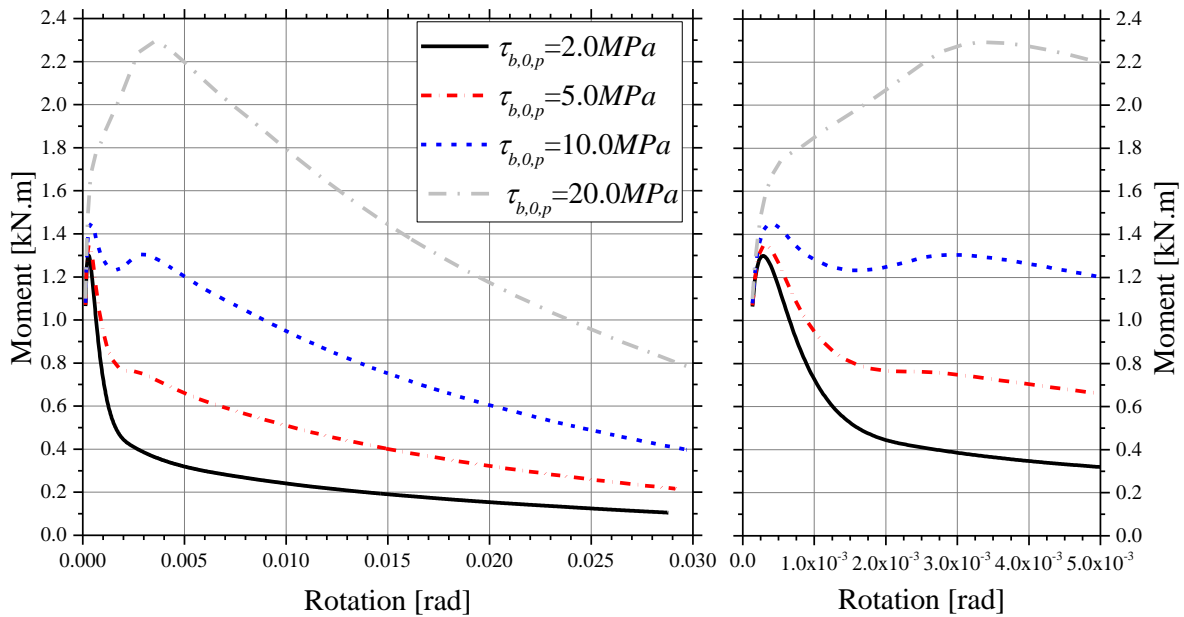


Figure 71 – Moment vs. rotation relationship of cross-section considering $\tau_{b,0,p} = 2, 5, 10, 20MPa$

Slip corresponding to bond strength of the fiber pullout local constitutive law

The influence of the slip corresponding to the bond strength of the pullout response, δ_p (Figure 63), in the flexural response of the cross-section of the case study, is analyzed considering four levels of δ_p , namely $\delta_p = 0.1, 0.5, 1.0, 5.0mm$. The bond stress vs. slip relationship adopted in the pullout response of aligned fiber is presented in Figure 72. The $M - \theta$ relationship of the cross-section is presented in Figure 73. It is evident that δ_p has a minor impact on the first peak of the flexural capacity of the cross section, but has a significant influence on this post-peak stage, with an increase of the flexural capacity, ductility and energy absorption with the δ_p .

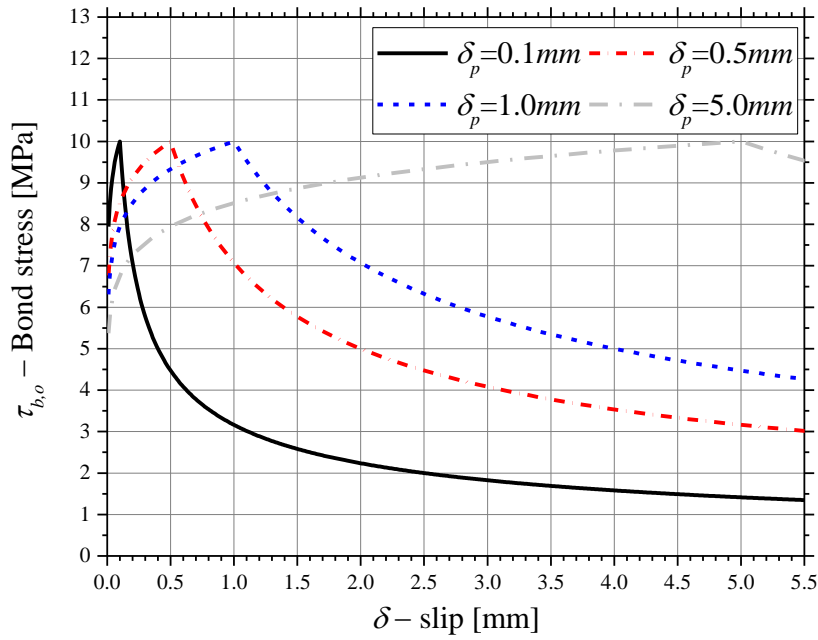


Figure 72 – Bond strength vs. slip ($\tau_{b,0} - \delta$) of the pullout response of an aligned fiber considering $\delta_p = 0.1, 0.5, 1.0, 5.0mm$.

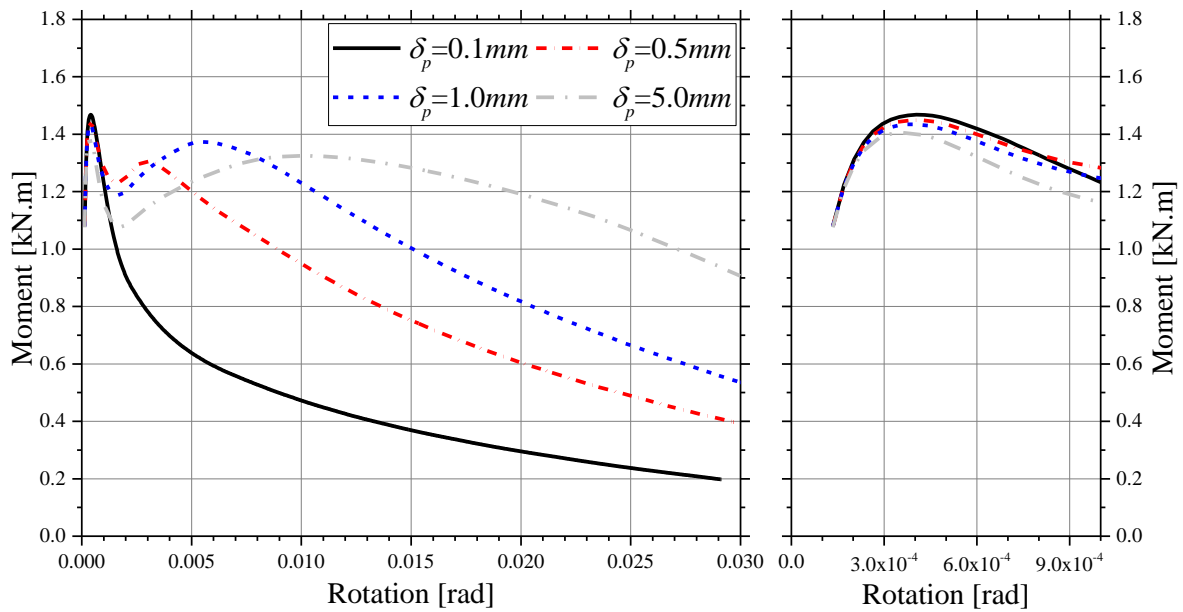


Figure 73 – Moment vs. rotation relationship of cross-section considering $\delta_p = 0.1, 0.5, 1.0, 5.0mm$.

Pre-peak exponent of the fiber pullout local constitutive law

The influence of the bond stress vs. slip gradient of the pre-peak fiber pullout local constitutive law (defined by the α parameter, Figure 63) on the $M - \theta$ response of the present case study is assessed in this section. For this purpose, values of $\alpha = 0.001, 0.01, 0.1, 1.0$ were considered. The bond stress vs. slip relationship adopted in the pullout response of aligned fiber is presented in Figure 74. As is seen in the $M - \theta$ presented in Figure 75, the exponent α influences the flexural capacity

of cross-section. The lower is α , the higher is the maximum resisting moment of the cross-section. This is due to the higher contribution of the fiber reinforcement, provided by a higher pre-peak bond strength up to δ_p is reached, when a lower value of α is adopted.

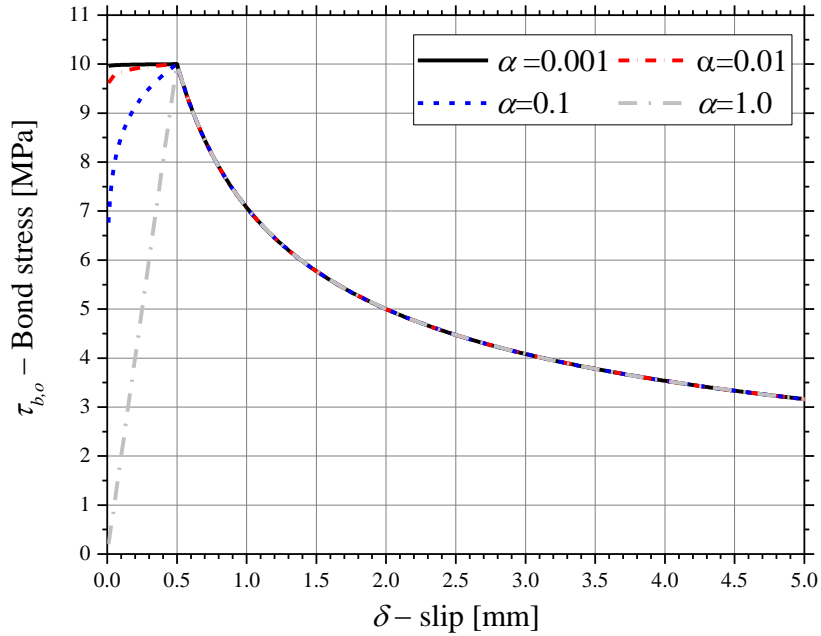


Figure 74 – Bond strength vs. slip ($\tau_{b,0} - \delta$) of the pullout response of an aligned fiber considering $\delta_p = 0.1, 0.5, 1.0, 5.0mm$.

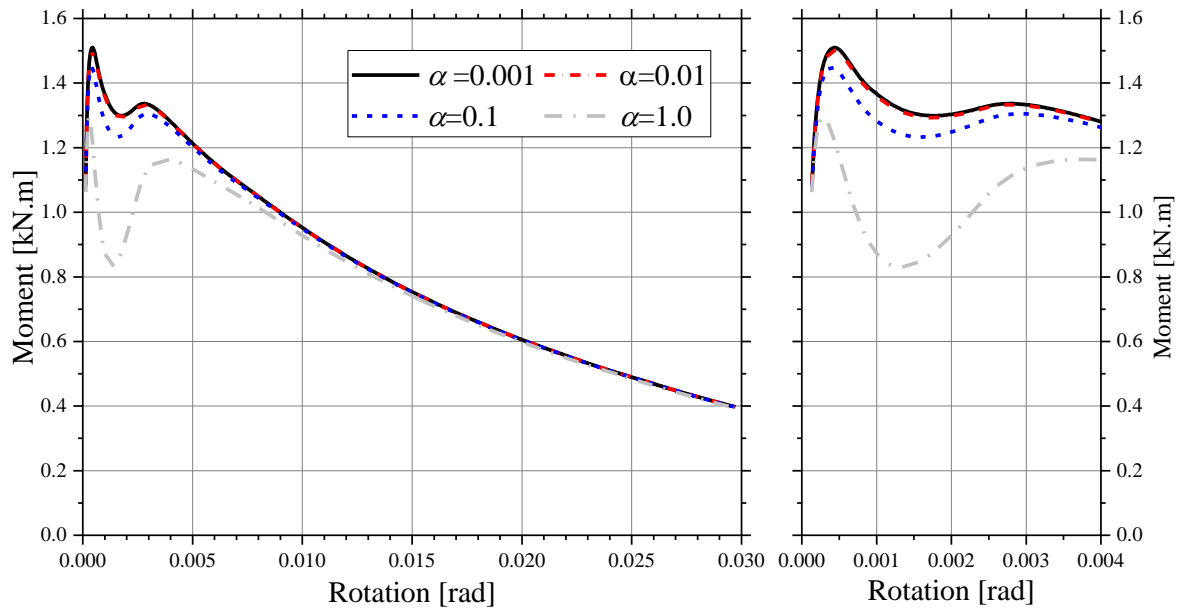


Figure 75 – Moment vs. rotation relationship of cross-section considering $\alpha = 0.001, 0.01, 0.1, 1.0$

Post-peak exponent of the fiber pullout local constitutive law

The influence of the value attributed to the β parameter, which defines the post-peak bond strength vs. slip rate, on the $M - \theta$ response of the present case study is assessed by adopting the following values for the $\beta = 0.1, 0.5, 1.0, 5.0$ (Figure 63). The bond stress vs. slip relationship adopted in the pullout response of aligned fiber is presented in Figure 76. Considering the corresponding obtained $M - \theta$ relationship of the cross-section presented in Figure 77, it is denoted that a sharper decrease of the post-peak $\tau_{b,0} - \delta$ relationship, which is obtained with a higher value of β , decreases the residual flexural capacity of the cross-section.

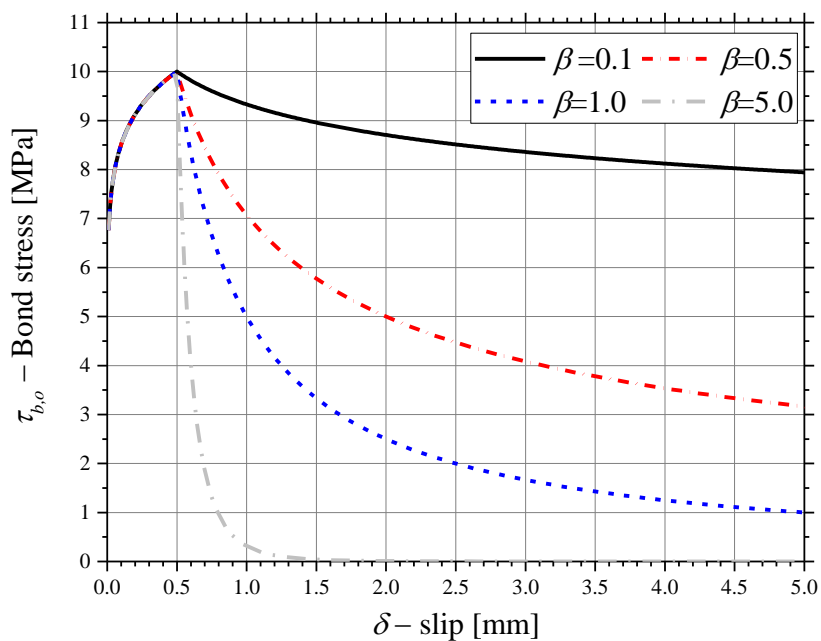


Figure 76 – Bond strength vs. slip ($\tau_{b,0} - \delta$) of the pullout response of an aligned fiber considering $\beta = 0.1, 0.5, 1.0, 5.0$.

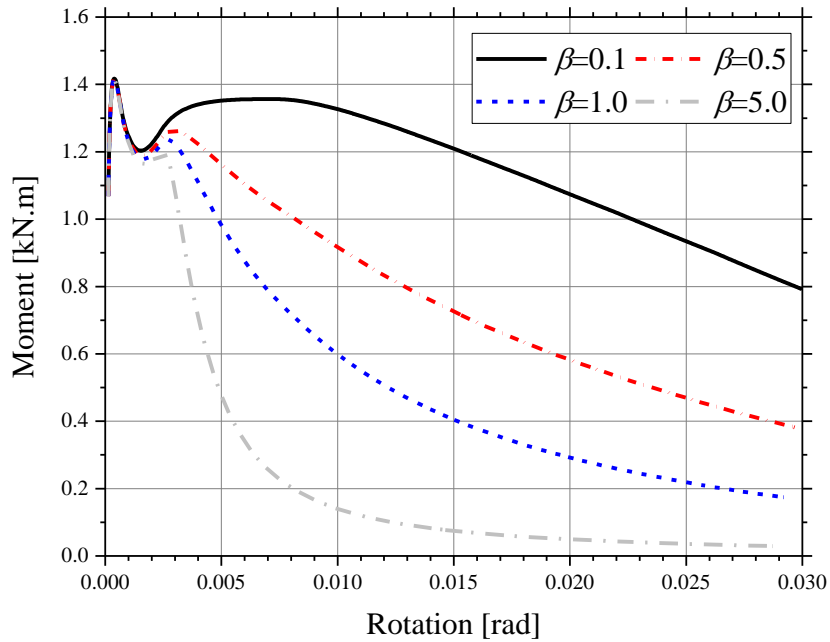


Figure 77 – Moment vs. rotation relationship of cross-section considering $\beta = 0.1, 0.5, 1.0, 5.0$.

5.2.5 Assessment of the predictive performance of the new model

In this section the predictive capacity of the NLMM107 model is assessed by comparing the flexural response of SFRC notched beams submitted to 3-point bending tests, with the numerical response determined with software *DOCROS*, where the NLMM107 was implemented. The experimental results and material properties of the SFRC beams were obtained from published work of several authors.

For each conducted analysis, the parameters of the NLMM107 model, namely those corresponding to the pullout response of aligned fibers described by the bond stress vs. slip ($\tau_{b,0} - \delta$) of aligned fibers, were obtained by a fitting procedure implemented in *DOCROS*, that resorts to the nonlinear least squares fitting routine *MPFIT* [109]. The data considered in the fitting procedure corresponded to the moment vs. crack tip opening displacement (CTOD) relationship that was derived from the experimental results of the bending tests. For most of the studied cases, the moment vs. CTOD relationship was obtained from the average force vs. midspan deflection results. The applied moment in the midspan cross-section is obtained from the expression:

$$M = \frac{F \cdot L}{4} \quad \text{Eq. (5.24)}$$

where L is the span length. The CTOD can be estimated by the expression proposed in [35]:

$$CTOD = CMOD \cdot \frac{h - ND}{h} \quad \text{Eq. (5.25)}$$

where ND is the notch depth, h is the beam height and $CMOD$ is the crack mouth opening displacement. The $CMOD$ can be determined as a function of the midspan deflection for bending tests performed according to the RILEM TC 162-TDF or EN 14651 from the expression proposed in [35]:

$$CMOD [mm] = 1.18 \cdot \delta_{MS} [mm] - 0.0416 \quad \text{Eq. (5.26)}$$

where δ_{MS} is the midspan deflection.

Given to the inexistence of information, the tensile strength of the concrete matrix is also a parameter to be derived during the fitting procedure.

Due to the existence of a notch in the SFRC members, executed after concrete casting, the fiber orientation factor as determined according to Eq. (5.10) needs to be adapted to notched beam cross-section, as is illustrated in Figure 78. In order to determine the fiber orientation factor of notched SFRC beams, it is resorted to the Eq. (5.27) and Eq. (5.28), respectively for the case where $l_f/2 > ND$ and $l_f/2 \leq ND$, where ND is the notch depth.

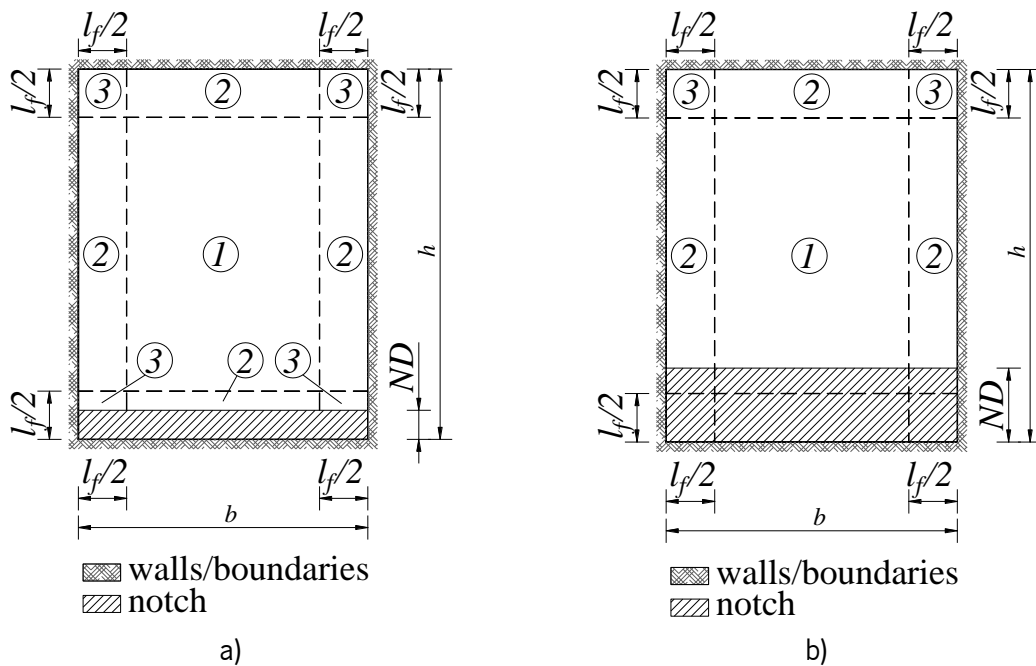


Figure 78 – Division of cross-section for determination of fiber orientation factor due to the existence of notch: a) $l_f/2 > ND$; b) $l_f/2 \leq ND$.

$$\eta = \frac{\eta_1 \cdot (b - l_f) \cdot (h - l_f) + \eta_2 \cdot \left[(b - l_f) \cdot (l_f - ND) + (h - l_f) \cdot l_f \right]}{b \cdot (h - ND)} + \frac{\eta_3 \cdot \left[2 \cdot \left(\frac{l_f}{2} \right)^2 + l_f \cdot \left(\frac{l_f}{2} - ND \right) \right]}{b \cdot (h - ND)} \quad , \frac{l_f}{2} > ND \quad \text{Eq. (5.27)}$$

$$\eta = \frac{\eta_1 \cdot (b - l_f) \cdot \left(h - \frac{l_f}{2} - ND \right)}{b \cdot (h - ND)} + \frac{\eta_2 \cdot \left[(b - l_f) \cdot \frac{l_f}{2} + \left(h - \frac{l_f}{2} - ND \right) \cdot l_f \right] + \eta_3 \cdot \frac{l_f^2}{2}}{b \cdot (h - ND)} \quad , \frac{l_f}{2} \leq ND < h - \frac{l_f}{2} \quad \text{Eq. (5.28)}$$

An additional aspect concerning the determination of the fiber orientation factor is related to the rheology of the concrete mixture. Due to the employment of self-compacting concrete in some of the cases in study, the fiber orientation factor adopted in the numerical models needs to reflect the increased flowability of these concrete mixtures. For this aspect is resorted to the work of [42], that idealizes the problem considering that the flowability of the self-compacting concrete as virtual layers with a thickness equal to the fiber length, with each layer acting as a virtual boundary that induce fiber alignment with the flow direction. Due to this, for the fiber orientation factor of zone 1 of the cross-section (Figure 58), is considered an orientation factor of $\eta_1 = 0.60$.

In Table 11 are presented the FRC material parameters and the parameters of the NLMM107 model, for each case study.

In Figure 79 and Figure 80 are illustrated the bond stress vs. slip relationship, $\tau_{b,0} - \delta$, of the pullout response of aligned fibers, that are obtained with the NLMM107 model parameters derived by the fitting procedure. For each case is also displayed the average bond stress, $\tau_{b,o,ave}$, determined up to the slip displacement correspondent to the maximum value of the CTOD obtained in the 3-point bending tests, and the maximum allowable bond stress vs. slip relationship, $\tau_{b,o,max} - \delta$. The maximum allowable bond stress, $\tau_{b,o,max}$, is determined from the expression that defines the fibers tensile failure criteria (Eq. (5.21)), namely:

$$\tau_{b,o,max}(w) = \frac{\overline{\sigma_{fu}} \cdot d_f}{4 \cdot L_{bf,o}(w)} \quad \text{Eq. (5.29)}$$

In Figure 81 and Figure 82 are presented the experimental and numerical response of the force vs. CTOD relationship of the FRC prisms submitted to 3-point bending, for all case studies.

Table 11 – Material properties of the FRC mixtures considered in the assessment of the predictive performance of the new model.

Reference	Mixture name	Fiber reinforcement properties					Concrete flowability	η	ξ	Material properties				Bond stress vs. slip relationship				
		Fiber type	V_f [%]	l_f [mm]	d_f [mm]	σ_{fu} [MPa]				E_c [MPa]	f_{cc} [MPa]	ε_{cc} [%]	ε_{cr} [%]	f_{ct} [MPa]	δ_p [mm]	$\tau_{b,0,p}$ [MPa]	α [$\times 10^{-3}$]	β
Pereira [110]	SFRSCC	HE	0.38	60	0.75	1100	SCC	0.645	0.0	35.85	61.60	3.00	6.00	3.21	0.745	13.75	1.0E-03	0.831
Lameiras [111]	SFRSCC A	HE	0.76	35	0.50	1300	SCC	0.619	0.0	35.83	65.78	5.87	12.00	1.83	0.502	5.13	1.640	1.404
Frazão et al. [112]	BACRFA	HE	0.76	35	0.50	1300	SCC	0.619	0.0	36.88	61.90	5.00	12.00	2.98	0.694	18.83	23.609	0.481
Valente et al. [113]	PreBeamTec	HE	0.76	33	0.55	1300	SCC	0.550	0.0	37.00	45.95	2.50	3.50	2.66	0.011	11.91	14.600	1.0E-06
Salehian [49]	c15_f45	HE	0.57	35	0.55	1300	SCC	0.619	0.0	23.31	13.12	3.50	17.50	2.29	0.700	10.23	1.340	0.499
	c25_f60	HE	0.76	35	0.55	1300	SCC	0.619	0.0	28.62	23.57	3.50	17.50	1.88	0.135	20.43	1.0E-03	0.281
	c45_f90	HE	1.15	35	0.55	1300	SCC	0.619	0.0	35.23	44.42	4.00	17.50	3.03	0.489	16.20	3.920	0.375
	c30_f45	HE	0.57	30	0.40	1000	SCC	0.616	0.0	29.63	26.18	3.50	17.50	5.36	1.004	13.33	1.0E-03	0.993
Soltanzadeh et al. [114]	HPFRC	HE	1.15	35	0.55	1100	SCC	0.619	0.0	36.06	67.84	2.60*	6.00*	6.99	1.797	17.30	1.0E-03	0.431
Frazão et al. [15]	RSFRC	R	1.00	20	0.15	2850	regular	0.530	0.0	24.31	39.42	2.30*	5.00*	1.18	0.467	7.19	0.679	0.281
Amin [41]	DA-0.5-S	S	0.50	13	0.20	1800	regular	0.531	0.0	34.70	63.70	2.50*	6.00*	2.91	0.432	17.11	1.0E-03	0.242
Pajak et al. [115]	0.5_S	S	0.50	12.5	0.40	1250	SCC	0.606	0.0	42.60*	80.10	2.70*	6.00*	2.06	0.818	8.48	1.0E-03	1.0E-06

Legend: HE – Hooked-end steel fibers; S – Straight steel fibers; R – recycled steel fibers; SCC – Self-compacting concrete; * - estimated values

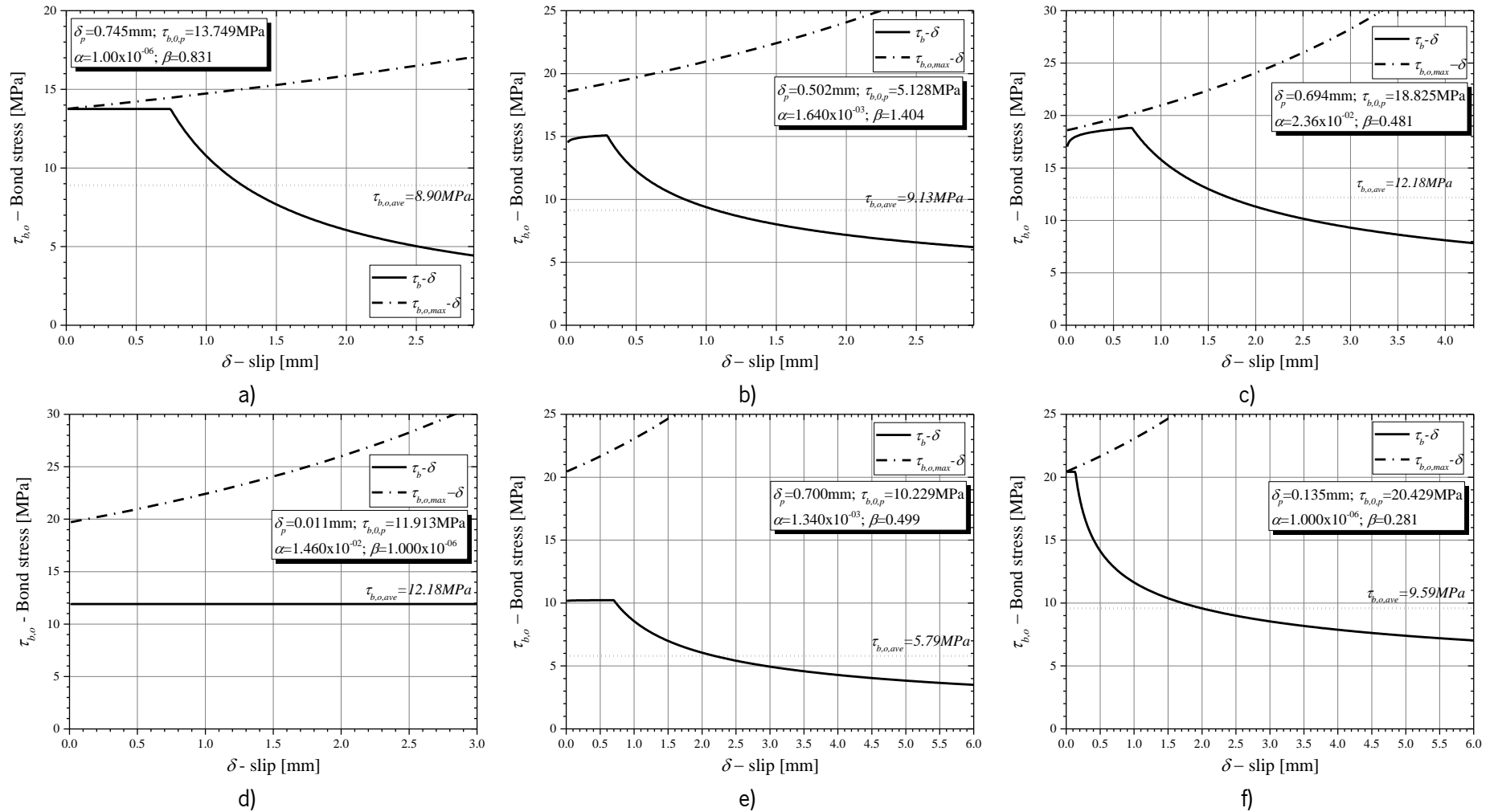


Figure 79 – Derived bond stress vs. slip ($\tau_{b,0} - \delta$) of the pullout response of an aligned fiber for the numerical model of the FRC studied in :a) Pereira [110]; b) Lameiras [111]; c) Frazão et al. [112]; d) Valente et al. [113]; e) mixture c15_f45 of Salehian [49]; f) mixture c25_f60 of Salehian [49].

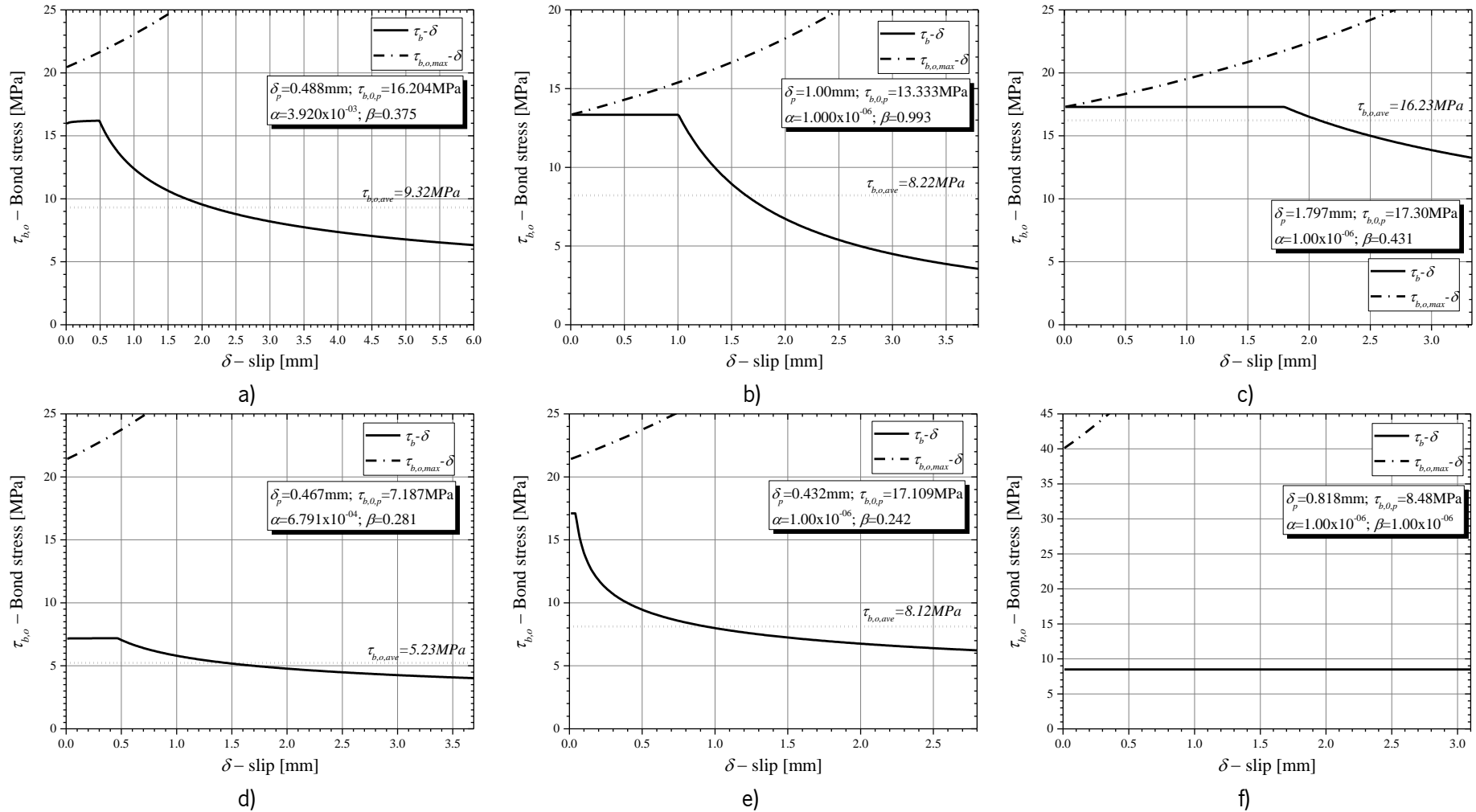


Figure 80 – Derived bond stress vs. slip ($\tau_{b,0} - \delta$) of the pullout response of an aligned fiber for the numerical model of the FRC studied in: a) mixture c45_f90 of Salehian [49]; b) mixture c30_f45 of Salehian [49]; c) Soltanzadeh et al. [114]; d) Frazão et al. [15]; e) Amin [41]; f) Pajak et al. [115].

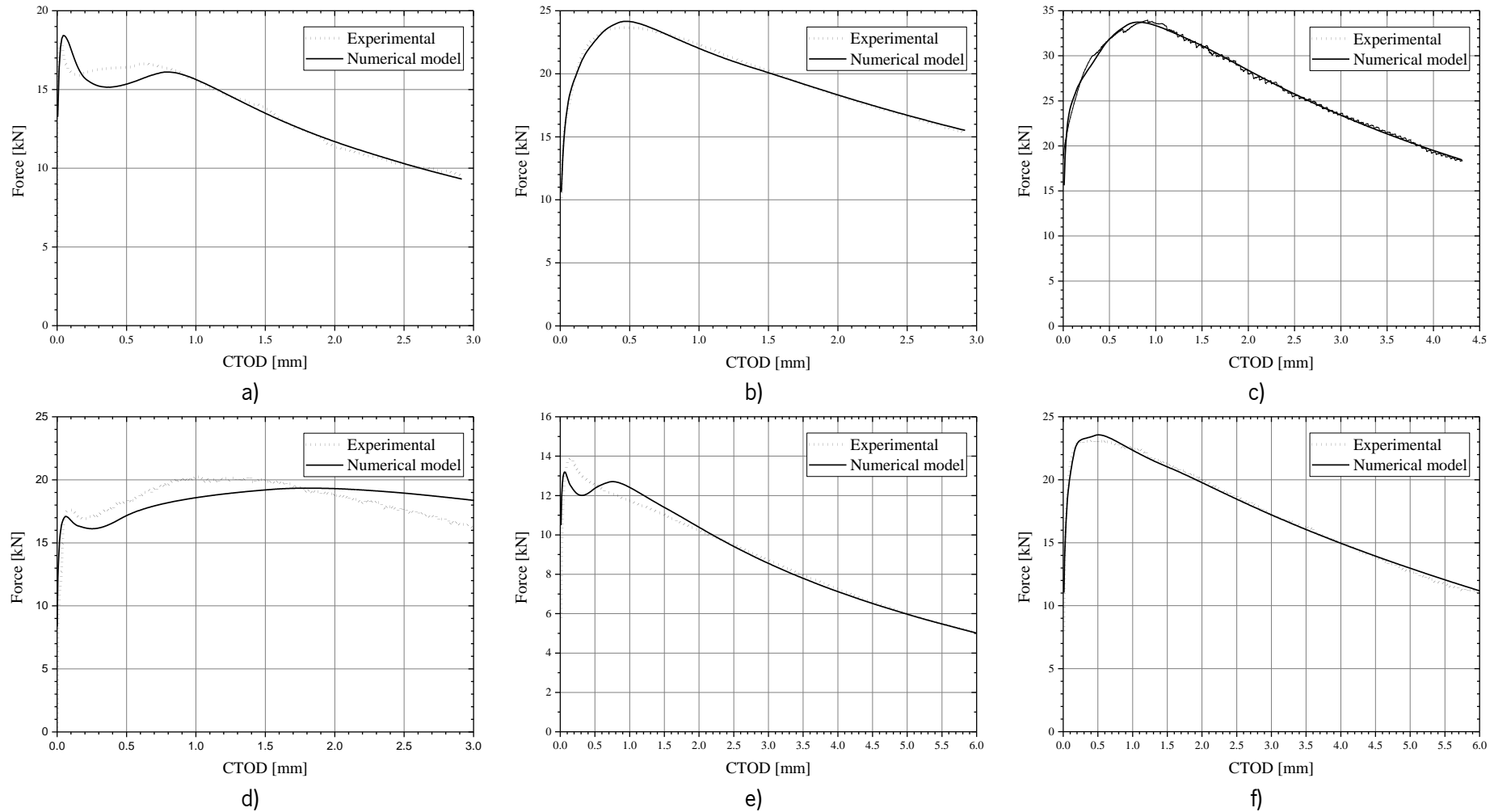


Figure 81 – Experimental and numerical model comparison of force vs. CTOD relationship of the FRC studied in: a) Pereira [110]; b) Lameiras [111]; c) Frazão et al. [112]; d) Valente et al. [113]; e) mixture c15_f45 of Salehian [49]; f) mixture c25_f60 of Salehian [49].

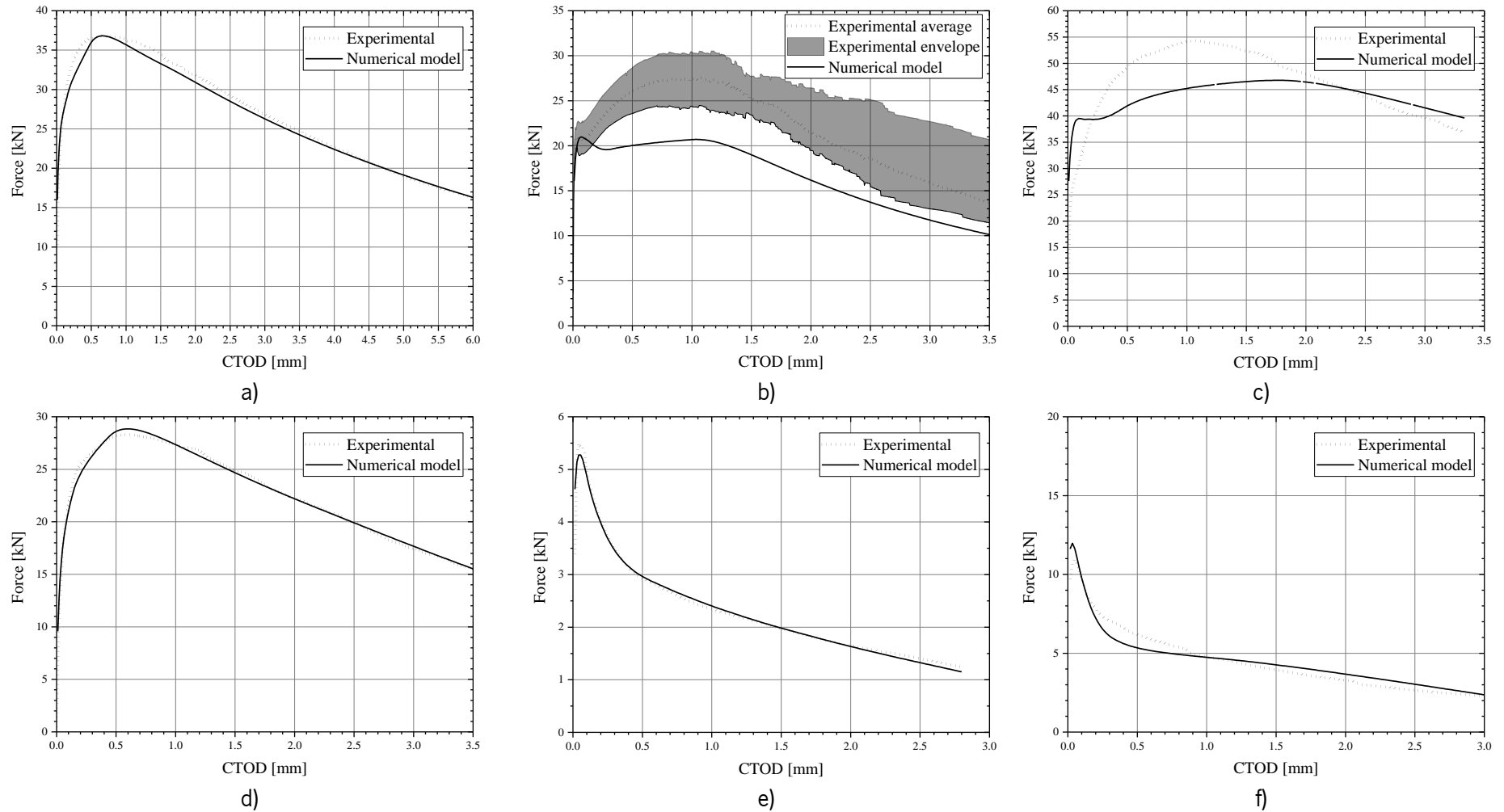


Figure 82 – Experimental and numerical model comparison of force vs. CTOD relationship of the FRC studied in: a) mixture c45_f90 of Salehian [49]; b) mixture c30_f45 of Salehian [49]; c) Soltanzadeh et al. [114]; d) Frazão et al. [15]; e) Amin [41]; f) Pajak et al. [115].

As demonstrated in Figure 81 and Figure 82, for the majority of the case studies, the application of the NLMM107 model predicted with very good accuracy the flexural response of the FRC prisms.

The main discrepancy between the experimental and numerical results are observed in the FRC studied in the work of Soltanzadeh et al. [114] and mixture c30_f45 of Salehian [49], with the numerical models exhibiting a lower flexural resistance when compared to the experimental values. Considering that the bond strength between the fibers cannot be increased, due to the maximum allowable bond stress, $\tau_{b,o,max}$, being reached at the initial stage of the fiber pullout response (Figure 80a) and b)), a further analysis to these results is conducted.

The numerical model determines the moment vs. CTOD considering the geometry and material properties at the notched cross-section of a FRC prisms, and assuming that the crack starts at the notch tip and propagates vertically along the notched section, as presented in Figure 83, which leads to a maximum crack surface area equal to $b \times h_{sp}$. However, the real situation, particularly for the case of high strength concrete matrix, the crack along the notched cross-section constantly changes direction and can bifurcate in two or more cracks. These phenomena, respectively known as crack tortuosity and crack branching [117], can significantly increase the fracture surface area leading to an increase of the total fiber pullout resistance by rising the number of fibers being solicited during the bending test. Ultimately, the overall flexural resistance of the FRC prisms submitted to 3-point bending tests is higher due to this diffusive crack path. Some real examples of the crack diffusivity observed in 3PNBBT are presented in Figure 84.

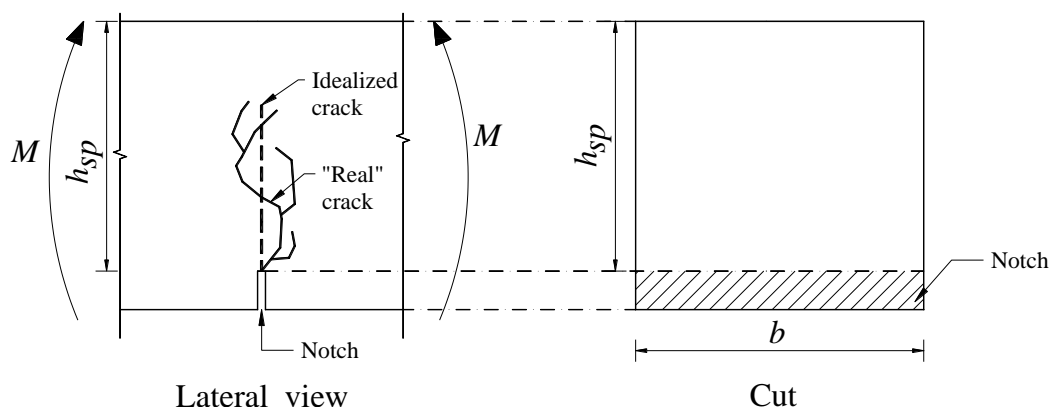


Figure 83 – Crack propagation in the cross-section of notched FRC prisms.

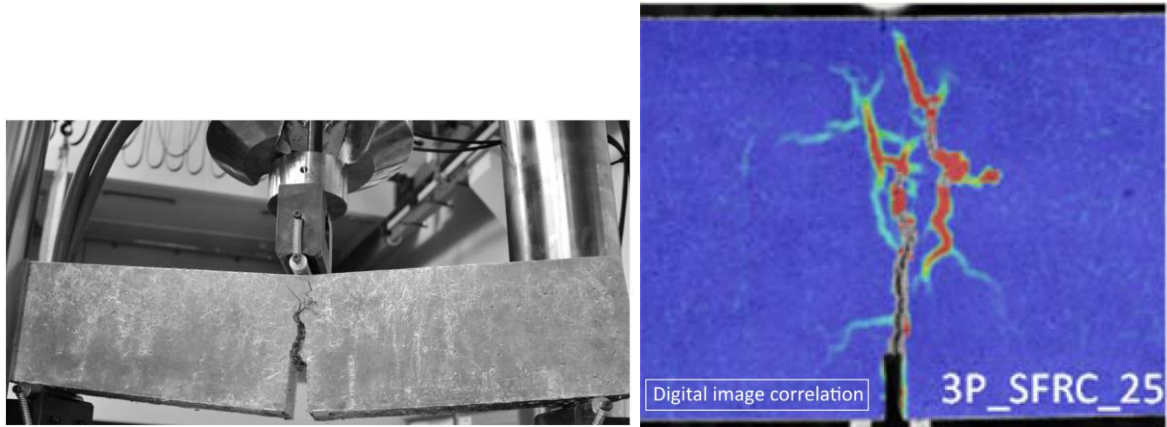


Figure 84 – Examples of crack tortuosity and branching of notched FRC prisms submitted to 3-point bending tests (extracted from [118], [119]).

In order to consider the increase of fibers being solicited due to crack diffusivity, the number of fibers in the idealized crack is multiplied by a crack diffusivity factor, κ . The expression Eq. (5.23) that defines the pullout resistance of the N_{f,φ_i}^j fibers with a mean orientation angle $\overline{\varphi_i}$ at the j^{th} cracked layer is modified to take into account the crack diffusivity factor, namely:

$$P_{\varphi_i}^j(w) = \kappa \cdot N_{f,\varphi_i}^j \cdot \pi \cdot d_f \cdot \tau_{bu,i} \cdot L_{bf,o}(w) \quad \text{Eq. (5.30)}$$

The parameter κ could be evaluated by performing a comprehensive experimental program that considers the performance of fiber pullout tests, 3PNBBT and direct tensile tests. For the fiber type and concrete matrix in analysis, the bond vs. slip relationship is derived from the pullout tests (Figure 85a). Afterwards, based on the moment vs. CTOD relationship obtained in the 3PNBBT and by assessing the number and orientation of each fiber in fracture surface of each specimen (Figure 85b), the crack diffusivity factor for FRC members in bending, κ_b , is obtained by performing an inverse analysis considering the concrete matrix tensile contribution and the fiber pullout resistance (Eq. (5.30)). Similarly, the crack diffusivity factor for FRC members in tension, κ_t , is obtained by performing an inverse analysis based on the $\sigma-w$ relationship obtained from direct tensile tests (Figure 85c).

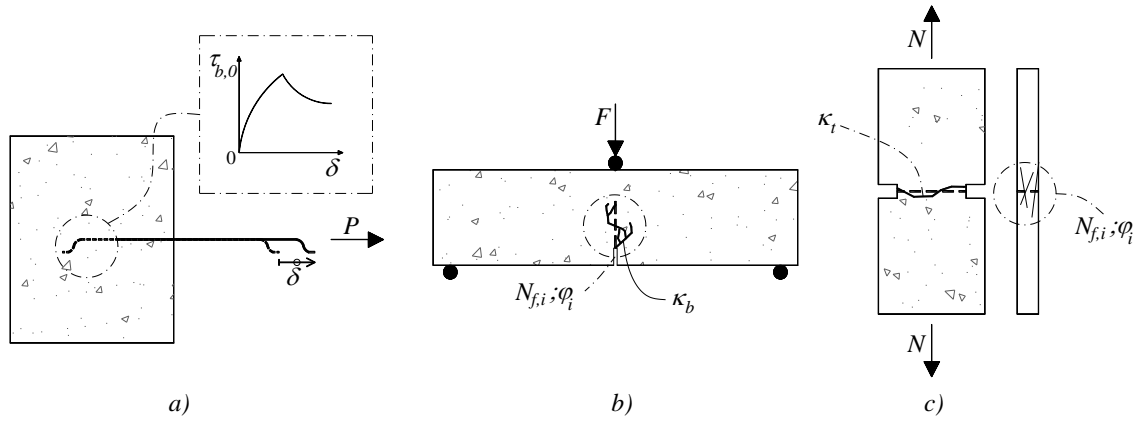


Figure 85 – Schematic representation of methodology to derive the crack diffusivity factor, κ . a) Fiber pullout tests; b) 3-point notched beam bending tests; c) Direct tensile tests.

In the absence of experimental results, the parameter κ must be empirically defined. In Figure 86 is presented the force vs. CTOD relationship of the FRC studied in the work of Soltanzadeh et al. [114] and the mixture c30_f45 of Salehian [49], considering a crack diffusivity factor equal to $\kappa = 1.20$. In Figure 87 is presented the corresponding pullout response of aligned fibers, with the parameters of NLMM107 obtained from the fitting procedure.

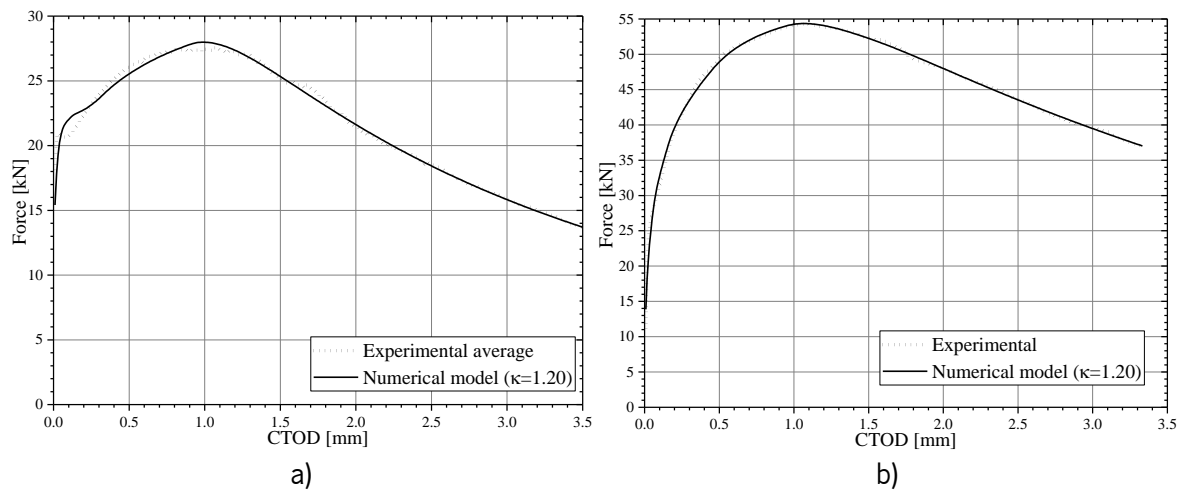


Figure 86 – Experimental and numerical model comparison of force vs. CTOD relationship considering $\kappa = 1.20$ for the FRC studied in: a) mixture c30_f45 of Salehian [49]; b) Soltanzadeh et al. [114].

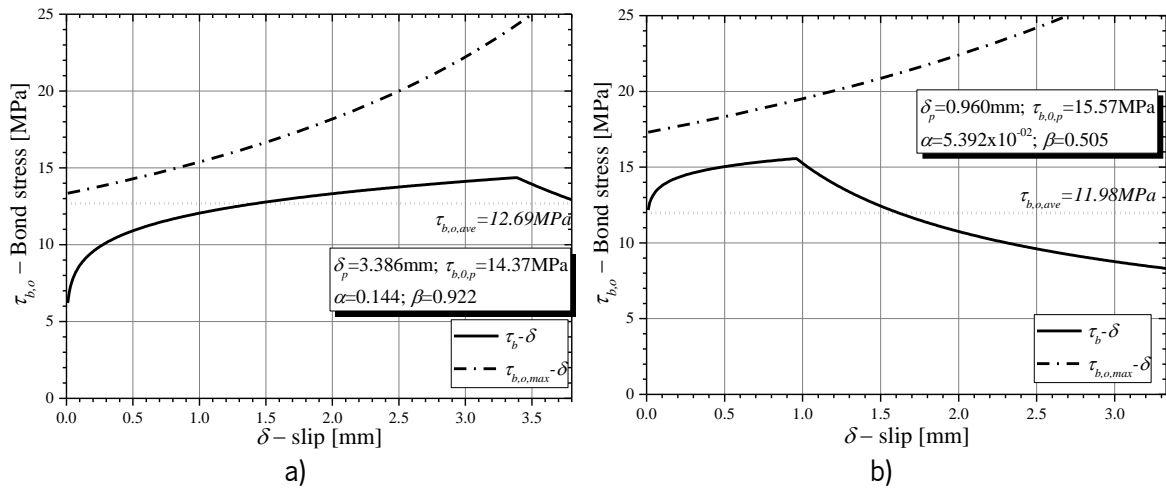


Figure 87 – Derived bond stress vs. slip ($\tau_{b,0} - \delta$) of the pullout response of an aligned fiber for the numerical model considering $\kappa = 1.20$ for the FRC studied in :a) mixture c30_f45 of Salehian [49]; b) Soltanzadeh et al. [114].

In Figure 88 is presented the $\tau_{b,0} - \delta$ model of the aligned fibers pullout response for all cases studied, which were obtained by adopting the fitting procedure. For the results of the mixture c30_f45 of Salehian [49] and of Soltanzadeh [116] are considered the parameters obtained in the model with $\kappa = 1.20$. The bond strength varies from 5.13 to 20.43MPa with the corresponding slide displacement ranging from 0.01 to 3.39mm. It is also denoted that in most cases, in order to obtain a good agreement between the experimental and numerical results, the pre-peak stage of the $\tau_{b,0} - \delta$ model presents a pseudo-plastic behavior, with the exponent α varying between 1×10^{-06} to 0.14. For the $\tau_{b,0} - \delta$ softening branch, the exponent β ranges between 1×10^{-06} to 1.40.

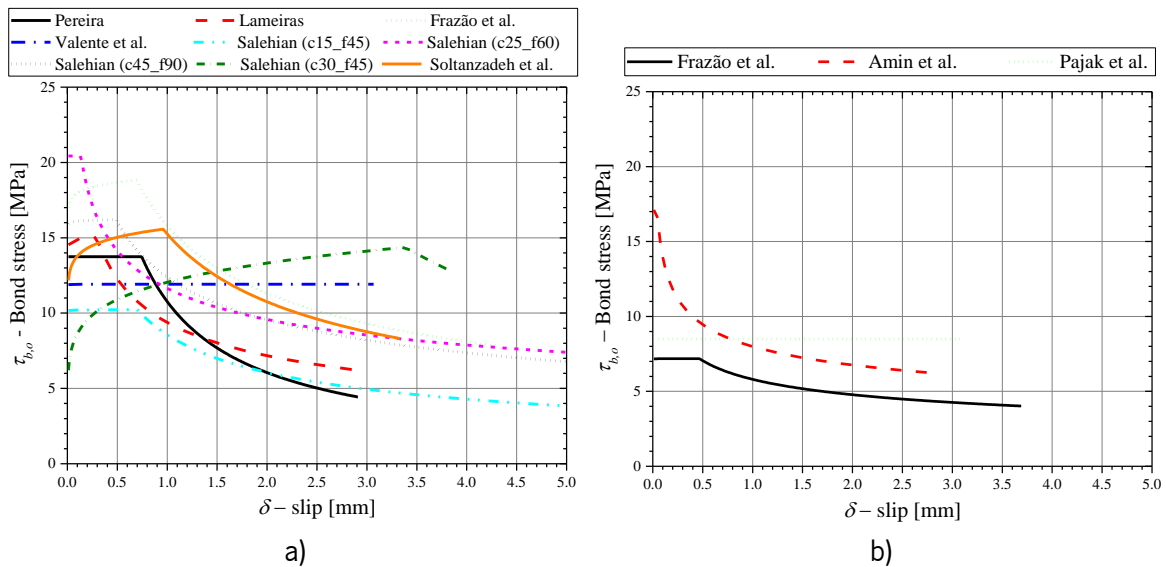


Figure 88 – Derived bond strength vs. slip ($\tau_{b,0} - \delta$) of the pullout response of an aligned fiber for the numerical model of all cases studies, according to type of fibers: a) hooked-end fibers; b) straight and recycled fibers.

In Figure 89 is compared the average bond strength, $\tau_{b,o,ave}$, up to the slip displacement correspondent to the maximum value of the CTOD obtained in the 3PNBBT and the average bond strength considered in the UVEM model [96] (Eq. (5.31), assuming that $f_{ctm} = 0.45 \cdot \sqrt{f_{cm}}$). As can be seen, the ratio $\tau_{b,o,ave} / \tau_{b,ave,UVEM}$ ranges between 1.0 and 2.2. The higher average bond strength derived from the fitting procedure, in comparison with the values considered in the UVEM model, can be justified by the different experimental data used to derive these parameters. While in the UVEM were considered the results of fiber pullout tests, in this study the parameters of the $\tau_{b,0} - \delta$ were derived from 3PNBBT. As previously illustrated in Figure 83 and Figure 84, due to crack tortuosity and branching the ratio between the total pullout resistance of the fibers and the number of fibers being solicited is higher in the numerical model than the observed in the 3PNBBT. Consequently, when performing the inverse analysis to derive the parameters of fiber pullout model, the bond stress is overestimated to compensate the increase of solicited fibers in the fracture surface.

$$\tau_{b,ave,UVEM} = \begin{cases} 2.5 \cdot f_{ctm} & ; \text{ for hooked-end fibers} \\ 1.2 \cdot f_{ctm} & ; \text{ for straight fibers} \end{cases} \quad \text{Eq. (5.31)}$$

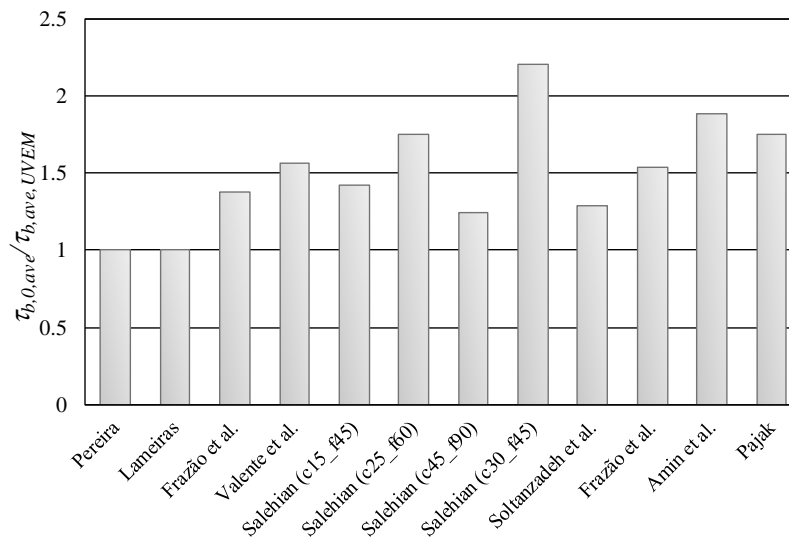


Figure 89 – Ratio between $\tau_{b,o,ave} / \tau_{b,ave,UVEM}$.

5.3 Moment-rotation procedure for analysis of cross-sections

In order to be possible to analyze the flexural response of structural members' cross-sections considering the NLMM107 model to simulate the FRC behavior, a moment-rotation procedure, $M - \theta$, was implemented in *DOCROS*. In this algorithm, after cracking in concrete is detected, is considered an incremental increase of the rotation of the cross-section, $\Delta\theta$, which leads to the

increase of crack width and the crack propagation across the cross-section height. At the p^{th} rotational increment, the rotation of member is equal to:

$$\theta^p = p \cdot \Delta\theta \quad \text{Eq. (5.32)}$$

The axial deformation of the j^{th} layer at the p^{th} rotation increment, D_j^p , w can be determined by the following relationship:

$$D_j^p = \theta^p \cdot (d_j - x) \quad \text{Eq. (5.33)}$$

where, d_j is the depth of the center of gravity of the j^{th} layer, and x is the neutral axis depth.

The corresponding strain of the j^{th} layer can be obtained by Eq. (5.34), considering that L_{cr} is the crack spacing of the FRC member.

$$\varepsilon_j^p = \frac{2 \cdot D_j^p}{L_{cr}} \quad \text{Eq. (5.34)}$$

For the cracked layers in the cross-section, the crack width is determined according to the expression:

$$w_j^p = 2 \cdot D_j^p - \frac{f_{ct}}{E_c} \cdot L_{cr} \quad \text{Eq. (5.35)}$$

In each rotational increment, the neutral axis position is determined according to an iterative process, considering the equilibrium of forces in each layer that discretizes the member cross-section, namely:

$$\sum_{i=1}^N F_j^p \approx 0 \quad \text{Eq. (5.36)}$$

The axial force of the j^{th} layer of the cross-section is determined based on the stress at the layer, namely:

$$F_j^p = \sigma_j^p \cdot b_j \cdot t_j \quad \text{Eq. (5.37)}$$

The resisting moment is determined according to Eq. (5.38).

$$M_{Rd} = \sum_{j=1}^N F_j^p \cdot d_j \quad \text{Eq. (5.38)}$$

The flexural stiffness of the cross-section, in the form of the moment vs. curvature ($M - \chi$) relationship, can be determined by evaluating the curvature of the cross-section, χ , at each rotational increment θ^p , according to Eq. (5.39).

$$\chi = \frac{\varepsilon_j^p - \varepsilon_{j-1}^p}{d_j - d_{j-1}} \quad \text{Eq. (5.39)}$$

5.3.1 Numerical simulation of FRC structural members

In the present section is assessed the capability of capturing the structural response of FRC members by adopting the NLMM107 model and the moment vs. rotation relationship of the members cross-section.

In the first study case is performed the numerical simulations of flexural tests of the R-FRC beams studied in [120]. The experimental program includes the characterization of the force vs. midspan deflection of three sets of R-FRC, considering different characteristics of the FRC. The FRC studied corresponds to the mixtures c15_f45, c25_f60 and c45_f90 presented in Table 11, for which the parameters of the NLMM107 model were already derived, namely the bond stress vs. slip relationship, $\tau_{b,0} - \delta$, of the pullout response of aligned fibers, based on the results of 3PNBBT.

The beams were submitted to 4-point bending tests, with a span length equal to 1400mm (Figure 90). The rectangular cross-section has 150mm of width and 100mm of height. The beams are longitudinally reinforced with one $\varnothing 8$ mm steel bar with 40mm of cover. The midspan central deflection was registered with an LVDT installed on an aluminum bar. During testing, the crack width at the reinforcement level was also registered.

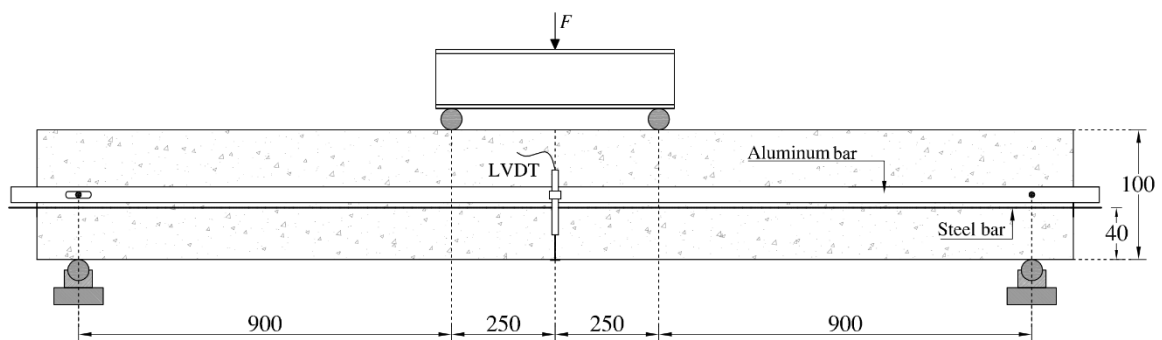


Figure 90 – R-FRC beams submitted to four-point bending tests (extracted from [120]).

The numerical simulation was performed by adopting the derived NLMM107 model parameters to obtain the moment vs. rotation and moment vs. curvature relationship of the cross-section of the beams studied in [120]. For the simulation of the steel reinforcement was adopted a linear-plastic model with the following parameters: yield stress: $f_{sy} = 575MPa$; Young's modulus: $E_s = 204.8GPa$; and ultimate strain: $\varepsilon_{su} = 32 \times 10^{-3}$.

In order to obtain the flexural response of the cross-section based in the presented moment-rotation procedure is necessary to determine the crack spacing, L_{cr} , of the R-FRC beams. The crack spacing of the beams was estimated considering the model presented in MC2010 and described in section 2.5.5 of this thesis, for which was determined that the mean crack spacing of the R-FRC beams is equal to $L_{cr} = 60mm$.

The numerical simulation of the bending tests is performed in the software *DEFDOCROS*, developed in [121], that derives the force-deflection of statically determinate structural elements based on the flexural stiffness, namely the moment vs. curvature ($M - \chi$) relationship, of the cross-section of the structural member. The beams are discretized by 2-noded Euler-Bernoulli elements, and for each segment is considered the $M - \chi$ relationship obtained in *DOCROS*.

In Figure 91 is presented the comparison of the force vs. midspan deflection obtained experimentally and in the numerical simulation. To be noticed that the experimental force-deflection response observed experimentally denotes that the failure did not occurred due to yielding of the steel reinforcement, pointing to the debonding of the steel bar. As the numerical model considers a perfect bond between the reinforcement bar and the surrounding FRC, are expected some divergences between the experimentally and numerically obtained force-deflection responses of the beams. These deviations are notorious in the response of mixtures c25_f60 and c45_f90, with the numerical model predicting the force-deflection response of the tested beams up to the maximum force observed experimentally. For the case of mixture c15_f45, it is evident that the numerical model could not accurately capture the experimental response of the tested beam.

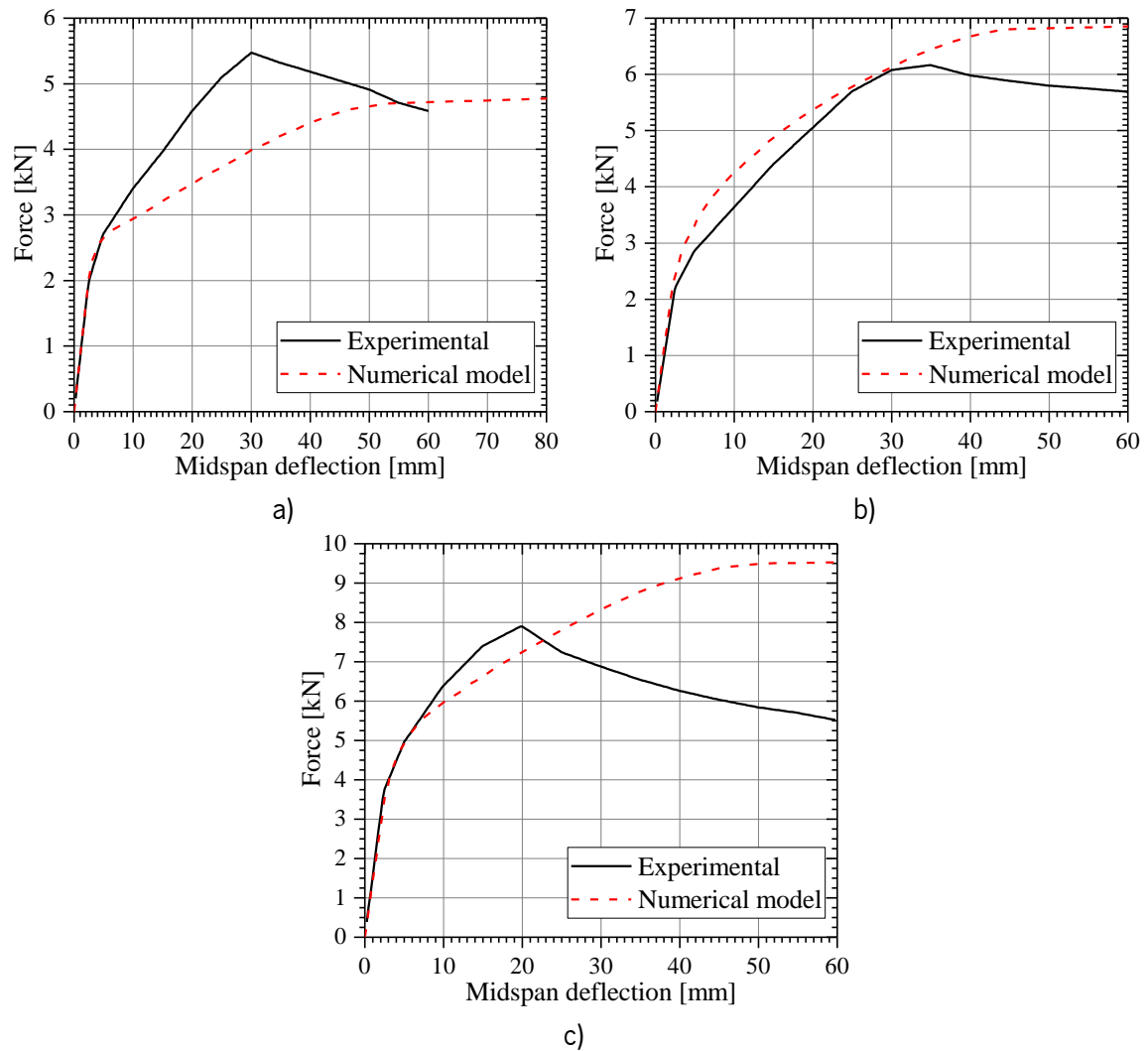


Figure 91 – Comparison between the experimental and numerical model force vs. midspan deflection for the R-FRC beams submitted to 4-point bending tests considering different FRC mixtures: a) c15_f45; b) c25_f60; and c) c45_f90 [114].

In Figure 92 is presented the comparison between the experimental and numerical derived moment vs. crack ($M - w$) width at reinforcement level of the tested beams. As it is observed, the numerical simulation was able to capture with a significant accuracy the $M - w$ response of the tested beams, particularly the case of mixtures c15_f45 and c25_f60. For the case of the mixture c45_f90, it is observed a more pronounced deviation between the experimental and numerical results.

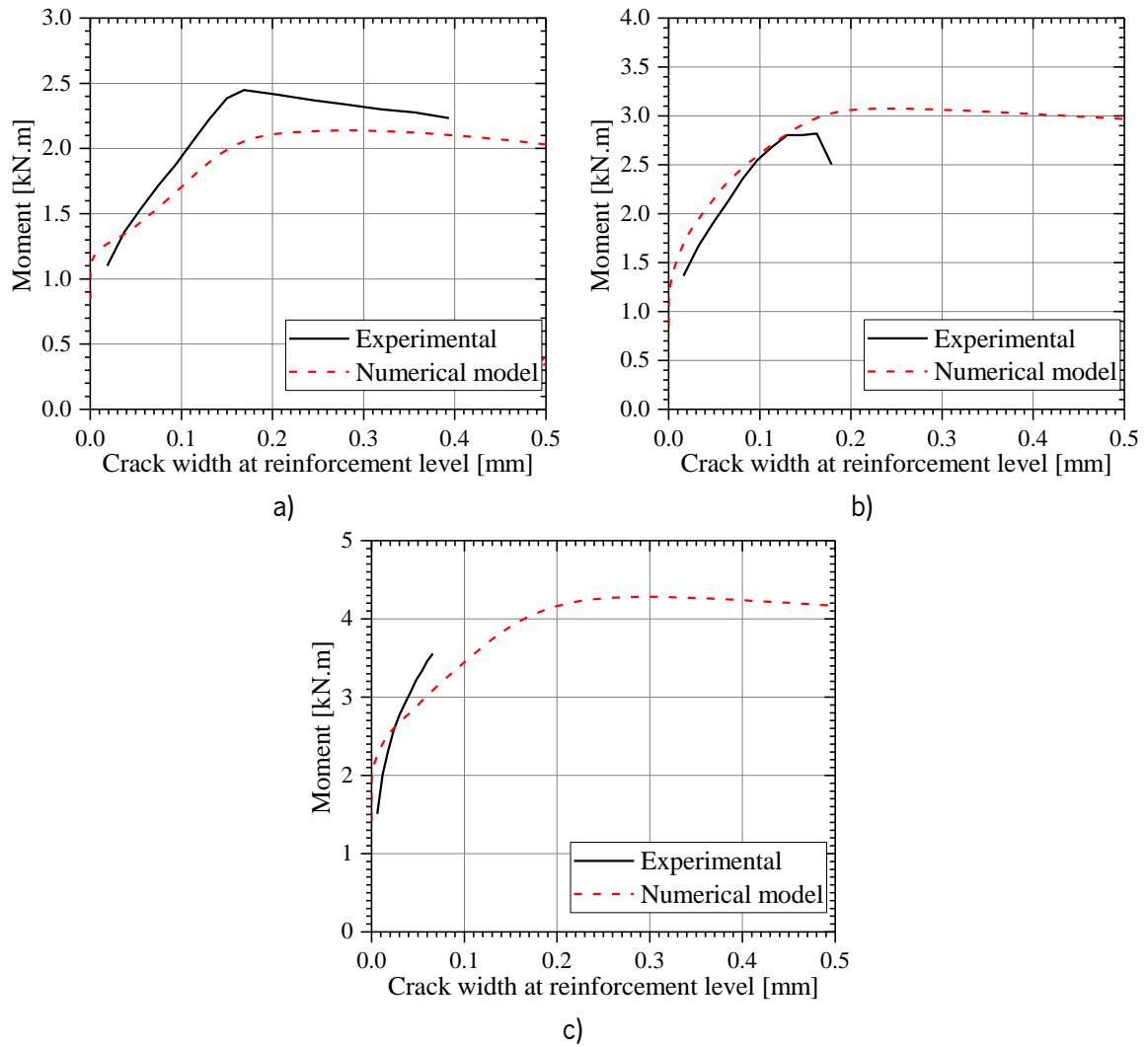


Figure 92 – Experimental and numerical model comparison of moment vs. crack width at reinforcement level for the R-FRC beams submitted to 4-point bending tests considering different FRC mixtures: a) c15_f45; b) c25_f60; and c) c45_f90 [114].

Next is presented the application of the NLMM107 model and the moment-rotation algorithm to predict the flexural response of a composite beam studied in [113]. The composite beams are formed by castellated U-shaped steel profiles with an upper flange and web formed by steel fiber reinforced self-compacting concrete. The steel profiles are formed by steel sheets with a thickness of 3mm. The web of the profiles is cut to form a castellated geometry, as presented in Figure 93.

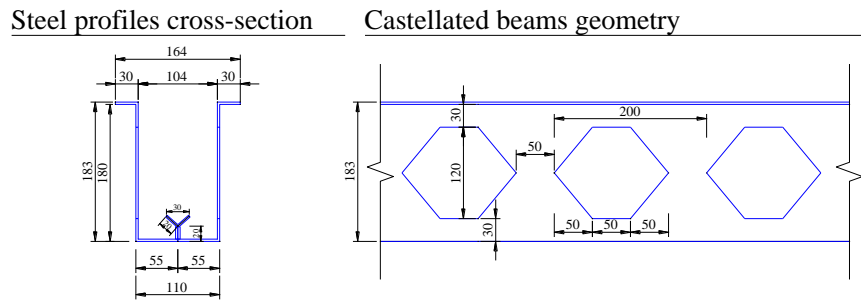


Figure 93 – Steel profiles geometry.

The self-compacting concrete adopted in the experimental program corresponds to the mixture presented in Table 11, denominated as PreBeamTec, for which the bond stress vs. slip relationship, $\tau_{b,0} - \delta$, of the pullout response of aligned fibers were already derived based on the 3PNBBT results.

The composite beams were submitted to 3-point bending tests, with a span length of 1100mm. The test setup and geometry of the beams are presented in Figure 94. The midspan deflection of the beam was registered with an LVDT installed on an aluminum bar (Figure 95). In addition, the deformation of the composite beam top and bottom face is also registered using strain gauges, placed at 50mm from the midspan of the composite beam.

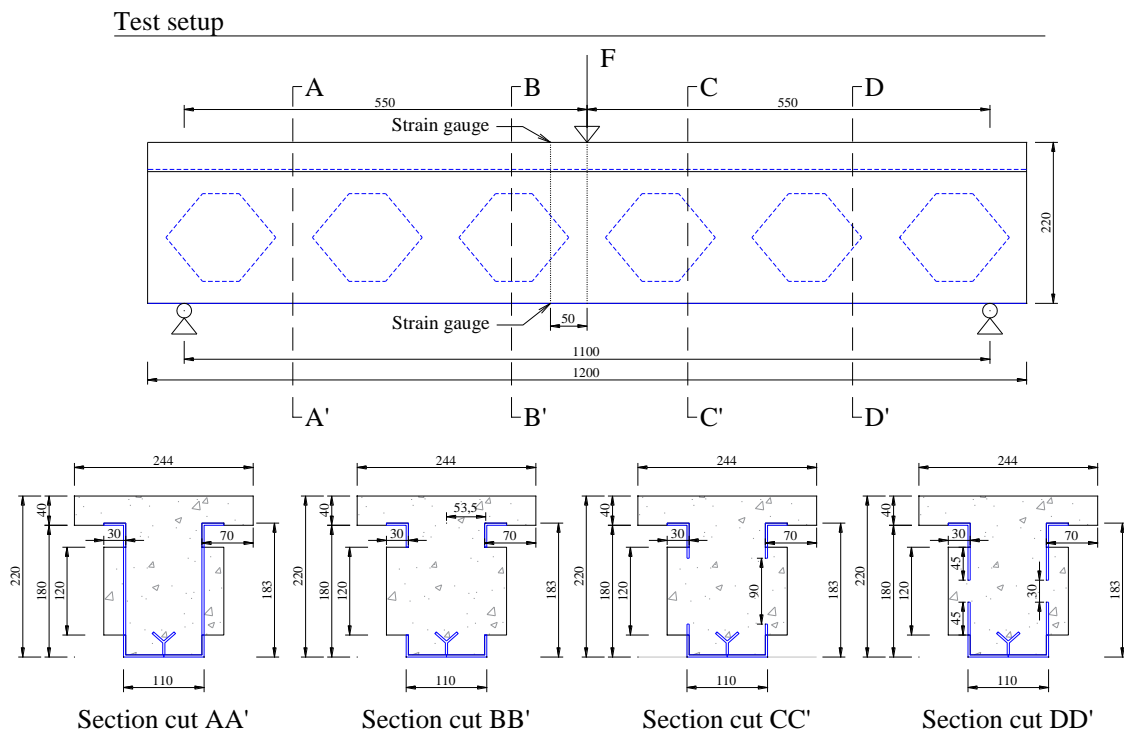


Figure 94 – 3-point bending test setup and section cuts of composite beam (dimension in mm) [113].



Figure 95 – Composite beam ready for testing [113].

The numerical simulation of the 3-point bending test of the composite beam was performed by estimating the moment vs. rotation and moment vs. curvature relationship of the cross-section of the composite beams. For the simulation of the concrete behavior was adopted the NLMM107 model, whose parameters correspond to mixture PreBeamTec presented in Table 11.

For the simulation of the steel reinforcement was adopted a linear-plastic model with the following parameters: yield stress: $f_{sy} = 235MPa$; Young's modulus: $E_s = 210GPa$; and ultimate strain: $\varepsilon_{su} = 10 \times 10^{-3}$.

In Figure 96 is presented the moment vs. curvature derived numerically using *DOCROS* at four section cuts of the composite beam, and the $M - \chi$ relationship obtained experimentally considering the deformation measured with the strain gauges at the top and bottom faces of the composite beam. The numerical relationship derived with *DOCROS* was obtained admitting a perfect bond between the castellated steel profile and the FRC, and for the moment-rotation calculation procedure was considered a crack spacing equal to the height of the beam ($L_{cr} = 220mm$). Knowing that the strain gauges are positioned between the beam's section cuts CC' and DD', it is clear the experimental $M - \chi$ relationship is stiffer and denotes a significantly higher flexural resistance than the observed numerically with *DOCROS*.

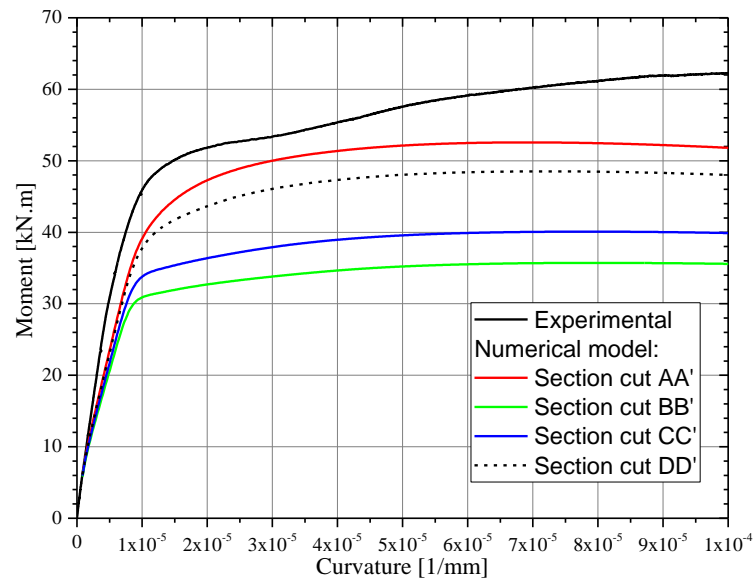


Figure 96 – Experimental and numerically derived moment vs. curvature relationship at four section cuts of the composite beam studied in [113].

Considering the $M - \chi$ relationship derived in *DOCROS*, the force vs. deflection of the composite beam when submitted to 3-point bending was obtained using the software *DEFDOCROS*. As it is presented in Figure 97, the numerical response could not capture the ultimate flexure capacity observed during the 3-point bending test. The discrepancy is based on the difference between the experimental and numerical $M - \chi$ relationship observed in Figure 96. However, up to a deflection value of $L/500 = 2.2\text{mm}$, which is normally considered in the verification of the limit states of deformation of concrete members, the force vs. deflection response obtained in *DEFDOCROS* is similar to the observed experimentally.

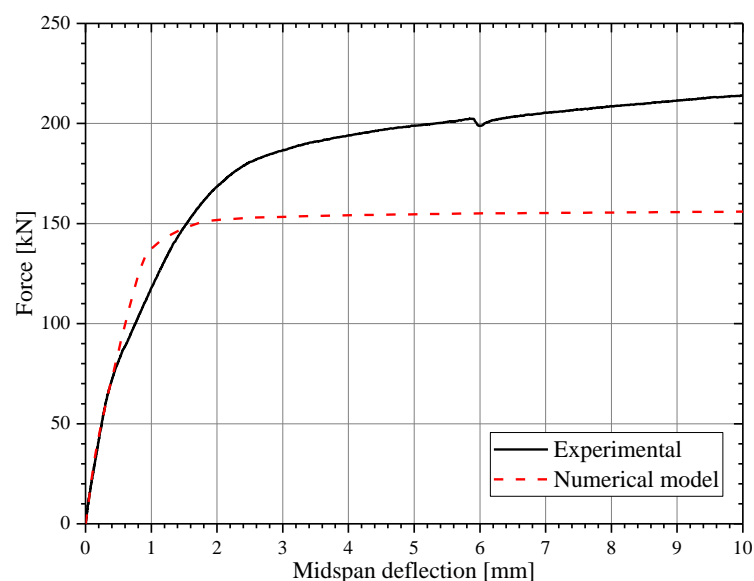


Figure 97 – Comparison between the force vs. midspan deflection of the composite beam submitted to 3-point bending studied in [113].

5.4 Concluding remarks

In the present chapter was proposed a model capable of describing the flexural behavior of 1D type FRC members considering the orientation of the fibers, the fibers segregation along the cross-section of these members, and the pullout constitutive model of each fiber bridging the two faces of a crack.

At the cross-section of a FRC member, the model is able to predict the distribution of the fibers in discrete orientation intervals, based on the evaluation of the orientation factor, which is a function of the length of the fibers and of the geometry and boundaries of the cross-section.

The model also includes a strategy to simulate the fiber segregation phenomena that can occur during FRC casting. This strategy relies in the definition of a unique parameter, denominated fiber segregation factor, where a linear variation of the fiber distribution along the depth of the cross-section is assumed.

The cross-section of the FRC member is divided into layers, and the number of fibers in each layer and within each orientation angle interval is determined by coupling the fiber orientation profile and segregation models.

In the proposed model, the fiber contribution to the post-cracking resistance of the FRC is determined according to the pullout resistance of the number of fibers in each layer and within each orientation angle interval. A new nonlinear bond vs. slip relationship is proposed to simulate the behavior of the interface between fiber and concrete matrix.

The components of the proposed model were coupled and implemented in a software for the analysis of cross-sections of R-FRC members failing in bending, considering a moment-rotation procedure.

The performance of the new model was assessed by comparing the flexural response SFRC notched beams submitted to 3-point bending tests. For the majority of the studied cases, a very good agreement between the experimental and numerical results was obtained. For the cases that displayed some discrepancies, the influence of cracking tortuosity and branching was addressed by defining a crack diffusivity factor. After adopting an empirical value for the crack diffusivity factor, a good agreement was obtained between the experimental and numerical results.

The chapter ends by assessing the capability of the new model to simulate the flexural response of FRC structural members. Although were obtained some discrepancies between the numerical and

experimental results, up to a certain level, the model was able to satisfactorily capture the experimental results for two case studies.

6 CREEP OF CEMENT BASED MATERIALS

6.1 Introduction

This chapter focus on the main aspects necessary to simulate the concrete creep effect by attending the viscoelastic response of cement based materials (CBM).

A review of fundamental concepts of creep, its driven mechanisms and main influencing factors for CBM are described.

An overview of the most widespread and significant existing creep prediction models is provided. Additionally, a new creep model capable of predicting the creep response of CBM, since their early ages, is presented.

A concrete constitutive model that couples the creep and cracking behavior of CBM is derived and implemented in a software based on the finite element method (FEM), and its predictive performance is assessed.

6.2 Time-dependent deformation

When in service, all CBM, e.g. concrete and mortar, experience the effect of instantaneous and time-dependent deformations. The total uniaxial deformation of a material at the time t , upon a sustained load since time t_0 can be divided in five components, as expressed in the Eq. (6.1):

$$\varepsilon(t) = \varepsilon_{ins}(t_0) + \varepsilon_{cr}(t) + \varepsilon_{sh}(t) + \varepsilon_T(t) + \varepsilon_{crco}(t) \quad \text{Eq. (6.1)}$$

where ε_{ins} is the instantaneous strain at loading, ε_{cr} is the creep strain, ε_{sh} is the shrinkage deformation, ε_T is the material deformation due to thermal expansion or contraction and ε_{crco} is the crack strain. The strains ε_{ins} , ε_{cr} and ε_{crco} are caused by the applied stress (or stress history), being commonly referred as mechanical strains, while the remaining components are stress independent strains. In Figure 98 are represented the CBM strain components along the time interval $[t_d, t]$, where t_d is the time where shrinkage starts, of an uncracked material submitted to a constant compressive stress applied at t_0 , considering a uniform temperature during all the time interval.

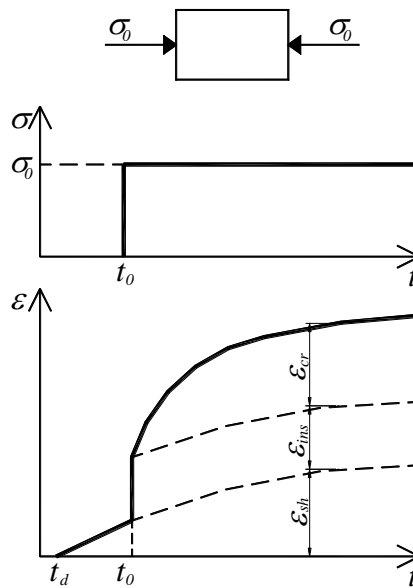


Figure 98 – CBM strain under constant load and temperature.

6.3 Creep fundamentals

All the CBM, e.g. concrete and mortar, exhibit a viscoelastic behavior characterized by an instantaneous and a time-dependent deformation upon loading. When submitted to a constant sustained stress, the time-dependent deformation of a CBM is depicted by a slow and continuous increase of deformation with time, at a decreasing rate, but without a maximum limiting bound (Figure 99a) [122]. This phenomenon is commonly referred as creep.

Alternatively, the viscoelastic behavior of a CBM can also be identified with the decrease of stress when the material is submitted to a constant strain (Figure 99b). The latter behavior is called relaxation. Both types of viscoelastic phenomena are driven by the same principles, and differ only on the boundary conditions of the problems [123], although for CBM the term creep is generally adopted when describing the time-dependent deformation apart from shrinkage and thermal volume changes, and for so it remains the focus of this work.

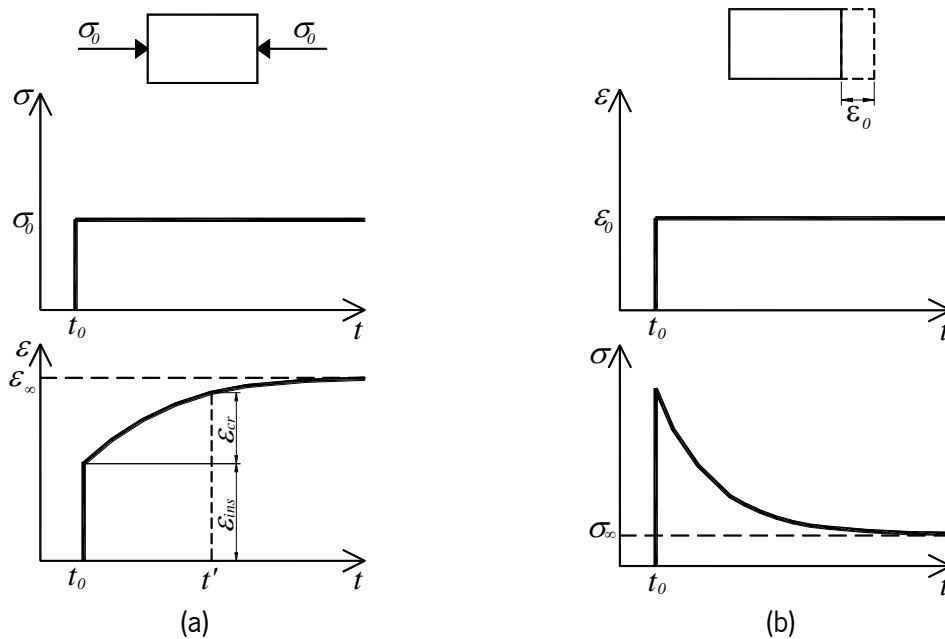


Figure 99 – Viscoelastic behavior: a) Creep; b) Relaxation.

The creep behavior depicted in Figure 99a is generally obtained when the applied stress is under the typical working stress level of CBM at serviceability limit state (SLS) loading conditions, which is generally 40-50% of the material strength. However, a more general form of the creep deformation can be obtained (Figure 100), considering that the sustained load is above 50% of the ultimate load. In this case, the creep deformation can be divided in three stages: a) primary creep (or transient creep), that is characterized by a decreasing rate of creep with time; b) secondary creep (or steady-state creep), where the time-strain rate due to creep is almost constant; c) tertiary creep (or accelerating creep), when the time-strain rate due to creep increases continuously up to the failure of the material. For typical values of working stress in CBM, primary and secondary creep stages are undifferentiated, and the tertiary stage is never reached [124], [125].

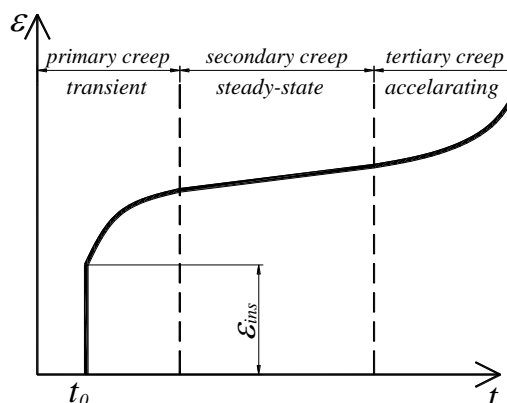


Figure 100 – General form of creep deformation.

For a previously loaded specimen, when the stress is removed at instant t_1 , only a partial recovery of the accumulated deformation is observed, which corresponds to the instantaneous response to the unloading, $\varepsilon_{ins,u}(t_1)$, and to a long-term reduction of the creep strain with a gradual decreasing rate, $\varepsilon_{cr,d}(t)$, (Figure 101). Upon unloading, the recoverable part of the creep strain is often named *delayed elastic strain* $\varepsilon_{cr,d}(t)$ and the irrecoverable part is often referred as *flow* $\varepsilon_{cr,f}(t)$ [123].

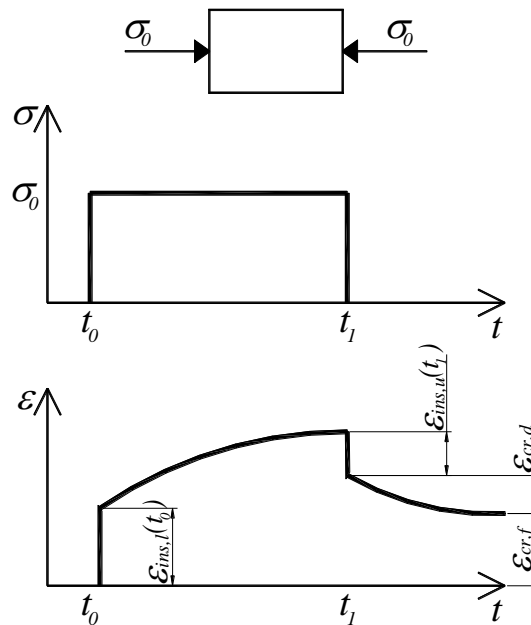


Figure 101 – Recoverable and irrecoverable components of creep strain.

A further fundamental concept in the study of creep is the *linearity*, which can be assumed if the applied stress level is less than about 40-50% of the material strength limit. A viscoelastic behavior can be considered linear when the principle of superposition and proportionality are fulfilled [126], which means that there is a linear relationship between stress and strain, as the one expressed in Eq. (6.2) [127].

$$\varepsilon(t) = J(t, t_0) \cdot \sigma(t_0) \quad \text{Eq. (6.2)}$$

where $J(t, t_0)$ is the uniaxial creep compliance function that characterizes a given CBM. The creep compliance is a function that represents the instantaneous plus the creep deformation at time t , caused by a unitary stress acting since time t_0 . The typical curves of the compliance function with respect to varying time t and loading ages t_0 are presented in Figure 102.

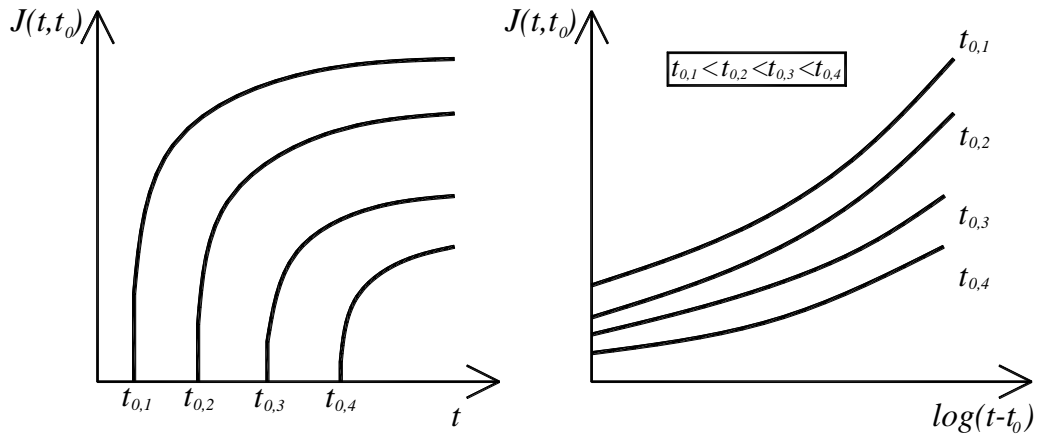


Figure 102 – Typical curves of creep compliance [128].

The meaning of proportionality is reflected in Eq. (6.3): a loading n times larger than another loading, shall also produce creep strains that are n times larger than those of the latter [127].

$$\begin{aligned} \varepsilon(n \cdot \sigma) &= n \cdot \varepsilon(\sigma) \\ n &= \text{const} \end{aligned} \quad \text{Eq. (6.3)}$$

where ε is the material strain and σ the applied stress. Considering the proportionality, it is possible to study a material submitted to a given stress level and extrapolate the viscoelastic behavior for distinct stress levels.

The superposition principle is illustrated in Figure 103 through an example with two independent loads/stresses applied: $\sigma_c(\tau_0)$ at instant τ_0 and $\sigma_c(\tau_1)$ at instant τ_1 . According to this principle, if a material is subjected to a loading history that corresponds to the combination of two independent load cases, the creep deformation corresponds to the cumulative effect of each individual load case (see curves a, b and c in Figure 103) [123], [126]. Overall, the superposition principle can be expressed mathematically by the following expression:

$$\varepsilon(\sigma^1 + \sigma^2) = \varepsilon(\sigma^1) + \varepsilon(\sigma^2) \quad \text{Eq. (6.4)}$$

where ε is the total strain, while σ^1 and σ^2 are the load cases.

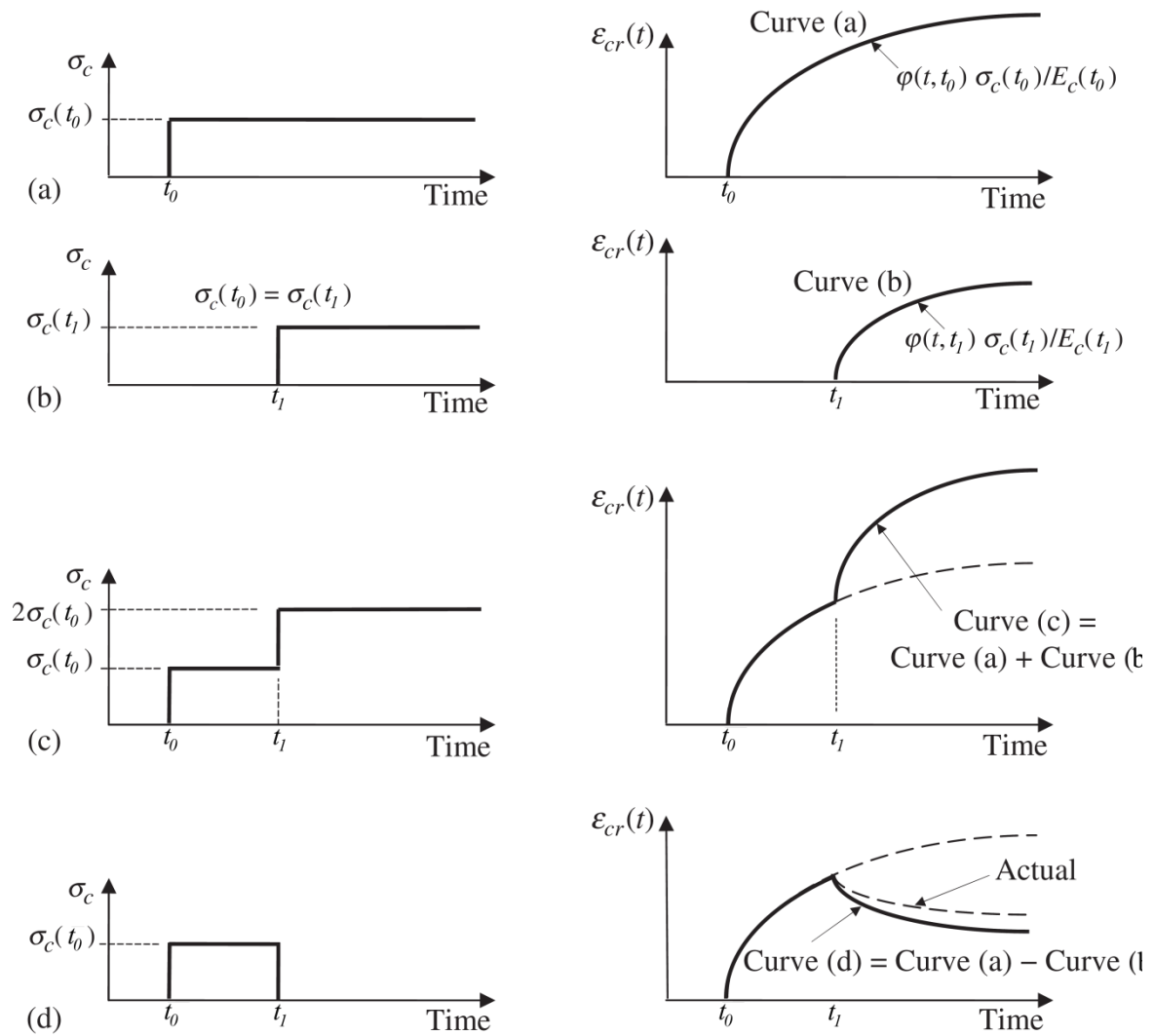


Figure 103 – Superposition principle of creep strains (adapted from [123]).

In general, the deformation of a material due to a nonconstant applied stress history can be estimated by application of the superposition principle. This principle was applied for the first time in concrete by McHenry [129]. McHenry stated that the strain produced by the stress increment applied at any time $t_{0,i}$, is not affected by any previous and subsequent applied stresses. According to the superposition principle, the total strain $\varepsilon(t)$ caused by a given stress history $\sigma(t)$ can be obtained by decomposing the history in small increments $d\sigma(t_{0,i})$ applied at various time instants $t_{0,i}$ (Figure 104), adding the corresponding strains based on Eq. (6.2) and the stress independent strains ε^0 , resulting in the following Stieltjes integral [122], [123], [128]:

$$\varepsilon(t) = \int_{t_0}^t J(t, t_{0,i}) \cdot d\sigma(t_{0,i}) + \varepsilon_0(t) \quad \text{Eq. (6.5)}$$

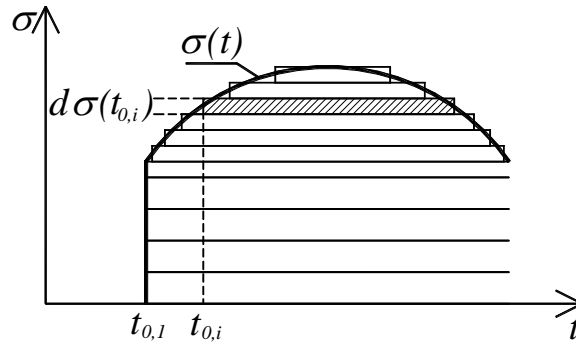


Figure 104 – Decomposition of time varying stress history.

Assuming that a material remains stress free until, at some time instant $t_{0,1}$, a finite stress σ_1 is applied in a sudden jump, and subsequently the stress $\sigma(t)$ varies continuously, Eq. (6.5) can be written in terms of the Riemann integral [122]:

$$\varepsilon(t) = \sigma_1 \cdot J(t, t_{0,1}) + \int_{t_{0,1}}^t J(t, t_0) \cdot \frac{d\sigma(t_0)}{dt_0} dt_0 + \varepsilon_0(t) \quad \text{Eq. (6.6)}$$

If the strain history $\varepsilon(t)$ is known, then Eq. (6.5) or Eq. (6.6) represent an integral equation for the stress history $\sigma(t)$, known as the Volterra integral equation [122]. The compliance function $J(t, t_0)$ is the kernel of the integral equation [122], [128]. Due to the aging nature of CBM materials, the creep compliance $J(t, t_0)$ is a function dependent on two variables (t and t_0), and the use of the Laplace transform is ineffective to resolve the Volterra integral equation [130]. Nonetheless, in general the strain history $\varepsilon(t)$ is not prescribed and Eq. (6.5) or Eq. (6.6) represents a uniaxial stress-strain relationship for creep [122].

Based on the theory of linear viscoelasticity, the superposition principle has been applied to materials with aging (aging linear viscoelasticity) [128]. Materials with aging are those whose mechanical properties are age dependent, such as the case of concrete and others CBM [126]. The fact that $J(t, t_0)$ is a two variable dependent function (t and t_0) is a consequence of aging, which adds a significant complexity in the process of deriving accurate creep prediction models. If no aging is considered, then the compliance function can be only expressed as function of the duration period $t - t_0$, $J(t, t_0)$. The concept of aging is further developed in the following sections.

The use of the superposition principle for the analysis of creep problems is restricted to the following conditions [131]:

- The stresses are within the service stress range (typically for stress/strength ratio lower than 40%);
- The strains do not decrease in value;
- There is no drying creep;
- Although possible, the stress increase after initial loading must exhibit a smooth change (i.e. no sudden variations are allowed).

It has been reported [128], [131]–[134] that the violation of these conditions yields in inaccurate predictions of the creep behavior of concrete specimens. The particular case of using the superposition principle to predict the creep recovery response after partial or total unloading has revealed an overestimation of the creep recovery when compared to experimental results [131], [132]. The latter phenomenon is represented in Figure 103d.

If the conditions of linearity are not fulfilled, it is then stated that the material exhibits a nonlinear viscoelastic behavior. The study of nonlinear viscoelastic behavior is not included within the scope of the present document.

Disregarding the influence of the remaining time-dependent deformations, namely shrinkage and thermal volume changes, the total deformation $\varepsilon(t)$ of an uncracked uniaxial loaded CBM material is expressed by:

$$\varepsilon(t) = \varepsilon_{ins}(t_0) + \varepsilon_{cr}(t) \quad \text{Eq. (6.7)}$$

For stress-strength ratio lower than 40% the instantaneous strain is defined by:

$$\varepsilon_{ins}(t_0) = \frac{\sigma(t_0)}{E(t_0)} \quad \text{Eq. (6.8)}$$

and the creep compliance can be expressed as:

$$J(t, t_0) = \frac{1}{E(t_0)} + \frac{\varepsilon_{cr}(t)}{\sigma(t_0)} \quad \text{Eq. (6.9)}$$

To the second term of Eq. (6.9) is called *specific creep* $C(t, t_0)$ and represents the creep strain at time t produced by a sustained unit stress applied at time t_0 . In Figure 105 are represented some examples of specific creep curves for a material loaded at different loading ages.

$$C(t, t_0) = \frac{\varepsilon_{cr}(t)}{\sigma(t_0)} \quad \text{Eq. (6.10)}$$

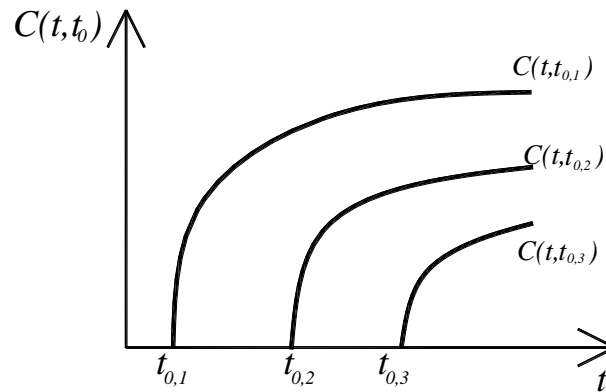


Figure 105 – Example of specific creep curves for a material loaded at different time instants.

Commonly, the creep deformation of CBM is quantified by the creep coefficient $\varphi(t, t_0)$. This coefficient is defined as the relation between the creep strain $\varepsilon_{cr}(t)$ evaluated at the instant t and the instantaneous strain $\varepsilon_{ins}(t_0)$ at the instant t_0 , namely:

$$\varphi(t, t_0) = \frac{\varepsilon_{cr}(t)}{\varepsilon_{ins}(t_0)} \quad \text{Eq. (6.11)}$$

Based on Eq. (6.2), Eq. (6.7), Eq. (6.8) and Eq. (6.11) the creep compliance and the creep coefficient can be related by the following expression:

$$J(t, t_0) = \frac{1}{E(t_0)} \cdot [1 + \varphi(t, t_0)] \quad \text{Eq. (6.12)}$$

Introducing Eq. (6.12) in Eq. (6.2), the total deformation $\varepsilon(t)$ at time t of a material submitted to a constant stress state $\sigma(t_0)$ since time t_0 is obtained by the following expression:

$$\varepsilon(t) = \sigma(t_0) \cdot \frac{[1 + \varphi(t, t_0)]}{E(t_0)} \quad \text{Eq. (6.13)}$$

The inverse of the second term of Eq. (6.13) is known as *effective modulus*, $E(t_0)/(1+\varphi(t,t_0))$ [123]. When considering the existence of the other remaining time-dependent deformations, the shrinkage strain, thermal dilation strains and cracking strains must be added to Eq. (6.13).

From Eq. (6.11) and Eq. (6.8) is possible to determine the creep strain at a given time instant t , resultant from a constant stress state $\sigma(t_0)$ applied since time t_0 , based on the creep coefficient $\varphi(t,t_0)$ and on the material elastic modulus $E(t_0)$ at the corresponding loading age:

$$\varepsilon_{cr}(t) = \frac{\sigma(t_0)}{E(t_0)} \cdot \varphi(t,t_0) \quad \text{Eq. (6.14)}$$

6.4 Creep mechanisms and influencing factors in CBM

The mechanisms that control creep behavior of CBM materials remain to be fully understood. According to [135], [136], some of these mechanisms can be:

- Sliding of the colloidal sheets in the cement gel between the layers of absorbed water – viscous flow;
- Expulsion and decomposition of the interlayer water within the cement gel – seepage;
- Elastic deformation of the aggregate and the gel crystals as viscous flow and seepage occurring within the cement gel – delayed elasticity;
- Local fracture within the cement gel involving the breakdown (and formation) of physical bonds – micro-cracking;
- Mechanical deformation theory;
- Plastic flow;
- Solidification theory;
- Microprestress of creep sites in cement gel microstructure.

More recently [137], the creep deformation of concrete has been strongly linked to the dissolution-precipitation process that acts at nanoscale contact regions of calcium-silicate-hydrates (C-S-H) particles. Based on nanoscale analysis techniques, it has been showed that the creep rates are related with the dissolution rates of C-S-H. The physical mechanisms rely on dissolution of C-S-H particles in high stress regions and their re-precipitation in low stress regions.

When submitted to sustained stress for long periods of time, concrete creep deformation can reach about 50% in the first 2-3 months and about 90% in 2-3 years after loading [123]. Afterwards, the strain rate is almost negligible [123].

It is known that creep deformation of CBM can be decomposed in two parts: a) basic creep; b) drying creep. The basic creep is associated to the stress state of the material and can be identified in sealed specimens in which all moisture interactions with the external environment are avoided. Basic creep is considered as a material constitutive property and independent from the specimens size and shape [138]. The drying creep is related to the time dependent deformation coupled with the drying effect of the CBM specimens, and is experimentally determined after subtracting shrinkage, elastic, thermal and basic creep components from the total measured strain [123], [138].

It is believed that the basic creep component is related with the debonding and rebonding at the highly stressed sites within the C-S-H microstructure [122]. While the drying component is related with the increase of stress at the C-S-H sites, and consequently of the rate of bond failure [122].

To the best of the knowledge on the matter, it is known that the creep deformation magnitude and rate of change is influenced by different factors such as: material composition, and environmental and loading conditions [123], [128]. In general, the creep deformation of high strength concrete is lower than normal strength counterparts. Additionally, the higher aggregate content and maximum aggregate size, and the lower water-cement ratio, also reduce the creep deformation of CBM [123]. Regarding the element geometry, the creep is more significant in thin structural specimens, such as slabs, which exhibit higher surface-area/volume ratios [123], [139]. In addition to relative humidity, the environment temperature is also an important factor in creep phenomena. The rise in temperature increases the deformation of the cement paste and accelerates drying and consequently increases the creep. The dependence of creep deformations to the temperature is more pronounced in high temperatures and has low relevance between 0 °C and 20 °C. At room temperature of 40 °C, the creep in concrete has been reported to be 25% higher than that at 20 °C [123].

Regarding the CBM creep response upon unloading, the delayed elastic strain is thought to be a result of the elastic recovery of the CBM aggregates [123]. For concrete specimens loaded for long periods of time, the delayed elastic recovery can reach approximately 40-50% of the instantaneous strain of the material [123]. The flow (irrecoverable) strain is thought to be caused by irreversible changes in

the material microstructure that occur during the hydration process, rupture of the interparticles bonds by moisture seepage and micro-cracking [140].

The creep deformation of CBM is highly influenced by the loading age of the specimens. For early ages, the creep strain magnitude is higher than for specimens loaded at later ages (Figure 106), considering specimens submitted to equal stress levels. To this behavior is called *aging* (or *maturing*).

Bazant physical explanation for aging is based on the solidification-microprestress theory [141]–[144], being related with the microstructural changes in the concrete pores. While the short-term aging is related to the volume growth of the hydration products in concrete pores (solidification concept), the long-term aging effect is assigned to the relaxation of the microprestress that is generated by the disjoining pressure of adsorbed water in the micropores and from the volume changes of the hydration products [143].

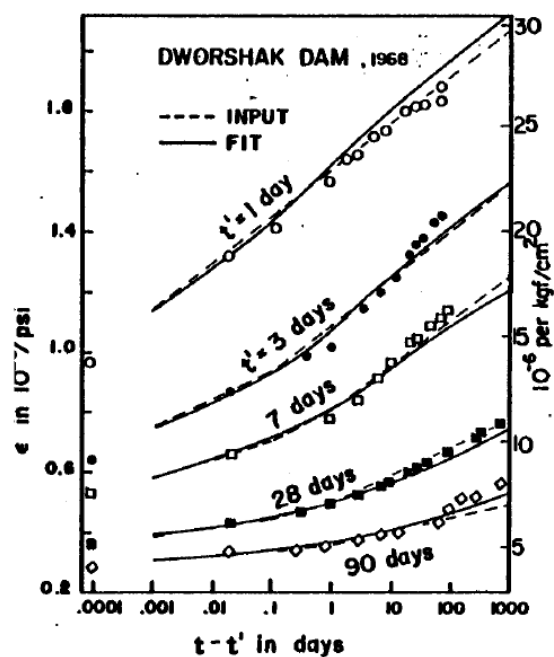


Figure 106 – Example of the dependence of creep strain of concrete specimens with the loading age (extracted from [130]).

In Figure 107 is displayed the typical response of the specimens when submitted to loading and total unloading periods, given to the aging effect of CBM. It is noticeable that due to the increase of material stiffness ($E(t_0) < E(t_e)$), the instantaneous deformation of the material is smaller for older ages of the CBM [$\varepsilon_{ins}(t_e) < \varepsilon_{ins}(t_0)$]. Additionally, the creep deformation recovery after total unloading is smaller than the creep deformation at the loading stage [$\varepsilon_{cr}(\Delta t, t_e) < \varepsilon_{cr}(\Delta t, t_0)$], for similar load

duration periods Δt , inducing an irreversible deformation of the CBM. The aging effect is particularly noticeable when comparing CBM specimens loaded since very early ages ($t_0 < 3days$) [145].

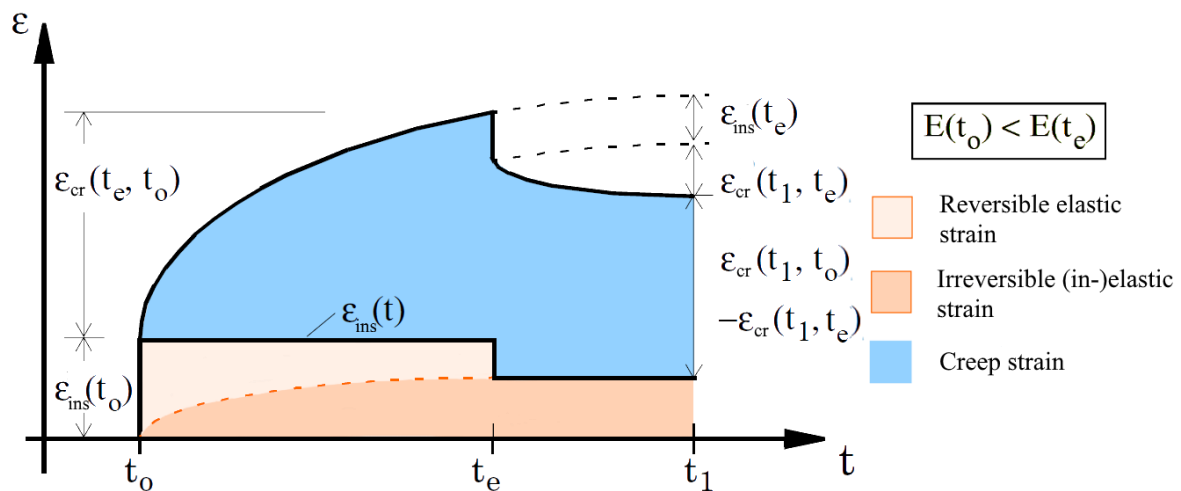


Figure 107 – Example of loading-unloading creep response of aging material (adapted from [146]).

Additionally, the creep deformation of CBM is influenced by the stress level applied to the specimens. If the applied stress level is on the linear domain of the stress-strain relationship of the material, it is possible to state that the creep deformation is proportional to the stress, according to Eq. (6.2) [139]. Otherwise, the creep deformation exhibits a nonlinear response, and the creep deformation increases at a faster rate [123]. For CBM materials the maximum stress limit value where creep exhibits a linear response is about 40-50% of the material strength, compressive or tensile [128], [130].

Although the main topics in CBM creep assessment are related with compressive stress states, the consideration of creep effect in tension is of great interest, especially in the analysis of the cracking risk of structures since early ages, due to the effects of shrinkage, temperature variations and load actions. Although some experimental research has been carried to evaluate the difference between concrete specimens submitted to compressive and tensile creep tests, a consensus between the researchers has not been reported [147], as some findings evidenced that creep is higher in compression, others have reached opposite conclusions, and similar response have also been pointed out [148].

The main mechanisms that rule the behavior of CBM creep in tension are common to creep in compression, namely i) micro-diffusion of water between capillary pores; and ii) long-term sliding of the calcium-silicates-hydrates, with the addition of micro-cracking [147]. Additionally, the creep in

tension has also evidenced to be influenced by the same type of factors as creep in compression, namely loading age, temperature, mix proportions and stress/strength ratio [145], [147].

6.5 Creep compliance prediction models

In order to assess the performance of creep sensitive structures or structural components it is of key importance to adopt accurate prediction models that can simulate the creep behavior of CBM, namely the creep compliance.

In this section are presented some the most widespread creep prediction models, including an analysis of the capabilities and drawbacks of each model. Additionally, a new model capable of predicting the creep behavior of CBM since early ages is also proposed.

Regarding the use of creep prediction models, it is highly desirable that the models used in the analysis of structures follow the guidelines presented in [149]. More recently, these guidelines have been reviewed [150]. The main recommendations that a creep prediction model should comply are:

- The model should describe creep in terms of the creep compliance function $J(t, t_0)$, rather than by the creep coefficient $\varphi(t, t_0)$ [149];
- Basic and drying creep components should be given by independent terms in the model formulation. The total creep deformation results from adding the instantaneous deformation with the basic and drying creep components [149];
- The creep compliance function must satisfy certain thermodynamics restrictions:
 - o The creep compliance $J(t, t_0)$ is always monotonically increasing function, which is mathematically translated into [128]:

$$\frac{\partial J(t, t_0)}{\partial t} \geq 0 \quad \text{Eq. (6.15)}$$

- o The rate of the creep compliance $\frac{\partial J(t, t_0)}{\partial t}$ decreases with time [128]:

$$\frac{\partial^2 J(t, t_0)}{\partial t^2} \leq 0 \quad \text{Eq. (6.16)}$$

- For increasing loading ages there is a decrease of the creep compliance magnitude for similar load duration periods $t - t_0$, as is illustrated in Figure 108 and is mathematically expressed by [128]:

$$\left[\frac{\partial J(t, t_0)}{\partial t_0} \right]_{t-t_0} \leq 0 \quad \text{Eq. (6.17)}$$

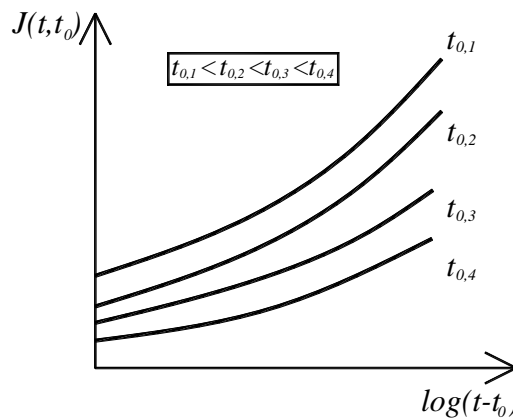


Figure 108 – Dependence of creep compliance rate with loading age t_0 in the $\log(t - t_0)$ time scale (based on [128, Fig. 2.1]).

- Drying creep should approach a final asymptotic value [149], [150];
- The basic creep model should be able to describe the experimental data through the entire ranges of loading ages t_0 and load duration $t - t_0$, namely:
 - The final basic creep value is not limited, i.e. does not possess any asymptotic final value [149];
 - A power function is recommended to describe well the short-term duration experimental creep data, while for long-term duration an asymptotic approach to a logarithmic function is suggested [149], [150];
 - The transition between the short-term and long-term durations shall be centered on a specific creep value, rather than on a specific time duration [149], [150];
 - The aging effect on creep can be described by a power function of the loading age t_0 , with a small negative exponent (approximately equal to $-\frac{1}{3}$) [149], [150];
- It is advisable that creep curves reveal a nondivergence property. Although this is not strictly necessary on a theoretical basis, by coupling the superposition principle with the creep models

that exhibit divergence, a nonmonotonic recovery of creep strain upon total unloading can be attained (Figure 109) [149];

- Divergence occurs when creep curves, for the same time t and for a higher loading age t_0 , exhibits a smaller slope than a creep curve of a lower loading age (Figure 109), which can be mathematically expressed as [151]:

$$\frac{\partial J(t, t_{0,2})}{\partial t} < \frac{\partial J(t, t_{0,1})}{\partial t}, \quad t_{0,2} > t_{0,1} \quad \text{Eq. (6.18)}$$

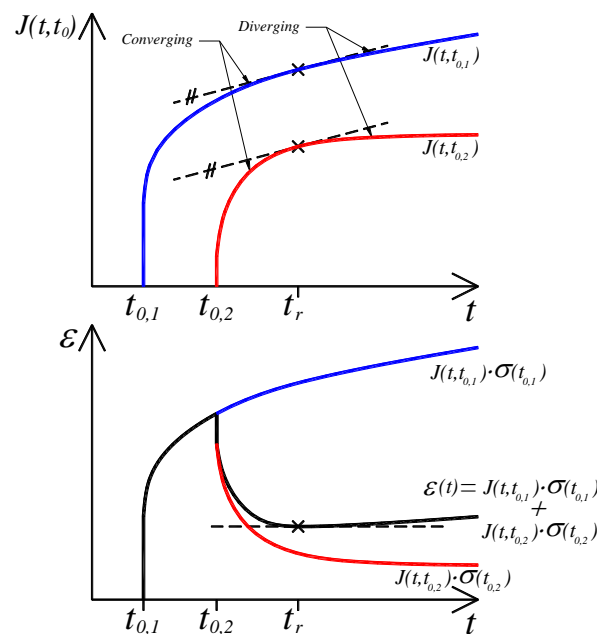


Figure 109 – Example of divergence of creep curves and nonmonotonic recovery of creep strain upon total unloading (t_r - point of recovery reversal) (adapted from [151, Fig. 1]).

- The creep model shall also be suitable for implementation in numerical computation, namely to expand the creep expression into a Dirichlet series, making it possible to characterize creep in a rate-type form corresponding to a Kelvin or Maxwell chain model [149];
- It is also preferable that the Dirichlet series expansion process can avoid ill-posed problems with nonunique solution, and always outputs positive and increasing Kelvin chain moduli with time (which grant nondivergence property) [149]. These problems can arise due to the age dependence of the Kelvin chain moduli, and are avoided if the age dependence is given by an external parameter, by means of some transformation of time [149], [150];
- The creep model must be continuous regarding its involving variables [149];

- The mathematical form of the prediction model should be based on a theory that can physically explain the process involved in the creep phenomenon [149], [150];
- The creep model accuracy should be assessed by using a comprehensive database that includes all the relevant creep tests available in the literature, namely the data bank developed in the Northwestern University [149], [150]. The model should achieve the lowest possible coefficient of variation, and its value must be supplied with the model formulation [150]. The validity of the model cannot be acknowledged from a partial selection of data tests, to which the model presents a good fit [149], [150];
- The application of the creep models in the analysis and design of creep sensitive structures should be coupled with the use of confidence limits, such as 95%. This means that when applying such confidence limit in the design of a structure, the probability of not exceeding a specified structural response (e.g. maximum midspan deflection of a beam or slab) is equal to 95%. [149];
- The most important parameters of the model should be calibrated according to short-term creep tests and then extrapolating the data for long-term [149], [150]. In situations where is considered that creep deformation plays a critical role in the behavior of structures, it is mandatory to adopt this methodology [136], [138].

6.5.1 Existing models

This section presents five existing creep models that have a widespread use and encompass the state-of-the-art theories to predict the creep of concrete, especially its basic component. The identified models are: (i) the Double Power Law (DPL); (ii) the Model Code 2010 model (MC2010); (iii) the Eurocode 2 model (EC2); (iv) the B3 model; (v) and its recent updated form, the B4 model. These models have almost exclusively been derived for concrete. However, as the creep is mostly caused by the deformation of the cement paste, it is considered that the existing models can be applied to other CBM, as mortar, including the use of fiber reinforced cement composites (FRC).

Amongst these creep prediction models a division can be drawn based on the followed approach applied to describe creep: (i) the DPL, EC2 and MC2010 models follow the classical approach that treats the material parameters involved in creep as empirical functions of time and loading age; (ii) the B3 and B4 models that follows a phenomenological approach, where the materials parameters

are determined based on the existing physical, chemical and thermodynamic understanding on concrete creep phenomenon and its microstructure.

6.5.1.1 Double Power Law

The Double Power Law was proposed in 1976 by Bažant and Osman [152], and it is based on the evidence that creep of concrete can be described by power functions of load duration $(t - t_0)$ and inverse power functions of loading age t_0 to describe aging effect [153].

It is a simple and versatile model, which is primordially used to simulate concrete basic creep component, based on material parameters that should be derived from a data-fitting procedure to the experimental creep data. The model allows good adjustments with experimental information associated to the basic creep [152], however its formulation is not supported in any physical understanding of creep.

Since its origin, the model received relevant updates, in order to increase creep prediction accuracy for long-time duration, by considering a transition from a power function for short-time duration to a logarithmic function for long-time duration.

In Table 12 are presented the original and updated equations of the model. It is also relevant to remark that over the years the DPL model suffered several updates related with factors that influence the creep deformation along time, namely: drying creep [154]; temperature effect in basic [155] and drying creep [156]; and cyclic creep and nonlinearity [157].

Table 12 – Basic creep compliance evolution of DPL model.

Models	Creep compliance
Double Power Law[152], [158]	$J(t, t_0) = \frac{1}{E_0} + \frac{\phi_1}{E_0} \cdot (t_0^{-m} + \alpha) \cdot (t - t_0)^n \quad \text{Eq. (6.19)}$
Log Double Power Law[158]	$J(t, t_0) = \frac{1}{E_0} + \frac{\psi_0}{E_0} \cdot \ln \left[1 + \psi_1 (t_0^{-m} + \alpha) \cdot (t - t_0)^n \right]$ Eq. (6.20)
Triple Power Law[159]	$J(t, t_0) = \frac{1}{E_0} + \frac{\phi_1}{E_0} \cdot (t_0^{-m} + \alpha) \left[(t - t_0)^n - B(t, t_0; n) \right]$ Eq. (6.21)

Variables:

- ϕ_1 , m , n and α are materials parameters (see references);
- $E_0 \approx 1.5E_{c,28}$, is the asymptotic elastic modulus [158];
- $E_{c,28}$, is the static elastic modulus of concrete at 28 days of age;
- ψ_0 and ψ_1 are constants (see reference [158]);
- $B(t, t_0; n)$ – binominal integral (see reference [159]).

Care must be taken, as the DPL and its succeeding variants resort to the concept of the asymptotic modulus E_0 , and not to the conventional static elastic modulus E . The E_0 represents the true elastic instantaneous response of the material, while the conventional elastic modulus E corresponds to a modulus obtained from compression tests with loading durations of 1 to 5 minutes, that incorporates the instantaneous and short-time creep response of the material within this time interval [158]. In Figure 110 is illustrated the concept of E_0 , that corresponds to the asymptotic value of the creep curve $J(t, t_0)$ vs. $\log(t - t_0)$, as $\log(t - t_0) \rightarrow -\infty$ or $(t - t_0) \rightarrow 0$ [158].

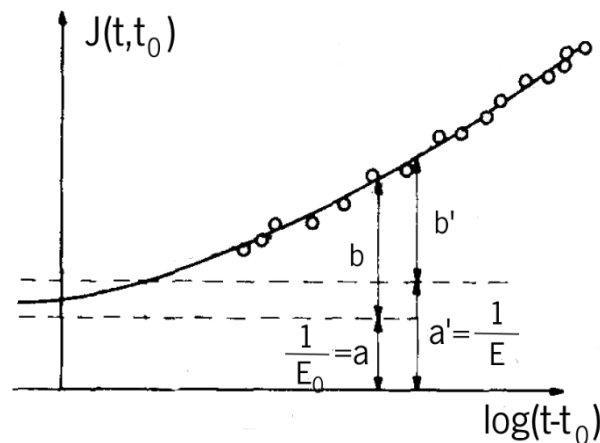


Figure 110 – Creep curve in log-time scale (a - true elastic deformation; b - true creep; a' - conventional elastic deformation; b' – conventional creep) (adapted from [158, Fig. 1]).

It should be noticed that the original DPL model and its succeeding improvements have revealed divergence of the creep curves, at least for some time periods [159].

Bažant and Osman [152] expanded the DPL creep compliance model into a Dirichlet series approximation. The DPL creep compliance expressed by a Dirichlet series takes the form:

$$J(t, t_0) = \frac{1}{E_s(t_0)} + \sum_{\mu=1}^N \frac{1}{E_{\mu}(t_0)} \cdot \left(1 - e^{-\frac{(t-t_0)}{\tau_{\mu}}} \right) \quad \text{Eq. (6.22)}$$

$$\frac{1}{E_s(t_0)} = \frac{1}{E_0} + a(n) \cdot \left(\frac{\tau_1}{0.002} \right)^n \cdot \frac{\varphi_1}{E_0} \cdot t_0^{-m} \quad \text{Eq. (6.23)}$$

For $\mu < N$:

$$\frac{1}{E_{\mu}(t_0)} = b(n) \cdot \left(\frac{\tau_1}{0.002} \right)^n \cdot \frac{\varphi_1}{E_0} \cdot 10^{n \cdot (\mu-1)} \cdot t_0^{-m} \quad \text{Eq. (6.24)}$$

For $\mu = N$:

$$\frac{1}{E_{\mu}(t_0)} = 1.2 \cdot b(n) \cdot \left(\frac{\tau_1}{0.002} \right)^n \cdot \frac{\varphi_1}{E_0} \cdot 10^{n \cdot (\mu-1)} \cdot t_0^{-m} \quad \text{Eq. (6.25)}$$

where E_0 , $a(n)$, $b(n)$, φ_1 , m and n are material parameters; $E_s(t_0)$ is the modulus of the isolated spring of the Kelvin generalized model; $E_{\mu}(t_0)$ are the modulus of each Kelvin chain; and τ_{μ} are the chosen retardation times.

The retardation time controls the growth of creep strain after stress is imposed; the shorter the retardation time, the more rapid the creep straining [160]. The retardation times of each Kelvin chain corresponds to the time after loading for the strain to reach $(1-1/e) = 63.2\%$ of its equilibrium value, corresponding to the maximum creep deformation obtained by each Kelvin chain. The retardation times for each chain are usually selected as $\tau_{\mu} = 10^{\mu-1} \cdot \tau_1$ ($\mu = 1, 2, \dots, N$) [128].

Although the DPL model origin goes back to 1976 and several research about creep has been carried since then, the original model and its variants remain still widely used due to its simplicity and versatility when compared to the remaining existing models. This model have been successfully applied to predict the creep compliance of CBM in several research works, e.g. [161]–[164].

6.5.1.2 Eurocode 2

Another creep prediction model available is the Eurocode 2 (EC2) model, that is part of the design rules for concrete structures in EU-countries [37]. This model is based on the creep model of *fib* Model Code 1990 [165].

The EC2 creep model, similarly to the MC2010 model, allows the determination of the creep coefficient function $\varphi(t, t_0)$. However, the EC2 model does not separate the time-dependent deformation in the basic and drying creep components.

The model formulation is presented in Table 14. Due to its mathematical expressions, it is possible to state that creep coefficient presents a limiting value. Additionally, the model lacks theoretical support. It was also verified that the derived creep curves may violate the nondivergence condition [166].

When comparing the prediction capability of the model in an extensive creep database, a coefficient of variation equal to 20% was attained [37].

Table 13 - Creep coefficient function based on EC2 model [37].

Creep coefficient:	
$\varphi(t, t_0) = \varphi_0 \cdot \beta_c(t, t_0)$	Eq. (6.26)
$\varphi_0 = \varphi_{RH} \cdot \beta(f_{cm}) \cdot \beta(t_0)$	Eq. (6.27)
$\varphi_{RH} = \left\{ \begin{array}{l} 1 + \frac{1 - RH / 100}{0.1 \cdot \sqrt[3]{h_0}} \quad , \text{ for } f_{cm} \leq 35 \text{ MPa} \\ \left[1 + \frac{1 - RH / 100}{0.1 \cdot \sqrt[3]{h_0}} \cdot \alpha_1 \right] \cdot \alpha_2 \quad , \text{ for } f_{cm} > 35 \text{ MPa} \end{array} \right\}$	Eq. (6.28)
$\beta(f_{cm}) = \frac{16.8}{\sqrt{f_{cm}}}$	Eq. (6.29)
$\beta(t_0) = \frac{1}{0.1 + (t_{0,adj})^{0.2}}$	Eq. (6.30)
$\beta_c(t, t_0) = \left[\frac{t - t_0}{\beta_H + t - t_0} \right]^{0.3}$	Eq. (6.31)
$\beta_H = \left\{ \begin{array}{l} 1.5 \cdot \left[1 + (0.012 \cdot RH)^{18} \right] \cdot h_0 + 250 \leq 1500 \quad , \text{ for } f_{cm} \leq 35 \text{ MPa} \\ 1.5 \cdot \left[1 + (0.012 \cdot RH)^{18} \right] \cdot h_0 + 250 \alpha_3 \leq 1500 \alpha_3 \quad , \text{ for } f_{cm} > 35 \text{ MPa} \end{array} \right\}$	Eq. (6.32)
$\alpha_1 = \left(\frac{35}{f_{cm}} \right)^{0.7} ; \alpha_2 = \left(\frac{35}{f_{cm}} \right)^{0.2} ; \alpha_3 = \left(\frac{35}{f_{cm}} \right)^{0.5}$	Eq. (6.33)
$h_0 = 2 \cdot A_c / u$	Eq. (6.34)
Effect of type of cement and curing temperature:	
$t_{0,adj} = t_{0,T} \cdot \left[\frac{9}{2 + (t_{0,T})^{1.2}} + 1 \right]^\alpha \geq 0.5 \text{ days}$	Eq. (6.35)
$t_{0,T} = \sum_{i=1}^n \Delta t_i \cdot e^{\frac{13.65 - 4000}{273 + T(\Delta t_i)}}$	Eq. (6.36)
Parameters definition:	
f_{cm} - concrete compressive strength at an age of 28 days, in MPa;	
$t_{0,adj}$ - adjusted age at loading, considering temperature and type of cement, in days;	
RH - relative humidity of the ambient environment, in %;	
h_0 - notational size, in mm	
A_c - cross-section section, in mm ² ;	
u - perimeter of the member in contact with the atmosphere, in mm;	
Δt_i - is the number of days where the temperature T prevails;	
$T(\Delta t_i)$ - is the average temperature during the time period Δt_i , in °C;	

$$\alpha = \begin{cases} -1, & \text{cement type S} \\ 0, & \text{cement type N} \\ 1, & \text{cement type R} \end{cases} \text{ - is a coefficient that depends on the type of cement}$$

6.5.1.3 Model Code 2010

The creep model proposed by the Model Code 2010 (MC2010) [30] consists of an update version of the one described in the CEB-FIP Model Code 1990 [165].

The model intends to describe the creep behavior of concrete by considering separately the effect of its basic and drying components. The first is considered to be a function of the concrete compressive strength, while the latter is related with the size and ambient relative humidity. In both parts, the aging effect of concrete is considered by relating the creep deformation with the loading age t_0 .

Additionally, the MC2010 creep prediction model also takes into account the temperature history, cement type and the nonlinear effect of high stress levels.

The model formulation was empirically derived from calibration to laboratory tests. The mathematical expressions to obtain the creep coefficient function $\varphi(t, t_0)$ are presented in Table 14. The creep compliance can be obtained using Eq. (6.12).

Table 14 – Creep coefficient function based on MC2010 model [30].

Creep coefficient:	
$\varphi(t, t_0) = \varphi_{bc}(t, t_0) + \varphi_{dc}(t, t_0)$	Eq. (6.37)
where:	
$\varphi_{bc}(t, t_0)$ - basic creep coefficient;	
$\varphi_{dc}(t, t_0)$ - drying creep coefficient.	
Basic Creep:	
$\varphi_{bc}(t, t_0) = \beta_{bc}(f_{cm}) \cdot \beta_{bc}(t, t_0)$	Eq. (6.38)
$\beta_{bc}(f_{cm}) = \frac{1.8}{(f_{cm})^{0.7}}$	Eq. (6.39)
$\beta_{bc}(t, t_0) = \ln \left(\left(\frac{30}{t_{0,adj}} + 0.035 \right)^2 \cdot (t - t_0) + 1 \right)$	Eq. (6.40)
Drying Creep:	
$\varphi_{dc}(t, t_0) = \beta_{dc}(f_{cm}) \cdot \beta(RH) \cdot \beta_{dc}(t_0) \cdot \beta_{dc}(t, t_0)$	Eq. (6.41)
$\beta(RH) = \frac{1 - \frac{RH}{100}}{\sqrt[3]{0.1 \cdot \frac{h_0}{100}}}$	Eq. (6.42)
$\beta_{dc}(f_{cm}) = \frac{412}{(f_{cm})^{1.4}}$	Eq. (6.43)
$\beta_{dc}(t_0) = \frac{1}{0.1 + (t_{0,adj})^{0.2}}$	Eq. (6.44)
$\beta_{dc}(t, t_0) = \left[\frac{t - t_0}{\beta_H + (t - t_0)} \right]^{\gamma(t_0)}$	Eq. (6.45)
$\beta_H = 1.5 \cdot h + 250 \cdot \alpha_{f_{cm}} \leq 1500 \cdot \alpha_{f_{cm}}$	Eq. (6.46)
$\alpha_{f_{cm}} = \left(\frac{35}{f_{cm}} \right)^{0.5}$	Eq. (6.47)
$\gamma(t_0) = \frac{1}{2.3 + \frac{3.5}{\sqrt{t_{0,adj}}}}$	Eq. (6.48)
$h_0 = 2 \cdot A_c / u$	Eq. (6.49)

Effect of temperature and curing temperature:

$$t_{0,adj} = t_{0,T} \cdot \left[\frac{9}{2 + (t_{0,T})^{1.2}} + 1 \right]^{\alpha} \geq 0.5 \text{ days} \quad \text{Eq. (6.50)}$$

$$t_{0,T} = \sum_{i=1}^n \Delta t_i \cdot e^{\frac{13.65 - 4000}{273 + T(\Delta t_i)}} \quad \text{Eq. (6.51)}$$

Effect of high stress $0.4 f_{cm}(t_0) < |\sigma_c| \leq 0.6 f_{cm}(t_0)$:

$$\varphi_{\sigma}(t, t_0) = \varphi(t, t_0) \cdot e^{1.5(k_{\sigma} - 0.4)} \quad \text{Eq. (6.52)}$$

$$k_{\sigma} = \frac{|\sigma_c|}{f_{cm}(t_0)} \quad \text{Eq. (6.53)}$$

Parameters definition:

 f_{cm} - average concrete compressive strength at an age of 28 days, in MPa; $f_{cm}(t_0)$ - average concrete compressive strength at the loading age t_0 , in MPa; $t_{0,adj}$ - adjusted age at loading, considering temperature and type of cement, in days; RH - relative humidity of the ambient environment, in %; h_0 - notational size, in mm A_c - cross-section section, in mm²; u - perimeter of the member in contact with the atmosphere, in mm; Δt_i - is the number of days where the temperature T prevails; $T(\Delta t_i)$ - is the average temperature during the time period Δt_i , in °C; σ_c - concrete stress, in MPa;

$$\alpha = \left. \begin{array}{l} -1, \text{ strength class 32.5N} \\ 0, \text{ strength class 32.5R, 42.5N} \\ 1, \text{ strength class 42.5R, 52.5N, 52.5R} \end{array} \right\} \text{ - is a coefficient that depends on the type of cement}$$

As result of the mathematical equations, the model considers that the maximum value of the basic creep component is unlimited, i.e. $\lim_{t \rightarrow \infty} \beta_{bc}(t, t_0) = +\infty$, while for the drying creep there is a limiting value $\lim_{t \rightarrow \infty} \beta_{dc}(t, t_0) = 1$ [167].

The prediction accuracy of the model was tested on a creep test databank, revealing a reasonable good approximation for the time development of creep up to a loading duration of 50 years, with the model exhibiting a coefficient of variation equal to 25% [30].

It was also verified that the MC2010 model violates the condition of nondivergence of creep curves [166].

6.5.1.4 B3 model

Nowadays, one of the most widespread prediction creep models is the model B3. This model is based on the solidification theory [141], [142] and microprestress relaxation [143], [144]. It was proposed by Bažant, and is presented as simpler, more accurate and with higher theoretical support than other existing models [168]. This model complies with general guidelines formulated by RILEM for creep and shrinkage prediction models [149], [150].

One of the most important aspects of the solidification theory, and consequently of the B3 model, is the assumption that the chemical constituents of the cement paste are not aging, and aging effect observed in the experimental data is a consequence of the volume growth and interlinking of layers with nonaging viscoelastic properties [128], [141]. Aging creep takes place exclusively in the cement paste, while the aggregates deform elastically [169].

On the other hand, the microprestress concept is related to the development of tensile stress in the cement paste microstructure (micropores in hardened cement gel) as result of the volume changes during the hydration process. The microprestress is originated since the early stages of microstructure formation and gradually reduces due to relaxation [169]. This relaxation results in long-term aging creep deformation (viscous flow) of concrete.

According to the solidification theory, the creep deformation is considered as a sum of an aging and nonaging viscoelastic strains and aging viscous strain (flow) [141], [142], consequently the uniaxial total strain can be obtained from [141]:

$$\varepsilon = \frac{\sigma}{E_0} + \varepsilon_{cr} + \varepsilon_0 \quad \text{Eq. (6.54)}$$

$$\varepsilon_{cr} = \varepsilon_{cr,v} + \varepsilon_{cr,f} \quad \text{Eq. (6.55)}$$

in which, σ is the applied stress; E_0 is the asymptotic modulus; σ/E_0 is the elastic strain; ε^{cr} is the creep strain; $\varepsilon_{cr,v}$ is the viscoelastic aging and nonaging creep strain component; $\varepsilon_{cr,f}$ is the viscous flow creep strain component; and ε_0 is the sum of hygrothermal strain, drying shrinkage, autogeneous shrinkage (chemical strain), thermal dilation and eventually cracking strain. For high stress levels, the relation between stress and both creep strain subcomponents ($\varepsilon_{cr,v}, \varepsilon_{cr,f}$) becomes nonlinear.

The creep compliance function defined according to B3 model [170] is presented in Table 15, and its application is recommended for structures highly sensitive to creep effects. Alternatively, for structures of medium sensitivity, a short-form formulation is available in [171]. As can be seen in Table 15, the creep compliance function is dependent on some constitutive parameters q_1, \dots, q_5 , that should be calibrated from data of short-time creep tests or, in the absence of this information, by using prediction expressions statistically derived from existing databases. These prediction expressions use as input the information of the concrete mix and strength.

Table 15 – Creep compliance function based on B3 model [170].

Creep compliance:	
$J(t, t_0) = q_1 + C_0(t, t_0) + C_d(t, t_0, t_d)$	Eq. (6.56)
where:	
q_1 - instantaneous strain due to unit stress;	
$C_0(t, t_0)$ - compliance function for basic creep;	
$C_d(t, t_0, t_d)$ - compliance function for drying creep.	
Instantaneous component:	
$q_1 = 1/E_0$	Eq. (6.57)
Basic creep compliance function:	
$C_0(t, t_0) = q_2 \cdot Q(t, t_0) + q_3 \cdot \ln[1 + (t - t_0)^n] + q_4 \cdot \ln\left(\frac{t}{t_0}\right)$	Eq. (6.58)
Drying creep compliance function:	
$C_d(t, t_0, t_d) = q_5 \cdot \left(e^{-8 \cdot H(t)} - e^{-8 \cdot H(t_d)} \right)^{0.5} \text{ for } t > t_d'$	Eq. (6.59)
$t_d' = \max(t_0, t_d)$	Eq. (6.60)
$H(t) = 1 - (1 - h)S(t)$	Eq. (6.61)
$S(t) = \tanh\left(\frac{t - t_d}{\tau_{sh}}\right)^{0.5}$	Eq. (6.62)
$\tau_{sh} = k_t \cdot (k_s \cdot D)^2$	Eq. (6.63)
$D = 2 \cdot V/S$	Eq. (6.64)
$k_t = 8.5 \cdot (t_d)^{-0.08} \cdot (f_c)^{-1/4} \text{ [days/cm}^2\text{]}$	Eq. (6.65)
Parameters prediction based on concrete mix and strength:	
$q_1 = \frac{0.6 \times 10^6}{E_{c,28}}$	Eq. (6.66)
$q_2 = 185.4 \cdot c^{0.5} \cdot (f_{cm})^{-0.9}$	Eq. (6.67)

$$q_3 = 0.29 \cdot \left(\frac{w}{c}\right)^4 \cdot q_2 \quad \text{Eq. (6.68)}$$

$$q_4 = 20.3 \cdot \left(\frac{a}{c}\right)^{-0.7} \quad \text{Eq. (6.69)}$$

$$q_5 = 7.57 \times 10^5 \cdot (f_c)^{-1} \cdot |\varepsilon_{sh\infty}|^{-0.6} \quad \text{Eq. (6.70)}$$

Parameters definition:

E_0 - asymptotic modulus;

q_1 - parameter that characterizes the strain for extremely short load duration;

q_2 - parameter that characterizes the aging viscoelastic compliance;

q_3 - parameter that characterizes the nonaging viscoelastic compliance;

q_4 - parameter that characterizes the flow compliance;

q_5 - parameter that characterizes the drying creep;

$Q(t, t_0)$ - Binomial function that results from the integration of the basic creep compliance rate

$\frac{\partial C_0(t, t_0)}{\partial t}$, and can be estimated from [170, Ch. 1.71.1];

V/S - volume-to-surface ratio;

w/c - water-cement ratio, by weight;

a/c - aggregate-cement ratio, by weight;

$\varepsilon_{sh\infty}$ - ultimate shrinkage strain, calculated according to [41, Eq. 1.19] ;

h - relative humidity of the environment, expressed as a decimal number $0 \leq h \leq 1$;

$k_s = \left\{ \begin{array}{l} 1.00, \text{ for an infinite slab} \\ 1.15, \text{ for an infinite cylinder} \\ 1.25, \text{ for an infinite square prism} \\ 1.30, \text{ for a sphere} \\ 1.55, \text{ for a cube} \end{array} \right\}$ - is a cross-section shape factor

The B3 model also provides guidance for considering the parameters statistical uncertainties [170]. Additionally, the model also presents formulation to consider the effects of temperature [172], cyclic loading and environmental humidity variation [173], and nonlinear dependence of creep on stress [141].

When compared to other creep prediction models, the B3 model presents some improvements, namely [141], [142]:

- The fact that the material viscoelastic properties are age independent agrees with the thermodynamics laws, which can only be formulated for materials that have constant properties with time;
- When the model formulation is expanded to a Dirichlet series (which concept is presented in section 6.6), its coefficients (spring moduli and dashpot viscosities) are always nonnegative and nondecreasing positive functions with time, complying with the laws of thermodynamics;
- The model formulation grants the nondivergence of creep curves at constant stress for different loading ages;
- Due to the nondivergence property, the application of superposition principle to simulate the creep recovery after unloading yields in monotonic creep recovery curves;
- Consideration of the nonlinear relation between stress and creep deformation, by relating the creep rate as a function of the stress level. This method has a better agreement with existing experimental data to describe the nonlinear response of creep, related with the creep rate increase for high stress levels and also the for creep recovery after unloading.

6.5.1.5 B4 model

More recently, an update of the B3 model was proposed [174], [175]. The improvements of the creep model, named B4 model, were driven by the need to improve the long-term creep prediction capability, as an analysis of the midspan deflection of 69 large-span prestressed bridges revealed that the existing codes and models exhibit significant underestimation of long-term creep [175], [176]. Additionally, the B4 model also includes the effect of modern concrete compositions on creep (different types of cement, admixtures and aggregates) [175].

Compared to the B3 model and pertaining the creep behavior of concrete, the B4 model consists on the refinement of the prediction parameters (q_1, \dots, q_5) that associate creep dependence on strength and mix composition. In this context, two sets of parameters predictors are proposed, being based on (i) mix composition and (ii) strength. While the former is aimed to be used in detailed creep analysis, the latter is mainly focused to be applied in the design process, or when the mix composition information is absent or unknown [176].

The prediction parameters were calibrated resorting to an extensive statistical optimization of an extended database of laboratory and multi-decade structural observations of the 69 bridges [176]. The two sets of expressions proposed to obtain the prediction parameters of the B4 model are presented in Table 16. The instantaneous and basic creep compliance function components are equal to the ones proposed in the B3 model (Table 15), while the drying creep has some slightly differences (only changes are presented in Table 16). In [175] is also presented the methodology to include the effect of temperature on basic and drying creep.

Table 16 – Creep compliance function based on B4 model [175].

Instantaneous component:	
$q_1 = \frac{P_1}{E(t = 28days)}$	Eq. (6.71)v
Drying creep compliance function:	
$C_d(t, t_o, t_d) = q_5 \cdot \left(e^{-p_5 \cdot H(t, t_d)} - e^{-p_5 \cdot H(t_d, t_d)} \right)^{0.5} \text{ for } t_o' > t_d$	Eq. (6.72)
$H(t, t_d) = 1 - (1 - h) \cdot \tanh \sqrt{\frac{t - t_d}{\tau_{sh}}}$	Eq. (6.73)
$\tau_{sh} = \tau_0 \cdot k_{\tau a} \cdot \left(k_s \cdot \frac{D}{1mm} \right)^2$	Eq. (6.74)
Parameters prediction based on mix proportions:	
$q_2 = \frac{P_2}{1GPa} \cdot \left(\frac{w/c}{0.38} \right)^{P_{2w}}$	Eq. (6.75)
$q_3 = p_3 \cdot q_2 \cdot \left(\frac{a/c}{6} \right)^{P_{3a}} \cdot \left(\frac{w/c}{0.38} \right)^{P_{3w}}$	Eq. (6.76)
$q_4 = \frac{P_4}{1GPa} \cdot \left(\frac{a/c}{6} \right)^{P_{4a}} \cdot \left(\frac{w/c}{0.38} \right)^{P_{4w}}$	Eq. (6.77)
$q_5 = \frac{P_5}{1GPa} \cdot \left(\frac{a/c}{6} \right)^{P_{5a}} \cdot \left(\frac{w/c}{0.38} \right)^{P_{5w}} \cdot k_h \cdot \varepsilon_{sh\infty}(t_d) ^{P_{5c}}$	Eq. (6.78)
$\tau_0 = \tau_{cem} \cdot \left(\frac{a/c}{6} \right)^{P_{\tau a}} \cdot \left(\frac{w/c}{0.38} \right)^{P_{\tau w}} \cdot \left(\frac{6.5 \cdot c}{\rho} \right)^{P_{\tau c}}$	Eq. (6.79)
Parameters prediction based on strength mix:	
$q_2 = \frac{s_2}{1GPa} \cdot \left(\frac{f_c^{28}}{40MPa} \right)^{s_{2f}}$	Eq. (6.80)
$q_3 = s_3 \cdot q_2 \cdot \left(\frac{f_c^{28}}{40} \right)^{s_{3f}}$	Eq. (6.81)

$$q_4 = \frac{s_4}{1GPa} \cdot \left(\frac{\overline{f_c^{28}}}{40MPa} \right)^{s_{4f}} \quad \text{Eq. (6.82)}$$

$$q_5 = \frac{s_5}{1GPa} \cdot \left(\frac{\overline{f_c^{28}}}{40MPa} \right)^{s_{5f}} \cdot \left| k_h \cdot \varepsilon_{sh\infty}(t_d) \right|^{p_{5\varepsilon}} \quad \text{Eq. (6.83)}$$

$$\tau_0 = \tau_{s,ce} \cdot \text{days} \left(\frac{\overline{f_c^{28}}}{40MPa} \right)^{s_{\tau f}} \quad \text{Eq. (6.84)}$$

Parameters definition:

q_1 - parameter that characterizes the strain for extremely short load duration;

q_2 - parameter that characterizes the aging viscoelastic compliance;

q_3 - parameter that characterizes the nonaging viscoelastic compliance;

q_4 - parameter that characterizes the flow compliance;

q_5 - parameter that characterizes the drying creep;

$p_1, \dots, p_{5\dots}$ - cement type dependent factor, that can be taken from (see Appendix F);

$s_2, \dots, s_{5\dots}$ - cement type dependent factor, that can be taken from (see Appendix F);

$\tau_{ce}, p_{\tau\dots}, \tau_{s,ce}, s_{\tau f}$ - cement type dependent factor, that can be taken from (see Appendix F);

$k_{\tau a}$ - aggregate type dependent correction factor, that can be taken from (see Appendix F);

$$k_h = \left\{ \begin{array}{ll} 1-h^3 & h \leq 0.98 \\ 12.94(1-h) - 0.2 & 0.98 \leq h \leq 1 \end{array} \right\} - \text{humidity dependence correction factor;}$$

w/c - water-cement ratio, by weight;

a/c - aggregate-cement ratio, by weight;

c - cement content (kg/m^3);

h - relative humidity of the environment, expressed as a decimal number $0 \leq h \leq 1$;

ρ - mass density of concrete, in kg/m^3 ;

$\varepsilon_{sh\infty}(t_d)$ - ultimate shrinkage strain, calculated according to Eq. (F.1) from (see Appendix F).

According to [166], the B4 model outputs the most accurate creep predictions when applied to the Northwestern University creep database, compared to the B3 model and MC2010, amongst other models. Other studies [138], [177], [178], also pointed to the increased performance of the models based on the solidification-microprestress theory.

6.5.2 Proposed model

As previously stated, the DPL model is capable of producing adequate prediction of the basic creep component of CBM. In this work is presented a basic creep model based on the Dirichlet series expansion of the DPL model [152], capable of predicting the aging creep behavior of CBM since early age.

The proposed model, henceforward referred as ACC (aging creep compliance) model, formulates the creep compliance in view of the elements of the Kelvin chain according to the following expressions:

$$J(t, t_0) = \frac{1}{E_s(t_0)} + \sum_{\mu=1}^N \frac{1}{E_{\mu}(t_0)} \cdot \left(1 - e^{-\frac{t-t_0}{\tau_{\mu}}} \right) \quad \text{Eq. (6.85)}$$

$$\frac{1}{E_{\mu}(t_0)} = b_{\mu} \cdot \left(\frac{\tau_1}{0.002} \right)^{n_{\mu}} \cdot \frac{\varphi_{1,\mu}}{E_s(t_0)} \cdot 10^{n_{\mu}(\mu-1)} \cdot t_0^{-m_{\mu}}, \text{ for } \mu < N \quad \text{Eq. (6.86)}$$

$$\frac{1}{E_{\mu}(t_0)} = 1.2 \cdot b_{\mu} \cdot \left(\frac{\tau_1}{0.002} \right)^{n_{\mu}} \cdot \frac{\varphi_{1,\mu}}{E_s(t_0)} \cdot 10^{n_{\mu}(\mu-1)} \cdot t_0^{-m_{\mu}}, \text{ for } \mu = N \quad \text{Eq. (6.87)}$$

where b_{μ} , n_{μ} , $\varphi_{1,\mu}$ and m_{μ} are the defining coefficients of the model, which are calibrated from the experimental creep test data; N is the number of Kelvin chains; τ_{μ} is the retardation time of the μ^{th} Kelvin chain; $E_s(t_0)$ is the modulus of the isolated spring of the Kelvin generalized model, and $E_{\mu}(t_0)$ are the modulus of each Kelvin chain.

While in the original model [152], the defining coefficients are fixed for all Kelvin chains, the present model uses a different values for these coefficients in each Kelvin chain. The expression to compute the modulus of the isolated spring of the Kelvin generalized model $E_s(t_0)$ is different than the proposed in the original model. Its value is determined with the following expression:

$$E_s(t_0) = \lambda \cdot E(t_0) \quad \text{Eq. (6.88)}$$

where $E(t_0)$ corresponds to the Young Modulus of the material evaluated at the loading age t_0 and λ is the scaling factor ($\lambda \geq 1.0$).

To determine the defining coefficients of the ACC model $\underline{\psi} = [b_{\mu} \quad n_{\mu} \quad \varphi_{1,\mu} \quad m_{\mu}]$, $\mu = 1, \dots, N$, a nonlinear least square method (NLSM) is applied to the experimental creep compliance curves. This

fitting procedure considers the following input data: number of Kelvin chains N , the retardation times τ_μ , the Young's modulus $E(t_0)$, and the scaling factor, λ .

The number of Kelvin chains should be adequately selected, so that their corresponding retardation times cover the entire scale of simulation [128]. It is further noted that, according to [128], is advisable that the retardation times are uniformly spread over the logarithmic time scale.

The objective function of the NLSM takes the following form:

$$\Phi = \sum_{i=1}^L \sum_{j=1}^{M_L} \left(J(t_{j,i}, t_{0,i})_{num} - J(t_{j,i}, t_{0,i})_{exp} \right)^2 \quad \text{Eq. (6.89)}$$

where L is the total number of experimental creep compliance functions to be fitted; M_L is the number of discrete points considered for fitting each creep function (from experimental data); $J(t_{j,i}, t_{0,i})_{exp}$ are the experimental values of the creep compliance corresponding to the loading age $t_{0,i}$ for each time step $t_{j,i}$; $J(t_{j,i}, t_{0,i})_{num}$ are the creep compliance estimated values determined according to Eq. (6.85)-Eq. (6.87). The meaning of variables L and M_L is exemplified in Figure 111 as illustrative case. The number of discrete points, M_L , should be the enough to accurately capture the trend of each creep function. The coefficients of the model can be obtained through the minimization of the following the expression:

$$\frac{\partial \Phi}{\partial \underline{\psi}} = 0 \quad \text{Eq. (6.90)}$$

$$\underline{\psi} = [b_\mu \quad n_\mu \quad \varphi_{1,\mu} \quad m_\mu], \quad \mu = 1, \dots, N$$

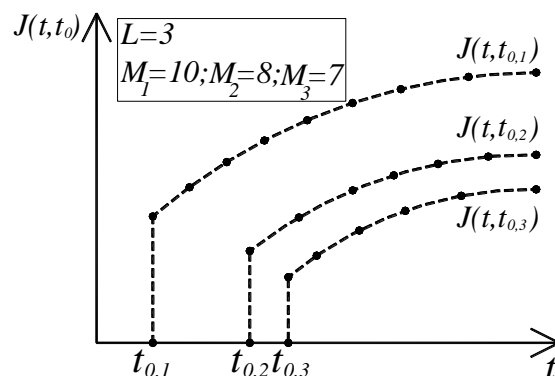


Figure 111 – Example of three creep functions ($L = 3$) to be fitted, where each function is defined by different number of points: $M_1=10$; $M_2=8$; $M_3=7$.

The ACC model performance was appraised in the research carried out in [179], [180], regarding its application for predicting, since early age, the creep behavior of concrete samples ($t_0 > 9h$) and epoxy adhesive ($t_0 \geq 1day$). As can be seen in Figure 112 and Figure 113, the model yielded satisfactory results. In [179] it was also verified that the ACC model inherited the handicap of its source model (DPL) related to the violation of the nondivergence condition.

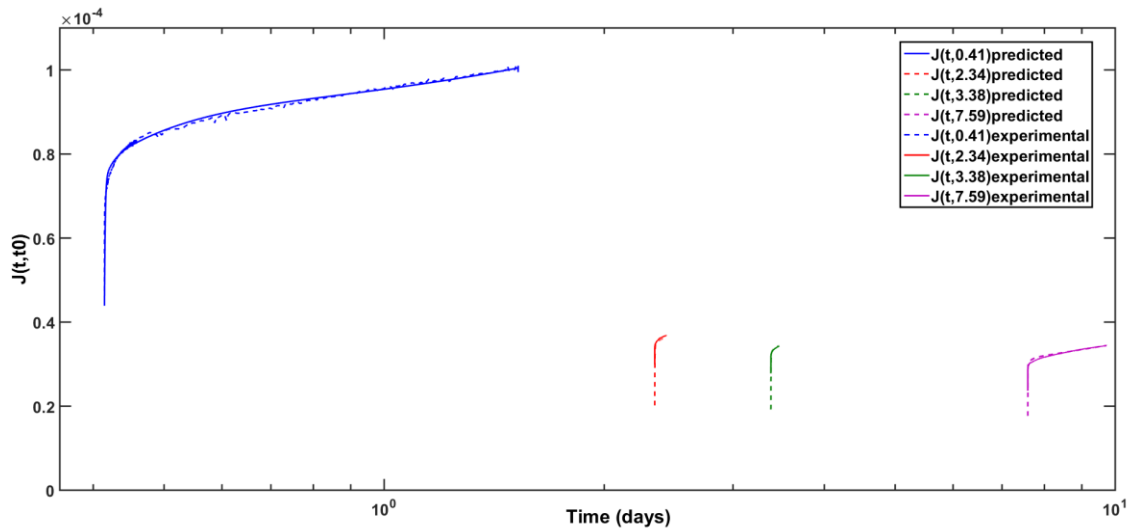


Figure 112 – Estimation of the creep function using the ACC model based on the experimental results of concrete samples (extracted from [179]).

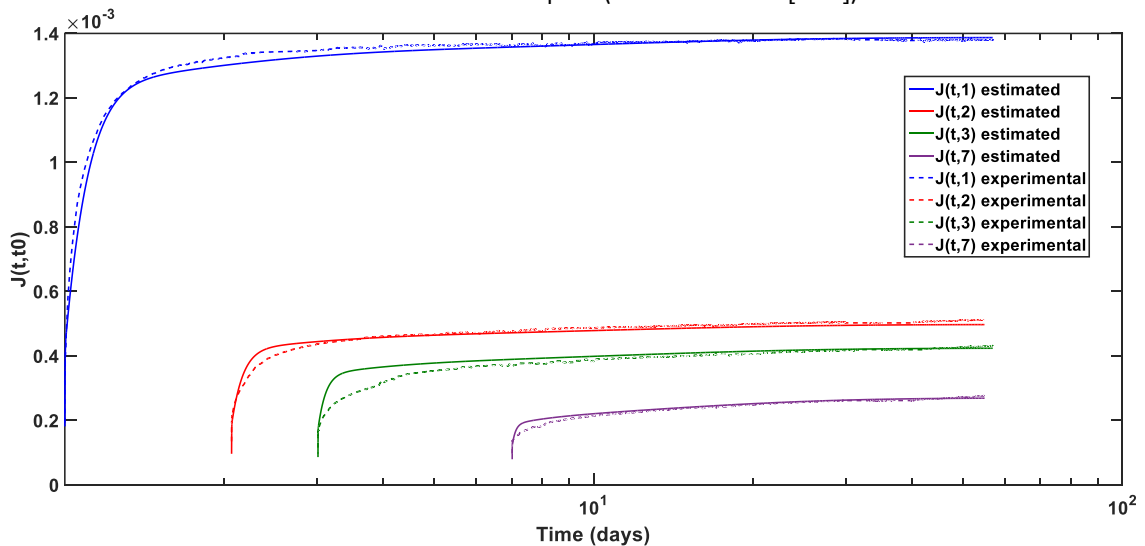


Figure 113 – Estimation of the creep function using the ACC model based on the experimental results of epoxy samples (extracted from [179]).

Additionally, the performance of the ACC model has also been appraised in another two sets of experimental creep data extracted from the Northwestern University data bank. In Figure 114 and Figure 115 it is possible to verify that the ACC model captures adequately the evolution of the creep compliance with the load duration and loading age of these two sets of creep tests.

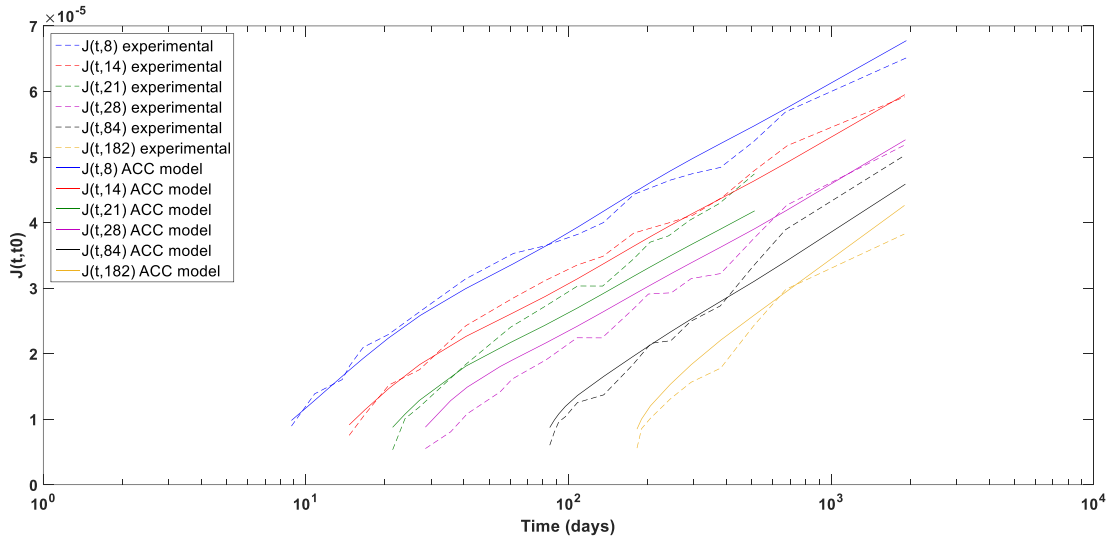


Figure 114 – Estimation of the creep function using the ACC model based on the experimental results [181] of concrete samples.

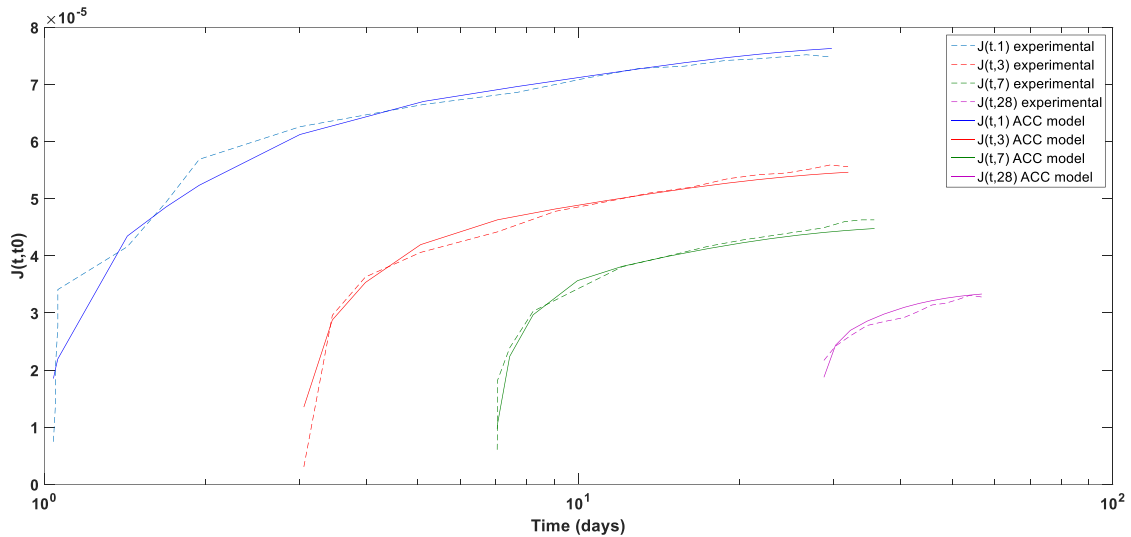


Figure 115 – Estimation of the creep function using the ACC model based on the experimental results [182] of concrete samples.

Furthermore, a comparison between the evolution of basic creep with time duration and loading age of the ACC and B4 models is performed. The creep compliance curves of the B4 model was determined considering the following sets of parameters: i) parameters prediction based on concrete strength; ii) cement type R; iii) $E(t = 28days) = 24.87GPa$; iv) $m = 0.5$; v) $n = 0.1$; vi) $\%c = 0.6$; vii) $\%c = 7$; viii) $\overline{f_c^{28}} = 28MPa$. The defining coefficients of the ACC model were determined by a NLSM to fit the B4 model creep curves, considering the following parameters: i) $E(t = 3days) = 27.7GPa$; ii) $E(t = 7days) = 30.8GPa$; iii) $E(t = 28days) = 34.0GPa$; iv) $E(t = 200days) = 36.2GPa$; v) $E(t = 2000days) = 37.1GPa$; vi) $\lambda = 1.75$; vii) $N = 10$; viii) $\tau_1 = 1 \times 10^{-3}$; ix) $\tau_\mu = \tau_1 \cdot 10^{\mu-1}$. As can be seen in Figure 116, the ACC model reveals a good agreement with the B4 model particularly for short and medium-term time duration. However, for long-

term creep estimation, the ACC model exhibits a deviation from the B4 creep curves. This shortcoming of the model is related with the different mathematical formulation of the models. For long-term duration the B4 model approaches a logarithmic function, while the ACC model, that is based on the original DPL model, uses power curves for all time durations.

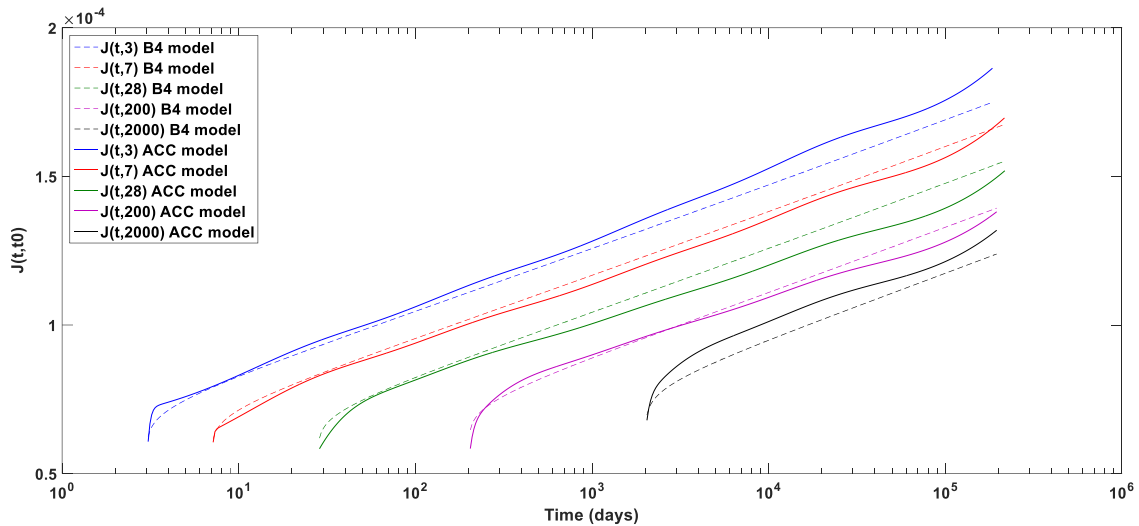


Figure 116 – Comparison between ACC and B4 models creep curves.

6.6 Numerical implementation for structural analysis

Different computational approaches exist for the analysis of the time-dependent deformation of structures, namely [123], [136]: (i) one-step approximate solution using the effective modulus method; (ii) one-step approximate solution using the age-adjusted effective modulus method; (iii) step-by-step solution according to the integral-type creep law based on the principle of superposition; (iv) step-by-step solution according to a rate-type creep law based on the Kelvin or Maxwell chain rheological models. Preferentially, for more advanced and complex analysis, the choice for a method usually resorts to the (iii) integral-type or (iv) rate-type creep law.

The analysis of structural effects of time-dependent behavior of a CBM structure submitted to varying stress histories is based on the resolution of the integral stress-strain relationship based on the superposition principle (Eq. (6.5)). However, the adoption of this type of formulation results in the need to store the complete history of stress and strains during the numerical simulations, resulting in highly time and resource consuming computational tasks, particularly in the analysis of large structures with finite element method (FEM) [122], [131]. On the other hand, the computation process can be more efficient, if the integral-type relationship is converted into a rate-type relation, with the

additional advantage that the latter approach is more adequate for the consideration of the drying effects (varying pore humidity and temperature) on creep and aging [130], [136].

To achieve this purpose, Eq. (6.5) can be converted to a system of differential equations (rate-type creep law) when the kernel $J(t, t_0)$ assumes the degenerated form, which consists of a sum of products of functions of t and t_0 , called Dirichlet series (or Prony series). The degenerated kernel has the form [130], [183]:

$$J(t, t_0) = \frac{1}{E_s(t_0)} + \sum_{\mu=1}^N \frac{1}{E_{\mu}(t_0)} \left(1 - e^{-\frac{(t-t_0)}{\tau_{\mu}}} \right) \quad \text{Eq. (6.91)}$$

where $E_s(t_0)$ and $E_{\mu}(t_0)$ are coefficients dependent of the loading age t_0 , both with units of elastic moduli; τ_{μ} are constants called retardation times; μ is the number of series; and N is the total number of series. An approximation of a creep function based on Dirichlet series is illustrated in Figure 117.

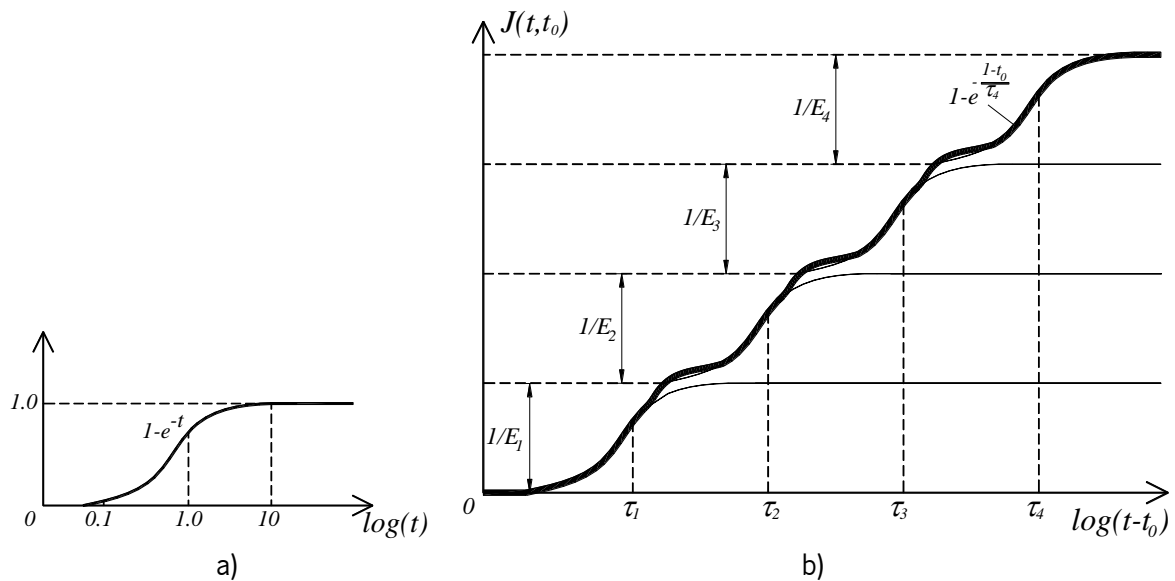


Figure 117 – Dirichlet series approximation of the creep function. a) curve of a single exponential in log-time; b) decomposition of the creep function (adapted from [128, Fig. 2.7]).

In fact, the conversion of an integral-type creep law to a rate-type creep law based on expressing the creep compliance as a Dirichlet series, results into a differential equation that can be interpreted as a Kelvin Generalized rheological model, formed by springs and dashpots (Figure 118) [183], [184]. In Eq. (6.91) and Figure 118, $E_s(t_0)$ is the modulus that influences the instantaneous response of the

creep function, while $E_\mu(t_0)$ are the moduli of each series (Kelvin chains). More information about the particular behavior of the Kelvin chain model components can be found in [126], [127], [185].

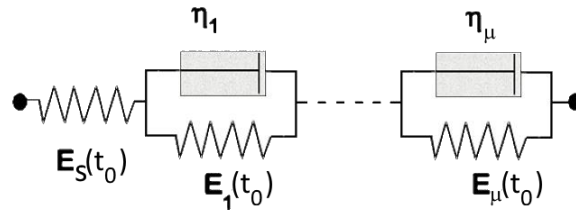


Figure 118 – Kelvin generalized model.

Upon insertion of the Dirichlet series expansion (Eq. (6.91)) and considering that $d\sigma(t_0) = \frac{d\sigma(t_0)}{dt_0} dt_0 = \dot{\sigma}(t_0) dt_0$, Eq. (6.5) results in [183]:

$$\varepsilon(t) = \int_0^t \left[\frac{1}{E_s(t_0)} + \sum_{\mu=1}^N \frac{1}{E_\mu(t_0)} \cdot \left(1 - e^{-\frac{(t-t_0)}{\tau_\mu}} \right) \right] \cdot \dot{\sigma}(t_0) dt_0 + \varepsilon_0(t) \quad \text{Eq. (6.92)}$$

Rearranging Eq. (6.92), leads to:

$$\varepsilon(t) = \int_0^t \left[\frac{1}{E_s(t_0)} + \sum_{\mu=1}^N \frac{1}{E_\mu(t_0)} \right] \cdot \dot{\sigma}(t_0) dt_0 - \sum_{\mu=1}^N \varepsilon_\mu^*(t) + \varepsilon_0(t) \quad \text{Eq. (6.93)}$$

with:

$$\varepsilon_\mu^*(t) = e^{-\frac{t}{\tau_\mu}} \cdot \int_0^t e^{\frac{t_0}{\tau_\mu}} \cdot \frac{1}{E_\mu(t_0)} \cdot \dot{\sigma}(t_0) dt_0 \quad \text{Eq. (6.94)}$$

where $\varepsilon_\mu^*(t)$ may be considered as a hidden state variable that represents the past history.

The time t can be subdivided into F discrete times t_0, t_1, \dots, t_F , with time steps given by $\Delta t_n = t_n - t_{n-1}$. By considering that $\dot{\sigma}(t_0)$ and $E_\mu(t_0)$ remain constant within each time step Δt_n , but allowing it to change discontinuously in each discrete time t_n , Eq. (6.94) can take the form [183]:

$$\varepsilon_\mu^*(t_n) = e^{-\frac{t_n}{\tau_\mu}} \cdot \sum_{st=1}^n \frac{\dot{\sigma}(t_{st})}{E_\mu(t_{st}^*)} \cdot \int_{t_{st-1}}^{t_{st}} e^{-\frac{t_0}{\tau_\mu}} dt_0 \quad \text{Eq. (6.95)}$$

with $t_{st} \leq t_{st}^* \leq t_{st+1}$, using a generalized midpoint rule. Eq. (6.95) can be exactly integrated, yielding [183]:

$$\varepsilon_{\mu}^*(t_n) = e^{-\frac{t_n}{\tau_{\mu}}} \cdot \sum_{st=1}^n \left(e^{-\frac{t_{st}}{\tau_{\mu}}} \cdot \left(1 - e^{-\frac{\Delta t_{st}}{\tau_{\mu}}} \right) \frac{\tau_{\mu} \cdot \Delta \sigma(t_{st})}{\Delta t_{st} \cdot E_{\mu}(t_{st}^*)} \right) \quad \text{Eq. (6.96)}$$

Based on Eq. (6.96), a recurrent formula can be defined to express the hidden state variable value at time t_n , based on its value in the preceding time step t_{n-1} , which surpasses the need to store the hidden variable value at each time step, namely [183]:

$$\varepsilon_{\mu}^*(t_n) = \left(1 - e^{-\frac{\Delta t_n}{\tau_{\mu}}} \right) \cdot \frac{\tau_{\mu} \cdot \Delta \sigma(t_n)}{\Delta t_n \cdot E_{\mu}(t_n^*)} + \varepsilon_{\mu}^*(t_{n-1}) \cdot e^{-\frac{\Delta t_n}{\tau_{\mu}}}; \quad \mu = 1, \dots, N \quad \text{Eq. (6.97)}$$

Eq. (6.97) evidences that in order to determine the value of the hidden variable of each Kelvin chain $\varepsilon_{\mu}^*(t_n)$ for the time t_n , there is only the need to know (or store) its value from the preceding time step $\varepsilon_{\mu}^*(t_{n-1})$. This procedure is optimal for implementation in FEM software for the analysis of creep problems of large structures.

The initial value of the state variable is determined from the expression:

$$\varepsilon_{\mu}^*(t_1) = \frac{\Delta \sigma(t_1)}{E_{\mu}(t_1)} \quad \text{Eq. (6.98)}$$

Based on Eq. (6.93), it is possible to derive the total incremental strain $\Delta \varepsilon(t_n)$ in each time step Δt_n [183]:

$$\Delta \varepsilon(t_n) = \left[\frac{1}{E_s(t_n^*)} + \sum_{\mu=1}^N \frac{1}{E_{\mu}(t_n^*)} \right] \cdot \Delta \sigma(t_n) - \sum_{\mu=1}^N \Delta \varepsilon_{\mu}^*(t_n) + \Delta \varepsilon_0(t_n) \quad \text{Eq. (6.99)}$$

with $t_{n-1} \leq t_n^* \leq t_n$, using a generalized midpoint rule.

The incremental value of the state variable $\Delta \varepsilon_{\mu}^*(t_n)$ can be expressed by:

$$\Delta \varepsilon_{\mu}^*(t_n) = \varepsilon_{\mu}^*(t_n) - \varepsilon_{\mu}^*(t_{n-1}) = \left(1 - e^{-\frac{\Delta t_n}{\tau_{\mu}}} \right) \cdot \frac{\tau_{\mu} \cdot \Delta \sigma(t_n)}{\Delta t_n \cdot E_{\mu}(t_n^*)} + \varepsilon_{\mu}^*(t_{n-1}) \cdot \left(e^{-\frac{\Delta t_n}{\tau_{\mu}}} - 1 \right) \quad \text{Eq. (6.100)}$$

By introducing Eq. (6.100) into Eq. (6.99) leads to:

$$\Delta \varepsilon(t_n) = \left[\frac{1}{E_s(t_n^*)} + \sum_{\mu=1}^N \frac{1}{E_\mu(t_n^*)} \right] \cdot \Delta \sigma(t_n) - \sum_{\mu=1}^N \left(1 - e^{-\frac{\Delta t_n}{\tau_\mu}} \right) \cdot \frac{\tau_\mu \cdot \Delta \sigma(t_n)}{\Delta t_n \cdot E_\mu(t_n^*)} + \varepsilon_\mu^*(t_{n-1}) \cdot \left(e^{-\frac{\Delta t_n}{\tau_\mu}} - 1 \right) + \Delta \varepsilon_0(t_n)$$

$$\Leftrightarrow \text{Eq. (6.101)}$$

$$\Delta \varepsilon(t_n) = \left[\frac{1}{E_s(t_n^*)} + \sum_{\mu=1}^N \frac{1}{E_\mu(t_n^*)} \left(1 - \left(1 - e^{-\frac{\Delta t_n}{\tau_\mu}} \right) \cdot \frac{\tau_\mu}{\Delta t_n} \right) \right] \cdot \Delta \sigma(t_n) - \sum_{\mu=1}^N \varepsilon_\mu^*(t_{n-1}) \cdot \left(e^{-\frac{\Delta t_n}{\tau_\mu}} - 1 \right) + \Delta \varepsilon_0(t_n)$$

By arranging Eq. (6.101), a fictitious linear elastic stress-strain law can be obtained [183]:

$$\Delta \varepsilon(t_n) = \frac{\Delta \sigma(t_n)}{\bar{E}(t_n)} + \Delta \bar{\varepsilon}(t_n) + \Delta \varepsilon_0(t_n) \quad \text{Eq. (6.102)}$$

in which $\bar{E}(t_n)$ represents a pseudo-instantaneous elastic modulus (Eq. (6.103)), and $\Delta \bar{\varepsilon}(t_n)$ represents a pseudo-inelastic strain increment (Eq. (6.104)) [183].

$$\frac{1}{\bar{E}(t_n)} = \frac{1}{E_s(t_n^*)} + \sum_{\mu=1}^N \frac{1}{E_\mu(t_n^*)} \cdot \left[1 - \left(1 - e^{-\frac{\Delta t_n}{\tau_\mu}} \right) \cdot \frac{\tau_\mu}{\Delta t_n} \right] \quad \text{Eq. (6.103)}$$

$$\Delta \bar{\varepsilon}(t_n) = \sum_{\mu=1}^N \varepsilon_\mu^*(t_{n-1}) \cdot \left(1 - e^{-\frac{\Delta t_n}{\tau_\mu}} \right) \quad \text{Eq. (6.104)}$$

For the numerical implementation of the material stress-strain constitutive relation into FEM software (based on displacement method) it is customary to explicitly derive the stress increment as a function of the strain increment. Considering this, Eq. (6.102) can take the form:

$$\Delta \sigma(t_n) = \bar{E}(t_n) \cdot \left[\Delta \varepsilon(t_n) - \Delta \bar{\varepsilon}(t_n) - \Delta \varepsilon_0(t_n) \right] \quad \text{Eq. (6.105)}$$

Considering that $\bar{\sigma}(t_n) = -\bar{E}(t_n) \Delta \bar{\varepsilon}(t_n)$, Eq. (6.105) can be rewritten as:

$$\Delta \sigma(t_n) = \bar{E}(t_n) \cdot \left[\Delta \varepsilon(t_n) - \Delta \varepsilon_0(t_n) \right] + \bar{\sigma}(t_n) \quad \text{Eq. (6.106)}$$

The multiaxial generalization of the problem can be obtained by introducing the matrix \underline{C} that relates the stress and strains components of the material. Conversely, in the previous equations Eq. (6.93)-

Eq. (6.106) the strain and stress variables represent vectors, and the stress vector must be coupled to the dimensionless compliance matrix \underline{C} . Introducing the matrix \underline{C} in Eq. (6.102) leads to:

$$\Delta \underline{\varepsilon}(t_n) = \frac{\underline{C} \Delta \underline{\sigma}(t_n)}{\underline{E}(t_n)} + \Delta \underline{\varepsilon}^-(t_n) \quad \text{Eq. (6.107)}$$

Assuming that the matrix $\underline{D} = \underline{C}^{-1}$, the multiaxial generalization of Eq. (6.106) and Eq. (6.97) take the form:

$$\Delta \underline{\sigma}(t_n) = \underline{E}^-(t_n) \underline{D} [\Delta \underline{\varepsilon}(t_n) - \Delta \underline{\varepsilon}_0(t_n)] + \underline{\sigma}^-(t_n) \quad \text{Eq. (6.108)}$$

$$\underline{\varepsilon}_\mu^*(t_n) = \left(1 - e^{-\frac{\Delta t_n}{\tau_\mu}} \right) \frac{\tau_\mu \underline{C} \Delta \underline{\sigma}(t_n)}{\Delta t_n E_\mu(t_n^*)} + \underline{\varepsilon}_\mu^*(t_{n-1}) e^{-\frac{\Delta t_n}{\tau_\mu}} \quad \text{Eq. (6.109)}$$

with $\underline{\sigma}^-(t_n) = -\underline{E}^-(t_n) \Delta \underline{\varepsilon}^-(t_n)$.

For the tridimensional case, the compliance matrix \underline{C} is given by [186]:

$$\underline{C} = \begin{bmatrix} 1 & -\nu & -\nu & 0 & 0 & 0 \\ -\nu & 1 & -\nu & 0 & 0 & 0 \\ -\nu & -\nu & 1 & 0 & 0 & 0 \\ 0 & 0 & 0 & 2(1+\nu) & 0 & 0 \\ 0 & 0 & 0 & 0 & 2(1+\nu) & 0 \\ 0 & 0 & 0 & 0 & 0 & 2(1+\nu) \end{bmatrix} \quad \text{Eq. (6.110)}$$

In order to perform accurate numerical simulations of creep sensitive structures, it is necessary to adopt a creep compliance prediction model that can simulate the aging effect of CBM. As presented in Eq. (6.103), in every time step Δt_n it is necessary to supply the moduli of each Kelvin chain $E_\mu(t_n^*)$ for $\mu = 1, \dots, N$ and $E_s(t_n^*)$. This can be performed via the creep compliance prediction models, as the ones presented in section 6.5, that can return $J(t_j, t_n^*)$, with $t_j \geq t_n^*$. In the absence of analytical expressions, the evaluation of the Kelvin chains modulus can be performed with a nonnegative least-square method [187], [188], where the moduli $E_\mu(t_n^*)$ of each chain are determined, given that the appropriate retardation times τ_μ are provided, similarly to the procedure described in section 6.5.2.

6.7 Coupling of creep and thermo-mechanical models

In this section is presented the formulation for the coupling of the creep model with a thermo-mechanical model for simulation of CBM elements and structures.

The mechanical model corresponds to the 3D multidirectional fixed smeared crack model capable of simulating the crack initiation and propagation in structures that are discretized with solid finite element. The formulation of the model is presented in [189], [190] and is based on the decomposition of strain components for the cracked concrete, namely in the cracks $\underline{\varepsilon}_{crco}$ and concrete between cracks $\underline{\varepsilon}_{co}$ [191]–[193].

$$\underline{\varepsilon}(t) = \underline{\varepsilon}_{co}(t) + \underline{\varepsilon}_{crco}(t) \quad \text{Eq. (6.111)}$$

The uncracked concrete strain component, $\underline{\varepsilon}_{co}$, can be further decomposed, which incorporates the elastic, creep, shrinkage and thermal deformation contribution, namely:

$$\underline{\varepsilon}_{co}(t) = \overbrace{\underline{\varepsilon}_{ins}(t_0) + \underline{\varepsilon}_{cr}(t)}^{\underline{\varepsilon}_m(t)} + \overbrace{\underline{\varepsilon}_{sh}(t) + \underline{\varepsilon}_T(t)}^{\underline{\varepsilon}_0(t)} \quad \text{Eq. (6.112)}$$

where $\underline{\varepsilon}_{ins}$, $\underline{\varepsilon}_{cr}$, $\underline{\varepsilon}_{sh}$ and $\underline{\varepsilon}_T$ are the elastic, creep, shrinkage and thermal strain vectors. The sum of the elastic and creep components is designated as mechanical strain $\underline{\varepsilon}_m(t)$ and the sum of shrinkage and thermal components is designated as stress-independent strain $\underline{\varepsilon}_0(t)$ [128], [190].

The formulation presented in previous section has been devoted to determine the stress-strain relationship of uncracked part of a cracked CBM. Introducing the incremental form of Eq. (6.111) in Eq. (6.108), results in the constitutive law of the cracked cement based materials coupled with the remaining time-dependent deformations (creep, shrinkage and temperature variations), namely:

$$\Delta \underline{\sigma}(t_n) = \bar{E}(t_n) \underline{D} [\Delta \underline{\varepsilon}(t_n) - \Delta \underline{\varepsilon}_0(t_n) - \underline{\varepsilon}_{crk}(t_n)] + \bar{\sigma}(t_n) \quad \text{Eq. (6.113)}$$

Regarding the multidirectional fixed smeared crack concept, for a three-dimensional case, at the crack plane (local axis) it is considered that the incremental strain vector has three components regarding the displacements smeared out in the cracks (Figure 119), namely [189], [190]:

$$\Delta \underline{\varepsilon}_{crk}^l = [\Delta \varepsilon_n \quad \Delta \gamma_{t1} \quad \Delta \gamma_{t2}]^T \quad \text{Eq. (6.114)}$$

where $\Delta\varepsilon_n$ is the incremental strain related with the opening displacement w ; $\Delta\gamma_{t_1}$ and $\Delta\gamma_{t_2}$ are the incremental strains related with the sliding displacements s_1 and s_2 , in the t_1 and t_2 directions, respectively.

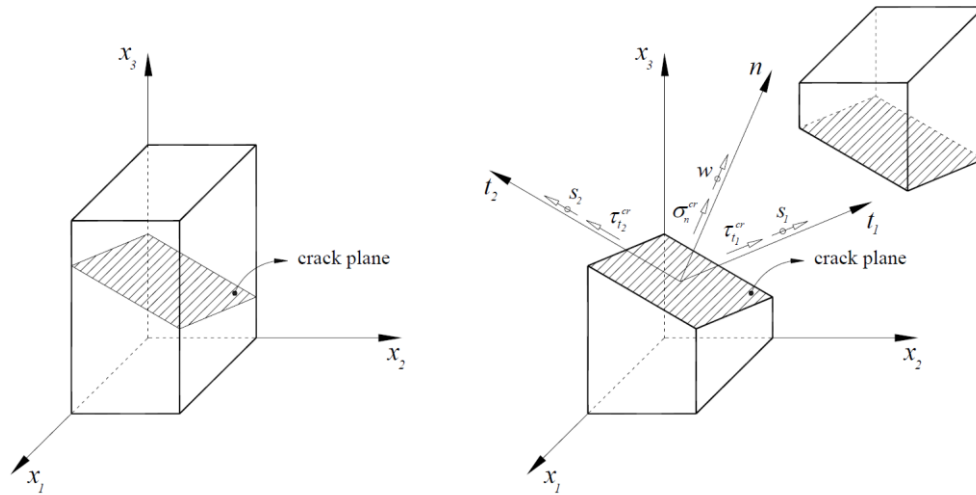


Figure 119 – Displacement, stress components and local coordinate system of a crack.

In the global coordinate system the incremental strain vector $\Delta\underline{\varepsilon}_{crk}$ is defined by [190]:

$$\Delta\underline{\varepsilon}_{crk} = [\Delta\varepsilon_{crk}^1 \quad \Delta\varepsilon_{crk}^2 \quad \Delta\varepsilon_{crk}^3 \quad \Delta\gamma_{crk}^{23} \quad \Delta\gamma_{crk}^{31} \quad \Delta\gamma_{crk}^{12}]^T \quad \text{Eq. (6.115)}$$

The local and global incremental strain vectors are related by:

$$\Delta\underline{\varepsilon}_{crk} = [\underline{T}_{crk}]^T \Delta\underline{\varepsilon}_{crk}^l \quad \text{Eq. (6.116)}$$

where \underline{T}_{crk} is the matrix that transforms the strain and stress components from the global coordinate system to the local crack coordinate system, and its components can be obtained according to the formulation presented in [190], [194].

Regarding the incremental stress vector at the crack plane $\Delta\underline{\sigma}_{crk}^l$, it is defined by [190]:

$$\Delta\underline{\sigma}_{crk}^l = [\Delta\sigma_{crk}^n \quad \Delta\tau_{crk}^{t_1} \quad \Delta\tau_{crk}^{t_2}]^T \quad \text{Eq. (6.117)}$$

where $\Delta\sigma_{crk}^n$ is the mode I incremental crack normal stress, related with the crack opening mode; $\Delta\tau_{crk}^{t_1}$ and $\Delta\tau_{crk}^{t_2}$ are the sliding mode incremental crack shear stress in t_1 and t_2 directions, respectively.

The incremental stress vector in the global coordinate system $\Delta\underline{\sigma}$ is defined by [190]:

$$\Delta \underline{\sigma} = \begin{bmatrix} \Delta \sigma^1 & \Delta \sigma^2 & \Delta \sigma^3 & \Delta \tau^{23} & \Delta \tau^{31} & \Delta \tau^{12} \end{bmatrix}^T \quad \text{Eq. (6.118)}$$

The local and global incremental stress vectors are related by [190]:

$$\Delta \underline{\sigma}_{crk}^l = \underline{T}_{crk} \Delta \underline{\sigma} \quad \text{Eq. (6.119)}$$

At the crack, the relationship between the incremental stress and strain vectors is given by [190]:

$$\Delta \underline{\sigma}_{crk}^l = \underline{D}_{crk} \Delta \underline{\varepsilon}_{crk}^l \quad \text{Eq. (6.120)}$$

where \underline{D}_{crk} is the crack constitutive matrix that incorporates the fracture mode I stiffness modulus, \underline{D}_{crk}^n and the sliding stiffness modulus according to t_1 and t_2 directions, \underline{D}_{crk}^{t1} and \underline{D}_{crk}^{t2} .

Incorporating Eq. (6.113) in Eq. (6.119) yields in [190]:

$$\Delta \underline{\sigma}_{crk}^l = \underline{T}_{crk} \left[\bar{\underline{E}}(t_n) \underline{D} [\Delta \underline{\varepsilon}(t_n) - \Delta \underline{\varepsilon}_0(t_n) - \underline{\varepsilon}_{crk}(t_n)] + \bar{\underline{\sigma}}(t_n) \right] \quad \text{Eq. (6.121)}$$

Further incorporation of Eq. (6.116) and Eq. (6.120) in Eq. (6.121) results in [190]:

$$\Delta \underline{\varepsilon}_{crk}^l(t_n) = \frac{\underline{T}_{crk} \left[\bar{\underline{E}}(t_n) \underline{D} [\Delta \underline{\varepsilon}(t_n) - \Delta \underline{\varepsilon}_0(t_n)] + \bar{\underline{\sigma}}(t_n) \right]}{\underline{D}_{crk} + \underline{T}_{crk} \bar{\underline{E}}(t_n) \underline{D} [\underline{T}_{crk}]^T} \quad \text{Eq. (6.122)}$$

The incorporation of Eq. (6.122) in Eq. (6.116) returns the crack incremental strain in the global coordinate system [190]:

$$\Delta \underline{\varepsilon}_{crk} = [\underline{T}_{crk}]^T \frac{\underline{T}_{crk} \left[\bar{\underline{E}}(t_n) \underline{D} [\Delta \underline{\varepsilon}(t_n) - \Delta \underline{\varepsilon}_0(t_n)] + \bar{\underline{\sigma}}(t_n) \right]}{\underline{D}_{crk} + \underline{T}_{crk} \bar{\underline{E}}(t_n) \underline{D} [\underline{T}_{crk}]^T} \quad \text{Eq. (6.123)}$$

The inclusion of Eq. (6.123) in Eq. (6.113) completes the relationship between the incremental stress and strain of cracked CBM considering the time-dependent deformation, namely [190]:

$$\Delta \underline{\sigma}(t_n) = \left(\underline{I} - \frac{\bar{\underline{E}}(t_n) \underline{D} [\underline{T}_{crk}]^T}{\underline{D}_{crk} + \underline{T}_{crk} \bar{\underline{E}}(t_n) \underline{D} [\underline{T}_{crk}]^T} \underline{T}_{crk} \right) \cdot \left[\bar{\underline{E}}(t_n) \underline{D} [\Delta \underline{\varepsilon}(t_n) - \Delta \underline{\varepsilon}_0(t_n)] + \bar{\underline{\sigma}}(t_n) \right] \quad \text{Eq. (6.124)}$$

where \underline{I} is the identity matrix. In order to resolve Eq. (6.124) a nonlinear transient analysis must be performed, since the strain components are time dependent. The computational strategy adopted in FEMIX for the resolution of this type of problems is presented in [190], [195].

For the evaluation of the incremental stress-independent strain, $\Delta \underline{\varepsilon}_0(t_n)$, it is necessary to consider the incremental thermal and shrinkage strains.

The incremental shrinkage strain $\Delta \underline{\varepsilon}_{sh}(t_n)$ is computed from the existing concrete shrinkage models. The Eurocode 2 [37] and B3 [168] shrinkage models are available in FEMIX.

The incremental thermal strain $\Delta \underline{\varepsilon}_T(t_n)$ is computed from the temperature field the structure is submitted at a certain instant t , by adopting a thermal model (e.g. [190]). The thermal model allows the simulation of heat transfer in structures by conduction, convection and radiation. The implementation of the heat transfer model to the finite element method formulation is presented in [190], [195]. In addition, the model allows the consideration of the heat development during the hydration process of cement based materials using the Arrhenius law [195], [196].

For the evolution of the concrete Young's modulus, compressive strength and tensile strength can be adopted the recommendations proposed in Eurocode 2 [37], while for the fracture energy the estimation proposed in [195] can be taken, while no more reliable approach is available from experimental evidence.

6.8 Implementation of ACC model in FEMIX

Due to the potentialities demonstrated by the ACC model to simulate the aging creep behavior of CBM, this model was implemented in FEMIX for the simulation of the creep behavior of CBM structures.

The main routines of the model are:

- Read discrete creep compliance curves determined for distinct loading ages;
- Determine the model's defining coefficients based on optimization technique;
- Estimate the creep compliance $J(t, t_0)_{num}$ and the moduli of each Kelvin chain $E_\mu(t_0)$ for all the loading ages t_0 considered.

Following the nomenclature adopted for the material models used in FEMIX, all data and code routines related to the ACC model incorporates the acronym NLMM174.

In order to use the model in FEMIX is necessary the following input data:

- Name of the NLMM174 material model;
- Number, L , and name of files containing the discrete values of the creep compliance to be fitted by the model. Each file contains the following data:
 - o Loading age $t_{0,i}$;
 - o Modulus of elasticity at the loading age $E_0(t_0)$;
 - o Number of discrete points for fitting each creep function at the loading age M_L ;
 - o Set of points of the creep compliance $J(t, t_0)_{\text{exp}}$ corresponding to the loading age t_0 for each time step $t_{j,i}$;
- Number of Kelvin chains N ;
- Retardation times of each Kelvin chain $\tau_\mu, \mu = 1, \dots, N$;
- Scaling factor λ .

When analyzing a structure it is possible to consider different creep behavior for the CBM material adopted in different structural elements by defining different NLMM174 material models to the finite elements that discretize the structural elements.

The fitting procedures implemented in FEMIX resorts to the nonlinear least squares fitting routine MPFIT [109] for the determination of defining coefficients of each NLMM174 material model. In the fitting routine, the model derivatives $\partial J(t, t_0) / \partial \psi$ are numerically approximated using the finite differences technique that is available in MPFIT. In order to guarantee the output of always positive Kelvin chain moduli $E_\mu(t_0)$ during the fitting procedure, the allowed solutions for the parameters b_μ and $\varphi_{1,\mu}$ are constrained to $b_\mu, \varphi_{1,\mu} = [1 \times 10^{-16}; +\infty[$.

After determination of the defining coefficients, it is possible to simulate the creep of CBM materials with the remaining thermo-mechanical model according to the formulation presented in the previous section. For the resolution of Eq. (6.124) during the nonlinear transient analysis of the structure, at each time step the value of $\bar{E}(t_n)$ is determined by using Eq. (6.103), considering that $t_n^* = (t_n + t_{n-1})/2$. The value of $E_s(t_n^*)$ is determined from Eq. (6.88), with the possibility of considering the evolution of the Young's modulus at each t_n^* by adopting the maturity model of Eurocode 2 [37] that is implemented in FEMIX under the acronym NLMM173. The value of $E_\mu(t_n^*)$

is determined from Eq. (6.86) and Eq. (6.87) for each Kelvin chain $\mu = 1, \dots, N$ using the defining coefficients of each NLMM174 model derived during the fitting procedure.

6.8.1 Numerical examples

6.8.1.1 Concrete sample under compressive creep test

The performance of the creep prediction model is appraised by performing the numerical simulation of creep compression tests of a concrete specimen and by comparing the numerical results of the deformation of the specimen with the experimental results. The experimental campaign was developed under the FCT project EXPL/ECM-EST/1323/2013 whose detailed description is presented in [197]. Concisely, the experimental program consisted in the casting of concrete cylinders with 150mm of diameter and 300mm of height. The specimens were tested in a creep testing rig, and the applied load was monitored with 100kN load cells. The specimens were internally monitored with vibrating-wire strain gauges to measure the longitudinal strains and temperature at the concrete core. The experimental program also included the assessment of the evolution of the concrete Young's modulus since early age, by resorting to the EMM-ARM test setup [197].

In Figure 120 is presented the creep compliance curves, $J(t, t_0)$, determined by fitting the parameters of the NLMM174 creep model to the experimental creep compliance functions, according to the fitting procedure implemented in FEMIX. The estimated creep functions were obtained considering 5 Kelvin chains with the retardation times $\tau = \{0.001; 0.01; 0.1; 1; 10\} \text{ days}$, the Young's modulus $E_0(t_0 = 0.41 \text{ days}) = 15184 \text{ MPa}$, $E_0(t_0 = 2.34 \text{ days}) = 33044 \text{ MPa}$, $E_0(t_0 = 3.38 \text{ days}) = 34692 \text{ MPa}$ and $E_0(t_0 = 7.59 \text{ days}) = 37695 \text{ MPa}$, and a factor $\lambda = 1.5$.

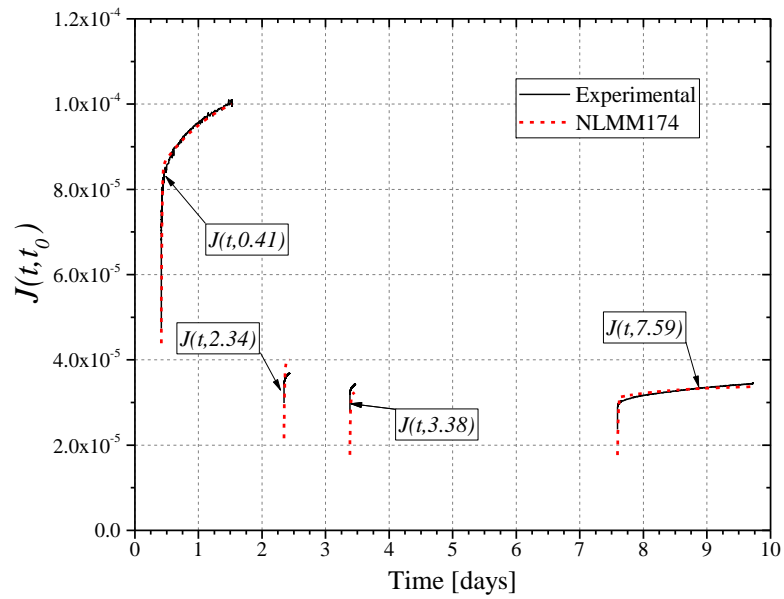


Figure 120 – Comparison between estimated and experimental creep compliance curves of concrete studied in [197].

The numerical simulation of the creep test is performed by assuming a representative 20-node solid element, with 1x1x1 Gauss Legendre integration scheme, submitted to the stress history recorded during the creep tests. In Figure 121 is presented the load history of one specimen of the experimental program, which was considered in the numerical simulation.

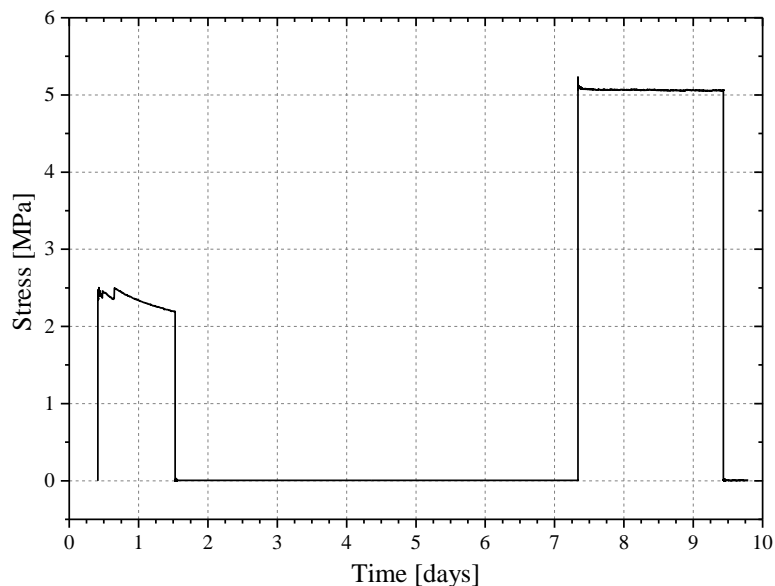


Figure 121 – Load history of concrete specimen [197].

In Figure 122 is presented the longitudinal strain determined numerically and deformation registered experimentally resorting to the vibrating-wire strain gauges after removing the shrinkage and thermal deformation of the specimen. As can be seen, there is a good agreement between the numerical and

experimental results, which highlight the potentiality of the NLMM174 model to simulate the aging basic creep behavior of CBM structures since early ages.

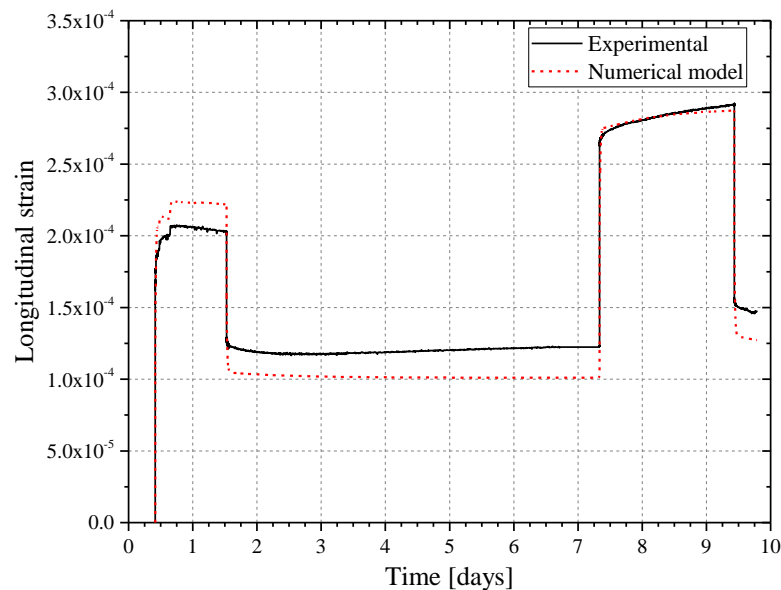


Figure 122 – Experimental and numerical model comparison of the longitudinal strain of the concrete specimen submitted to the creep test.

6.8.1.2 Reinforced concrete beam under flexure creep test

In the following numerical application, the performance of the creep prediction model is assessed by conducting a numerical simulation of a flexurally reinforced concrete beam submitted to bending up to a period of about two years. The total deformation obtained in the numerical simulation is compared with the experimental results of the beam with the reference CB-59 of experimental campaign conducted in [198].

The geometry, reinforcements, and test setup are presented in Figure 123. The beam is longitudinally reinforced with two $\varnothing 10$ steel bars as tensile reinforcement and two $\varnothing 6$ steel bars as compressive reinforcement. Transverse reinforcements are also adopted in the form of steel stirrups placed in the entire length of the beam with a spacing of 75mm. The material properties of the steel reinforcements were assessed in [198] and are presented in Table 17.

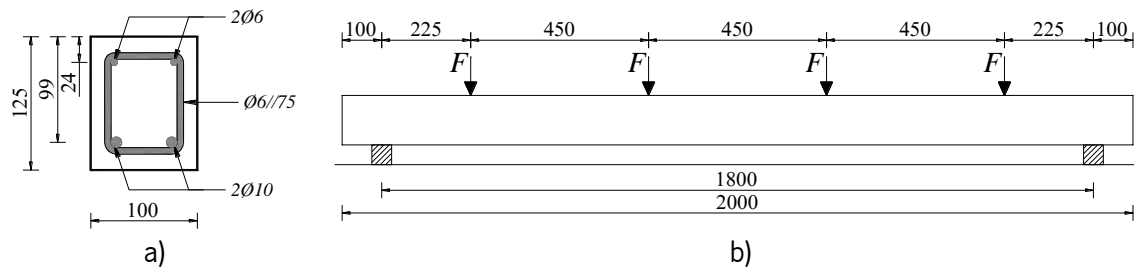


Figure 123 – Beam geometry, reinforcement, support and loading configuration (dimensions in mm) [198].

Table 17 – Properties of the steel reinforcements [198].

Type of reinforcement	Yield strength [MPa]	Modulus of elasticity [GPa]
Tensile longitudinal reinforcement	520	194
Compressive longitudinal reinforcement	525	183
Transverse reinforcement	212	200

According to [198] the concrete used to cast the beam had a cement content of 394kg/m^3 (ordinary Portland cement), a water-cement ratio of 0.53 and an aggregate-cement ratio of 4.56. The concrete cube's compressive strength at 28 days of age was found to be about 40MPa, and the measured Young's modulus at 28 days of age was equal to 27.2GPa, with the flexural tensile strength of 4.67MPa [198].

After casting, the beam was stored in the laboratory, staying covered with wet gunny sacks for 7 days after casting. The beam was loaded 28 days after casting, according to the test setup presented in Figure 123b. The loads were applied using concrete blocks and steel plates at four points along the beam span (1800mm). The total applied load is equal to 15.8kN ($F = 3.95\text{kN}$), which corresponds to a load level equal to 59% of the computed ultimate flexural capacity of the beam [198].

The midspan deflection of the beam was taken as the average of two dial gauges placed in a fixed reference frame, with the readings being regularly recorded up to a period of about two years [198].

In order to perform the numerical simulation of the creep flexural test, a finite element model of the concrete beam was formed with 20-node solid elements and the steel reinforcements were discretized by 3-node linear elements. For the solid elements a $2 \times 2 \times 2$ Gauss Legendre integration scheme was adopted, while for the steel linear elements were adopted 2 integration points with the Gauss Legendre integration technique. Due to the symmetry of the beam, only half-length of the beam is simulated. A

total of 1008 solid elements and 224 linear elements are used to simulate the reinforced concrete beam. The lateral view of the finite element mesh is presented in Figure 124.

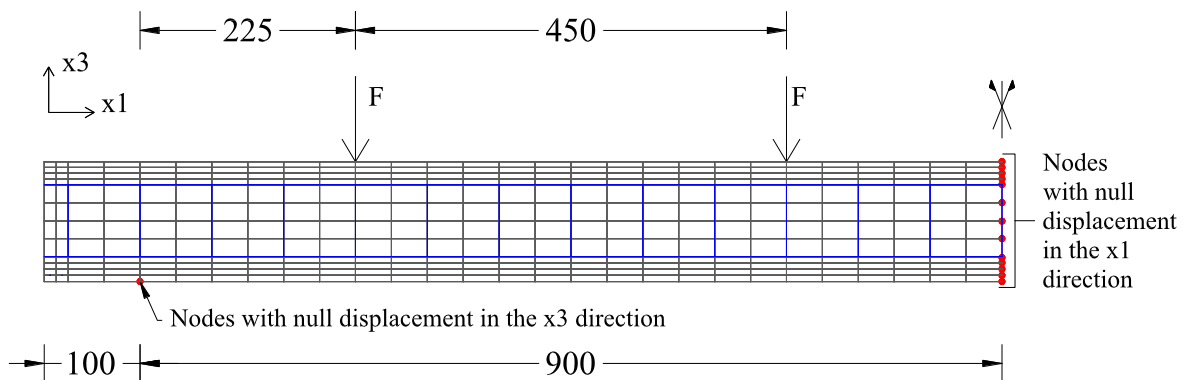


Figure 124 – Finite element mesh: line elements in blue line; solid elements in black line; supports in red circles (dimensions in mm).

For the simulation of the concrete aging creep behavior is adopted the NLMM174 model, as previously presented. Due to the inexistence of creep compliance curves for the concrete mixture studied in [198], the B4 model is employed to predict the creep behavior of the concrete, based on its mix proportions (vide section 6.5.1.5). The creep compliance curves are then considered to determine the ACC model coefficients that are used in the NLMM174 model. In Figure 125 is presented the creep compliance curves $J(t, t_0)$ for four loading ages ($t_0 = \{21, 28, 56, 120\} \text{ days}$), determined by the B4 model and by the NLMM174 creep model. The estimated NLMM174 creep functions were obtained considering 7 Kelvin chains with the retardation times $\tau = \{0.001; 0.01; 0.1; 1; 10; 100; 1000\} \text{ days}$, the Young's modulus $E_0(t_0 = 21 \text{ days}) = 26949 \text{ MPa}$, $E_0(t_0 = 28 \text{ days}) = 27200 \text{ MPa}$, $E_0(t_0 = 56 \text{ days}) = 27682 \text{ MPa}$ and $E_0(t_0 = 120 \text{ days}) = 28057 \text{ MPa}$, and a factor $\lambda = 1.0$.

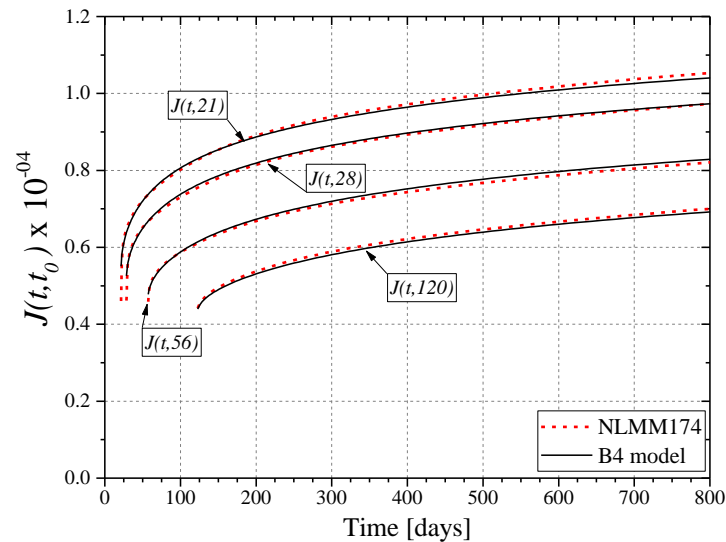
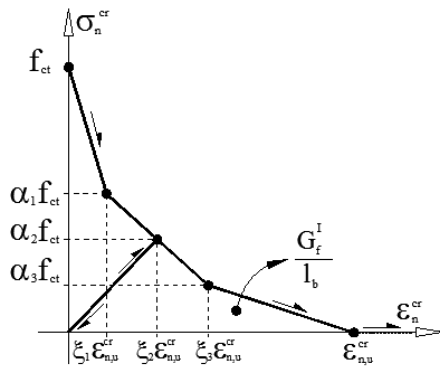


Figure 125 – Comparison between the creep compliance curves obtained by the B4 model and by the NLMM174 model for the concrete studied in [198].

In addition, the creep model is combined with the 3D multidirectional fixed smeared crack model [189] to simulate the nonlinear behavior of concrete in tension. The smeared crack model considers the post-cracking residual strength of the concrete by adopting the trilinear diagram presented in Figure 126. The concrete tensile strength was calculated with the expression that relates the flexural tensile strength and the tensile strength proposed in MC2010 (Eq. (6.125) with $h_b = 100mm$), and the concrete post-cracking diagram and value of fracture energy were also determined according to the models proposed by MC2010 for plain concrete [30]. For the employment of the smeared crack model was adopted a crack bandwidth equal to the cubic root of the integration points volume. For the shear stress-strain relationship was adopted the concept of shear retention [190], considering a cubic degradation of the fracture mode II modulus with the increase of crack normal strain.

For the compressive behavior of concrete, considering the relatively small load level that the beam is submitted, is considered in linear-elastic stage. For the same reason, it was also admitted a linear-elastic response to simulate the steel reinforcements elements, assuming $E_s = 200GPa$ and $\nu = 0.30$.

The concrete shrinkage deformation is not considered, as this phenomenon is particularly relevant for the analysis of early age problems, and for the loading age adopted in the creep test ($t_0 = 28days$), it is expected to have a minor impact in the obtained results.



f_{ct}	2.81 MPa	
G_F	0.142 N/mm	
ξ_1	0.20	
α_1	0.20	
$\sigma - w$	ξ_2	0.40
	α_2	0.15

Figure 126 – Trilinear tensile-softening diagram.

$$f_{ctm} = \alpha_{fl} \cdot f_{ctm,fl}$$

$$\alpha_{fl} = \frac{0.06 \cdot h_b^{0.7}}{1 + 0.06 \cdot h_b^{0.7}} \quad \text{Eq. (6.125)}$$

In order to assess the instantaneous deformation of the beam, to evaluate the stress level on the steel reinforcement elements and determine the initial cracking status of the concrete beam, a static analysis was conducted considering the self-weight of the beam and the loads applied during the creep test. The latter are simulated as line loads applied along the width of the beam's cross section, with a value of $F = 39.5 \text{ N/mm}$.

In Figure 127 is displayed the vertical displacement of the beam obtained from the static analysis of the numerical model. The instantaneous midspan deflection reported in [198] was about 6.70mm, which was about $\Delta_{ins} = 1.11 \text{ mm}$ higher than the maximum vertical displacement obtained in the numerical simulation ($\delta = 5.59 \text{ mm}$). The discrepancy between the experimental and numerical results can be justified by the apparatus used to register the beam deformation during the experimental campaign, which does not register the deformation of the beam's reaction structure, as well as the settlement of the beam's supports.

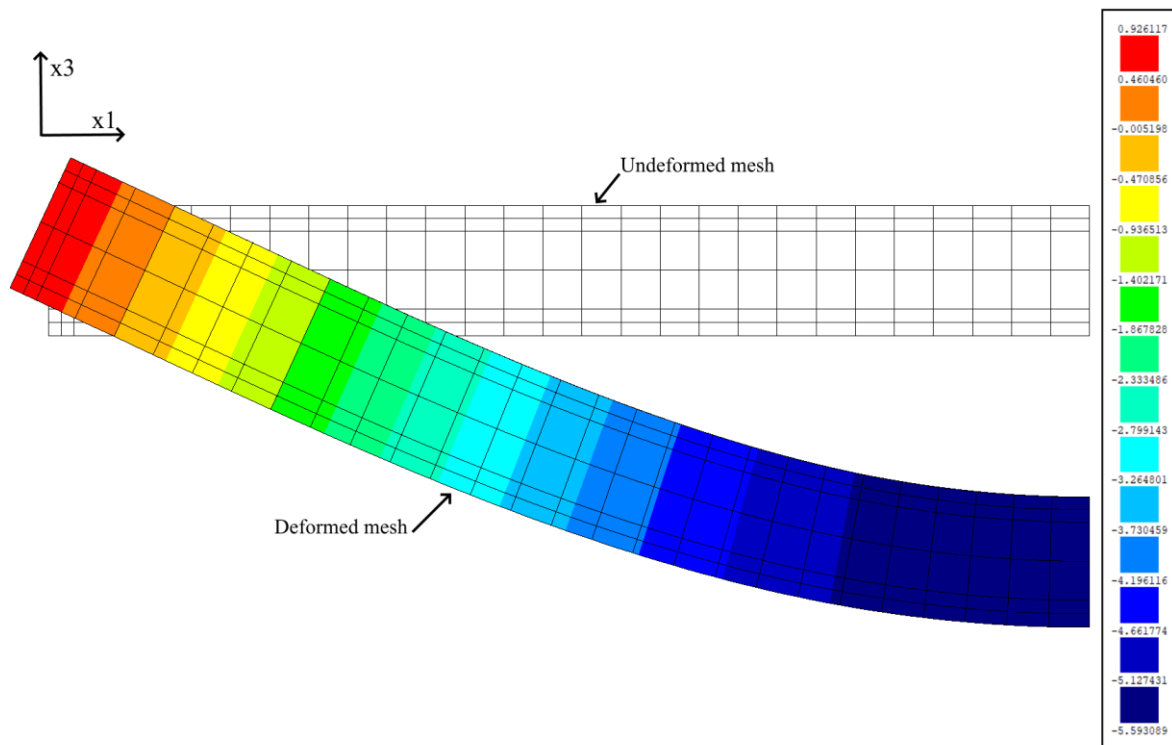


Figure 127 – Displacement along x_3 obtained in the static analysis (displacements in mm, deformed mesh with 50x magnification factor).

From the static analysis was also possible to verify the maximum stress level in the steel reinforcements. As presented in Table 18, the stress level is considerably lower than the steel yield strength, which validates the adoption of a linear-elastic material model to simulate the steel reinforcement elements. Furthermore, due to low ratio between the stress and yield strength obtained for the instantaneous response, it is expected that the stress in the steel reinforcements remain in the elastic stage during the duration of the creep test.

Table 18 – Maximum stress level of the steel reinforcements obtained in the static analysis.

Type of reinforcement	Stress [MPa]	Yield strength [MPa]	Stress/Yield strength ratio [%]
Tensile longitudinal reinforcement	194.7	520	37.4
Compressive longitudinal reinforcement	-68.6	-525	13.0
Transverse reinforcement	8.5	212	4.0

From the static analysis, it is also possible to verify that a significant number of concrete elements are cracked for the considered load level. In Figure 128 is display the crack pattern obtained from the numerical model, where the maximum computed crack width is about 0.034mm for a solid element in the midspan zone of the finite element mesh.

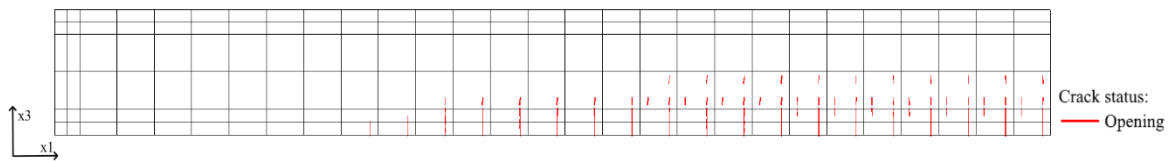


Figure 128 – Crack pattern obtained in the static analysis (only displayed cracks with computed crack width higher than 0.005mm).

Subsequently, a transient analysis was performed considering that the loads of creep tests are applied at the age of 28 days, and the deformation of the beam, considering the concrete creep and cracking, is obtained for the subsequent time steps up to the age of 750 days. In Figure 129 the instantaneous deformation of the beam ($t_0 = 28days$) and at $t = 750days$ are compared.

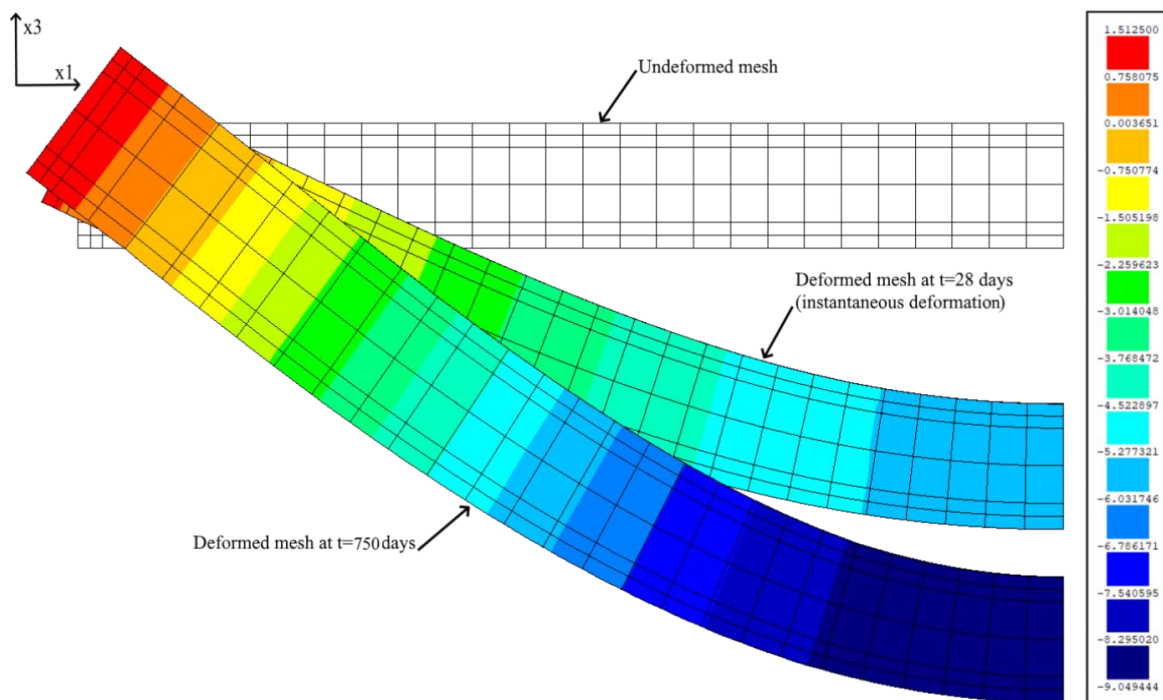


Figure 129 – Displacement along x_3 obtained in the transient analysis (displacements in mm, deformed meshes with 50x magnification factor).

In Figure 130 are plotted the evolution of the midspan deflection of the beam with time. In addition to the experimental results of [198] and the obtained results from the numerical simulation, it is also plotted a curve that increases the numerically obtained midspan deflection by adding the difference between the experimental and numerical instantaneous midspan deflection ($\Delta_{ins} = 1.1mm$). As can be seen, by adding Δ_{ins} , is achieved a good agreement between the numerical response and the experimental results.

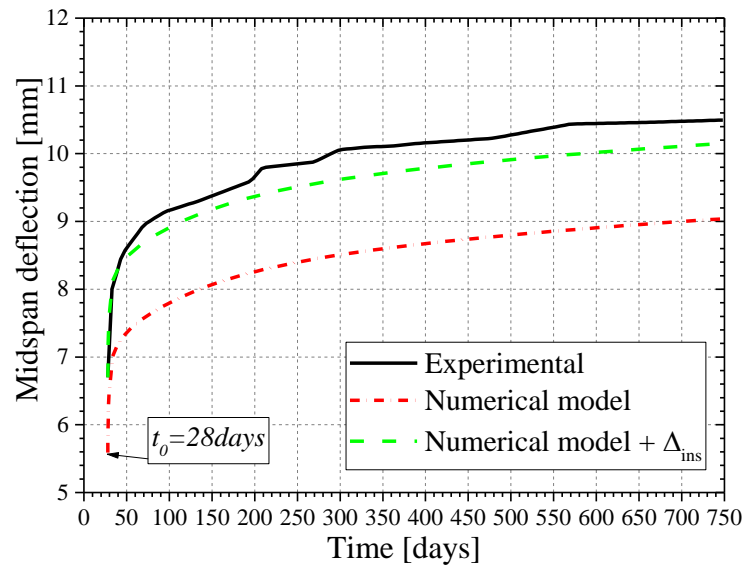


Figure 130 – Evolution of midspan deflection of the reinforced concrete beam.

In Table 19 is summarized the maximum stress level in the steel reinforcements obtained in the transient analysis at the time $t = 750days$. As expected, the steel yield stress is not achieved, and when compared to the stress level at $t_0 = 28days$ (Table 18), a significant increase is attained.

Table 19 – Maximum stress level of the steel reinforcements obtained in the transient analysis for $t = 750days$.

Type of reinforcement	Stress [MPa]	Yield strength [MPa]	Stress/Yield strength ratio [%]
Tensile longitudinal reinforcement	246.2	520	47.3
Compressive longitudinal reinforcement	-165.0	-525	31.4
Transverse reinforcement	16.3	212	7.7

In Figure 131 is display the crack pattern obtained from the transient analysis for $t = 750days$. Compared to the cracking pattern obtained at the loading age $t_0 = 28days$, presented in Figure 128, it is verified the localization of crack opening characterized by the progressive opening of some cracks, while the neighboring cracks started to close. The maximum computed crack width at $t = 750days$ is about 0.063mm which represent an increase of about 1.85x regarding the maximum crack width computed at $t_0 = 28days$ due to the consideration of concrete creep deformation between cracks.

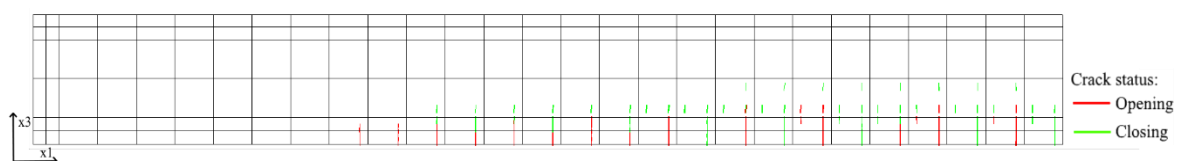


Figure 131 – Crack pattern obtained in the transient analysis for $t = 750days$ (only displayed cracks with computed crack width higher than 0.005mm).

6.9 Concluding remarks

The present chapter is mainly dedicated to the description of a new creep model, designated by Aging Creep Compliance model (ACC), and to the assessment of its predictive performance when applied at material and structural level. In addition, a review of creep fundamentals and of the mechanisms that influence viscoelastic behavior of cement based materials (CBM) are briefly overviewed. The most widespread creep compliance models are presented, including its capabilities and drawbacks.

The ACC is based on the Dirichlet series expansion of the DPL model, and is capable of predicting the aging creep behavior of CBM and structures, since early age. The ACC model uses different values for these coefficients in each Kelvin chain, which are obtained by a nonlinear least square method applied to the experimental creep compliance curves. The ACC model was integrated into the FEMIX computer program, with the code designation of NLMM174 (Non-Linear Material Model 174), and can be coupled to the other time dependent constitutive models governing the behavior CBM since their early age up to hardened stage, like maturation, shrinkage, thermal variation and cracking.

The good predictive performance of the ACC at material level was demonstrated by simulating experimental tests of laboratory scale. For demonstrating its suitability when coupled with a cracking model, a reinforced concrete beam experimentally tested under creep loading conditions was simulated.

7 IMPLEMENTATION OF A CYCLIC-HYSTERETIC CONSTITUTIVE MODEL FOR SIMULATING THE CONTACT BETWEEN DIFFERENT MATERIALS

To simulate the contact between different materials, a new constitutive model was developed and implemented in the Finite Element Method (FEM) software – *FEMIX*. In the scope of this research, the main goal is to apply this constitutive model to simulate the behavior of the interface between concrete slabs supported on ground and the respective granular layers of the pavements.

The constitutive model is applicable to the isoparametric zero-thickness interface finite elements available in *FEMIX* library, namely the 4 or 6-noded interface linear element and the 8 or 16-noded interface surface element, that are illustrated in Figure 132.

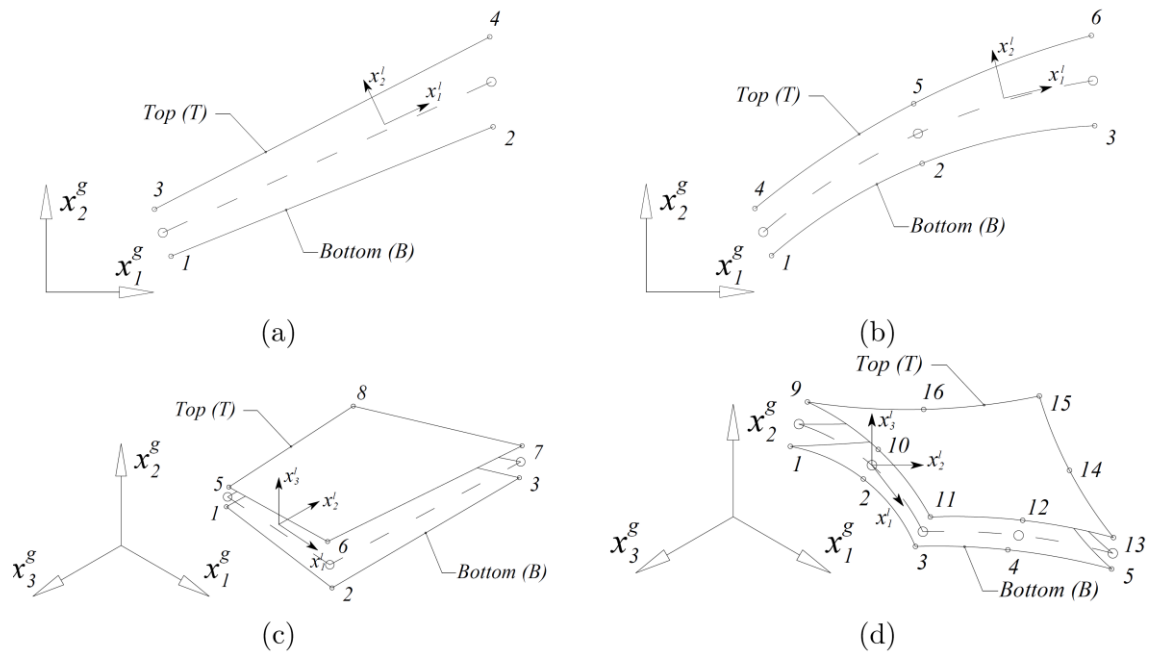


Figure 132 – Isoparametric zero-thickness finite elements available in *FEMIX*: a) linear 4-node; b) quadratic 6-node; c) Lagrangian 8-node; d) Serendipity 16-node (extracted from [199]).

7.1 Numerical implementation

At the integration point level of a linear interface finite element is considered the following relationship:

$$\underline{\sigma} = \begin{bmatrix} \tau_1 \\ \sigma_n \end{bmatrix} = \underline{D} \Delta u' \quad \text{Eq. (7.1)}$$

where $\underline{\sigma}$ is the stress vector, with the tangential (τ_1) and normal (σ_n) components in the local coordinate system. In this equation: $\Delta\underline{u}'$ is the vector of the relative displacements of the interface elements that comprises a sliding s and opening w components; and \underline{D} is the constitutive matrix:

$$\underline{D} = \begin{bmatrix} D_t & 0 \\ 0 & D_n \end{bmatrix} \quad \text{Eq. (7.2)}$$

where D_t and D_n are the tangential and normal stiffness, respectively.

For the surface interface elements, a third stress and displacement component are considered, and the constitutive matrix is updated, namely:

$$\underline{\sigma} = \begin{bmatrix} \tau_1 \\ \tau_2 \\ \sigma_n \end{bmatrix} = \underline{D} \Delta\underline{u}' \quad \text{Eq. (7.3)}$$

$$\Delta\underline{u}' = [s_1 \quad s_2 \quad w]^T \quad \text{Eq. (7.4)}$$

$$\underline{D} = \begin{bmatrix} D_{t_1} & 0 & 0 \\ 0 & D_{t_2} & 0 \\ 0 & 0 & D_n \end{bmatrix} \quad \text{Eq. (7.5)}$$

The constitutive model assumes that no tensile stresses can be transferred between the interface, and a linear-elastic behavior is considered when the interface element is in compression, as defined by the following expression:

$$\begin{cases} D_n = 0 & w > 0 \\ D_n = k_n & w \leq 0 \end{cases} \quad \text{Eq. (7.6)}$$

where k_n is a user defined value.

To simulate the shear strength vs. sliding response ($\tau - s$) of the interface was implemented a cyclic hysteretic model. It is considered that the envelope of the cyclic response of the interface is described by the monotonic response presented in Figure 133.

The monotonic response is based on the work of [200], that is characterized by a linear-elastic branch up to the slide displacement s_0 , followed by a pre-peak nonlinear branch up to the slide displacement corresponding to peak shear stress s_m , and, finally, a post-peak nonlinear branch. The shear-sliding

response is defined by Eq. (7.7), and the tangent stiffness at any point of the curve is obtained by Eq. (7.8), where the subscript i represents the relative sliding displacement and shear stress according to the local axis of the interface element. For the case of surface interface elements, no relationship between the two shear components is considered, and the response of the interface elements in each local axis of the finite elements is considered independently. For the case of linear interface elements, only one direction is considered, i.e. $i = 1$.

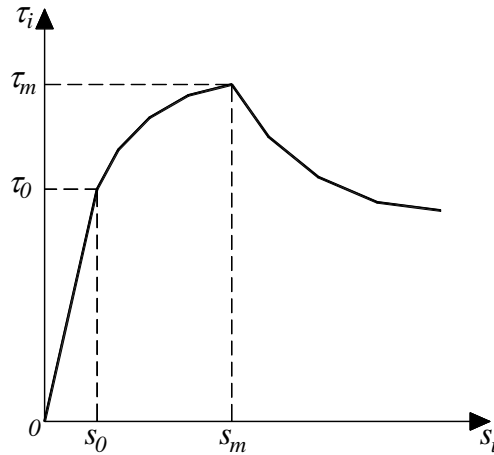


Figure 133 – Shear stress vs. relative sliding displacement ($\tau - s$) monotonic response of the constitutive model.

$$\tau_i = \begin{cases} \frac{\tau_0}{s_0} \cdot s_i & ; 0 \leq |s_i| \leq s_0 \\ \tau_m \cdot \left(\frac{s_i}{s_m} \right)^{\alpha_1} & ; s_0 < |s_i| < s_m, \quad i = 1, 2 \\ \tau_m \cdot \left(\frac{s_i}{s_m} \right)^{-\alpha_2} & ; |s_i| > s_m \end{cases} \quad \text{Eq. (7.7)}$$

$$D_{t,i} = \begin{cases} \frac{\tau_0}{s_0} & ; 0 \leq |s_i| \leq s_0 \\ \alpha_1 \cdot \frac{\tau_m}{s_m} \cdot \left(\frac{s_i}{s_m} \right)^{\alpha_1 - 1} & ; s_0 < |s_i| < s_m, \quad i = 1, 2 \\ -\alpha_2 \cdot \frac{\tau_m}{s_m} \cdot \left(\frac{s_i}{s_m} \right)^{-\alpha_2 - 1} & ; |s_i| > s_m \end{cases} \quad \text{Eq. (7.8)}$$

In Eq. (7.7) and Eq. (7.8) the slide displacement s_0 and s_m are user defined values, which correspond, respectively, to the slide at the end of the linear-elastic branch and to the slide corresponding to peak shear strength of the interface. In addition, α_1 and α_2 are parameters that

define the shape of the pre-peak and post-peak nonlinear branches, respectively, as can be seen in Figure 134.

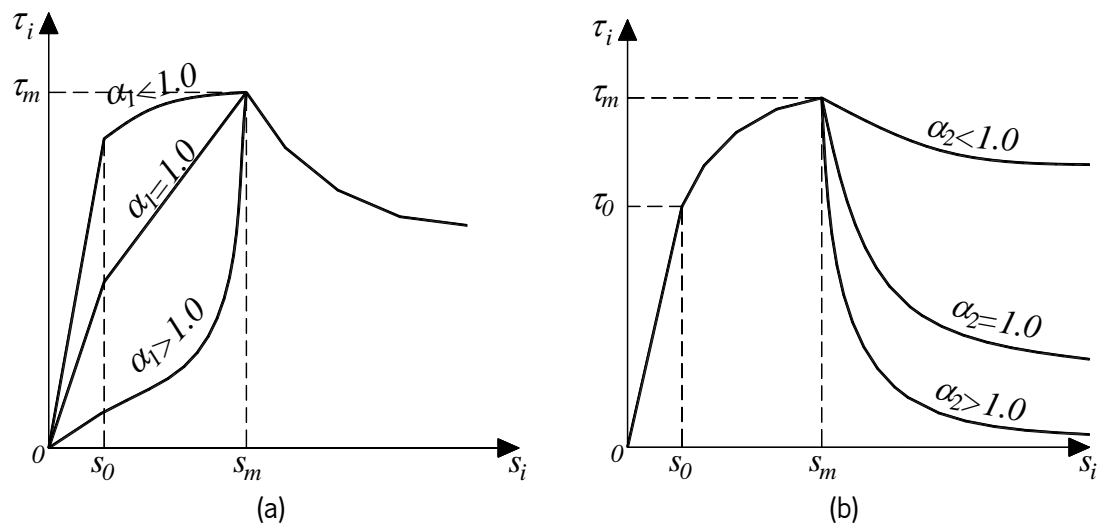


Figure 134 – Schematic representation of the influence of the value of parameters α_1 and α_2 in the shape of the $\tau - s$ relationship.

The value of the shear stress at the end of the elastic branch τ_0 is determined from the expression that defines the pre-peak nonlinear branch assuming $s_i = s_0$, as follows:

$$\tau_0 = \tau_m \cdot \left(\frac{s_0}{s_m} \right)^{\alpha_1} \quad \text{Eq. (7.9)}$$

The peak shear stress, τ_m , is determined according to the Mohr-Coulomb failure criterion, namely:

$$\tau_m = \sigma_n \cdot \mu + c \quad \text{Eq. (7.10)}$$

where μ is the friction coefficient that is taken equal to the tangent of the angle of internal friction, $\mu = \tan \phi$, and c is the material cohesion of the interface between the materials in contact.

Previous research [201]–[204] pointed out the existence of an interrelation between the friction coefficient and the relative displacement of the concrete pavements and subbase interface. Due to this, in the constitutive model is considered that the friction coefficient varies with the accumulated relative sliding displacement s_a , as presented in Figure 135, Eq. (7.11), Eq. (7.12) and Eq. (7.13). The mathematical formulation of this relationship is based on the curve proposed in Model Code 1990 for the stress-strain relationship of plain concrete [165].

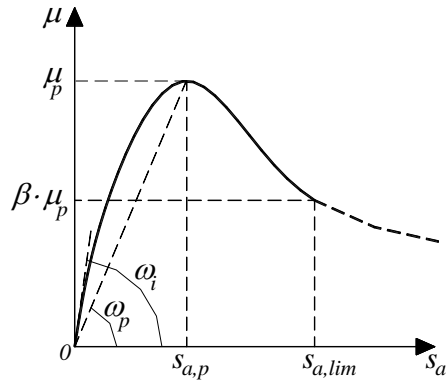


Figure 135 –Relationship between friction coefficient and accumulated relative sliding displacement ($\mu - s_a$) of the interface.

$$\mu = \begin{cases} \frac{\frac{\omega_i}{\omega_p} \cdot \frac{s_a}{s_{a,p}} - \left(\frac{s_a}{s_{a,p}}\right)^2}{1 + \left(\frac{\omega_i}{\omega_p} - 2\right) \cdot \frac{s_a}{s_{a,p}}} \cdot \mu_p & , s_a \leq s_{a,lim} \\ \frac{\frac{\omega_i}{\omega_p} \cdot \frac{s_{a,lim}}{s_{a,p}} - \left(\frac{s_{a,lim}}{s_{a,p}}\right)^2}{1 + \left(\frac{\omega_i}{\omega_p} - 2\right) \cdot \frac{s_{a,lim}}{s_{a,p}}} \cdot \mu_p & , s_a > s_{a,lim} \end{cases} \quad \text{Eq. (7.11)}$$

$$s_{a,lim} = \left[\frac{1}{2} \cdot \left[(1 - \beta) \cdot \frac{\omega_i}{\omega_p} + 2 \cdot \beta \right] + \left[\frac{1}{4} \cdot \left[(1 - \beta) \cdot \frac{\omega_i}{\omega_p} + 2 \cdot \beta \right]^2 - \beta \right]^{0.5} \right] \cdot s_{a,p} \quad \text{Eq. (7.12)}$$

$$\omega_p = \frac{\mu_p}{s_{a,p}} \quad \text{Eq. (7.13)}$$

In order to apply Eq. (7.11) and Eq. (7.12) is necessary to input the maximum friction coefficient μ_p and the corresponding sliding displacement $s_{a,p}$, the ratio between the maximum friction coefficient and the residual friction coefficient β and the initial tangent slope of the $\mu - s_a$ curve ω_i .

The accumulated relative sliding displacement, s_a , is determined according to the following expression:

$$s_a = \sum_{j=1}^N \left| \sqrt{(s_{1,j})^2 + (s_{2,j})^2} - \sqrt{(s_{1,j-1})^2 + (s_{2,j-1})^2} \right| \quad \text{Eq. (7.14)}$$

where N is the number of load combinations.

The hysteretic model is based on the work developed in [205] to describe the hysteric behavior of steel, where the unloading and reloading curves are defined by the Menegotto-Pinto model [206]. The Menegotto-Pinto model is used to calculate a curve that connects two tangents with a variable radius of curvature at the intersection of those two tangents, whose formulation is presented in Appendix G. The steel constitutive model was implemented in *FEMIX* in the research carried out by Varma [121].

The hysteretic model is presented in Figure 136. The complete cyclic model is defined by 10 rules, with 2 rules governing the monotonic envelope (1,2), and the remaining are set to describe the hysteretic response, namely reversal (3,4), returning (5,6), first transition (7,8) and second transitions curves (9,10). Considering the value of the relative sliding displacement, shear stress and tangent stiffness of the initial and target points of the curve, the shear stress and tangent stiffness of curves 3 to 10 can be determined according to the formulation presented in Appendix G.

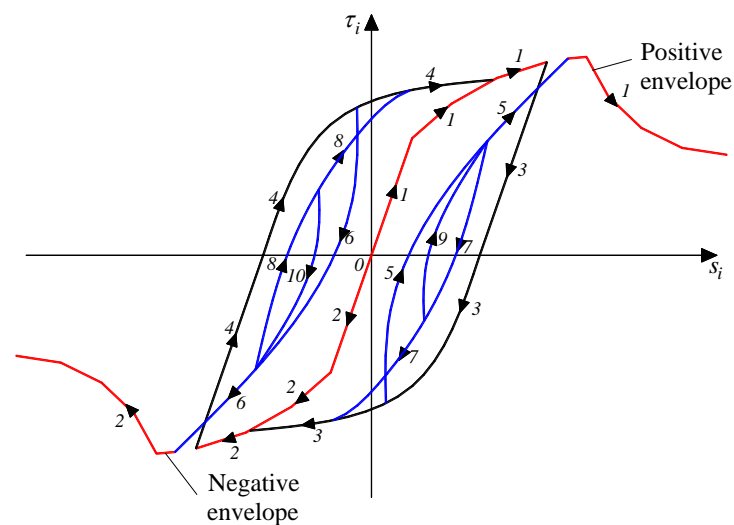


Figure 136 – Representation of the types of curves considered in the cyclic hysteretic model.

The positive (rule 1) and negative (rule 2) envelopes are defined by Eq. (7.7). When an unloading occurs, if the relative sliding displacement is on the first branch of the envelope response, i.e. $0 \leq |s_i| \leq s_0$, is admitted a elastic recovery, without inelastic deformation. When the relative sliding displacement surpasses the elastic branch, and an unloading occurs, the reversal curves (rule 3 or 4) are applied.

In Figure 137 are presented the parameters that are considered in the rule 3, which are calculated according to Eq. (7.15).

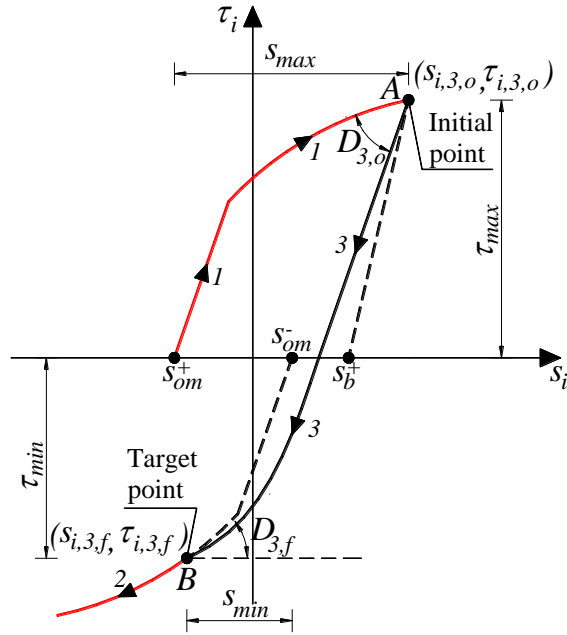


Figure 137 – Representation of parameters of reversal curve 3.

$$s_b^+ = s_{om}^+ + s_{max} - \frac{\tau_{max}}{\tau_0/s_0}, \text{ with } s_{max} \geq s_0$$

$$k_{rev}^- = \exp\left(-\frac{s_{max}}{5.0(s_0)^2}\right)$$

$$s_{om}^- = s_{om}^+ \cdot k_{rev}^- + s_b^+ \cdot (1 - k_{rev}^-)$$

$$s_{i,3,o} = s_{om}^+ + s_{max}$$

$$\tau_{i,3,o} = \tau_{max}$$

$$s_{i,3,f} = s_{om}^- + s_{min}, \text{ with } |s_{min}| \geq s_0$$

$$\tau_{i,3,f} = \tau_i(s_{i,3,f})$$

$$D_{3,f} = D_{t,i}(s_{i,3,f})$$

$$R = 16 \cdot (s_0)^{1/3} \cdot (1 - 0.01 \cdot \Delta s_{a3})$$

$$D_{3,o} = (1 - 0.3 \cdot \Delta s_{a3}) \cdot \frac{\tau_0}{s_0}$$

$$\Delta s_{a3} = \frac{|s_{i,3,f} - s_{i,3,o}|}{2 \cdot s_m} \quad \text{Eq. (7.15)}$$

Similarly, in Figure 138 are represented the parameters that are considered in the rule 4, and in Eq. (7.16) are indicated the formulas to calculate these parameters.

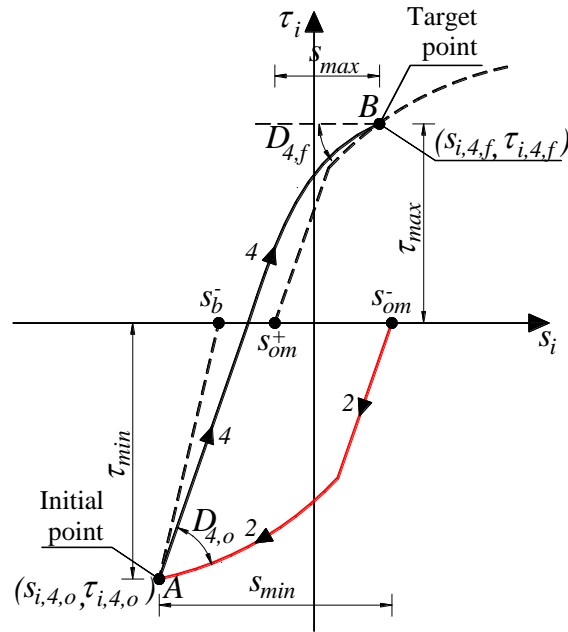


Figure 138 – Representation of parameters of reversal curve 4.

$$s_b^- = s_{om}^- + s_{min} - \frac{\tau_{min}}{\tau_0/s_0} \text{ with } s_{min} \leq -s_0$$

$$k_{rev}^+ = \exp\left(-\frac{|s_{min}|}{5.0(s_0)^2}\right)$$

$$s_{om}^+ = s_{om}^- \cdot (1 - k_{rev}^+) + s_b^- \cdot k_{rev}^+$$

$$s_{i,4,o} = s_{om}^- + s_{min}$$

$$\tau_{i,4,o} = \tau_{min}$$

$$s_{i,4,f} = s_{om}^+ + s_{max}, \text{ with } |s_{max}| \geq s_0$$

$$\tau_{i,4,f} = \tau_i(s_{i,4,f})$$

$$D_{4,f} = D_{i,i}(s_{i,4,f})$$

$$R = 16 \cdot (s_0)^{1/3} \cdot (1 - 0.01 \cdot \Delta s_{a4})$$

$$D_{4,o} = (1 - 0.3 \cdot \Delta s_{a4}) \cdot \frac{\tau_0}{s_0}$$

$$\Delta s_{a4} = \frac{|s_{i,4,f} - s_{i,4,o}|}{2 \cdot s_m} \quad \text{Eq. (7.16)}$$

When the reversal from the positive envelope to the negative envelope is not completed (path A-B' in Figure 139), is applied the returning curve (rule 5) from rule 3 to the positive envelope (rule 1). The parameters of rule 5 are presented in Figure 139 and are calculated according to Eq. (7.17).

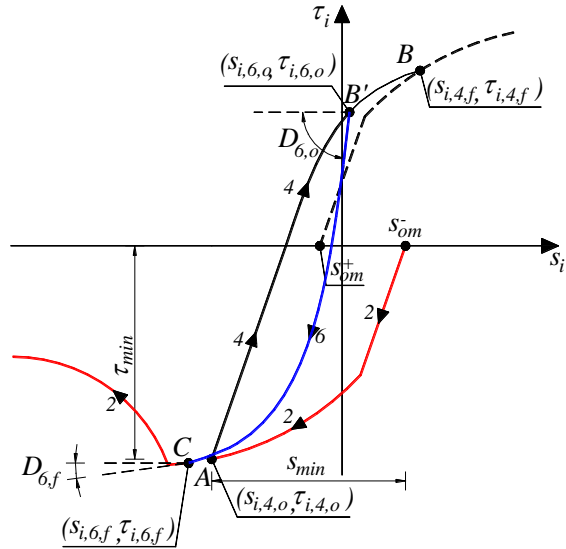


Figure 140 – Representation of parameters of returning curve 6.

$$\Delta s_{rev}^- = s_{i,4,o} - s_{i,6,o} - \frac{\tau_0}{1.2 \cdot \tau_0 / s_0}$$

$$s_{i,6,f} = s_{om}^- + s_{min} + \Delta s_{rev}^-$$

$$\tau_{i,6,f} = \tau_i(s_{i,6,f})$$

$$D_{6,f} = D_{i,i}(s_{i,6,f})$$

Eq. (7.18)

$$R = 20 \cdot (s_0)^{1/3} \cdot (1 - 0.2 \cdot \Delta s_{a6})$$

$$D_{6,o} = (1 - 0.1 \cdot \Delta s_{a6}) \cdot \frac{\tau_0}{s_0}$$

$$\Delta s_{a6} = \frac{|s_{i,6,f} - s_{i,6,o}|}{2 \cdot s_m}$$

When a reversal from a returning curve (rule 5 and 6) occurs, it is activated the first transition curve.

In Figure 141 and Eq. (7.19) are presented the parameters considered in rule 7 that are required when a reversal in rule 6 occurs. It is noted that the target point of rule 7 ($s_{i,7,f}, \tau_{i,7,f}$) is determined by applying a new reversal curve (3*) based on the formulation of rule 3, connecting points D'-B''.

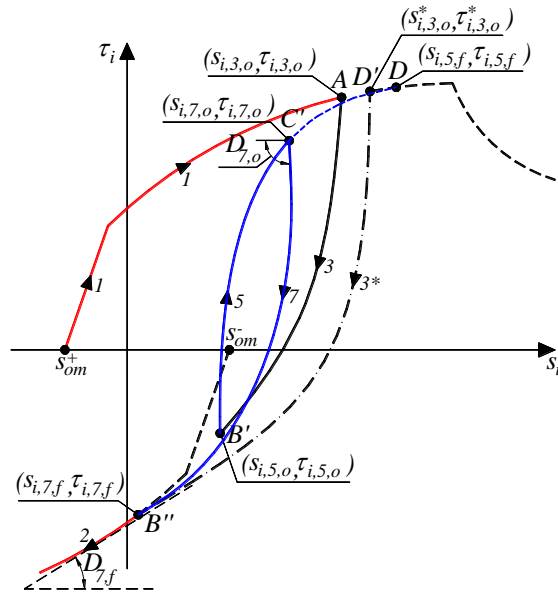


Figure 141 – Representation of parameters of first transition curve 7.

$$\begin{aligned}
 s_{i,3,o}^* &= s_{i,5,f} \cdot \frac{s_{i,7,o} - s_{i,5,o}}{s_{i,5,f} - s_{i,5,o}} + s_{i,3,o} \cdot \frac{s_{i,5,f} - s_{i,7,o}}{s_{i,5,f} - s_{i,5,o}} \\
 \tau_{i,3,f}^* &= \tau_i(s_{i,3,f}^*) \\
 D_{7,f} &= D_{i,i}(s_{i,7,f}) \\
 R &= 16 \cdot (s_0)^{1/3} \cdot (1 - 0.1 \cdot \Delta s_{a7}) \\
 D_{7,o} &= (1 - 0.3 \cdot \Delta s_{a7}) \cdot \frac{\tau_0}{s_0} \\
 \Delta s_{a7} &= \frac{|s_{i,7,f} - s_{i,7,o}|}{2 \cdot s_m}
 \end{aligned} \tag{7.19}$$

Conversely, in Figure 142 and Eq. (7.20) is presented the first transition curve that is activated when a reversal from rule 6 occurs. In this situation the target point for rule 8 $(s_{i,8,f}, \tau_{i,8,f})$ is determined from a new reversal curve 4*, based on the formulation of rule 4, with the initial point $(s_{i,4,o}^*, \tau_{i,4,o}^*)$ being calculated from the expression in Eq. (7.20).

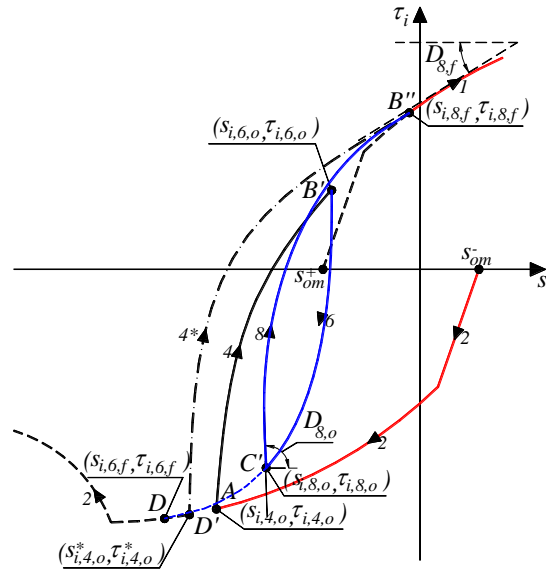


Figure 142 – Representation of parameters of first transition curve 8.

$$\begin{aligned}
 s_{i,4,o}^* &= s_{i,6,f} \cdot \frac{s_{i,8,o} - s_{i,6,o}}{s_{i,6,f} - s_{i,6,o}} + s_{i,4,o} \cdot \frac{s_{i,6,f} - s_{i,8,o}}{s_{i,6,f} - s_{i,6,o}} \\
 \tau_{i,4,f}^* &= \tau_i(s_{i,4,f}^*) \\
 D_{8,f} &= D_{t,i}(s_{i,8,f}) \\
 R &= 16 \cdot (s_0)^{1/3} \cdot (1 - 0.1 \cdot \Delta s_{a7}) \\
 D_{8,o} &= (1 - 0.3 \cdot \Delta s_{a8}) \cdot \frac{\tau_0}{s_0} \\
 \Delta s_{a8} &= \frac{|s_{i,8,f} - s_{i,8,o}|}{2 \cdot s_m}
 \end{aligned} \tag{7.20}$$

When a reversal from rule 7 occurs, a second transition curve is enabled (rule 9), aiming the returning branch of rule 5. The schematic representation of the second transition curve 9 is presented in Figure 143, and the defining parameters of rule 9 are presented in Eq. (7.21). To be noticed that the target point of rule 9 is the initial point of rule 7 $(s_{i,7,o}, \tau_{i,7,o})$, and the tangent stiffness $D_{9,f}$ of the target point is determined according to rule 5 formulation $(D_{9,f} = D_t^{*5}(s_{i,7,o}))$.

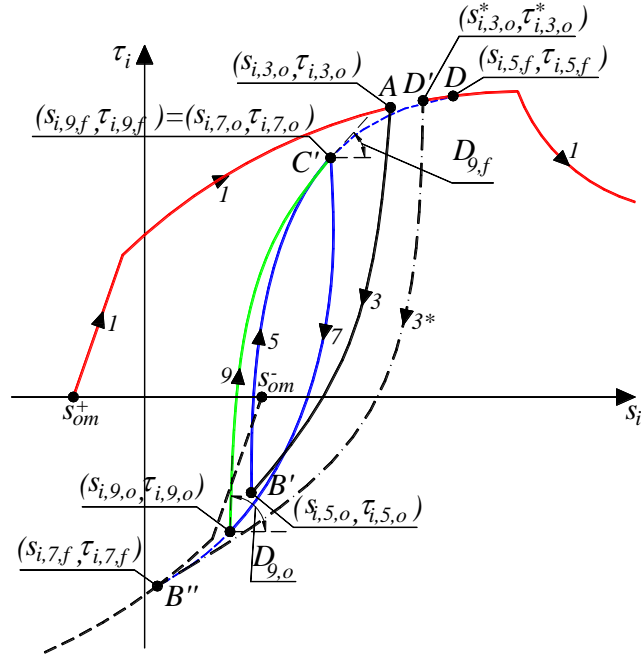


Figure 143 – Representation of parameters of second transition curve 9.

$$s_{i,9,f} = s_{i,7,o}$$

$$\tau_{i,9,f} = \tau_{i,7,o}$$

$$\Delta s_{a9} = \frac{|s_{i,9,f} - s_{i,9,o}|}{2 \cdot s_m}$$

Eq. (7.21)

$$D_{9,o} = (1 - 0.1 \cdot \Delta s_{a9}) \cdot \frac{\tau_0}{s_0}$$

$$R = 20 \cdot (s_0)^{1/3} \cdot (1 - 0.2 \cdot \Delta s_{a9})$$

$$D_{9,f} = D_t^{*5} (s_{i,7,o})$$

Analogously, when a reversal from rule 8 occurs, a second transition curve is enabled (rule 10), aiming the returning branch (rule 6). The schematic representation of the second transition curve 10 is presented in Figure 144, and the defining parameters of rule 9 are provided in Eq. (7.22).

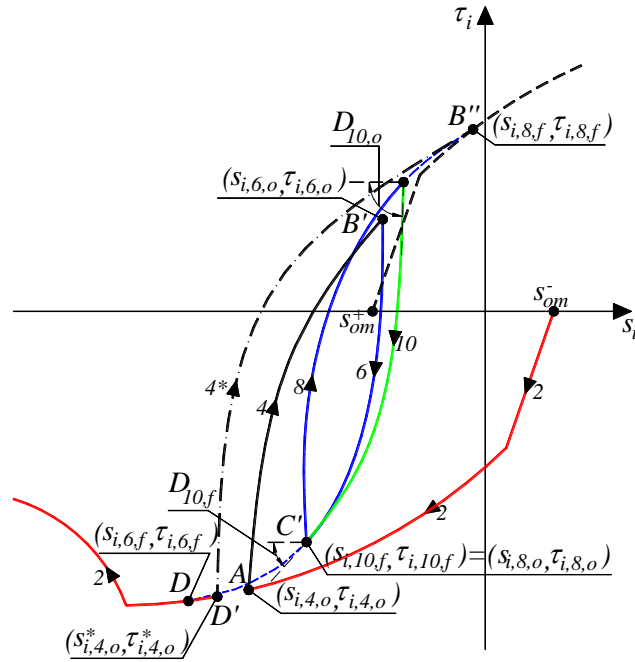


Figure 144 – Representation of parameters of second transition curve 10.

$$s_{i,10,f} = s_{i,8,o}$$

$$\tau_{i,10,f} = \tau_{i,8,o}$$

$$\Delta s_{a10} = \frac{|s_{i,10,f} - s_{i,10,o}|}{2 \cdot s_m}$$

Eq. (7.22)

$$D_{10,o} = (1 - 0.1 \cdot \Delta s_{a10}) \cdot \frac{\tau_0}{s_0}$$

$$R = 20 \cdot (s_0)^{1/3} \cdot (1 - 0.2 \cdot \Delta s_{a10})$$

$$D_{10,f} = D_t^{*6} (s_{i,8,o})$$

If a reversal from a second transition curve occurs, a new first transition curve is adopted, keeping the target point of the first transition curve unchanged. In Figure 145a is represented the reversal from rule 9, where a new rule 7 is adopted with a target point equal to $(s_{i,7,f}, \tau_{i,7,f})$. Similarly, in Figure 145b is represented the reversal from rule 10, being adopted a new rule 8 with a target point equal to $(s_{i,8,f}, \tau_{i,8,f})$.

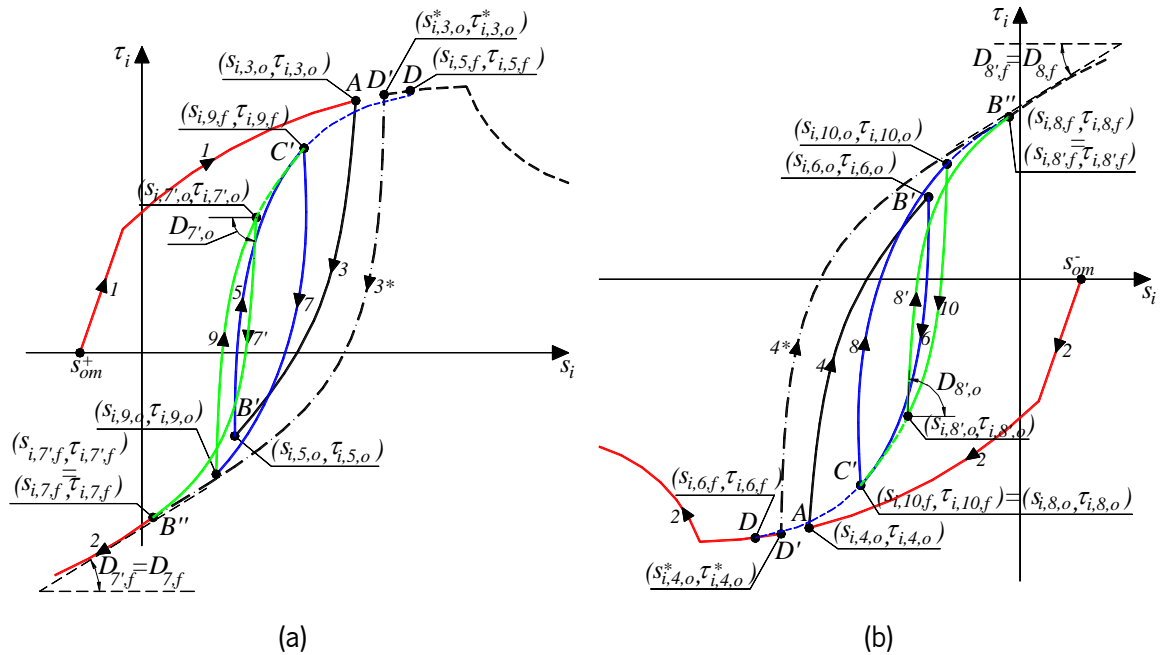


Figure 145 – Representation of reversal from second transition curves of: a) Rule 9; b) Rule 10.

7.2 Numerical example

The adequate functioning of the developed constitutive model for interface finite elements, designated by NLMM306 in the programming philosophy of FEMIX, is assessed in this section by simulating some examples.

In Figure 146 is presented the geometry, load and support conditions of the first analyzed example. This example aims basically to demonstrate the correct hysteretic functioning of the implemented model in a situation where the interface is subjected to constant normal compressive stress and several loading/unloading sliding loading conditions. The mesh is composed by two 8-node plane stress elements (element no. 1 and 2) with 10mm of thickness and one quadratic 6-node interface element (element no.3), being coincident the pair of nodes that form the interface element. For the interface element is considered a Gauss-Legendre integration scheme with 2 integration points (IP), and for the plane stress finite elements is considered a 2x2 IP Gauss-Legendre integration scheme.

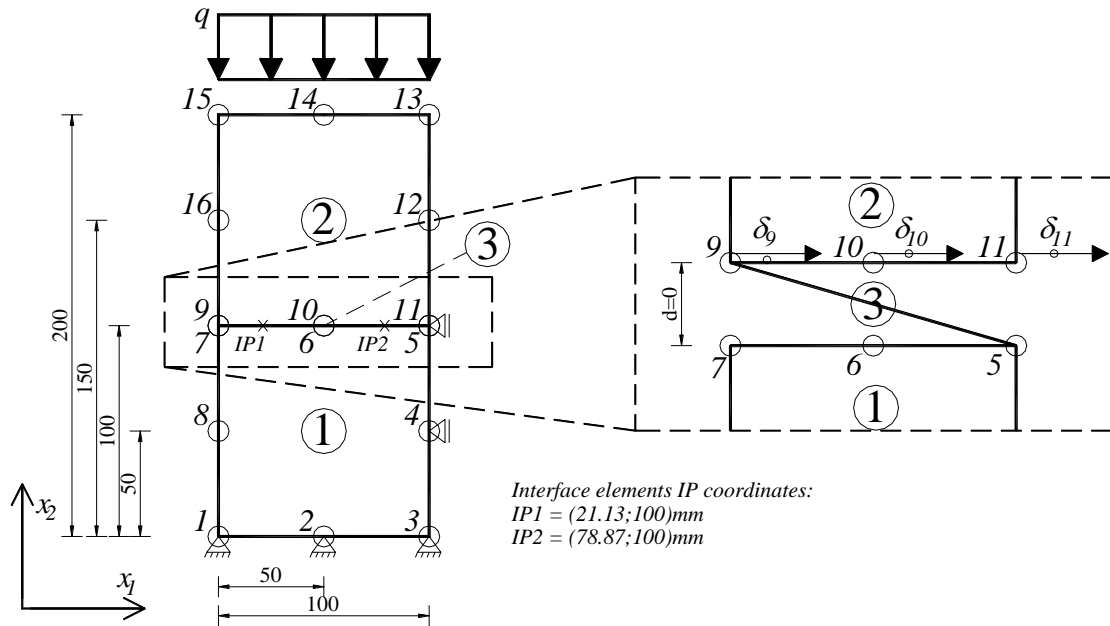


Figure 146 – Geometry, load and support conditions considered in the numerical model (dimensions in mm).

For the 8-node plane stress elements is considered a linear elastic material model, considering a Young's modulus of 300 GPa and a null Poisson's coefficient. In Table 17 is presented the parameters of the NLMM306 constitutive model adopted in the interface element.

Table 20 – Material properties of the constitutive model of the interface.

s_o	0.1 mm
s_m	0.2 mm
c	0.50 MPa
α_1	0.2
α_2	0.3
ω_i	5 mm ⁻¹
μ_p	0.466
$s_{a,p}$	0.15 mm
β	0.9
k_n	100x10 ³ N/mm

In Figure 147 is presented the evolution of the friction coefficient of the IP no (IP2) of the interface element, considering the adopted parameters of the NLMM306 constitutive model.

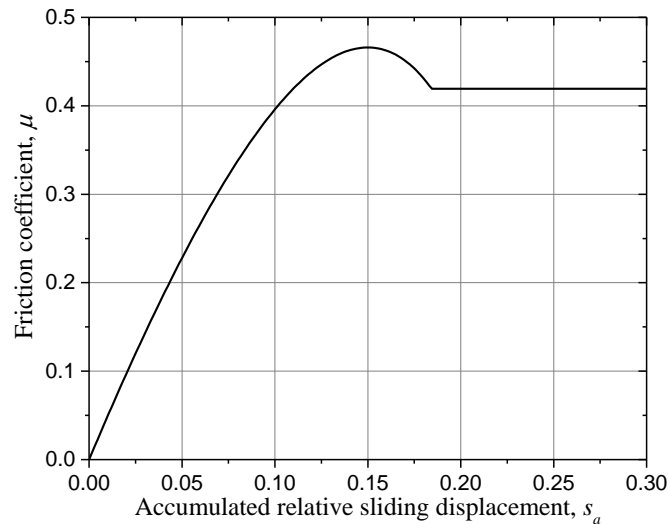


Figure 147 – Evolution of friction coefficient with the accumulated sliding displacement.

In the top edge of element no. 2 is applied an uniformly distributed load with the value of $q = 1000N / mm$ in the $-x_2$ global axis direction, which applies a normal compressive stress at each integration point of the interface element equal to 100MPa. On nodes 9, 10 and 11 is applied a horizontal prescribed displacement (values will be presented in each set of load combinations), whose value is equal to the relative sliding displacement of the IP of the interface element.

7.2.1 Load combinations - set A

In Figure 148a is presented the prescribed displacement applied at nodes 9, 10 and 11 for the set A of load combinations. The corresponding relative sliding displacement vs. shear stress response of the IP2 of the interface element is presented in Figure 148b, from which is noticeable the application of the rule 1 and 3 of the NLMM306 model.

The analysis of Figure 148b reveals that due to the variation of the friction coefficient (Figure 147), the first branch of the constitutive model also assumes a nonlinear relationship between $\tau - s$. The nonlinear behavior of the first branch of the $\tau - s$ relationship is justified as follows:

- The slope of the elastic branch is a function of the shear stress τ_0 , as expressed in Eq. (7.8) ;
- The shear stress τ_0 is determined according to Eq. (7.9) considering the peak shear stress τ_m ;
- The peak shear stress is a function of the friction coefficient, μ ;
- The friction coefficient is a function of the accumulated sliding displacement, s_a ;

- The accumulated sliding displacement is obtained from Eq. (7.14), which increases with the variation of the relative sliding displacement of the interface element IP.

For this example, the positive curvature of the first branch of the $\tau - s$ is explained by the progressive increase of the tangential stiffness with the increase of the sliding displacement, up to reaching a sliding displacement of $s_0 = 0.10mm$, as shown in Figure 149;

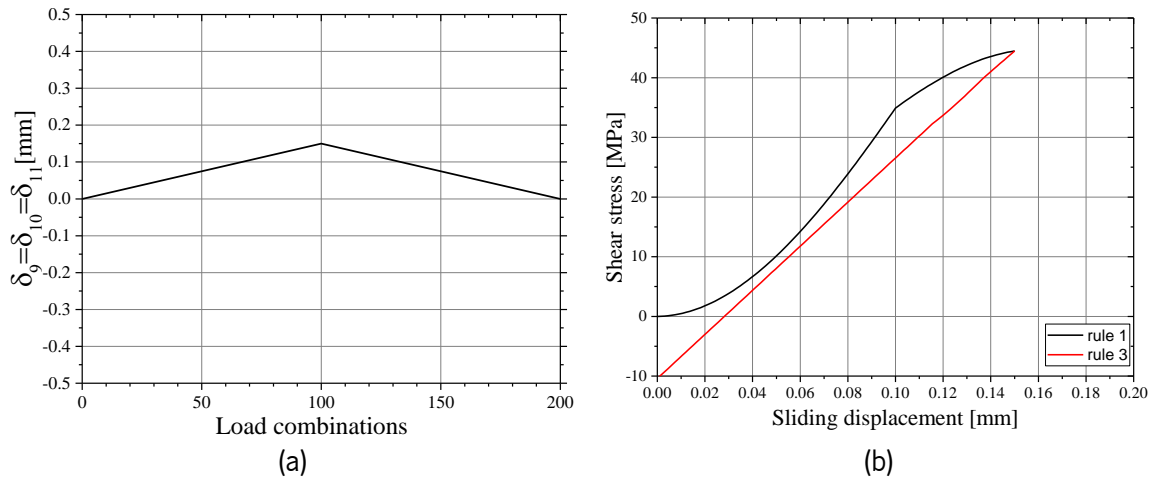


Figure 148 – a) Prescribed horizontal displacement at node 9, 10 and 11 for the set A of load combinations. b) Shear stress vs sliding displacement at the IP2 of the interface element.

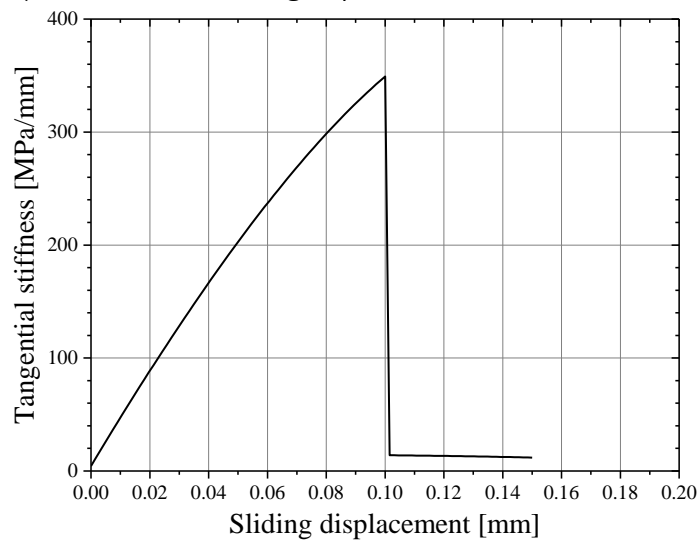


Figure 149 – Tangential stiffness at the IP2 of the interface element up to load combination 100.

7.2.2 Load combinations - set B

In Figure 150b is presented the $\tau - s$ relationship at the IP2 of the interface element corresponding to the prescribed displacement applied in nodes 9, 10 and 11 according to Figure 150a. From this numerical simulation is clearly demonstrated the hysteretic response of the NLMM306 constitutive

model, as the response encloses the positive (rule 1) and negative (rule 2) envelopes and the reversal curves considered in rules 3 and 4.

Until load combination no. 100 is adopted rule 1, and the relative sliding displacement is lower than s_0 . Due to the monotonic response did not reach the pre-peak nonlinear branch, as $s \leq s_0$, after load combination no. 101 and until relative sliding displacement becomes negative, is still applicable rule 1, being followed by rule 2 when $s < 0$. At the load combination no. 201 occurs a reversal of the sliding displacement, and rule 4 is activated until the positive envelope (rule 1) is reached. At load combination no. 301 a new reversal of the relative sliding displacement takes place and rule 3 is activated. However, due to the model restriction (lack of convergence of the iterative process of the Menegotto-Pinto model, see Appendix G), a linear interpolation in rule 3 is adopted. After reaching the negative envelope at load combination no. 400, a new reversal curve (rule 4) is adopted until the positive envelope is reached again (rule 1).

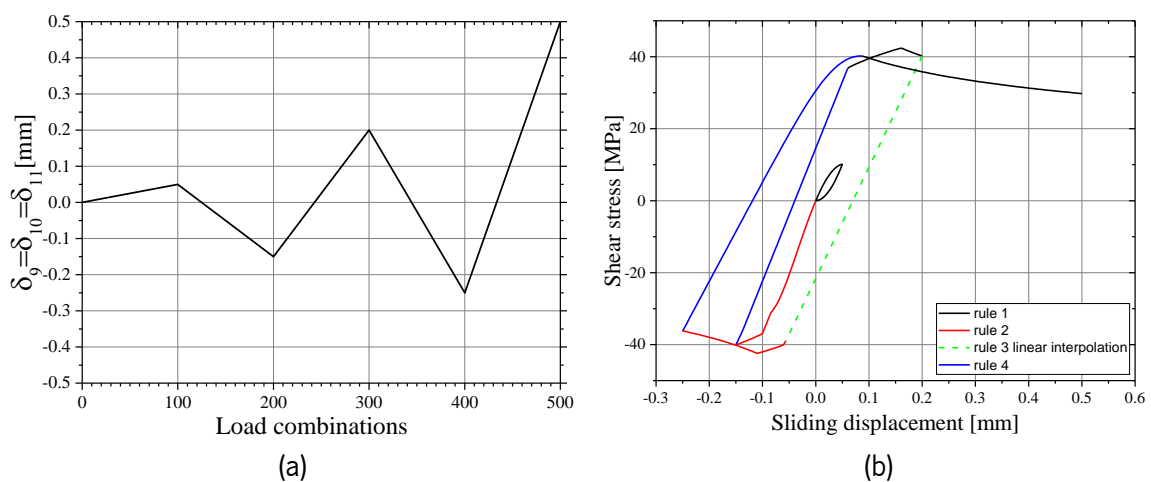


Figure 150 – a) Prescribed horizontal displacement at node 9, 10 and 11 for the set B of load combinations; b) Shear stress vs sliding displacement at the IP2 of the interface element.

7.2.3 Load combinations - set C

In Figure 151 is presented the set C of load combinations that demonstrates the application of the reversal, returning, first and second transition curves. The evolution of the prescribed displacement applied in nodes 9, 10 and 11 considered in the numerical example is presented in Figure 151a, and the corresponding $\tau - s$ relationship of IP2 of the interface element is presented in Figure 151b. The applied prescribed displacement yields a response on the integration point that starts in the positive

envelope and ends in the negative envelope, with unloading and reloading stages in between, with rules path of: 1→3→2→4→6→8→10→6→2.

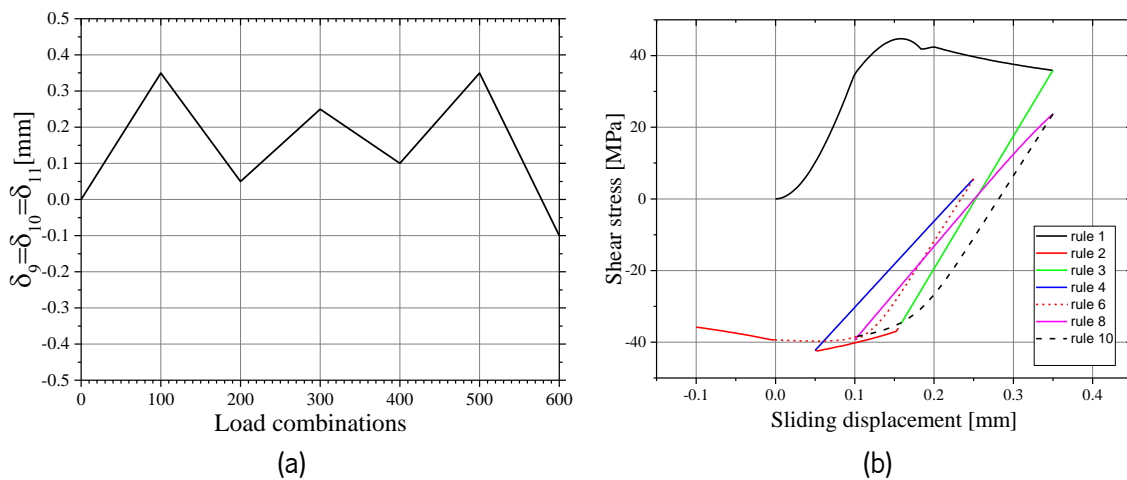


Figure 151 – a) Prescribed horizontal displacement at node 9, 10 and 11 for the set C of load combinations; b) Shear stress vs sliding displacement at the IP2 of the interface element.

7.3 Numerical application

The example in this section aims to assess the capability of the new interface constitutive model to simulate the behavior of concrete slabs supported on ground submitted to push-off tests. The results of the numerical simulation are compared with the data of the experimental program presented in [201].

In [201] were conducted several push-off tests of concrete slabs with different geometries and with different materials between the concrete slabs and the granular base layers. It is simulated the test series no. 1 of the slab 1, which corresponds to a rectangular slab with 3.65x3.15m² plant dimensions and with 152.4mm of thickness. In the interface between the slab and the granular base was placed a double layer of polyethylene sheets. The push-off test consisted in the application of a horizontal load on the center of the lateral edge of the slab, while the displacement of the slab was registered in four points by using dial gages disposed according to the schematic representation shown in Figure 7.20. The horizontal load was applied with a stressing ram, and the applied load was registered with a 444kN load cell. In Figure 152 is presented the test setup.

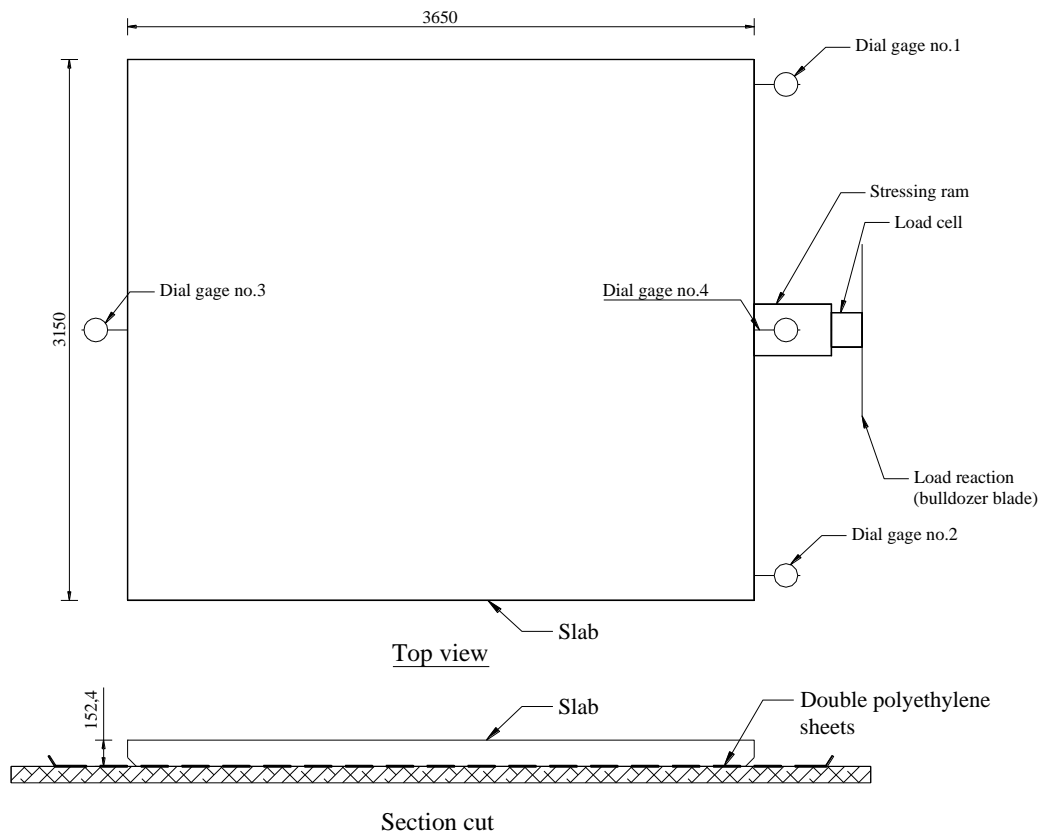


Figure 152 – Test setup of slab tested in [201] (dimensions in mm).

In order to perform the numerical simulation of the push-off test, a finite element model of the concrete slab was formed with 4-node of Reissner-Mindlin shell elements, considering a 2x2 Gauss-Legendre integration scheme. For the simulation of the contact conditions between the concrete slab and the granular layers of the pavement, 8-node surface interface finite elements were introduced between the elements of the slab and the supports that materialize the foundation of the pavement. For the surface interface finite elements was adopted a Gauss-Legendre 2x2 integration scheme. The finite element mesh is shown in Figure 153, being formed by 270 shell elements and 270 interface elements.

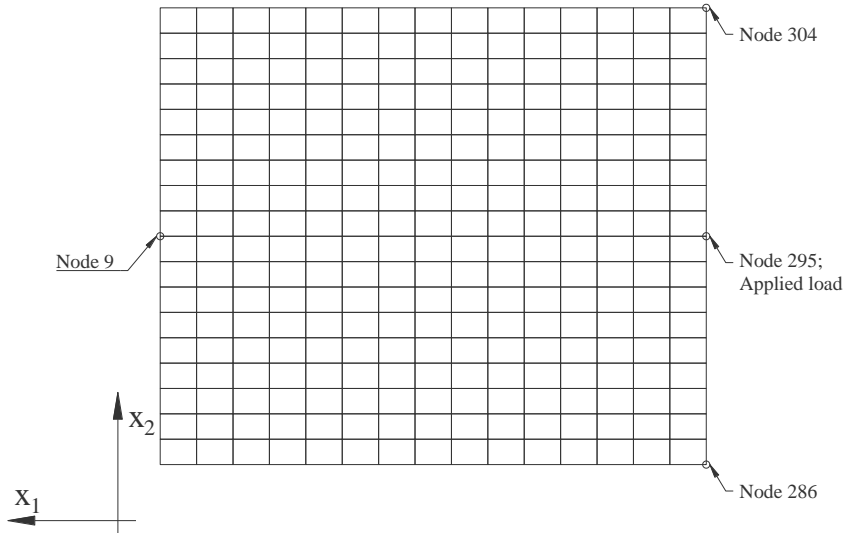


Figure 153 – Finite element mesh.

The simulation is carried under displacement control. Resorting to the arc-length technique [207], the magnitude of the point load applied at node 295 is determined in order that the incremental displacement of the node 9 is equal to $\delta_9^{x_1} = 2 \times 10^{-3} \text{ mm}$ in each iteration. The self-weight of the slab is also considered during the analysis.

For the simulation of the concrete behavior is admitted a linear-elastic response, assuming a Young's modulus $E_c = 30.0 \text{ GPa}$ and Poisson's ratio $\nu = 0.20$. Based on the information collected in [201], the slab's concrete density is equal to $\rho_c = 2070 \text{ kg} / \text{m}^3$.

The NLMM306 constitutive model is considered for simulating the behavior of the interface elements, with the parameters presented in Table 21.

Table 21 - Material properties of the constitutive model of the interface.

s_o	$1 \times 10^{-3} \text{ mm}$
s_m	0.125 mm
c	0.0 MPa
α_1	0.10
α_2	0.01
ω_i	10 mm^{-1}
μ_p	0.472
$s_{a,p}$	0.125 mm
β	0.99
k_n	$1 \times 10^9 \text{ N/mm}$

In Figure 154 is presented the relationship between the applied horizontal load and the average displacement in the x_1 direction of the nodes 9, 286, 295 and 304 of the mesh (Figure 153), similarly to the procedure employed in [201]. The very good agreement between the numerical model and experimental results reveals the capability of the NLMM306 constitutive model to simulate the behavior of the interface between concretes slabs supported on ground.

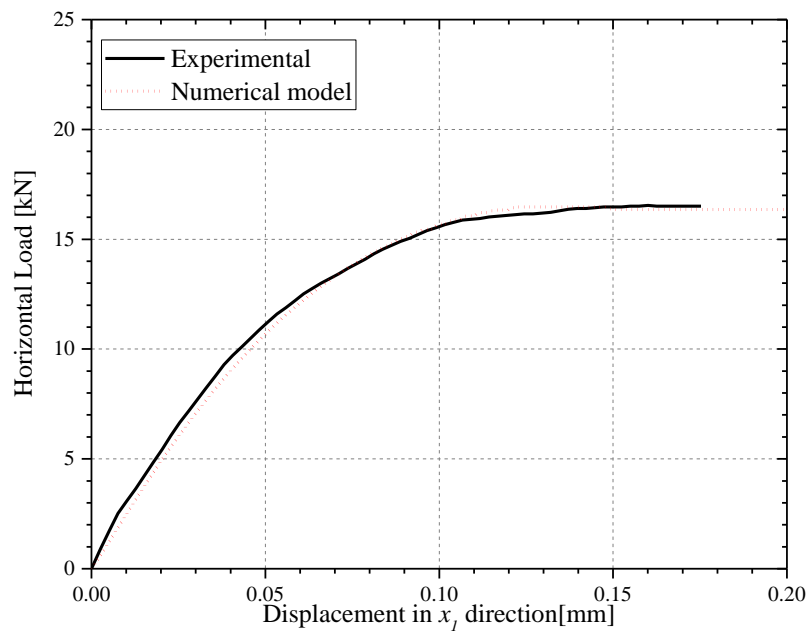


Figure 154 – Horizontal load vs. displacement in the x_1 direction relationship of the slab.

7.4 Concluding remarks

This chapter was dedicated to the description of a new constitutive model for simulating the contact between different materials. The constitutive model was implemented in *FEMIX* to be adopted in zero-thickness interface elements.

To simulate the shear strength vs. sliding response of the interface was implemented a cyclic hysteretic model. Within the model, the maximum shear stress is defined according to the Mohr-Coulomb law, while being adopted a nonlinear variation of the friction coefficient as a function of the sliding displacement of the interface.

The hysteretic response of the model was demonstrated by conducting simulations of simplified numerical examples, and some of the model's particularities were presented.

The capability of the model to simulate the interface of concrete slabs supported on ground was assessed by performing the numerical simulation of a push-off test. It was verified a good agreement between the numerical and experimental response of the force vs. sliding displacement of the concrete slab.

8 CONCLUSIONS

8.1 Main conclusions

The present thesis has focused on the development and implementation of numerical tools that can be applied in the analysis and design of FRC structures.

In this scope, the development of a software which is based on the most recent guidelines and recommendations for the design of FRC members, *FRCcalc*, can represent a significant resource for the design community. Based on a user-friendly interface, the program allows to conduct fast and detailed analysis of the ultimate and serviceability limit state safety verifications of FRC structural members, filling a gap in the availability of a software to conduct analysis of FRC members. In addition, the possibility to run comparative analysis between the structural performance of a concrete element with traditional reinforcements and fiber reinforcements can, based on the improved performance of FRC, promote the increase of prescription of FRC at the design stage.

One of the most promising application of fiber reinforcements relies on the replacement of conventional shear reinforcements of concrete. In this aim, it was conducted an assessment of the reliability of the shear prediction models available on MC2010, by comparison with the experimental results of an extended version of a database of FRC elements shear tests. For the database under analysis, both models revealed a satisfactory approximation to the experimental results, and in average both models exhibited very similar predictive performance. A significant finding of the research relied on the fact that, in the majority of the cases, both shear prediction models returned safe estimations of the shear resistance of the FRC beams of the database. In addition, after application of the partial safety factor for FRC, both models always return safe predictions, which confirms the reliability of the shear models for the design of FRC structures.

For the analysis of the flexural response of FRC members, an approach that couples the influence of fiber orientation and segregation, and the contribution of the pullout resistance of each fiber bridging a crack was developed. A novel local constitutive model for the pullout response of the fibers was proposed, which can be adapted to simulate the interface behavior between different types of fibers and concrete matrix properties. By adopting a fitting procedure to derive the values that define the parameters of the local bond strength vs. displacement of aligned fibers, the integrated model was

able to capture the flexural response of steel fiber reinforced concrete notched beams submitted to 3-point bending tests. Although some discrepancies were found in its application to simulate the flexural response of FRC structural members for two case studies, it is believed that the followed approach can simulate more realistically the post-cracking response of FRC in comparison to the already available models, e.g. generalized stress vs. crack width relationships. The performance of the model would greatly benefit from the characterization of the pullout response of aligned and inclined fibers, which is being a major research topic in the more recent years.

One of major reasons for the use of fiber reinforcements is the capability of fibers to transfer stresses across cracks, increasing the stiffness of cracked structural elements, which ultimately limits crack opening and reduces structural member's deformation. In order to estimate the crack opening and deformation of FRC structural members under sustained loading, a new basic creep model – ACC model – based on the Dirichlet series expansion of the DPL model was developed for predicting the aging creep behavior of CBM, since early age. The model was integrated in *FEMIX*, which can be coupled with other time dependent constitutive models governing the behavior CBM since their early age up to hardened stage, like maturation, shrinkage, thermal variation and cracking. The good predictive performance of the ACC was demonstrated at material and structural levels. For this last situation, of more interest in structural design practice, the long term deflection of a reinforced concrete beam submitted to flexural creep test was predicted with good accuracy, in a complex scenario where cracking has also occurred. For the case of FRC members, the model can be adopted to simulate creep of concrete in compression and in tension between cracks.

Until now, the widest use of FRC resides in its application in slabs of pavements supported on ground, mainly for industrial buildings. In this topic, is of paramount importance to adequately simulate the support conditions of the slabs, since the stress state and crack propagation developed in the slabs are significantly influenced by the restriction promoted by the granular layers of their foundation system. In this scope, it was implemented in *FEMIX* a constitutive model that can simulate the contact between different materials, namely concrete slabs supported on ground. The model adopts a cyclic-hysteretic response based on Mohr-Coulomb law, while a variable friction coefficient is adopted. In addition, only shear and compressive stresses are permitted in the interface between materials. This model can be used with the available models in *FEMIX* to simulate FRC cracking,

creep, shrinkage, maturation and thermal variation, and perform extremely thorough analysis for the assessment of the behavior of FRC pavements.

8.2 Possible future developments

The work conducted in this thesis can be further developed, and the following list of research topics is proposed:

- Upgrade the design capabilities of *FRCcalc* to allow the analysis of T and I-shaped FRC cross-sections, the use of prestressed reinforcements, and the use of fiber reinforced polymer reinforcement bars. Addition of a new module in *FRCcalc* for conducting comparative analysis of the economic aspects of concrete elements with traditional reinforcements and fiber reinforcements. In addition, a special module aimed for the design of FRC slabs supported on ground, submitted to the typical load conditions, could also reveal a great interest due to the widespread use of fiber reinforcements in this type of structures, namely in industrial buildings;
- The fiber pullout resistance model, used in the analysis of FRC structures, should be extended to the use of non-steel based fiber reinforcements, particularly glass and synthetic fibers;
- In the fiber segregation model, further research can be carried out by assessing the performance improvement of the numerical tool by adopting a nonlinear distribution of fibers along the cross-section height. The reliability of these models should be assessed with experimental results;
- A creep model for concrete in compression and for the fiber-matrix interface can be implemented in the numerical tool presented in chapter 5, in order to adequately predict the long term deflection and crack opening of FRC members.
- Coupling a tension-stiffening model, similar to the one proposed in [25], [208], with the fiber orientation profile, fiber segregation and fiber pullout resistance models to improve the capability to simulate the flexural and cracking behavior of FRC members, including members flexurally reinforced with conventional reinforcements (R-FRC). A new software based on the force method can be developed for the analysis of a R-FRC structures, where the flexibility

matrix of the structure is updated according to the moment-rotation relationship outputted by *DOCROS*;

- The integrated approach that adopts the fiber orientation profile, fiber segregation model and fiber pullout resistance can be implemented in FEM-based software, as *FEMIX*, to be used in the analysis of more complex structural elements. In addition, the model formulation could also be improved in order to consider Mode II fracture of FRC based on the work of [209].
- Development of a time-dependent model to simulate the evolution of the post-cracking behavior of FRC since early ages. This model can be implemented in the available smeared crack model that is applied for the simulation of the crack opening and propagation of FRC, and be coupled with the thermo, maturation, creep and shrinkage models that are adopted in the simulation of cement based materials since early ages.

REFERENCES

- [1] A. M. Brandt, "Fibre reinforced cement-based (FRC) composites after over 40 years of development in building and civil engineering," *Compos. Struct.*, vol. 86, no. 1–3, pp. 3–9, Nov. 2008.
- [2] J. P. Romualdi and J. A. Mandel, "Tensile Strength of Concrete Affected by Uniformly Distributed and Closely Spaced Short Lengths of Wire Reinforcement," *J. Proc.*, vol. 61, no. 6, pp. 657–672, Jun. 1964.
- [3] Ronald F. Zollo, "Fiber-reinforced concrete: an overview after 30 years of development," *Cem. Concr. Compos.*, vol. 19, no. 2, pp. 107–122, 1997.
- [4] J. A. O. Barros, "Comportamento do betão reforçado com fibras - análise experimental e simulação numérica / Behavior of fiber reinforced concrete - experimental and numerical analysis," PhD Thesis, Department of Civil Engineering, FEUP, Portugal, 1995.
- [5] J. A. O. Barros and J. Sena-Cruz, "Fracture energy of steel fiber-reinforced concrete," *Mech. Compos. Mater. Struct.*, vol. 8, no. 1, pp. 29–45, 2001.
- [6] A. M. Brandt, *Cement based composites: materials, mechanical properties, and performance*, 2nd ed. Milton Park, Abingdon, Oxon: Taylor & Francis, 2009.
- [7] N. Banthia, "Fiber reinforced concrete," *ACI SP-142ACI Detroit MI*, pp. 91–119, 1994.
- [8] H. Mazaheripour, J. A. O. Barros, F. Soltanzadeh, and J. Sena-Cruz, "Deflection and cracking behavior of SFRSCC beams reinforced with hybrid prestressed GFRP and steel reinforcements," *Eng. Struct.*, vol. 125, pp. 546–565, Oct. 2016.
- [9] C. Frazão, J. Barros, A. Camões, A. C. Alves, and L. Rocha, "Corrosion effects on pullout behavior of hooked steel fibers in self-compacting concrete," *Cem. Concr. Res.*, vol. 79, pp. 112–122, Jan. 2016.
- [10] S. Grunewald, *Performance-based design of self-compacting fibre reinforced concrete*. Delft: Delft University Press, 2004.
- [11] N. Van Chanh, "Steel fiber reinforced concrete," in *Faculty of Civil Engineering Ho chi minh City university of Technology. Seminar Material*, 2004, pp. 108–116.
- [12] F. Bencardino, L. Rizzuti, G. Spadea, and R. N. Swamy, "Stress-Strain Behavior of Steel Fiber-Reinforced Concrete in Compression," *J. Mater. Civ. Eng.*, vol. 20, no. 3, pp. 255–263, 2008.
- [13] Y. Mohammadi, S. P. Singh, and S. K. Kaushik, "Properties of steel fibrous concrete containing mixed fibres in fresh and hardened state," *Constr. Build. Mater.*, vol. 22, no. 5, pp. 956–965, May 2008.
- [14] Ş. Yazıcı, G. İnan, and V. Tabak, "Effect of aspect ratio and volume fraction of steel fiber on the mechanical properties of SFRC," *Constr. Build. Mater.*, vol. 21, no. 6, pp. 1250–1253, Jun. 2007.
- [15] C. Frazão, J. Barros, J. A. Bogas, and K. Pilakoutas, "An experimental investigation on the post-cracking behaviour of Recycled Steel Fibre Reinforced Concrete," in *3rd FRC International Workshop Fibre Reinforced Concrete: from Design to Structural Applications*, Desenzano del Garda, Italy, 2018, p. 10.
- [16] A. Conforti, F. Minelli, and G. A. Plizzari, "Wide-shallow beams with and without steel fibres: A peculiar behaviour in shear and flexure," *Compos. Part B Eng.*, vol. 51, pp. 282–290, Aug. 2013.
- [17] J.-H. Hwang, D. H. Lee, H. Ju, K. S. Kim, T. H.-K. Kang, and Z. Pan, "Shear Deformation of Steel Fiber-Reinforced Prestressed Concrete Beams," *Int. J. Concr. Struct. Mater.*, vol. 10, no. S3, pp. 53–63, Sep. 2016.
- [18] Y.-K. Kwak, M. O. Eberhard, W.-S. Kim, and J. Kim, "Shear strength of steel fiber-reinforced concrete beams without stirrups," *ACI Struct. J.*, vol. 99, no. 4, pp. 530–538, 2002.
- [19] J. A. O. Barros, B. N. Moraes Neto, G. S. S. A. Melo, and C. M. V. Frazão, "Assessment of the effectiveness of steel fibre reinforcement for the punching resistance of flat slabs by experimental research and design approach," *Compos. Part B Eng.*, vol. 78, pp. 8–25, Sep. 2015.
- [20] K.-H. Tan, P. Paramasivam, and K.-C. Tan, "Cracking characteristics of reinforced steel fiber concrete beams under short- and long-term loadings," *Adv. Cem. Based Mater.*, vol. 2, no. 4, pp. 127–137, Jul. 1995.
- [21] S. A. Altoubat and D. A. Lange, "Creep, shrinkage and cracking of restrained concrete at early age," *Urbana*, vol. 51, p. 61801, 2001.
- [22] P. H. Bischoff, "Tension Stiffening and Cracking of Steel Fiber-Reinforced Concrete," *J. Mater. Civ. Eng.*, vol. 15, no. 2, pp. 174–182, Apr. 2003.
- [23] P. Schumacher, "Rotation capacity of self-compacting steel fiber reinforced concrete," PhD Thesis, Delft University, Delft, Holland, 2006.
- [24] F. Minelli, G. Tiberti, and G. Plizzari, "Crack Control in RC Elements with Fiber Reinforcement," *ACI Spec. Publ.*, vol. 280, p. 18, 2011.
- [25] H. Mazaheripour, J. A. O. Barros, and J. Sena-Cruz, "Tension-stiffening model for FRC reinforced by hybrid FRP and steel bars," *Compos. Part B Eng.*, vol. 88, pp. 162–181, Mar. 2016.
- [26] G. Plizzari, "Bond and splitting crack development in normal and high strength fibre reinforced concrete," in *Proceedings of ASCE Engineering Mechanics Division Conference*, The Johns Hopkins University, 1999.

- [27] L. Lourenço, J. A. Barros, and S. P. F. Santos, "High strength and ductile fibrous concrete of enhanced fire resistance," presented at the Conference of Sociedade Portuguesa de Materiais, FEUP, Porto, Portugal, 2007.
- [28] L. Lourenço, "Betão reforçado com fibras : aplicações e técnicas de inspeção e reforço de elementos estruturais afetados pela ação de um fogo," Tese de doutoramento, Universidade do Minho, Guimarães, Portugal, 2013.
- [29] F. Soltanzadeh, A. E. Behbahani, H. Mazaheripour, and J. A. O. Barros, "Shear resistance of SFRSCC short-span beams without transversal reinforcements," *Compos. Struct.*, vol. 139, pp. 42–61, Apr. 2016.
- [30] fib-federation internationale du beton, *fib Model Code for Concrete Structures 2010*. John Wiley & Sons, 2013.
- [31] RILEM TC 162-TDF, "Final recommendation of RILEM TC 162-TDF: Test and design methods for steel fibre reinforced concrete," *Mater. Struct.*, vol. 36, no. 262, p. 8, 2003.
- [32] S. H. Ahmad *et al.*, "Design Considerations for Steel Fiber Reinforced Concrete," ACI 544.4R-88, 1988.
- [33] M. di Prisco, G. Plizzari, and L. Vandewalle, "Fibre reinforced concrete: new design perspectives," *Mater. Struct.*, vol. 42, no. 9, pp. 1261–1281, Nov. 2009.
- [34] European Committee for Standardization, *Test method for metallic fibered concrete - Measuring the flexural tensile strength (limit of proportionality (LOP), residual)*, vol. EN 14651. 2005.
- [35] RILEM TC 162-TDF, "Recommendations of RILEM TC 162-TDF: Test and design methods for steel fibre reinforced concrete: bending test," *Mater. Struct.*, vol. 35, no. 253, pp. 579–582, 2002.
- [36] European Committee for Standardization, *Concrete Part 1: Specification, performance, production and conformity*, vol. EN 206-1. 2005.
- [37] European Committee for Standardization, *Eurocode 2: Design of concrete structures Part 1-1: General rules and rules for buildings*, vol. NP EN 1992-1-1. 2010.
- [38] J. A. O. Barros, M. Taheri, and H. Salehian, "A model to simulate the moment–rotation and crack width of FRC members reinforced with longitudinal bars," *Eng. Struct.*, vol. 100, pp. 43–56, Oct. 2015.
- [39] M. di Prisco, M. Colombo, and D. Dozio, "Fibre-reinforced concrete in fib Model Code 2010: principles, models and test validation," *Struct. Concr.*, vol. 14, no. 4, pp. 342–361, Dec. 2013.
- [40] A. Blanco, P. Pujadas, A. de la Fuente, S. Cavalaro, and A. Aguado, "Application of constitutive models in European codes to RC–FRC," *Constr. Build. Mater.*, vol. 40, pp. 246–259, Mar. 2013.
- [41] Ali Amin, "Post cracking behaviour of steel fibre reinforced concrete : from material to structure," PhD Thesis, University of New South Wales, Sydney, Australia, 2015.
- [42] F. Laranjeira de Oliveira, "Design-oriented constitutive model for steel fiber reinforced concrete," PhD Thesis, Universitat Politècnica de Catalunya, Catalunya, Spain, 2010.
- [43] L. Ferrara, Y.-D. Park, and S. P. Shah, "Correlation among fresh state behavior, fiber dispersion, and toughness properties of SFRCs," *J. Mater. Civ. Eng.*, vol. 20, no. 7, pp. 493–501, 2008.
- [44] L. Ferrara and A. Meda, "Relationships between fibre distribution, workability and the mechanical properties of SFRC applied to precast roof elements," *Mater. Struct.*, vol. 39, no. 4, pp. 411–420, Aug. 2007.
- [45] P. Stähli, R. Custer, and J. G. M. van Mier, "On flow properties, fibre distribution, fibre orientation and flexural behaviour of FRC," *Mater. Struct.*, vol. 41, no. 1, pp. 189–196, Jan. 2008.
- [46] A. Abrishambaf, V. M. C. F. Cunha, and J. A. O. Barros, "The influence of fibre orientation on the post-cracking tensile behaviour of steel fibre reinforced self-compacting concrete," *Fract. Struct. Integr. J.*, vol. Volume 31, no. 1, pp. 38–53, 2015.
- [47] R. Lameiras, J. A. O. Barros, and M. Azenha, "Influence of casting condition on the anisotropy of the fracture properties of Steel Fibre Reinforced Self-Compacting Concrete (SFRSCC)," *Cem. Concr. Compos.*, vol. 59, pp. 60–76, May 2015.
- [48] Amin Abrishambaf, Joaquim A. O. Barros, and Vitor M. C. F. Cunha, "A state of art study on the fibre orientation and distribution in steel fibre reinforced concrete," University of Minho. School of Engineering, Azurem, 4800-085 Guimarães, Portugal, 13-DEC/E-16, Nov. 2013.
- [49] H. Salehian, "Evaluation of the performance of steel fibre reinforced self-compacting concrete in elevated slab systems; from the material to the structure," PhD Thesis, University of Minho, 2015.
- [50] J. A. Barros, L. A. Lourenço, F. Soltanzadeh, and M. Taheri, "Steel-fibre reinforced concrete for elements failing in bending and in shear," *Eur. J. Environ. Civ. Eng.*, vol. 18, no. 1, pp. 33–65, 2014.
- [51] F. Soltanzadeh, H. Mazaheripour, J. BARROS, M. Taheri, and S. Jose, "Experimental study on shear behavior of HPFRC beams reinforced by hybrid pre-stressed GFRP and steel bars," in *7th International Conference on Fiber Reinforced Polymer (FRP) Composites in Civil Engineering (CICE 2014)*, 2014.
- [52] M. Imam, L. Vandewalle, F. Mortelmans, and D. Van Gemert, "Shear domain of fibre-reinforced high-strength concrete beams," *Eng. Struct.*, vol. 19, no. 9, pp. 738–747, Sep. 1997.
- [53] K. Noghabai, "Beams of fibrous concrete in shear and bending: experiment and model," *J. Struct. Eng.*, vol. 126, no. 2, pp. 243–251, 2000.
- [54] P. Adebar, S. Mindess, D. St Pierre, and B. Olund, "Shear tests of fiber concrete beams without stirrups," *ACI Struct. J.*, vol. 94, no. 1, Jan. 1997.

- [55] Stephen Foster, "Design of FRC beams for shear using the VEM and the draft Model Code approach," in *Shear and punching shear in RC and FRC elements (workshop proceedings)*, Lausanne: fédération internationale du béton, 2010, pp. 195–210.
- [56] Marco di Prisco, Giovanni Plizzari, and Lucie Vandewalle, "MC2010: Overview on the shear provisions for FRC," in *Shear and punching shear in RC and FRC elements (workshop proceedings)*, Lausanne: fédération internationale du béton, 2010, pp. 61–76.
- [57] S. J. Foster, Y. L. Voo, and K. T. Chong, "FE Analysis of Steel Fiber Reinforced Concrete Beams Failing in Shear: Variable Engagement Model," *Spec. Publ.*, vol. 237, pp. 55–70, Aug. 2006.
- [58] E. C. Bentz, F. J. Vecchio, and M. P. Collins, "Simplified modified compression field theory for calculating shear strength of reinforced concrete elements," *ACI Struct. J.*, vol. 103, no. 4, p. 614, 2006.
- [59] V. Sigrist, E. Bentz, M. F. Ruiz, S. Foster, and A. Muttoni, "Background to the *fib* Model Code 2010 shear provisions - part I: beams and slabs," *Struct. Concr.*, vol. 14, no. 3, pp. 195–203, Sep. 2013.
- [60] S. J. Foster, A. Agarwal, and A. Amin, "Design of steel fiber reinforced concrete beams for shear using inverse analysis for determination of residual tensile strength," *Struct. Concr.*, Sep. 2017.
- [61] A. Amin, S. J. Foster, and A. Muttoni, "Derivation of the σ - w relationship for SFRC from prism bending tests," *Struct. Concr.*, vol. 16, no. 1, pp. 93–105, Mar. 2015.
- [62] ASTM International, *Standard Test Method for Flexural Performance of Fiber-Reinforced Concrete (Using Beam With Third-Point Loading)*, vol. ASTM C1609. 2012.
- [63] Italian Board for Standardization, *Steel Fiber Reinforced Concrete—Part I: Definitions, Classification Specification and Conformity—Part II: Test Method for Measuring First Crack Strength and Ductility Indexes*, vol. UNI 11039. 2003.
- [64] Bernardo Nunes de Moraes Neto, "Punching behaviour of flat slabs of steel fibre reinforced concrete submitted to symmetric loading," PhD thesis, Universidade de Brasília, Brasília, Brasil, 2013.
- [65] B. N. Moraes Neto, J. A. O. Barros, and G. S. S. A. Melo, "A model for the prediction of the punching resistance of steel fibre reinforced concrete slabs centrally loaded," *Constr. Build. Mater.*, vol. 46, pp. 211–223, Sep. 2013.
- [66] Y. H. Moussa, "Steel fiber efficiency for flexural reinforcement of reinforced concrete beams with minimum reinforcement ratio," MSc thesis, Universidade Federal do Pará, Belém, Brasil, 2017.
- [67] Aurelio Muttoni and Miguel Fernández Ruiz, "MC2010: The Critical Shear Crack Theory as a mechanical model for punching shear design and its application to code provisions," in *Shear and punching shear in RC and FRC elements (workshop proceedings)*, Lausanne: fédération internationale du béton, 2010, pp. 31–59.
- [68] *Structural concrete: textbook on behaviour, design and performance. Vol. 1: [...]*, 2. ed. Lausanne: International Federation for Structural Concrete (fib), 2009.
- [69] V. Ciampi, R. Eligehausen, V. V. Bertero, and E. P. Popov, *Analytical model for concrete anchorages of reinforcing bars under generalized excitations*. College of Engineering, University of California, 1982.
- [70] M. Pepe, H. Mazaheripour, J. Barros, J. Sena-Cruz, and E. Martinelli, "Numerical calibration of bond law for GFRP bars embedded in steel fibre-reinforced self-compacting concrete," *Compos. Part B Eng.*, vol. 50, pp. 403–412, Jul. 2013.
- [71] A. W. Beeby, "The influence of the parameter ϕ/p_{eff} on crack widths," *Struct. Concr.*, vol. 5, no. 2, pp. 71–83, Jun. 2004.
- [72] *Structural concrete: textbook on behaviour, design and performance. Vol. 2: [...]*, 2. ed. Lausanne: International Federation for Structural Concrete (fib), 2010.
- [73] L. Vandewalle, "Cracking behaviour of concrete beams reinforced with a combination of ordinary reinforcement and steel fibers," *Mater. Struct.*, vol. 33, no. 3, pp. 164–170, 2000.
- [74] *Microsoft Office Excel*. Microsoft.
- [75] C. A. A. Basto and J. A. O. Barros, "Numeric simulation of sections submitted to bending," Department of Civil Engineering, School of Engineering, University of Minho Guimarães,, Portugal, Technical Report 08-DEC/E-46, 2008.
- [76] S. J. Foster and A. Argarwal, "Database for testing shear models for SFRC beams and one-way slabs without stirrups," School of Civil and Environmental Engineering, UNSW Sydney, Sydney, Australia, 2017.
- [77] H. H. Dinh, G. J. Parra-Montesinos, and J. K. Wight, "Shear Strength Model for Steel Fiber Reinforced Concrete Beams without Stirrup Reinforcement," *J. Struct. Eng.*, vol. 137, no. 10, pp. 1039–1051, Oct. 2011.
- [78] E. Cuenca, "On Shear Behavior of Structural Elements Made of Steel Fiber Reinforced Concrete," PhD Thesis, Universitat Politècnica de València, Valencia, Spain, 2015.
- [79] J. Rosenbusch and M. Teutsch, "Shear design with- method," *Proc. RILEM TC*, pp. 105–117, 2003.
- [80] F. Minelli, "Plain and fiber reinforced concrete beams under shear loading: Structural behavior and design aspects," PhD Thesis, Department of Civil Engineering, University of Brescia, Brescia, Italy, 2005.

- [81] H. Aoude, M. Belghiti, W. D. Cook, and D. Mitchell, "Response of steel fiber-reinforced concrete beams with and without stirrups," *ACI Struct. J.*, vol. 109, no. 3, p. 359, 2012.
- [82] K. Jain and B. Singh, "Investigation of steel fibres as minimum shear reinforcement," *Proc. Inst. Civ. Eng. - Struct. Build.*, vol. 167, no. 5, pp. 285–299, May 2014.
- [83] K. Jain and B. Singh, "Deformed steel fibres as minimum shear reinforcement – a comparative appraisal," *Mag. Concr. Res.*, vol. 66, no. 22, pp. 1170–1182, Nov. 2014.
- [84] K. Al-lami, "Experimental Investigation of Fiber Reinforced Concrete Beams," MSc Thesis, Portland State University, 2000.
- [85] T. Greenough and M. Nehdi, "Shear behavior of fiber-reinforced self-consolidating concrete slender beams," *Mater. J.*, vol. 105, no. 5, pp. 468–477, 2008.
- [86] Bryan Erick Barragán, "Failure and toughness of Steel Fiber Reinforced Concrete under tension and shear," PhD Thesis, Universitat Politècnica de Catalunya, Barcelona, Spain, 2002.
- [87] A. Bertozzi and A. Reggia, "Steel fibers for the minimum shear reinforcement of the beams," MSc Thesis, University of Brescia, Brescia, Italy, 2006.
- [88] A. Conforti, "Variable truss model for the shear design of fibre reinforced concrete beams: experimental and analytical study," MSc Thesis, University of Brescia, Brescia, Italy, 2008.
- [89] F. Minelli, G. A. Plizzari, and F. J. Vecchio, "Influence of steel fibers on full-scale RC beams under shear loading," in *Fracture Mechanics of Concrete Structures – High Performance Concrete, Brick-Masonry and Environmental Aspects*, London, 2007, pp. 1523–1531.
- [90] A. Conforti, F. Minelli, and G. A. Plizzari, "Influence of Width-to-Effective Depth Ratio on Shear Strength of Reinforced Concrete Elements without Web Reinforcement," *ACI Struct. J.*, vol. 114, no. 4, Jul. 2017.
- [91] Stephen J. Foster, Ankit Agarwal, and Ali Amin, "Design of SFRC Beams for Shear using Inverse Analysis for determination of Residual Tensile Strength," *Struct. Concr.*, vol. 19, no. 1, pp. 129–140, 2017.
- [92] L. Vandewalle and D. Dupont, "BENDING TEST AND INTERPRETATION," in *International RILEM Workshop on Test and Design Methods for Steel Fibre Reinforced Concrete - Background and Experiences*, 2003, pp. 1–13.
- [93] MP. Collins, "Evaluation of shear design procedures for concrete structures," A Report prepared for the CSA technical committee on reinforced concrete design, Canada, Mar. 2001.
- [94] D. Häbler and Barros, J.A.O, "Exploring the possibilities of steel fibre reinforced self-compacting concrete for the flexural strengthening of masonry structural elements," *Int. J. Archit. Herit. Conserv. Anal. Restor.*, pp. 26–53.
- [95] T. N. S. Htut and S. J. Foster, "Unified model for mixed mode fracture of steel fibre reinforced concrete," in *Proceedings of the 7th International Conference on Fracture Mechanics Concrete and Concrete Structures (FramCoS-7)*, Jeju, Korea, 2010, pp. 1469–1477.
- [96] T. Htut and S. J. Foster, "Fracture of steel fibre reinforced concrete - the unified variable engagement model," The University of the New South Wales, UNSW Sydney, Australia, R-460, 2012.
- [97] Seong-Cheol Lee, Jae-Yeol Cho, and Frank J. Vecchio, "Diverse Embedment Model for Steel Fiber-Reinforced Concrete in Tension: Model Verification," *ACI Mater. J.*, vol. 108, no. 5, 2011.
- [98] J. A. O. Barros, R. K. Varma, J. M. Sena-Cruz, and A. F. M. Azevedo, "Near surface mounted CFRP strips for the flexural strengthening of RC columns: Experimental and numerical research," *Eng. Struct.*, vol. 30, no. 12, pp. 3412–3425, Dec. 2008.
- [99] F. Laranjeira, A. Aguado, C. Molins, S. Grünwald, J. Walraven, and S. Cavalaro, "Framework to predict the orientation of fibers in FRC: A novel philosophy," *Cem. Concr. Res.*, vol. 42, no. 6, pp. 752–768, Jun. 2012.
- [100] H.- Krenchel, "Fibre spacing and specific fibre surface," in *Proceedings of Rilem Symposium on Fibre Reinforced Cement and Concrete*, 1975, pp. 69–79.
- [101] D. Dupont and L. Vandewalle, "Distribution of steel fibres in rectangular sections," *Cem. Concr. Compos.*, vol. 27, no. 3, pp. 391–398, Mar. 2005.
- [102] M. G. Alberti, A. Enfedaque, and J. C. Gálvez, "On the prediction of the orientation factor and fibre distribution of steel and macro-synthetic fibres for fibre-reinforced concrete," *Cem. Concr. Compos.*, vol. 77, pp. 29–48, Mar. 2017.
- [103] T. Htut, "Fracture processes in steel fibre reinforced concrete," PhD Thesis, School of Civil and Environmental Engineering, The University of New South Wales, UNSW Sydney, Australia, 2010.
- [104] T. S. Ng, S. J. Foster, M. L. Htet, and T. N. S. Htut, "Mixed mode fracture behaviour of steel fibre reinforced concrete," *Mater. Struct.*, vol. 47, no. 1–2, pp. 67–76, Jan. 2014.
- [105] S. J. Foster, G. G. Lee, and T. N. S. Htut, "Radiographic imaging for the observation of Modes I and II fracture in Fibre Reinforced Concrete," in *The 6th International Conference on Fracture Mechanics of Concrete and Concrete Structures*, Catania, Italy, 2007, pp. 1457–1465.
- [106] T. N. S. Htut and S. J. Foster, "X-Ray Imaging for the Observation of Mode I Fracture in Fibre Reinforced Concrete," in *The 5th Australasian Congress on Applied Mechanics*, Brisbane, Australia, 2007, pp. 120–125.

- [107] G. G. Lee and S. J. Foster, "Behaviour of steel fibre reinforced mortar in shear I: Direct shear testing," The University of the New South Wales, Sydney, Australia, R-444, 2006.
- [108] P. Marti, T. Pfyler, V. Sigrist, and T. Ulaga, "Harmonized test procedures for steel fibre-reinforced concrete," *ACI Mater. J.*, vol. 96, no. 6, pp. 676–685, 1999.
- [109] C. B. Markwardt, "Non-linear least squares fitting in IDL with MPFIT," in *Astronomical Data Analysis Software and Systems XVIII*, Quebec, Canada, 2009, vol. 411, pp. 251–254.
- [110] E. Pereira, "Steel Fibre Reinforced Self-compacting Concrete: from material to mechanical behaviour," 2006.
- [111] R. M. Lameiras, "Sandwich structural panels comprising thin-walled SFRSCC and GFRP connectors: from material features to structural behaviour," PhD Thesis, Universidade do Minho, Guimarães, Portugal, 2016.
- [112] C. M. V. Frazão, A. Camões, and J. Barros, "Durabilidade do betão auto-compactável reforçado com fibras de aço," *Durability of steel fiber reinforced self-compacting concrete*, 2013.
- [113] Tiago Valente, Delfina Gonçalves, Inês Costa, Rui Costa, and Luís Costa, "Relatório Projeto PreBeamTec - Análise numérica e caracterização experimental," CiviTest - Pesquisa de Materiais para a Engenharia Civil, Lda - Serralharia Cunha, Lda, Braga, Relatório Interno (Confidencial), 2017.
- [114] F. Soltanzadeh, J. A. O. Barros, and R. F. C. Santos, "High performance fiber reinforced concrete for the shear reinforcement: Experimental and numerical research," *Constr. Build. Mater.*, vol. 77, pp. 94–109, Feb. 2015.
- [115] M. Pająk and T. Ponikiewski, "Flexural behavior of self-compacting concrete reinforced with different types of steel fibers," *Constr. Build. Mater.*, vol. 47, pp. 397–408, Oct. 2013.
- [116] F. Soltanzadeh, "High Performance Fiber Reinforced Concrete for the Replacement of Shear Stirrups," PhD Thesis, Universidade do Minho, Guimarães, Portugal, 2016.
- [117] C. G. Berrocal, I. Löfgren, K. Lundgren, N. Görander, and C. Halldén, "Characterisation of bending cracks in R/FRC using image analysis," *Cem. Concr. Res.*, vol. 90, pp. 104–116, Dec. 2016.
- [118] P. Smarzewski and D. Barnat-Hunek, "Fracture properties of plain and steel-polypropylene-fiber-reinforced high-performance concrete," *Mater. Tehnol.*, vol. 49, no. 4, pp. 563–571, Aug. 2015.
- [119] S. Finazzi, I. Paegle, G. Fischer, and F. Minelli, "Influence of bending test configuration on cracking behavior of FRC," in *Proceedings of the 3rd All-Russia (International) Conference on Concrete and Reinforced Concrete*, vol. 3, pp. 196–205.
- [120] M. Taheri and J. Barros, "Experimental and numerical evaluation of flexural response of SFRSCC members reinforced with longitudinal steel and GFRP bars," University of Minho. School of Engineering, Technical Report, May 2015.
- [121] Varma, Rajendra Kumar, "Numerical models for the simulation of the cyclic behaviour of RC structures incorporating new advanced materials," PhD Thesis, Universidade do Minho, 2013.
- [122] M. Jirasek and Z. P. Bazant, *Inelastic Analysis of Structures*, 1st edition. John Wiley & Sons Ltd, 2001.
- [123] R. I. Gilbert and G. Ranzi, *Time-dependent behaviour of concrete structures*. London ; New York: Spon, 2011.
- [124] K.-W. Lee, *Nonlinear Time Dependent Design and Analysis of Slender Reinforced Concrete Columns*. Cuuillier Verlag, 2004.
- [125] J. Newman and B. S. Choo, *Advanced concrete technology 1 : Concrete Properties*, vol. 1, 4 vols. Butterworth-Heinemann, 2003.
- [126] G. J. Creus, *Viscoelasticity—basic theory and applications to concrete structures*, vol. 16. Springer Science & Business Media, 2012.
- [127] D. Roylance, *Mechanics of Materials*. Wiley, 1995.
- [128] Z. P. Bazant and R. L'Hermite, *Mathematical modeling of creep and shrinkage of concrete*. John Wiley & Sons Ltd, 1988.
- [129] D. McHenry, "A new aspect of creep in concrete and its application to design," in *Proc. ASTM*, 1943, vol. 43, pp. 1069–1084.
- [130] Z. P. Bazant, "Theory of creep and shrinkage in concrete structures: A precis of recent developments," *Mech. Today*, vol. 2, pp. 1–93, 1975.
- [131] Z. P. Bazant and F. H. Wittmann, *Creep and Shrinkage in Concrete Structures*. John Wiley & Sons Ltd, 1982.
- [132] L. L. Yue and L. Taerwe, "Two-function method for the prediction of concrete creep under decreasing stress," *Mater. Struct.*, vol. 26, no. 5, pp. 268–273, 1993.
- [133] Z. P. Bazant and S.-S. Kim, "Nonlinear creep of concrete—adaptation and flow," *J. Eng. Mech. Div.*, vol. 105, no. 3, pp. 429–446, 1979.
- [134] Z. P. Bazant, T. Tsubaki, and Z. Celep, "Singular history integral for creep rate of concrete," *J. Eng. Mech.*, vol. 109, no. 3, pp. 866–884, 1983.
- [135] A. M. Neville, W. H. Dilger, and J. J. Brooks, *Creep of plain and structural concrete*. Construction press, 1983.
- [136] Z. P. Bazant, "Prediction of concrete creep and shrinkage: past, present and future," *Nucl. Eng. Des.*, vol. 203, no. 1, pp. 27–38, 2001.

- [137] I. Pignatelli, A. Kumar, R. Alizadeh, Y. Le Pape, M. Bauchy, and G. Sant, "A dissolution-precipitation mechanism is at the origin of concrete creep in moist environments," *J. Chem. Phys.*, vol. 145, no. 5, p. 054701, Aug. 2016.
- [138] N. J. Gardner, "Guide for Modeling and Calculating Shrinkage and Creep in Hardened Concrete," ACI, ACI 209.2R-08, 2008.
- [139] P. Monteiro, *Concrete: Microstructure, Properties, and Materials*. McGraw-Hill Publishing, 2006.
- [140] Adriaan Greeff Van Zijl, "Computational modelling of masonry creep and shrinkage," PhD Thesis, University of Delft, 2000.
- [141] Z. P. Bažant and S. Prasannan, "Solidification Theory for Concrete Creep. I: Formulation," *J. Eng. Mech.*, vol. 115, no. 8, pp. 1691–1703, 1989.
- [142] Z. P. Bažant and S. Prasannan, "Solidification Theory for Concrete Creep. II: Verification and Application," *J. Eng. Mech.*, vol. 115, no. 8, pp. 1704–1725, 1989.
- [143] Z. P. Bažant, A. B. Hauggaard, S. Baweja, and F.-J. Ulm, "Microprestress-Solidification Theory for Concrete Creep. I: Aging and Drying Effects," *J. Eng. Mech.*, vol. 123, no. 11, pp. 1188–1194, 1997.
- [144] Z. P. Bažant, A. B. Hauggaard, and S. Baweja, "Microprestress-Solidification Theory for Concrete Creep. II: Algorithm and Verification," *J. Eng. Mech.*, vol. 123, no. 11, pp. 1195–1201, 1997.
- [145] L. Østergaard, D. A. Lange, S. A. Altoubat, and H. Stang, "Tensile basic creep of early-age concrete under constant load," *Cem. Concr. Res.*, vol. 31, no. 12, pp. 1895–1899, Dec. 2001.
- [146] B. Eirle and K. Schikora, "Computational viscoelasticity of aging materials," presented at the European Conference on Computational Mechanics, Munchen, Germany, 1999.
- [147] A. Hilaire, F. Benboudjema, A. Darquennes, Y. Berthaud, and G. Nahas, "Modeling basic creep in concrete at early-age under compressive and tensile loading," *Nucl. Eng. Des.*, vol. 269, pp. 222–230, Apr. 2014.
- [148] A. M. Neville, "Creep of Concrete : Plain, Reinforced, and Prestressed," Feb. 1971.
- [149] RILEM TC 107, "TC 107 - Guidelines for characterizing concrete creep and shrinkage in structural design codes or recommendations," *Mater. Struct.*, vol. 28, pp. 52–55, 1995.
- [150] Z. P. Bazant, "Criteria for rational prediction of creep and shrinkage of concrete," *ACI Spec. Publ.*, vol. 194, pp. 237–260, 2000.
- [151] Z. P. Bažant and S. S. Kim, "Can the creep curves for different loading ages diverge?," *Cem. Concr. Res.*, vol. 8, no. 5, pp. 601–611, Sep. 1978.
- [152] Z. P. Bažant and E. Osman, "Double power law for basic creep of concrete," *Matér. Constr.*, vol. 9, no. 1, pp. 3–11, 1976.
- [153] F. Wittmann, "Bestimmung Physikalischer Eigenschaften des Zementsteins," *Dtsch. Aussch. Fuer Stahlbeton*, no. 232, 1974.
- [154] Z. P. Bažant and L. Panula, "Practical prediction of time-dependent deformations of concrete - Part III: Drying Creep," *Mater. Struct.-Mater. Constr.*, vol. 11, no. 66, pp. 415–424, 1978.
- [155] Z. P. Bazant and L. Panula, "Practical prediction of time-dependent deformations of concrete - Part IV: Temperature effect on Basic Creep," *Mater. Struct.-Mater. Constr.*, vol. 11, no. 66, pp. 425–434, 1978.
- [156] Z. P. Bažant and L. Panula, "Practical prediction of time-dependent deformations of concrete - Part V: Temperature effect on Drying Creep," *Matér. Constr.*, vol. 12, no. 69, pp. 169–174, 1979.
- [157] Z. P. Bazant and L. Panula, "Practical prediction of time-dependent deformation of concrete - Part VI: Cyclic creep, nonlinearity and statistical scatter," *Mater. Struct.-Mater. Constr.*, vol. 12, no. 69, pp. 175–183, 1979.
- [158] E. Eo, "Log Double Power Law for Concrete Creep," 1985.
- [159] Z. P. Bažant and J.-C. Chern, "Triple Power Law for Concrete Creep," *J. Eng. Mech.*, vol. 111, no. 1, pp. 63–83, 1985.
- [160] Piaras Kelly, *Solid Mechanics Part I: An Introduction to Solid Mechanics*. Department of Engineering Science, University of Auckland.
- [161] K. Li, Y. Ju, J. Han, and C. Zhou, "Early-age stress analysis of a concrete diaphragm wall through tensile creep modeling," *Mater. Struct.*, vol. 42, no. 7, pp. 923–935, Aug. 2009.
- [162] R. Faria, M. Azenha, and J. A. Figueiras, "Modelling of concrete at early ages: Application to an externally restrained slab," *Cem. Concr. Compos.*, vol. 28, no. 6, pp. 572–585, Jul. 2006.
- [163] H.-S. Chiu, J.-C. Chern, and K.-C. Chang, "Long-term deflection control in cantilever prestressed concrete bridges. I: control method," *J. Eng. Mech.*, vol. 122, no. 6, pp. 489–494, 1996.
- [164] I. Pane and W. Hansen, "Early age creep and stress relaxation of concrete containing blended cements," *Mater. Struct.*, vol. 35, no. 2, pp. 92–96, 2002.
- [165] Comité Euro-International du Béton, *CEB-FIP Model Code 1990*. Thomas Telford, 1993.
- [166] R. Wendner, M. H. Hubler, and Z. P. Bažant, "Statistical justification of model B4 for multi-decade concrete creep using laboratory and bridge databases and comparisons to other models," *Mater. Struct.*, vol. 48, no. 4, pp. 815–833, Apr. 2015.

- [167] F. Mola and L. M. Pellegrini, "The new model for creep of concrete in FIP Model Code 2010," in *Proceedings of the 37th Conference: Our World in Concrete & Structures*, 2012, pp. 53–66.
- [168] Z. P. Bazant and S. Baweja, "Creep and shrinkage prediction model for analysis and design of concrete structures— model B3," *Mater. Struct.*, vol. 28, no. 6, pp. 357–365, Jul. 1995.
- [169] M. Jirásek and P. Havlásek, "Microprestress–solidification theory of concrete creep: Reformulation and improvement," *Cem. Concr. Res.*, vol. 60, pp. 51–62, Jun. 2014.
- [170] Z. P. Bazant and S. Baweja, "Creep and shrinkage prediction model for analysis and design of concrete structures: Model B3," *ACI Spec. Publ.*, vol. 194, pp. 1–84, 2000.
- [171] Zdenek P. Bazant and Sandeep Baweja, "TC 107-GCS - Guidelines for the formulation of creep and shrinkage models - Addendum to Recommendations: Short form of creep and shrinkage predictin model B3 for structures of medium sensitivity," *Mater. Struct.*, vol. 29, no. 194, pp. 587–593, 1996.
- [172] Z. P. Bazant and J. K. Kim, "Improved prediction model for time-dependent deformations of concrete: Part 4- Temperature effects," *Mater. Struct.*, vol. 25, no. 2, pp. 84–94, 1992.
- [173] Z. P. Bazant, J.-K. Kim, and L. Panula, "Improved prediction model for time-dependent deformations of concrete: Part 5–Cyclic load and cyclic humidity," *Mater. Struct.*, vol. 25, no. 147, pp. 163–169, 1992.
- [174] R. Wendner, M. H. Hubler, and Z. P. Bažant, "The B4 Model for Multi-decade Creep and Shrinkage Prediction," in *Mechanics and Physics of Creep, Shrinkage, and Durability of Concrete: A Tribute to Zdeněk P. Bažant*, Cambridge, Massachusetts, 2013, pp. 429–436.
- [175] RILEM Technical Committee TC-242-MDC (Zdeněk P. Bažant, chair), "RILEM draft recommendation: TC-242-MDC multi-decade creep and shrinkage of concrete: material model and structural analysis*: Model B4 for creep, drying shrinkage and autogenous shrinkage of normal and high-strength concretes with multi-decade applicability," *Mater. Struct.*, vol. 48, no. 4, pp. 753–770, Apr. 2015.
- [176] R. Wendner, M. H. Hubler, and Z. P. Bazant, "Statistical justification of Model B4 for multi-decade concrete creep and comparisons to other models using laboratory and bridge databases," *RILEM Mater Struct Accept.*, 2014.
- [177] L. Vandewalle, "Concrete creep and shrinkage at cyclic ambient conditions," *Cem. Concr. Compos.*, vol. 22, no. 3, pp. 201–208, Jun. 2000.
- [178] Z. P. Bažant and S. Baweja, "Justification and refinements of model B3 for concrete creep and shrinkage 1. statistics and sensitivity," *Mater. Struct.*, vol. 28, no. 7, pp. 415–430, Aug. 1995.
- [179] P. Silva, T. Valente, and M. Azenha, "Analytical and numerical evaluation of creep data," Universidade do Minho. Escola de Engenharia. Departamento de Engenharia Civil, Guimarães, Portugal, 2015.
- [180] Patrícia Silva, Tiago Valente, Miguel Azenha, José Sena-Cruz, and Joaquim Barros, "Viscoelastic Response of an Epoxy Adhesive for Construction since its Early Ages : Experiments and Modelling," *Compos. Part B Eng.*, vol. 116, pp. 266–277, May 2017.
- [181] A. H. Bryant and C. Vadhanavikkit, "Creep, Shrinkage-Size, and Age at Loading Effects," *Mater. J.*, vol. 84, no. 2, pp. 117–123, Mar. 1987.
- [182] Y. Lee, S.-T. Yi, M.-S. Kim, and J.-K. Kim, "Evaluation of a basic creep model with respect to autogenous shrinkage," *Cem. Concr. Res.*, vol. 36, no. 7, pp. 1268–1278, Jul. 2006.
- [183] Z. P. Bazant and S. T. Wu, "Dirichlet series creep function for aging concrete," *J. Eng. Mech.*, vol. 99, no. em2, 1973.
- [184] Z. P. Bazant and J.-C. Chern, "Rate-type concrete creep law with reduced time," *J. Eng. Mech.*, vol. 110, no. 3, pp. 329–340, 1984.
- [185] R. Christensen, *Theory of Viscoelasticity: An Introduction*. Elsevier, 2012.
- [186] Rui Póvoas, "Modelos Não-lineares de Análise e Dimensionamento," PhD Thesis, FEUP, Porto, 1991.
- [187] R. Bro and S. De Jong, "A fast non-negativity-constrained least squares algorithm," *J. Chemom.*, vol. 11, no. 5, pp. 393–401, 1997.
- [188] D. Chen and R. J. Plemmons, "Nonnegativity Constraints in Numerical Analysis," presented at the Symposium on the Birth of Numerical Analysis, 2009.
- [189] A. V. Gouveia, J. A. Barros, Á. F. Azevedo, and J. Sena-Cruz, "Multi-fixed smeared 3d crack model to simulate the behavior of fiber reinforced concrete structures," presented at the CCC 2008 - Challenges for Civil Construction, Porto, 2008.
- [190] A. Ventura-Gouveia, "Constitutive models for the material nonlinear analysis of concrete structures including time dependent effects," PhD Thesis, Department of Civil Engineering, University of Minho, 2011.
- [191] R. De Borst and P. Nauta, "Non-orthogonal cracks in a smeared finite element model," *Eng. Comput.*, vol. 2, no. 1, pp. 35–46, 1985.
- [192] R. De Borst, "Smeared cracking, plasticity, creep, and thermal loading—A unified approach," *Comput. Methods Appl. Mech. Eng.*, vol. 62, no. 1, pp. 89–110, May 1987.
- [193] J. G. Rots, "Computational modeling of concrete fracture," Dissertation, Technische Hogeschool Delft, Delft, 1988.

- [194] V. D. da Silva, *Mechanics and strength of materials*. Berlin ; New York: Springer, 2006.
- [195] Ventura-Gouveia, A, Barros, J.A.O., and Azevedo, A.F.M., "Thermo-mechanical model for the material nonlinear analysis of cement based materials," in *Framcos-9*, Berkeley, California USA, 2016.
- [196] H. W. Reinhardt, J. Blaauwendraad, and J. Jongedijk, "Temperature development in concrete structures taking account of state dependent properties," in *Int. conf. concrete at early ages, Paris, France*, 1982.
- [197] Ricardo Oliveira, Miguel Azenha, José Granja, and Erika Guimarães, "Report 3 Task 3 – Experimental program and round robin testing," University of Minho. School of Engineering, Guimarães, Portugal, 2015.
- [198] K. H. Tan and M. K. Saha, "Long-Term Deflections of Reinforced Concrete Beams Externally Bonded with FRP System," *J. Compos. Constr.*, vol. 10, no. 6, pp. 474–482, Dec. 2006.
- [199] M. Coelho, "Bond behaviour of NSM FRP systems in concrete," PhD Thesis, Universidade do Minho, Guimarães, Portugal, 2016.
- [200] Joaquim A. O. Barros and Marco di Prisco, "Assessing the possibilities of fibre reinforced concrete for underground prefabricated structures," Universidade do Minho. Escola de Engenharia. Departamento de Engenharia Civil., Guimarães, Portugal, Research carried out within the ambit of the sabbatical licence Report 09-DEC/E-12, Oct. 2009.
- [201] W. S. Chia, B. F. McCullough, and N. H. Burns, "Field evaluation of subbase friction characteristics," Center of Transportation Research Bureau of Engineering Research The University of Texas at Austin, Research Report 401-5, 1986.
- [202] J. W. Wesevich, B. F. McCullough, and N. H. Burns, "Stabilized subbase friction study for concrete pavements," Center of Transportation Research Bureau of Engineering Research The University of Texas at Austin, Research Report 459-1, 1987.
- [203] Y. Chan Suh, S. Woo Lee, and M. Soo Kang, "Evaluation of Subbase Friction for Typical Korean Concrete Pavement," *Transp. Res. Rec. J. Transp. Res. Board*, vol. 1809, pp. 66–73, Jan. 2002.
- [204] S. R. Maitra, K. S. Reddy, and L. S. Ramachandra, "Experimental evaluation of interface friction and study of its influence on concrete pavement response," *J. Transp. Eng.*, vol. 135, no. 8, pp. 563–571, 2009.
- [205] G. A. Chang and J. B. Mander, "Seismic Energy Based Fatigue Damage Analysis of Bridge Columns: Part 1 - Evaluation of Seismic Capacity," 1994.
- [206] M. Menegotto and P. E. Pinto, "Method of analysis for cyclically loaded R.C. plane frames including changes in geometry and non-elastic behaviour of elements under combined normal force and bending," 1973.
- [207] V. Gouveia, J. Barros, Á. Azevedo, and J. S. Cruz, *Implementação da técnica do arc-length e métodos relacionados no programa de elementos finitos FEMIX*. Escola Superior de Tecnologia do Instituto Politécnico de Viseu, 2006.
- [208] H. Mazaheripour, "Structural behavior of hybrid GFRP and steel reinforced FRC prestressed beams," Universidade do Minho, 2015.
- [209] J. A. O. Barros and S. J. Foster, "An integrated approach for predicting the shear capacity of fibre reinforced concrete beams," *Eng. Struct.*, vol. 174, pp. 346–357, Nov. 2018.

APPENDIX A

In Table 22 are presented the reference values of concrete mechanical properties based on the existing strength classes.

Table 22 – Reference values of concrete mechanical properties for each strength class [30].

Strength classes	f_{ck} [MPa]	ε_{c3} [-]	ε_{cu3} [-]	E_c [GPa]	f_{ctm} [MPa]
C12/16	12.0	1.750E-03	3.50E-03	27.0	1.6
C16/20	16.0	1.750E-03	3.50E-03	29.0	1.9
C20/25	20.0	1.750E-03	3.50E-03	30.0	2.2
C25/30	25.0	1.750E-03	3.50E-03	31.0	2.6
C30/37	30.0	1.750E-03	3.50E-03	33.0	2.9
C35/45	35.0	1.750E-03	3.50E-03	34.0	3.2
C40/50	40.0	1.750E-03	3.50E-03	35.0	3.5
C45/55	45.0	1.750E-03	3.50E-03	36.0	3.8
C50/60	50.0	1.750E-03	3.50E-03	37.0	4.1
C55/67	55.0	1.800E-03	3.10E-03	38.0	4.2
C60/75	60.0	1.900E-03	2.90E-03	39.0	4.4
C70/85	70.0	2.000E-03	2.70E-03	41.0	4.6
C80/95	80.0	2.200E-03	2.60E-03	42.0	4.8
C90/105	90.0	2.300E-03	2.60E-03	44.0	5.0

APPENDIX B

The rigid-plastic and linear models are derived from the observed results of 3PNBBT to describe the uniaxial tension behavior of FRC.

The rigid-plastic model is derived from an ultimate design analysis of FRC cross-section of the notched beams, and considers that the compressive force is concentrated in the top fiber of the section, while the tensile post-cracking strength of the FRC is distributed along the cross-section with a constant stress of f_{Ftu} (Figure 155) [30].

The value of f_{Ftu} can be obtained by equating the internal resisting moment of the cross-section, $M_{u,int}$, and the external applied moment, $M_{u,ext}$, considering the forces acting on the beam during the 3PNBBT at ULS. Considering that at ULS the ultimate crack opening of FRC is equal to $w_u = CMOD_3 = 2.5mm$, which and that considering a linear-elastic stress distribution in the specimen critical cross-section (notch zone) the maximum stress in the cross-section corresponds to the residual flexural strength f_{R3} [39] (Figure 155), the expression that yields in the relationship between f_{Ftu} and f_{R3} presented in Eq. (2.15), can be deduced from:

$$M_{u,ext} = M_{u,int} \Leftrightarrow \frac{f_{R3} \cdot b \cdot h_{sp}^2}{6} = \frac{f_{Ftu} \cdot b \cdot h_{sp}^2}{2} \Leftrightarrow f_{Ftu} = \frac{f_{R3}}{3} \quad \text{Eq. (B.1)}$$

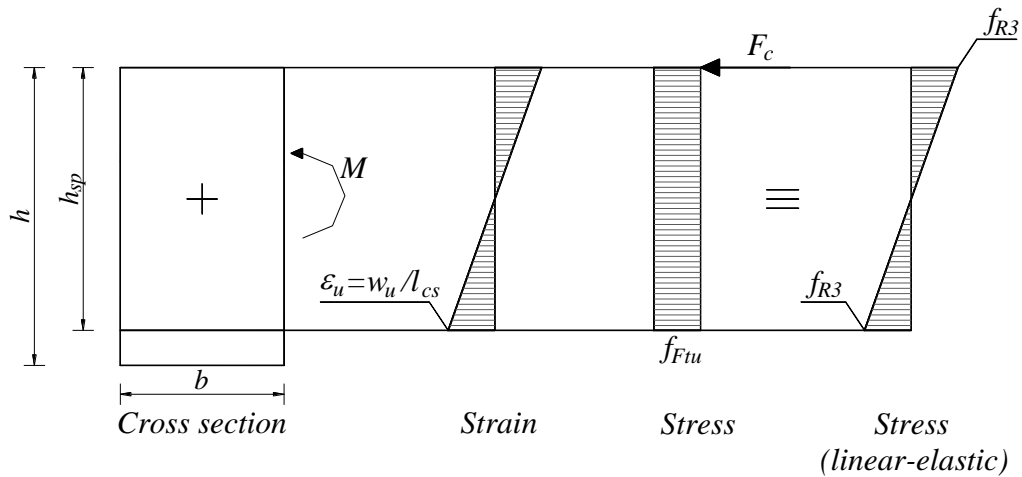


Figure 155 – Stress-strain distribution in 3PNBBT critical cross-section at ULS considering the rigid-plastic model for FRC.

The linear model is defined by two variables: the serviceability and ultimate residual tensile strength, f_{Fts} and f_{Ftu} , respectively. Each variable is defined according to different assumptions at SLS and ULS.

At SLS it is considered that the FRC in the notched beam cross-section assumes an elastoplastic stress distribution for FRC in tension and linear-elastic stress distribution in compression [30]. Considering a linear-elastic stress distribution assumed for the critical cross-section of 3PNBBT (Figure 156) at SLS, the serviceability residual tensile strength f_{Fts} can be derived from following set of equilibrium equations:

$$\begin{cases} \sum F = 0 \\ M_{s,int} = M_{s,ext} \end{cases} \Leftrightarrow \begin{cases} \sigma \cdot b \cdot x - \frac{f_{Fts} \cdot b \cdot q}{2} - f_{Fts} \cdot b \cdot (y - q) = 0 \\ f_{Fts} \cdot b \cdot y \cdot \left(\frac{2}{3} \cdot x + \frac{y}{2} \right) - \frac{f_{Fts} \cdot b \cdot q}{2} \cdot \left(\frac{1}{3} \cdot q + \frac{2}{3} \cdot x \right) = \frac{f_{R1} \cdot b \cdot h_{sp}^2}{6} \end{cases} \quad \text{Eq. (B.2)}$$

$$\sigma = E_c \cdot \chi \cdot x \quad \text{Eq. (B.3)}$$

$$q = \frac{f_{Fts} \cdot x}{\sigma} \quad \text{Eq. (B.4)}$$

$$\chi = \frac{w}{l_{cs} \cdot y} \quad \text{Eq. (B.5)}$$

where, $w = CMOD_1 = 0.5mm$ and $y = h_{sp} - x$.

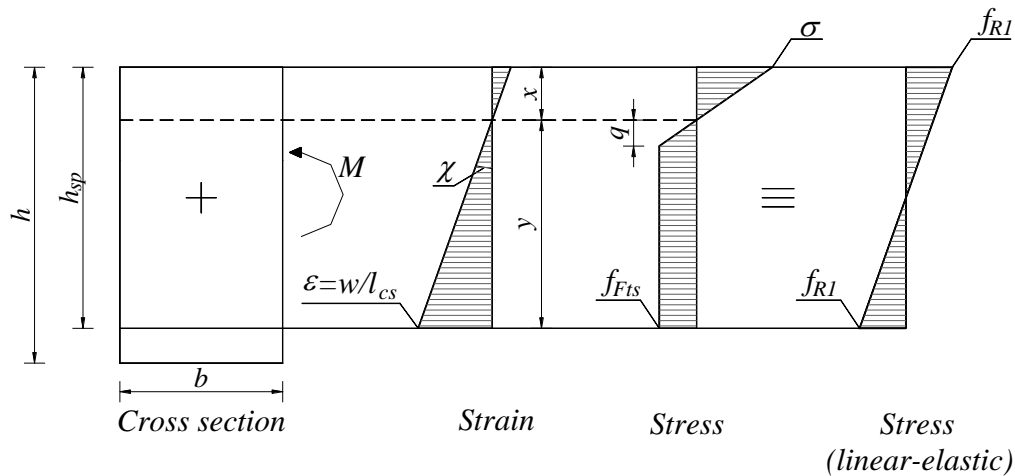


Figure 156 – Stress-strain distribution in 3PNBBT critical cross-section at SLS for determination of f_{Fts} .

The resolution of the set of equilibrium equations Eq. (B.2) yields a correlation between f_{Fts} and f_{R1} that depends on the Young's modulus, E_c , and of the structural characteristic length, l_{cs} , namely [39]:

$$f_{Fts} = k_a \cdot (E_c, l_{cs}) \cdot f_{R1} \quad \text{Eq. (B.6)}$$

Considering that $l_{cs} = h_{sp}$, the factor k_a changes with the Young's modulus, ranging between 0.362 and 0.375 (Figure 157), with an average value of $k_a = 0.37$ [39].

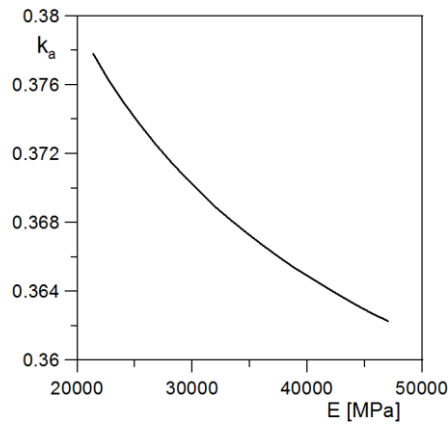


Figure 157 – Values of k_a for the linear model and considering $l_{cs} = h_{sp}$ (extracted from [39]).

At ULS it is considered that the compressive stress is concentrated in the top fiber of the critical cross-section, and that the FRC assumes a linear stress distribution along the cross-section. It is assumed that the tensile strength varies from $k_b \cdot f_{R1}$ at $w=0$, and f_{Ftu} at $w = w_u = 2.5mm$ [39]. Considering the rotational equilibrium of the cross-section, f_{Ftu} can be defined as:

$$\sum M_{u,int} = \sum M_{u,ext} \Leftrightarrow \frac{f_{Ftu} \cdot b \cdot h_{sp}^2}{2} + (k_b \cdot f_{R1} - f_{Ftu}) \cdot \frac{b \cdot h_{sp}^2}{3} = \frac{f_{R3} \cdot b \cdot h_{sp}^2}{6} \quad \text{Eq. (B.7)}$$

$$f_{Ftu} = 0.5 \cdot f_{R3} - \frac{k_b}{2} \cdot f_{R1}$$

Considering that the linear model has also to pass in the point $w = \text{CMOD}_1 = 0.5mm$, $f_{Fts} = k_a \cdot f_{R1} = 0.37 \cdot f_{R1}$, the value of k_b can be obtained from:

$$k_b = 0.529 - 0.143 \cdot \frac{f_{R3}}{f_{R1}} \quad \text{Eq. (B.8)}$$

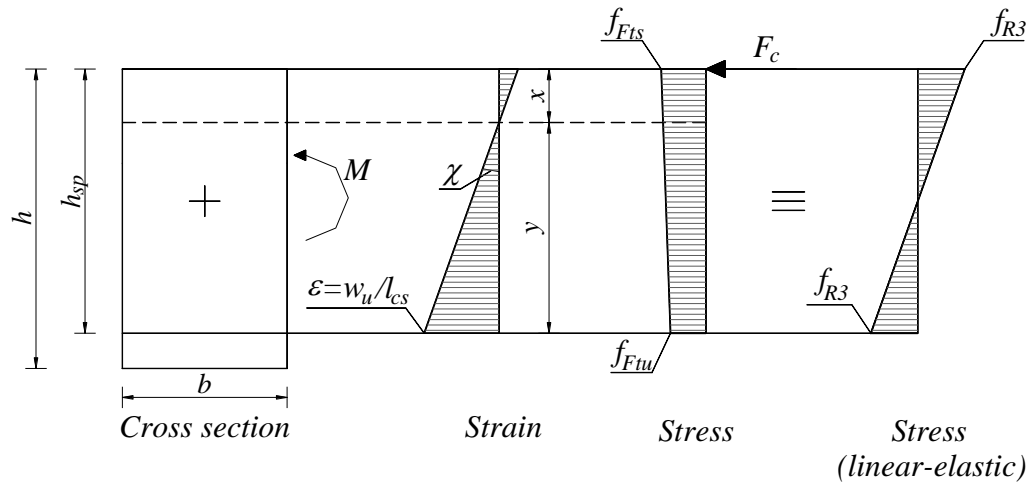


Figure 158 – Stress-strain distribution in 3PNBBT critical cross-section at SLS for determination of f_{Ftu} .

In order to obtain the expression presented in Eq. (2.16), it is introduced in Eq. (B.8) the lower limit of the expression presented in Eq. (2.3), $f_{R3} = 0.5 \cdot f_{R1}$, and k_b takes the value of:

$$k_b = 0.45 \quad \text{Eq. (B.9)}$$

Introducing the value of k_b in Eq. (B.7), the ultimate residual tensile strength for $w_u = 2.5\text{mm}$ can be obtained by:

$$f_{Ftu} = 0.5 \cdot f_{R3} - 0.225 \cdot f_{R1} \cong 0.5 \cdot f_{R3} - 0.2 \cdot f_{R1} \quad \text{Eq. (B.10)}$$

The expression presented in Eq. (2.17) corresponds to the ultimate residual tensile strength of the linear model that can be calculated for ultimate crack opening values that differ from $w_u \neq \text{CMOD}_3$.

APPENDIX C

In the present section are presented the derivation of the compatibility and equilibrium equations of the generic rectangular cross-section presented in Figure 35, that are implemented in the software *FRCCalc*.

Based on Figure 35 the forces and moment equilibrium equations in the cross-section are:

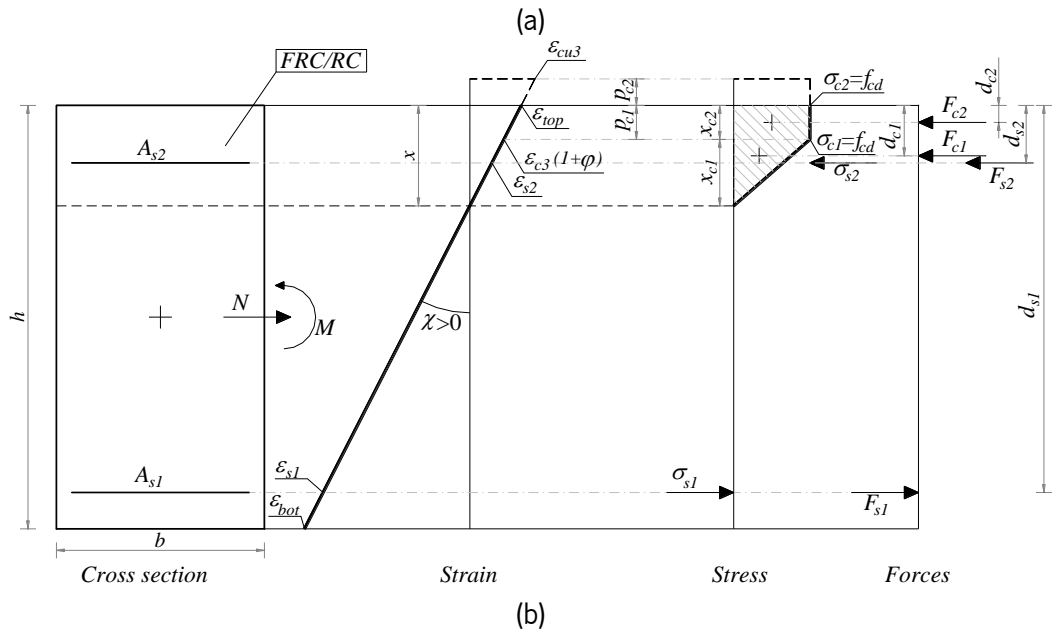
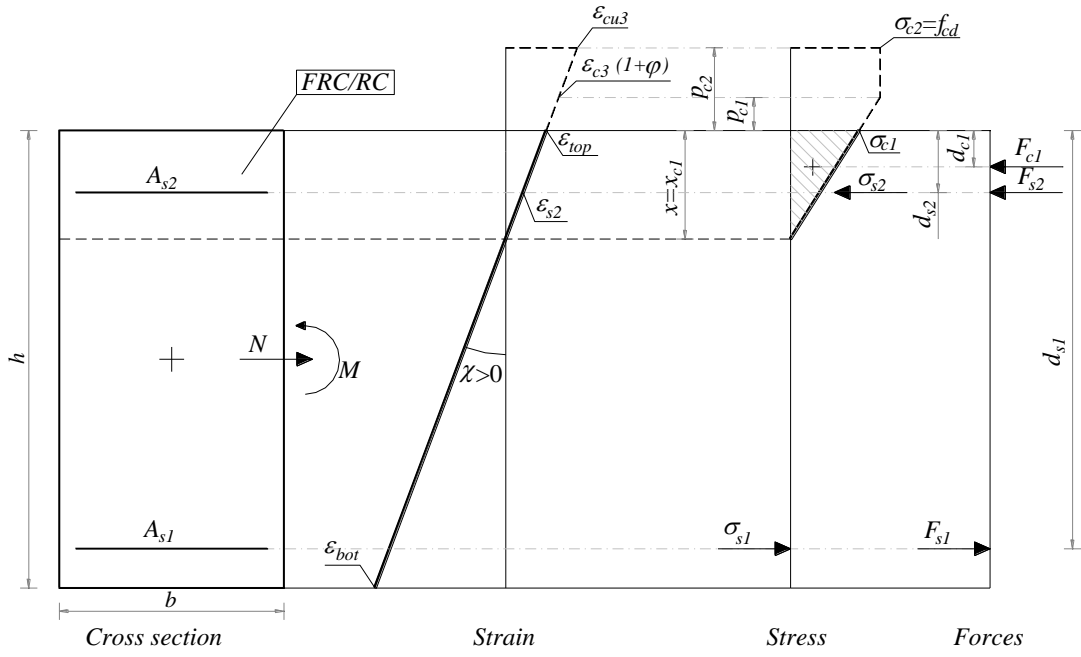
$$\left\{ \begin{array}{l} \sum F = N \\ \sum F_i \cdot d_i = M \end{array} \right\} \Leftrightarrow \left\{ \begin{array}{l} F_s + F_{t,u} + F_{t,r} + F_c = N \\ M_s + M_{t,u} + M_{t,r} + M_c + N \cdot \frac{h}{2} = M \end{array} \right. \quad \text{Eq. (C.1)}$$

From Figure 35 is also possible to define the following compatibility relationships:

$$\left\{ \begin{array}{l} \varepsilon_{top} = -\chi \cdot x \\ \varepsilon_i = \varepsilon_{top} + \chi \cdot p_i \end{array} \right. \quad \text{Eq. (C.2)}$$

where d_i is the depth of the resultant internal forces, relatively to the top fiber of the cross-section; and χ is the curvature of the cross-section.

By specifying the bilinear diagram for concrete in compression (section 2.3.1), the distribution of compressive stress (σ_{c1}, σ_{c2}), forces (F_{c1}, F_{c2}) and forces depth (d_{c1}, d_{c2}) in the cross-section is presented in Figure 159 and Figure 160, for situations where the neutral axis position is inside the cross-section and member presents positive and negative curvature respectively. For situations where the neutral axis position is outside the cross-section is assumed a virtual compressive force between the neutral axis and the face of the cross-section ($F_{c1,v}, F_{c2,v}$), as can be seen in Figure 161 and Figure 162.



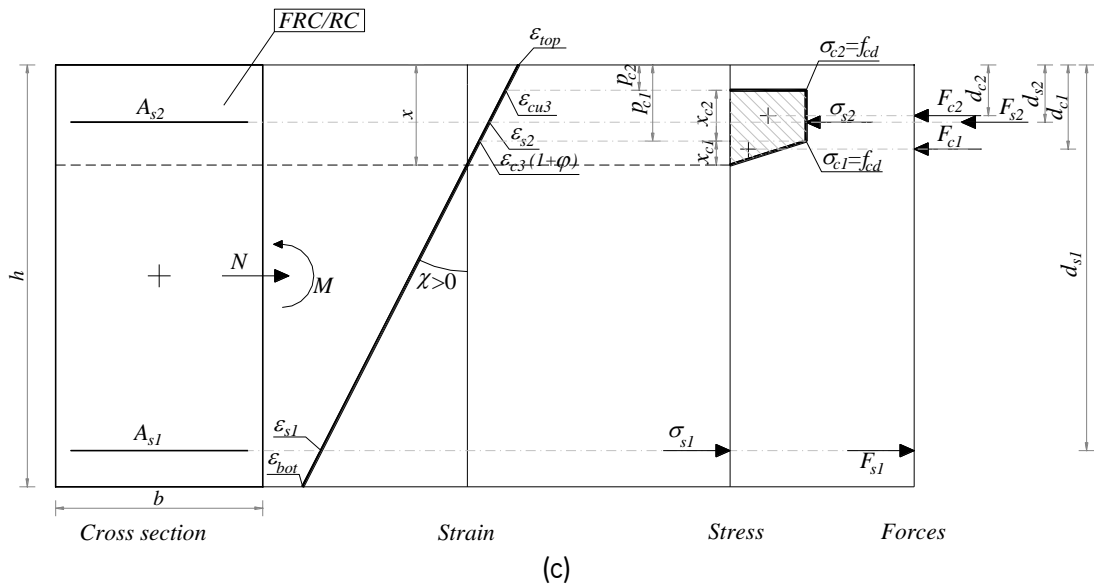
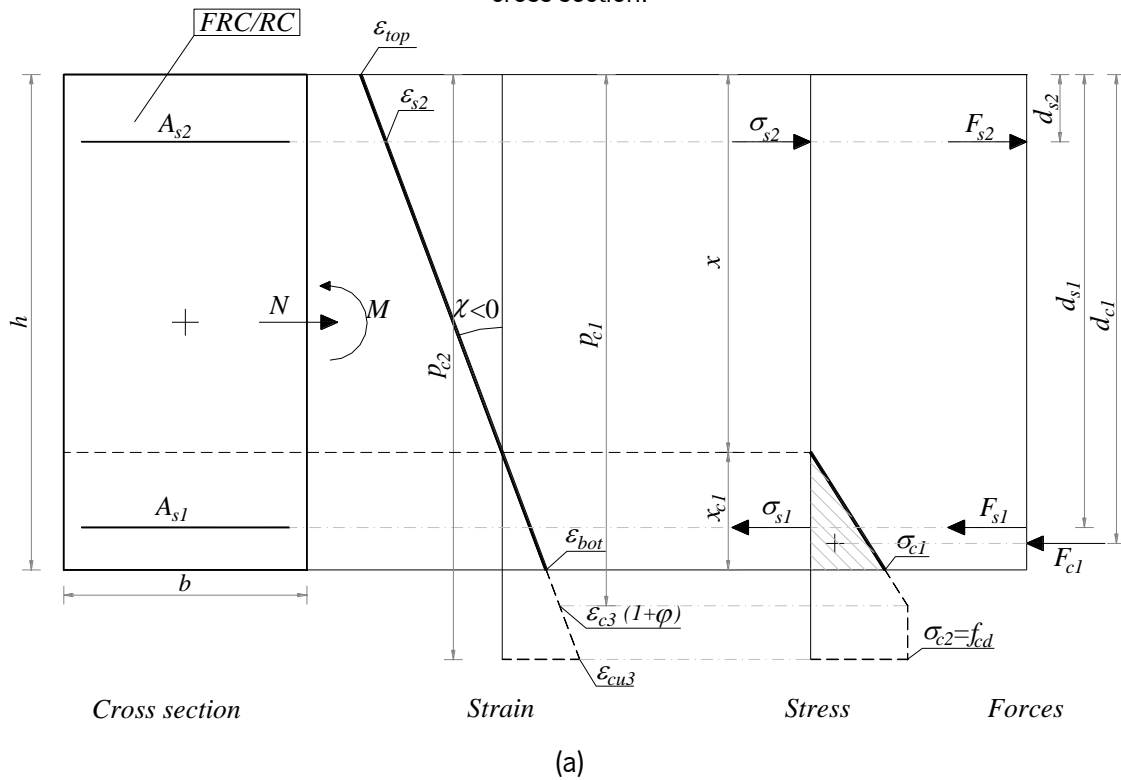
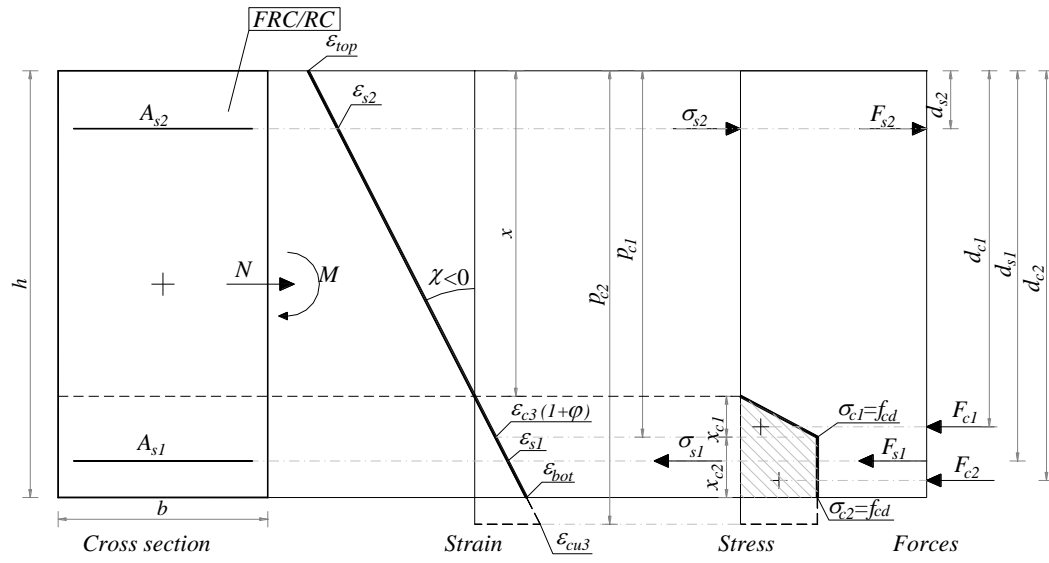
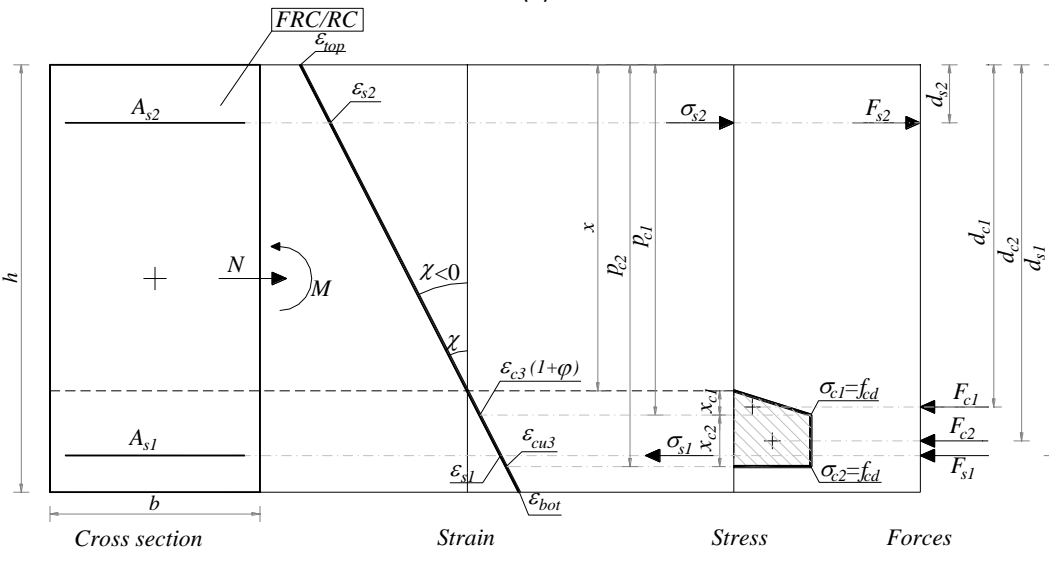


Figure 159 – Stress, strain, compressive forces and forces depth for the compressive zone of the cross-section applying the bilinear model, for positive curvature and neutral axis position inside the cross-section.



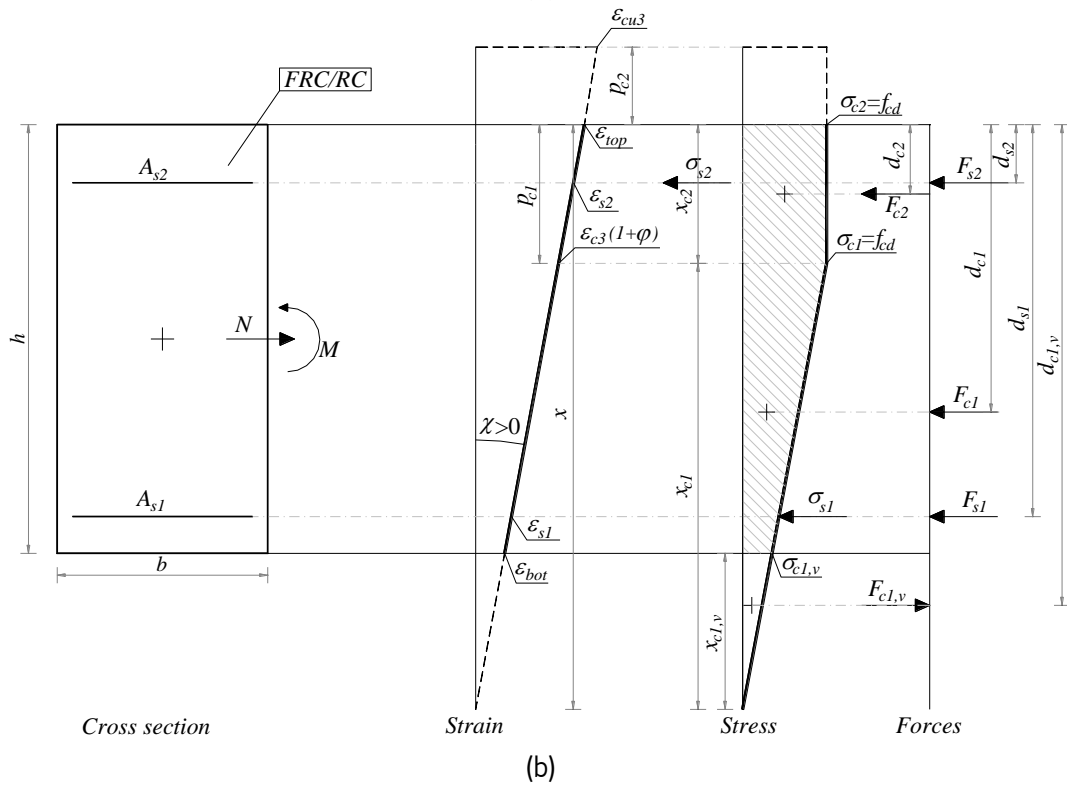
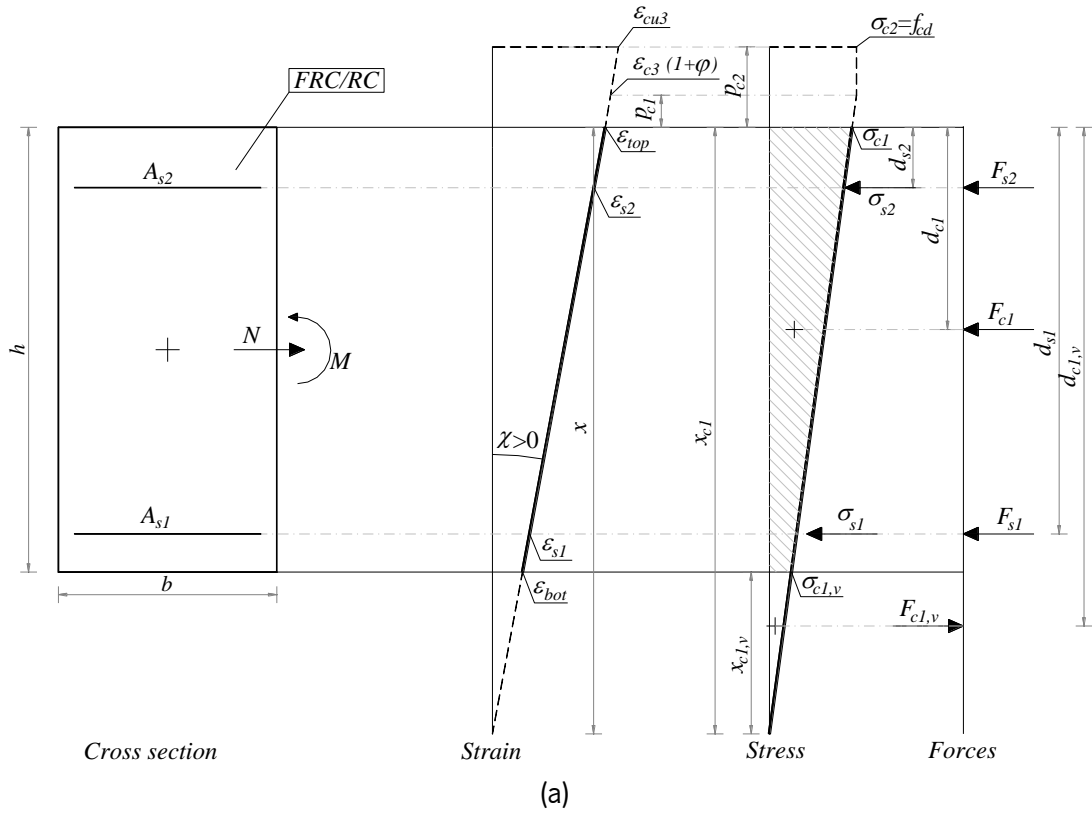


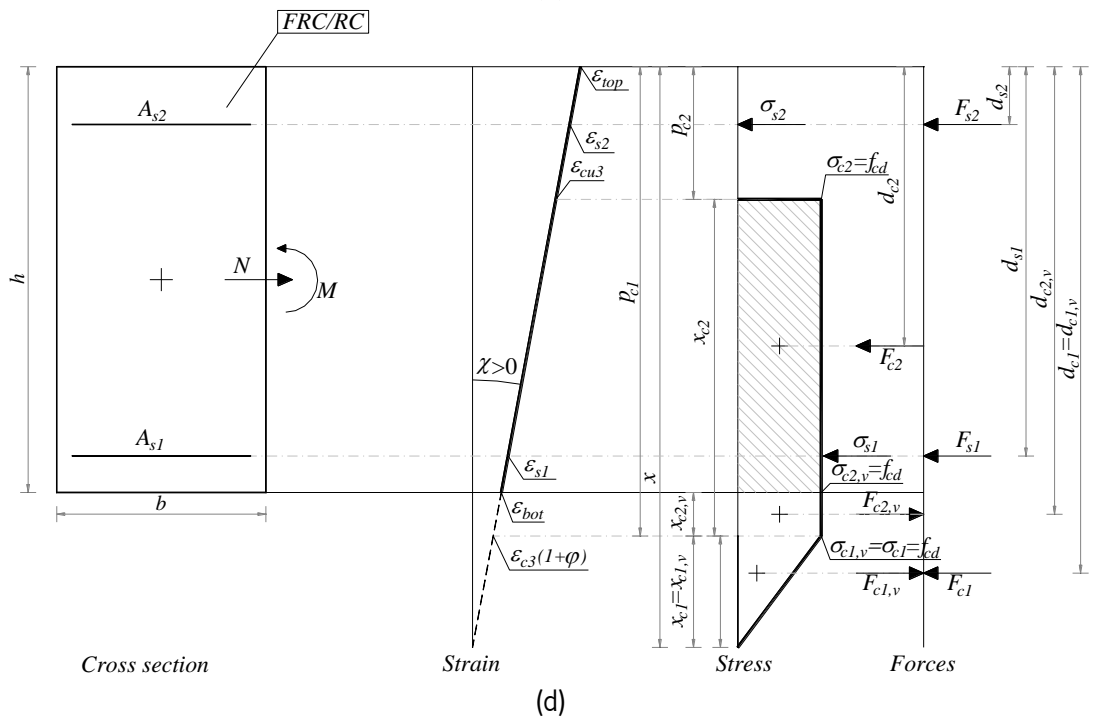
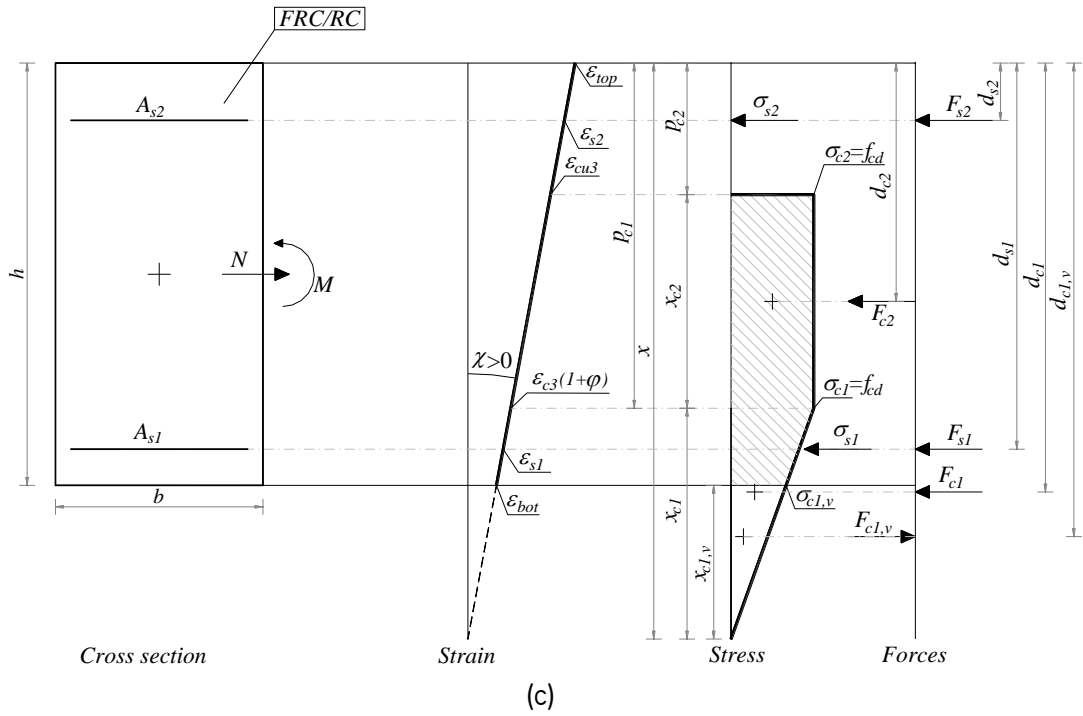
(b)

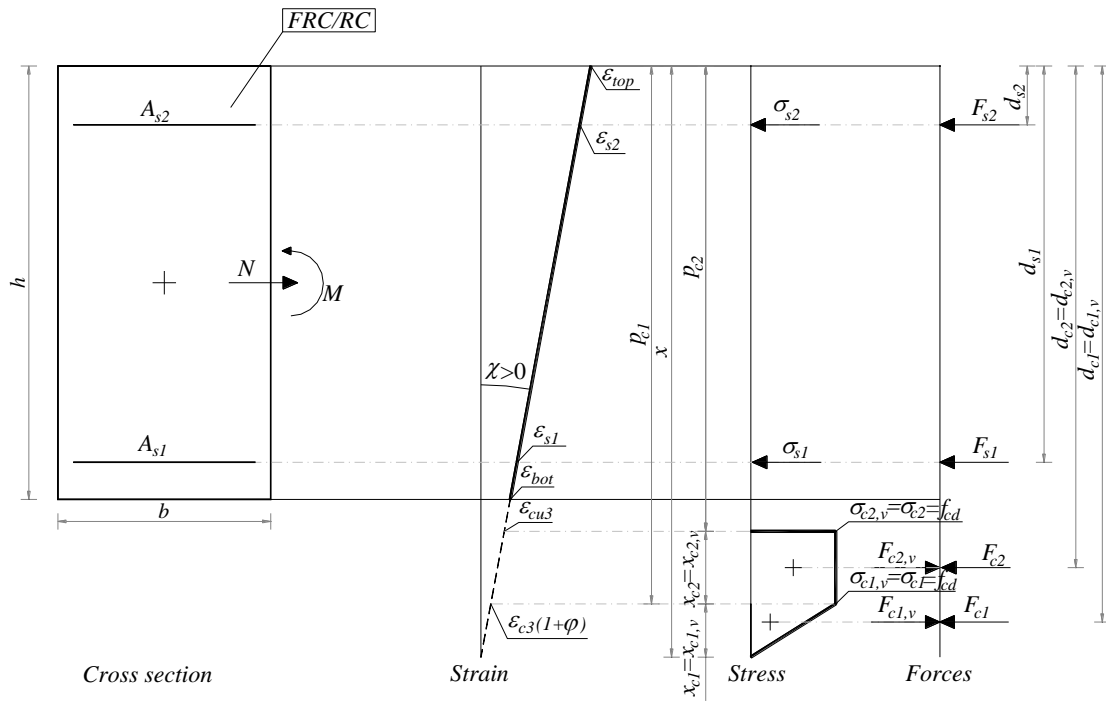


(c)

Figure 160 – Stress, strain, compressive forces and forces depth for the compressive zone of the cross-section applying the bilinear model, for negative curvature and neutral axis position inside the cross-section.

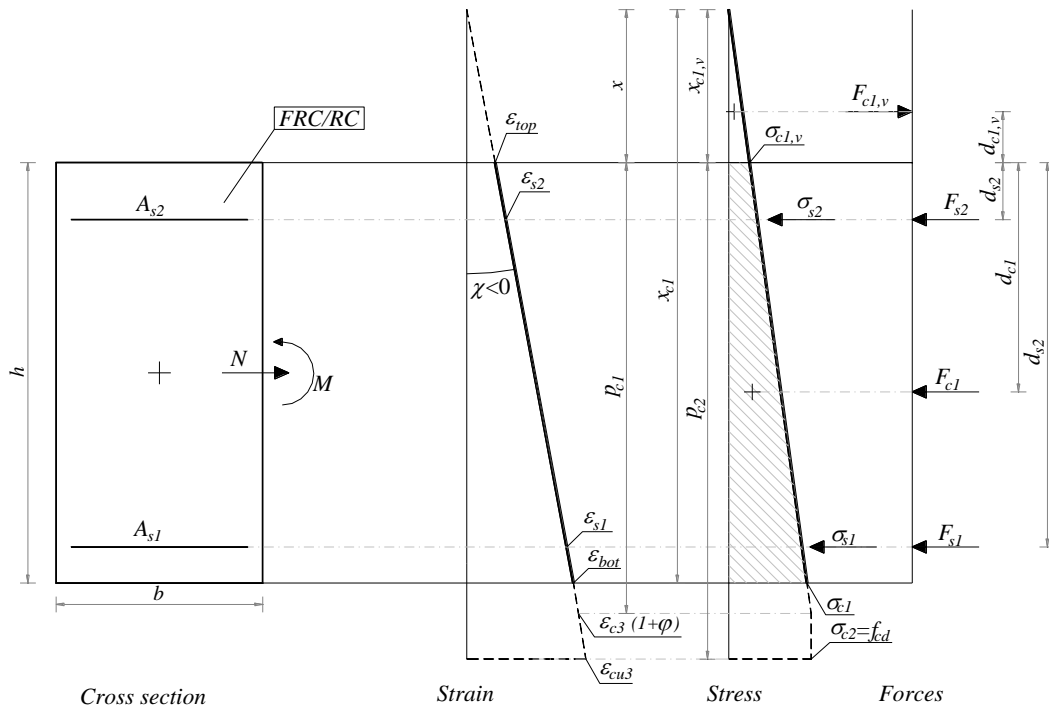




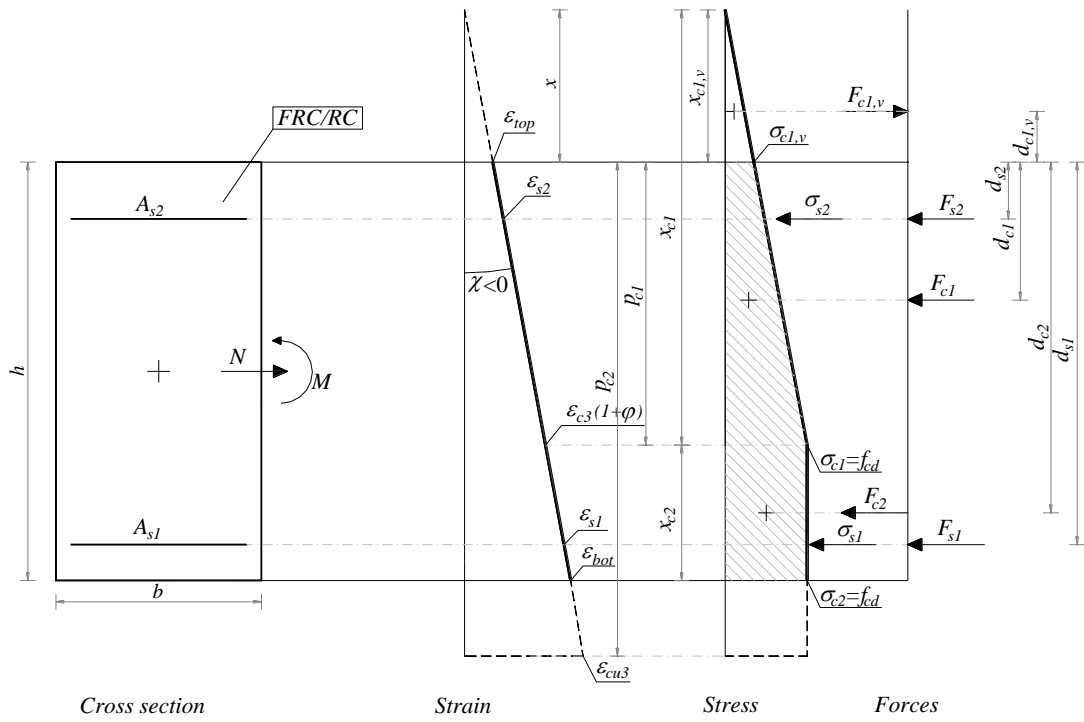


(e)

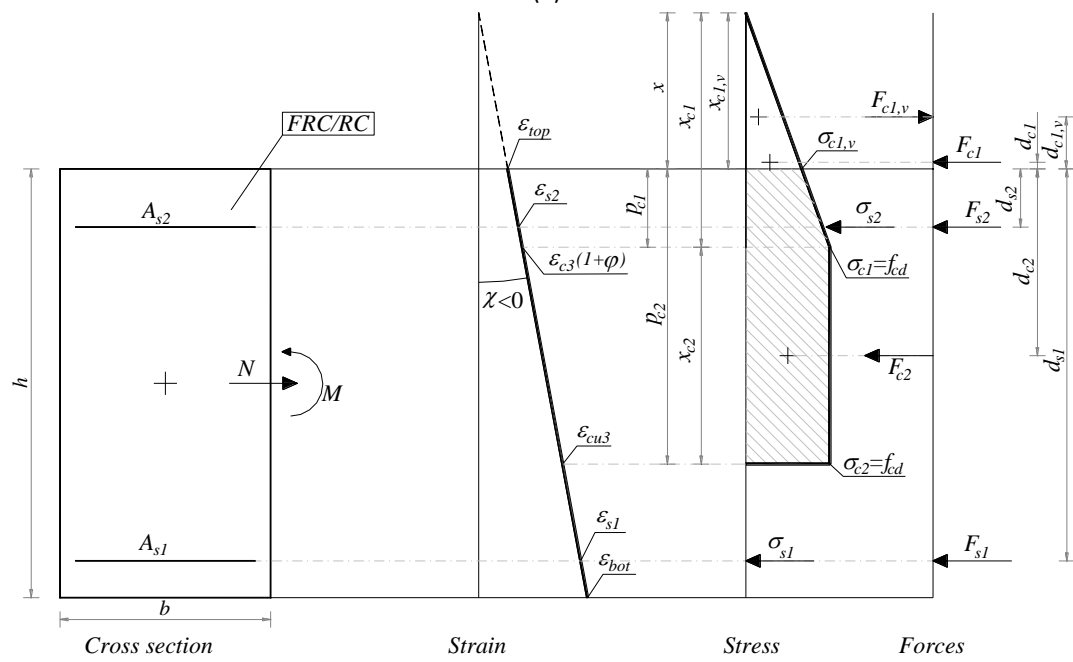
Figure 161 – Stress, strain, compressive forces and forces depth for the compressive zone of the cross-section applying the bilinear model, for positive curvature and neutral axis position outside the cross-section.



(a)



(b)



(c)

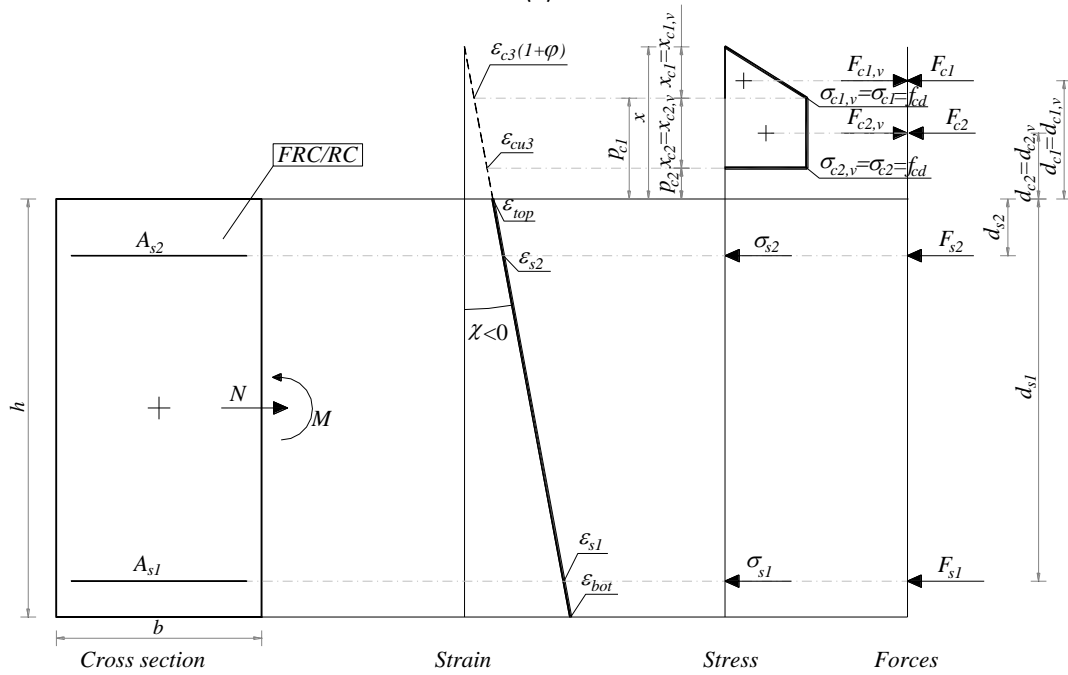
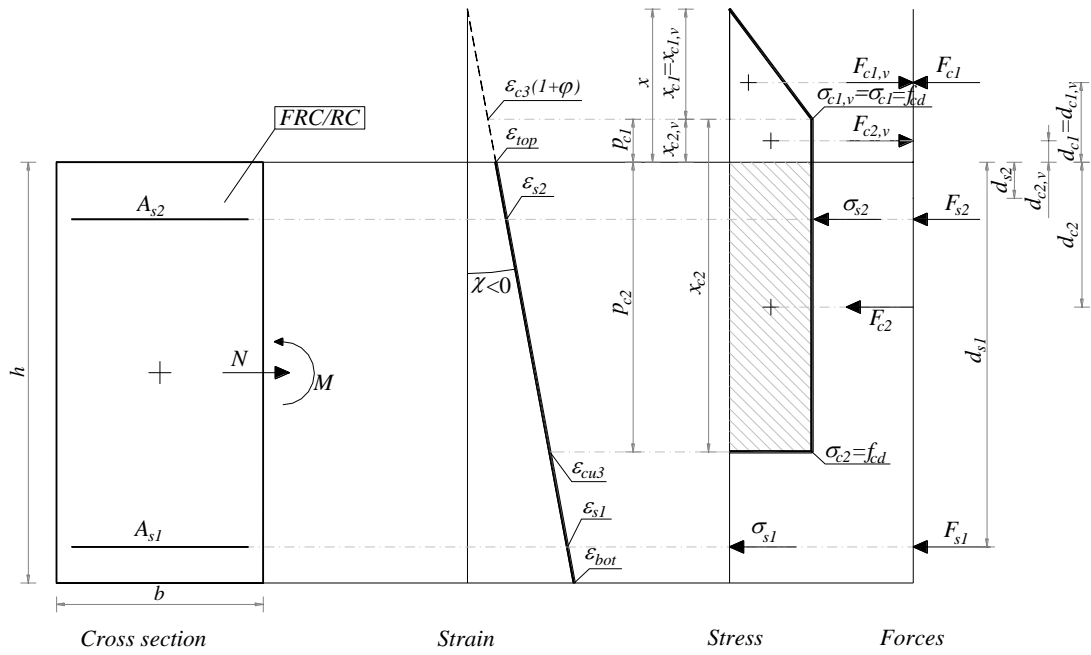


Figure 162 – Stress, strain, compressive forces and forces depth for the compressive zone of the cross-section applying the bilinear model, for negative curvature and neutral axis position outside the cross-section.

From Figure 159 to Figure 162 can be deduced the following relationships:

$$\begin{cases} p_{c1} = \frac{\varepsilon_{c3} \cdot (1 + \varphi_c) - \varepsilon_{top}}{\chi} \\ p_{c2} = \frac{\varepsilon_{cu3} \cdot (1 + \varphi_c) - \varepsilon_{top}}{\chi} \\ d_{\varepsilon_{c3}} = \left| \frac{\varepsilon_{c3} \cdot (1 + \varphi_c)}{\chi} \right| \end{cases} \quad \text{Eq. (C.3)}$$

$$\chi > 0: \begin{cases} x_{c1} = 0 & ; x < 0 \\ x_{c1} = x & ; x \geq 0 \wedge p_{c1} < 0 \\ x_{c1} = p_{c1} - x & ; x \geq 0 \wedge p_{c1} \geq 0 \end{cases}; \begin{cases} x_{c2} = 0 & x \leq 0 \\ x_{c2} = 0 & x > 0 \wedge p_{c2} < 0 \wedge p_{c1} < 0 \\ x_{c2} = p_{c1} & x > 0 \wedge p_{c2} < 0 \wedge p_{c1} \geq 0 \\ x_{c2} = p_{c1} - p_{c2} & x > 0 \wedge p_{c2} \geq 0 \end{cases} \quad \text{Eq. (C.4)}$$

$$\chi < 0: \begin{cases} x_{c1} = 0 & ; x \geq h \\ x_{c1} = h - x & ; x < h \wedge p_{c1} < 0 \\ x_{c1} = p_{c1} - x & ; x < h \wedge p_{c1} \geq 0 \end{cases}; \begin{cases} x_{c2} = 0 & x \leq 0 \\ x_{c2} = 0 & x > 0 \wedge p_{c2} < 0 \wedge p_{c1} < 0 \\ x_{c2} = p_{c1} & x > 0 \wedge p_{c2} < 0 \wedge p_{c1} \geq 0 \\ x_{c2} = p_{c1} - p_{c2} & x > 0 \wedge p_{c2} \geq 0 \end{cases}$$

$$\chi > 0: \begin{cases} x_{c1,v} = 0 & ; x < h \\ x_{c1,v} = x - h & ; x \geq h \wedge p_{c1} < h \\ x_{c1,v} = d_{\varepsilon_{c3}} & ; x \geq h \wedge p_{c1} \geq h \end{cases}; \begin{cases} x_{c2,v} = 0 & ; x \leq h \\ x_{c2,v} = p_{c1} - h & ; x > h \wedge p_{c1} > h \wedge p_{c2} < h \\ x_{c2,v} = p_{c1} - p_{c2} & ; x > h \wedge p_{c1} > h \wedge p_{c2} \geq h \end{cases} \quad \text{Eq. (C.5)}$$

$$\chi < 0: \begin{cases} x_{c1,v} = 0 & ; x > 0 \\ x_{c1,v} = 0 - x & ; x \leq 0 \wedge p_{c1} \geq 0 \\ x_{c1,v} = p_{c1} - x & ; x \geq h \wedge p_{c1} < 0 \end{cases}; \begin{cases} x_{c2,v} = 0 & ; x \geq 0 \\ x_{c2,v} = 0 - p_{c1} & ; x < 0 \wedge p_{c1} < 0 \wedge p_{c2} \geq 0 \\ x_{c2,v} = p_{c2} - p_{c1} & ; x < 0 \wedge p_{c1} < 0 \wedge p_{c2} < 0 \end{cases}$$

$$\begin{cases} \varepsilon_{c1} = -|\chi| \cdot x_{c1} \\ \varepsilon_{c2} = -|\chi| \cdot (x_{c1} + x_{c2}) \\ \varepsilon_{c1,v} = -|\chi| \cdot x_{c1,v} \\ \varepsilon_{c2,v} = -|\chi| \cdot (x_{c1,v} + x_{c2,v}) \end{cases} \quad \text{Eq. (C.6)}$$

$$\begin{cases} \sigma_{ci} = 0 & ; \varepsilon_{ci} \geq 0 \\ \sigma_{ci} = \frac{f_{cd}}{\varepsilon_{c3} \cdot (1 + \varphi_c)} \cdot \varepsilon_{ci} & ; \varepsilon_{c3} \cdot (1 + \varphi_c) \leq \varepsilon_{ci} < 0 \wedge \varepsilon_{ci} \geq \varepsilon_{cu3} \\ \sigma_{ci} = f_{cd} & ; \varepsilon_{cu3} \leq \varepsilon_{ci} < \varepsilon_{c3} \cdot (1 + \varphi_c) \\ \sigma_{ci} = 0 & ; \varepsilon_{ci} < \varepsilon_{cu3} \end{cases} ; i = 1, 2, 1v, 2v \quad \text{Eq. (C.7)}$$

$$\begin{cases} F_{c1} = 0.5 \cdot b \cdot x_{c1} \cdot \sigma_{c1} \\ F_{c2} = b \cdot x_{c2} \cdot \sigma_{c2} \\ F_{c1,v} = -0.5 \cdot b \cdot x_{c1,v} \cdot \sigma_{c1,v} \\ F_{c2,v} = -b \cdot x_{c2,v} \cdot \sigma_{c2,v} \\ F_c = F_{c1} + F_{c2} + F_{c1,v} + F_{c2,v} \end{cases} \quad \text{Eq. (C.8)}$$

$$\begin{cases} d_{c1} = x - \frac{2 \cdot x_{c1}}{3} & ; \chi > 0 \\ d_{c1} = x + \frac{2 \cdot x_{c1}}{3} & ; \chi < 0 \end{cases} ; \begin{cases} d_{c2} = x - x_{c1} - \frac{x_{c2}}{2} & ; \chi > 0 \\ d_{c2} = x + x_{c1} + \frac{x_{c2}}{2} & ; \chi < 0 \end{cases} \quad \text{Eq. (C.9)}$$

$$\begin{cases} d_{c1,v} = x - \frac{2 \cdot x_{c1,v}}{3} & ; \chi > 0 \wedge x > h \\ d_{c1,v} = x + \frac{2 \cdot x_{c1,v}}{3} & ; \chi < 0 \wedge x < 0 \end{cases} ; \begin{cases} d_{c2,v} = x - x_{c1,v} - \frac{x_{c2,v}}{2} & ; \chi > 0 \wedge x > h \\ d_{c2,v} = x + x_{c1,v} + \frac{x_{c2,v}}{2} & ; \chi < 0 \wedge x < 0 \end{cases} \quad \text{Eq. (C.10)}$$

$$\begin{cases} M_{c1} = F_{c1} \cdot d_{c1} \\ M_{c2} = F_{c2} \cdot d_{c2} \\ M_{c1,v} = F_{c1,v} \cdot d_{c1,v} \\ M_{c2,v} = F_{c2,v} \cdot d_{c2,v} \\ M_c = M_{c1} + M_{c2} + M_{c1,v} + M_{c2,v} \end{cases} \quad \text{Eq. (C.11)}$$

The design compressive strength of concrete, f_{cd} , is determined according to Eq. (2.9). In *FRCcalc* it is assumed that $\alpha_{cc} = 1.0$ and that for ULS analysis the partial safety factor assumes the value of $\gamma_c = 1.50$ and for SLS analysis the value is equal to $\gamma_c = 1.0$.

As can be deduced in Eq. (C.7) and Figure 159, in the model is considered the influence of creep of concrete under compression, in accordance with the methodology presented in section 2.3.1.

The stress and internal forces of the conventional steel rebars are also represented in Figure 159. Applying the elastic-perfectly plastic diagram for steel in compression and tension (section 2.3.2), the rebars stress (σ_{s1}, σ_{s2}), forces (F_{s1}, F_{s2}) and force depth (d_{s1}, d_{s2}) can be determined from the following expressions:

$$\begin{cases} \varepsilon_{s1_1} = \chi \cdot (d_{s1_1} - x) \\ \varepsilon_{s1_2} = \chi \cdot (d_{s1_2} - x) \\ \varepsilon_{s2_1} = \chi \cdot (d_{s2_1} - x) \\ \varepsilon_{s2_2} = \chi \cdot (d_{s2_2} - x) \end{cases} \quad \text{Eq. (C.12)}$$

$$\left\{ \begin{array}{l} \sigma_{sj} = -f_{yd} \quad ; \varepsilon_{sj} < -\frac{f_{yd}}{E_s} \\ \sigma_{sj} = E_s \cdot \varepsilon_{sj} \quad ; -\frac{f_{yd}}{E_s} \leq \varepsilon_{sj} \leq \frac{f_{yd}}{E_s} \\ \sigma_{sj} = f_{yd} \quad ; \varepsilon_{sj} > \frac{f_{yd}}{E_s} \end{array} \right. \quad j=1,2 \quad \text{Eq. (C.13)}$$

$$\left\{ \begin{array}{l} F_{s1_1} = A_{s1_1} \cdot \sigma_{s1_1} \\ F_{s1_2} = A_{s1_2} \cdot \sigma_{s1_2} \\ F_{s2_1} = A_{s2_1} \cdot \sigma_{s2_1} \\ F_{s2_2} = A_{s2_2} \cdot \sigma_{s2_2} \end{array} \right. \quad \text{Eq. (C.14)}$$

$$\left\{ \begin{array}{l} d_{s1_1} = h - c_{1_1} \\ d_{s1_2} = h - c_{1_2} \\ d_{s2_1} = c_{2_1} \\ d_{s2_2} = c_{2_2} \end{array} \right. \quad \text{Eq. (C.15)}$$

$$\left\{ \begin{array}{l} M_{s1_1} = F_{s1_1} \cdot d_{s1_1} \\ M_{s1_2} = F_{s1_2} \cdot d_{s1_2} \\ M_{s2_1} = F_{s2_1} \cdot d_{s2_1} \\ M_{s2_2} = F_{s2_2} \cdot d_{s2_2} \end{array} \right. \quad \text{Eq. (C.16)}$$

$$\{ F_s = F_{s1_1} + F_{s1_2} + F_{s2_1} + F_{s2_2} \} \quad \text{Eq. (C.17)}$$

$$\{ M_s = F_{s1_1} \cdot d_{s1_1} + F_{s1_2} \cdot d_{s1_2} + F_{s2_1} \cdot d_{s2_1} + F_{s2_2} \cdot d_{s2_2} \} \quad \text{Eq. (C.18)}$$

For FRC in tension, the stress-strain model to be adopted depends if a ULS and SLS analysis is being performed. In *FRCcalc* a generalized stress-strain distribution is adopted that is capable to be adapted to both ULS and SLS FRC in tension models. The generalized model is divided in 4 linear branches, which is presented in Figure 163.

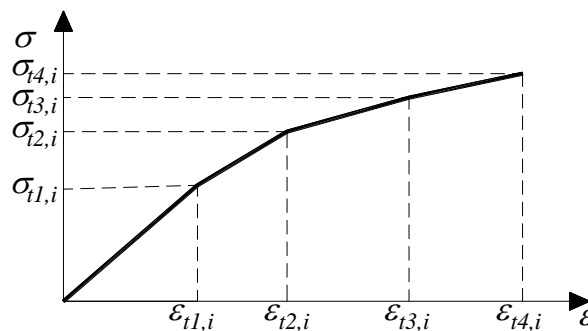
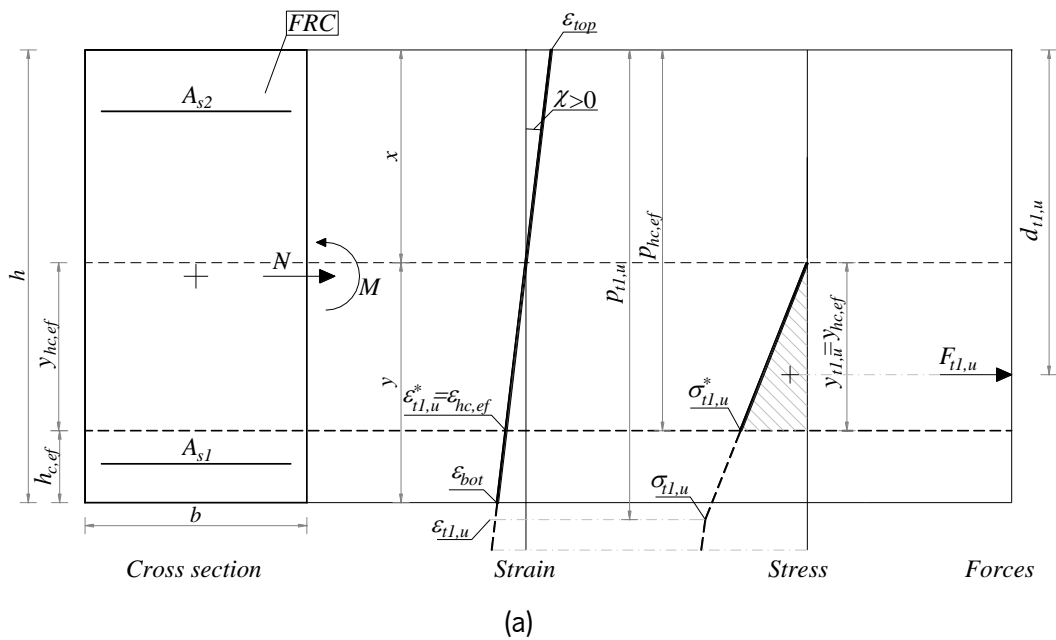
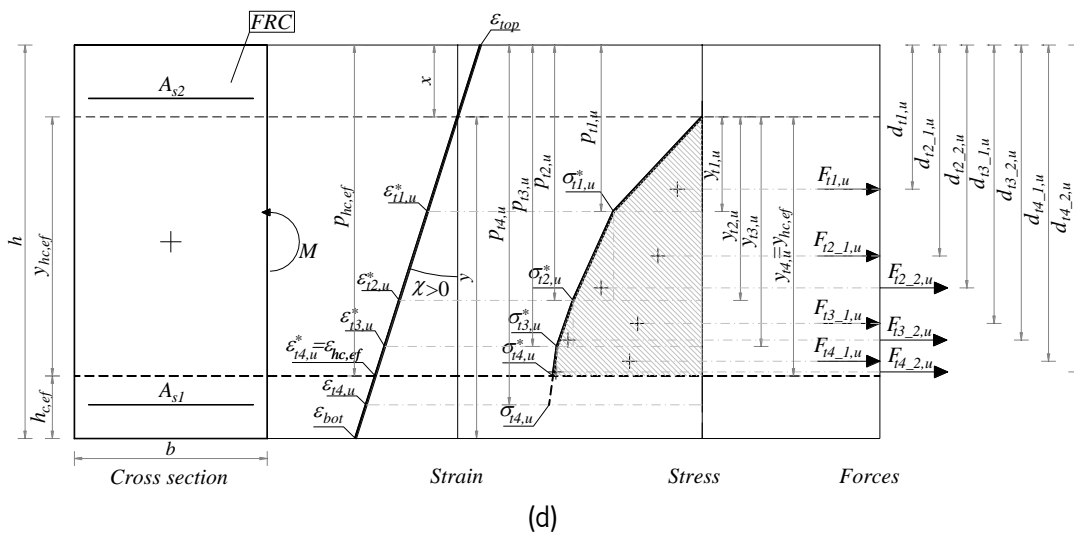
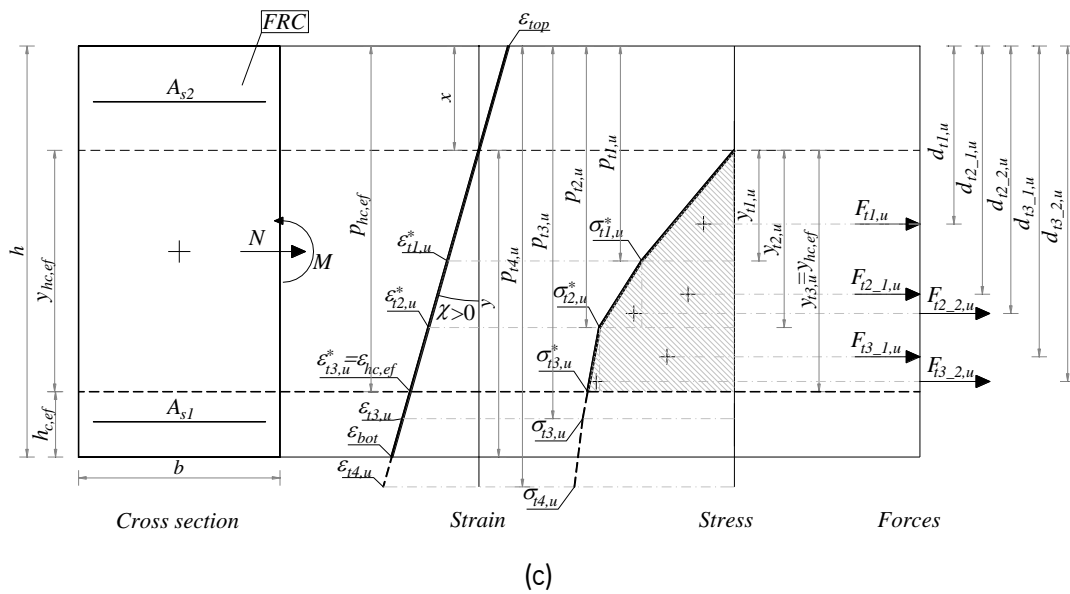
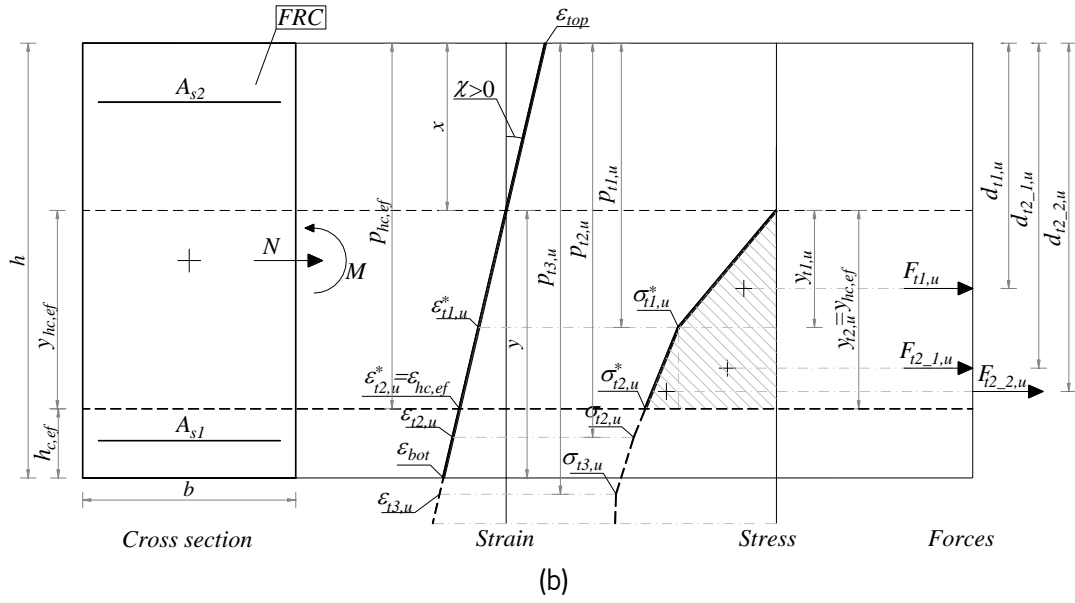


Figure 163 – Generalized multi-linear model for FRC in tension.

As presented in section 2.5.1, for FRC cross-section with longitudinal steel bars reinforcement the tensile zone should be divided in two zones. Consequently, an independent stress-strain relationship is applied for each zone. In Figure 163 the index i represents the tensile zones of the cross-section, where $i = r$ stands for reinforced zone, corresponding to the effective tension zone of the section, and $i = u$ is referred to the unreinforced zone, corresponding to the remaining part of the cross-section, i.e. zone between the height of the effective tensile zone and the neutral axis position.

The possible distribution of stresses, strains, tensile forces and force depth for the unreinforced tensile zone of the cross-section are represented in Figure 164 and Figure 165 for the situation where the neutral axis position is inside the cross-section and member presents positive and negative curvature respectively. For situations where the neutral axis position is outside the cross-section are assumed virtual tensile forces between the neutral axis and the face of the cross-section ($F_{ii,u,v}$), as can be seen in Figure 166 and Figure 167.





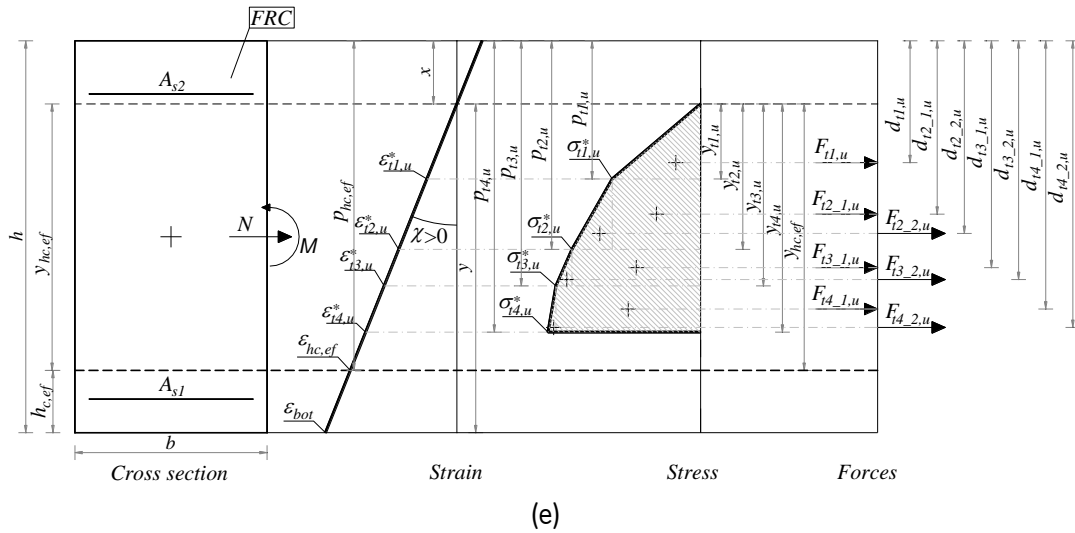
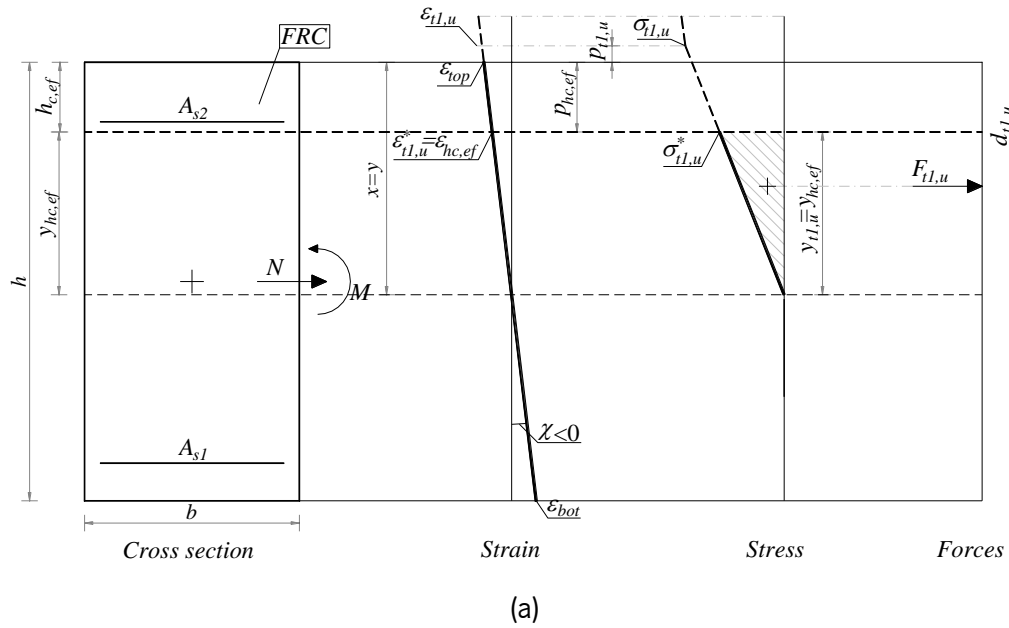
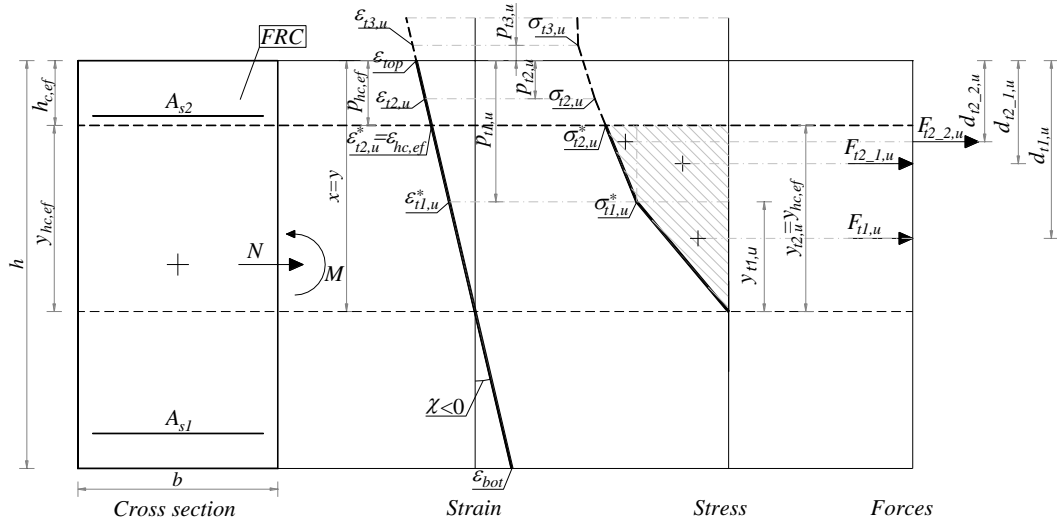
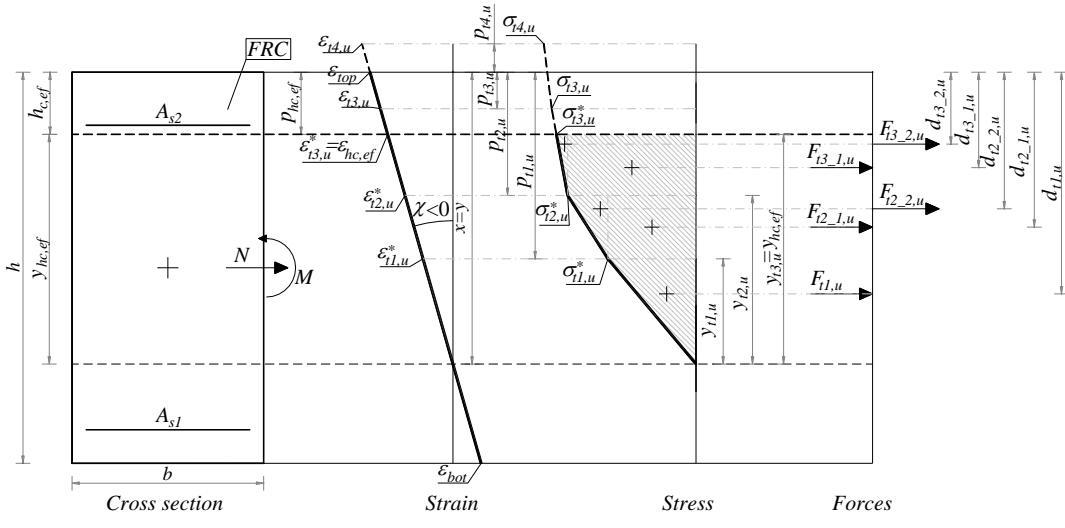


Figure 164 – Possible distribution of stresses, strains, tensile forces and forces levers for the unreinforced tensile zone of a FRC cross-section with longitudinal conventional reinforcement, adopting quadrilinear stress-strain diagram, for positive curvature and neutral axis position inside the cross-section.

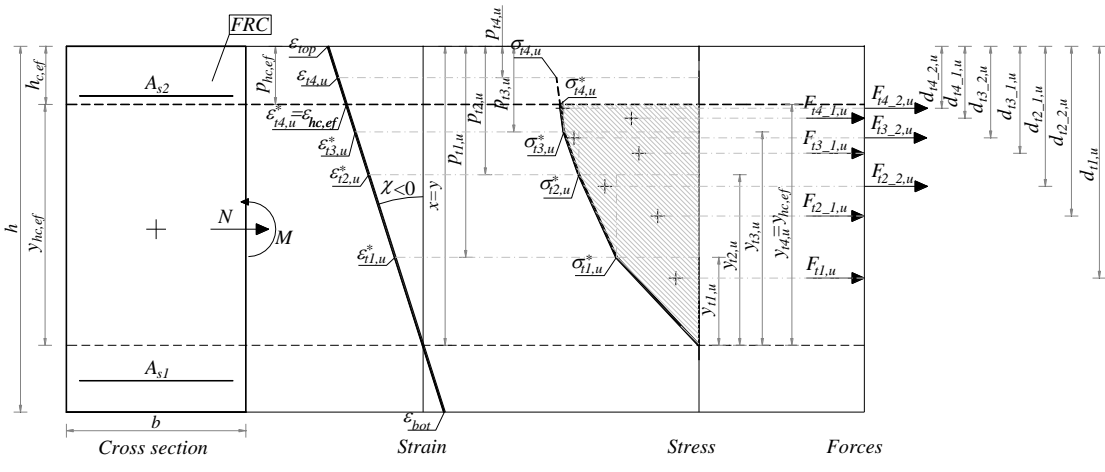




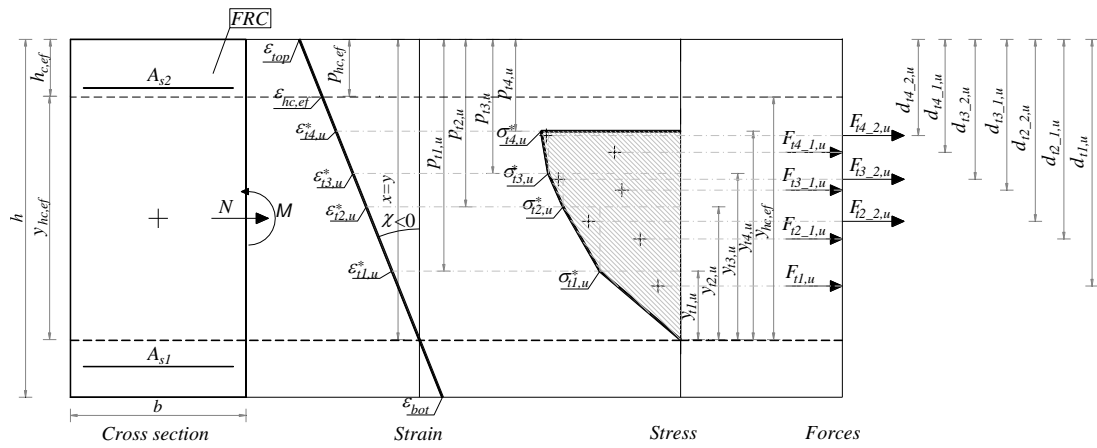
(b)



(c)

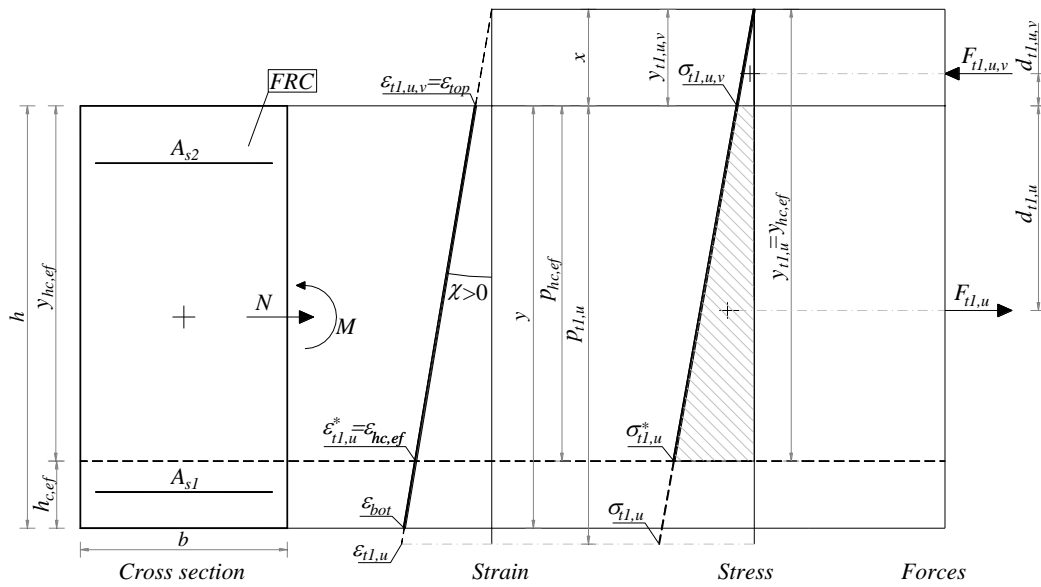


(d)

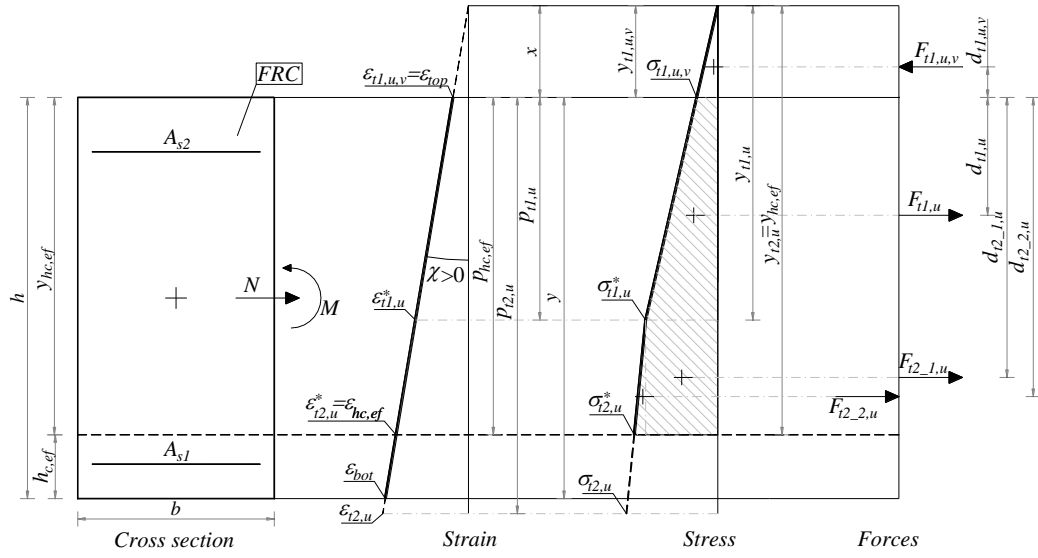


(e)

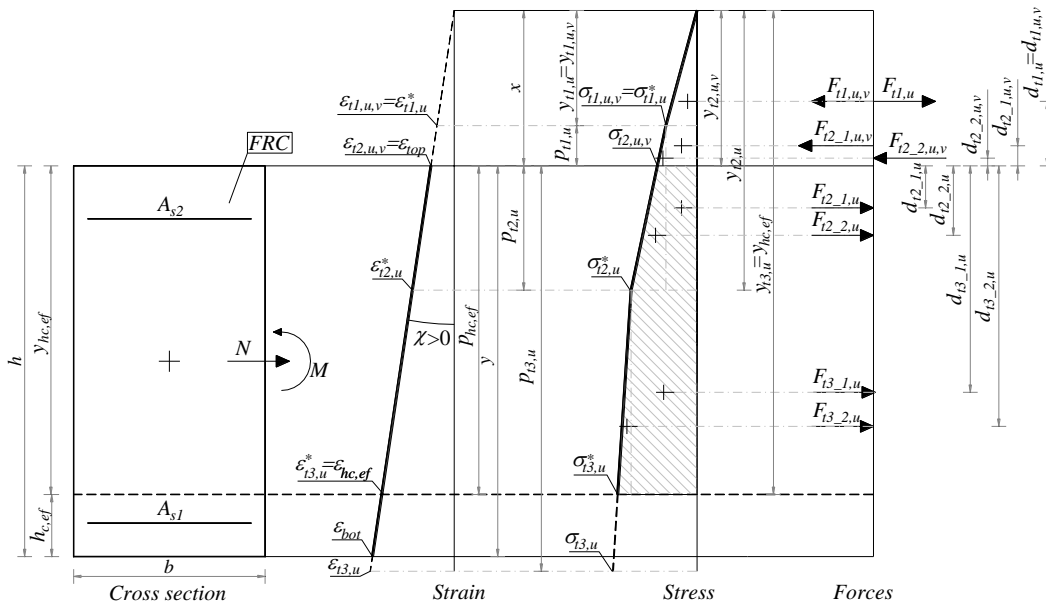
Figure 165 – Possible distribution of stresses, strains, tensile forces and forces levers for the unreinforced tensile zone of a FRC cross-section with longitudinal conventional reinforcement, adopting quadrilinear stress-strain diagram, for negative curvature and neutral axis position inside the cross-section.



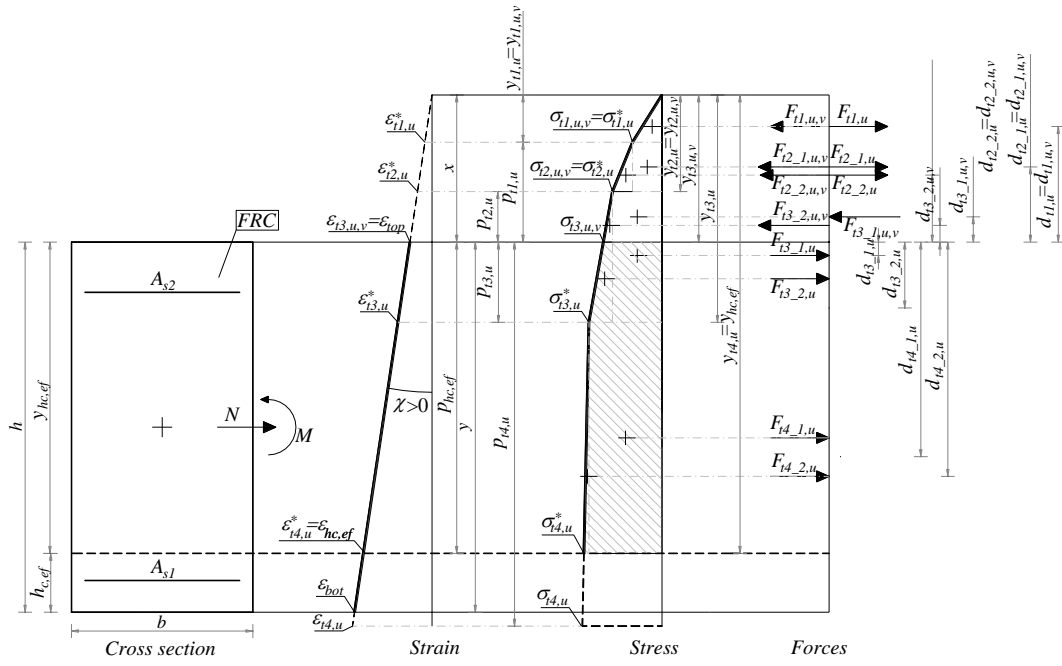
(a)



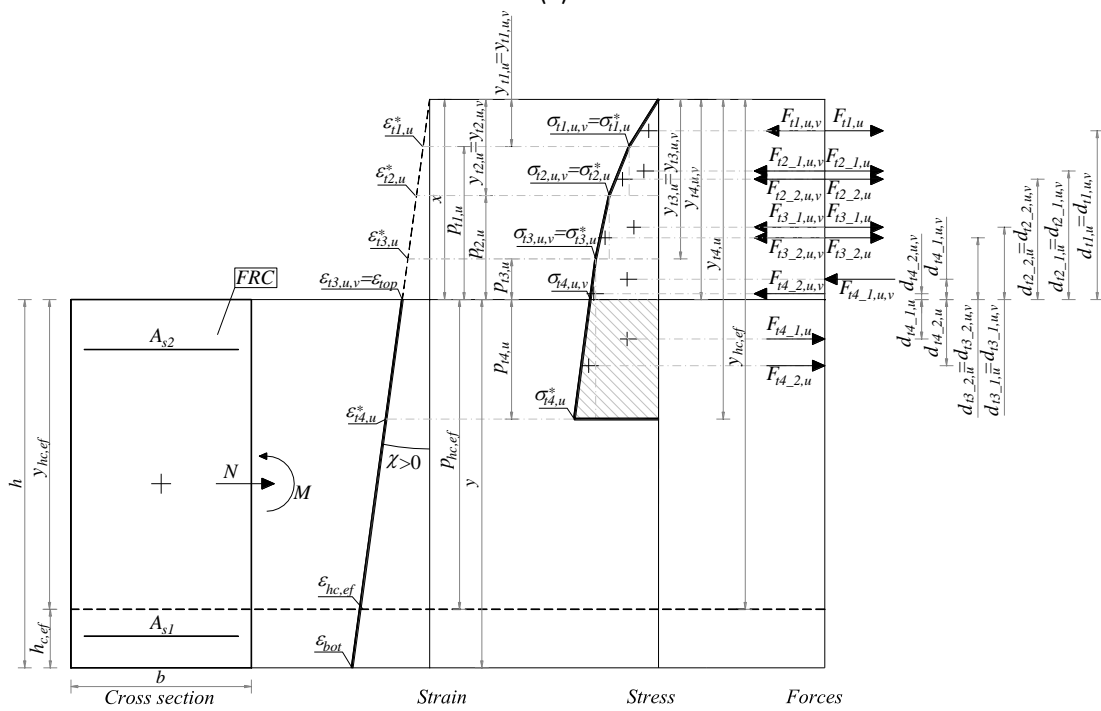
(b)



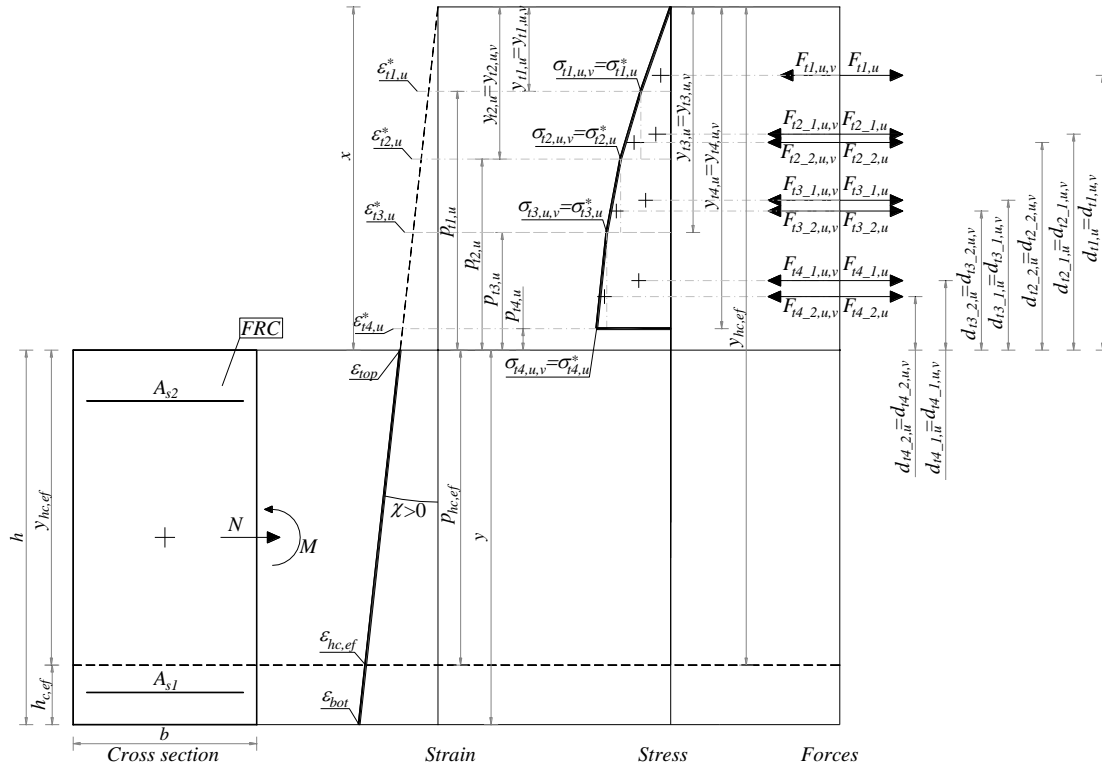
(c)



(d)

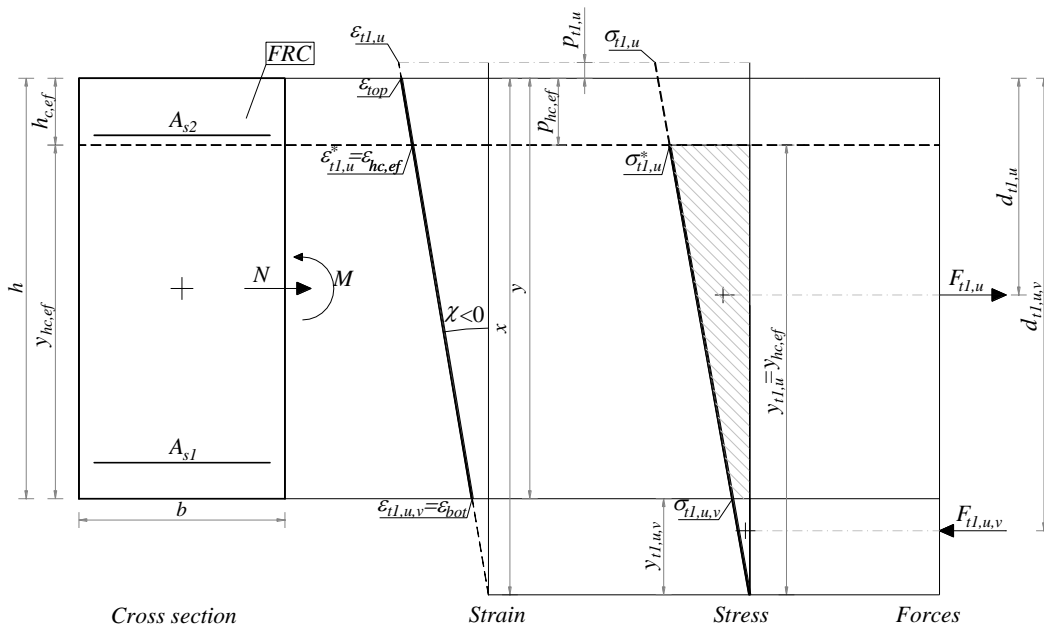


(e)

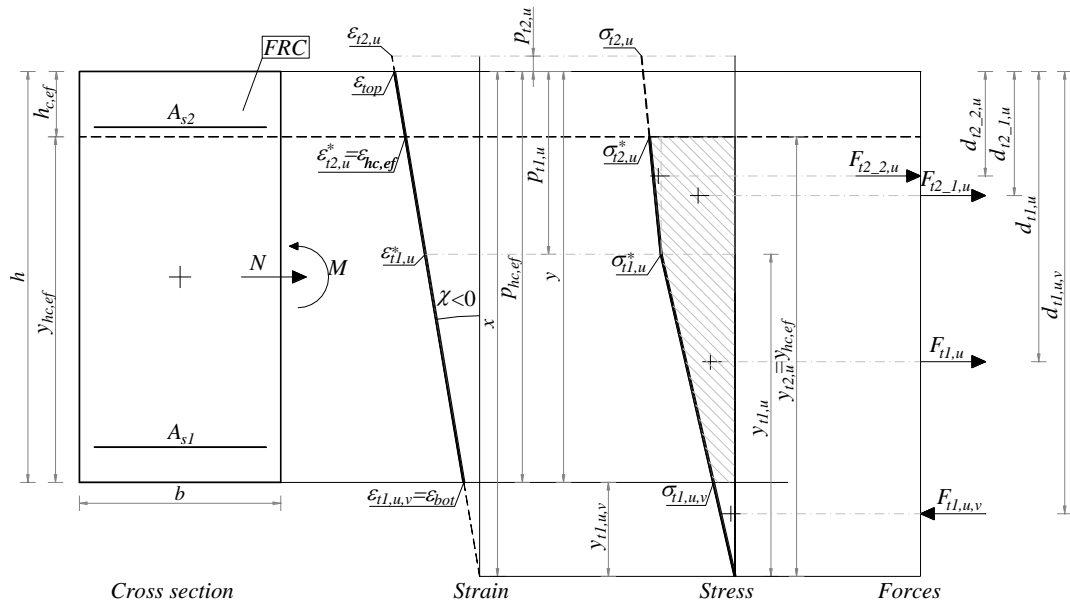


(f)

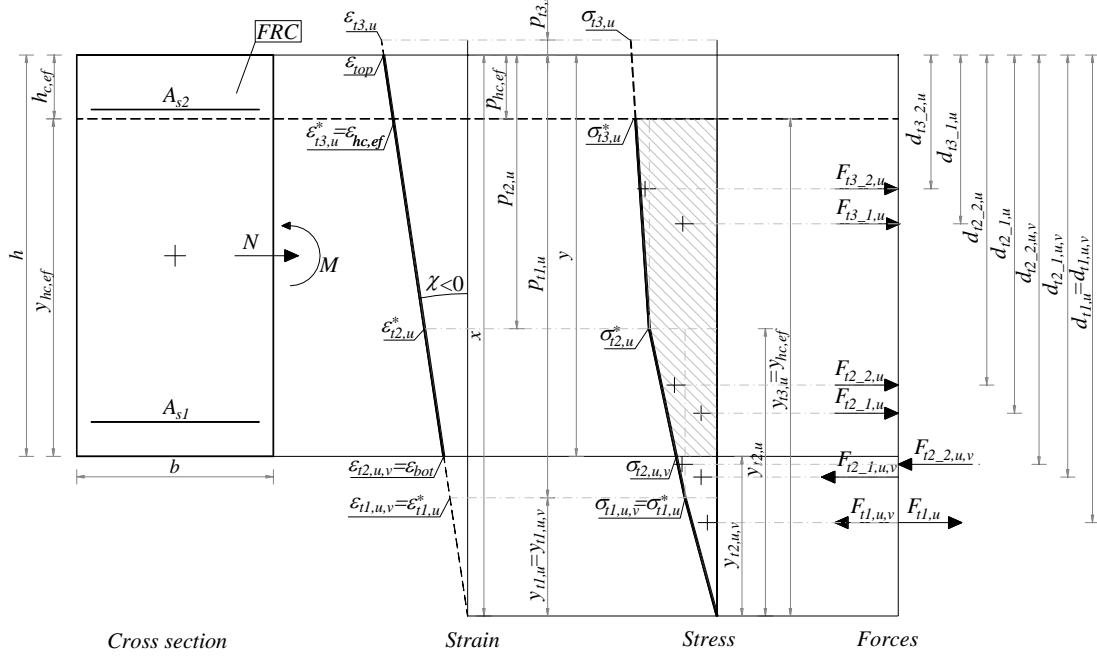
Figure 166 – Possible distribution of stresses, strains, tensile forces and forces levers for the unreinforced tensile zone of a FRC cross-section with longitudinal conventional reinforcement, adopting quadrilinear stress-strain diagram, for positive curvature and neutral axis position outside the cross-section.



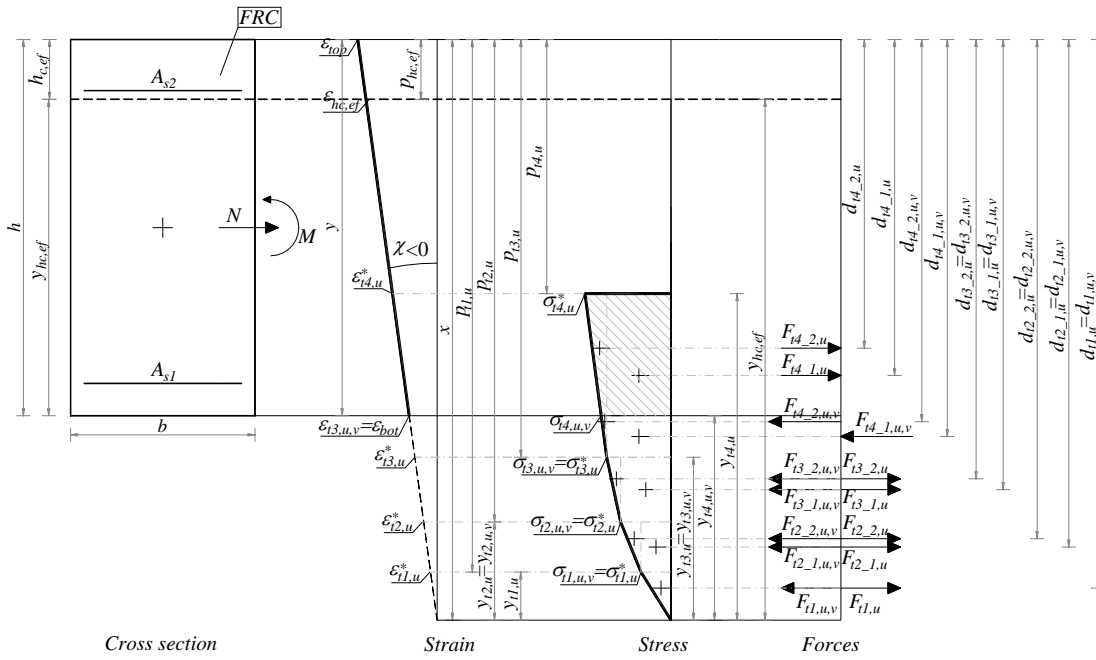
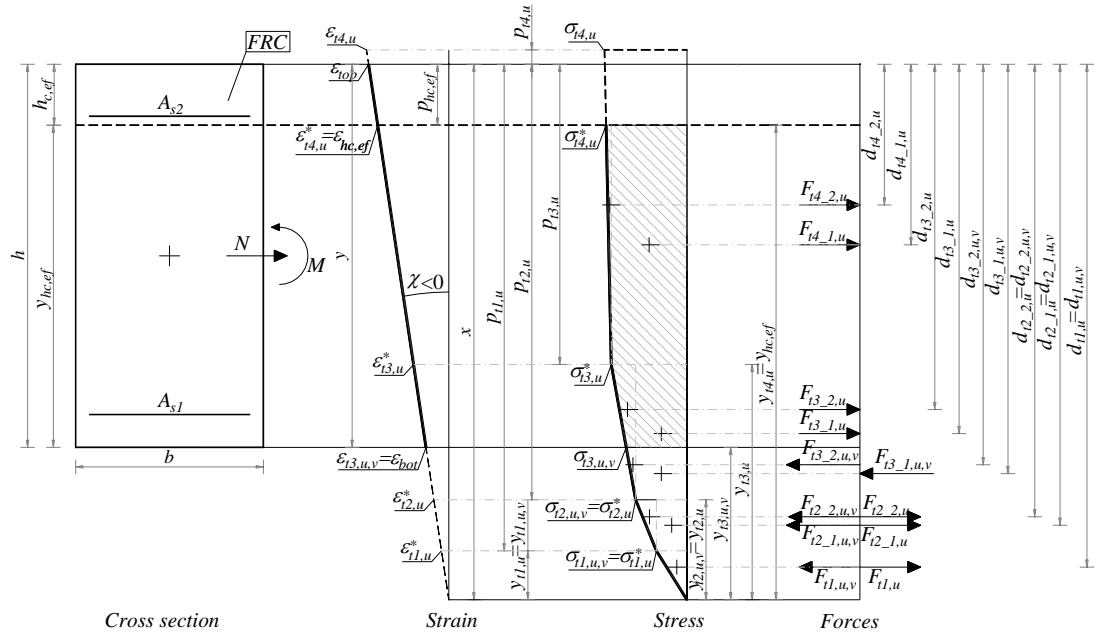
(a)

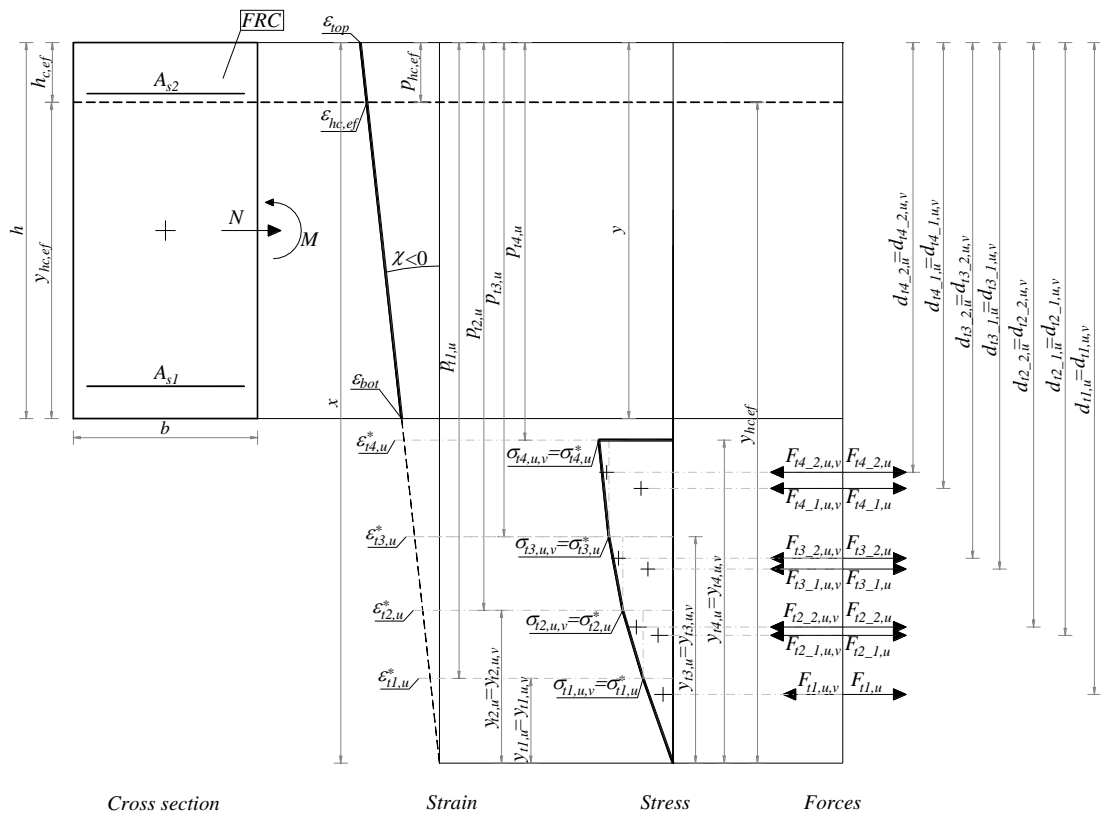


(b)



(c)

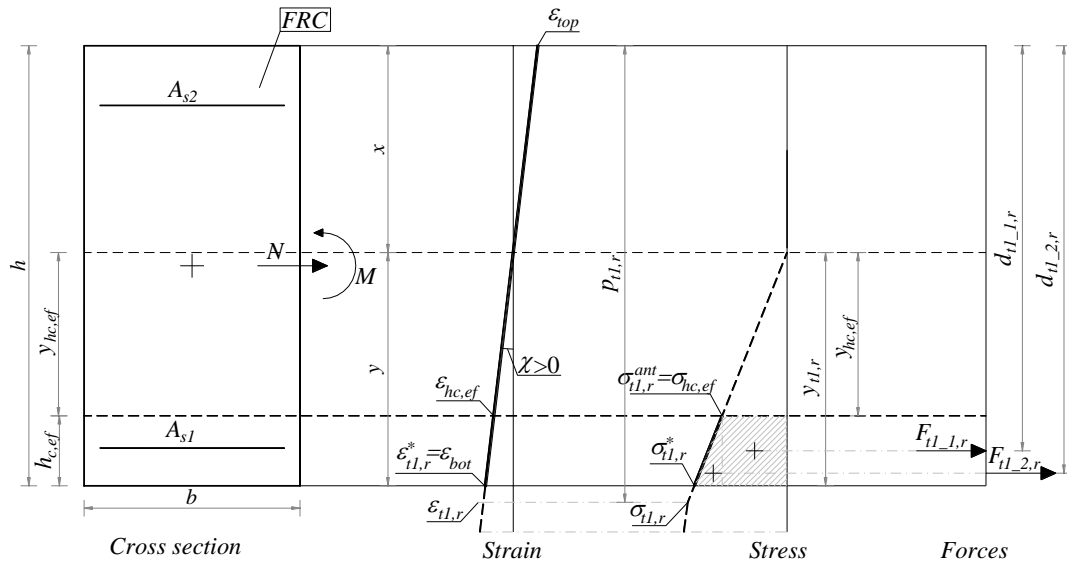




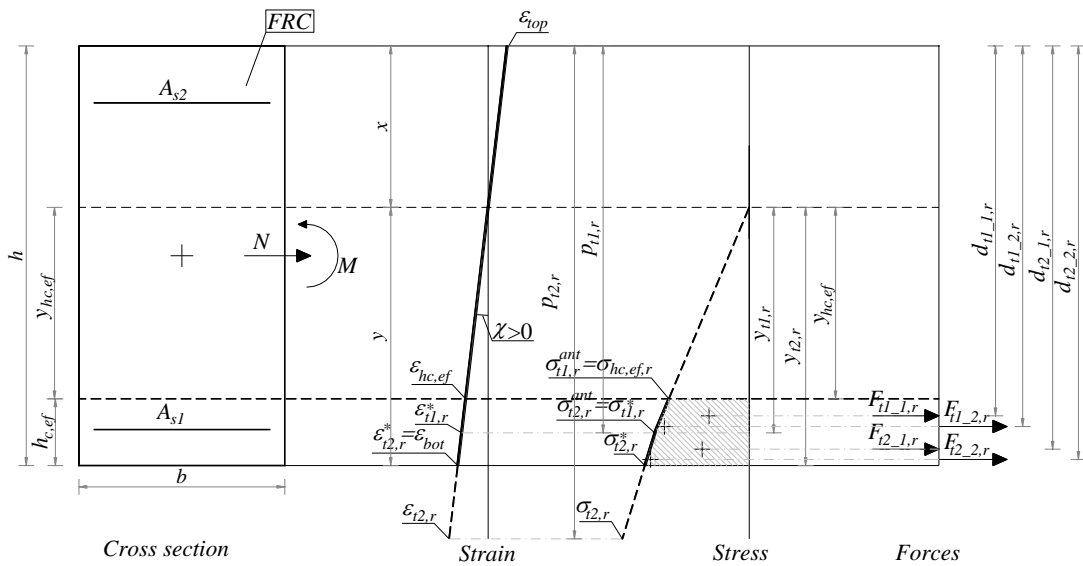
(f)

Figure 167 – Possible distribution of stresses, strains, tensile forces and forces levers for the unreinforced tensile zone of a FRC cross-section with longitudinal conventional reinforcement, adopting quadrilinear stress-strain diagram, for negative curvature and neutral axis position outside the cross-section.

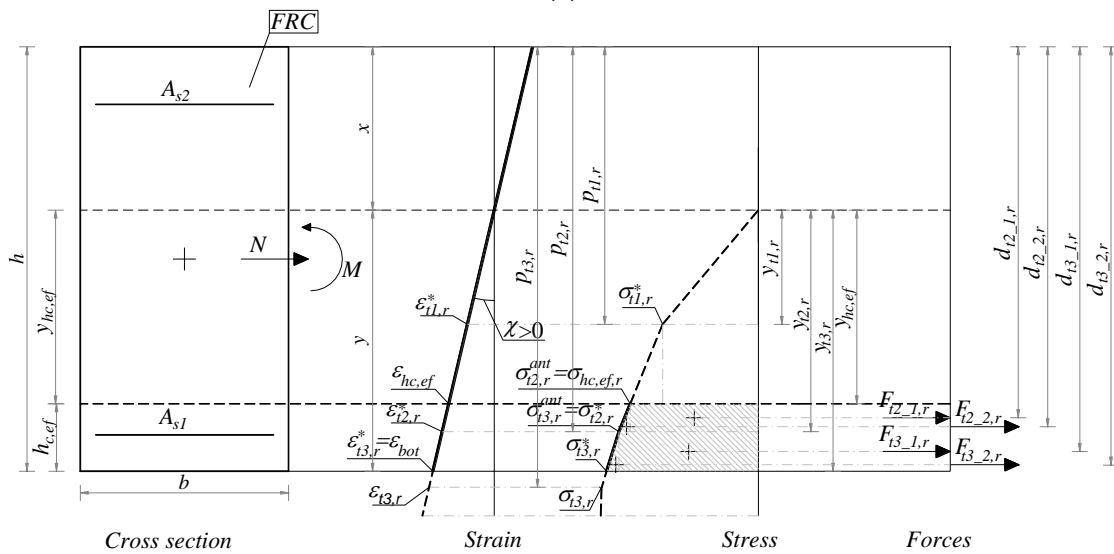
The possible distribution of stresses, strains, tensile forces and force depth for the reinforced tensile zone of the cross-section are represented in Figure 168 for the situation when quadrilinear tensile stress-strain diagram is adopted.



(a)



(b)



(c)

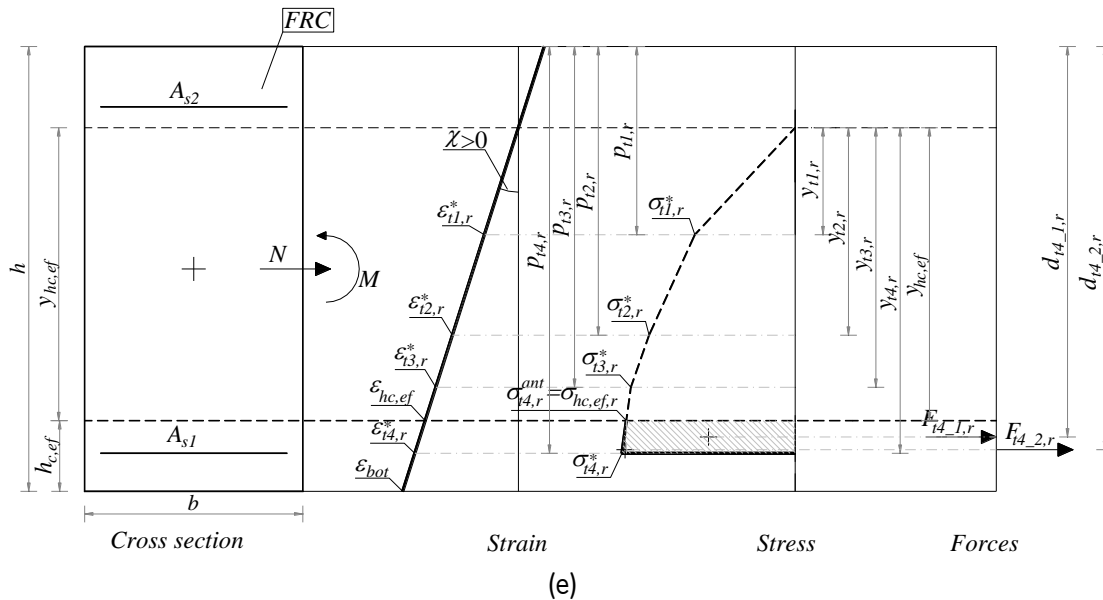
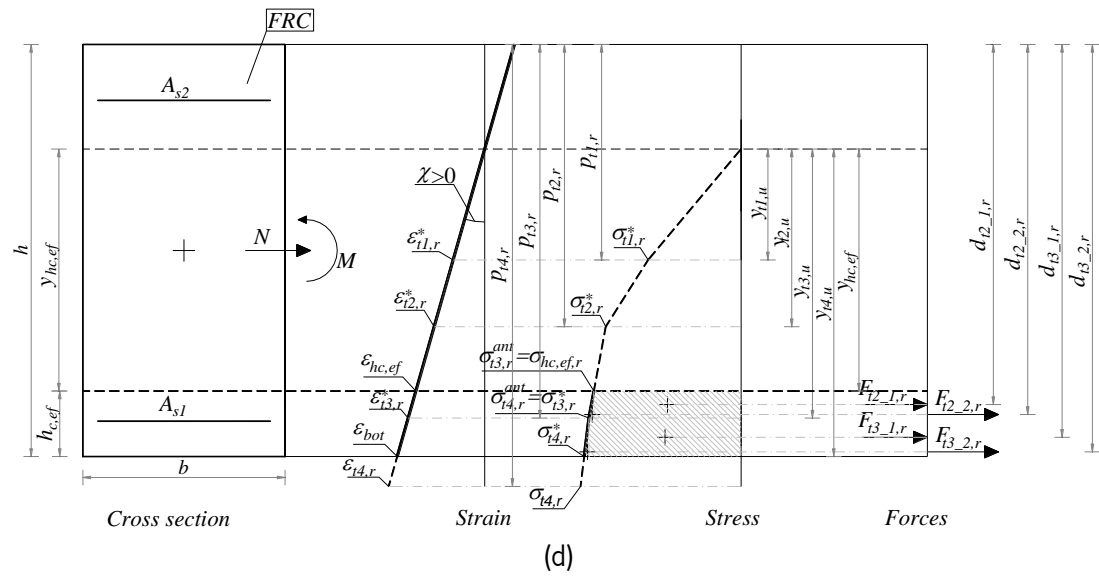


Figure 168 – Possible distribution of stresses, strains, tensile forces and forces levers for the reinforced tensile zone of a FRC cross-section with longitudinal conventional reinforcement, adopting quadrilinear stress-strain diagram.

From Figure 164 and Figure 168 it is possible to deduct the following relationships:

$$\begin{cases} p_{ij,u} = \frac{\epsilon_{ij,u} - \epsilon_{top}}{\chi} \\ p_{ij,r} = \frac{\epsilon_{ij,r} - \epsilon_{top}}{\chi} \end{cases}, j = 1, 2, 3, 4 \quad \text{Eq. (C.19)}$$

$$\begin{cases} p_{hc,ef} = h - h_{c,ef} & ; \chi > 0 \\ p_{hc,ef} = h_{c,ef} & ; \chi < 0 \end{cases} \quad \text{Eq. (C.20)}$$

$$\chi > 0 : \begin{cases} y_{t1,u} = 0 & ; x > p_{hc,ef} \\ y_{t1,u} = p_{hc,ef} - x & ; x \leq p_{hc,ef} \wedge p_{t1,u} > p_{hc,ef} \\ y_{t1,u} = p_{tj,u} - x & ; x \leq p_{hc,ef} \wedge p_{t1,u} \leq p_{hc,ef} \end{cases} ; \begin{cases} y_{tj,u} = 0 & ; p_{tj-1,u} > p_{hc,ef} \\ y_{tj,u} = p_{hc,ef} - x & ; p_{tj-1,u} \leq p_{hc,ef} \wedge p_{tj,u} > p_{hc,ef} \\ y_{tj,u} = p_{tj,u} - x & ; p_{tj-1,u} \leq p_{hc,ef} \wedge p_{tj,u} \leq p_{hc,ef} \end{cases} , j = 2, 3, 4 \\
 \chi < 0 : \begin{cases} y_{t1,u} = 0 & ; x < p_{hc,ef} \\ y_{t1,u} = x - p_{hc,ef} & ; x \geq p_{hc,ef} \wedge p_{t1,u} < p_{hc,ef} \\ y_{t1,u} = x - p_{t1,u} & ; x \geq p_{hc,ef} \wedge p_{t1,u} \geq p_{hc,ef} \end{cases} ; \begin{cases} y_{tj,u} = 0 & ; p_{tj-1,u} < p_{hc,ef} \\ y_{tj,u} = x - p_{hc,ef} & ; p_{tj-1,u} \geq p_{hc,ef} \wedge p_{tj,u} < p_{hc,ef} \\ y_{tj,u} = x - p_{tj,u} & ; p_{tj-1,u} \geq p_{hc,ef} \wedge p_{tj,u} \geq p_{hc,ef} \end{cases}$$

Eq. (C.21)

$$\chi > 0 : \begin{cases} y_{tj,u,v} = 0 & x > 0 \\ y_{tj,u,v} = 0 - x & x \leq 0 \wedge 0 - x \leq y_{tj,u} \\ y_{tj,u,v} = y_{tj,u} & x \leq 0 \wedge 0 - x > y_{tj,u} \end{cases} \\
 \chi < 0 : \begin{cases} y_{tj,u,v} = 0 & x < h \\ y_{tj,u,v} = x - h & x \geq h \wedge x - h \leq y_{tj,u} \\ y_{tj,u,v} = y_{tj,u} & x \geq h \wedge x - h > y_{tj,u} \end{cases}$$

Eq. (C.22)

$$\begin{cases} y_{hc,ef} = p_{hc,ef} - x & ; \chi > 0 \\ y_{hc,ef} = x - p_{hc,ef} & ; \chi < 0 \end{cases}$$

Eq. (C.23)

$$\{ \varepsilon_{hc,ef} = |\chi| \cdot y_{hc,ef}$$

Eq. (C.24)

$$\begin{cases} \varepsilon_{tj,i}^* = |\chi| \cdot y_{tj,i} & , i = u, r \\ \varepsilon_{tj,u,v} = |\chi| \cdot y_{tj,u,v} \end{cases} , j = 1, 2, 3, 4$$

Eq. (C.25)

$$\begin{cases} \sigma_{t1,i}^* = \frac{\sigma_{t1,i}}{\varepsilon_{t1,i}} \cdot \varepsilon_{t1,i}^* & ; \varepsilon_{t1,i}^* \leq \varepsilon_{t1,i} \\ \sigma_{tj,i}^* = \sigma_{tj-1,i} + \frac{\sigma_{tj,i} - \sigma_{tj-1,i}}{\varepsilon_{tj,i} - \varepsilon_{tj-1,i}} \cdot (\varepsilon_{tj,i}^* - \varepsilon_{tj-1,i}) & ; \varepsilon_{tj-1,i} < \varepsilon_{tj,i}^* \leq \varepsilon_{tj,i} \end{cases} , i = u, r \quad \text{Eq. (C.26)} \\
 , j = 2, 3, 4$$

$$\begin{cases} \sigma_{t1,u,v} = \frac{\sigma_{t1,u}}{\varepsilon_{t1,u}} \cdot \varepsilon_{t1,u,v} & ; \varepsilon_{t1,u,v} \leq \varepsilon_{t1,u} \\ \sigma_{tj,u,v} = \sigma_{tj-1,u} + \frac{\sigma_{tj,u} - \sigma_{tj-1,u}}{\varepsilon_{tj,u} - \varepsilon_{tj-1,u}} \cdot (\varepsilon_{tj,u,v} - \varepsilon_{tj-1,u}) & ; \varepsilon_{tj-1,u} < \varepsilon_{tj,u,v} \leq \varepsilon_{tj,u} \end{cases} , j = 2, 3, 4 \quad \text{Eq. (C.27)}$$

$$\begin{cases} F_{t1,u} = 0.5 \cdot b \cdot \sigma_{t1,u}^* \cdot y_{t1,u} \\ F_{tj-1,u} = b \cdot \sigma_{tj-1,u}^* \cdot (y_{tj,u} - y_{tj-1,u}) \\ F_{tj-2,u} = 0.5 \cdot b \cdot (\sigma_{tj,u}^* - \sigma_{tj-1,u}^*) \cdot (y_{tj,u} - y_{tj-1,u}) \end{cases} , j = 2, 3, 4 \quad \text{Eq. (C.28)}$$

$$\begin{cases} F_{t1,u,v} = -0.5 \cdot b \cdot \sigma_{t1,u,v} \cdot y_{t1,u,v} \\ F_{tj-1,u,v} = -b \cdot \sigma_{tj-1,u,v} \cdot (y_{tj,u,v} - y_{tj-1,u,v}) \\ F_{tj-2,u,v} = -0.5 \cdot b \cdot (\sigma_{tj,u,v} - \sigma_{tj-1,u,v}) \cdot (y_{tj,u,v} - y_{tj-1,u,v}) \end{cases} , j = 2, 3, 4 \quad \text{Eq. (C.29)}$$

$$\chi > 0: \begin{cases} y_{ij,r} = 0 & ; p_{ij,r} \leq p_{hc,ef} \\ y_{ij,r} = p_{ij,r} - x & ; p_{ij,r} > p_{hc,ef} \wedge p_{ij,r} \leq h \\ y_{ij,r} = h - x & ; p_{ij,r} > p_{hc,ef} \wedge p_{ij,r} > h \end{cases}, j = 1, 2, 3, 4 \quad \text{Eq. (C.30)}$$

$$\chi < 0: \begin{cases} y_{ij,r} = 0 & ; p_{ij,r} \geq p_{hc,ef} \\ y_{ij,r} = x - p_{ij,r} & ; p_{ij,r} < p_{hc,ef} \wedge p_{ij,r} > 0 \\ y_{ij,r} = x & ; p_{ij,r} < p_{hc,ef} \wedge p_{ij,r} \leq 0 \end{cases}$$

$$\begin{cases} y_{t1,r}^{ant} = y_{hc,ef} & ; y_{hc,ef} < y_{t1,r} \\ y_{t1,r}^{ant} = 0 & ; y_{hc,ef} \geq y_{t1,r} \\ y_{ij,r}^{ant} = y_{hc,ef} & ; y_{hc,ef} > y_{ij-1,r} \\ y_{ij,r}^{ant} = y_{ij-1,r} & ; y_{hc,ef} \leq y_{ij-1,r} \end{cases}, j = 2, 3, 4 \quad \text{Eq. (C.31)}$$

$$\begin{cases} \sigma_{hc,ef,r} = \frac{\sigma_{t1,r}}{\varepsilon_{t1,r}} \cdot \varepsilon_{hc,ef} & ; \varepsilon_{hc,ef} \leq \varepsilon_{t1,r} \\ \sigma_{hc,ef,r} = \sigma_{t1,r} + \frac{\sigma_{t2,r} - \sigma_{t1,r}}{\varepsilon_{t2,r} - \varepsilon_{t1,r}} \cdot (\varepsilon_{hc,ef} - \varepsilon_{t1,r}) & ; \varepsilon_{t1,r} < \varepsilon_{hc,ef} \leq \varepsilon_{t2,r} \\ \sigma_{hc,ef,r} = \sigma_{t2,r} + \frac{\sigma_{t3,r} - \sigma_{t2,r}}{\varepsilon_{t3,r} - \varepsilon_{t2,r}} \cdot (\varepsilon_{hc,ef} - \varepsilon_{t2,r}) & ; \varepsilon_{t2,r} < \varepsilon_{hc,ef} \leq \varepsilon_{t3,r} \\ \sigma_{hc,ef,r} = \sigma_{t3,r} + \frac{\sigma_{t4,r} - \sigma_{t3,r}}{\varepsilon_{t4,r} - \varepsilon_{t3,r}} \cdot (\varepsilon_{hc,ef} - \varepsilon_{t3,r}) & ; \varepsilon_{t3,r} < \varepsilon_{hc,ef} \leq \varepsilon_{t4,r} \end{cases} \quad \text{Eq. (C.32)}$$

$$\begin{cases} \sigma_{t1,r}^{ant} = \sigma_{hc,ef,r} & ; y_{hc,ef} < y_{t1,r} \\ \sigma_{t1,r}^{ant} = 0 & ; y_{hc,ef} \geq y_{t1,r} \\ \sigma_{ij,r}^{ant} = \sigma_{hc,ef,r} & ; y_{hc,ef} > y_{ij-1,r} \\ \sigma_{ij,r}^{ant} = \sigma_{ij-1,r} & ; y_{hc,ef} \leq y_{ij-1,r} \end{cases}, j = 2, 3, 4 \quad \text{Eq. (C.33)}$$

$$\begin{cases} F_{ij-1,r} = 0 & ; y_{ij,r} < y_{hc,ef} \\ F_{ij-1,r} = b \cdot \sigma_{ij,r}^{ant} \cdot (y_{ij,r} - y_{ij-1,r}^{ant}) & ; y_{ij,r} \geq y_{hc,ef} \\ F_{ij-2,r} = 0 & ; y_{ij,r} < y_{hc,ef} \\ F_{ij-2,r} = 0.5 \cdot b \cdot (\sigma_{ij,r}^* - \sigma_{ij,r}^{ant}) \cdot (y_{ij,r} - y_{ij-1,r}^{ant}) & ; y_{ij,r} \geq y_{hc,ef} \end{cases} j = 1, 2, 3, 4 \quad \text{Eq. (C.34)}$$

$$\begin{cases} F_{tu} = \sum_{j=1}^4 F_{ij,u} + \sum_{j=1}^4 F_{ij,u,v} \\ F_{tr} = \sum_{j=1}^4 F_{ij,r} \\ F_t = F_{tu} + F_{tr} \end{cases} \quad \text{Eq. (C.35)}$$

$$\chi > 0: \begin{cases} d_{t1,u} = x + \frac{2}{3} \cdot y_{t1,u} \\ d_{tj-1,u} = x + y_{tj-1,u} + \frac{(y_{tj,u} - y_{tj-1,u})}{2} \\ d_{tj-2,u} = x + y_{tj-1,u} + \frac{2 \cdot (y_{tj,u} - y_{tj-1,u})}{3} \end{cases}, j = 2, 3, 4$$

$$\chi < 0: \begin{cases} d_{t1,u} = x + \frac{2}{3} \cdot y_{t1,u} \\ d_{tj-1,u} = x - y_{tj-1,u} - \frac{(y_{tj,u} - y_{tj-1,u})}{2} \\ d_{tj-2,u} = x - y_{tj-1,u} - \frac{2 \cdot (y_{tj,u} - y_{tj-1,u})}{3} \end{cases}, j = 2, 3, 4$$

Eq. (C.36)

$$\chi > 0: \begin{cases} d_{t1,u,v} = x + \frac{2}{3} \cdot y_{t1,u,v} \\ d_{tj-1,u,v} = x + y_{tj-1,u,v} + \frac{(y_{tj,u,v} - y_{tj-1,u,v})}{2} \\ d_{tj-2,u,v} = x + y_{tj-1,u,v} + \frac{2 \cdot (y_{tj,u,v} - y_{tj-1,u,v})}{3} \end{cases}, j = 2, 3, 4$$

$$\chi < 0: \begin{cases} d_{t1,u,v} = x + \frac{2}{3} \cdot y_{t1,u,v} \\ d_{tj-1,u,v} = x - y_{tj-1,u,v} - \frac{(y_{tj,u,v} - y_{tj-1,u,v})}{2} \\ d_{tj-2,u,v} = x - y_{tj-1,u,v} - \frac{2 \cdot (y_{tj,u,v} - y_{tj-1,u,v})}{3} \end{cases}, j = 2, 3, 4$$

Eq. (C.37)

$$\chi > 0: \begin{cases} d_{tj-1,r} = x + y_{tj,r}^{ant} + \frac{(y_{tj,r} - y_{tj,r}^{ant})}{2} \\ d_{tj-1,r} = x + y_{tj,r}^{ant} + \frac{2 \cdot (y_{tj,r} - y_{tj,r}^{ant})}{3} \end{cases}, j = 1, 2, 3, 4$$

$$\chi < 0: \begin{cases} d_{tj-1,r} = x - y_{tj,r}^{ant} - \frac{(y_{tj,r} - y_{tj,r}^{ant})}{2} \\ d_{tj-1,r} = x - y_{tj,r}^{ant} - \frac{2 \cdot (y_{tj,r} - y_{tj,r}^{ant})}{3} \end{cases}$$

Eq. (C.38)

$$\begin{cases} M_{tu} = \sum_{j=1}^4 F_{tj,u} \cdot d_{tj,u} + \sum_{j=1}^4 F_{tj,u,v} \cdot d_{tj,u,v} \\ M_{tr} = \sum_{j=1}^4 F_{tj,r} \cdot d_{tj,r} \end{cases}$$

Eq. (C.39)

APPENDIX D

D.3 Determination of structural characteristic length

In Table 23 is presented the algorithm for the determination of the structural characteristic length of FRC member. The calculation procedure is based on the methodology presented in section 2.3.3.

The structural characteristic length of an FRC cross-section without longitudinal conventional reinforcements is equal to the cross-section height, $l_{cs}^u = h$.

For FRC cross-section with longitudinal steel rebars, the structural characteristic zone is evaluated for the two zones of the cross-section: (i) a reinforced zone limited between the bottom fiber and the height of the effective tensile zone, $h_{c,ef}$; (ii) and an unreinforced zone limited by the height of the effective tensile zone of the cross-section and extreme compressive (top) fiber of the cross-section.

The value of l_{cs}^r is the minimum between mean crack spacing, s_m , and the distance between the cross neutral axis-position and the extreme tensile (bottom) fiber of the cross-section, y . The neutral axis position is determined considering the bending moment corresponding to the serviceability criteria (data input) and disregarding the FRC tensile strength. The value of l_{cs}^u is equal to the distance between top fiber of the cross-section and the height of the effective tensile zone of the cross-section.

Table 23 – Algorithm for determination of structural characteristic length of FRC member.

ROUTINE TITLE: <i>Calc_structural_length</i>
INPUT: <ul style="list-style-type: none"> • Class with geometry and material data, <i>cData</i>.
OUTPUT: <ul style="list-style-type: none"> • Structural characteristic length of the unreinforced zone, l_{cs}^u, and of the reinforced zone, l_{cs}^r.
<p>I) Determine if longitudinal conventional reinforcements are adopted in the cross-section. Is $(M_{Ed,crack} > 0 \wedge A_{s1_1} = 0 \wedge A_{s1_2} = 0) \vee (M_{Ed,crack} < 0 \wedge A_{s2_1} = 0 \wedge A_{s2_2} = 0)$?</p> <p>i) <i>Yes</i>: Set $l_{cs}^u = h$. Go to II).</p> <p>ii) <i>No</i>:</p>

- i) Read variable corresponding to the creep coefficient, φ_c , from *cData*.
- ii) Set analyze type to RC cross-section: $CS_type = RC$.
- iii) Set analysis state to SLS: $Analysis_type = SLS$.
- iv) Resolve cross-section equilibrium equations disregarding tensile strength of FRC:
Call routine $Calc_section(cData, CS_type, Analysis_type, \varphi, M_{Ed,crack}, N_{Ed,crack})$, and retrieve neutral axis position, x , and curvature, χ .
- v) Calculate $y = h - x$.
- vi) Determine f_{Ftsm} from Eq. (2.113) and Eq. (2.16).
- vii) Determine mean crack spacing s_{rm} : Call routine $Calc_lsmax(cData, f_{Ftsm}, y)$. Retrieve s_{rm} .
- viii) Determine the height of the effective tensile zone, $h_{c,ef}$, considering the distance between neutral axis and extreme fiber of cross-section in tension, y . Call routine $Calc_effective_height(cData)$. Retrieve $h_{c,ef}$.
- ix) Set $l_{cs}^r = \min(s_{rm}, y)$.
- x) Set $l_{cs}^u = h - h_{c,ef}$.

II) **End.**

In Table 24 is presented the algorithm that is used to set the formula to determine the height of effective tensile zone of the cross-section. This procedure is based on the approximated method presented in section 2.5.5. The set of formulas that allow to determine the effective tensile zone height are exported to an Excel worksheet, whose value is updated considering the type of element in analysis, geometrical data of the cross-section and distance y .

Table 24 – Algorithm to set the formulas for effective height of tensile zone of cross-section.

ROUTINE TITLE: <i>Calc_effective_height</i>
INPUT: <ul style="list-style-type: none"> • Class with geometry and material data, <i>cData</i>.
OUTPUT: <ul style="list-style-type: none"> • Height of effective tensile zone, $h_{c,eff}$.
<p>I) Read in <i>cData</i> the type of element to be analyzed: <i>Elem_Type</i></p> <p>II) Define formula for $h_{c,eff}$. Check value of <i>Elem_Type</i>?</p> <p>i) <i>Elem_Type</i> = "Beam" :</p> <p>1) If $\chi > 0$:</p> <p>a) If $A_{s1_1} > 0 \wedge A_{s1_2} > 0$: $h_{c,eff} = \min\left(2.5 \cdot \min(c_{1_1}, c_{1_2}), \frac{y}{3}\right)$. End.</p> <p>b) If $A_{s1_1} > 0 \wedge A_{s1_2} = 0$: $h_{c,eff} = \min\left(2.5 \cdot c_{1_1}, \frac{y}{3}\right)$. End.</p> <p>c) If $A_{s1_1} = 0 \wedge A_{s1_2} > 0$: $h_{c,eff} = \min\left(2.5 \cdot c_{1_2}, \frac{y}{3}\right)$. End.</p> <p>d) $A_{s1_1} = 0 \wedge A_{s1_2} = 0$: $h_{c,eff} = 0$. End.</p> <p>2) If $\chi < 0$:</p> <p>a) If $A_{s2_1} > 0 \wedge A_{s2_2} > 0$: $h_{c,eff} = \min\left(2.5 \cdot \min(c_{2_1}, c_{2_2}), \frac{y}{3}\right)$. End.</p> <p>b) If $A_{s2_1} > 0 \wedge A_{s2_2} = 0$: $h_{c,eff} = \min\left(2.5 \cdot c_{2_1}, \frac{y}{3}\right)$. End.</p> <p>c) If $A_{s2_1} = 0 \wedge A_{s2_2} > 0$: $h_{c,eff} = \min\left(2.5 \cdot c_{2_2}, \frac{y}{3}\right)$. End.</p> <p>d) If $A_{s2_1} = 0 \wedge A_{s2_2} = 0$: $h_{c,eff} = 0$. End.</p> <p>ii) <i>Elem_Type</i> = "Slab" :</p> <p>1) If $\chi > 0$:</p>

a) If $A_{s1-1} > 0 \wedge A_{s1-2} > 0$:

$$h_{c,eff} = \min \left(2.5 \cdot \left(\min(c_{1-1}, c_{1-2}) + 0.5 \cdot \left(\frac{\phi_{1-1}^2 \cdot A_{s1-1} + \phi_{1-2}^2 \cdot A_{s1-2}}{\phi_{1-1} \cdot A_{s1-1} + \phi_{1-2} \cdot A_{s1-2}} \right) \right), y/3 \right)$$

End.

b) If $A_{s1-1} > 0 \wedge A_{s1-2} = 0$: $h_{c,eff} = \min \left(2.5 \cdot (c_{1-1} + 0.5 \cdot \phi_{1-1}), y/3 \right)$. End.

c) If $A_{s1-1} = 0 \wedge A_{s1-2} > 0$: $h_{c,eff} = \min \left(2.5 \cdot (c_{1-2} + 0.5 \cdot \phi_{1-2}), y/3 \right)$. End.

d) If $A_{s1-1} = 0 \wedge A_{s1-2} = 0$: $h_{c,eff} = 0$. End.

2) If $\chi < 0$:

a) If $A_{s2-1} > 0 \wedge A_{s2-2} > 0$:

$$h_{c,eff} = \min \left(2.5 \cdot \left(\min(c_{2-1}, c_{2-2}) + 0.5 \cdot \left(\frac{\phi_{2-1}^2 \cdot A_{s2-1} + \phi_{2-2}^2 \cdot A_{s2-2}}{\phi_{2-1} \cdot A_{s2-1} + \phi_{2-2} \cdot A_{s2-2}} \right) \right), y/3 \right)$$

End.

b) If $A_{s2-1} > 0 \wedge A_{s2-2} = 0$: $h_{c,eff} = \min \left(2.5 \cdot (c_{2-1} + 0.5 \cdot \phi_{2-1}), y/3 \right)$. End.

c) If $A_{s2-1} = 0 \wedge A_{s2-2} > 0$: $h_{c,eff} = \min \left(2.5 \cdot (c_{2-2} + 0.5 \cdot \phi_{2-2}), y/3 \right)$. End.

d) If $A_{s2-1} = 0 \wedge A_{s2-2} = 0$: $h_{c,eff} = 0$. End.

iii) *Elem_Type* = "Wall" :

1) If $\chi > 0$:

a) If $A_{s1-1} > 0 \wedge A_{s1-2} > 0$:

$$h_{c,eff} = \min \left(2.5 \cdot \left(\min(c_{1-1}, c_{1-2}) + 0.5 \cdot \left(\frac{\phi_{1-1}^2 \cdot A_{s1-1} + \phi_{1-2}^2 \cdot A_{s1-2}}{\phi_{1-1} \cdot A_{s1-1} + \phi_{1-2} \cdot A_{s1-2}} \right) \right), h/2 \right)$$

End.

b) If $A_{s1-1} > 0 \wedge A_{s1-2} = 0$: $h_{c,eff} = \min \left(2.5 \cdot (c_{1-1} + 0.5 \cdot \phi_{1-1}), h/2 \right)$. End.

c) If $A_{s1_1} = 0 \wedge A_{s1_2} > 0$: $h_{c,eff} = \min\left(2.5 \cdot (c_{1_2} + 0.5 \cdot \phi_{1_2}), h/2\right)$. End.

d) If $A_{s1_1} = 0 \wedge A_{s1_2} = 0$: $h_{c,eff} = 0$. End.

2) If $\chi < 0$:

a) If $A_{s2_1} > 0 \wedge A_{s2_2} > 0$:

$$h_{c,eff} = \min\left(2.5 \cdot \left(\min(c_{2_1}, c_{2_2}) + 0.5 \cdot \left(\frac{\phi_{2_1}^2 \cdot A_{s2_1} + \phi_{2_2}^2 \cdot A_{s2_2}}{\phi_{2_1} \cdot A_{s2_1} + \phi_{2_2} \cdot A_{s2_2}}\right)\right), h/2\right)$$

End.

b) If $A_{s2_1} > 0 \wedge A_{s2_2} = 0$: $h_{c,eff} = \min\left(2.5 \cdot (c_{2_1} + 0.5 \cdot \phi_{2_1}), h/2\right)$. End.

c) If $A_{s2_1} = 0 \wedge A_{s2_2} > 0$: $h_{c,eff} = \min\left(2.5 \cdot (c_{2_2} + 0.5 \cdot \phi_{2_2}), h/2\right)$. End.

d) If $A_{s2_1} = 0 \wedge A_{s2_2} = 0$: $h_{c,eff} = 0$. End.

D.4 Definition constitutive models

The definition of the constitutive models for concrete in compression, FRC in tension and steel in tension and compression are based on the formulation presented in section 2.3. In Table 25 to Table 28 are presented the algorithms used in *FRCcalc* to define the mentioned constitutive models. The formulas that define the constitutive models are exported to an Excel worksheet, and for each iteration of the calculation procedure the stresses are updated according to the strains of each characteristic point of the cross-section.

Table 25 – Algorithm for definition of constitutive model for concrete in compression.

ROUTINE TITLE: <i>model_SigmaC</i>
INPUT: <ul style="list-style-type: none"> • Class with geometry and material data, <i>cData</i>. • Variable that defines type of limit state analysis to be performed, <i>Analysis_type = ULS/SLS</i>.
OUTPUT: <ul style="list-style-type: none"> • Formula for σ_{c1}, σ_{c2}, x_{c1} and x_{c2}.

<p>I) Read concrete creep coefficient, φ_c, from <i>cData</i>.</p> <p>II) Define partial safety factor for concrete in compression. Check value of <i>Analysis_type</i>?</p> <p>i) <i>Analysis_type</i> = <i>SLS</i>: Set $\gamma_c = 1.0$.</p> <p>ii) <i>Analysis_type</i> = <i>ULS</i>: Set $\gamma_c = 1.5$.</p> <p>III) Set $\alpha_{cc} = 1.0$.</p> <p>IV) Determine design value for concrete compressive strength: $f_{cd} = \alpha_{cc} \cdot f_{ck} / \gamma_c$.</p> <p>V) Set formula for p_{c1}, p_{c2} and $d_{\varepsilon_{c3}}$ according to Eq. (C.3).</p> <p>VI) Set formula for x_{c1}, x_{c2}, $x_{c1,v}$ and $x_{c2,v}$ according to Eq. (C.4) and Eq. (C.5).</p> <p>VII) Set formula for ε_{c1}, ε_{c2}, $\varepsilon_{c1,v}$ and $\varepsilon_{c2,v}$ according to Eq. (C.6).</p> <p>VIII) Set formula for σ_{c1}, σ_{c2}, $\sigma_{c1,v}$ and $\sigma_{c2,v}$ according to Eq. (C.7).</p> <p>IX) End.</p>
--

Table 26 – Algorithm for definition of constitutive model for steel in compression or tension.

ROUTINE TITLE: <i>model_SigmaS</i>
<p>INPUT:</p> <ul style="list-style-type: none"> • Class with geometry and material data, <i>cData</i>. • Variable that defines type of limit state analysis to be performed, <i>Analysis_type</i> = <i>ULS/SLS</i>. • Variable <i>j</i>, that represents if the model is for bottom (<i>j</i>=1) or top (<i>j</i>=2) reinforcements.
<p>OUTPUT:</p> <ul style="list-style-type: none"> • Formula for $\sigma_{s,j}$.
<p>I) Define partial safety factor for concrete in compression. Check value of <i>Analysis_type</i>?</p> <p>i) <i>Analysis_type</i> = <i>SLS</i>: Set $\gamma_s = 1.0$.</p> <p>ii) <i>Analysis_type</i> = <i>ULS</i>: Set $\gamma_s = 1.15$.</p>

I)	Determine design value of steel yield strength: $f_{yd} = f_{yk} / \gamma_s$.
II)	Set formula for $\sigma_{s,j}$ according to Eq. (C.13).
III)	End.

Table 27 – Algorithm for definition of constitutive model for FRC in tension at ULS.

ROUTINE TITLE: <i>model_FRC_ULS</i>	
INPUT:	<ul style="list-style-type: none"> • Class with geometry and material data, <i>cData</i>. • Variable <i>i</i> that defines the zone of tensile zone of the cross-section (<i>i</i> = 1 corresponds to unreinforced zone; <i>i</i> = 2 corresponds to reinforced zone limited by the effective tension zone height). • Variable <i>z</i> that defines the number of divisions of the tensile zone of the cross-section. • $l_{cs,i}$, structural characteristic length of zone <i>i</i> .
OUTPUT:	<ul style="list-style-type: none"> • Values of $\sigma_{tj,i}$ of the quadrilinear model, $j = 1, 2, 3, 4$. • Formulas for $y_{tj,i}$, $\sigma_{bot,i}$ and $\sigma_{h,i}$.
I)	Set partial safety factor: $\gamma_F = 1.5$
II)	Determine characteristic tensile strength: $f_{ctk} = 0.7 \cdot f_{ctm}$
III)	Determine values for the model characteristic points: <ul style="list-style-type: none"> i) Set $\sigma_{t1,i} = 0.9 \cdot f_{ctk} / \gamma_F$ and $\varepsilon_{t1,i} = \sigma_{t1,i} / E_c$. ii) Set $\sigma_{t2,i} = f_{ctk} / \gamma_F$ and $\varepsilon_{t1,i} = 0.15\text{‰}$. iii) Set $\sigma_{t3,i} = 0.45 \cdot f_{r1k} / \gamma_F$ and $\varepsilon_{t3,i} = 0.15\text{‰}$. iv) Determine ultimate crack opening for zone <i>i</i> , based on Eq. (2.18) and considering $\varepsilon_{fu} = 0.02$: $w_{u,i} = \min(2.5; l_{cs,i} \cdot 0.02)$.

v) Set $\sigma_{t4,i} = \max\left(0; f_{Ftsk} - \frac{w_{u,i}}{2.5} \cdot (f_{Ftsk} - 0.5 \cdot f_{R3k} + 0.2 \cdot f_{R1k})\right)$ and

$$\varepsilon_{t4,i} = w_{u,i} / l_{cs,i} .$$

vi) If $z = 2$: Set formulas for tensile stress at division of tensile zone, $\sigma_{hc,ef,r}$ from Eq. (C.32).

vii) Value of i ?

1) $i = 1$:

a) Set formulas for distance between cross-section top edge and end of each quadrilinear branch of the model, $p_{j,u}$, $j = 1, 2, 3, 4$ from Eq. (C.19).

b) Set formulas for distance between neutral axis and end of each quadrilinear branch of the model, $y_{j,u}$, $j = 1, 2, 3, 4$ from Eq. (C.21) and

$y_{j,u,v}$, $j = 1, 2, 3, 4$ from Eq. (C.22).

c) Set formulas for stress corresponding to the distance $y_{j,u}$, $\sigma_{ij,u}^*$ from Eq. (C.26), respectively.

d) Set formulas for $\sigma_{ij,u,v}$ $j = 1, 2, 3, 4$ from Eq. (C.27).

2) $i = 2$:

a) Set formulas for $p_{hc,ef}$ (Eq. (C.20)), $y_{hc,ef}$ (Eq. (C.23)), $\varepsilon_{hc,ef}$ (Eq. (C.24)) and $\sigma_{hc,ef,r}$ (Eq. (C.32)).

e) Set formulas for distance between cross-section top edge and end of each quadrilinear branch of the model, $p_{j,r}$, $j = 1, 2, 3, 4$ from Eq. (C.19).

f) Set formulas for distance between neutral axis and end of each quadrilinear branch of the model, $y_{j,r}$, $j = 1, 2, 3, 4$ from Eq. (C.30) and

$y_{j,r}^{ant}$, $j = 1, 2, 3, 4$ from Eq. (C.31).

b) Set formulas for $\sigma_{ij,r}^{ant}$ from Eq. (C.33).

IV) End.

Table 28 – Algorithm for definition of constitutive model for FRC in tension at SLS.

ROUTINE TITLE: <i>model_FRC_SLS</i>
<p>INPUT:</p> <ul style="list-style-type: none"> • Class with geometry and material data, <i>cData</i>. • Variable <i>i</i> that defines the zone of tensile zone of the cross-section (<i>i</i> = 1 corresponds to unreinforced zone; <i>i</i> = 2 corresponds to reinforced zone limited by the effective tension zone height). • Variable <i>z</i> that defines the number of divisions of the tensile zone of the cross-section. • $l_{cs,i}$, structural characteristic length of zone <i>i</i>.
<p>OUTPUT:</p> <ul style="list-style-type: none"> • Values of $\sigma_{ij,i}$ of the quadrilinear model, $j = 1, 2, 3, 4$. • Formulas for $y_{ij,i}$, $\sigma_{bot,i}$ and $\sigma_{h,i}$.
<p>I) Set partial safety factor: $\gamma_F = 1.0$.</p> <p>II) Determine serviceability residual tensile strength: $f_{Ftsk} = 0.45 \cdot f_{R1k}$.</p> <p>III) Determine characteristic tensile strength: $f_{ctk} = 0.7 \cdot f_{cm}$.</p> <p>IV) Determine mean compressive strength: $f_{cm} = f_{ck} + 8$.</p> <p>V) Determine fracture energy: $G_F = \frac{73 \cdot f_{cm}^{0.18}}{1000}$.</p> <p>VI) Determine values for the model characteristic points:</p> <p>i) Set $\sigma_{t1,i} = 0.9 \cdot f_{ctk} / \gamma_F$ and $\varepsilon_{t1,i} = \sigma_{t1,i} / E_c$.</p> <p>ii) Set $\sigma_{t2,i} = f_{ctk} / \gamma_F$ and $\varepsilon_{t2,i} = 0.15\text{‰}$.</p> <p>iii) Set $\sigma_{t4,i} = f_{Ftsk}$ and $\varepsilon_{t4,i} = 0.5 / l_{cs,i}$.</p> <p>iv) Determine ultimate crack opening for zone based on Eq. (2.18) and considering.</p> $\varepsilon_{fu} = 0.02 : w_{u,i} = \min(2.5; l_{cs,i} \cdot 0.02).$

$$v) \text{ Set } \sigma_{E,i} = \max \left(0; f_{Ftsk} - \frac{w_{u,i}}{2.5} \cdot (f_{Ftsk} - 0.5 \cdot f_{R3k} + 0.2 \cdot f_{R1k}) \right) \text{ and}$$

$$\varepsilon_{E,i} = w_{u,i} / l_{cs,i} \cdot$$

vi) Determine type of case for SLS model:

1) Is $f_{Ftsk} < f_{ctk}$?

a) *No: Go to 2).*

b) *Yes: Case=1:*

$$b.1) \text{ Set } \sigma_{Q,i} = 0.2 \cdot f_{ctk} \text{ and } \varepsilon_{Q,i} = \frac{G_F}{f_{ctk} \cdot l_{cs,i}} + \left(\varepsilon_{t2,i} - \frac{0.8 \cdot f_{ctk}}{E_c} \right).$$

$$b.2) \text{ Set } m_{ED,i} = \frac{\sigma_{E,i} - \sigma_{t4,i}}{\varepsilon_{E,i} - \varepsilon_{A,i}} \text{ and } b_{ED,i} = \sigma_{E,i} - m_{ED,i} \cdot \varepsilon_{E,i}.$$

$$b.3) \text{ Set } m_{BQ,i} = \frac{\sigma_{Q,i} - \sigma_{t2,i}}{\varepsilon_{Q,i} - \varepsilon_{2,i}} \text{ and } b_{BQ,i} = \sigma_{Q,i} - m_{BQ,i} \cdot \varepsilon_{Q,i}.$$

b.4) Is $\varepsilon_{Q,i} < \varepsilon_{t2,i}$?

- Yes: Set $\varepsilon_{t3,i} = \varepsilon_{t2,i} + 1 \times 10^{-16}$ and $\sigma_{t3,i} = m_{ED,i} \cdot \varepsilon_{t3,i} + b_{ED,i}$
(Figure 15). **Go to ix).**

- No: **Go to b.5).**

b.5) Determine point C coordinates):

$$\varepsilon_{C,i} = \frac{b_{DE,i} - b_{BQ,i}}{m_{BQ,i} - m_{DE,i}} \text{ and } \sigma_{C,i} = m_{DE,i} \cdot \varepsilon_{C,i} + b_{DE,i}.$$

b.6) Is $\varepsilon_{C,i} < \varepsilon_{t2,i}$?

- No: Set $\sigma_{t3,i} = \sigma_{C,i}$ and $\varepsilon_{t3,i} = \varepsilon_{C,i}$ (Figure 14a). **Go to ix).**

- Yes: Set $\sigma_{t3,i} = \sigma_{t2,i}$ and $\varepsilon_{t3,i} = \varepsilon_{t2,i} + 1 \times 10^{-16}$ (Figure 16). **Go to ix).**

2) Check if Case=2 or 3. Is $\frac{\sigma_{t4} - \sigma_{t1}}{\varepsilon_{t4} - \varepsilon_{t1}} \leq \frac{\sigma_{t2} - \sigma_{t1}}{\varepsilon_{t2} - \varepsilon_{t1}}$?

a) Yes: Case=2. **Go to viii);**

b) No: Case=3. **Go to vii).**

vii) Determine point A' : $\sigma_{A',i} = 0.9 \cdot f_{Ftsk}$ and $\varepsilon_{A',i} = \frac{\sigma_{A',i}}{E_c}$, and set $\sigma_{t2,i} = \sigma_{A',i}$

and $\varepsilon_{t2,i} = \varepsilon_{A',i}$.

viii) Determine mid-point between point B and D (Figure 14a,b). Set

$$\sigma_{t3,i} = \sigma_{t2,i} + \frac{\sigma_{t4,i} - \sigma_{t2,i}}{2} \text{ and } \varepsilon_{t3,i} = \varepsilon_{t2,i} + \frac{\varepsilon_{t4,i} - \varepsilon_{t2,i}}{2}.$$

ix) If $z = 2$: Set formulas for tensile stress at division of tensile zone, $\sigma_{hc,ef,r}$ from Eq. (C.32).

x) Value of i ?

3) $i = 1$:

a) Set formulas for distance between cross-section top edge and end of each quadrilinear branch of the model, $p_{j,u}$, $j = 1, 2, 3, 4$ from Eq. (C.19).

b) Set formulas for distance between neutral axis and end of each quadrilinear branch of the model, $y_{j,u}$, $j = 1, 2, 3, 4$ from Eq. (C.21) and $y_{j,u,v}$, $j = 1, 2, 3, 4$ from Eq. (C.22).

c) Set formulas for stress corresponding to the distance $y_{j,u}$, $\sigma_{ij,u}^*$ from Eq. (C.26), respectively.

d) Set formulas for $\sigma_{ij,u,v}$ $j = 1, 2, 3, 4$ from Eq. (C.27).

4) $i = 2$:

c) Set formulas for $p_{hc,ef}$ (Eq. (C.20)), $y_{hc,ef}$ (Eq. (C.23)), $\varepsilon_{hc,ef}$ (Eq. (C.24)) and $\sigma_{hc,ef,r}$ (Eq. (C.32)).

e) Set formulas for distance between cross-section top edge and end of each quadrilinear branch of the model, $p_{j,r}$, $j = 1, 2, 3, 4$ from Eq. (C.19).

- f) Set formulas for distance between neutral axis and end of each quadrilinear branch of the model, $y_{ij,r}$, $j = 1, 2, 3, 4$ from Eq. (C.30) and

$$y_{ij,r}^{ant}, \quad j = 1, 2, 3, 4 \text{ from Eq. (C.31).}$$

- d) Set formulas for $\sigma_{ij,r}^{ant}$ from Eq. (C.33).

VII) End.

D.5 Calculate neutral axis position and curvature for cross-section under bending and axial force

In the following section are presented the algorithm used to calculate the neutral axis position and curvature, considering the acting bending moment, M , and axial force N in the FRC or RC cross-section. This calculation routine is based on the plain section analysis presented in section 3.2.

In Table 29 is presented the main algorithm of the calculation routine, which calls the routines that defines the formulas of the constitutive models, equilibrium and compatibility equations, as well as the routine that resolves the equilibrium equations.

Table 29 – Algorithm to determine neutral axis and curvature of a FRC or RC cross-section.

ROUTINE TITLE: <i>Calc_section</i>
<p>INPUT:</p> <ul style="list-style-type: none"> • Class with geometry and material data, <i>cData</i>. • Variable that defines type of cross-section to be analyzed, $CS_type = FRC/RC$. • Variable that defines type of limit state analysis to be performed, $Analysis_type = ULS/SLS$. • Variable corresponding to the creep coefficient, φ_c. • Bending moment, M_{Ed}, and axial force, N_{Ed}.
<p>OUTPUT:</p> <ul style="list-style-type: none"> • Neutral axis, x. • Curvature, χ. • Stresses, strain forces and depth of forces in characteristic points of the cross-section.
<p>l) Define concrete compressive constitutive model. Call <i>model_SigmaC(Analysis_type, φ_c, cData)</i>.</p>

- II) If $A_{s1_1} > 0 \vee A_{s1_2} > 0$:Set $j = 1$.Call *model_SigmaS*(j , *Analysis_type*, *cData*).
- III) If $A_{s2_1} > 0 \vee A_{s2_2} > 0$:Set $j = 2$.Call *model_SigmaS*(j , *Analysis_type*, *cData*).
- IV) Check type of analysis to be performed: Is $CS_type = FRC$?
- i) *Yes*: **Go to V**).
- ii) *No*: Set $z = 0$. **Go to VI**).
- V) Define FRC tensile constitutive model:
- i) Check if longitudinal conventional tensile reinforcements are adopted in the cross-section. Is $(M_{Ed} > 0 \wedge A_{s1_1} = 0 \wedge A_{s1_2} = 0) \vee (M_{Ed} < 0 \wedge A_{s2_1} = 0 \wedge A_{s2_2} = 0)$?
- Yes* : $z = 1$.
- No* : $z = 2$.
- ii) Define formula for the height of effective tensile zone. Call routine *Calc_effective_height*(*cData*).
- iii) Determine structural characteristic length. Call routine *Calc_structural_length*(*cData*). If $z = 1$, retrieve l_{cs}^u . If $z = 2$, retrieve l_{cs}^u and l_{cs}^r .
- iv) Set $i = 1$.
- v) Define structural characteristic length for zone i :
- If $i = 1$: $l_{cs,i} = l_{cs}^u$.
- If $i = 2$: $l_{cs,i} = l_{cs}^r$.
- vi) Is $i \leq z$?
- Yes*: **Go to vii**).
- No*: **Go to VI**).
- vii) Check value of *Analysis_type* ?
- a) *Analysis_type* = *SLS*: Call routine *model_FRC_SLS*(*cData*, i , z , $l_{cs,i}$).
- b) *Analysis_type* = *ULS*: Call routine *model_FRC_ULS*(*cData*, i , z , $l_{cs,i}$).

viii)	$i = i + 1$. Go to v).
VI)	Define equilibrium equations in the cross-section. Call <i>Formula_Forces</i> (<i>cData</i> , <i>z</i> , <i>CS_type</i> , N_{Ed}) and <i>Formula_Moment</i> (<i>cData</i> , <i>z</i> , <i>CS_Type</i> , M_{Ed} , N_{Ed}).
VII)	Define compatibility equations in the cross-section. Call <i>Formula_Compatibility</i> ().
VIII)	Resolve equilibrium equations. Call <i>resolve_x_curvature</i> (M_{Ed}). Return neutral axis position, x , and curvature, χ .
IX)	Import data of resolution of equilibrium and compatibility equations (stresses, strains, forces, depth of forces) to <i>cData</i> .
X)	End.

In Table 30 and Table 31 are presented the subroutines to define the formulas of the equilibrium equations for a FRC and RC cross-section.

Table 30 – Algorithm to set the formulas for forces in a FRC cross-section.

ROUTINE TITLE: <i>Formula_Forces</i>	
INPUT:	
<ul style="list-style-type: none"> • Class with geometry and material data, <i>cData</i>. • Variable z that defines the total number of divisions of the tensile zone of the cross-section. • Variable that defines type of cross-section to be analyzed, $CS_type = FRC/RC$. • Axial force, N. 	
OUTPUT:	
<ul style="list-style-type: none"> • Formula for sum of forces in the cross-section. 	
I)	Define formulas for concrete in compression forces in the cross-section according to Eq. (C.8).
II)	Define formulas for reinforcement steel bars forces in the cross-section according to Eq. (C.14).
III)	Check type of cross-section to be analyzed. Value of CS_type ?
i)	$CS_type = FRC$. Go to IV).
ii)	$CS_type = RC$. Set $F_{t,u} = F_{t,u,v} = F_{t,r} = 0$. Go to V).

IV)	Define formulas for FRC in tension forces in the cross-section according to Eq. (C.35).
V)	Define formula for sum of forces in cross-section according to Eq. (C.1), considering the value of N .
VI)	End.

Table 31 – Algorithm to set the formulas for forces depth and moments in a FRC cross-section.

ROUTINE TITLE: <i>Formula_Moments</i>	
INPUT:	<ul style="list-style-type: none"> • Class with geometry and material data, $cData$. • Variable z that defines the total number of divisions of the tensile zone of the cross-section. • Variable that defines type of cross-section to be analyzed, $CS_type = FRC/RC$. • Axial force, N and bending moment, M.
OUTPUT:	<ul style="list-style-type: none"> • Formula for sum of moments in the cross-section.
I)	Define formulas for depth and moment of forces for concrete in compression in the cross-section according to Eq. (C.9) and Eq. (C.11).
II)	Define formulas for depth and moment of forces of reinforcement steel bars in the cross-section according to Eq. (C.15) and Eq. (C.16).
III)	Check type of cross-section to be analyzed. Value of CS_type ?
	<ul style="list-style-type: none"> i) $CS_type=FRC$. Go to IV). ii) $CS_type=RC$. Go to V).
IV)	Define formulas for depth and moment of forces of FRC in tension in the cross-section according to Eq. (C.36) to Eq. (C.39).
V)	Define formula for sum of moments in cross-section according to Eq. (C.1), considering the value of M and N .
VI)	End.

In Table 32 is presented the algorithm that defines the formulas of the compatibility equations in the cross-section, based on Eq. (C.2).

Table 32 – Algorithm to set the formulas compatibility equations.

ROUTINE TITLE: <i>Formula_Compatibility</i>
INPUT: not applicable
OUTPUT: <ul style="list-style-type: none"> • Formulas for compatibility equations in the cross-section.
<p>I) Define formula for top and bottom fibers of the cross-section:</p> $\varepsilon_{top} = -\chi \cdot x$ $\varepsilon_{bot} = \varepsilon_{top} + \chi \cdot h$ <p>II) Define formula for curvature of the cross-section: $\chi = -\frac{\varepsilon_{top}}{x}$.</p> <p>III) End.</p>

In Table 33 is presented the algorithm that is used to resolve the equilibrium equations and find the solution for the neutral axis position, x , and cross-section curvature, χ , for a given acting bending moment, M . This procedure resorts to Microsoft Excel Solver algorithm to apply an iterative approach to find the solution for the problem $(\min(x, \chi))$, given specific constraints $(\sum F = N; \sum M = M)$.

Table 33 – Algorithm to resolve the equilibrium equations and find solution for neutral axis position and cross-section curvature.

ROUTINE TITLE: <i>resolve_x_and_curvature</i>
INPUT Bending moment, M_{Ed} .
OUTPUT: <ul style="list-style-type: none"> • Neutral axis, x ; • Curvature, χ .
<p>I) Set changing variables equal to neutral axis and curvature: <i>changing variables</i> = $x; \chi$.</p> <p>II) Set objective function equal to the sum of the neutral axis and curvature: <i>objective</i> = $\min(x + \chi)$.</p> <p>III) Set constraints of the iterative model based on the equilibrium equations Eq. (C.1).</p> <p>IV) Set initial values of neutral axis and curvature equal to:</p>

$$\begin{cases} x = \frac{h}{2} \\ M_{Ed} > 0: \chi = \frac{2 \cdot \varepsilon_{c3}}{10 \cdot h}; M_{Ed} < 0: \chi = -\frac{2 \cdot \varepsilon_{c3}}{10 \cdot h} \end{cases}$$

- V) Set $iIter = 1$.
- VI) Set maximum number for changing the initial values of iterative algorithm, $nIterMax = 20$.
- VII) Call *Excel Solver* module. Return state variable of convergence $Solver_out$.
- VIII) Convergence check: Value of $Solver_out$?
- i) $Solver_out = OK$: **End**.
- ii) $Solver_out = KO$ and $iIter \leq nIterMax$: Change initial solution: $x = iIter \cdot \frac{h}{20}$ and $M_{Ed} > 0: \chi = \frac{2 \cdot \varepsilon_{c3}}{10 \cdot h}; M_{Ed} < 0: \chi = -\frac{2 \cdot \varepsilon_{c3}}{10 \cdot h}$. Set $iIter = iIter + 1$. **Go to VII**).
- iii) $Solver_out = KO$ and $iIter > nIterMax$: No convergence. Send error message. **End**.

D.6 Determination of moment-curvature relationship

In the following section are presented the algorithms used to calculate the resisting moment vs. curvature relationship of a FRC or RC cross-section under bending without axial force. The calculation procedure resorts to an iterative approach to determine the neutral axis position in the cross-section, considering an incremental strain value of the top fiber of the cross-section. At each strain increment, the height of the effective tensile zone of the cross-section is updated. After resolution of the equilibrium equations, the curvature of the cross-section is determined from the compatibility equations (Eq. (C.2)).

Table 34 – Algorithm to determine the moment-curvature relationship of a FRC or RC cross-section.

ROUTINE TITLE: <i>Calc_M_curv</i>
<p>INPUT:</p> <ul style="list-style-type: none"> • Class with geometry and material data, <i>cData</i> . • Variable that defines type of cross-section to be analyzed, $CS_type = FRC/RC$; • Variable that defines type of limit state analysis to be performed, $Analysis_type = ULS/SLS$.
<p>OUTPUT:</p> <ul style="list-style-type: none"> • Relationship of M vs. χ of the cross-section.
<p>I) Define concrete compressive constitutive model. Call <i>model_SigmaC(Analysis_type , φ_c , cData)</i>.</p> <p>II) If $A_{s1-1} > 0 \vee A_{s1-2} > 0$:Set $j = 1$.Call <i>model_SigmaS(j , Analysis_type , cData)</i>.</p> <p>III) If $A_{s2-1} > 0 \vee A_{s2-2} > 0$:Set $j = 2$.Call <i>model_SigmaS(j , Analysis_type , cData)</i>.</p> <p>IV) Check type of analysis to be performed: Is $CS_type = "FRC"$?</p> <p style="padding-left: 40px;">i) <i>Yes: Go to V).</i></p> <p style="padding-left: 40px;">ii) <i>No: Set $z = 0$. Go to VI).</i></p> <p>V) Define FRC tensile constitutive model:</p> <p style="padding-left: 40px;">i) Check if longitudinal conventional tensile reinforcements are adopted in the cross-section. Is $A_{s1-1} = 0 \wedge A_{s1-2} = 0$?</p> <p style="padding-left: 80px;">1) <i>Yes : $z = 1$.</i></p> <p style="padding-left: 80px;">2) <i>No : $z = 2$.</i></p> <p style="padding-left: 40px;">ii) Define formula for height of effective tensile zone. Call routine <i>Calc_effective_height(cData)</i>.</p> <p style="padding-left: 40px;">iii) Determine structural characteristic length. Call routine <i>Calc_structural_length(cData)</i>. If $z = 1$, retrieve l_{cs}^u . If $z = 2$, retrieve l_{cs}^u and l_{cs}^r .</p> <p style="padding-left: 40px;">iv) Set $i = 1$.</p>

v) Define structural characteristic length for zone i :

$$\text{If } i = 1 : l_{cs,i} = l_{cs}^u .$$

$$\text{If } i = 2 : l_{cs,i} = l_{cs}^r .$$

vi) Is $i \leq z$?

1) **Yes: Go to vii).**

2) **No: Go to VI).**

vii) Check value of *Analysis_type* ?

1) *Analysis_type* = *SLS*: Call routine *model_FRC_SLS*(*cData*, i , z , $l_{cs,i}$).

2) *Analysis_type* = *ULS*: Call routine *model_FRC_ULS*(*cData*, i , z , $l_{cs,i}$).

viii) $i = i + 1$.

ix) **Go to v).**

VI) Set initial values of solution: $x_{init} = \frac{h}{10} [m]$.

VII) Set $x = x_{init}$ and $M = 0$.

VIII) Read N from *cData*: $N = N_{Ed,ULS}$.

IX) Define equilibrium equations in the cross-section. Call *Formula_Forces*(*cData*, z , *CS_type*, N) and *Formula_Moment*(*cData*, z , *CS_type*, M , N).

X) Define equilibrium equations in the cross-section. Call *Formula_Compatibility*().

XI) Is $N = 0$:

i) No: $\varepsilon_N = 0$.

ii) Yes: Determine strain in the cross-section when submitted to axial force only *Strain_Axial_Force*(N). Return ε_N .

XII) Set $\varepsilon_{top} = \varepsilon_N$ and strain increment equal to: $\varepsilon_{inc} = \frac{\varepsilon_{c3}}{30}$.

XIII) Set strain at top fiber $\varepsilon_{top} = \varepsilon_{top} + \varepsilon_{inc}$.

XIV)	Check if concrete in compression fails: <ol style="list-style-type: none"> i) If $\varepsilon_{top} < \varepsilon_{cu3}$: Failure. End. ii) If $\varepsilon_{top} \geq \varepsilon_{cu3}$: Proceed to step XV)
XV)	Set maximum number of iterations in each strain increment for changing the initial values of iterative algorithm, $nIterMax = 30$.
XVI)	Resolve equilibrium equations. Call $resolve_x(x, nIterMax)$. Return convergence check, $conv_check$, neutral axis position, x , and respective moment, M .
XVII)	Import data of resolution of equilibrium and compatibility equations (curvature, stresses, strains, forces and depth of forces) to $cData$.
XVIII)	Test convergence: Value of $conv_check$? <ol style="list-style-type: none"> i) $conv_check=KO$: Send error message. End. ii) $conv_check=OK$: <ol style="list-style-type: none"> 1) If $CS_type = FRC$: Check failure of FRC is reached. Call $check_FRCfailure(cData)$ and return variable $FRC_failure_check$: <ol style="list-style-type: none"> a) If $FRC_failure_check=Yes$: End. b) If $FRC_failure_check =NO$: Proceed to step 2). 2) Store results $(M, \chi, x, h_{c.ef}, \varepsilon_{top})$ in Excel worksheet. 3) Set $M = 0$. Go to step XIII).

In Table 35 is presented the algorithm used to resolve the equilibrium equations and find the solution for the neutral axis position, x , considering an imposed compressive strain in the top fiber of the section, and determine respective resisting bending moment of the cross-section, M . This procedure resorts to Microsoft Excel Solver algorithm to apply an iterative approach to find the solution for the problem $(\min(x))$, given specific constraints $(\sum F = N)$.

Table 35 – Algorithm to resolve the equilibrium equations and find solution for neutral axis position and bending moment.

ROUTINE TITLE: <i>resolve_x</i>
<p>INPUT:</p> <ul style="list-style-type: none"> • Initial values for solution, x_{init}. • Maximum number of iterations, $nIterMax$.
<p>OUTPUT:</p> <ul style="list-style-type: none"> • Neutral axis, x. • Bending moment, M.
<p>I) Set changing variables equal to neutral axis: <i>changing variable</i> = x.</p> <p>II) Set objective function equal to the sum of the forces in the cross-section equal to N : $objective = \sum F_i = N$.</p> <p>III) Set initial values of neutral axis and moment equal to:</p> $\{x = x_{init}$ <p>IV) Set $iIter=1$.</p> <p>V) Call <i>Excel Solver</i> module.</p> <p>VI) Convergence check: Value of <i>Solver_out</i>?</p> <p>i) <i>Solver_out</i> = <i>OK</i> : Determine the resisting bending moment, M, using Eq. (C.1). End.</p> <p>ii) <i>Solver_out</i> = <i>KO</i> and $iIter < nIterMax$: Change initial solution: $x = x_{init} - iIter \cdot x_{init}$. Go to V).</p> <p>iii) <i>Solver_out</i>=<i>KO</i> and $iIter > nIterMax$: No convergence. Send error message. End.</p>

In Table 36 is presented the algorithm to check if tensile failure of FRC is reached, i.e. if the strain at bottom fiber of cross-section exceeds the ultimate strain of the quadrilinear model.

Table 36 – Algorithm to check if tensile failure of FRC is reached.

ROUTINE TITLE: <i>check_FRCfailure</i>
INPUT: <ul style="list-style-type: none"> • Class with geometry and material data, <i>cData</i> .
OUTPUT: <ul style="list-style-type: none"> • State variable regarding the convergence check, <i>FRC_failure_check</i> .
<p>l) Check if longitudinal conventional reinforcements are adopted in the cross-section. Is $(M > 0 \wedge A_{s1_1} = 0 \wedge A_{s1_2} = 0) \vee (M < 0 \wedge A_{s2_1} = 0 \wedge A_{s2_2} = 0)$?</p> <p>i) <i>Yes</i> :</p> <ol style="list-style-type: none"> 1) If $\varepsilon_{bot} > \varepsilon_{t4,r}$: <i>FRC_failure_check=YES. End.</i> 2) If $\varepsilon_{bot} \leq \varepsilon_{t4,r}$: <i>FRC_failure_check=NO. End.</i> <p>ii) <i>No</i> :</p> <ol style="list-style-type: none"> 1) If $\varepsilon_{bot} > \varepsilon_{t4}$: <i>FRC_failure_check=YES. End.</i> 2) If $\varepsilon_{bot} \leq \varepsilon_{t4}$: <i>FRC_failure_check=NO. End.</i>

D.7 Determination of shear resistance

In the present section are presented the algorithms to determine the shear resistance of FRC and RC cross-sections.

The calculation routines for FRC cross-sections are based on the design assumptions provided in section 2.5.2. For FRC cross-sections with longitudinal conventional reinforcements (only bottom reinforcements are considered for shear resistance contribution), the two design formulations are available in *FRCcalc*: the empirical based model and the model based on the VEM/SMCFT. In Table 37 is presented the algorithm of the main routine adopted for determination of the shear resistance of FRC cross-sections.

Table 37 – Algorithm to determine shear resistance of FRC cross-section.

ROUTINE TITLE: <i>FRC_shear</i>
INPUT: <ul style="list-style-type: none"> • Class with geometry and material data, <i>cData</i>.
OUTPUT: <ul style="list-style-type: none"> • Shear resistance of FRC cross-section, V_{Rd}.
<p>l) Check if longitudinal conventional reinforcements are adopted in the cross-section. Is $A_{s1-1} = 0 \wedge A_{s1-2} = 0$?</p> <p>i) <i>Yes</i>:</p> <ol style="list-style-type: none"> 1) Determine shear resistance of FRC cross-section without longitudinal reinforcement: Call <i>Calc_Shear_FRC_NoReinf(cData)</i>. Return $V_{Rd,F}$. 2) $V_{Rd} = V_{Rd,F}$. End. <p>ii) <i>No</i>:</p> <ol style="list-style-type: none"> 1) Determine shear resistance of FRC cross-section with longitudinal reinforcement, based on empirical model (Eq. (2.37)): Call <i>Calc_Shear_FRC_LongReinf(cData)</i>. Return V_{Rd}. 2) Store results V_{Rd} in Excel worksheet. 3) Determine shear resistance of FRC cross-section with longitudinal reinforcement with or without transverse reinforcements, based on VEM/SMCFT model: Call <i>Calc_FRC_Shear_MCFT(cData)</i>. Return $V_{Rd,c}$, $V_{Rd,f}$, $V_{Rd,s}$ and V_{Rd}. 4) Store results $V_{Rd,c}$, $V_{Rd,f}$, $V_{Rd,s}$ and V_{Rd} in Excel worksheet. End.

In Table 38 is presented the algorithm to determine the shear resistance of a FRC cross-section without longitudinal and transversal conventional reinforcements.

Table 38 – Algorithm to determine shear resistance of FRC cross-section without longitudinal and shear reinforcements.

ROUTINE TITLE: <i>Calc_Shear_FRC_NoReinf</i>	
INPUT:	
<ul style="list-style-type: none"> • Class with geometry and material data, <i>cData</i> . 	
OUTPUT:	
<ul style="list-style-type: none"> • Shear resistance of FRC cross-section without longitudinal and transversal reinforcements, $V_{Rd,F}$. 	
I)	Determine f_{Ftuk} based on Eq. (2.17) and Eq. (2.16), considering $w_u = 1.5mm$.
II)	Set partial safety factor equal to : $\gamma_F = 1.5$.
III)	Based on Eq. (2.76) $V_{Rd,F}$ for a rectangular cross-section:
	$V_{Rd,F} = \frac{f_{Ftuk} \cdot b \cdot h}{1.5 \cdot \gamma_F} \quad \text{Eq. (D.1)}$
IV)	End.

In Table 39 is presented the algorithm to determine the shear resistance of a FRC cross-section with longitudinal conventional reinforcements, based on the empirical model (Eq. (2.37)).

Table 39 – Algorithm to determine shear resistance of FRC cross-section with longitudinal reinforcement, based on empirical model.

ROUTINE TITLE: <i>Calc_Shear_FRC_LongReinf</i>	
INPUT:	
<ul style="list-style-type: none"> • Class with geometry and material data, <i>cData</i> . 	
OUTPUT:	
<ul style="list-style-type: none"> • Shear resistance of FRC cross-section with longitudinal and transverse reinforcements, V_{Rd} 	
I)	Set partial safety factor for FRC equal to : $\gamma_F = 1.5$.
II)	Determine d :
	<p>a. If $A_{s1_1} > 0 \wedge A_{s1_2} > 0$: $d = \frac{d_{s1_1} \cdot A_{s1_1} + d_{s1_2} \cdot A_{s1_2}}{A_{s1_1} + A_{s1_2}}$;</p> <p>b. If $A_{s1_1} > 0 \wedge A_{s1_2} = 0$: $d = d_{s1_1}$;</p>

$$c. \text{ If } A_{s1-1} = 0 \wedge A_{s1-2} > 0: d = d_{s1-2}.$$

- III) Calculate size effect factor: $k = 1 + \sqrt{\frac{200}{d [mm]}} \leq 2.0$.
- IV) Determine longitudinal reinforcement ratio: $\rho_{sl} = \frac{A_{s1-1} + A_{s1-2}}{b \cdot d}$.
- V) Determine f_{Ftk} based on Eq. (2.17) and Eq. (2.16), considering $w_u = 1.5mm$.
- VI) Determine characteristic value of concrete tensile strength: $f_{ctk} = 0.7 \cdot f_{ctm}$.
- VII) Obtain $N_{Ed,Shear,ULS}$ from *cData*. Set axial force equal to $N_{Ed} = -1 \cdot N_{Ed,Shear,ULS}$.
- VIII) Determine $\sigma_{cp} = N_{Ed} / A_c < 0.2 \cdot f_{cd}$.
- IX) Determine $V_{Rd,F}$ based on Eq. (2.37).
- X) Determine v_{min} based on Eq. (2.39).
- XI) Determine $V_{Rd,F,min}$ based on Eq. (2.38).
- XII) Check if $V_{Rd,F} \leq V_{Rd,F,min}$:
- Yes: $V_{Rd,F} = V_{Rd,F,min}$.
 - No: **Proceed to step XIII).**
- XIII) Check if $\frac{A_{sw}}{s_w} > 0$:
- No: Set $V_{Rd,s} = 0$. Set $V_{Rd} = V_{Rd,F}$ **End.**
 - Yes:
 - Determine z :
 - If $A_{s1-1} > 0 \wedge A_{s1-2} > 0: z = \frac{(0.9 \cdot d_{s1-1})^2 \cdot A_{s1-1} + (0.9 \cdot d_{s1-2})^2 \cdot A_{s1-2}}{0.9 \cdot d_{s1-1} \cdot A_{s1-1} + 0.9 \cdot d_{s1-2} \cdot A_{s1-2}}$.
 - If $A_{s1-1} > 0 \wedge A_{s1-2} = 0: z = 0.9 \cdot d_{s1-1}$.

$$3. \text{ If } A_{s1-1} = 0 \wedge A_{s1-2} > 0: z = 0.9 \cdot d_{s1-2}.$$

- c. Set $\Delta e = 0$.
- d. Obtain $N_{Ed} = N_{Ed,Shear,ULS}$, $V_{Ed} = V_{Ed,Shear,ULS}$, $M_{Ed} = M_{Ed,Shear,ULS}$ and d_g from *cData*.
- e. Determine ε_x from Eq. (2.49).
- f. Determine $\theta = \min((20^\circ + 10000 \cdot \varepsilon_x), 45^\circ)$.
- g. Determine $\varepsilon_1(\varepsilon_x)$ according to Eq. (2.74).
- h. Determine k_ε according to Eq. (2.73).
- i. Determine $V_{Rd,s}$ according to Eq. (2.71).
- j. Check if $V_{Rd,F} > V_{Rd,s}$:
 - i. Yes: $V_{Rd} = V_{Rd,F}$.
 - ii. No: $V_{Rd} = V_{Rd,s}$.
- k. Check if $V_{Rd} > V_{Rd,max}$:
 - i. Yes: $V_{Rd} = V_{Rd,F,max}$. **End.**
 - ii. No: **End.**

In Table 40 is presented the algorithm to determine the shear resistance of a FRC cross-section with longitudinal conventional reinforcements and with or without transverse reinforcements, based on the VEM/SMCFT model. For the determination of the tensile strength of FRC is considered the model presented in Eq. (2.54) and assuming that the post-cracking residual flexural strength f_{R2k} and f_{R4k} are obtained according to the standard EN 14651 [34].

Table 40 – Algorithm to determine shear resistance of FRC cross-section with longitudinal reinforcement and with or without transversal reinforcements, based on VEM/SMCFT model.

ROUTINE TITLE: <i>Calc_FRC_Shear_MCFT</i>
<p>INPUT:</p> <ul style="list-style-type: none"> • Class with geometry and material data, <i>cData</i>. • Transverse reinforcement area, A_{sw}.
<p>OUTPUT:</p> <ul style="list-style-type: none"> • Contribution of concrete matrix for shear resistance, $V_{Rd,c}$. • Contribution of fiber reinforcements for shear resistance, $V_{Rd,f}$. • Contribution of transverse reinforcements for shear resistance, $V_{Rd,s}$. • Shear resistance of FRC cross-section with longitudinal reinforcements and with or without transversal reinforcements, V_{Rd}.
<p>I) Set partial safety factor for FRC equal to: $\gamma_F = 1.5$.</p> <p>II) Determine d :</p> <p>a. If $A_{s1-1} > 0 \wedge A_{s1-2} > 0$: $d = \frac{d_{s1-1} \cdot A_{s1-1} + d_{s1-2} \cdot A_{s1-2}}{A_{s1-1} + A_{s1-2}}$.</p> <p>b. If $A_{s1-1} > 0 \wedge A_{s1-2} = 0$: $d = d_{s1-1}$.</p> <p>c. If $A_{s1-1} = 0 \wedge A_{s1-2} > 0$: $d = d_{s1-2}$.</p> <p>III) Set $A_{s'} = A_{s1-1} + A_{s1-2}$.</p> <p>IV) Determine z :</p> <p>a. If $A_{s1-1} > 0 \wedge A_{s1-2} > 0$: $z = \frac{(0.9 \cdot d_{s1-1})^2 \cdot A_{s1-1} + (0.9 \cdot d_{s1-2})^2 \cdot A_{s1-2}}{0.9 \cdot d_{s1-1} \cdot A_{s1-1} + 0.9 \cdot d_{s1-2} \cdot A_{s1-2}}$.</p> <p>b. If $A_{s1-1} > 0 \wedge A_{s1-2} = 0$: $z = 0.9 \cdot d_{s1-1}$.</p> <p>c. If $A_{s1-1} = 0 \wedge A_{s1-2} > 0$: $z = 0.9 \cdot d_{s1-2}$.</p> <p>V) Set $\Delta e = 0$.</p>

- VI) Obtain $N_{Ed} = N_{Ed,Shear,ULS}$, $V_{Ed} = V_{Ed,Shear,ULS}$, $M_{Ed} = M_{Ed,Shear,ULS}$ and d_g from *cData*.
- VII) Determine transverse reinforcement ratio: $\rho_{sw} = \frac{A_{sw}}{b \cdot s \cdot \sin \alpha}$.
- VIII) Determine longitudinal reinforcement ratio: $\rho_{sl} = \frac{A_{sl}}{b \cdot d}$.
- IX) Determine k_{dg} according to Eq. (2.45).
- X) Set formulas for $k_v(\bar{\varepsilon}_x)$ according to Eq. (2.44).
- XI) Set formula for $\theta = \theta_{\min}$ according to:
- $$\theta = \min\left(\left(29^\circ + 7000 \cdot \bar{\varepsilon}_x\right), 45^\circ\right) \quad \text{Eq. (D.2)}$$
- XII) Set formula for $v_{Rd,c}$ according to Eq. (2.43): $v_{Rd,c} = \min\left(k_v \cdot \sqrt{f_{ck}}, 8\right)$.
- XIII) Set formula for $w_u(\bar{\varepsilon}_x)$ according to Eq. (2.70).
- XIV) Obtain f_{R2k} and f_{R4k} from *cData*.
- XV) Set $\alpha = 5/12$ and $k_G = 0.6$.
- XVI) Set formula for $\xi(w_u)$ according to Eq. (2.55).
- XVII) Set formula for $f_{Tk}(w_u)$ according Eq. (2.54).
- XVIII) Set $k_{fd} = 0.8$.
- XIX) Set formula for $v_{Rd,f}$ according to Eq. (2.53).
- XX) Set formula for $V_{Rd,F}$ according to Eq. (2.42).
- XXI) Obtain $\frac{A_{sw}}{s_w}$, α and f_{wyd} from *cData*.
- XXII) Check if $\frac{A_{sw}}{s_w} > 0$:
- a. Yes: Set formula for $V_{Rd,s}$ according to Eq. (2.71).

b. No: Set $V_{Rd,s} = 0$.

XXIII) Set formula for V_{Rd} according to Eq. (2.41).

XXIV) Set formula for $\varepsilon_x(\theta)$ according to Eq. (2.48).

XXV) Run iterative procedure:

i) Set initial values of $\overline{\varepsilon}_x = \frac{f_{wyk}}{10 \cdot E_s}$.

ii) Set changing variables: *changing variables* = $\overline{\varepsilon}_x$.

iii) Set objective function: *objective* = $\varepsilon_x - \overline{\varepsilon}_x < 1 \times 10^{-6}$.

iv) Set constraints of the iterative model: $0.0 \leq \overline{\varepsilon}_x \leq 0.003$.

v) Call *Excel Solver* module.

vi) Convergence check: Value of *Solver_out*?

a) *Solver_out* = OK : Go to XXVI).

b) *Solver_out*=KO: No convergence. Send error message. **End**.

XXVI) Determine concrete matrix contribution to shear resistance $V_{Rd,c} = \frac{V_{rd,c}}{\gamma_c} \cdot z \cdot b$.

XXVII) Determine $V_{Rd,f} = \frac{V_{rd,f}}{\gamma_c} \cdot z \cdot b$.

XXVIII) Determine η_{fc} according to Eq. (2.75).

XXIX) Determine ε_1 according to Eq. (2.74).

XXX) Determine k_c according to Eq. (2.73).

XXXI) Determine $V_{Rd,max}$ based on Eq. (2.72).

XXXII) Check if $V_{Rd} > V_{Rd,max}$:

i) Yes: $V_{Rd} = V_{Rd,max}$. **End**.

ii) No: **End.**

In Table 41 is presented the algorithm of the main routine to determine the shear resistance of a RC cross-section.

Table 41 – Algorithm to determine shear resistance of RC cross-section.

ROUTINE TITLE: <i>RC_shear</i>
INPUT: <ul style="list-style-type: none"> • Class with geometry and material data, <i>cData</i>.
OUTPUT: <ul style="list-style-type: none"> • Shear resistance of RC cross-section, V_{Rd}.
<p>I) Check if transverse reinforcements are provided. Is $A_{sw} = 0$?</p> <p>i) Yes: Determine shear resistance of RC cross-section without transverse reinforcements, based on Level II of approximation: Call <i>Calc_Shear_RC_Vcd(cData)</i>. Return $V_{Rd,c}$. Set $V_{Rd} = V_{Rd,c}$.</p> <p>ii) No: Determine shear resistance of RC cross-section with transverse reinforcements based on Level III of approximation: Call <i>Calc_Shear_RC_Vcd_and_Vwd(cData)</i>. Return $V_{Rd,c}$, $V_{Rd,s}$ and V_{Rd}.</p> <p>II) End.</p>

In Table 42 is presented the algorithm to determine the shear resistance of a RC cross-section with longitudinal reinforcements (only bottom reinforcements are considered) and without transverse reinforcements, that is based on the level of approximation II presented in §7.3.3.2 MC2010 [30].

Table 42 – Algorithm to determine shear resistance of RC cross-section with longitudinal reinforcement.

ROUTINE TITLE: <i>Calc_Shear_RC_Vcd</i>
INPUT: <ul style="list-style-type: none"> • Class with geometry and material data, <i>cData</i>.
OUTPUT: <ul style="list-style-type: none"> • Shear resistance of RC cross-section with longitudinal reinforcements and without transverse reinforcements, V_{cd}.
<p>I) Set partial safety factor for FRC equal to $\gamma_c = 1.5$:</p> <p>II) Determine d .</p> <p style="padding-left: 40px;">a. If $A_{s1-1} > 0 \wedge A_{s1-2} > 0$: $d = \frac{d_{s1-1} \cdot A_{s1-1} + d_{s1-2} \cdot A_{s1-2}}{A_{s1-1} + A_{s1-2}}$.</p> <p style="padding-left: 40px;">b. If $A_{s1-1} > 0 \wedge A_{s1-2} = 0$: $d = d_{s1-1}$.</p> <p style="padding-left: 40px;">c. If $A_{s1-1} = 0 \wedge A_{s1-2} > 0$: $d = d_{s1-2}$.</p> <p>III) Set $A_{s'l} = A_{s1-1} + A_{s1-2}$.</p> <p>IV) Determine z :</p> <p style="padding-left: 40px;">a. If $A_{s1-1} > 0 \wedge A_{s1-2} > 0$: $z = \frac{(0.9 \cdot d_{s1-1})^2 \cdot A_{s1-1} + (0.9 \cdot d_{s1-2})^2 \cdot A_{s1-2}}{0.9 \cdot d_{s1-1} \cdot A_{s1-1} + 0.9 \cdot d_{s1-2} \cdot A_{s1-2}}$.</p> <p style="padding-left: 40px;">b. If $A_{s1-1} > 0 \wedge A_{s1-2} = 0$: $d = 0.9 \cdot d_{s1-1}$.</p> <p style="padding-left: 40px;">c. If $A_{s1-1} = 0 \wedge A_{s1-2} > 0$: $d = 0.9 \cdot d_{s1-2}$.</p> <p>V) Set $\Delta e = 0$.</p> <p>VI) Obtain $N_{Ed} = N_{Ed,Shear,ULS}$, $V_{Ed} = V_{Ed,Shear,ULS}$, $M_{Ed} = M_{Ed,Shear,ULS}$ and d_g from <i>cData</i>.</p> <p>VII) Determine k_{dg} according to Eq. (2.45).</p> <p>VIII) Determine ε_x according to Eq. (2.48).</p>

IX)	Determine k_v according to Eq. (2.44).	
X)	Determine $v_{Rd,c}$ according to Eq. (2.43): $v_{Rd,c} = \min(k_v \cdot \sqrt{f_{ck}}, 8)$.	
XI)	Determine $V_{Rd,c}$ according to:	
	$V_{Rd,c} = \frac{v_{Rd,c}}{\gamma_c} \cdot b \cdot z$	Eq. (D.3)
XII)	End.	

In Table 43 is presented the algorithm to determine the shear resistance of a RC cross-section with longitudinal (only bottom reinforcements are considered) and transverse reinforcements, that is based on the level of approximation III presented in §7.3.3.3 MC2010 [30].

Table 43 – Algorithm to determine shear resistance of RC cross-section with longitudinal and transverse reinforcements.

ROUTINE TITLE: <i>Calc_Shear_RC_Vcd_and_Vwd</i>	
INPUT:	
<ul style="list-style-type: none"> • Class with geometry and material data, <i>cData</i>. 	
OUTPUT:	
<ul style="list-style-type: none"> • Contribution of concrete matrix for shear resistance, $V_{Rd,c}$. • Contribution of transverse reinforcements for shear resistance, $V_{Rd,s}$. • Shear resistance of RC cross-section with longitudinal and transverse reinforcements, V_{Rd}. 	
I)	Set partial safety factor for RC equal to: $\gamma_c = 1.5$.
II)	Determine d :
	d. If $A_{s1-1} > 0 \wedge A_{s1-2} > 0$: $d = \frac{d_{s1-1} \cdot A_{s1-1} + d_{s1-2} \cdot A_{s1-2}}{A_{s1-1} + A_{s1-2}}$.
	e. If $A_{s1-1} > 0 \wedge A_{s1-2} = 0$: $d = d_{s1-1}$.
	f. If $A_{s1-1} = 0 \wedge A_{s1-2} > 0$: $d = d_{s1-2}$.
III)	Set $A_{st} = A_{s1-1} + A_{s1-2}$.
IV)	Determine z :

$$\text{a. If } A_{s1-1} > 0 \wedge A_{s1-2} > 0: z = \frac{(0.9 \cdot d_{s1-1})^2 \cdot A_{s1-1} + (0.9 \cdot d_{s1-2})^2 \cdot A_{s1-2}}{0.9 \cdot d_{s1-1} \cdot A_{s1-1} + 0.9 \cdot d_{s1-2} \cdot A_{s1-2}}.$$

$$\text{b. If } A_{s1-1} > 0 \wedge A_{s1-2} = 0: d = 0.9 \cdot d_{s1-1}.$$

$$\text{c. If } A_{s1-1} = 0 \wedge A_{s1-2} > 0: d = 0.9 \cdot d_{s1-2}.$$

V) Set $\Delta e = 0$.

VI) Obtain $N_{Ed} = N_{Ed,Shear,ULS}$, $V_{Ed} = V_{Ed,Shear,ULS}$, $M_{Ed} = M_{Ed,Shear,ULS}$ and d_g from *cData*.

VII) Obtain $\frac{A_{sw}}{s_w}$, α and f_{wyd} from *cData*.

VIII) Determine k_{dg} according to Eq. (2.45).

IX) Set formulas for $k_v(\bar{\varepsilon}_x)$ according to:

$$k_v = \frac{0.4}{1 + 1500 \cdot \bar{\varepsilon}_x} \left(1 - \frac{V_{Ed}}{V_{Rd,max}(\theta)} \right) \geq 0 \quad \text{Eq. (D.4)}$$

X) Set formula for $\theta = \theta_{\min}$ according to:

$$\theta = \min\left(\left(20^\circ + 10000 \cdot \bar{\varepsilon}_x\right), 45^\circ\right) \quad \text{Eq. (D.5)}$$

XI) Set formula for $v_{Rd,c}$ according to Eq. (2.43).

XII) Set formula for $V_{Rd,c}$ according to Eq. (D.3).

XIII) Set formula for η_{fc} according to Eq. (2.75).

XIV) Set formula for $\varepsilon_1(\bar{\varepsilon}_x)$ according to Eq. (2.74).

XV) Set formula for k_ε according to Eq. (2.73).

XVI) Set formula for $V_{Rd,max}$ according to Eq. (2.72)

XVII) Set formula for $V_{Rd,s}$ according to Eq. (2.71).

XVIII) Set formula for V_{Rd} according to:

$$V_{Rd} = V_{Rd,c} + V_{Rd,s} \quad \text{Eq. (D.6)}$$

- XIX) Set formula for $\varepsilon_x(\theta)$ according to Eq. (2.48).
- XX) Run iterative procedure:
- i) Set initial values of $\bar{\varepsilon}_x = \frac{f_{wyk}}{10 \cdot E_s}$.
 - ii) Set changing variables: *changing variables* = $\bar{\varepsilon}_x$.
 - iii) Set objective function: *objective* = $\varepsilon_x - \bar{\varepsilon}_x < 1 \times 10^{-6}$.
 - iv) Set constraints of the iterative model: $0.0 \leq \bar{\varepsilon}_x \leq 0.003$.
 - v) Call *Excel Solver* module.
 - vi) Convergence check: Value of *Solver_out*?
 - a) *Solver_out* = OK : Go to XXI).
 - b) *Solver_out*=KO: No convergence. Send error message. End.
- XXI) Check if $V_{Rd} > V_{Rd,max}$:
- i) Yes: $V_{Rd} = V_{Rd,max}$. End.
 - ii) No: End.

D.8 Calculation of bond transfer length and crack spacing

In Table 44 is presented the routine to determine the bond transfer length and the mean crack spacing of a FRC and RC cross-section, considering the methodology presented in section 2.5.5.

Table 44 – Algorithm to determine the bond transfer length in a FRC and RC cross-section.

ROUTINE TITLE: <i>Calc_Ismax</i>
<p>INPUT:</p> <ul style="list-style-type: none"> • Class with geometry and material data, <i>cData</i>. • Serviceability residual tensile strength, f_{Fism}. • Distance between neutral axis and bottom fiber of cross-section, y. • Acting bending moment, M_{Ed}.
<p>OUTPUT:</p> <ul style="list-style-type: none"> • Bond transfer length, $l_{s,max}$. • Mean spacing between cracks, s_{rm}. • Reinforcement ratio of effective tensile zone, $\rho_{s,ef}$.
<p>I) Determine height of effective tensile zone based on routine <i>Calc_effective_height(cData)</i>, considering the distance between neutral axis and bottom fiber of cross-section, y. Return $h_{c,ef}$.</p> <p>II) Determine area of effective tensile zone: $A_{c,ef} = h_{c,ef} \cdot b$.</p> <p>III) Set $A_{s,ef} = 0$. Determine reinforcement area inside effective tensile zone:</p> <p style="padding-left: 40px;">i) If $M_{Ed} > 0$:</p> <p style="padding-left: 80px;">i. If $h_{c,ef} > c_{1-1}$: $A_{s,ef} = A_{s,ef} + A_{s1-1}$.</p> <p style="padding-left: 80px;">ii. If $h_{c,ef} > c_{1-2}$: $A_{s,ef} = A_{s,ef} + A_{s1-2}$.</p> <p style="padding-left: 80px;">iii. If $h_{c,ef} > h - c_{2-1}$: $A_{s,ef} = A_{s,ef} + A_{s2-1}$.</p> <p style="padding-left: 80px;">iv. If $h_{c,ef} > h - c_{2-2}$: $A_{s,ef} = A_{s,ef} + A_{s2-2}$.</p> <p style="padding-left: 40px;">ii) If $M_{Ed} < 0$:</p> <p style="padding-left: 80px;">i. If $h_{c,ef} > c_{2-1}$: $A_{s,ef} = A_{s,ef} + A_{s2-1}$.</p> <p style="padding-left: 80px;">ii. If $h_{c,ef} > c_{2-2}$: $A_{s,ef} = A_{s,ef} + A_{s2-2}$.</p> <p style="padding-left: 80px;">iii. If $h_{c,ef} > h - c_{1-1}$: $A_{s,ef} = A_{s,ef} + A_{s1-1}$.</p>

<p>iv. If $h_{c,ef} > h - c_{1-2}$: $A_{s,ef} = A_{s,ef} + A_{s1-2}$.</p> <p>iii) If $A_{s,ef} = 0$ Send error message. End.</p> <p>IV) Determine reinforcement ratio of effective tensile zone: $\rho_{s,ef} = \frac{A_{s,ef}}{A_{c,ef}}$.</p> <p>V) Set empirical value to consider influence of concrete cover, $k = 1.0$.</p> <p>VI) Read loading type and cracking stage from <i>cData</i>. Determine $\tau_{bms}(f_{ctm})$ according to Table 3.</p> <p>VII) If $f_{Fism} - f_{ctm} < 0$ set $f_{Fism} - f_{ctm} = 0$.</p> <p>VIII) Determine $l_{s,max}$ based on Eq. (2.177).</p> <p>IX) Determine mean crack spacing, $s_{rm} = 1.5 \cdot l_{s,max}$.</p> <p>X) End.</p>

D.9 Determination of design crack width at SLS

In Table 45 and Table 46 are presented the algorithms to determine the design crack width of the FRC and RC cross-sections, considering the load combination corresponding to cracking serviceability criteria. The calculation procedure is based in the methodology presented in section 2.5.5.

Table 45 – Main algorithm to determine the design crack width of a FRC and RC cross-section at SLS.

ROUTINE TITLE: <i>Calc_crack_width_SLS</i>
<p>INPUT:</p> <ul style="list-style-type: none"> • Class with geometry and material data, <i>cData</i>. • Variable that defines type of cross-section to be analyzed, $CS_type = FRC/RC$. • Variable corresponding to the creep coefficient, φ_c . • Bending moment, $M_{Ed,crack}$, corresponding to the load combination corresponding to the cracking serviceability criteria.

<p>OUTPUT:</p> <ul style="list-style-type: none"> • Design crack width, w_d.
<p>I) Set $Analysis_type=SLS$.</p> <p>II) Call $Calc_Section(CData, CS_type, Analysis_type, \varphi_c, M_{Ed,crack})$. Return y and stress in steel longitudinal reinforcements (σ_{si}, $i=1_1,1_2,2_1,2_2$).</p> <p>III) Type of cross-section in analysis. Check CS_type value:</p> <p>i) If $CS_type=FRC$: Determine serviceability residual tensile strength,</p> $f_{Ftsm} = \frac{0.45 \cdot f_{R1k}}{0.7}.$ <p>ii) If $CS_type=RC$: Set $f_{Ftsm} = 0$.</p> <p>IV) Determine bond transfer length $l_{s,max}$. Call routine $Calc_lsmax(cData, f_{Ftsm}, y, M_{Ed,crack})$. Return $l_{s,max}$, $\rho_{s,ef}$ and $h_{c,ef}$.</p> <p>V) Determine design crack width w_d. Call routine $Calc_crack_width(cData, f_{Ftsm}, \sigma_{si}, l_{s,max}, \rho_{s,ef}, h_{c,ef}, M_{Ed,crack})$.</p>

Table 46 – Algorithm to determine the design crack width of a FRC and RC cross-section.

<p>ROUTINE TITLE: $Calc_crack_width$</p>
<p>INPUT:</p> <ul style="list-style-type: none"> • Class with geometry and material data, $cData$. • Serviceability residual tensile strength, f_{Ftsm}. • Stress of steel longitudinal reinforcements, σ_{si}, $i=1_1,1_2,2_1,2_2$. • Bond transfer length, $l_{s,max}$. • Reinforcement ratio in the effective tensile zone, $\rho_{s,ef}$. • Height of the effective tensile zone, $h_{c,ef}$. • Acting bending moment, M_{Ed}.
<p>OUTPUT:</p> <ul style="list-style-type: none"> • Design crack width, w_d.

- I) Read variable corresponding to the creep coefficient, φ_c , from *cData*.
- II) Determine concrete effective modulus according to $E_{c,ef} = \frac{E_c}{(1 + \varphi_c)}$.
- III) Determine modular ratio: $\alpha_E = \frac{E_s}{E_c}$.
- IV) Determine σ_{sr} according to Eq. (2.112).
- V) Read shrinkage strain, ε_{sh} from *cData*.
- VI) Read loading type and cracking stage from *cData*. Determine η_r and β according to Table 3.
- VII) Determine σ_s :
- a. If $M_{Ed} > 0$:
- i. If $A_{s1-1} > 0 \wedge A_{s1-2} > 0$:
1. If $h_{c,ef} > c_{1-1} \wedge h_{c,ef} > c_{1-2}$: $\sigma_s = \frac{\sigma_{s1-1} \cdot A_{s1-1} + \sigma_{s1-2} \cdot A_{s1-2}}{A_{s1-1} + A_{s1-2}}$; Go to VIII).
 2. If $h_{c,ef} > c_{1-1}$: $\sigma_s = \sigma_{s1-1}$; Go to VIII).
 3. If $h_{c,ef} > c_{1-2}$: $\sigma_s = \sigma_{s1-2}$; Go to VIII).
- ii. If $A_{s1-1} > 0$: $\sigma_s = \sigma_{s1-1}$; Go to VIII).
- iii. If $A_{s1-2} > 0$: $\sigma_s = \sigma_{s1-2}$; Go to VIII).
- b. If $M_{Ed} < 0$:
- i. If $A_{s2-1} > 0 \wedge A_{s2-2} > 0$:
1. If $h_{c,ef} > c_{2-1} \wedge h_{c,ef} > c_{2-2}$: $\sigma_s = \frac{\sigma_{s2-1} \cdot A_{s2-1} + \sigma_{s2-2} \cdot A_{s2-2}}{A_{s2-1} + A_{s2-2}}$; Go to VIII).
 2. If $h_{c,ef} > c_{2-1}$: $\sigma_s = \sigma_{s2-1}$; Go to VIII).

<p>3. If $h_{c,ef} > c_{2-2}$: $\sigma_s = \sigma_{s2-2}$; Go to VIII).</p> <p>ii. If $A_{s2-1} > 0$: $\sigma_s = \sigma_{s2-1}$; Go to VIII).</p> <p>iii. If $A_{s2-2} > 0$: $\sigma_s = \sigma_{s2-2}$; Go to VIII).</p> <p>VIII) Determine $\varepsilon_{sm} - \varepsilon_{cm} - \varepsilon_{cs}$ according to Eq. (2.120).</p> <p>IX) Determine design crack width w_d according to Eq. (2.119).</p> <p>X) End.</p>
--

D.10 Determination of moment-crack width relationship

In Table 47 is presented the algorithm that determines the moment vs. crack width relationship for a FRC and RC cross-section. The calculation procedure resorts to an iterative approach to determine the neutral axis position and bending moment in the cross-section, considering at each step an incremental value of the top compressive fiber strain. At each strain increment, the height of the effective tensile zone of the cross-section is updated. After resolution of the equilibrium equations, the tensile stress is determined, and the bond transfer length and design crack width are calculated based in the methodology presented in section 2.5.

Table 47 – Algorithm to determine moment-crack width relationship of FRC and RC cross-section.

ROUTINE TITLE: <i>Calc_M_crack</i>
<p>INPUT:</p> <ul style="list-style-type: none"> • Class with geometry and material data, <i>cData</i>. • Variable that defines type of cross-section to be analyzed, $CS_type = FRC/RC$;
<p>OUTPUT:</p> <ul style="list-style-type: none"> • Relationship of M vs. w_d of the cross-section.
<p>I) Read variable corresponding to the creep coefficient, φ_c , from <i>cData</i>.</p> <p>II) Set analysis state to SLS: <i>Analysis_type=SLS</i>.</p> <p>III) Define concrete compressive constitutive model. Call <i>model_SigmaC(Analysis_type , φ_c , cData)</i>.</p>

- IV) If $A_{s1-1} > 0 \vee A_{s1-2} > 0$:Set $j = 1$.Call *model_SigmaS*(j , *Analysis_type*, *cData*).
- V) If $A_{s2-1} > 0 \vee A_{s2-2} > 0$:Set $j = 2$.Call *model_SigmaS*(j , *Analysis_type*, *cData*).
- VI) Check type of analysis to be performed: Is $CS_type = FRC$?
- i) *Yes*: **Go to VII**) .
- ii) *No*: Set $f_{Ftsm} = 0$ and $z = 0$. **Go to VIII**) .
- VII) Define FRC tensile constitutive model:
- i) Determine $f_{Ftsm} = \frac{0.45 \cdot f_{R1k}}{0.7}$.
- ii) Check if longitudinal conventional tensile reinforcements are adopted in the cross-section. Is $A_{s1-1} = 0 \wedge A_{s1-2} = 0$?
- 1) *Yes* : $z = 1$. **Go to iv**).
- 2) *No* : $z = 2$. **Go to iii**).
- iii) Define formula for height of effective tensile zone. Call routine *Calc_effective_height*(*cData*).
- iii) Determine structural characteristic length. Call routine *Calc_structural_length*(*cData*). Retrieve l_{cs}^u and/or l_{cs}^r .
- iv) Set $i = 1$.
- v) Define structural characteristic length for zone i :
- $i = 1$: $l_{cs,i} = l_{cs}^u$.
- $i = 2$: $l_{cs,i} = l_{cs}^r$.
- vi) Is $i \leq z$?
- Yes*: **Go to vii**).
- No*: **Go to VIII**).
- vii) Call routine *model_FRC_SLS*(*cData*, i , z , $l_{cs,i}$).
- viii) $i = i + 1$.

- ix) **Go to v).**
- XIX) Read N from $cData$: $N = N_{Ed,crack}$.
- VIII) Determine moment at crack initiation. Call $Calc_M_crack_init(cData, N)$. Return M_{crack} , x_{crack} and $\varepsilon_{top,crack}$.
- IX) Set initial values of solution: $x_{init} = x_{crack}$ and $M = 0$.
- X) Define equilibrium equations in the cross-section. Call $Formula_Forces(cData, z, CS_type, N)$ and $Formula_Moment_FRC(cData, z, CS_type, M, N)$.
- XI) Define equilibrium equations in the cross-section. Call $Formula_Compatibility()$.
- XII) Set $x = x_{init}$.
- XIII) Set $\varepsilon_{top} = \varepsilon_{top,crack}$ and strain increment equal to: $\varepsilon_{inc} = \frac{\varepsilon_{cu3}}{30}$.
- XIV) Set strain at top fiber $\varepsilon_{top} = \varepsilon_{top} + \varepsilon_{inc}$.
- XV) Check if concrete in compression fails:
- i) If $\varepsilon_{top} < \varepsilon_{cu3}$: Failure. **End.**
 - ii) If $\varepsilon_{top} \geq \varepsilon_{cu3}$: **Proceed to step XVI).**
- XVI) Set maximum number of iterations in each strain increment for changing the initial values of iterative algorithm, $nIterMax = 30$.
- XVII) Resolve equilibrium equations. Call $resolve_x(x, nIterMax)$. Return convergence check ($conv_check$), neutral axis position, x , moment, M .
- XVIII) Import data of resolution of equilibrium and compatibility equations (curvature, stresses, strains, forces and depth of forces) to $cData$, namely $\sigma_{si}, i = 1_1, 1_2, 2_1, 2_2$ and y .
- XIX) Test convergence: Value of $conv_check$?
- i) $conv_check=KO$: Send error message. **End.**
 - ii) $conv_check=OK$:

- 1) If $CS_type = FRC$: Check failure of FRC is reached. Call $check_FRCfailure(cData)$ and return variable $FRC_failure_check$:
 - a) If $FRC_failure_check = Yes$: **End.**
 - b) If $FRC_failure_check = NO$: **Proceed to step 2).**
- 2) Determine bond transfer length $l_{s,max}$. Call routine $Calc_lsmax(cData, f_{Fism}, y, M)$. Return $l_{s,max}$, $\rho_{s,ef}$ and $h_{c,ef}$.
- 3) Determine design crack width w_d . Call routine $Calc_crack_width(cData, f_{Fism}, \sigma_{si}, l_{s,max}, \rho_{s,ef}, h_{c,ef}, M)$.
- 4) Store results $(M, w_d, \chi, x, h_{c,ef}, \varepsilon_{top})$ in Excel worksheet.
- 5) Set $M = 0$. **Go to XIV).**

D.11 Determination of bending moment corresponding to crack initiation

In Table 48 is presented the algorithm to determine the bending moment corresponding to crack initiation of a FRC and RC cross-section with axial force. In this particular case, as the pre-cracking stress-strain relationship for FRC is independent of the structural characteristic length is adopted a unique stress-strain relationship for FRC in tension (i. e. $z = 1$), even if longitudinal conventional steel reinforcements are adopted.

Table 48 – Algorithm to determine the moment at crack initiation.

ROUTINE TITLE: <i>Calc_M_cracking</i>
<p>INPUT:</p> <ul style="list-style-type: none"> • Class with geometry and material data, <i>cData</i>. • Axial force, <i>N</i>.
<p>OUTPUT:</p> <ul style="list-style-type: none"> • Bending moment at crack initiation, M_{crack}. • Position of neutral axis at crack initiation, x_{crack}. • Strain of top fiber of cross-section at crack initiation, $\varepsilon_{top,crack}$.
<p>I) Define concrete compressive constitutive model. Call <i>model_SigmaC(Analysis_type, φ_c, cData)</i>.</p> <p>II) If $A_{s1-1} > 0 \vee A_{s1-2} > 0$:Set $j = 1$.Call <i>model_SigmaS(j, Analysis_type, cData)</i>.</p> <p>III) If $A_{s2-1} > 0 \vee A_{s2-2} > 0$:Set $j = 2$.Call <i>model_SigmaS(j, Analysis_type, cData)</i>.</p> <p>IV) Define FRC/RC tensile constitutive model:</p> <p style="padding-left: 40px;">i) Set $z = 1$.</p> <p style="padding-left: 40px;">ii) Call routine <i>model_FRC_SLS(cData, i, z, l_{cs}^u)</i>.</p> <p>V) Set $CS_type = FRC$.</p> <p>VI) Set $M = 0$.</p> <p>VII) Define equilibrium equations in the cross-section. Call <i>Formula_Forces(cData, z, CS_type, N)</i> and <i>Formula_Moment(cData, z, CS_type, M , N)</i>.</p> <p>VIII) Define equilibrium equations in the cross-section. Call <i>Formula_Compatibility()</i>.</p> <p>IX) Set maximum number of iterations, $nIterMax = 30$.</p> <p>X) Set $\varepsilon_{bot} = \varepsilon_{t2} = 0.15\text{‰}$.</p> <p>XI) Set formulas:</p>

$\chi = \frac{\varepsilon_{bot}}{y}$ $\varepsilon_{top} = \chi \cdot x$	Eq. (D.7)
<p>XII) Resolve equilibrium equations. Call <i>resolve_x(x, nIterMax)</i>. Return convergence state variable (<i>conv_check</i>), neutral axis position, <i>x</i>, moment, <i>M</i>.</p>	
<p>XIII) Set $M_{crack} = M$ and $x_{crack} = x$.</p>	
<p>XIV) Determine $\varepsilon_{top,crack}$ based on Eq. (D.7).</p>	
<p>XV) End.</p>	

D.12 Verification of stress limitation criteria

In Table 49 is presented the algorithm adopted to verify the stress limitation criteria at SLS verification of FRC and RC cross-sections. The calculation procedure is based on methodology presented in section 2.5.4.

Table 49 – Algorithm of routine of stress limitation serviceability verifications.

ROUTINE TITLE: <i>Calc_FRC_stress_limitation</i>
<p>INPUT:</p> <ul style="list-style-type: none"> • Class with geometry and material data, <i>cData</i>. • Variable that defines type of cross-section to be analyzed, <i>CS_type</i> = “FRC” or “RC”. • Variable corresponding to the creep coefficient, φ_c. • Bending moment, $M_{sd,char}$, and axial force, $N_{sd,char}$, corresponding to the characteristic load combination. • Bending moment, $M_{sd,qperm}$, and axial force, $N_{sd,qperm}$, corresponding to the quasi-permanent load combination.
<p>OUTPUT:</p> <ul style="list-style-type: none"> • Variables of state of SLS verifications: <i>Check_Conc_Stress_Char</i>, <i>Check_Conc_Stress_QPerm</i>, <i>Check_Steel_Stress_Char</i> and <i>Check_FRC_Stress_Char</i>.
<p>1) Set <i>Analysis_type=SLS</i>.</p>

II) Verification of concrete compressive stress limitation:

i) Call $Calc_Section(CData, CS_type, Analysis_type, \varphi_c = 0, M_{Ed, char}, N_{Ed, char})$. Return σ_{c1} . Set $\sigma_{c1, char} = \sigma_{c1}$.

ii) Is $|\sigma_{c1, char}| < 0.6 \cdot |f_{ck}|$?

1) Yes: $Check_Conc_Stress_Char=OK$.

2) No: $Check_Conc_Stress_Char=KO$.

iii) Call $Calc_Section(CData, CS_type, Analysis_type, \varphi = 0, M_{Ed, qperm}, N_{Ed, qperm})$. Return σ_{c1} . Set $\sigma_{c1, qperm} = \sigma_{c1}$.

iv) $|\sigma_{c1, qperm}| < 0.4 \cdot |f_{ck}|$?

1) Yes: $Check_Conc_Stress_QPerm=OK$.

2) No: $Check_Conc_Stress_QPerm=KO$.

III) Verification of steel tensile stress limitation:

i) Call $Calc_Section(CData, CS_type, Analysis_type, \varphi, M_{Ed, char}, N_{Ed, char})$. Return $\sigma_{si}, i = 1_1, 1_2, 2_1, 2_2$.

ii) If $M_{Ed, char} > 0$:

a. If $A_{s1_1} > 0 \wedge A_{s1_2} > 0$:

1) Is $\sigma_{s1_1} < 0.8 \cdot f_{syk} \wedge \sigma_{s1_2} < 0.8 \cdot f_{syk}$

Yes: $Check_Steel_Stress_Char=OK$. Go To IV).

No: $Check_Steel_Stress_Char=KO$. Go To IV).

b. If $A_{s1_1} > 0$:

1) Is $\sigma_{s1_1} < 0.8 \cdot f_{syk}$

Yes: $Check_Steel_Stress_Char=OK$. Go To IV).

No: $Check_Steel_Stress_Char=KO$. Go To IV).

c. If $A_{s1-2} > 0$:

1) Is $\sigma_{s1-2} < 0.8 \cdot f_{syk}$

Yes: *Check_Steel_Stress_Char=OK. Go To IV).*

No: *Check_Steel_Stress_Char=KO. Go To IV).*

iii) If $M_{Ed,char} < 0$:

a. If $A_{s2-1} > 0 \wedge A_{s2-2} > 0$:

1) Is $\sigma_{s2-1} < 0.8 \cdot f_{syk} \wedge \sigma_{s2-2} < 0.8 \cdot f_{syk}$

Yes: *Check_Steel_Stress_Char=OK. Go To IV).*

No: *Check_Steel_Stress_Char=KO. Go To IV).*

b. If $A_{s2-1} > 0$:

1) Is $\sigma_{s2-1} < 0.8 \cdot f_{syk}$

Yes: *Check_Steel_Stress_Char=OK. Go To IV).*

No: *Check_Steel_Stress_Char=KO. Go To IV).*

c. If $A_{s2-2} > 0$:

1) Is $\sigma_{s2-2} < 0.8 \cdot f_{syk}$

Yes: *Check_Steel_Stress_Char=OK. Go To IV).*

No: *Check_Steel_Stress_Char=KO. Go To IV).*

IV) Set $f_{Ftsk} = 0.45 \cdot f_{R1k}$ and $f_{ctk} = 0.7 \cdot f_{ctm}$.

V) Check if FRC has strain-hardening behavior: Is $f_{Ftsk} \geq f_{ctk}$:

i) Yes: Verification of FRC tensile stress limitation:

1) Call *Calc_Section(CData, CS_type, Analysis_type, φ , $M_{Ed,char}$, $N_{Ed,char}$).*

- 2) Check if longitudinal conventional reinforcements in tension are adopted in the cross-section. Is

$$(M > 0 \wedge A_{s1_1} = 0 \wedge A_{s1_2} = 0) \vee (M < 0 \wedge A_{s2_1} = 0 \wedge A_{s2_2} = 0) ?$$

- a) *Yes*: Set $\sigma_{t,FRC} = \sigma_{t4}$.
- b) *No*: Set $\sigma_{t,FRC} = \sigma_{t4,reif}$.

3) Is $|\sigma_{t,FRC}| < 0.6 \cdot |f_{Ftsk}|$?

- a) *Yes*: *Check_FRC_Stress_Char=OK. End.*
- b) *No*: *Check_FRC_Stress_Char=KO. End.*
- ii) *No*: *Check_FRC_Stress_Char=OK. End.*

APPENDIX E

Table 50 – Database of beams shear tests and results of theoretical models.

Ref.,	Sample			Cross-section				Concrete					Passive reinforcement			Experimental test					MC2010_MCFT							MC2010_EEN				
	Code	Type		b_w [mm]	h [mm]	d [mm]	f_{cm} [MPa]	d_g [mm]	V_f [%]	l_f/d_f	f_{R1m} [MPa]	f_{R2m} [MPa]	f_{R3m} [MPa]	f_{R4m} [MPa]	A_{sl} [mm ²]	f_{syk} [MPa]	z_s [mm]	a/d	$V_{u,exp}$ [kN]	k_{dg}	k_v	ϵ_x	θ [°]	w_u [mm]	$V_{Rd,c}$ [kN]	f_{Fum} [MPa]	$V_{Rd,f}$ [kN]	$V_{u,model}$ [kN]	λ	f_{Fum} [MPa]	$V_{u,model}$ [kN]	λ
[77]	1	B18-3a	R	152.4	457.2	381	31.0	10	1.50	54.55	6.60	6.31	5.29	4.45	1552	448	342.9	3.43	150.76	1.23	0.17	7.65E-04	34.36	1.06	49.54	1.45	88.72	138.26	1.09	1.98	129.81	1.16
	2	B18-3b	R	152.4	457.2	381	31.0	10	1.50	54.55	6.60	6.31	5.29	4.45	1552	448	342.9	3.43	Excluded due to possible flexural-shear failure													
	3	B18-3c	R	152.4	457.2	381	44.9	10	1.50	54.55	6.60	6.31	5.29	4.45	1552	448	342.9	3.43	193.32	1.23	0.16	8.33E-04	34.83	1.13	56.92	1.57	94.25	151.16	1.28	1.98	137.33	1.41
	4	B18-3d	R	152.4	457.2	381	44.9	10	1.50	54.55	6.60	6.31	5.29	4.45	1552	448	342.9	3.43	191.77	1.23	0.16	8.33E-04	34.83	1.13	56.92	1.57	94.25	151.16	1.27	1.98	137.33	1.40
	5	B27-1a	R	203.2	685.8	607	50.8	10	0.75	54.55	5.70	5.27	3.55	2.73	2534	455	546.3	3.52	Excluded due to possible flexural-shear failure													
	6	B27-1b	R	203.2	685.8	607	50.8	10	0.75	54.55	5.70	5.27	3.55	2.73	2534	455	546.3	3.52	341.94	1.23	0.14	8.42E-04	34.90	1.34	108.68	1.06	134.47	243.16	1.41	1.41	249.53	1.37
	7	B27-2a	R	203.2	685.8	607	28.7	10	0.75	80.00	5.23	5.70	5.79	5.59	2534	455	546.3	3.52	Excluded due to possible flexural-shear failure													
	8	B27-2b	R	203.2	685.8	607	28.7	10	0.75	80.00	5.23	5.70	5.79	5.59	2534	455	546.3	3.52	Excluded due to possible flexural-shear failure													
	9	B27-4a	R	203.2	685.8	607	29.6	10	0.75	80.00	5.86	5.74	6.14	5.90	1940	448	546.3	3.52	Excluded due to possible flexural-shear failure													
	10	B27-4b	R	203.2	685.8	607	29.6	10	0.75	80.00	5.86	5.74	6.14	5.90	1940	448	546.3	3.52	229.54	1.23	0.12	1.08E-03	36.53	1.64	71.86	1.41	168.64	240.50	0.95	2.19	237.38	0.97
	11	B18-2d	R	152.4	457.2	381	38.1	10	1.00	54.55	6.60	6.31	5.29	4.45	1552	448	342.9	3.50	153.20	1.23	0.16	8.29E-04	34.80	1.13	52.59	1.57	94.51	147.10	1.04	1.98	133.89	1.14
	12	B18-5a	R	152.4	457.2	381	49.2	10	1.00	80.00	6.60	6.31	5.29	4.45	1552	448	342.9	3.43	176.38	1.23	0.16	8.42E-04	34.89	1.14	59.23	1.56	93.73	152.96	1.15	1.98	139.32	1.27
	13	B18-5b	R	152.4	457.2	381	49.2	10	1.00	80.00	6.60	6.31	5.29	4.45	1552	448	342.9	3.43	Excluded due to possible flexural-shear failure													
[78]	14	H1000 FRC50	R	250	1000	940	32.1	16	0.64	62.50	5.40	5.60	5.00	4.50	2513	555	846	3.00	289.52	1.00	0.11	1.03E-03	36.20	1.75	132.71	0.97	223.32	356.04	0.81	1.82	354.91	0.82
	15	H1000 FRC75	R	250	1000	940	33.1	16	1.00	62.50	6.00	6.10	6.00	5.50	2513	555	846	3.00	367.07	1.00	0.10	1.15E-03	37.05	1.92	125.78	1.23	274.99	400.78	0.92	2.16	373.60	0.98
	16	H1500 FRC50	R	250	1500	1440	32.1	16	0.64	62.50	5.40	5.60	5.00	4.50	3619	518	1296	3.00	521.28	1.00	0.09	9.67E-04	35.77	2.06	169.69	0.86	310.18	479.87	1.09	1.82	500.32	1.04
	17	H1500 FRC75	R	250	1500	1440	33.1	16	1.00	62.50	6.00	6.10	6.00	5.50	3619	518	1296	3.00	593.28	1.00	0.08	1.11E-03	36.80	2.32	158.05	1.15	399.93	557.98	1.06	2.16	526.66	1.13
	18	H500 FRC50	R	250	500	440	32.1	16	0.64	62.50	5.40	5.60	5.00	4.50	1232	500	396	3.00	Excluded due to possible flexural-shear failure													
[79]	19	H500 FRC75	R	250	500	440	33.1	16	0.96	62.50	6.00	6.10	6.00	5.50	1232	500	396	3.00	235.00	1.00	0.13	1.22E-03	37.53	1.52	75.04	1.30	133.83	208.87	1.13	2.16	203.45	1.16
	20	2.3_2	R	200	300	260	40.04	16	0.25	66.67	1.85(*)	1.85(*)	1.72(*)	1.65(*)	690	500	234	2.50	Excluded due to possible flexural-shear failure													
	21	2.3_3	R	200	300	260	38.68	16	0.76	66.67	4.6(*)	4.45(*)	3.87(*)	3.48(*)	690	500	234	2.50	Excluded due to possible flexural-shear failure													
	22	2.4_2	R	200	300	260	40.04	16	0.25	66.67	1.85(*)	1.85(*)	1.72(*)	1.65(*)	1086	500	234	2.50	Excluded due to possible flexural-shear failure													
	23	2.6_2	R	200	300	260	41.168	16	0.25	66.67	1.89(*)	1.88(*)	1.73(*)	1.67(*)	1086	500	234	4.04	Excluded due to possible flexural-shear failure													
	24	2.6_3	R	200	300	260	40.296	16	0.76	66.67	4.73(*)	4.53(*)	3.9(*)	3.5(*)	1086	500	234	4.04	Excluded due to possible flexural-shear failure													
	25	3.1_1	R	200	300	260	37.696	16	0.51	66.67	3.21(*)	3.15(*)	2.84(*)	2.61(*)	1698	500	234	3.50	189.00	1.00	0.23	5.65E-04	32.95	0.73	65.56	0.74	42.52	108.08	1.75	1.04	110.74	1.71
	26	3.1_1 F2	R	200	300	260	38.8	16	0.51	66.67	3.27(*)	3.2(*)	2.86(*)	2.63(*)	1698	500	234	3.50	Excluded due to possible flexural-shear failure													
	27	3.1_2	R	200	450	410	37.696	16	0.51	66.67	3.21(*)	3.15(*)	2.84(*)	2.61(*)	2781	500	369	3.34	249.00	1.00	0.22	5.05E-04	32.53	0.74	97.96	0.73	67.90	165.86	1.50	1.04	158.01	1.58
	28	20_50	R	200	500	460	38.8	16	0.51	66.67	3.27(*)	3.2(*)	2.86(*)	2.63(*)	2730	500	414	3.37	272.00	1.00	0.20	5.56E-04	32.89	0.82	103.44	0.73	74.73	178.17	1.53	1.05	174.45	1.56
	29	3.1_3	R	200	600	560	37.696	16	0.51	66.67	3.21(*)	3.15(*)	2.84(*)	2.61(*)	3276	500	504	3.48	265.00	1.00	0.19	5.54E-04	32.88	0.87	116.86	0.71	88.87	205.73	1.29	1.04	203.00	1.31
	30	3.1_3 F2	R	200	600	560	38.8	16	0.51	66.67	3.27(*)	3.2(*)	2.86(*)	2.63(*)	3276	500	504	3.48	383.00	1.00	0.19	5.59E-04	32.91	0.88	118.05	0.72	89.69	207.74	1.84	1.05	204.47	1.87
	31	8_50	T	200	500	460	38.8	16	0.51	66.67	3.27(*)	3.2(*)	2.86(*)	2.63(*)	2800	500	414	3.37	338.00	1.00	0.20	5.46E-04	32.82	0.81	104.28	0.73	75.11	179.39	1.88	1.05	174.45	1.94
	32	3.2_1	T	200	500	460	37.696	16	0.51	66.67	3.21(*)	3.15(*)	2.84(*)	2.61(*)	2800	500	414	3.37	286.00	1.00	0.20	5.41E-04	32.78	0.81	103.23	0.72	74.38	177.61	1.61	1.04	173.20	1.65
	33	10_50 F2	T	200	500	460	38.8	16	0.51	66.67	3.27(*)	3.2(*)	2.86(*)	2.63(*)	2800	500	414	3.37	265.00	1.00	0.20	5.46E-04	32.82	0.81	104.28	0.73	75.11	179.39	1.48	1.05	174.45	1.52
	34	3.2_2	T	200	500	460	37.696	16	0.51	66.67	3.21(*)	3.15(*)	2.84(*)	2.61(*)	2800	500	414	3.37	Excluded due to possible flexural-shear failure													
	35	15_50 F2	T	200	500	460	38.8	16	0.51	66.67	3.27(*)	3.2(*)	2.86(*)	2.63(*)	2800	500	414	3.37	276.00	1.00	0.20	5.46E-04	32.82	0.81	104.28	0.73	75.11	179.39	1.54	1.05	174.45	1.58
	36	23_50 F2	T	200	500	460	38.8	16	0.51	66.67	3.27(*)	3.2(*)	2.86(*)	2.63(*)	2800	500	414	3.37	Excluded due to possible flexural-shear failure													
	37	3.2_3	T	200	500	460	37.696	16	0.51	66.67	3.21(*)	3.15(*)	2.84(*)	2.61(*)	2800	500	414	3.37	Excluded due to possible flexural-shear failure													
38	3.2_4	T	200	500	460	37.696	16	0.51	66.67	3.21(*)	3.15(*)	2.84(*)	2.61(*)	2800	500	414	3.37	Excluded due to possible flexural-shear failure														
[80]	39	HSC-FRC1	R	200	480	435	61.1	15	0.64	48.39	2.90	4.86	2.81	2.65	905	512	391.5	2.51	188.51	1.03	0.15	9.39E-04	35.58	1.23	94.08	0.56	49.27	143.36	1.31	1.02	146.74	1.28
	40	NSC1-FRC1	R	200	480	435	24.8	20	0.38	50.00	2.50	2.73(*)	2.40	2.48(*)	905	512	391.5	2.51	131.51	0.89	0.17	8.18E-04	34.73	1.06	67.54	0.62	56.13	123.67	1.06	0.87	118.52	1.11

Ref.	Sample		Cross-section				Concrete							Passive reinforcement			Experimental test				MC2010 MCFT								MC2010 EEN			
	Code	Type	b_w [mm]	h [mm]	d [mm]	f_{cm} [MPa]	d_g [mm]	V_f [%]	l_f/d_f	f_{R1m} [MPa]	f_{R2m} [MPa]	f_{R3m} [MPa]	f_{R4m} [MPa]	A_{st} [mm ²]	f_{syk} [MPa]	z_s [mm]	a/d	$V_{u,exp}$ [kN]	k_{dg}	k_v	ϵ_s	θ [°]	w_u [mm]	$V_{Rd,c}$ [kN]	f_{Fnum} [MPa]	$V_{Rd,f}$ [kN]	$V_{u,model}$ [kN]	λ	f_{Fnum} [MPa]	$V_{u,model}$ [kN]	λ	
[81] 41	NSC2-FRC1	R	200	480	435	33.5	20	0.38	50.00	2.60	1.82(*)	2.29	1.64(*)	905	512	391.5	2.51	117.01	0.89	0.18	7.84E-04	34.49	1.02	80.36	0.41	37.76	118.12	0.99	0.84	124.17	0.94	
[81] 42	NSC3-FRC1	R	200	480	435	38.6	20	0.38	50.00	3.34	1.98(*)	2.73	1.76(*)	905	512	391.5	2.51	138.51	0.89	0.17	8.21E-04	34.75	1.06	84.07	0.44	40.11	124.18	1.12	1.02	133.02	1.04	
[81] 43	HSC-FRC2	R	200	480	435	58.3	15	0.64	78.95	6.50	6(*)	5.39	5.01(*)	905	512	391.5	2.51	220.01	1.03	0.14	1.15E-03	37.08	1.46	81.09	1.18	97.74	178.83	1.23	2.01	170.36	1.29	
[81] 44	A0.5%	R	150	250	202	21.3	16	0.50	54.55	2.81(*)	2.81(*)	2.8(*)	2.55(*)	400	478	181.8	2.97	48.04	1.00	0.19	8.70E-04	35.09	0.97	24.03	0.77	23.92	47.96	1.00	1.01	53.75	0.89	
[81] 45	A1%	R	150	250	202	19.6	16	1.00	54.55	3.63(*)	3.72(*)	3.73(*)	3.39(*)	400	478	181.8	2.97	57.04	1.00	0.18	9.51E-04	35.66	1.05	21.89	1.01	30.85	52.74	1.08	1.34	57.15	1.00	
[81] 46	B0.5%	R	300	500	437	21.3	16	0.50	54.55	2.81(*)	2.81(*)	2.8(*)	2.55(*)	2000	429	393.3	3.09	159.16	1.00	0.17	7.65E-04	34.35	1.03	94.66	0.77	105.76	200.42	0.79	1.01	205.07	0.78	
[81] 47	B1%	R	300	500	437	19.6	16	1.00	54.55	3.63(*)	3.72(*)	3.73(*)	3.39(*)	2000	429	393.3	3.09	202.86	1.00	0.16	8.44E-04	34.91	1.12	86.02	1.01	136.32	222.34	0.91	1.34	218.07	0.93	
[41] 48	B25-0-0-0	R	300	700	622	34	10	0.32	66.67	2.39	2.52	2.56	2.26	3694	540	559.8	2.81	282.82	1.23	0.17	5.41E-04	32.79	0.96	166.38	0.58	120.23	286.61	0.99	0.91	314.55	0.90	
[41] 49	B50-0-0-0	R	300	700	622	36	10	0.64	66.67	6.74	8.58	8.07	7.91	3694	540	559.8	2.81	352.82	1.23	0.14	7.69E-04	34.38	1.26	144.07	1.37	269.73	413.80	0.85	2.83	426.75	0.83	
[82] 50	DI-N-HO-35-0.75	R	150	300	251	28.1	12.5	0.75	63.64	3.15	3.33	3.01	2.69	1202	500	225.9	3.49	113.90	1.12	0.22	5.79E-04	33.05	0.75	39.88	0.93	38.88	78.76	1.45	1.09	77.68	1.47	
[82] 51	DI-N-HO-35-0.75	R	150	300	251	25.3	12.5	0.75	63.64	3.15	3.33	3.01	2.69	1202	500	225.9	3.49	80.01	1.12	0.22	5.68E-04	32.98	0.74	38.18	0.94	39.07	77.24	1.04	1.09	76.34	1.05	
[82] 52	F-I-N-HO-35-1.50	R	150	300	251	28.1	12.5	1.50	63.64	5.88	6.30	5.26	4.43	1202	500	225.9	3.49	112.01	1.12	0.21	6.74E-04	33.72	0.84	37.05	1.36	55.19	92.24	1.21	1.93	90.36	1.24	
[82] 53	F-I-N-HO-35-1.50	R	150	300	251	27.3	12.5	1.50	63.64	5.88	6.30	5.26	4.43	1202	500	225.9	3.49															
[82] 54	G-I-N-HO-60-0.50	R	150	300	251	27.5	12.5	0.50	80.00	2.89	3.09	2.94	2.71	1202	500	225.9	3.49	65.70	1.12	0.23	5.61E-04	32.93	0.73	40.01	0.87	36.31	76.33	0.86	1.05	76.73	0.86	
[82] 55	G-I-N-HO-60-0.50	R	150	300	251	24.9	12.5	0.50	80.00	2.89	3.09	2.94	2.71	1202	500	225.9	3.49	78.13	1.12	0.23	5.51E-04	32.86	0.72	38.40	0.87	36.46	74.86	1.04	1.05	75.47	1.04	
[82] 56	H-N-HO-60-1.00	R	150	300	251	26.3	12.5	1.00	80.00	4.40	4.98	4.81	4.64	1202	500	225.9	3.49															
[82] 57	H-I-N-HO-60-1.00	R	150	300	251	27.1	12.5	1.00	80.00	4.40	4.98	4.81	4.64	1202	500	225.9	3.49	105.61	1.12	0.21	6.63E-04	33.64	0.83	36.68	1.33	54.03	90.71	1.16	1.71	86.88	1.22	
[82] 58	K-I-M-HO-35-0.75	R	150	300	251	53.4	12.5	0.75	63.64	6.00	5.12	3.99	3.24	1202	500	225.9	3.49	113.90	1.12	0.20	7.45E-04	34.21	0.91	48.52	1.35	53.79	102.31	1.11	1.56	94.99	1.20	
[82] 59	K-I-M-HO-35-0.75	R	150	300	251	54.1	12.5	0.75	63.64	6.00	5.12	3.99	3.24	1202	500	225.9	3.49	126.70	1.12	0.20	7.46E-04	34.22	0.91	48.79	1.35	53.74	102.52	1.24	1.56	95.28	1.33	
[82] 60	P-I-M-HO-35-1.50	R	150	300	251	64.6	12.5	1.50	63.64	8.52	7.59	6.20	5.09	1202	500	225.9	3.49															
[82] 61	P-I-M-HO-35-1.50	R	150	300	251	59.9	12.5	1.50	63.64	8.52	7.59	6.20	5.09	1202	500	225.9	3.49	160.96	1.12	0.18	8.76E-04	35.13	1.04	47.02	1.92	74.16	121.18	1.33	2.37	108.75	1.48	
[82] 62	AA-I-M-HO-60-0.50	R	150	300	251	49.5	12.5	0.50	80.00	4.54	5.88	5.50	4.87	1202	500	225.9	3.49	153.05	1.12	0.19	7.85E-04	34.50	0.95	45.41	1.59	62.72	108.13	1.42	1.92	98.43	1.55	
[82] 63	N-I-M-HO-60-1.00	R	150	300	251	53.4	12.5	1.00	80.00	7.29	8.93	8.70	7.59	1202	500	225.9	3.49	128.96	1.12	0.18	8.85E-04	35.20	1.05	44.12	2.04	78.47	122.59	1.05	3.05	113.49	1.14	
[82] 64	N-I-M-HO-60-1.00	R	150	300	251	51	12.5	1.00	80.00	7.29	8.93	8.70	7.59	1202	500	225.9	3.49	157.95	1.12	0.18	8.73E-04	35.11	1.03	43.46	2.01	77.36	120.81	1.31	3.05	112.32	1.41	
[83] 65	H35-1	R	150	300	251	27.9	12.5	1.00	63.64	3.17	3.34	3.07	2.76	1202	500	225.9	3.49	110.13	1.12	0.22	5.78E-04	33.05	0.75	39.76	0.93	38.91	78.67	1.40	1.11	77.95	1.41	
[83] 66	H35-2	R	150	300	251	26.2	12.5	1.00	63.64	3.17	3.34	3.07	2.76	1202	500	225.9	3.49															
[83] 67	H60-1	R	150	300	251	26.25	12.5	1.00	80.00	3.89	4.45	4.38	4.21	1202	500	225.9	3.49															
[83] 68	H60-2	R	150	300	251	27.12	12.5	1.00	80.00	3.89	4.45	4.38	4.21	1202	500	225.9	3.49	105.61	1.12	0.21	6.45E-04	33.51	0.81	37.21	1.24	50.87	88.08	1.20	1.55	84.57	1.25	
[16] 69	W750 FRC25-1	O	750	250	210	38	16	0.32	62.50	3.01	3.20	2.99	2.69	1913	537	189	2.50	348.36	1.00	0.19	8.71E-04	35.10	0.98	165.67	0.71	114.55	280.22	1.24	1.08	301.63	1.15	
[16] 70	W750 FRC25-2	O	750	250	210	38	16	0.32	62.50	3.01	3.20	2.99	2.69	1913	537	189	2.50	364.36	1.00	0.19	8.71E-04	35.10	0.98	165.67	0.71	114.55	280.22	1.30	1.08	301.63	1.21	
[16] 71	W750 FRC35-1	O	750	250	210	36.9	16	0.45	62.50	3.52	3.87	3.62	3.24	1913	537	189	2.50	352.86	1.00	0.18	9.13E-04	35.39	1.02	158.94	0.85	135.66	294.60	1.20	1.30	313.87	1.12	
[16] 72	W750 FRC35-2	O	750	250	210	36.9	16	0.45	62.50	3.52	3.87	3.62	3.24	1913	537	189	2.50	363.36	1.00	0.18	9.13E-04	35.39	1.02	158.94	0.85	135.66	294.60	1.23	1.30	313.87	1.16	
[16] 73	W1000 FRC25-1	R	1000	250	210	38	16	0.32	62.50	3.01	3.20	2.99	2.69	2625	537	189	2.50	491.15	1.00	0.19	8.55E-04	34.99	0.96	223.23	0.71	153.86	377.09	1.30	1.08	406.08	1.21	
[16] 74	W1000 FRC25-2	R	1000	250	210	38	16	0.32	62.50	3.01	3.20	2.99	2.69	2625	537	189	2.50	482.65	1.00	0.19	8.55E-04	34.99	0.96	223.23	0.71	153.86	377.09	1.28	1.08	406.08	1.19	
[16] 75	W1000 FRC35-1	R	1000	250	210	36.9	16	0.45	62.50	3.52	3.87	3.62	3.24	2625	537	189	2.50	483.15	1.00	0.19	8.96E-04	35.27	1.00	214.19	0.85	182.28	396.47	1.22	1.30	422.55	1.14	
[16] 76	W1000 FRC35-2	R	1000	250	210	36.9	16	0.45	62.50	3.52	3.87	3.62	3.24	2625	537	189	2.50	509.65	1.00	0.19	8.96E-04	35.27	1.00	214.19	0.85	182.28	396.47	1.29	1.30	422.55	1.21	
[82] 77	MH35-1	R	150	300	251	53.2	12.5	1.00	63.64	7.51	6.74	5.46	4.35	1202	500	225.9	3.49	145.14	1.12	0.19	8.22E-04	34.76	0.99	45.90	1.73	67.57	113.48	1.28	2.09	102.28	1.42	
[82] 78	MH35-2	R	150	300	251	55.3	12.5	1.00	63.64	7.51	6.74	5.46	4.35	1202	500	225.9	3.49	166.61	1.12	0.19	8.26E-04	34.79	0.99	46.67	1.73	67.39	114.06	1.46	2.09	103.21	1.61	
[82] 79	MH60-1	R	150	300	251	53.4	12.5	1.00	80.00	7.13	8.94	8.87	7.59	1202	500	225.9	3.49	128.96	1.12	0.18	8.85E-04	35.20	1.05	44.12	2.04	78.47	122.59	1.05	3.09	113.91	1.13	
[82] 80	MH60-2	R	150	300	251	51	12.5	1.00	80.00	7.13	8.94	8.87	7.59	1202	500	225.9	3.49	157.95	1.12													

Ref.	Sample		Cross-section			Concrete								Passive reinforcement			Experimental test		MC2010 MCFT												MC2010 EEN		
	Code	Type	b_w [mm]	h [mm]	d [mm]	f_{cm} [MPa]	d_g [mm]	V_f [%]	l_f/d_f	f_{R1m} [MPa]	f_{R2m} [MPa]	f_{R3m} [MPa]	f_{R4m} [MPa]	A_{st} [mm ²]	f_{syk} [MPa]	z_s [mm]	a/d	$V_{u,exp}$ [kN]	k_{dg}	k_v	ϵ_s	θ [°]	w_u [mm]	$V_{Rd,c}$ [kN]	f_{Fnum} [MPa]	$V_{Rd,f}$ [kN]	$V_{u,model}$ [kN]	λ	f_{Fnum} [MPa]	$V_{u,model}$ [kN]	λ		
	87	20x60-SFRC-S2	O	200	600	540	38.8	25	0.51	66.67	3.27(*)	3.2(*)	2.86(*)	2.63(*)	2945	500	486	3.50	Excluded due to possible flexural-shear failure														
	88	T10x50-SFRC-S1	O	200	500	460	37.7	25	0.51	66.67	3.21(*)	3.15(*)	2.84(*)	2.61(*)	2413	500	414	3.37	285.60	0.78	0.20	6.19E-04	33.33	0.83	103.62	0.72	72.39	176.02	1.62	1.04	173.20	1.65	
	89	T10x50-SFRC-S2	R	200	500	460	38.8	25	0.51	66.67	3.27(*)	3.2(*)	2.86(*)	2.63(*)	2413	500	414	3.37	264.60	0.78	0.20	6.25E-04	33.37	0.84	104.65	0.73	73.07	177.73	1.49	1.05	174.45	1.52	
	90	T15x50-SFRC-S2	O	200	500	460	38.8	25	0.51	66.67	3.27(*)	3.2(*)	2.86(*)	2.63(*)	2413	500	414	3.37	276.10	0.78	0.20	6.25E-04	33.37	0.84	104.65	0.73	73.07	177.73	1.55	1.05	174.45	1.58	
	91	T23x50-SFRC-S2	R	200	500	460	38.8	25	0.51	66.67	3.27(*)	3.2(*)	2.86(*)	2.63(*)	2413	500	414	3.37	Excluded due to possible flexural-shear failure														
	92	T15x75-SFRC-S1	R	200	500	460	37.7	25	0.51	66.67	3.21(*)	3.15(*)	2.84(*)	2.61(*)	2413	500	414	3.37	Excluded due to possible flexural-shear failure														
	93	T15x100-SFRC-S1	R	200	500	460	37.7	25	0.51	66.67	3.21(*)	3.15(*)	2.84(*)	2.61(*)	2413	500	414	3.37	Excluded due to possible flexural-shear failure														
[18]	94	FNB2-2	R	125	250	212	30.8	19	0.51	62.50	2.7(*)	2.69(*)	2.56(*)	2.35(*)	469	442	190.8	2.00	Excluded due to possible flexural-shear failure														
	95	FNB2-3	R	125	250	212	30.8	19	0.51	62.50	2.7(*)	2.69(*)	2.56(*)	2.35(*)	469	442	190.8	3.00	67.58	0.91	0.21	7.22E-04	34.05	0.83	28.13	0.62	17.58	45.71	1.48	0.93	53.41	1.27	
[85]	96	SHE-50-0.75	R	200	300	265	38	10	0.75	50.00	3.51(*)	3.43(*)	3.06(*)	2.8(*)	1020	400	238.5	3.02	105.47	1.23	0.19	7.27E-04	34.09	0.92	56.52	0.76	43.01	99.53	1.06	1.13	113.17	0.93	
	97	SHE-50-1.0	T	200	300	265	42.2	10	1.00	50.00	4.8(*)	4.56(*)	3.89(*)	3.51(*)	1020	400	238.5	3.02	Excluded due to possible flexural-shear failure														
	98	FRC-20 H50_1	T	200	500	455	24.4	20	0.25	50.00	1.47	2.13(*)	1.54	1.93(*)	901	500	409.5	2.50	154.00	0.89	0.18	7.80E-04	34.46	1.03	71.06	0.49	46.33	117.39	1.31	0.55	108.76	1.42	
	99	FRC-20 H50_2	T	200	500	455	24.4	20	0.25	50.00	1.47	2.13(*)	1.54	1.93(*)	901	500	409.5	2.50	Excluded due to possible flexural-shear failure														
	100	FRC-40 H50_1	T	200	500	455	20.6	20	0.51	50.00	3.10	2.6(*)	2.94	2.36(*)	901	500	409.5	2.50	125.00	0.89	0.17	8.00E-04	34.60	1.05	64.41	0.59	56.18	120.59	1.04	1.07	123.35	1.01	
[87]	101	FRC-40 H50_2	T	200	500	455	20.6	20	0.51	50.00	3.10	2.6(*)	2.94	2.36(*)	901	500	409.5	2.50	133.00	0.89	0.17	8.00E-04	34.60	1.05	64.41	0.59	56.18	120.59	1.10	1.07	123.35	1.08	
	102	FRC-60 H50_1	T	200	500	455	19.2	20	0.76	50.00	4.40	2.97(*)	4.62	2.7(*)	901	500	409.5	2.50	Excluded due to possible flexural-shear failure														
	103	FRC-60 H50_2	R	200	500	455	19.2	20	0.76	50.00	4.40	2.97(*)	4.62	2.7(*)	901	500	409.5	2.50	Excluded due to possible flexural-shear failure														
	104	FRC-20 H100	R	200	1000	910	24.4	20	0.25	50.00	1.47	2.13(*)	1.54	1.93(*)	1893	500	819	2.50	258.00	0.89	0.15	6.82E-04	33.77	1.17	120.39	0.48	93.34	213.73	1.21	0.55	195.30	1.32	
[88]	105	FRC	R	200	450	435	40.7	20	0.38	50.00	2.08	2.04(*)	1.91	1.79(*)	1357	500	391.5	3.10	140.00	0.89	0.18	7.51E-04	34.26	0.99	90.60	0.46	42.39	132.98	1.05	0.70	141.80	0.99	
[89]	106	FRC-100	R	200	1000	910	55	20	0.25	50.00	2.47	1.77(*)	2.52	1.41(*)	1875	512	819	2.50	339.00	0.89	0.14	7.62E-04	34.33	1.28	170.64	0.35	67.39	238.04	1.42	0.90	254.41	1.33	
[90]	107	W105 FRC25-14	O	105	250	210	35.3	16	0.32	62.50	2.17	1.96(*)	2.23	1.75(*)	309	541	189	2.50	39.00	1.00	0.21	7.01E-04	33.91	0.82	25.13	0.46	10.78	35.91	1.09	0.80	40.84	0.96	
	108	W210 FRC25-14	O	210	250	210	35.3	16	0.32	62.50	2.17	1.96(*)	2.23	1.75(*)	617	541	189	2.50	98.00	1.00	0.21	7.01E-04	33.91	0.82	50.27	0.46	21.56	71.83	1.36	0.80	81.67	1.20	
	109	W315 FRC25-14	O	315	250	210	35.3	16	0.32	62.50	2.17	1.96(*)	2.23	1.75(*)	926	541	189	2.50	142.00	1.00	0.21	7.01E-04	33.91	0.82	75.40	0.46	32.34	107.74	1.32	0.80	122.51	1.16	
	110	W420 FRC25-14	O	420	250	210	35.3	16	0.32	62.50	2.17	1.96(*)	2.23	1.75(*)	1235	541	189	2.50	196.00	1.00	0.21	7.01E-04	33.91	0.82	100.54	0.46	43.12	143.66	1.36	0.80	163.34	1.20	
	111	W525 FRC25-14	O	525	250	210	35.3	16	0.32	62.50	2.17	1.96(*)	2.23	1.75(*)	1544	541	189	2.50	261.00	1.00	0.21	7.01E-04	33.91	0.82	125.67	0.46	53.90	179.57	1.45	0.80	204.18	1.28	
	112	W630 FRC25-14	O	630	250	210	35.3	16	0.32	62.50	2.17	1.96(*)	2.23	1.75(*)	1852	541	189	2.50	353.00	1.00	0.21	7.01E-04	33.91	0.82	150.81	0.46	64.68	215.49	1.64	0.80	245.01	1.44	
	113	W735 FRC25-14	O	735	250	210	35.3	16	0.32	62.50	2.17	1.96(*)	2.23	1.75(*)	2161	541	189	2.50	376.00	1.00	0.21	7.01E-04	33.91	0.82	175.94	0.46	75.46	251.40	1.50	0.80	285.85	1.32	

Legend: R- Rectangular cross-section; T – T-shape cross-section; (*) - Values estimated according to [66].

APPENDIX F

In this appendix are presented the factors that are used to determine the prediction parameters of the B4 model that were calibrated from optimization process to existing creep database [175].

In Table 51 are presented the B4 creep model parameters that are dependent on the cement type.

Table 51 – B4 model creep parameters dependent on cement type [175].

Type of cement	R	RS	SL
p_1	0.70	0.60	0.80
p_2	58.6×10^{-3}	17.4×10^{-3}	40.5×10^{-3}
p_3	39.3×10^{-3}	39.3×10^{-3}	39.3×10^{-3}
p_4	3.4×10^{-3}	3.4×10^{-3}	3.4×10^{-3}
p_5	777×10^{-6}	94.6×10^{-6}	496×10^{-6}
p_{5H}	8.00	1.00	8.00*
p_{2w}	3.00	3.00	3.00
p_{3a}	-1.10	-1.10	-1.10
p_{3w}	0.40	0.40	0.40
p_{4a}	-0.90	-0.90	-0.90
p_{4w}	2.45	2.45	2.45
$p_{5\varepsilon}$	-0.85	-0.85	-0.85
p_{5a}	-1.00	-1.00	-1.00
p_{5w}	0.78	0.78	0.78
τ_{cem} (days)	0.016	0.080	0.010
$\tau_{s,cem}$ (days)	0.027	0.027	0.032
$p_{\tau a}$	-0.33	-0.33	-0.33
$p_{\tau w}$	-0.06	-2.40	3.55
$p_{\tau c}$	-0.10	-2.70	3.80
ε_{cem}	360×10^{-6}	860×10^{-6}	410×10^{-6}
$p_{\varepsilon a}$	-0.80	-0.80	-0.80
$p_{\varepsilon w}$	1.10	-0.27	1.00
$p_{\varepsilon c}$	0.11	0.11	0.11
s_2	14.2×10^{-3}	29.9×10^{-3}	11.2×10^{-3}
s_3	0.976	0.976	0.976
s_4	4.00×10^{-3}	4.00×10^{-3}	4.00×10^{-3}
s_5	1.54×10^{-3}	41.8×10^{-6}	150×10^{-6}
s_{2f}	-1.58	-1.58	-1.58
s_{3f}	-1.61	-1.61	-1.61

s_{4f}	-1.16	-1.16	-1.16
s_{5f}	-0.45	-0.45	-0.45
$s_{\tau f}$	0.21	1.55	-1.84

The following expressions are used to determine the ultimate shrinkage strain [175]:

$$\varepsilon_{sh\infty}(\tilde{t}_0) = -\varepsilon_0 \cdot k_{\varepsilon a} \frac{E(7\beta_{Th} + 600 \cdot \beta_{Ts})}{E(\tilde{t}_0 + \tau_{sh} \cdot \beta_{Ts})} \quad \text{Eq. (F.1)}$$

$$\tilde{t}_0 = t_0 \cdot \beta_{Th} \quad \text{Eq. (F.2)}$$

$$\beta_{Th} = e^{\left(\frac{U_h}{R} \left(\frac{1}{293} - \frac{1}{T_{cur} + 273} \right) \right)} \quad \text{Eq. (F.3)}$$

$$\beta_{Ts} = e^{\left(\frac{U_s}{R} \left(\frac{1}{293} - \frac{1}{T + 273} \right) \right)} \quad \text{Eq. (F.4)}$$

$$\varepsilon_0 = \varepsilon_{cem} \left(\frac{a/c}{6} \right)^{p_{\varepsilon a}} \cdot \left(\frac{w/c}{0.38} \right)^{p_{\varepsilon w}} \cdot \left(\frac{6.5 \cdot c}{\rho} \right)^{p_{\varepsilon c}} \quad \text{Eq. (F.5)}$$

where $T_{cur} \in [20^\circ C, 30^\circ C]$ is the temperature at curing; $E(t)$ is the Young's modulus evaluated at t days; U_h is the activation energy of hydration; U_s is the activation energy of moisture diffusion; T is the average environmental temperature before load application; ε_{cem} can be obtained from Table 51; and $\rho = 2.350 \text{ kg/m}^3$. The coefficient $k_{\varepsilon a}$ is dependent of the type of aggregate and can be estimated from Table 52.

Table 52 – B4 model shrinkage parameter dependent on aggregate type [175].

Type of aggregates	Diabase	Quartzite	Limestone	Sandstone	Granite	Quartz Diorite
$k_{\varepsilon a}$	0.76*	0.71	0.95	1.60	1.05	2.20*
$k_{\tau a}$	0.06*	0.59	1.80	2.30	4.00	15.0*

* - denotes uncertain fitted parameters

APPENDIX G

In this section is presented the formulation of the Menegotto-Pinto model. This model describes a curve (connecting two tangents with a variable radius of curvature at the intersection point of these tangents). In Eq. (G.1) is presented the Menegotto-Pinto equation to describe a curve that connects the initial (s_o, τ_o) and final (s_f, τ_f) points, while in Eq. (G.2) is presented the equation that expresses the tangent stiffness of the Menegotto-Pinto curve at any point.

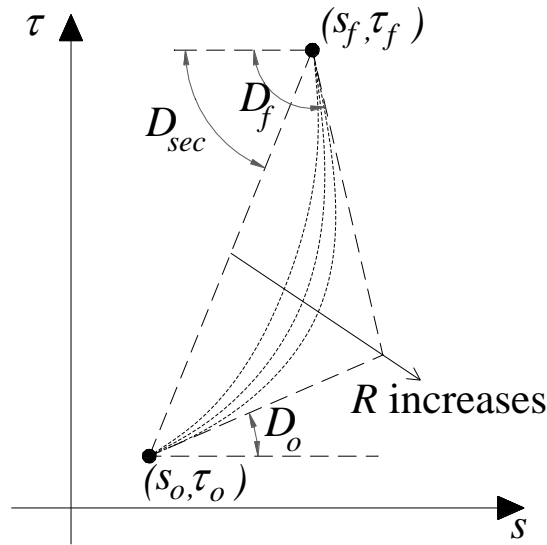


Figure 169 – Menegotto-Pinto curve.

$$\tau = \tau_o + D_o \cdot (s - s_o) \cdot \left[Q + \frac{1 - Q}{\left[1 + \left| D_o \cdot \frac{s - s_o}{\tau_{ch} - \tau_o} \right|^R \right]^{1/R}} \right] \quad \text{Eq. (G.1)}$$

$$D_t = \frac{\partial \tau}{\partial s} = D_{sec} - \frac{D_{sec} - Q \cdot D_o}{1 + \left| D_o \cdot \frac{s - s_o}{\tau_{ch} - \tau_o} \right|^R} \quad \text{Eq. (G.2)}$$

In Eq. (G.1) and Eq. (G.2), τ_{ch} , Q and R are parameters that control the shape of the curve, and are calculated as shown in Figure 170.

When the Newton-Raphson iterative algorithm fails to resolve the nonlinear equation, the Menegotto-Pinto model is replaced by a linear model that connects the initial and target points with a slope equal to D_{sec} .

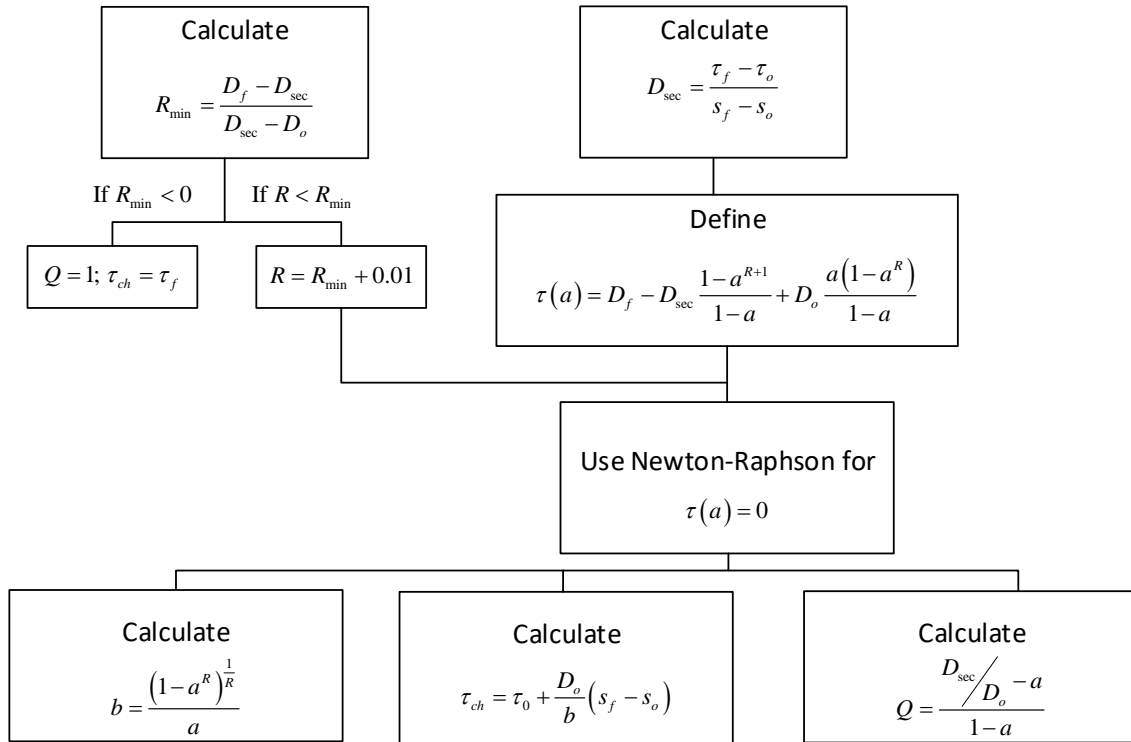


Figure 170 – Algorithm to determine the parameters that control the shape of the Menegotto-Pinto curve.